Universidade de Brasília
Instituto de Geociências
Programa de Pós-graduação em Geologia

Evolução sedimentar Cenozoica do sistema fonte-sedimentação Andes-Amazônia-Margem Equatorial Sul-Americana

The Cenozoic sedimentary evolution of the Andes-Amazon-South America Equatorial Margin Source to Sink system

Evolution sédimentaire cénozoïque du système Andes-Amazonie-marge équatoriale

MICHELE ANDRIOLLI CUSTÓDIO

n° 207

Orientador: Prof. Dr. Roberto Ventura Santos

Co-orientador: Prof. Dr. Martin Roddaz

Brasília, 09/01/2024

Universidade de Brasília
Instituto de Geociências
Programa de Pós-graduação em Geologia

Evolução sedimentar Cenozoica do sistema fonte-sedimentação Andes-Amazônia-Margem Equatorial Sul-Americana

The Cenozoic sedimentary evolution of the Andes-Amazon-South America Equatorial Margin Source to Sink system

Evolution sédimentaire cénozoïque du système Andes-Amazonie-marge équatoriale

MICHELE ANDRIOLLI CUSTÓDIO

Tese apresentada ao Programa de Pós-Graduação em Geologia – Instituto de Geociências – IG da Universidade de Brasília – UnB como requisito parcial obrigatório para a obtenção do título de Doutora em Geologia.

Área de concentração: Geologia Regional

Orientador: Prof. Dr. Roberto Ventura Santos

Co-orientador: Prof. Dr. Martin Roddaz

Université Fédérale
Toulouse Midi-Pyrénées

THÈSE

En vue de l'obtention du

DOCTORAT DE L'UNIVERSITÉ DE TOULOUSE

Délivré par :

Université Toulouse 3 Paul Sabatier (UT3 Paul Sabatier)

Cotutelle internationale: Université de Brasilia

Présentée et soutenue par :
Michele ANDRIOLLI CUSTÓDIO
le mardi 19 décembre 2023

Titre :

Evolution du système Andes-Amazonie-Océan Atlantique au cours du Cénozoïque

---

École doctorale et discipline ou spécialité :
ED SDU2E : Sciences de la Terre et des Planètes Solides

Unité de recherche :
GET - Géosciences Environnement Toulouse

Directeur/trice(s) de Thèse :

Martin RODDAZ et Roberto VENTURA SANTOS

Jury :
Mme Cécile GAUTHERON, Rapporteure
Mme Dilce ROSSETTI, Rapporteure
M. Christian GORINI, Président du jury
M. Jérôme VIERS, Examinateur
M. Abdel SIFFEDINE, Invité
M. Martin RODDAZ, Directeur de thèse
M. Roberto VENTURA SANTOS, Co-directeur de thèse

Ficha catalográfica elaborada automaticamente,
com os dados fornecidos pelo(a) autor(a)

Ae Andriolli Custódio, Michele
Evolução sedimentar Cenozoica do sistema fonte-sedimentação Andes-Amazônia-Margem Equatorial Sul-Americana / Michele Andriolli Custódio; orientador Roberto Ventura Santos; co-orientador Martin Roddaz. -- Brasília, 2023.
292 p.

Tese(Doutorado em Geologia) -- Universidade de Brasília, 2023.

1. Paleogeno. 2. norte da plataforma da América do Sul. 3. Bacia da Foz do Amazonas. 4. paleogeografia. 5. proveniência sedimentar. I. Ventura Santos, Roberto , orient. II. Roddaz, Martin, co-orient. III. Título.

AGRADECIMENTOS

“O presente trabalho foi realizado com apoio da Coordenação de Aperfeiçoamento de Pessoal de Nível Superior-Brasil (CAPES) – Código de Financiamento 001”

This study was financed in part by the Coordenação de Aperfeiçoamento de Pessoal de Nível Superior - Brasil (CAPES) - Finance Code 001”

This Phd has also been supported by the CAPES-COFECUB program Te 924/18 “Paléo-Amazone: evolution Néogène de l'Amazonie Brésilienne” which give me the opportunity to stay 18 months at the *Geosciences Environnement Toulouse* (Toulouse - France).

Externo meus agradecimentos aos meus orientadores Prof. Dr. Martin Roddaz e Prof. Dr. Roberto Ventura Santos, por todo o suporte na realização de trabalhos de campo, pelas orientações científicas na condução de toda a presente pesquisa, por meio de discussões, interpretações, escrita e re-escrita dos artigos científicos e da tese de doutorado e, principalmente por toda paciência, respeito, compreensão e companheirismo ao me orientar da melhor forma possível ao longo destes quatro anos.

A Universidade Federal do Amazonas (UFAM) pelo suporte institucional e financeiro para a plena realização da presente pesquisa de doutorado.

Ao corpo docente e técnico do Departamento de Geociências (DEGEO/UFAM) por autorizarem a liberação integral da pesquisadora pelo período de 4 anos para efetiva realização do presente doutorado.

Ao Programa de Pós-Graduação em Geologia (PPGG) do Instituto de Geociências (IG) da Universidade de Brasilia (UnB), pelo apoio acadêmico, indispensável à realização desta tese de doutorado.

Aos funcionários(as) e amigos(as) do Laboratório de Estudos Geodinâmicos, Geocronológicos e Ambientais (LEGGA) por possibilitarem o uso das instalações, equipamentos e realização das análises necessários ao desenvolvimento do presente projeto de doutorado, bem como, pelos bons momentos de descontração e amizade (Alanielson, Paulinha, Mariana, Jeane, Leticia, Felipo, Gilvan, Vanessa, André, André Alvim - Foguinho, Leandro, Alisson e Jô).

A *Université Toulouse III Paul Sabatier* e ao Laboratório *Geosciences Environnement Toulouse* pelo apoio institucional e científico ao longo do período estadia no país estrangeiro (Cotutela), bem como, a todos os funcionários e colegas de trabalho

que pelo suporte acadêmico que contribuiram direta ou indiretamente para o presente doutorado.

A Agência Nacional do Petróleo (ANP) e Petrobras por terem disponibilizado os dados técnicos e amostras de calhas pertencentes a Bacia da Foz do Amazonas.

Agradeço a colaboração científica nos trabalhos de campo e colaboração nos artigos científicos, dos pesquisadores(as) doutores(as) Prof. Dr. Elton Luiz Dantas, Prof. Dr. Pierre-Olivier Antoine, Laurent Marivaux, Narla Stutz, François Pujos, Aldo Benites-Palomino, Christian Hurtado, Mélanie Louterbach, Guilherme Oliveira Gonçalves e Carlos Jaramillo.

Agradeço aos amigos Talia Rodrigues, Wagner de Oliveira, Dayane Evellin, Marine Knoll, Gabriel Moizinho, Calimeria do Carmo, Pierre Bentaberry, Alexandre Rosa, Antoine, Mariana Rodrigues, Carolina Maia, Artur, Paulinha e André Alvim que compartilharam comigo momentos, bons e ruins, ao longo do desenvolvimento da presente tese de doutorado. Em especial a minha amiga Daniela Cristina (*in memoriam*). Danoca, como você dizia "o céu é o limite", agora você brilha e encanta ai de cima.

Finalmente, e a parte mais importante da minha vida e trajetória, agradeço imensamente a minha FAMÍLIA, que é e sempre foi a minha base para trilhar o caminho da vida, seja na parte pessoal e profissional. Meus avós, Marcinda e Orlando, obrigada por serem meu exemplo de pessoas honestas e trabalhadoras e, que apesar de não entenderem muito deste universo da Geologia, sempre me apoiaram nas minhas decisões, ainda que parecesse bem incomum para vocês, rsrs. Pai (*in memoriam*), Mãe, meu irmão Matheus, minha cunhada Isabella e a pitica (Manuella), de nada teria valido a pena e eu não teria nem ao menos iniciado e conseguido, sem presença e apoio de cada um de vocês, obrigada por tudo e por tanto. Pai, o que eu mais queria na vida é que você pudesse estar por aqui, junto comigo! Sou quase "dotôra" pai, queria poder comemorar mais essa junto com você com uma boa cervejinha gelada acompanhada de um salaminho como a gente sempre fez rsrs, mas tenho certeza que você vai me acompanhar e continuar me protegendo ai de cima. Te levo junto comigo pra sempre! Amo muito vocês !

RÉSUMÉ

Le système « source to sink » (S2S) Andes-Amazone-Marge équatoriale sud-américaine (AAMESA) qui s'étend sur environ 3 200 km et est situé au nord de la plate-forme sud-américaine, un des plus grands systèmes S2S au monde. Actuellement, le système AAMESA est contrôlé par les Andes d'un point de vue sédimentaire, car 95 % du flux annuel moyen de sédiments en suspension fournis par l'Amazone à l'océan Atlantique provient d'affluents andins. Malgré de récents progrès détaillant les influences des processus de construction et d'érosion des Andes sur l'origine et l'évolution et l'enregistrement sédimentaire du système S2S AAMESA à la fin du Crétacé-début du Paléocène en Amazonie occidentale et l'établissement du fleuve Amazone transcontinental à la fin du Miocène (Néogène) en Amazonie orientale, l'histoire géologique et en particulier configurations pré néogène et pliocène du système AAMESA restent à préciser. L'objectif principal de cette thèse est de proposer une une reconstruction paléogéographique du système Andes-Amazonie-Marge équatoriale au cours du Cénozoïque à partir de nouvelles données stratigraphiques, sédimentologiques et de provenance obtenues sur un des bassins constituant le système de bassin d'avant-pays rétroarc amazonien (Bassin de Huallaga, nord Pérou) et sur le bassin principal de la marge équatoriale amazonienne (Foz de Amazonas). Nous montrons que du Paléocène à l'Éocène inférieur (Danien - Yprésien) (66 – 43.5 Ma), un hiatus de dépôt s'est développé dans les bassins d'avant retroarc amazonien lié à un épisode de quiescence tectonique dans les Andes. Cette quiescence tectonique est contemporaine de la formation des surfaces latéritiques "sul-americano" en Amazonie centrale et aux faibles taux de sédimentation dans le bassin de Foz do Amazonas La reprise du soulèvement et de l'érosion des Andes péruviennes à l'Éocène moyen ou tardif (Lutétien - Bartonien) (43.5 – 37.6 Ma) a été enregistrée dans la sédimentation du bassin d'avant-pays retroarc amazonien par la présence de detritus provenant des arcs magmatiques de la Cordillère Occidentale et par une transgression au Bartonien marquée par la présence de dépôts tidaux sur des dépôts continentaux lacustres. Le début du soulèvement de la Cordillère Orientale est enregistré dans les sédiments du bassin d'avant-pays retroarc amazonien (bassin de Huallaga) il y a 30 Ma, au Rupélien. Du Rupélien au Miocène moyen, la Cordillère Orientale continue à se soulever, créant un relief topographique capable de jouer le rôle de barrière orographique aux flux atmosphérique en provenance de l'Océan Atlantique. Ce soulevèment continue peut avoir provoquer la présence de climats plus humides en Amazonie occidentale ce qui pourrait avoir favoriser la la formation de

surfaces latéritiques en Amazonie centrale entre l'Oligocène et le Miocène inférieur, en relation avec la phase intense d'altération ayant eu lieue entre 30 et 18 Ma. Nos données de provenance enregistrent une nouvelle période d'exhumation de la Cordillère Orientale du Miocène supérieur à l'actuel. Cette période se marque dans l'enregistrement sédimentaire du bassin d'avant-pays retroarc amazonien par des detritus provenant exclusivement de la Cordillère Orientale.Cette période de réjuvenation du relief de la Cordillère orientale est liée à une période de propagation du prisme orogénique amazonien en direction du craton. Elle induit une réorganisation du réseau de drainage amazonien et constitue probablement un des moteurs de la transcontinentalisation de l'Amazone au miocène moyen-supérieur. Finalement, le système AAMESA n'existe en termes de "source-to-sink" (S2S) qu'à partir du Miocène supérieur, avec l'établissement transcontinental du fleuve Amazone. La période précédente est marquée par la domination de deux systèmes différents, représentés par le craton amazonien oriental et la région NE de l'Amérique du Sud (province de Borborema, craton de São Luis, ceinture de Gurupi).

Mots-clés : Paléogène ; plateau sud-américain ; bassin de la Foz do Amazonas ; paléogéographie ; provenance sédimentaire.

RESUMO

O sistema fonte-sedimentação (S2S) Andes-Amazônia-Margem Equatorial Sul-Americana (AAMESA), que se estende por cerca de 3.200 km e está localizado ao norte da plataforma Sul-Americana, é um dos maiores sistemas S2S do mundo. Atualmente, o sistema AAMESA é controlado pelos Andes do ponto de vista sedimentar, pois 95% do fluxo médio anual de sedimentos suspensos fornecidos pela Amazônia ao Oceano Atlântico provêm de afluentes andinos. Apesar dos avanços científicos que detalham as influências dos processos de construção e erosão dos Andes na sua origem, evolução e registro sedimentar do sistema S2S AAMESA desde o final do Cretáceo ao início do Paleoceno na Amazônia Ocidental e o estabelecimento do rio Amazonas transcontinental no final do Mioceno (Neógeno) na Amazônia Oriental, a história geológica e, em particular, as configurações pré-Neogeno e Plioceno do sistema AAMESA ainda não foram esclarecidas. O principal objetivo desta tese é propor uma reconstrução paleogeográfica do sistema AAMESA durante o Cenozoico, com base em novos dados

estratigráficos, sedimentológicos e de proveniência sedimentar obtidos de uma das bacias que constituem o sistema de bacias do *foreland* do retroarco Amazônico (Bacia Huallaga, norte do Peru) e da principal bacia da margem equatorial amazônica (Bacia da Foz do Amazonas). Mostramos que, do Paleoceno ao Eoceno Inferior (Daniano - Ypresiano) (66 – 43.5 Ma), desenvolveu-se um hiato deposicional nas bacias do retroarco Amazônico ligado a um episódio de quiescência tectônica nos Andes. Essa quiescência tectônica é contemporânea à formação das superfícies lateríticas "Sul-Americanas" na Amazônia Central, e às baixas taxas de sedimentação na Bacia da Foz do Amazonas. A retomada da elevação e erosão dos Andes peruanos no Eoceno médio a tardio (Luteciano - Bartoniano) (43.5 – 37.6 Ma) foi registrada na bacia de *foreland* do retroarco Amazônico pela presença de detritos dos arcos magmáticos da Cordilheira Ocidental e pela transgressão Bartoniana, esta marcada por depósitos de maré intercalados a depósitos lacustres continentais. O início da elevação da Cordilheira Oriental na Bacia Huallaga ocorreu no Rupeliano (30 Ma). Do Rupeliano ao Mioceno Médio, a Cordilheira Oriental continuou a se elevar, criando relevo topográfico capaz de atuar como barreira orográfica aos fluxos atmosféricos do Oceano Atlântico. Essa elevação contínua pode ter resultado em climas mais úmidos no oeste da Amazônia, o que poderia ter favorecido a formação de superfícies lateríticas na Amazônia Central entre o Oligoceno e o Mioceno Inferior, em relação à intensa fase de alteração que ocorreu entre 30 e 18 Ma. Nossos dados de proveniência registram um novo período de exumação da Cordilheira Oriental desde o Mioceno Superior até os dias atuais. Esse período de rejuvenescimento do relevo da Cordilheira Oriental está ligado à propagação do prisma orogênico amazônico em direção ao cráton. Esse evento levou a uma reorganização da rede de drenagem Amazônica e é provavelmente uma das forças motrizes por trás da transcontinentalização da Amazônia no Mioceno Médio-Superior. Por fim, o sistema AAMESA não existia como um S2S até o Mioceno tardio, quando houve o estabelecimento transcontinental do rio Amazonas. O período anterior foi marcado pelo domínio de dois sistemas diferentes, representados pelo cráton Amazônico Oriental e pela região nordeste da América do Sul (província Borborema, cráton São Luís, cinturão Gurupi).

Palavras-chave: Paleogeno; norte da plataforma da América do Sul; Bacia da Foz do Amazonas; paleogeografia, proveniência sedimentar

ABSTRACT

The Andes-Amazon-South American Equatorial Margin (AAMESA) source-sedimentation system (S2S), which extends for around 3,200 km and is located north of the South American platform, is one of the largest S2S systems in the world. Currently, the AAMESA system is controlled by the Andes from a sedimentary point of view, as 95% of the average annual flow of suspended sediment supplied by the Amazon to the Atlantic Ocean comes from Andean tributaries. Despite scientific advances detailing the influences of Andean construction and erosion processes on the origin, evolution and sedimentary record of the S2S AAMESA system from the end of the Cretaceous to the beginning of the Paleocene in Western Amazonia and the establishment of the transcontinental Amazon River at the end of the Miocene (Neogene) in Eastern Amazonia, the geological history and, in particular, the pre-Neogene and Pliocene configurations of the AAMESA system have yet to be clarified. The main objective of this thesis is to propose a paleogeographic reconstruction of the Andes-Amazon-Equatorial Margin system during the Cenozoic, based on new stratigraphic, sedimentological and sedimentary provenance data obtained from one of the basins that make up the foreland basin system of the Amazonian backarc (Huallaga Basin, northern Peru) and the main basin of the Amazonian equatorial margin (Foz do Amazonas Basin). We show that, from the Paleocene to the Lower Eocene (Danian - Ypresian) (66 - 43.5 Ma), a depositional hiatus developed in the basins of the Amazonian backarc linked to an episode of tectonic quiescence in the Andes. This tectonic quiescence is contemporaneous with the formation of the "South American" laterite surfaces in Central Amazonia and the low sedimentation rates in the Foz do Amazonas Basin. The resumption of uplift and erosion of the Peruvian Andes in the middle to late Eocene (Lutetian - Bartonian) (43.5 - 37.6 Ma) was recorded in the sedimentation of the foreland basin of the Amazonian backarc by the presence of debris from the magmatic arcs of the Cordillera Occidental and by a Bartonian transgression marked by the presence of tidal deposits in continental lacustrine deposits. The beginning of the rise of the Eastern Cordillera is recorded in the sediments of the foreland basin of the Amazonian backarc (Huallaga Basin) 30 Ma ago, in the Rupelian. From the Rupelian to the Middle Miocene, the Eastern Cordillera continued to rise, creating a topographic relief capable of acting as an orographic barrier

to atmospheric flows from the Atlantic Ocean. This continuous elevation may have led to the presence of wetter climates in western Amazonia, which could have favored the formation of laterite surfaces in central Amazonia between the Oligocene and the Lower Miocene, in relation to the intense phase of alteration that occurred between 30 and 18 Ma. Our provenance data record a new period of exhumation of the Cordillera Oriental from the Upper Miocene to the present day. This period of rejuvenation of the relief of the Eastern Cordillera is linked to a period of propagation of the Amazonian orogenic prism towards the craton. This led to a reorganization of the Amazon drainage network and is probably one of the driving forces behind the transcontinentalization of Amazonia in the Middle-Upper Miocene. Finally, the AAMESA system did not exist in "source-to-sink" (S2S) terms until the late Miocene, with the transcontinental establishment of the Amazon River. The preceding period was marked by the dominance of two different systems, represented by the Eastern Amazon craton and the NE region of South America (Borborema province, São Luís craton, Gurupi belt).

Keywords: Paleogene; northern South American plate; Foz do Amazonas Basin; paleogeography; sediment provenance

SUMÁRIO

1. INTRODUÇÃO / INTRODUCTION 12

PRÉSENTATION 12
1.1 CONTEXTUALIZAÇÃO DO TEMA 16
1.1.1 Sistema Fonte – Sedimentação (source-to-sink) *17*
1.2 INTRODUÇÃO E RELEVÂNCIA DO ESTUDO 19
1.3 CONTEXTO GEOLÓGICO 22
1.3.1 Eventos orogênicos e evolução das Bacias Amazônicas Ocidentais *22*
1.3.2 Evolução da Margem Equatorial Sul-Americana: Bacia da Foz do Amazonas *27*
1.4 OBJETIVOS 31
REFERÊNCIAS 31

2. MATERIAIS E MÉTODOS / MATÉRIEL ET MÉTHODES 43

RÉSUMÉ 43
2.1 AQUISIÇÃO DE DADOS 44
2.1.1 Definição da área de estudo e trabalhos de campo *44*
2.1.2 Dados técnicos e amostras de poços *45*
2.2 INTERPRETAÇÃO PALEOAMBIENTAL 48
2.2.1 Análise sedimentológica *48*
2.2.2 Análise de isótopos estáveis *48*
2.2.3 Análise paleontológica *50*
2.3 PROVENIÊNCIA SEDIMENTAR 51
2.3.1 Geoquímica elementar *51*
2.3.2 Análise isotópica de Sm-Nd *53*
2.3.3 Análise isotópica de U-Pb *55*
REFERÊNCIAS 57

3. RECONSTRUÇÕES PALEOAMBIENTAL E PALEOGEOGRÁFICA DO PALEÓGENO DA AMAZÔNIA OCIDENTAL 64

RÉSUMÉ 64
RESUMO 65
3.1 ABSTRACT 67
3.2 INTRODUCTION 68
3.3 GEOLOGICAL BACKGROUND 71
3.3.1 Tectonic setting and stratigraphy of the Huallaga Basin *71*
3.3.2 Stratigraphy of other Western Amazonian basins *73*
3.4 MATERIALS AND METHODS 75
3.4.1 Sedimentology *75*
3.4.2 Stable isotopes *76*
3.4.3 Palynological analysis *77*
3.4.4 U-Pb ages *77*
3.5 RESULTS 79
3.5.1 Sedimentary facies *79*
3.5.1.1 Facies association 1 (FA1) *83*
3.5.1.2 Facies association 2 (FA2) *85*
3.5.1.3 Facies association 3 (FA3) *88*
3.5.1.4 Facies association 4 (FA4) *88*
3.5.2 Depositional environments *89*
3.5.2.1 Tide-dominated environment: The fluvial-tidal transition zone *89*
3.5.2.2 Lacustrine environment *90*
3.5.3 Oxygen and carbon stable isotopes *91*

3.5.4 Biostratigraphic constraints: Paleontological content of the Juanjuí Maastrichtian–Eocene section *94*
3.5.5 U-Pb ages *96*
3.6 DISCUSSION 97
3.6.1 Age of the deposits *97*
3.6.2 Paleogeographic implications *98*
3.7 CONCLUSIONS 102
3.8 ACKNOWLEDGEMENTS 103
REFERENCES 103

4. HISTORIA EROSIVA DA REGIAO NORTE DOS ANDES AMAZÖNICOS PERUANOS (MAASTRICHTIANO – CENOZOICO): IMPLICAÇOES PARA EVOLUÇAO DA CORDILHEIRA ORIENTAL 113

RÉSUMÉ 113
RESUMO 114
4.1 ABSTRACT 116
4.2 INTRODUCTION 117
4.3 GEOLOGICAL SETTING 120
4.3.1 Tectonic setting of the Huallaga Basin *121*
4.3.2 Stratigraphic framework *122*
4.4. MATERIALS AND METHODS 124
4.4.1 Sedimentology *124*
4.4.2 Major and trace elements analyses *125*
4.4.3 Sm-Nd isotopes compositions *126*
4.4.4 Zircon U-Pb dating *126*
4.4.5 Sedimentation rates *128*
4.5 RESULTS 130
4.5.1 Depositional systems from sedimentary analysis *130*
4.5.1.1 Facies association 5: Channels deposits *130*
4.5.1.2 Facies association 6: Floodplain deposits *132*
4.5.1.3 Facies association 7: Crevasse splay deposits *133*
4.5.2 Major and trace element concentrations and Sm-Nd isotopes *134*
4.5.3 U-Pb ages *138*
4.5.4 Sedimentation Rates based on MLA ages *140*
4.6 DISCUSSION 142
4.6.1 Interpretation of sedimentary provenance *142*
4.6.2 Erosional history of the Amazonian Andes during the late Cretaceous – Cenozoic *145*
4.6.2.1 Maastrichtian Andean mountain building *145*
4.6.2.2 Paleocene-to-late Eocene: tectonic quiescence and erosion of the Western Cordillera *146*
4.6.2.3 Early Oligocene (Rupelian)-Middle Miocene: uplift and erosion of the Eastern Cordillera . *149*
4.6.2.4 Late Miocene to present-day accelerated exhumation of the EC, drainage reorganization and the onset of the transcontinental Amazon River *151*
4.6.3 Comparison with the sedimentary record of the Amazon Fan *151*
4.7 CONCLUSIONS 153
ACKNOWLEDGMENT 154
REFERENCES 154

5. PROVENIÊNCIA SEDIMENTAR DA BACIA DA FOZ DO AMAZONAS: IMPLICAÇÕES PARA O SISTEMA FONTE – DEPOSIÇÃO NO NOROESTE DA MARGEM EQUATORIAL BRASILEIRA 165

RÉSUMÉ 165
RESUMO 166
5.1 ABSTRACT 167
5.2 INTRODUCTION 168

5.3 GEOLOGICAL SETTING....170
5.3.1 Cenozoic sequence of the Foz do Amazonas Basin....172
5.3.2 Potential sources....174
5.4 MATERIALS AND METHODS....176
5.4.1 Data acquisition....176
5.4.2 Whole-rock Sm-Nd isotopes....177
5.4.3 Detrital zircon geochronology....178
5.5 RESULTS....179
5.5.1 Sm-Nd isotopes....181
5.5.2 U-Pb isotopes....181
5.5.2.1 Paleogene....182
5.5.2.2 Neogene (Middle – late Miocene to early Pliocene)....182
5.5.2.3 Quaternary (Pleistone to Recent)....182
5.6 DISCUSSION....183
5.6.1 Interpretation of source areas....184
5.7 CONCLUSIONS....190
REFERENCES....191

6. SÍNTESE E DISCUSSÃO....200

RÉSUMÉ....200
6.1 EVOLUÇÃO ESPAÇO-TEMPORAL DO SISTEMA ANDES-AMAZÖNIA-MARGEM EQUATORIAL SUL-AMERICANA....202
6.1.1 Paleoceno ao Eoceno inferior (Daniano – Ypresiano) (66 – 47.8 Ma)....202
6.1.2 Eoceno médio a superior (Lutetiano – Bartoniano) (43.5 – 37.6 Ma)....204
6.1.3 Oligoceno inferior (Rupeliano) a Mioceno médio (~30 – 12 Ma)....206
6.1.4 Mioceno superior ao Recente (~12 Ma – Recente)....210

REFERÊNCIAS....212

7. CONCLUSÃO E PERSPECTIVAS....218

RÉSUMÉ....218
7.1 CONCLUSÃO....219
7.2 PERSPECTIVAS....221

ANEXOS CAPITULO 3....223

ANEXOS CAPITULO 4....234

ANEXOS CAPITULO 5....280

LISTA DE FIGURAS E TABELAS

CAPÍTULO 1

Figura 1. 1 Representação esquemática do Sistema Fonte-Sedimentação e os três principais segmentos, as zonas de erosão (erosional engine), transferência (trajectory) e deposição (sinks) (Caracciolo, 2020) 18
Figura 1. 2 Mapa de localização do sistema fonte-deposição no eixo Andes – Amazônia – Margem Equatorial Sul-Americana (AAMESA). A) Mapa regional do relevo e principais unidades geotectônicas da região norte da Plataforma Sul-Americana, exibindo à oeste o cinturão orogênico Andino; na zona central-norte o Cráton Amazônico; os Arcos de Iquitos, Purus e Gurupá e a nordeste, a Margem Equatorial Sul-

Americana com destaque do limite da Bacia da Foz do Amazonas. Em destaque, a Amazônia Ocidental e Oriental estão representadas por contornos tracejados. Em detalhe, os números (1) – Artigo 1°; (2) – Artigo 2° e (3) – Artigo 3°. B) Seção geológica esquemática da região norte da Plataforma Sul-Americana, exibindo (perfil W-E) a cadeia de montanhas Andinas; a zona-subandina, da Amazônia Ocidental, com as bacias de retroarco de antepaís (Bacia de Huallaga-Marañón-Acre); as bacias intracratônicas (Bacia do Solimões e Amazonas) e a margem passiva (Bacia da Foz do Amazonas). Crédito da imagem de relevo NASA/JPL/NIMA (https://photojournal.jpl.nasa.gov/catalog/PIA03388). Figuras modificadas de Albert et al., 2018; Hoorn et al., 2017; Bajolet et al., 2022. 20

Figura 1. 3 Contexto espaço-temporal dos principais eventos geológicos ocorridos na Plataforma Sul-Americana durante o Mesozoico-Cenozoico. A) Mapa tectônico da América do Sul, contendo os limites das placas tectônicas de Nazca e Sul-Americana, bem como, o Arco Magmático Andino (incluindo as zonas vulcânicas a norte, central e sul) (modificado de Horton, 2018). B) Principais eventos tectônicos globais e amazônicos ocorridos ao longo do Meso-Cenozoico, na escala do tempo geológico, que impactaram na evolução e configuração geológica das regiões da Amazônia Ocidental e Oriental. ...24

Figura 1. 4 Principais unidades morfoestruturais presente ao Norte dos Andes Centrais. A) Mapa morfotectônico do Cinturão Orogênico Andino segmentado, de oeste à leste, pelo Arco Magmático Andino (Cordilheira Ocidental) (<0.145 Ga); Cinturão Paleozoico plutônico e metamórfico (0.5 – 0.26 Ga) e pela Zona Subandina (sistema de bacias de antepaís). B) Seção transversal esquemática da região Norte dos Andes Centrais exibindo a configuração tectônica da margem oeste da América do Sul, zona dos Andes Amazônicos, incluindo a geometria da placa de subducção de Nazca sob a placa Sul-Americana, a espessura crustal (~25-50 km), região do retroarco, geometrias estruturais da frente de empurrão orogênico, configuração do sistema de bacias amazônicas de antepaís (Modificado de Horton, 2018; Armijo et al., 2015).....25

Figura 1. 5 Configuração estrutural do sistema de bacias amazônicas de antepaís (Amazonian Retroarc Foreland Basin). A) Seção esquemática transversal da geometria do sistema de bacias de antepaís, com as zonas de deposição wedge-top, foredeep, forebulge e backbulge, exibindo as principais áreas de erosão e de bypass. B) Seção esquemática transversal do sistema de bacias amazônicas de antepaís representando as bacias amazônicas ocidentais correlacionadas com as respectivas zonas de deposição. Em destaque, a Bacia de Huallaga, localizada na zona de deposição wedge-top, também denominada Zona Subandina (SAZ), situada na região mais proximal e deformada, dentro do sistema de bacias amazônicas de antepaís (modificada de Roddaz et al., 2010; DeCelles and Giles, 1996). 27

Figura 1. 6 A) Reconstrução paleogeográfica da fase de rifteamento e ruptura dos continentes Sul-Americano e Africano durante o Cretáceo Superior (~ 84 Ma). B) Reconstrução estrutural da Margem Equatorial Sul-Americana, com destaque para os principais lineamentos e falhas associados. C) Mapa paleogeográfico da fase rifte durante a abertura do Oceano Atlântico Sul e Equatorial, indicando as principais zonas de cisalhamento ao longo da dorsal meso-oceânica no limite entre as placas tectônicas Sul-Americana e Africana. Destaque para as potenciais áreas-fontes de sedimentos para a Amazônia Ocidental e Oriental, localizadas na região norte da Plataforma Sul-Americana, sendo representadas, de oeste à leste, pela Cordilheira Andina, Cratón do Amazonas e Província Borborema. As áreas foco do

estudo estão destacadas por retângulos vermelhos (1 – Bacia de Huallaga) e (2 – Bacia da Foz do Amazonas). Figura baseada e modificada no modelo de Moulin et al. (2010) e Rosa et al. (2023). 28
Figura 1. 7 Mapa geológico regional das unidades Meso-Cenozoicas da costa da Amazônia Oriental, localizadas na Margem Equatorial Sul-Americana, destacando os principais compartimentos estruturais, limites das bacias sedimentares e do Cratón Amazônico. (Modificado de Moizinho et al., 2022; Nogueira et al., 2021; Soares Júnior et al., 2011). 30

CAPÍTULO 2

Figura 2. 1 Fotos representativas da área de estudo, equipe de trabalho e procedimentos de coleta e preparação de amostras realizados na região de Juanjuí, Bacia de Huallaga (Peru)..... 45
Figura 2. 2 Fluxograma dos processos de Solicitação de Acesso aos Dados Técnicos (SDT) e Solicitação de Acesso às Amostras (SAA) junto à Agência Nacional de Petróleo, Gás Natural e Biocombustíveis (ANP) e à Petrobras. 47
Figura 2. 3 Características geoquímicas e isotópicas de distintas fontes definidos por McLennan et al., (1993) 52
Figura 2. 4 Variações das razões Eu/Eu*, Th/Sc, Cr/Th para sedimentos finos e grossos de origem félsica e básica (Cullers, 2000). 53
Figura 2. 5 Realização dos procedimentos métodologicos necessários na lixiviação sequencial para extração da fração carbonática, dos óxidos de Fe – Mn, do carbono orgânico e da fração detrítica dos sedimentos, realizados no IFREMER. A) Adição de água MiliQ (MQ H2O) para condução do preparo das amostras; B) Tubos falcon de 50 ml contendo as frações sólidas das amostras em reação com ácido acético 10% para a separação da fração carbonática; C) Etapa de centrifugar as amostras com rotação de 3000 rpm / 2 minutos. 54
Figura 2. 6 Materiais e procedimentos realizados na concentração e separação dos cristais de zircões detríticos, realizados no laboratório Géosciences Environnement Toulouse (GET). A) Separador Magnético Isodinâmico de Frantz, utilizado na separação dos minerais magnéticos dos não-magnéticos. B) Separação dos zircões com método densimétrico utilizando líquido denso (Diiodomethane, 99+, d = 3.32 g/mL). 56

CAPÍTULO 3

Figure 3. 1 Map of the geographic extent of the major morphotectonic provinces of the northern South Ameria, from west to east, the retroarc foreland basins (Colombia, Ecuador and Peru countries), the intracratonic and passive margin basins (Brazil), partially bounded by structural arches (dashed lines). Northern and Southern Amazon Craton are represented by the Guiana and Brazilian shields, respectively (modified and compiled from Albert et al., 2018; Moreno et al., 2020; Roddaz et al., 2010). The red lines indicate the location of figs 3 A and 3B. 70

Figure 3. 2 Geological map of the studied area modified from the INGEMMET Geological Map of Peru available at http://geocatmin.ingemmet.gob.pe/geocatmin/. A) Regional geologic map of the Huallaga Basin, which is separated to the west from the Eastern Cordillera and limited, to east, from Marañón Basin by the Chazuta thrust and the Cushabatay High. The red rectangle indicate the location of the Juanjuí stratigraphic section. Location of the large dinosaur tracks is represented by TAR33; B) Detailed geological map showing the Mesozoic-Cenozoic geological contacts and the stratigraphic position of the Juanjui studied section. 72

Figure 3. 3 Comparative chronostratigraphic diagram showing the stratigraphic nomenclature, age, lithology, tectonic setting, and stratigraphic discontinuities for (A) the Ecuadorian and Peruvian Subandean Amazonian basins and (B) Peruvian Amazonian foreland basins. The chronostratigraphic diagram (A) was constructed based on Baby et al. (2013); Calvès et al. (2018); Roddaz et al. (2010), Hurtado et al. (2018); Hermoza et al. (2005); Louterbach et al. (2014), and Calderón et al. (2017a, 2017b). The chronostratigraphic diagram (B) is based on Moreno et al. (2020; 2022) and George et al. (2019). 74

Figure 3. 4 Synthetic Juanjuí stratigraphic section through the late Cretaceous (Maastrichtian) to late middle Eocene (Bartonian) at the Huallaga Basin, constructed from field observations, with location of the analyzed samples for C-O isotopic compositions, paleontological content (biostratigraphic constraints) and U-Pb zircon dating. Siliciclastic facies: massive clast-supported conglomerate (Gcm); trough cross-stratified sandstone (St), planar cross-stratified sandstone (Sp), climbing ripple cross-laminated sandstone (Sr), bioturbated sandstone (Smb), heterolithic facies (H), herringbone cross-stratified sandstone (Hb), fines (F) and paleosol (P). Carbonate microfacies: peloidal mudstone (Mp); wackestone with peloids and ostracods (Wpo); wackestone with ostracods and charophytes (Woc); and pisolitic grainstone (Gps). FA= Facies association. See text and Table 1 for details. 81

Table 3. 1 Summary of the descriptions and interpretations of each sedimentary silicilastic facies and carbonate microfacies. 80

Figure 3. 5 Representative photographs of the siliciclastic facies. A) Massive clast-supported conglomerate (Gcm) with an erosive base, limited between fines with no structures (Fm) (below) and sandstones with through cross-stratification (St) (above); B) Massive conglomerates with scattered clasts (Gcm); C) Fine-grained sandstone with through cross-stratification; D) Fine-grained sandstone with climbing ripples; E) Highly bioturbated deposits (Smb) covering the primary structures in fines bodies; F) Thin mudstone layer drape on foresets of cross-bedded (St) fine-grained sandstones with regular variations (neap-spring influence); G) Heterolithic facies (H) with flaser bedding; H) Fine to medium-grained sandstones with bi-directional herringbone cross-stratification (Hb). 84

Figure 3. 6 Fine-grained facies; paleosols and palynological content. (A) Overall m-scale view of massive mudstones and siltstones, with red to purple colors, interbedded with cm-dm tabular carbonate beds. (B) Massive siltstones, presenting purple to green-grey colors, latter probably related to weathering processes. (C) Paleosols with incipient horizontal lamination, mottled horizons. (D) Cricotriporites aff. macroporus, slide 47176_A, England Finder (EF) W13; (E) Araucariacites sp., slide 47176_A, EF N12/2; (F) Ulmoideipites krempii, slide 47176_A, EF S8/4; (G) Echimonocolpites protofranciscoi, slide

47176_A, EF Q12/1; (H) Proxapertites psilatus, slide 47179_B, EF F15; (I) Balmeisporites minutus, slide 47179_B, EF S33/4; (J) Momipites africanus, slide 47179_B, EF M5/2. Scale bar= 10um. 86
Figure 3. 7 Representative photographs of carbonate microfacies. A) General view of the carbonate outcrops; B) Mudstone deposits with scattered peloids (Mp) with clotted texture (HUA63B); C) Dark-brown wackestones with peloids and ostracods (Wpo) (HUA63C), characterized by disarticulated valves of ostracods oriented parallel to bedding of rock; D) Wackestone with scattered bioclasts as fragmented ostracods and charophytes (Woc) (JUA5A); E) Geopetal structure and recrystallized by spar marked in the inner part of charophytes (JUA5B); F) Moldic porosity is identified as secondary pores in charophytes (JUA5C); G) Fragments of pisoids partially replaced by pyrite (?) (JUA 2B). Mi= micrite; Pl= peloids; Ost= ostracod; Chpy= charophyte; Psd= pisoid. 87
Figure 3. 8 Selected vertebrate-related findings and vertebrate fossils of interest from the Maastrichtian–Paleogene Juanjuí section, San Martín, Peru. A) Paddling-turtle track at TAR-29 (=HUA-63; Maastrichtian). The turtle was moving to the right. The same carbonated layer provided the regurgitation ball seen in B; B) Regurgitation ball (of an aquatic bird?), with fish bones and scales both gathered and split all around (TAR-29 = HUA-63; Maastrichtian); C) Pucapristis hoffstetteri, tooth in occlusal view (TAR-41, Maastrichtian); D) Ouledia sp., tooth in occlusal view (TAR-30 sup. = HUA-473; Lutetian); E) Stephanodus sp., pharyngeal tooth in lateral view (TAR-30 sup. = HUA-473; Lutetian); F) Polypterid polypteriform, fragmentary ganoin scale in external view (TAR-42 = JUA 14; Bartonian). Scale bar = 1 mm (C, E) and 0.5 mm (D, F). 93
Figure 3. 9 Carbon versus oxygen isotopes cross plot of Miocene (Alvim et al., 2021) and Eocene fossil and carbonates samples. Black boxes represent stable isotopes values of modern mollusks from North Atlantic seawater, Great Lakes, and North American rivers (Keith et al., 1964), the San Francisco Bay estuary (Ingram et al., 1996) and the Black Sea (Varol, 2015). 94
Table 3. 2 Table showing the number and percentage U-Pb ages of zircons grains by distinct geochronological events in potential source areas on the Amazon craton and the northern central Andes. Temporal ranges of events according to Bahlburg et al. (2009), Chew et al. (2008) and Reimann et al. (2010). (n) is the number of samples analyzed for the time interval. 96
Figure 3. 10 Schematic composite section and 3D sketch representing the paleoenvironmental reconstruction of the (A) Maastrichtian – Paleogene stratigraphic unconformity, (B) Lutetian lacustrine setting, (C) The Bartonian transition from lacustrine system to the tide-dominated setting, represented by the distal part in a fluvial-tidal transition zone. See text for details. 100
Figure 3. 11 Paleogeographic maps of Western Amazonia in Paleocene (A) Eocene (B) times. A) During the Paleocene, the northern part of the Western Amazonian basins are characterized by the presence of a regional unconformity while the southern part experienced shallow marine transgression (Louterbach et al., 2014). B) During the Eocene, the northern part likely experienced shallow marine embayment during short time-intervals through a connection with the Caribbean Sea while the southern part (the Madre de Dios Basin) is characterized by the absence of Eocene deposits (Louterbach, 2014). 101

CAPÍTULO 4

Figure 4. 1 Map of the geographic extent of the major potential source areas of the Western Amazonia, from the west to east, the Western Cordillera (Andean Magmatic Arch), Eastern Cordillera (retroarc fold-thrust belt) and Western Amazon Craton (Guyana and Brazilian shields). The actual Huallaga River is represented by the thicker blue line. 120

Figure 4. 2 Geologic map of the Huallaga foreland basin. Cenozoic sedimentary sections described in this study are localized along the Huallaga river (Juanjui Section). Additional set of data is localized near Tarapoto city, such as Abra Machungo, Juan Guerra and Shapaja areas. See details about cordinates position in Supplementary Data S1. 122

Figure 4. 3 Comparative chronostratigraphic diagram showing the stratigraphic nomenclature, age and stratigraphic discontinuities for the Huallaga and Marañón basins (modified from Roddaz et al., 2010). The circles indicate the stratigraphic position of the samples on the stratigraphic sections and the outcrops: black – Juanjuí section; red – Shapaja ; blue – Abra Machungo and Juan Guerra area. 124

Figure 4. 4 Juanjuí stratigraphic section of the Huallaga Basin. The related chronostratigraphic ages, paleocurrents data, depositional systems, ƐNd values and measures of sedimentation rates obtained are indicated along the section. See text for more details. 128

Table 4. 1 Facies Association and Interpretation for the Cenozoic sequence of Western Amazonia (Huallaga basin, Peru). The FA1, FA2, FA3, FA4 were previously described and interpreted by Custódio et al. (2023). 130

Figure 4. 5 Representative photographs of the Facies Associations of Channel deposits (FA5) and Floodplain deposits (FA6). A) General outcrop view along the road cutting, showing the vertical and lateral stacking pattern of the Facies Associations (FA5; FA6). B) Representative photograph of the FA5, represented by a m-scale amalgamated sigmoidal clinoform, showing internally tangential cross-beds, defined as a lateral-accretion architectural. C) View of the fining-upward beds, ranging from 3 to 0.2m, grading from coarse-grained sandstones trough cross-beds (St), passing to the top to planar (Sp) and climbing ripple (Sr) sandstones. Outcrop HUA 470. 131

Figure 4. 6 A) General outcrop (JUA27) view along the road cutting, showing vertical fining upward beds and lateral variations of the sedimentary facies associated to archictetural channels. B) Sedimentary section with Facies Associations code (see Table 1 for details). 132

Table 4. 2 Major and trace element concentrations of sedimentary rocks analyzed in Huallaga Basin, Peru. 135

Table 4. 3 Sm-Nd isotopic compositions of sedimentary rocks analyzed in this study. 136

Figure 4. 7 Geochemical data. A) Major and selected trace element contents of analyzed samples normalized to PAAS (Taylor and McLennan, 1985; McLennan, 2001; Pourmand et al., 2012). From left to right on the diagram, these include the major elements (SiO2, TiO2, Al2O3, Fe2O3, MnO, MgO, CaO, Na2O, K2O and P2O5), LILE (Rb, Cs, Ba, Sr, Th and U), HFSE (Y, Zr, Nb, Hf), and TTE (Sc, Cr, Co, V and Ni). B) Rare Earth Element (REE) contents of studied samples normalized to PAAS (Taylor and McLennan, 1985; McLennan, 2001; Pourmand et al., 2012). 137

Table 4. 4 Calculated ages of the samples using the 'Maximum Likelihood Age' (MLAs) method, following Vermeesch (2021). 139
Table 4. 5 Calculated sedimentation rates for the Cenozoic sequence of Huallaga Basin, northern Peruvian retroforeland basin. Maximum sedimentation rates calculated from GENEX 1D basin modelling software. Maximum sedimentation rates are based on stratigraphic thickness, time as well as compaction.....140
Table 4. 6 Table showing the number and porcentage U-Pb ages of zircons grains by distinct geochronological events in potential source areas on the Amazon craton and the northern central Andes. Temporal ranges of events according to Bahlburg et al. (2009), Chew et al. (2008).....141
Figure 4. 8 Distribution of zircon U-Pb age proportions (bars) for the whole Cenozoic deposits of Huallaga Basin, Western Amazonia.....143
Figure 4. 9 Non-matrix metric multi-dimensional scaling (MDS) plot (Vermeesch, 2013) of detrital zircon ages from Cretaceous to Recent deposits in the studied area. The four groups indicate samples with similar detrital zircon age populations (see discussion in the text). The solid line connecting samples indicate the closest neighbors. 145
Figure 4. 10 Detrital-zircon age spectra of the late Cretaceous – Cenozoic samples from the Huallaga Basin. 147
Figure 4. 11 Cross section of Huallaga Basin based on Calves et al., 2018 ; Eude et al., 2015 ; Hermoza et al., 2005. The cross-sections exhibits the Cretaceous – Cenozoic stages of tectonic loadings related to the eastward propagation of the orogenic wedge ; unconformity event ; basin morphology ; paleoenvironmental and paleogeographic changes due to the shifts in provenance areas. 149

CAPITULO 5

Figure 5. 1 Simplified geologic map of the northern South American plate showing main geotectonic units. From source-to-sink is exhibited the Andes mountain chain, intracratonis basins, Amazon Craton, Borborema Province (NE Brazil) and the Brazilian Equatorial Margin. The red box, in detail, indicates the geographic location of the Foz do Amazonas Basin (study area). 170
Figure 5. 2 Stratigraphic chart of the Foz do Amazonas Basin (simplified from Figueiredo et al., 2007). The red box indicates the geologic time interval investigated in this study.....173
Figure 5. 3 The potential source-areas to source-to-sink Andes – Amazon – Brazilian Equatorial Margin system located in northern South American plate (Caxito et al., 2020; Dantas et al., 2013; Cordani and Teixeira, 2007; Klein et al., 2005; Dantas et al., 2004; Brito Neves et al., 2003; Van Schumus et al., 2003; Santos et al., 2000; Tassinari and Macambira, 1999; Brito Neves et al., 1995; Rodrigues et al., 2023; Moizinho et al., 2022; Hurtado et al., 2018; Costa, 2000; Palheta et al., 2009; Klein et al., 2020a, b; Litty et al., 2017; Navarro et al., 2010; Bettencourt et al., 2010; Chiaradia, 2009).....176
Figure 5. 4 Geological map of study area and adjacent basins, indicating the geographic location of the five (5) studied cores (blue circles), exhibiting simplified codes. Small dashed lines show the modern shelf

break. The onshore and offshore basins are bounded by large dashed lines, while the strutures zones are limited by dark solid lines. (18) 1APS0018AP; (23) 1APS0023AP; (24) 1APS0024AP; (25) 1APS25AP and (33E) 1APS33EAP. 177
Figure 5. 5 Regional Central-NW cross-section displaying all five wells studied in the Foz do Amazonas Basin. In detail, litotratigraphic units (Figureiredo et al., 2007); stratigraphic surfaces; cuttings locations (U-Pb, Sm-Nd); distribution of the ƐNd(0) isotopic compositions along the interval. The colored lines indicate the stratigraphic surfaces (surfaces Spn and Sn1 to Sn5) proposed by Cruz et al. (2019). Well 33E after Figueiredo et al. (2009). 179
Figure 5. 6 Histograms of the zircon ages distribution displayed as Kernel density estimate plots (KDE) of each sample analyzed in this study correlated with potetial sources. 183
Figure 5. 7 Multidimensional scaling (MDS) (Vermeesch, 2013) map for U–Pb ages of detrital zircons in the Foz do Amazonas Basin and catchment areas from Paleocene to Holocene. Sedimentary units of Bragantina Platform (Moizinho et al., 2022), Northern and Central Andes (Pepper et al., 2016; Mappes, 2009); Amazon Craton (Mapes et al., 2005) and the Holocene of Foz do Amazonas Baisn studied by Mason et al. (2019). The green and blue circles indicate similar detrital zircon age populations (see discussion in the tex and supplementary data). The solid line connecting samples indicate the closest neighbors. The stress values of the configuration indicate a fair goodness of fit (Vermeesch, 2013). 187

CAPITULO 6

Figura 6. 1 Mapa da reconstrução paleogeográfica da porção norte da América do Sul, detalhes das areas source-to-sink durante o Paleoceno ao Eoceno inferior (66 – 47.8 Ma). 204
Figura 6. 2 Mapa da reconstrução paleogeográfica da porção norte da América do Sul, detalhes das areas source-to-sink durante o Eoceno médio a superior (43.5 – 37.6 Ma). 206
Figura 6. 3 Mapa da reconstrução paleogeográfica da porção norte da América do Sul, detalhes das áreas source-to-sink durante o Oligoceno (~30 – 23 Ma). 209
Figura 6. 4 Mapa da reconstrução paleogeográfica da porção norte da América do Sul, detalhes das areas source-to-sink durante o Mioceno inferior a médio (23 – 12 Ma). 210
Figura 6. 5 Mapa da reconstrução paleogeográfica da porção norte da América do Sul, detalhes das areas source-to-sink durante o Miocene superior (~ 12 Ma). 212

CAPITULO 7

Figura 7.1 Esboço esquemático dos principais eventos geológicos ocorridos espaço-temporalmente no sistema fonte-sedimentação Andes-Amazônia-Margem Equatorial Sul-Americana ao longo do Cenozoico.....221

CAPÍTULO 1

INTRODUÇÃO

Introduction

1. INTRODUÇÃO / INTRODUCTION

PRÉSENTATION

Les systèmes sédimentaires et en particulier les bassins sont maintenant souvent analysés en termes de systèmes « *source-to-sink* » (S2S) c'est-à-dire en étudiant les zones sources qui par érosion produisent le sédiment, le transport de ces sédiments et leur piégeage dans les bassins qu'ils soient continentaux ou marins (Figure 1.1) (Sømme et al., 2009). C'est l'interaction entre les variations tectoniques et climatiques qui en façonnant les paysages anciens contrôle la production, le transport et le piégeage des particules issues des zones zource du S2S s (Caracciolo, 2020; Allen, 2017; Sømme et Jackson, 2013; Sømme et al., 2009). L'évolution temporelle et spatiale des S2S est régie par des processus dynamiques et des mécanismes de rétroaction liés à des facteurs internes et externes au système comme les changements paléogéographiques, les soulèvements tectoniques et des changements climatiques (Allen, 2017; 2008; Sømme et al., 2009).

Bien que l'enregistrement des dépôts dans le système S2S puisse documenter avec précision l'érosion dans les zones sources, les processus physico-chimiques comme l'altération, le tri hydrodynamique ou la diagénèse intervenant lors du transfert de sédiments et leur piegeage dans les bassins peuvent potentiellement masquer l'origine des sédiments (Sklar et al., 2017; Moquet et al., 2011; Jerolmack e Paola, 2010; Johnsson, 1993).

Il est possible de réduire et/ou d'éliminer ces biais concernant la provenance sédimentaire en couplant plusieurs méthodes d'analyses (*multi-proxy*), telles que les analyses sédimentologiques (caractérisation des faciès, pétrographie, mesures des paléocourants) (Miall, 1978, 1996, 2006), les analyses des minéraux lourds (p. ex. Augustsson et al, 2018 ; Augustsson et Reker, 2012 ; Garzanti, 2019, 2016 ; Garzanti et Andò, 2007), la géochimie élémentaire (éléments majeurs, traces et terres rares (ETR), (e.g. McLennan et al., 1993 ; Roddaz et al., 2006 ; Roddaz et al. 2021), les datations isotopiques (e. Hurtado et al. 2018 ; Vermeesch et Garzanti, 2015 ; von Eynatten et Dunkl, 2012 ; Weltje, 2012 ; Weltje et von Eynatten, 2004), ainsi que des études liées à la paléontologie et à la palynologie (Custódio et al, 2023; Paula de Sá et al., 2020).

En analysant la provenance des sédiments préservés dans les bassins des systèmes S2S sur les temps géologiques, les géologues peuvent déduire l'histoire de l'érosion des

chaines de montagnes, comme cela a été fait en Himalaya (Bergmann et al., 2016), dans les bassins d'avant-pays pour les Alpes (Lu et al., 2019) ou les Pyrénées (Valero et al., 2020 ; Odlum et al., 2019). Dansle cas des Andes, l'étude de la provenance des sédiments a non seulement permis de reconstituer l'histoire érosive de la chaine de montagne (voir Horton, 2018 et références à l'intérieur) mais aussi a permis de dater le début de l'érosion de la chaine andine amazonienne (Louterbach et al., 2018 ; Hurtado et al., 2018), de mettre en évidence l'activité flexurale du forebulge d'Iquitos (Roddaz et al., 2005), de dater le début de la transcontinentalisation de l'Amazone en déterminant la provenance des sédiments du cône de l'Amazone (Figuereido et al., 2009 ; Hoorn et al., 2017, van Soelen et al., 2017). Ainsi, les outils de provenance sont des outils puissants si on cherche a comprendre l'évolution des systèmes S2S à l'échelle des temps géologiques afin de mieux comprendre et discuter le rôle respectif du climat et de la tectonique sur les flux d'érosion (e.g. Caracciolo et al., 2020; Chew et al., 2020).

Dans cette optique, le S2S Andes-Amazone-Marge équatoriale sud-américaine (AAMESA) qui s'étend sur environ 3 200 km et est situé au nord de la plate-forme sud-américaine, peut être considéré comme un exemple type puisqu'il s'agit de l'un des plus grands systèmes S2S au monde (Figure 1.2). Ce système abrite une partie la deuxième plus grande chaine de montagne au monde (les Andes), le réseau fluvial le plus important de la planète, la plus grande forêt tropicale de la planète et l'un des plus grands deltas en eau profonde du monde (delta-fan de l'Amazone) (Val et al., 2021). Actuellement, le système AAMESA est contrôlé par les Andes d'un point de vue sédimentaire, car 95 % du flux annuel moyen de sédiments en suspension fournis par l'Amazone à l'océan Atlantique provient d'affluents andins (2/3 et 1/3 des fleuves Solimões et Madeira, respectivement) (Filizola e Guyot, 2004).

L'origine et l'évolution géologique du S2S AAMESA dans sa partie occidentale sont fortement liées à l'histoire géologique des Andes amazoniennes dont les traces du début de l'érosion sont enregistrées au Maatrichtien (Huratado et al., 2018 ; Louterbach et al., 2018) et dont les processus de formation et de propagation au cours du Cénozoïque ne sont pas continues (Mora et al., 2010 ; Eude et al., 2015 ; Horton, 2018). Dans sa partie centrale et orientale, l'évolution cénozoïque du sytème dépend des mouvements verticaux post fragmentation du Gondwana qui ont affecté le craton amazonien et la marge équatoriale (Alves et al., 2020; Fellin et al., 2023; Rossetti et al., 2019, 2012; 2013;

Rossetti, 2014; Rossetti and Valeriano, 2007) (Figure 1.3). L'origine et l'évolution géologique du S2S AAMESA sont également liées à l'histoire géologique du fleuve Amazone, qui a connu plusieurs changements de direction au cours du Méso-Cénozoïque (Hurtado et al., 2018; Rodrigues et al., 2023; Caputo et Soares, 2016; Sacek, 2014; Shepard, et al., 2010; Potter, 1997).

Entre l'Albien et le début du Maastrichtien, le réseau hydrographique amazonien est contrôlé par le soulèvement de l'Arc Purus (région orientale des cratons brésilien et guyanais) (Hurtado et al., 2018 ; Rodrigues et al., 2023). Entre la fin du Maastrichtien et le début du Paléocène (~70 - 61 Ma), les rivières andines-amazoniennes ont développé un drainage parallèle aux Andes (Hurtado et al. 2018; Louterbach et al. 2018) sous l'effet probable d'une augmentation de l'éosion dans les Andes amazoniennes en relation avec une période de chargement tectonique (Louterbach et al., 2014, 2018). Les premières preuves de l'existence de la transcontinentalisation du fleuve Amazone, c'est-à-dire de l'existence d'un fleuve amazonien d'origine andine traversant le continent sud-américain pour aller se jeter dans l'Océan Atlantique, sont enregistrées par l'arrivée des premiers sédiments andins dans le cône amazonien (bassin de Foz do Amazonas), dont les âges existants indiquent qu'elle s'est produite entre 11.8 et 8.7 Ma (Figueiredo et al., 2009; Hoorn et al., 2017; van Soelen et al., 2017).

Le timing du début de la transcontinentalisation ne correspond pas avec l'augmentation des taux de sédimentation dans le cône de l'Amazone puisque ces derniers ont au moins quadruplés après la fin du Pliocène c'est-à-dire bien après que l'Amazone soit devenue transcontinentale (Figueiredo et al., 2009 ; Rouby et al., 2023). Avant la transcontinentalisation du fleuve Amazone, l'environnement sédimentaire de l'Amazonie occidentale au cours du Miocène moyen (Madre de Dios, Ucayali, Huallaga, Oriente, Llanos, Acre et Solimões) était caractérisé par la présence d'une zone humide marécageuse, le système Pebas (Hoorn et al., 2010 ; Wesselingh et al., 2001, 2006) qui a occasionnellement enregistré des incursions marines (Alvim et al., 2021; Hoorn et al., 2010; Hoorn, 1993, 1994; Hovikoski et al., 2011; Jaramillo et al., 2017; Boonstra et al., 2015). Dans l'est de l'Amazonie, plusieurs bassins intracratoniques et de la marge équatoriale ont enregistré une augmentation massive des apports sédimentaires au cours du Miocène moyen (Mabesoone et al., 1972 ; Bigarella, 1975 ; Rossetti et al., 2013). Au Miocène inférieur (~18.3 Ma), un fleuve Amazone d'origine andine pourrait avoir connu

une connexion temporaire avec l'Océan Atlantique comme le montre les données de provenance et de marqueurs organiques analysées sur des sédiments du forage IODP 825 de Ceara Rise (van Soelen et al., 2017). Des études récentes montrent que l'accumulation de sédiments au Miocène sur la marge équatoriale de l'Amazonie orientale a été régie par l'activité néotectonique liée à la phase post-rift (Bezerra et al., 2001 ; Rossetti et Goes, 2004 ; Rossetti, 2006 ; Nogueira et al., 2010 ; Rossetti et al., 2012 ; Rossetti et al., 2013).

Malgré de récents progrès détaillant les influences des processus de construction et d'érosion des Andes sur l'origine et l'évolution et l'enregistrement sédimentaire du système S2S AAMESA à la fin du Crétacé-début du Paléocène en Amazonie occidentale (Custódio et al., 2023 ; Rodrigues et al., 2023 ; Calvès et al., 2018 ; Hurtado et al., 2018 ; Horton et al., 2018a, Louterbach et al, 2017) et l'établissement du fleuve Amazone transcontinental à la fin du Miocène (Néogène) en Amazonie orientale (Cruz et al., 2019 ; Figueiredo et al., 2009 ; Gorini et al., 2014 ; Hoorn et al., 2017 ; van Soelen et al., 2017), les configurations pré néogène et pliocène du système AAMESA restent à préciser. En particulier, plusieurs questions restent ouvertes sur l'évolution sédimentaire du système S2S AAMESA au cours du Paléogène et notamment sur les changements paléogéographiques et paléoenvironnementaux survenus en Amazonie occidentale au cours du Paléogène, sur l'histoire de l'érosion des Andes amazoniennes au cours du Cénozoïque et son influence sur le développement du fleuve transcontinental Amazone et les sources de sédiments paléogènes sur la marge équatoriale. Si on arrive à avoir des précisions sur ces thématiques, on pourra alors éventuellement s’intéresser aux relations entre l’évolution paléogène des bassins d’avant-pays retroarc de l’Amazonie occidentale et ceux de la marge équatoriale.

Cette thèse vise à réaliser une reconstruction paléogéographique du système S2S Andes - Amazonie - Marge équatoriale Sud-Américaine (AAMESA) au cours du Cénozoïque. Pour ce faire, nous avons déterminé la provenance des échantillons d’affleurement et de puits des sédiments cénozïques des bassins Huallaga (faisant partie du bassin d’avant-pays retroarc amazonien nord péruvien) et de Foz de Amazonas (marge équatoriale) afin d’identifier les zones sources alimentant le système S2S au cours du cénozoïque. Nous avons aussi redefini les s paléoenvironnements cénozoïques amazoniens, en particulier en Amazonie Occidentale (Bassin de Huallaga) à partir de nouvelles contraintes isotopiques et sédimentologiques.

Cette thèse se divise en sept chapitres :

Le présent chapitre introductif (Chapitre 1) traite du contexte théorique et des implications du système S2S, de l'importance scientifique de cette recherche et énumère les objectifs spécifiques à atteindre pour permettre de proposer une reconstruction paléogéographique au cours du Cénozoïque dans la partie septentrionale de la plate-forme sud-américaine.

Le Chapitre 2 détaille les conditions d'acquisition des données, le matériel et méthodes utilisés au cours de cette thèse.

Le Chapitre 3 apporte de nouvelles contraintes chronologiques et paléonenvionnementales sur la paléogeographie de l'Amazonie occidentale Ce chapitre se présente sous la forme d'un article publié à *Journal of South American Earth Sciences* « New stratigraphic and paleoenvironmental constraints on the Paleogene paleogeography of Western Amazonia » (https://doi.org/10.1016/j.jsames.2023.104256).

Le Chapitre 4 apporte de nouveaux jalons sur l'histoire érosive Maastrichtienne à Actuelle de la partie nord des Andes amazoniennes à partir de la provenance sédimentaire. En particulier, il apporte de nouvelles contraintes sur la formation et l'érosion de la Cordillère Orientale. Ce chapitre se présente sous la forme d'un manuscrit en cours de soumission à *Gondwana Research* intitulé « Maastrichtian-Cenozoic erosional history of the Northern Peruvian Amazonian Andes: Implications for the Eastern Cordillera evolution (Huallaga Basin, Northern Peru) ».

Le Chapitre 5 traite de la reconstitution du paleo réseau de drainage Amazonien Paléogène Oriental à partir de la provenance des sédiments du bassin Foz de Amazonas, marge équatoriale de l'Amérique du Sud. Les données présentées ici sont sous la forme d'un 'article en préparation. Les données présentées sont préliminaires, car des données complémentaires (datations U-Pb sur zircons supplémentaires et datations biostratigraphiques) sont en cours d'analyse.

Le Chapitre 6 présente une synthèse et discussion sur la paléogéographie de la partie nord de la plate-forme sud-américaine dans le contexte de l'origine et de l'évolution du système S2S AAMESA au cours du Cénozoïque.

Le Chapitre 7 (conclusion) rassemble les principales conclusions de cette thèse et propose quelques perspectives.

1.1 CONTEXTUALIZAÇÃO DO TEMA

1.1.1 Sistema Fonte – Sedimentação (*source-to-sink*)

Os sistemas sedimentares e, em particular, as bacias, são agora frequentemente analisados em termos de sistemas "*source-to-sink*" (S2S), ou seja, estudando as zonas de origem dos sedimentos por erosão, seu transporte e aprisionamento em bacias, sejam elas continentais ou marinhas (Figura 1.1) (Sømme et al., 2009). É a interação entre as variações tectônicas e climáticas que, ao moldar as paisagens antigas, controla a produção, o transporte e o aprisionamento de partículas das zonas de origem de S2S (Caracciolo, 2020; Allen, 2017; Sømme e Jackson, 2013; Sømme et al., 2009). A evolução temporal e espacial do S2S é governada por processos dinâmicos e mecanismos de retroalimentação ligados a fatores internos e externos ao sistema, como mudanças paleogeográficas, elevação/subsidência tectônica e variação do nível do mar (Allen, 2017; 2008; Sømme et al., 2009).

O S2S é composto por segmentos geneticamente relacionados: zona de erosão (*erosional engine*), zona de transferência (*transfer zone*) e área de deposição (*long-term sink*), os quais se conectam pela trajetória dos sedimentos (Figura 1.1) (Caracciolo, 2020; Allen and Heller, 2012). A sua evolução é refletida por modificações paleogeograficas ocorridas dentro de um ou vários segmentos adjacentes (Sømme et al., 2009). Essa relação entre processo e resposta é a força motriz por trás do desenvolvimento dos segmentos e da evolução do sistema na escala de tempo geológico (Allen and Heller, 2012; Sømme et al., 2009).

Embora o registro de deposição no S2S possa documentar com precisão a erosão nas áreas de origem, os processos físico-químicos, como intemperismo, classificação hidrodinâmica ou diagênese envolvidos na transferência de sedimentos e aprisionamento em bacias, podem mascarar a origem dos sedimentos (Sklar et al., 2017; Moquet et al., 2011; Jerolmack e Paola, 2010; Johnsson, 1993). É possível reduzir e/ou eliminar esses vieses estudando a proveniência sedimentar por meio da integração de vários métodos analíticos (*multi-proxy*), como análises sedimentológicas (caracterização de fácies, petrografia, medições de paleocorrentes) (Miall, 1978, 1996, 2006), análises de minerais pesados (Augustsson et al., 2018; Augustsson e Reker, 2012; Garzanti, 2019, 2016; Garzanti e Andò, 2007), geoquímica elementar (elementos principais, traços e terras raras (REE), (e.g. McLennan et al, 1993; Roddaz et al., 2006;. 2021), datação isotópica (e.g.

Hurtado et al. 2018; Vermeesch e Garzanti, 2015; von Eynatten e Dunkl, 2012; Weltje, 2012; Weltje e von Eynatten, 2004), bem como estudos relacionados à paleontologia e palinologia (Custódio et al, 2023; Paula de Sá et al., 2020).

Ao analisar a proveniência dos sedimentos preservados nos sistemas S2S ao longo do tempo geológico, é possível fazer deduções sobre a história de erosão das cadeias de montanhas, como foi feito no Himalaia (Bergmann et al., 2016), nas bacias foreland dos Alpes (Lu et al., 2019) ou nos Pirineus (Valero et al., 2020; Odlum et al., 2019). No caso dos Andes, estudos de proveniência dos sedimentos do cone amazônico não só possibilitaram a reconstrução da história erosiva da cordilheira (p.e., Horton, 2018a), mas também a datação do início da erosão da Cordilheira Andina Amazônica (Louterbach et al., 2017; Hurtado et al, 2018), a flexão do *forebulge* de Iquitos (Roddaz et al., 2005), e, datar o início da transcontinentalização da Amazônia (Figueiredo et al., 2009; Hoorn et al., 2017, van Soelen et al., 2017). Ferramentas de proveniência sedimentar são poderosas no entendimento da evolução dos sistemas S2S em uma escala de tempo geológico, contribuindo em discussões sobreo controle climático e tectônico nos processos de erosão (e.g. Caracciolo et al., 2020; Chew et al., 2020; Insel et al., 2010).

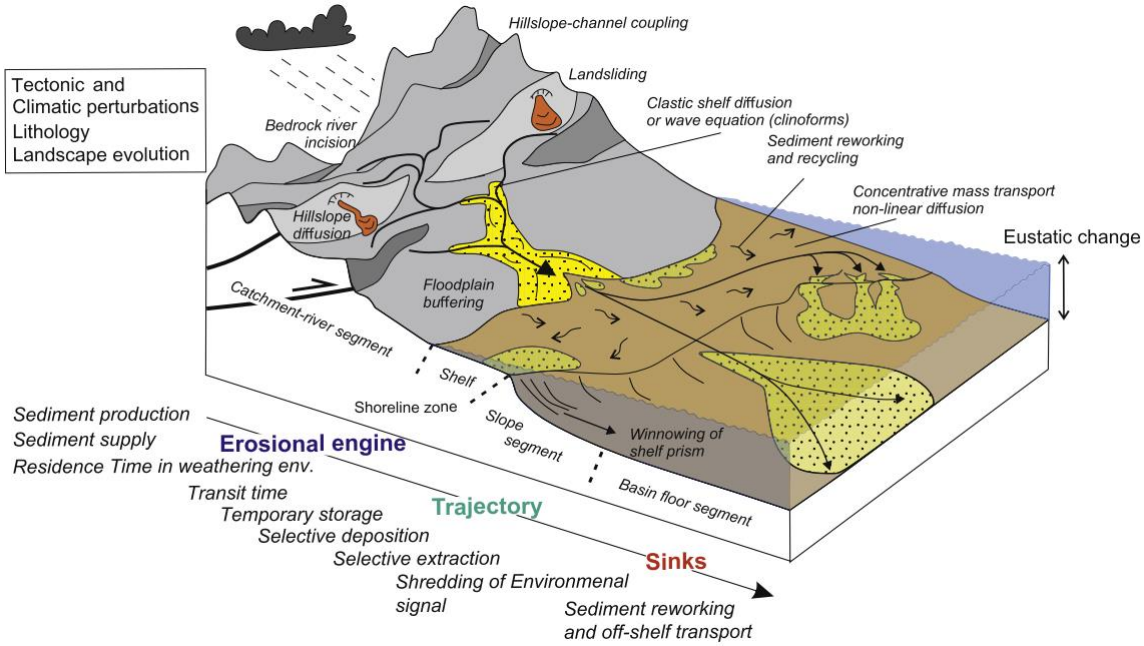


Figura 1. 1 Representação esquemática do sistema S2S e os três principais segmentos, as zonas de erosão (*erosional engine*), transferência (*trajectory*) e deposição (*sinks*) (Caracciolo, 2020)

1.2 INTRODUÇÃO E RELEVÂNCIA DO ESTUDO

O sistema S2S do eixo Andes-Amazônia-Margem Equatorial Sul-Americana (AAMESA) se estende por cerca de 3.200 km e está localizado ao norte da plataforma Sul-Americana, representando um dos maiores sistemas S2S do mundo (Figura 1.2). Esse sistema abriga parte da segunda maior cadeia de montanhas (i.e., os Andes), o maior sistema fluvial, a maior floresta tropical e um dos maiores leques submarinos da Terra (a foz do Amazonas) (Val et al., 2021).

Atualmente, o S2S do eixo AAMESA hospeda o volumoso rio Amazonas, que ocupa o primeiro lugar na transferência de massa global dos continentes para os oceanos. De fato, esse rio fornece cerca de 20% da água (Callède et al., 2004), ~10% da carga dissolvida (Gaillardet et al., 2007) e ~3% da carga suspensa (Milliman e Syvitski, 1992) para os oceanos do mundo. Mais de 95% do fluxo médio anual de sedimentos em suspensão fornecido pelo Amazonas tem contribuição de afluentes andinos (2/3 e 1/3 dos rios Solimões e Madeira), respectivamente (Filizola e Guyot, 2004). O sistema S2S do eixo AAMESA conecta a Amazônia Ocidental, a Cordilheira dos Andes e o Cráton Amazônico (escudos brasileiro e da Guiana) à Bacia da Foz do Amazonas na Amazônia Oriental (Figura 1.2). Dada a sua magnitude, importância e complexidade, este sistema tem sido objeto de vários estudos recentes que abordam sua evolução (van Soelen et al. 2017; Albert et al. 2018; Hurtado et al. 2018; Louterbach et al. 2017; Bajolet et al. 2022; Custódio et al., 2023; Rodrigues et al., 2023).

A origem e a evolução geológica do S2S do eixo AAMESA em sua parte ocidental estão fortemente ligadas à história geológica dos Andes Amazônicos, onde há evidências de início de erosão no Maastrichtiano (Hurtado et al., 2018; Louterbach et al., 2017), cujos processos de formação e propagação durante o Cenozoico não são contínuos (Mora et al., 2010; Eude et al., 2015; Horton, 2018). Em suas partes central e oriental, a evolução cenozoica do S2S do eixo AAMESA esteve condicionada a movimentos verticais após a quebra do *Gondwana*, que afetou o Cráton Amazônico e a Margem Equatorial (Alves et al., 2020; Fellin et al., 2023; Rossetti et al., 2012, 2013, 2022; Rossetti e Valeriano, 2007). A origem e a evolução geológica do S2S da AAMESA também estão ligadas à história geológica do rio Amazonas, que passou por várias mudanças de sentido durante o Meso-Cenozoico (Hurtado et al., 2018; Rodrigues et al., 2023; Caputo e Soares, 2016; Sacek, 2014; Shepard, et al., 2010; Potter, 1997).

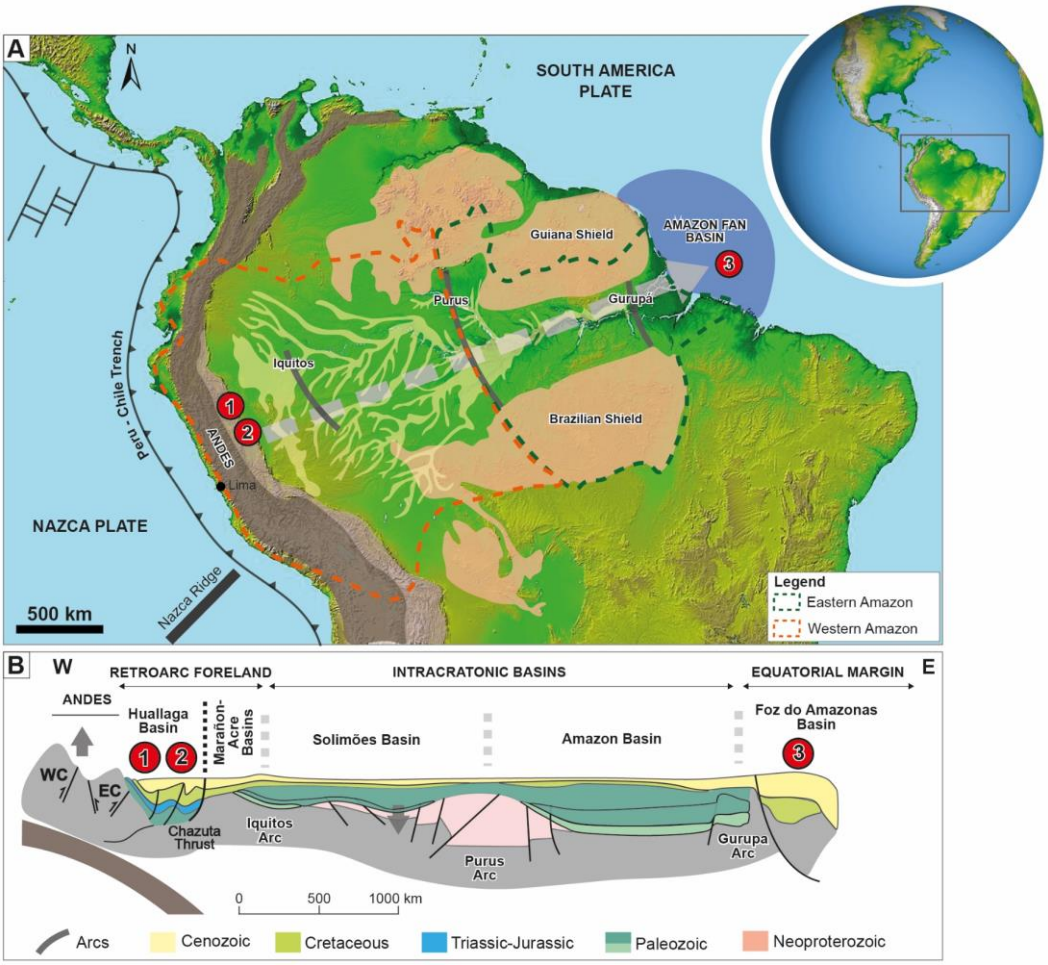


Figura 1. 2 Mapa de localização do sistema fonte-deposição (S2S) no eixo Andes – Amazônia – Margem Equatorial Sul-Americana (AAMESA). A) Mapa regional do relevo e principais unidades geotectônicas da região norte da Plataforma Sul-Americana, exibindo: o cinturão orogênico Andino à oeste; o Cráton Amazônico e os arcos de Iquitos, Purus e Gurupá na zona centro-leste; a Margem Equatorial Sul-Americana a nordeste, esta se limitando com a Bacia da Foz do Amazonas. Em destaque, a Amazônia Ocidental e Oriental estão representadas por contornos tracejados. Em detalhe, os números (1) – Artigo 1°; (2) – Artigo 2° e (3) – Artigo 3°. B) Seção geológica esquemática da região norte da Plataforma Sul-Americana, exibindo (perfil W-E) a cadeia de montanhas Andinas; a zona-subandina, da Amazônia Ocidental, com as bacias de retroarco de antepaís (Bacia de Huallaga-Marañón-Acre); as bacias intracratônicas (Bacia do Solimões e Amazonas) e a margem passiva (Bacia da Foz do Amazonas). Crédito da imagem de relevo NASA/JPL/NIMA (https://photojournal.jpl.nasa.gov/catalog/PIA03388). Figuras modificadas de Albert et al., 2018; Hoorn et al., 2017; Bajolet et al., 2022.

Entre o Albiano e o início do Maastrichtiano, a rede hidrográfica amazônica foi controlada pela elevação do Arco do Purus (região oriental dos crátons do Brasil e da Guiana) (Fig. 1.2) (Hurtado et al., 2018; Rodrigues et al., 2023). Entre o final do Maastrichtiano e o início do Paleoceno (~70 - 61 Ma), os rios andino-amazônicos

desenvolveram a drenagem (Hurtado et al. 2018; Louterbach et al. 2017) sob o provável efeito de um aumento da erosão nos Andes amazônicos decorrente de um período de soerguimento tectônico (Louterbach et al., 2014; 2017). A primeira evidência da transcontinentalização do rio Amazonas, ou seja, a existência de um rio amazônico de origem andina atravessando o continente sul-americano para desaguar no Atlântico, é registrada pela chegada dos primeiros sedimentos Andinos na foz do Amazonas (Bacia da Foz do Amazonas), propostamente ocorrida entre 11.8 e 8.7 Ma (Figueiredo et al, 2009; Hoorn et al., 2017; van Soelen et al., 2017). O estabelecimento do rio Amazonas como transcontinental é controverso, variando entre o Mioceno inicial (18.3 Ma) (van Soelen et al, 2017); Mioceno tardio (11.8 a 11.3 Ma) (Figueiredo et al., 2009); (9.4 a 9.0 Ma) (Hoorn et al., 2017; 1995); Plioceno tardio (ca. 2.5 Ma) (Campbell, 2010).

O início da transcontinentalização do rio Amazonas não corresponde ao aumento das taxas de sedimentação em sua foz, uma vez que elas aumentaram pelo menos quatro vezes após o final do Plioceno, ou seja, bem depois que o Amazonas se tornou transcontinental (Figueiredo et al., 2009; Rouby et al., 2023). No Mioceno Médio, ou seja, antes desse evento, uma ampla área de sedimentação da Amazônia ocidental, correspondentes às bacias de Madre de Dios, Ucayali, Huallaga, Oriente, Llanos, Acre e Solimões, era caracterizada por ambientes úmidos pantanosos, conhecidos como o sistema Pebas (Hoorn et al, 2010; Wesselingh et al., 2001, 2006). Essas regiões ocasionalmente registravam incursões marinhas (Alvim et al., 2021; Hoorn et al., 2010; Hoorn, 1993, 1994; Hovikoski et al., 2011; Jaramillo et al., 2017; Boonstra et al., 2015). No leste da Amazônia, várias bacias terrestres e áreas de plataforma registraram um aumento na entrada de sedimentos durante o Mioceno Médio (Mabesoone et al., 1972; Bigarella, 1975; Rossetti et al., 2013). No Mioceno Inferior (~18.3 Ma), o rio Amazonas de origem andina pode ter experimentado uma conexão temporária com o Oceano Atlântico, conforme demonstrado por dados de proveniência e marcadores orgânicos analisados em sedimentos do furo de sondagem IODP 825 no Ceará *Rise* (van Soelen et al., 2017). Estudos recentes mostram que a acumulação de sedimentos miocênicos na costa leste da Amazônia Oriental foi governada pela atividade neotectônica relacionada à fase pós-rifte (Bezerra et al., 2001; Rossetti et Goes, 2004 ; Rossetti, 2006 ; Nogueira et al., 2010 ; Rossetti et al., 2012 ; 2013).

Avanços recentes detalharam as influências da construção Andina e dos processos erosivos na origem e evolução do registro sedimentar do sistema S2S do eixo AAMESA

no final do Cretáceo e início do Paleoceno na Amazônia Ocidental (Custódio et al., 2023; Rodrigues et al., 2023; Horbe et al., 2019; Calvès et al., 2018; Hurtado et al., 2018; Horton et al, 2018a, Louterbach et al., 2017). Apesar disso, e da proposta de estabelecimento do rio Amazonas transcontinental no final do Mioceno (Neogeno) no leste da Amazônia (Mason et al., 2019, 2022; Cruz et al., 2019; Figueiredo et al., 2009; Gorini et al., 2014; Hoorn et al., 2017; van Soelen et al., 2017), as configurações pré-Neogeno e Plioceno do sistema AAMESA ainda precisam ser esclarecidas. Em particular, várias questões permanecem em aberto sobre a evolução sedimentar do sistema S2S do eixo AAMESA durante o Paleógeno e, especialmente, sobre as mudanças paleogeográficas e paleoambientais que ocorreram na Amazônia ocidental durante o Paleógeno. Além disso, a história de erosão dos Andes amazônicos durante o Cenozoico e sua influência no desenvolvimento do rio Amazonas transcontinental e as fontes de sedimentos do Paleógeno na margem equatorial Sul-Americana, é ainda pouco detalhada. Se formos capazes de esclarecer essas questões, poderemos então analisar as relações entre a evolução paleogênica das bacias *foreland* do retroarco da Amazônia Ocidental e as da margem Equatorial brasileira.

O objetivo desta tese é compreender como a evolução geológica das porções oeste e norte da América do Sul influenciaram as configurações paleoambientais e paleogeográficas do sistema S2S do eixo AAMESA durante o Cenozoico, com foco no Paleógeno. Para isso, determinamos a proveniência de sedimentos cenozoicos em afloramento e de poços derivados das bacias de Huallaga (parte da bacia *foreland* do retroarco amazônico do norte do Peru) e Foz de Amazonas (margem equatorial), a fim de identificar as fontes de sedimentos do sistema S2S. Também redefinimos os paleoambientes do Cenozoico amazônico, particularmente na Amazônia Ocidental (Bacia do Huallaga), usando novos dados isotópicos e sedimentológicos.

1.3 CONTEXTO GEOLÓGICO

1.3.1 Eventos orogênicos e evolução das bacias Amazônicas ocidentais

A América do Sul experimentou eventos orogênicos distintos ao longo da sua história geológica, que desempenharam papel importante na configuração atual de sua paisagem. A fase inicial é caracterizada pela Orogênese Gondwânica que compreendeu uma ampla gama de eventos ocorridos do Neoproterozoico ao Paleozoico (Trompette,

2000). Ela resultou na formação de várias cadeias montanhosas em algumas regiões do *Gondwana*, que contribuiram como área-fonte de sedimentos. A orogênese Gondwânica incluiu as orogenias Pan Africana-Brasiliana (Neoproterozoico), Pampeana (Cambriano) e Famatiniana (Ordoviciano) (Chew et al., 2016). Estes eventos orogênicos foram seguidos por fases de metamorfismo permo-triássico (Chew et al., 2016) e magmatismo jurássico ao longo da margem ocidental da América do Sul (Kontak et al., 1990).

A orogênese Andina, que é mais recente, iniciou no final do Mesozoico (Cretáceo), levando à formação do atual sistema de cadeia de montanhas de alta elevação (Evenstar et al., 2023; Boschman, 2021; Faccenna et al., 2017; DeCelles et al., 2009; Garzione, 2008; Gregory-Wodzicki, 2000; Jaillard et al., 2000; Jaillard e Soler, 1996). Caracterizado como sistema orogênico Andino, o mesmo resulta do processo de subducção da placa de Nazca sob a placa continental Sul-Americana, esta última tendo sido impulsionada para oeste pela ruptura do *Gondwana* e abertura do Oceano Atlântico Sul (Figura 1.3) (Horton, 2018b; Mora et al., 2010; Jaillard et al., 2000; Almeida et al., 2000; Jaillard and Soler, 1996). A dinâmica da atividade tectônica, ocorrida durante o Meso-Cenozoico esteve atrelada à formação de arcos vulcânicos e deformação da placa Sul-Americana sobrejacente, que moldaram a paisagem e impactaram na origem e evolução da Cordilheira dos Andes e bacias de retroarco de antepaís (Figura 1.3) (Custódio et al., 2023; Vallejo et al., 2021; Macellari, 2021; Mora et al., 2020; Moreno et al., 2020; Tcheumeleu et al., 2020; Horton et al., 2020; Gutiérrez et al., 2019; George et al., 2019; Hurtado et al., 2018; Calvès et al., 2018; Louterbach et al., 2017; Perez et al., 2016; Pfiffner and Gonzalez, 2013; Delgado et al., 2012; Roddaz et al., 2010; Bayona et al., 2008; Hermoza et al., 2005; Christophoul et al., 2002; Jaillard, 1993). A deformação relacionada ao processo de subducção, ao longo da margem pré-Andina, foi policíclica, de longa duração e de extensão regional (Chew, et al., 2016) e, pode ter progredido de norte em sentido aos Andes centrais e sul (Figura 1.3) (Chen et al., 2019).

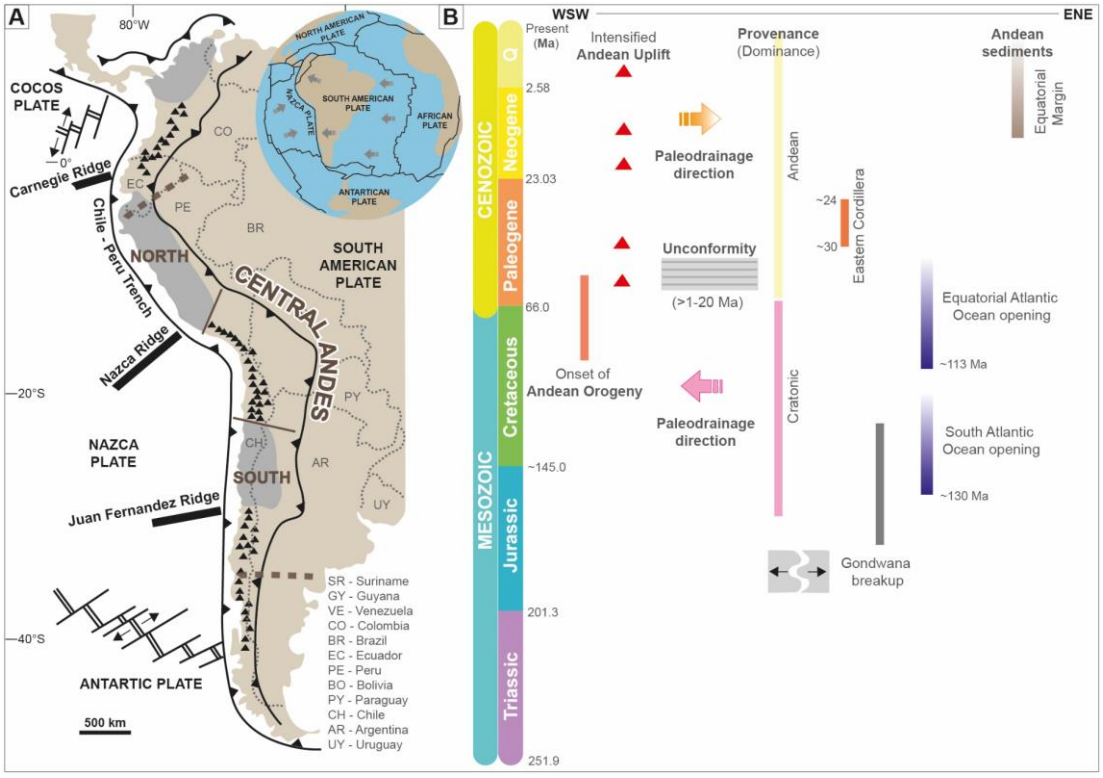


Figura 1. 3 Contexto espaço-temporal dos principais eventos geológicos ocorridos na Plataforma Sul-Americana durante o Mesozoico-Cenozoico. A) Mapa tectônico da América do Sul, contendo os limites das placas tectônicas de Nazca e Sul-Americana, bem como, o Arco Magmático Andino (incluindo as zonas vulcânicas a norte, central e sul) (modificado de Horton, 2018a). B) Principais eventos tectônicos globais e amazônicos ocorridos ao longo do Meso-Cenozoico que impactaram na evolução e configuração geológica da Amazônia Ocidental e Oriental.

O sistema orogênico Andino é segmentado, de oeste para leste, nas seguintes regiões (Figura 1.4): i) frente de arco *(forearc)*, ii) Arco Magmático Andino (Cordilheira Ocidental), iii) cinturão de cavalgamento de trás de arco (r*etroarc fold-thrust belt)* (Cordilheira Oriental). No caso dos Andes Centrais (Figuras 1.2) (Horton et al., 2016; Ramos and Folguera, 2009), ocorrem as seguintes regiões iv) altiplano (h*interland)*; e v) sistema de bacias de antepaís de retroarco (*Retroarc foreland basin system)* (Horton, 2018a).

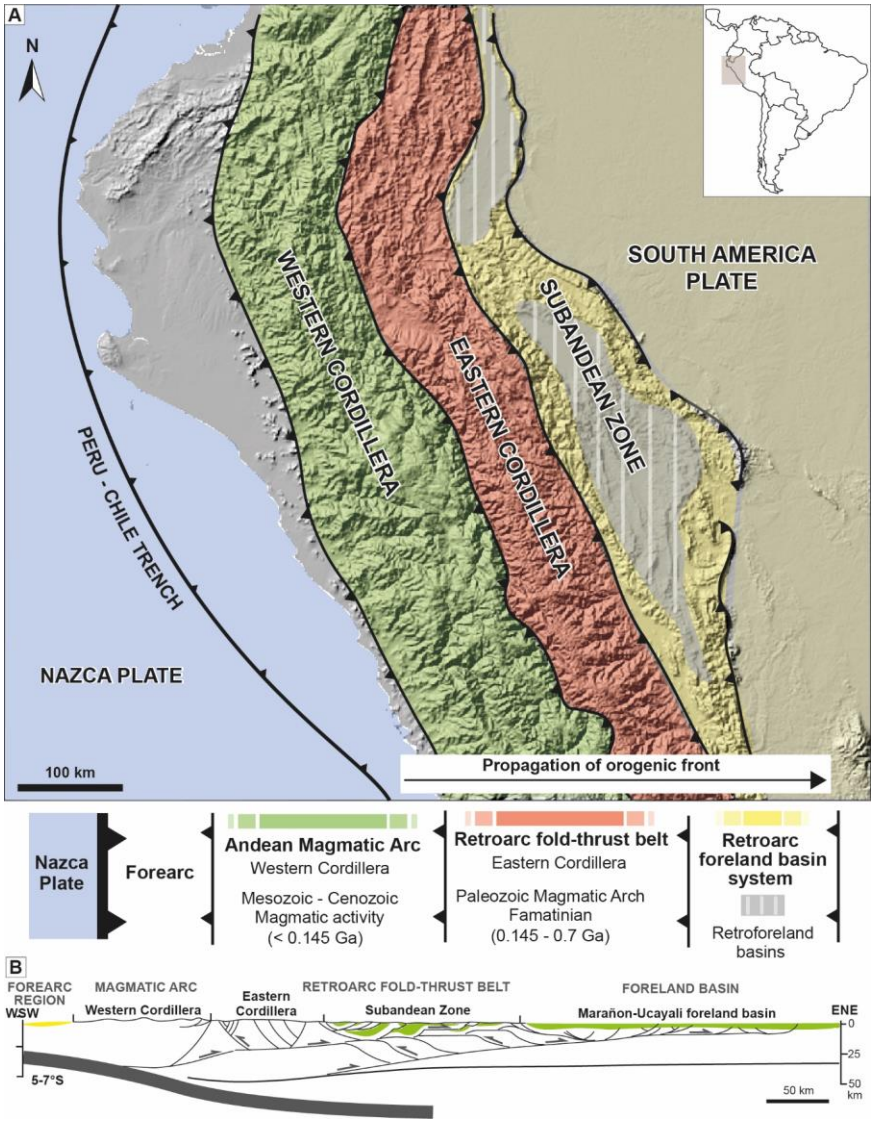


Figura 1. 4 Principais unidades morfoestruturais presente ao Norte dos Andes Centrais. A) Mapa morfotectônico do Cinturão Orogênico Andino segmentado, de oeste à leste, pelo Arco Magmático Andino (Cordilheira Ocidental) (<0.145 Ga); Cinturão Paleozoico plutônico e metamórfico (0.5 – 0.26 Ga) e pela Zona Subandina (sistema de bacias de antepaís). B) Seção transversal esquemática da região Norte dos Andes Centrais exibindo a configuração tectônica da margem oeste da América do Sul, zona dos Andes Amazônicos, incluindo a geometria da placa de subducção de Nazca sob a placa Sul-Americana, a espessura crustal (~25-50 km), região do retroarco, geometrias estruturais da frente de empurrão orogênico, configuração do sistema de bacias amazônicas de antepaís (Modificado de Horton, 2018a; Armijo et al., 2015).

Em particular, os Andes Centrais (Figuras 1.3) (15-25°S) apresentam configurações específicas, caracterizados por extremo encurtamento (> 150-300 km) e espessamento (> 50-70 km *deep Moho*) da crosta litosférica, devido ao aumento acentuado das taxas de encurtamento durante o Paleógeno (Horton, 2018a, b; Eude et al., 2015; Armijo et al., 2015; Beck and Zandt, 2002). A progressão, à leste, do encurtamento litosférico e espessamento

da cunha do cinturão orogênico Andino gerou subsidência flexural regional e condicionou a formação do sistema de bacias Amazônicas Ocidentais (*Amazonian Retroarc Foreland Basin*) no flanco leste dos Andes Centrais Norte (Figura 1.4) (Horton, 2018a; Roddaz et al., 2010; Horton and DeCelles, 1997). O preenchimento sedimentar deste sistema de bacias registrou o início da orogenia Andina e os aumentos no espaço de acomodação e sedimentação dos Andes Amazônicos, no Cretáceo Superior – Cenozoico Inferior (Figura 1.3B) (Hurtado et al., 2018; Louterbach et al., 2017).

Este sistema é dividido por quatro zonas deposicionais: *wedge-top*, *foredeep*, *forebulge*, e *backbulge* (Figura 1.5A) (DeCelles and Giles, 1996; Horton and DeCelles, 1997). No contexto da Amazônia Ocidental, a zona da frente de empurrão Andino é denominada Zona Sub-Andina (*wedge-top depozone*), sendo representada pelas bacias Huallaga (foco deste estudo) – Moyabamba –Marañón (Peru) (Figura 1.5B) (Calderón et al., 2017; Eude et al., 2015; Roddaz et al., 2010). A zona de deposição *foredeep* consiste nos sedimentos depositados entre a zona *wedge-top* e o *forebulge*, representada pelas bacias Llanos (Colômbia), Oriente (Equador), Madre de Dios (Peru), Beni-Mamore (Roddaz et al., 2010). Enquanto que o *forebulge* comprende uma estrutura elevada do embasamento, produto do soerguimento flexural decorrente das elevadas taxas de subsidência, representado pelo Arco de Iquitos (Figura 1.5B). Este arco corresponde ao limite entre as zonas *foredeep* e *backbulge* (DeCelles and Giles, 1996). A interação entre as unidades morfoestruturais acima apresentadas delinearam condições favoráveis para geração e deposição de sedimentos na Amazônia Ocidental.

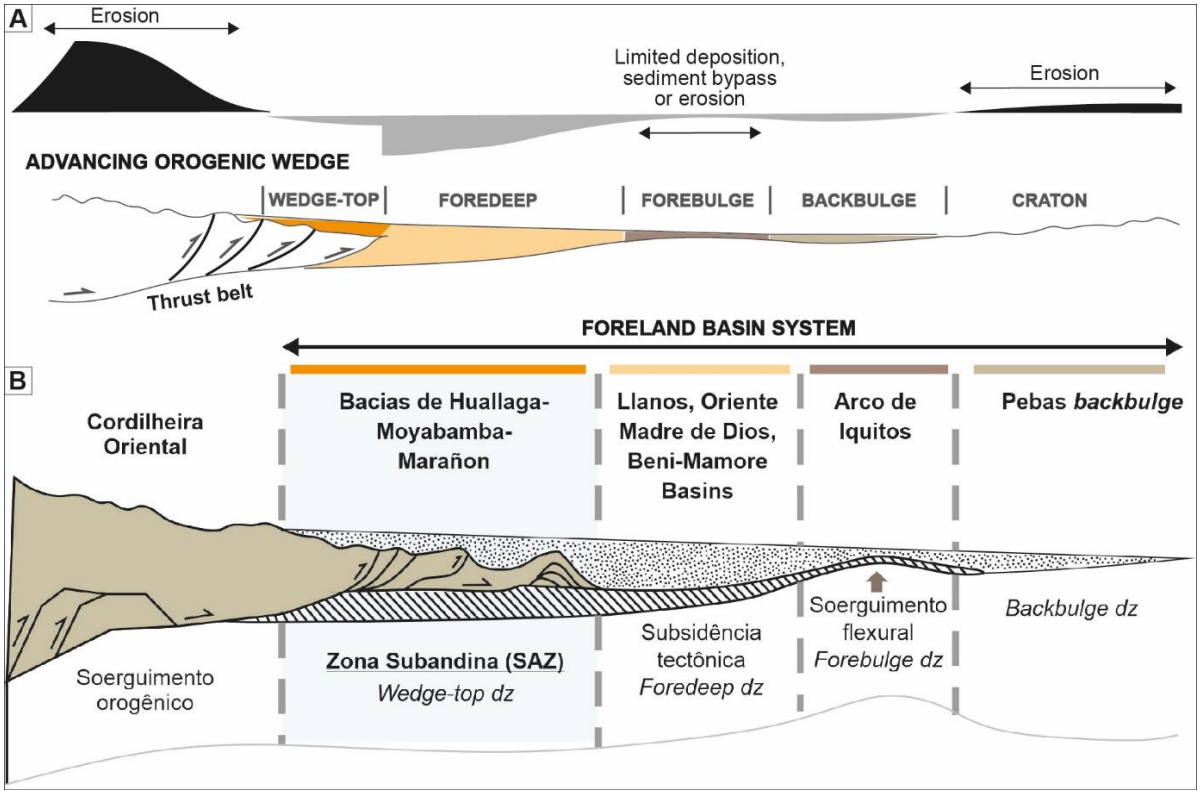


Figura 1. 5 Configuração estrutural do sistema de bacias amazônicas de antepaís (*Amazonian Retroarc Foreland Basin*). A) Seção esquemática transversal da geometria do sistema de bacias de antepaís, com as zonas de deposição wedge-top, foredeep, forebulge e backbulge, exibindo as principais áreas de erosão e de *bypass*. B) Seção esquemática transversal do sistema de bacias amazônicas de antepaís representando as bacias amazônicas ocidentais correlacionadas com as respectivas zonas de deposição. Em destaque, a Bacia de Huallaga, localizada na zona de deposição *wedge-top*, também denominada Zona Subandina (SAZ), situada na região mais proximal e deformada, dentro do sistema de bacias amazônicas de antepaís (modificada de Roddaz et al., 2010; DeCelles and Giles, 1996).

1.3.2 Evolução da Margem Equatorial Sul-Americana: Bacia da Foz do Amazonas

A Margem Equatorial Sul-Americana é uma ampla margem continental que se estende ao longo do Equador, desde a costa norte do Brasil até a Colômbia. A origem e evolução da Margem Atlântica Equatorial é relativamente jovem, com as rochas mais antigas datando do Triássico (Figueiredo et al., 2007; Soares Júnior et al., 2011). Durante o Mesozoico, a combinação de eventos de soerguimentos associados com magmatismo, seguidos por esforços distensivos, culminaram na fragmentação do supercontinente *Gondwana* (quebra dos continentes Sul-Americano e Africano) e, consequente expansão do assoalho oceânico, resultando na formação do Oceano Atlântico nas regiões sul e

equatorial, respectivamente (Figuras 1.2B; 1.5) (Darros de Matos, 2000; Hollanda et al., 2019; Soares Júnior et al., 2011, 2008; McHone, 2000; Nürnberg and Müller, 1991).

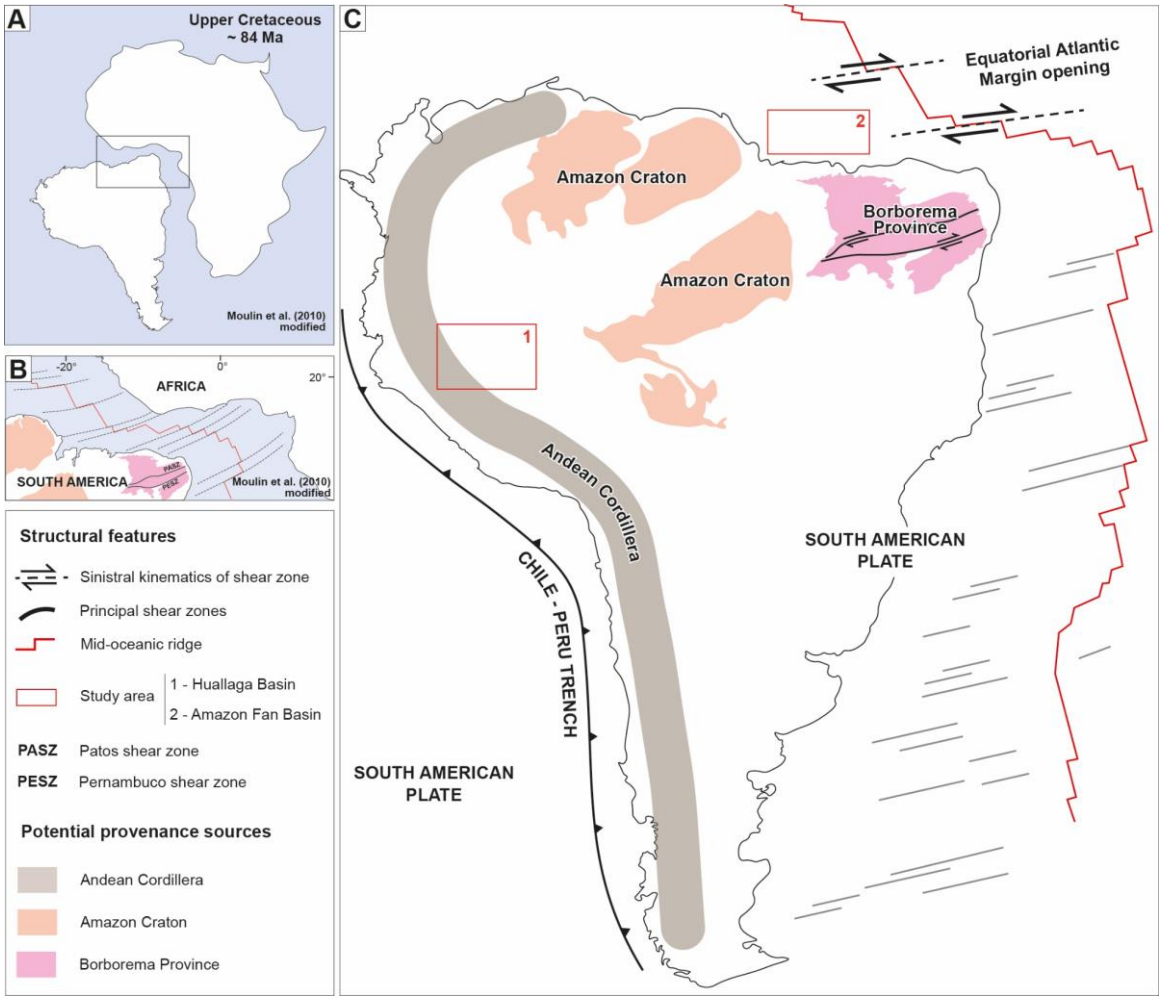


Figura 1. 6 A) Reconstrução paleogeográfica do rifteamento e ruptura dos continentes Sul-Americano e Africano durante o Cretáceo Superior (~ 84 Ma). B) Reconstrução estrutural da Margem Equatorial Sul-Americana, com destaque para os principais lineamentos e falhas associados. C) Mapa paleogeográfico da fase rifte durante a abertura do Oceano Atlântico Sul e Equatorial, indicando as principais zonas de cisalhamento ao longo da dorsal meso-oceânica no limite entre as placas tectônicas Sul-Americana e Africana. Destaque para as potenciais áreas-fontes de sedimentos para a Amazônia Ocidental e Oriental, localizadas na região norte da Plataforma Sul-Americana, sendo representadas, de oeste à leste, pela Cordilheira Andina, Cratón do Amazonas e Província Borborema. As áreas foco do estudo estão destacadas por retângulos vermelhos (1 – Bacia de Huallaga) e (2 – Bacia da Foz do Amazonas). Figura baseada e modificada no modelo de Moulin et al. (2010) e Rosa et al. (2023).

Os rifteamentos ocorridos ao longo do Mesozoico resultaram em considerável deformação diacrônica e formação de bacias sedimentares, em ambas as margens orientais e equatoriais da Plataforma Sul-Americana (Darros de Matos, 2000). No contexto

Ocidental da Margem Equatorial, reconstruções tectono-estratigráficas revelaram que a sua evolução geológica esteve condicionada a fases distensivas, ocorridas do Neotriássico ao final do Eocretáceo (Albiano), dando origem à diversas bacias sedimentares *onshore* (bacias de Barreirinhas, São Luís, Bragança-Viseu e Marajó), *offshore* (bacias do Pará-Maranhão e Foz do Amazonas), bem como a Plataforma Bragantina (Figura 1.7) (Soares Júnior et al., 2011; 2008; Costa et al., 2002; Nogueira et al., 2021).

Ao mesmo tempo que a Amazônia Ocidental na região oeste da América do Sul, Amazônia Ocidental, estava submetida a forte soerguimento do proto-Andes e do escudo brasileiro durante o Cretáceo Superior (Hurtado et al., 2018; Louterbach et al., 2017), a Margem Equatorial Sul-Americana, Amazônia Oriental, era provavelmente área de descarga de grande aporte sedimentar, provenientes da Província Borborema (Figura 1.6). Reconstruções paleogeográficas da região nordeste da plataforma sul-americana apontam expressivo evento regional de soerguimento e denudação, do embasamento Pré-Cambriano e bacias intracontinentais, ocorridos no intervalo do Cretáceo Superior ao Mioceno (Rosa et al., 2023; Japsen et al., 2012; Magnavita et al., 1994).

As deformações tectônicas intraplaca teriam ocorrido como resposta ao estresse envolvido com a ruptura do paleocontinente *Gondwana* e rotação do continente Sul-Americano no sentido horário em relação ao continente Africano e consequente abertura da Margem Equatorial (Figura 1.6) (Rosa et al., 2023; Moulin et al., 2010). A propagação dos campos de tensão intraplaca, reativaram antigas descontinuidades listosféricas, conduzindo a geração de bacias sedimentares intracontinentais, que foram submetidas posteriormente a eventos de inversão (Rosa et al., 2023; Marques et al., 2014). Esta inversão pode ter sido a responsável no soerguimento de potenciais áreas-fonte para a Margem Equatorial, sendo marcada por falhas reversas na Bacia do Rio do Peixe e Bacia do Araripe (Vasconcelos et al., 2019, Nogueira et al., 2015; Marques et al., 2014), soerguimento de sedimentos marinhos Cretáceos (Formação Romualdo) (Custódio et al., 2017; Assine et al., 2014) e mudança radical na paleodrenagem continental, que foi drasticamente alterada de leste-sudeste (ESE) para oeste (W), registrados na Chapada da Bacia do Araripe (Warren et al., 2021; Assine, 1994).

Durante os eventos de soerguimento ocorridos no nordeste da Plataforma Sul-Americana e regimes transtensionais impostos à Margem Equatorial, fases de rifteamento conduziram à origem e evolução da Bacia da Foz do Amazonas, na costa da Amazônia

Oriental (Figuras 1.6, 1.7) (Figueiredo et al., 2009; Brandão and Feijó, 1994). A configuração tectono-estratigráfica da Bacia da Foz do Amazonas revela que esta bacia evoluiu de uma fase rifte para uma fase drifte, no intervalo do Cretáceo Inferior ao Cretaceo Superior (Figueiredo et al., 2007).

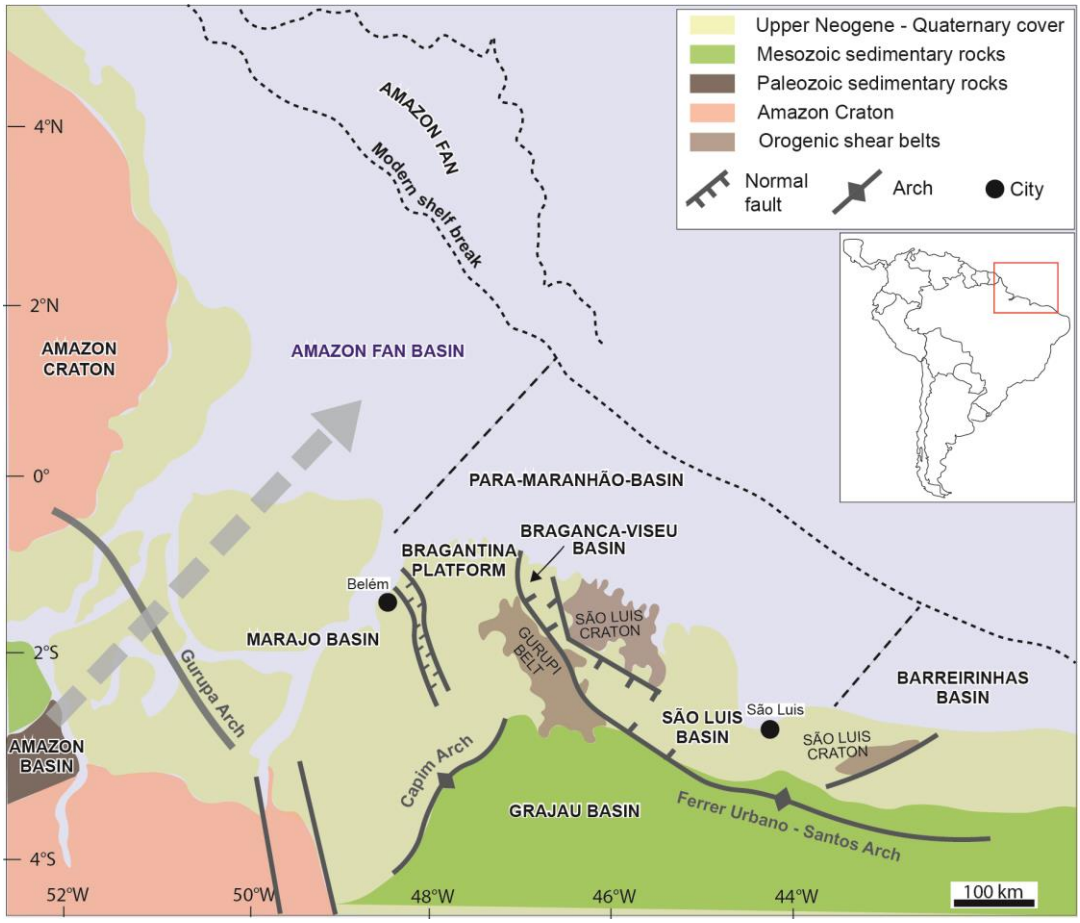


Figura 1. 7 Mapa geológico regional das unidades meso-cenozoicas da costa da Amazônia Oriental, localizadas na Margem Equatorial Sul-Americana, destacando os principais compartimentos estruturais, limites das bacias sedimentares e do Cratón Amazônico. (Modificado de Moizinho et al., 2022; Nogueira et al., 2021; Soares Júnior et al., 2011).

Já no Cenozoico, durante o Paleoceno ao Mioceno (~61.7 to ~8.0 Ma), foi a principal fase de desenvolvimento e consolidação de uma plataforma carbonática, relacionada a evento drifte ocorrido na bacia (Figueiredo et al., 2009; Cruz et al., 2019). No entando, uma grande área da Amazônia Oriental na Margem Equatorial da América do Sul foi afetada por expressivo aporte sedimentar, desta vez oriundos da Cordilheira dos Andes (Mason et al., 2019; 2022). Dados de proveniência sedimentar registram a chegada

dos primeiros sedimentos Andinos na Margem Equatorial (Bacia da Foz do Amazonas), somente no Mioceno superior, entre 11.8 e 8.7 Ma, atestando a consolidação do rio Amazonas como rio transcontinental e dando início ao desenvolvimento do Cone do Amazonas (Figura 1.3B) (Cruz et al., 2019; Hoorn et al., 2017; van Soelen et al., 2017; Stewart et al., 2016; Nogueira et al., 2013; Gorini et al., 2014; Figueiredo et al., 2009). Neste contexto de área-fonte e deposição do eixo Andes-Amazônia-Margem Equatorial Sul-Americana, a Bacia da Foz do Amazonas corresponde a região mais distal deste sistema (Amazônia Oriental).

1.4 OBJETIVOS

A proposta central desta tese consiste em compreender como a evolução geológica das porções oeste e norte da América do Sul influenciaram as configurações paleoambientais e paleogeográficas do sistema S2S do eixo AAMESA. Esse estudo foi baseado na integração de diferentes análises sedimentológicas, paleontológicas, geoquímicas elementar e isotópica. Objetivos específicos incluiram:

a) Compreender a evolução paleoambiental e paleogeográfica ocorridas na Amazônia Ocidental durante o Paleógeno (Capítulo 3);

b) Desvendar e documentar a história erosiva dos Andes Amazônicos durante o Cenozoico (Amazônia Ocidental) (Capítulo 4);

c) Definir as potenciais áreas-fonte de sedimentos na Bacia da Foz do Amazonas (noroeste da Margem Equatorial) e correlacionar com os eventos de soerguimentos e erosivos do norte da plataforma Sul-Americana durante o Cenozoico (Capítulo 5).

REFERÊNCIAS

Albert, J.S., Val, P., Hoorn, C., 2018. The changing course of the Amazon River in the Neogene: center stage for Neotropical diversification. Neotrop. Ichthyol. 16, 1–24. https://doi.org/10.1590/1982-0224-20180033.

Allen, P.A. 2008. Time scales of tectonic landscapes and their sediment routing systems. In: Landscape Evolution: Denudation, Climate and Tectonics Over Di¡erent Time and Space Scales (Ed. by K. Gallagher, S.J. Jones & J.Wainwright), Geol. Soc. London Spec. Publ., 296, 7-28

Allen, P.A., 2017. Sediment Routing Systems. The Fate of Sediments from Source to Sink. Cambridge University Press, Cambridge. https://doi.org/10.1017/9781316135754.

Allen, P.A., Heller, P.L., 2012. The timing, distribution and significance of tectonically generated gravels in terrestrial sediment routing systems. In: Busby, C., Azor, A. (Eds.), Syntectonic

Basin Development, Active to Ancient: Recent Advances. WileyBlackwell, Oxford, pp. 111–130.

Almeida, F.F.M. de, Brito Neves, B.B. de, Dal Ré Carneiro, C., 2000. The origin and evolution of the South American Platform. Earth-Science Reviews 50, 77–111. https://doi.org/10.1016/S0012-8252(99)00072-0

Alves, F.C., Rossetti, D.F., Valeriano, M.M. 2020. Detecting neotectonics in the lowlands of Amazonia through the analysis of river long profiles. Journal of South American Earth Sciences. https://doi.org/10.1016/j.jsames.2020.102553

Alvim, A.M.V., Santos, R.V., Roddaz, M., Antoine, P.-O., Ramos, M.I.F., do Carmo, D.A., Linhares, A.P., Negri, F.R., 2021. Fossil isotopic constraints (C, O and 87Sr/86Sr) on Miocene shallow-marine incursions in Amazonia. Palaeogeography, Palaeoclimatology, Palaeoecology 573, 110422. https://doi.org/10.1016/j.palaeo.2021.110422

Armijo, R., Lacassin, R., Coudurier-Curveur, A., Carrizo, D., 2015. Coupled tectonic evolution of Andean orogeny and global climate. Earth-Science Reviews 143, 1–35. https://doi.org/10.1016/j.earscirev.2015.01.005

Assine, M.L., 1994. Paleocorrentes e paleogeografia na Bacia do Araripe, Nordeste do Brasil. RBG 24, 223–232. https://doi.org/10.25249/0375-7536.1994223232

Assine, M.L., Neumann, H., Varejão, F.G., Mescolotti, P.C., 2014 Sequências deposicionais do Andar Alagoas da Bacia do Araripe, Nordeste do Brasil.

Augustsson, C., Reker, A., 2012. Cathodolumenescence Spectra of Quartz As Provenance Indicators Revisited. Journal of Sedimentary Research 82, 559–570. https://doi.org/10.2110/jsr.2012.51

Augustsson, C., Voigt, T., Bernhart, K., Kreißler, M., Gaupp, R., Gärtner, A., Hofmann, M., Linnemann, U., 2018. Zircon size-age sorting and source-area effect: The German Triassic Buntsandstein Group. Sedimentary Geology 375, 218–231. https://doi.org/10.1016/j.sedgeo.2017.11.004

Bajolet, F., Chardon, D., Rouby, D., Dall'Asta, M., Loparev, A., Couëffe, R., Roig, J.-Y., 2022. The sediment routing systems of Northern South America since 250 Ma. Earth-Science Reviews 232, 104139. https://doi.org/10.1016/j.earscirev.2022.104139

Bayona, G., Cortes, M., Jaramillo, C., Ojeda, G., Aristizabal, J.J., Reyes-Harker, A., 2008. An integrated analysis of an orogen-sedimentary basin pair: Latest Cretaceous-Cenozoic evolution of the linked Eastern Cordillera orogen and the Llanos foreland basin of Colombia. Geological Society of America Bulletin 120, 1171–1197. https://doi.org/10.1130/B26187.1

Beck, S.L., Zandt, G., 2002. The nature of orogenic crust in the central Andes: nature of orogenic crust. J. Geophys. Res. 107, ESE 7-1-ESE 7-16. https://doi.org/10.1029/2000JB000124

Bergmann, F., Schwenk, T., Spiess, V., France-Lanord, C. 2016. The Himalaya-Bengal Fan source to sink system - new insights by correlation of re-processed seismic data and IODP Expedition 354 results. EGU General Assembly 2016, held 17-22 April, 2016 in Vienna Austria, id. EPSC2016-18456.

Bezerra, F.H.R., Amaro, V.E., Vitafinzi, C., Saadi, A., 2001. Pliocene–Quaternary fault control of sedimentation and coastal plain morphology in NE Brazil. J. S. Am. Earth Sci. 14, 61–75.

Bigarella, J.J., 1975. The Barreiras Group in North-eastern Brazil. Anais da Acad. Brasil. de Cien. 47, 366–392.

Boonstra, M., Ramos, M.I.F., Lammertsma, E.I., Antoine, P.-O., Hoorn, C., 2015. Marine connections of Amazonia: evidence from foraminifera and dinoflagellate cysts (early to middle Miocene, Colombia/Peru). Palaeogeogr. Palaeoclimatol. Palaeoecol. 417, 176–194. https://doi.org/10.1016/j.palaeo.2014.10.032.

Boschman, L.M., 2021. Andean mountain building since the Late Cretaceous: A paleoelevation reconstruction. Earth-Science Reviews 220, 103640. https://doi.org/10.1016/j.earscirev.2021.103640

Brandão, J.A.S.L., Feijo, F.J., 1994. Bacia da Foz do Amazonas. Boletim de Geociências da Petrobras 8, 91–100.

Calderón, Y., Baby, P., Vela, Y., Hurtado, C., Eude, A., Roddaz, M., Brusset, S., Calvès, G., Bolaños, R., 2017. Petroleum systems restoration of the Huallaga-Marañon Andean retroforeland basin, Peru, in: Petroleum Systems Analysis—Case Studies, AAPG Memoir 114.

Callède, J., Guyot, J.-L., Ronchail, J., L'Hote, Y., Niel, H., de Oliveira, E., 2004. Evolution du debit de l'Amazonea Obidos de 1902 a 1999. Hydrol. Sci. J. 49, 85–97. https://doi.org/10.1623/hysj.49.1.85.53992

Calvès, G., Calderón, Y., Hurtado Enriquez, C., Brusset, S., Santini, W., Baby, P., 2018. Mass Balance of Cenozoic Andes-Amazon Source to Sink System—Marañón Basin, Peru. Geosciences 8, 167. https://doi.org/10.3390/geosciences8050167

Campbell, K.E. 2010. Late Miocene onset of the Amazon River and the Amazon deep-sea fan: Evidence from the Foz do Amazonas Basin: COMMENT. Geological Society of America. GEOLOGY FORUM, July 2010. doi: 10.1130/G30633C.1

Caputo, M.V., Soares, E.A.A., 2016. Eustatic and tectonic change effects in the reversion of the transcontinental Amazon River drainage system. Braz. J. Geol. 46, 301–328. https://doi.org/10.1590/2317-4889201620160066

Caracciolo, L., Chew, D., Andò, S., 2020. Sediment Generation and Sediment Routing Systems. Earth-Science Reviews 207, 103221. https://doi.org/10.1016/j.earscirev.2020.103221

Chew, D., O'Sullivan, G., Caracciolo, L., Mark, C., Tyrrell, S., 2020. Sourcing the sand: Accessory mineral fertility, analytical and other biases in detrital U-Pb provenance analysis. Earth-Science Reviews 202, 103093. https://doi.org/10.1016/j.earscirev.2020.103093

Chen, Y.-W., Wu, J., Suppe, J., 2019. Southward propagation of Nazca subduction along the Andes. Nature 565, 441–447. https://doi.org/10.1038/s41586-018-0860-1

Chew, D.M., Pedemonte, G., Corbett, E., 2016. Proto-Andean evolution of the Eastern Cordillera of Peru. Gondwana Research 35, 59–78. https://doi.org/10.1016/j.gr.2016.03.016

Christophoul, F., Baby, P., Dávila, C., 2002. Stratigraphic responses to a major tectonic event in a foreland basin: the Ecuadorian Oriente Basin from Eocene to Oligocene times. Tectonophysics 345, 281–298. https://doi.org/10.1016/S0040-1951(01)00217-7

Costa, J.B.S., Hasui, Y., Bemerguy, R.L., Soares-Júnior, A.V., Villegas, J.M.C., 2002. Tectonics and paleogeography of the Marajó Basin, northern Brazil. An. Acad. Bras. Ciênc. 74, 519–531. https://doi.org/10.1590/S0001-37652002000300013

Cruz, A.M., Reis, A.T., Suc, J.P., Silva, C.G., Praeg, D., Granjeon, D., Rabineau, M., Popescu, S.M., Gorini, C., 2019. Neogene evolution and demise of the Amapá carbonate platform, Amazon continental margin, Brazil. Marine and Petroleum Geology 105, 185–203. https://doi.org/10.1016/j.marpetgeo.2019.04.009

Custódio, M.A., Quaglio, F., Warren, L.V., Simões, M.G., Fürsich, F.T., Perinotto, J.A.J., Assine, M.L., 2017. The transgressive-regressive cycle of the Romualdo Formation (Araripe Basin): Sedimentary archive of the Early Cretaceous marine ingression in the interior of Northeast Brazil. Sedimentary Geology 359, 1–15. https://doi.org/10.1016/j.sedgeo.2017.07.010

Custódio, M.A., Roddaz, M., Santos, R.V., Antoine, P.-O., Marivaux, L., Stutz, N.S., Dantas, E.L., Jaramillo, C., Louterbach, M., Hurtado, C., Oliveira Gonçalves, G., 2023. New stratigraphic and paleoenvironmental constraints on the Paleogene paleogeography of Western Amazonia. Journal of South American Earth Sciences 124, 104256. https://doi.org/10.1016/j.jsames.2023.104256

Darros de Matos, R.M., 2000. Tectonic evolution of the equatorial South Atlantic, in: Mohriak, W., Taiwani, M. (Eds.), Geophysical Monograph Series. American Geophysical Union, Washington, D. C., pp. 331–354. https://doi.org/10.1029/GM115p0331

DeCelles, P.G., Ducea, M.N., Kapp, P., Zandt, G., 2009. Cyclicity in Cordilleran orogenic systems. Nature Geosci 2, 251–257. https://doi.org/10.1038/ngeo469

Delgado, A., Mora, A., Reyes-Harker, A., 2012. Deformation partitioning in the Llanos foreland basin during the Cenozoic and its correlation with mountain building in the hinterland.

Journal of South American Earth Sciences 39, 228–244. https://doi.org/10.1016/j.jsames.2012.04.011
DeCelles, P.G., Giles, K.A., 1996. Foreland basin systems. Basin Research 8, 105–123. https://doi.org/10.1046/j.1365-2117.1996.01491.x
Eude, A., Roddaz, M., Brichau, S., Brusset, S., Calderon, Y., Baby, P., Soula, J.-C., 2015. Controls on timing of exhumation and deformation in the northern Peruvian eastern Andean wedge as inferred from low-temperature thermochronology and balanced cross section: Exhumation And Deformation of North Peru. Tectonics 34, 715–730. https://doi.org/10.1002/2014TC003641
Evenstar, L.A., Hartley, A.J., Mather, A.E., 2023. Orogenic-orographic feedback and the rise of the Central Andes. Earth and Planetary Science Letters 602, 117931. https://doi.org/10.1016/j.epsl.2022.117931
Faccenna, C., Oncken, O., Holt, A.F., Becker, T.W., 2017. Initiation of the Andean orogeny by lower mantle subduction. Earth and Planetary Science Letters 463, 189–201. https://doi.org/10.1016/j.epsl.2017.01.041
Fellin, M.G., Zattin, M., Zuffa, G.G., De Ros, L.F., Cupertino, J.A., De Souza, R.S., Morais Neto, J.M., Dalmonte, C. 2023. New detrital petrographic and thermochronologic constraints on the Late Cretaceous–Neogene erosional history of the equatorial margin of Brazil: Implications for the surface evolution of a complex rift margin. Basin Research. 2023;00:1–27. DOI: 10.1111/bre.12808.
Figueiredo, J., Hoorn, C., van der Ven, P., Soares, E., 2009. Late Miocene onset of the Amazon River and the Amazon deep-sea fan: Evidence from the Foz do Amazonas Basin. Geology 37, 619–622. https://doi.org/10.1130/G25567A.1
Figueiredo, J.J.P., Zalán, P.V., Soares, E.F., 2007. Bacia Foz do Amazonas. Boletim de Geociências da Petrobras 15, 299–309.
Filizola, N., Guyot, J.L., 2004. The use of Doppler technology for suspended sediment discharge determination in the River Amazon / L'utilisation des techniques Doppler pour la détermination du transport solide de l'Amazone. Hydrol. Sci. J. 49, 143–153. https://doi.org/10.1623/hysj.49.1.143.53990
Gaillardet, J., Viers, J., Dupré, B., 2007. Trace element in river waters, in: J.I. Drever (Ed), Surface and Ground Water, Weathering, and soils, vol. 5, in: Holland, H.D., Turekian, K.K. (Eds), Treatise on Geochemistry, Pergamon, 225-272
Garzanti, E., 2019. Petrographic classification of sand and sandstone. Earth-Science Reviews 192, 545–563. https://doi.org/10.1016/j.earscirev.2018.12.014
Garzanti, E., 2016. From static to dynamic provenance analysis—Sedimentary petrology upgraded. Sedimentary Geology 336, 3–13. https://doi.org/10.1016/j.sedgeo.2015.07.010
Garzanti, E., Andò, S., 2007. Chapter 20 Heavy Mineral Concentration in Modern Sands: Implications for Provenance Interpretation, in: Developments in Sedimentology. Elsevier, pp. 517–545. https://doi.org/10.1016/S0070-4571(07)58020-9
Garzione, C.N., Hoke, G.D., Libarkin, J.C., Withers, S., MacFadden, B., Eiler, J., Ghosh, P., Mulch, A., 2008. Rise of the Andes. Science 320, 1304–1307. https://doi.org/10.1126/science.1148615
George, S.W.M., Horton, B.K., Jackson, L.J., Moreno, F., Carlotto, V., Garzione, C.N., 2019. Sediment provenance variations during contrasting Mesozoic-early Cenozoic tectonic regimes of the northern Peruvian Andes and Santiago-Marañón foreland basin, in: Andean Tectonics. Elsevier, pp. 269–296. https://doi.org/10.1016/B978-0-12-816009-1.00012-5
Gorini, C., Haq, B.U., dos Reis, A.T., Silva, C.G., Cruz, A., Soares, E., Grangeon, D., 2014. Late Neogene sequence stratigraphic evolution of the Foz do Amazonas Basin, Brazil. Terra Nova 26, 179–185. https://doi.org/10.1111/ter.12083
Gregory-Wodzicki, K.M., 2000. Uplift history of the Central and Northern Andes: A review. Geological Society of America Bulletin.
Gutiérrez, E.G., Horton, B.K., Vallejo, C., Jackson, L.J., George, S.W.M., 2019. Provenance and geochronological insights into Late Cretaceous-Cenozoic foreland basin development in

the Subandean Zone and Oriente Basin of Ecuador, in: Andean Tectonics. Elsevier, pp. 237–268. https://doi.org/10.1016/B978-0-12-816009-1.00011-3

Hermoza, W., Brusset, S., Baby, P., Gil, W., Roddaz, M., Guerrero, N., Bolaños, R. 2005. The Huallaga foreland basin evolution: Thrust propagation in a deltaic environment, northern Peruvian Andes. Journal of South American Earth Sciences 19, 21–34. https://doi.org/10.1016/j.jsames.2004.06.005

Hollanda, M.H.B.M., Archanjo, C.J., Macedo Filho, A.A., Fossen, H., Ernst, R. E., de Castro, D.L., Melo, A.C., Oliveira, A.L., 2019. The Mesozoic Equatorial Atlantic Magmatic Province (EQUAMP): A New Large Igneous Province in South America, in: Srivastava, R.K., Ernst, Richard E., Peng, P. (Eds.), Dyke Swarms of the World: A Modern Perspective, Springer Geology. Springer Singapore, Singapore, pp. 87–110. https://doi.org/10.1007/978-981-13-1666-1_3

Hoorn, C., 1993. Marine incursions and the influence of Andean tectonics on the Miocene depositional history of northwestern Amazonia: results of a palynostratigraphic study. Palaeogeography, Palaeoclimatology, Palaeoecology 105, 267–309. https://doi.org/10.1016/0031-0182(93)90087-Y

Hoorn, C., 1994. An environmental reconstruction of the paleo-Amazon River system (Middle-late Miocene, NW Amazonia). Palaeogeogr. Palaeoclimatol. Palaeoecol. 112, 187–238

Hoorn, C., Bogotá-A, G.R., Romero-Baez, M., Lammertsma, E.I., Flantua, S.G.A., Dantas, E.L., Dino, R., do Carmo, D.A., Chemale, F., 2017. The Amazon at sea: Onset and stages of the Amazon River from a marine record, with special reference to Neogene plant turnover in the drainage basin. Global and Planetary Change 153, 51–65. https://doi.org/10.1016/j.gloplacha.2017.02.005

Hoorn, C., Guerrero, J., Sarmiento, G.A., Lorente, M.A., 1995. Andean tectonics as a cause for changing drainage patterns in Miocene northern South America. Geol 23, 237. https://doi.org/10.1130/0091-7613(1995)023<0237:ATAACF>2.3.CO;2

Hoorn, C., Wesselingh, F.P., ter Steege, H., Bermudez, M.A., Mora, A., Sevink, J., Sanmartín, I., Sanchez-Meseguer, A., Anderson, C.L., Figueiredo, J.P., Jaramillo, C., Riff, D., Negri, F.R., Hooghiemstra, H., Lundberg, J., Stadler, T., Särkinen, T., Antonelli, A., 2010. Amazonia Through Time: Andean Uplift, Climate Change, Landscape Evolution, and Biodiversity. Science 330, 927–931. https://doi.org/10.1126/science.1194585

Horbe, A.M.C., Roddaz, M., Gomes, L.B., Castro, R.T., Dantas, E.L., do Carmo, D.A., 2019. Provenance of the Neogene sediments from the Solimões Formation (Solimões and Acre Basins), Brazil, Journal of South American Earth Sciences, Volume 93. https://doi.org/10.1016/j.jsames.2019.05.004.

Horton, B.K., 2018a. Sedimentary record of Andean mountain building. Earth-Science Reviews 178, 279–309. https://doi.org/10.1016/j.earscirev.2017.11.025

Horton, B.K., 2018b. Tectonic Regimes of the Central and Southern Andes: Responses to Variations in Plate Coupling During Subduction. Tectonics 37, 402–429. https://doi.org/10.1002/2017TC004624

Horton, B.K., DeCelles, P.G. 1997. The modern foreland basin system adjacent to the Central Andes. Geol 25, 895. https://doi.org/10.1130/0091-7613(1997)025<0895:TMFBSA>2.3.CO;2

Horton, B.K., Fuentes, F., Boll, A., Starck, D., Ramirez, S.G., Stockli, D.F., 2016. Andean stratigraphic record of the transition from backarc extension to orogenic shortening: A case study from the northern Neuquén Basin, Argentina. Journal of South American Earth Sciences 71, 17–40. https://doi.org/10.1016/j.jsames.2016.06.003

Horton, B.K., Parra, M., Mora, A., 2020. Construction of the Eastern Cordillera of Colombia: Insights from the Sedimentary Record, in: The Geology of Colombia. Servicio Geológico Colombiano, Bogotá, p. 22. https://doi.org/10.32685/pub.esp.37.2019.03

Hovikoski, J., P, W.F., Matti, R., Murray, G., B, V.H., 2011. Marine influence in Amazonia: Evidence from the Geological Record, in: Amazonia: Landscape and Species Evolution. Wiley-Blackwell, pp. 143–161. https://doi.org/10.1002/9781444306408.ch9

Hurtado, C., Roddaz, M., Santos, R.V., Baby, P., Antoine, P.-O., Dantas, E.L., 2018. Cretaceous-early Paleocene drainage shift of Amazonian rivers driven by Equatorial Atlantic Ocean opening and Andean uplift as deduced from the provenance of northern Peruvian sedimentary rocks (Huallaga basin). Gondwana Research 63, 152–168. https://doi.org/10.1016/j.gr.2018.05.012

Jaillard, E., 1993. L'évolution tectonique de la marge péruvienne au sénonien et paléocène et ses relations avec la géodynamique. Bulletin de la Societe Geologique de France 164, 819–830.

Jaillard, E., Hérail, G., Monfret, T., Dlaz-Martfnez, E. 2000. Tectonic evolution of the Andes of Ecuador, Peru, Bolivia and Northernmost Chile, in: Tectonic Evolution of South America. Rio de Janeiro, pp. 481–559.

Jaillard, E., Soler, P., 1996. Cretaceous to early Paleogene tectonic evolution of the northern Central Andes (0–18°S) and its relations to geodynamics. Tectonophysics 259, 41–53. https://doi.org/10.1016/0040-1951(95)00107-7

Japsen, P., Bonow, J.M., Green, P.F., Cobbold, P.R., Chiossi, D., Lilletveit, R., Magnavita, L.P., Pedreira, A., 2012. Episodic burial and exhumation in NE Brazil after opening of the South Atlantic. Geological Society of America Bulletin 124, 800–816. https://doi.org/10.1130/B30515.1

Jaramillo, C., Romero, I., D'Apolito, C., Bayona, G., Duarte, E., Louwye, S., Escobar, J., Luque, J., Carrillo-Briceño, J.D., Zapata, V., Mora, A., Schouten, S., Zavada, M., Harrington, G., Ortiz, J., Wesselingh, F.P., 2017. Miocene flooding events of western Amazonia. Sci. Adv. 3, e1601693. https://doi.org/10.1126/sciadv.1601693

Jerolmack, D.J., Paola, C., 2010. Shredding of environmental signals by sediment transport. Geophys. Res. Lett. 37, L19401. https://doi.org/10.1029/2010GL044638.

Johnsson, M.J., 1993. The system controlling the composition of clastic sediments. In: Johnsson, M.J., Basu, A. (Eds.), Processes Controlling the Composition of Clastic Sediments. 284. Geological Society of America, Special Paper, pp. 1–19.

Kontak, D.J., Clark, A.H., Farrar, E., Archibald, D.A., Baadsgaard, H. 1990. Late Paleozoic-early Mesozoic magmatism in the Cordillera de Carabaya, Puno, southeastern Peru: Geochronology and petrochemistry. Journal of South American Earth Sciences, Vol. 3, No. 4, pp. 213-230.

Louterbach, M., Roddaz, M., Antoine, P.-O., Marivaux, L., Adnet, S., Bailleul, J., Dantas, E., Santos, R.V., Chemale, F., Baby, P., Sanchez, C., Calderon, Y., 2017. Provenance record of late Maastrichtian-late Palaeocene Andean Mountain building in the Amazonian retroarc foreland basin (Madre de Dios basin, Peru). Terra Nova 30, 17–23. https://doi.org/10.1111/ter.12303

Lu, G.; Di Capua, A.; Winkler, W.; Rahn, M.; Guillong, M.; von Quadt, A.; Willet, S.D. Restoring the source-to-sink relationships in the Paleogene foreland basins in the Central and Southern Alps (Switzerland, Italy, France): A detrital zircon study approach. Int. J. Earth Sci. 2019, 108, 1817–1834.

Mabesoone, J.M., Campos, E., Silva, A., Beurlen, K., 1972. Estratigrafia e origem do Grupo Barreiras em Pernambuco, Paraíba e Rio Grande do Norte. Rev. Bras. Geoci. 2, 173–190.

Macellari, C.E., 2021. Recent uplift and the origin of hydrodynamic traps in the Llanos Basin of Colombia. Marine and Petroleum Geology 132, 105198. https://doi.org/10.1016/j.marpetgeo.2021.105198

Magnavita, L.P., Davison, I., Kusznir, N.J., 1994. Rifting erosion and uplift history of the Rec ncavo-Tucano-Jatob Rift northeast.pdf. Tectonics 13, 367–388.

Marques, F.O., Nogueira, F.C.C., Bezerra, F.H.R., de Castro, D.L., 2014. The Araripe Basin in NE Brazil: An intracontinental graben inverted to a high-standing horst. Tectonophysics 630, 251–264. https://doi.org/10.1016/j.tecto.2014.05.029

Martínez, F., López, C., Torres, C., González, R., Peña, M. 2023. Understanding the initial upper plate architecture and shortening distribution in subduction-related orogens:

Insights from the Central Andean forearc. Tectonophysics 863 (2023) 230001. https://doi.org/10.1016/j.tecto.2023.230001
Mason, C.C., Romans, B.W., Stockli, D.F., Mapes, R.W., Fildani, A., 2019. Detrital zircons reveal sea-level and hydroclimate controls on Amazon River to deep-sea fan sediment transfer. Geology 47, 563–567. https://doi.org/10.1130/G45852.1
Mason, C.C., Romans, B.W., Patterson, M.O., Stockli, D.F., Fildani, A., 2022. Cycles of Andean mountain building archived in the Amazon Fan. Nat Commun 13, 6983. https://doi.org/10.1038/s41467-022-34561-6
McLennan, S.M., Hemming, S., McDaniel, D.K., Hanson, G.N., 1993. Geochemical approaches to sedimentation, provenance, and tectonics, in: Geological Society of America Special Papers. Geological Society of America, pp. 21–40. https://doi.org/10.1130/SPE284-p21
McHone, J.G., 2000. Non-plume magmatism and rifting during the opening of the central Atlantic Ocean. Tectonophysics 316, 287–296. https://doi.org/10.1016/S0040-1951(99)00260-7
Miall, A.D., 1978. Lithofacies types and vertical profile models in braided river deposits: a summary. Fluv. Sedimentol. 5, 597–600.
Miall, A.D., 1996. The Geology of Fluvial Deposits, Sedimentary Facies, Basin Analysis and Petroleum Geology. Sprin-ger, Berlin.
Miall, A.D., 2006. The Geology of Fluvial Deposits. Springer Berlin Heidelberg, Berlin, Heidelberg. https://doi.org/10.1007/978-3-662-03237-4
Milliman, J.D., Syvitski, J.P.M., 1992. Geomorphyc/tectonic control of sediment discharge to the ocean: the importance of small mountainous rivers. J. Geol. 100, 525–544.
Moizinho, G.R., Vieira, L.C., Santos, R.V., Nogueira, A.C.R., Dantas, E.L., Roddaz, M., 2022. Provenance of Miocene-Pleistocene siliciclastic deposits in the Eastern Amazonia coast (Brazil) and paleogeographic implications. Palaeogeography, Palaeoclimatology, Palaeoecology 587, 110799. https://doi.org/10.1016/j.palaeo.2021.110799
Moquet, J.-S., Crave, A., Viers, J., Seyler, P., Armijos, E., Bourrel, L., Chavarri, E., Lagane, C., Laraque, A., Casimiro, W.S.L., Pombosa, R., Noriega, L., Vera, A., Guyot, J.-L., 2011. Chemical weathering and atmospheric/soil CO2 uptake in the Andean and Foreland Amazon basins. Chemical Geology 287, 1–26. https://doi.org/10.1016/j.chemgeo.2011.01.005
Mora, A., Baby, P., Roddaz, M., Parra, M., Brusset, S., Hermoza, W., Espurt, N., 2010. Tectonic History of the Andes and Sub-Andean Zones: Implications for the Development of the Amazon Drainage Basin, in: Hoorn, C., Wesselingh, F.P. (Eds.), Amazonia: Landscape and Species Evolution. Wiley-Blackwell Publishing Ltd., Oxford, UK, pp. 38–60. https://doi.org/10.1002/9781444306408.ch4
Mora, A., Villagómez, D., Parra, M., Caballero, V.M., Spikings, R., Horton, B.K., Mora-Bohorquez, J.A., Ketcham, R.A., Arias-Martinez, J.P., 2020. Late Cretaceous to Cenozoic Uplift of the Northern Andes: Paleogeographic Implications, in: The Geology of Colombia. Servicio Geológico Colombiano, Bogotá, pp. 89–121.
Moreno, F., Garzione, C.N., George, S.W.M., Horton, B.K., Williams, L., Jackson, L.J., Carlotto, V., Richter, F., Bandeian, A., 2020. Coupled Andean Growth and Foreland Basin Evolution, Campanian–Cenozoic Bagua Basin, Northern Peru. Tectonics 39. https://doi.org/10.1029/2019TC005967
Moulin, M., Aslanian, D., Unternehr, P., 2010. A new starting point for the South and Equatorial Atlantic Ocean. Earth-Science Reviews 98, 1–37. https://doi.org/10.1016/j.earscirev.2009.08.001
Nogueira, F.C., Bezerra, F.H.R., Fuck, R.A., 2010. Quaternary fault kinematics and chronology in intraplate northeastern Brazil. J. Geod. 49, 79–91. https://doi.org/10.1016/j.jog.2009.11.002.
Nogueira, A.R., Silveira, R., Guimarães, J.T.F., 2013. Neogene-Quaternary sedimentary and paleovegetation history of the eastern Solimões Basin, central Amazon region. J. South Am. Earth Sci. 46, 89–99.

Nogueira, A.C.R., Amorim, K.B., Góes, A.M., Truckenbrodt, W., Petri, S., Nogueira, A.A.E., Bandeira, J., Soares, J.L., Baía, L.B., Imbiriba Júnior, M., Bezerra, I.S., Ribas, C.C., Cracraft, J., 2021. Upper Oligocene-Miocene deposits of Eastern Amazonia: Implications for the collapse of Neogene carbonate platforms along the coast of northern Brazil. Palaeogeography, Palaeoclimatology, Palaeoecology 563, 110178. https://doi.org/10.1016/j.palaeo.2020.110178

Nogueira, F.C.C., Marques, F.O., Bezerra, F.H.R., de Castro, D.L., Fuck, R.A., 2015. Cretaceous intracontinental rifting and post-rift inversion in NE Brazil: Insights from the Rio do Peixe Basin. Tectonophysics 644–645, 92–107. https://doi.org/10.1016/j.tecto.2014.12.016

Nürnberg, D., Müller, R.D., 1991. The tectonic evolution of the South Atlantic from Late Jurassic to present. Tectonophysics 191, 27–53. https://doi.org/10.1016/0040-1951(91)90231-G

Odlum, M.L., Stockli, D.F., Capaldi, T.N., Thomson, K.D., Clark, J., Puigdefàbregas, C., Fildani, A. 2019. Tectonic and sediment provenance evolution of the South Eastern Pyrenean foreland basins during rift margin inversion and orogenic uplift, Tectonophysics, Volume 765, Pages 226-248 https://doi.org/10.1016/j.tecto.2019.05.008.

Paula de Sá, N., Carvalho, M.A., Correia, G.C. 2020. Miocene paleoenvironmental changes in the Solimões Basin, western Amazon, Brazil: A reconstruction based on palynofacies analysis, Palaeogeography, Palaeoclimatology, Palaeoecology, volume 537, https://doi.org/10.1016/j.palaeo.2019.109450.

Perez, N.D., Horton, B.K., McQuarrie, N., Stübner, K., Ehlers, T.A., 2016. Andean shortening, inversion and exhumation associated with thin- and thick-skinned deformation in southern Peru. Geol. Mag. 153, 1013–1041. https://doi.org/10.1017/S0016756816000121

Pfiffner, O., Gonzalez, L., 2013. Mesozoic–Cenozoic Evolution of the Western Margin of South America: Case Study of the Peruvian Andes. Geosciences 3, 262–310. https://doi.org/10.3390/geosciences3020262

Potter, P.E., 1997. The Mesozoic and Cenozoic paleodrainage of South America: a natural history. Journal of South American Earth Sciences 10, 331–344. https://doi.org/10.1016/S0895-9811(97)00031-X

Ramos, V.A., Folguera, A., 2009. Andean flat-slab subduction through time. SP 327, 31–54. https://doi.org/10.1144/SP327.3

Roddaz, M., Hermoza, W., Mora, A., Baby, P., Parra, M., Christophoul, F., et al., 2010. Cenozoic sedimentary evolution of the amazonian foreland basin system. Amazon. Landsc. Species Evol. Look Past 61–88. https://doi.org/10.1002/9781444306408. ch5.

Roddaz, M., Baby, P., Brusset, S., Hermoza, W., Maria Darrozes, J., 2005. Forebulge dynamics and environmental control in Western Amazonia: The case study of the Arch of Iquitos (Peru). Tectonophysics 399, 87–108. https://doi.org/10.1016/j.tecto.2004.12.017

Roddaz, M., Brusset, S., Baby, P., Hérail, G. (2006) Miocene tidal-influenced sedimentation to continental Pliocene sedimentation in the forebulge-backbulge depozones of the Beni-Mamore foreland basin (northern Bolivia). J S Am Earth Sci 20, 79–96.

Roddaz, M., Christophoul, F., Burgos Zambrano, J.D., Soula, J.-C., Baby, P., 2012. Provenance of late Oligocene to quaternary sediments of the Ecuadorian Amazonian foreland basin as inferred from major and trace element geochemistry and Nd–Sr isotopic composition. J. South Am. Earth Sci. 37, 136–153. https://doi.org/10.1016/j.jsames.2012.02.008

Roddaz, M., Dera, G., Mourlot, Y., Calvès, G., Kim, J.-H., Chaboureau, A.-C., Mounic, S., Raisson, F., 2021. Provenance constraints on the Cretaceous-Paleocene erosional history of the Guiana Shield as determined from the geochemistry of clay-size fraction of sediments from the Arapaima-1 well (Guyana-Suriname basin). Marine Geology 434, 106433. https://doi.org/10.1016/j.margeo.2021.106433

Rodrigues, M. de A., Roddaz, M., Santos, R.V., Louterbach, M., D'Apolito, C., Brusset, S., Dantas, E.L., Negri, F.R., 2023. New insights into the Cretaceous evolution of the Western Amazonian paleodrainage system. Sedimentary Geology 453, 106434. https://doi.org/10.1016/j.sedgeo.2023.106434

Rosa, M.C., Morales, N., Assine, M.L., 2023. Transtensional tectonics during the Gondwana breakup in northeastern Brazil: Early Cretaceous paleostress inversion in the Araripe Basin. Tectonophysics 846, 229666. https://doi.org/10.1016/j.tecto.2022.229666

Rossetti, D. F.; Valeriano, M. M. 2007. Evolution of the lowest amazon basin modeled from the integration of geological and SRTM topographic data. Catena, v. 70, p. 253-265.

Rossetti, D.F., Bezerra, F.H.R., Dominguez, J.M.L., 2013. Late Oligocene–Miocene transgressions along the equatorial and eastern margins of Brazil. Earth-Sci. Rev. 123, 87–112. https://doi.org/10.1016/j.earscirev.2013.04.005.

Rossetti, D.F., 2006. Evolução Sedimentar Miocenica nos Estados do Para e Maranhao. Rev. do Inst. Geociencias, USP 6 (2), 7–18. https://doi.org/10.5327/S1519874X2006000300003.

Rossetti, D.F., Goes, A.M., 2004. Geologia. In: Rossetti; Goes. (Org.). O Neogeno da Amazonia Oriental. 1ed. Bel´em: Editora Museu Goeldi, 1, pp. 13–52.

Rossetti, D.F., Souza, L.S.B., Elis, V.R., 2012. Neotectonics in the Northern Equatorial Brazilian margin. J. S. Am. Earth Sci. 37, 175–190. https://doi.org/10.1016/j.jsames.2012.03.004.

Rossetti, D.F., Vasconcelos, D.L., Bezerra, F.H.R., Valeriano, M.M., Alves, F.C., Molina, E.C. 2022. A large-scale domal relief due to intraplate neotectonic compression in central Amazonia, Geomorphology, Volume 407. https://doi.org/10.1016/j.geomorph.2022.108218.

Rouby, D., Loparev, A., Chardon, D., Bajolet, F., Dall'Asta, M., Paquet, F., Fillon, C., Roig, J.-Y., Ye, J., 2023. Sediment routing systems to the Atlantic rifted margin of the Guiana Shield. Geosphere. https://doi.org/10.1130/GES02561.1

Sacek, V., 2014. Drainage reversal of the Amazon River due to the coupling of surface and lithospheric processes. Earth and Planetary Science Letters 401, 301–312. https://doi.org/10.1016/j.epsl.2014.06.022

Shephard, G.E., Müller, R.D., Liu, L., Gurnis, M., 2010. Miocene drainage reversal of the Amazon River driven by plate–mantle interaction. Nature Geosci 3, 870–875. https://doi.org/10.1038/ngeo1017

Sklar, L.S., Riebe, C.S., Marshall, J.A., Genetti, J., Leclere, S., Lukens, C.L., Merces, V., 2017. The problem of predicting the particle size distribution of sediment supplied by hillslopes to rivers. Geomorphology 277, 31–49.

Soares Júnior, A.V., Costa, J.B.S., Hasui, Y., 2008. Evolução da Margem Atlântica Equatorial do Brasil: Três Fases Distensivas. Geociências 27, 427–437.

Soares Júnior, A.V., Hasui, Y., Costa, J.B.S., Machado, F.B., 2011. Evolução do rifteamento e paleogeografia da margem Atlântica Equatorial do Brasil: Triassico ao Holoceno. São Paulo 30.

Sømme, T.O., Helland-Hansen, W., Martinsen, O.J., Thurmond, J.B., 2009. Relationships between morphological and sedimentological parameters in source-to-sink systems: a basis for predicting semi-quantitative characteristics in subsurface systems. Basin Research 21, 361–387. https://doi.org/10.1111/j.1365-2117.2009.00397.x

Sømme, T.O., Jackson, C.A.-L., 2013. Source-to-sink analysis of ancient sedimentary systems using a subsurface case study from the Møre-Trøndelag area of southern Norway: Part 2 - sediment dispersal and forcing mechanisms. Basin Res 25, 512–531. https://doi.org/10.1111/bre.12014

Stewart, J.A., Gutjahr, M., James, R.H., Anand, P., Wilson, P.A., 2016. Influence of the Amazon River on the Nd isotope composition of deep water in the western equatorial Atlantic during the Oligocene–Miocene transition. Earth and Planetary Science Letters 454, 132–141. https://doi.org/10.1016/j.epsl.2016.08.037

Tcheumeleu, A.F., Fauquette, S., Castillo, A.A., Martinez, C., Moreno, F., Navarrete, R.E., Parra, F., Wesselingh, F.P., Salas-Gismondi, R., Varas-Malca, R., Roddaz, M., Antoine, P.-O., 2020. Depositional environments and landscapes of the upper Miocene Ipururo Formation at Shumanza, Subandean Zone, northern Peru. Palaeobio Palaeoenv 100, 719–735. https://doi.org/10.1007/s12549-019-00400-8

Trompette, R. 2000. Gondwana evolution; its assembly at around 600 Ma. Comptes Rendus de l'Académie des Sciences - Series IIA - Earth and Planetary Science, Volume 330, Issue 5, Pages 305-315. https://doi.org/10.1016/S1251-8050(00)00125-7

Val, P., Figueiredo, J., Melo, G., Flantua, S., Quesada, C.A., Reinfelder, Y.F., Albert, J.S., Guayasamin, J.M., Hoorn, C., 2021. Chapter 1: Geology and geodiversity of the Amazon: Three billion years of history, in: Nobre, C., Encalada, A., Anderson, E., Roca Alcazar, F.H., Bustamante, M., Mena, C., Peña-Claros, M., Poveda, G., Rodriguez, J.P., Saleska, S., Trumbore, S.E., Val, A., Villa Nova, L., Abramovay, R., Alencar, A., Rodriguez Alzza, A.C., Armenteras, D., Artaxo, P., Athayde, S., Barretto Filho, H.T., Barlow, J., Berenguer, E., Bortolotto, F., Costa, F. de A., Costa, M.H., Cuvi, N., Fearnside, P., Ferreira, J., Flores, B.M., Frieri, S., Gatti, L.V., Guayasamin, J.M., Hecht, S., Hirota, M., Hoorn, C., Josse, C., Lapola, D.M., Larrea, C., Larrea-Alcazar, D.M., Lehm Ardaya, Z., Malhi, Y., Marengo, J.A., Melack, J., Moraes R., M., Moutinho, P., Murmis, M.R., Neves, E.G., Paez, B., Painter, L., Ramos, A., Rosero-Peña, M.C., Schmink, M., Sist, P., ter Steege, H., Val, P., van der Voort, H., Varese, M., Zapata-Ríos, G. (Eds.), Amazon Assessment Report 2021. UN Sustainable Development Solutions Network (SDSN). https://doi.org/10.55161/POFE6241

Vallejo, C., Romero, C., Horton, B.K., Spikings, R.A., Gaibor, J., Winkler, W., Esteban, J.J., Thomsen, T.B., Mariño, E., 2021. Jurassic to Early Paleogene sedimentation in the Amazon region of Ecuador: Implications for the paleogeographic evolution of northwestern South America. Global and Planetary Change 204, 103555. https://doi.org/10.1016/j.gloplacha.2021.103555

Valero, L., Beamud, E., Garcés, M., Vinyoles, A., Sharma, N., Watkins, S. E., Tremblin, M., Puigdefàbregas, C., Guillocheau, F., Whitakker, A. C., López-Blanco, M., Arbués, P., and Castelltort, S.: Origin and propagation of sedimentary sequences throughout the Escanilla fluvial routing system (South Pyrenean foreland basin), EGU General Assembly 2020, Online, 4–8 May 2020, EGU2020-19537, https://doi.org/10.5194/egusphere-egu2020-19537, 2020.

van Soelen, E.E., Kim, J.-H., Santos, R.V., Dantas, E.L., Vasconcelos de Almeida, F., Pires, J.P., Roddaz, M., Sinninghe Damsté, J.S., 2017. A 30 Ma history of the Amazon River inferred from terrigenous sediments and organic matter on the Ceará Rise. Earth and Planetary Science Letters 474, 40–48. https://doi.org/10.1016/j.epsl.2017.06.025

Vasconcelos, D.L., Bezerra, F.H.R., Medeiros, W.E., de Castro, D.L., Clausen, O.R., Vital, H., Oliveira, R.G., 2019. Basement fabric controls rift nucleation and postrift basin inversion in the continental margin of NE Brazil. Tectonophysics 751, 23–40. https://doi.org/10.1016/j.tecto.2018.12.019

Vermeesch, P., Garzanti, E., 2015. Making geological sense of 'Big Data' in sedimentary provenance analysis. Chemical Geology 409, 20–27. https://doi.org/10.1016/j.chemgeo.2015.05.004

von Eynatten, H., Dunkl, I., 2012. Assessing the sediment factory: The role of single grain analysis. Earth-Science Reviews 115, 97–120. https://doi.org/10.1016/j.earscirev.2012.08.001

Warren, L.V., de Andrade, A.S.M., Varejão, F.G., Promenzio, P., Santos, M.G.M., Alessandretti, L., Assine, M.L., 2021. Sedimentary evolution of distributive fluvial systems within intraplate tectonic active basins: Case study of the Early Cretaceous Araripina Formation (Araripe Basin, NE Brazil). Journal of South American Earth Sciences 111, 103496. https://doi.org/10.1016/j.jsames.2021.103496

Wesselingh, F.P., Guerrero, J., Räsänen, M., Pitmann, L.R., Vonhof, H., 2006. Landscape evolution and depositional processes in the Miocene Amazonian Pebas lake/wetland system: evidence from exploratory boreholes in northeastern Peru. Scripta Geologica 133, 323–361.

Wesselingh, F.P., Räsänen, M.E., Irion, G., Vonhof, H.B., Kaandorp, R., Renema, W., Pittman, L.R., Gingras, M., 2001. Lake Pebas: a palaeoecological reconstruction of a Miocene, long-lived lake complex in western Amazonia. Cenozoic Research 1, 35–81.

Weltje, G.J., 2012. Quantitative models of sediment generation and provenance: State of the art and future developments. Sedimentary Geology 280, 4–20. https://doi.org/10.1016/j.sedgeo.2012.03.010
Weltje, G.J., von Eynatten, H., 2004. Quantitative provenance analysis of sediments: review and outlook. Sedimentary Geology 171, 1–11. https://doi.org/10.1016/j.sedgeo.2004.05.007

CAPÍTULO 2

MATERIAIS E MÉTODOS

Matériel et méthodes

2. MATERIAIS E MÉTODOS / MATERIEL ET METHODES

RÉSUMÉ

Ce chapitre traite de l'acquisition des échantillons (affleurements et puits) et de la méthodologie utilisée pour déterminer la provenance des sédiments et reconstituer les paléoenvironnements Cénozoïques amazoniens. A cause de la pandémie, une seule mission de terrain pour échantillonner et préciser les paléoenvironnements amazoniens a pu être effectuée (en août 2019). Les autres missions prévues ont dû être annulées. L'acquisition des échantillons de puits (« cuttings » auprès de l'ANP (Agence Nationale des pétrôles et gaz brésilienne qui s'occupe du stockage et de la mise à disposition des données du sous sol brésilien) s'est révélé particulièrement chronophage (deux ans de processus) à cause de la bureaucratie et de la pandémie. Les échantillons de puits furent finalement mis à disposition en mars 2023. En ce qui concerne, la partie méthodologie sensu stricto, j'ai choisi de ne pas présenter de résumé en français de chaque méthode utilisée car ces résumés se trouvent en anglais dans les chapitre suivants (article publié au *Journal of South American Earth Sciences* (https://doi.org/10.1016/j.jsames.2023.104256), article en cours de soumission à *Gondwana Research* et article en préparation).

De uma perspectiva *source-to-sink,* este projeto baseia-se numa abordagem integrada visando a reconstrução das variações ambientais e de fontes ocorridas ao longo do Cenozoico na área de estudo.

i) A primeira abordagem é uma análise paleoambiental para determinar as variações dos ambientes deposicionais em função das condições geodinâmicas ocorridas ao longo da evolução do sistema AAMESA;
ii) A segunda abordagem consiste no estudo da proveniência sedimentar para reconstrução paleogeográfica e determinação as principais áreas-fontes contribuintes de sedimentos ao sistema AAMESA ao longo do Cenozoico.

Neste cenário, dada a complexidade da área e do tema, foram delimitadas áreas-chaves, consideradas como setores representativos, para reconstruir a evolução geológica do sistema fonte – deposição AAMESA.

2.1 AQUISIÇÃO DE DADOS

2.1.1 Definição da área de estudo

A definição de setores representativos que permitessem a reconstituição da área-fonte e de deposição dos sedimentos no eixo AAMESA foi baseada em artigos científicos previamente publicados na literatura. As Bacias de Huallaga, localizada zona sub-Andina Peruana, porção leste da Cordilheira dos Andes e a Bacia da Foz do Amazonas, localizada na porção noroeste da Margem Equatorial Brasileira, registram nos depósitos os principais eventos geológicos ocorridos na porção norte da plataforma Sul-Americana; Amazônia Ocidental (proximal) e Oriental (distal), respectivamente (Figura 1.2) (Cruz et al., 2019; Hurtado et al., 2018; Horton, 2018; Hoorn et al., 2017; van Soelen et al., 2017; Stewart et al., 2016; Nogueira et al., 2013; Gorini et al., 2014; Figueiredo et al., 2009; Hermoza et al., 2005). Neste cenário, a análise dos depósitos Cenozoicos destas bacias fornece informações relevantes para a reconstrução da evolução do sistema *source-to-sink* AAMESA.

No que concerne aos dados adquiridos em campo, uma seção estratigráfica completa do final do Cretáceo ao longo do Cenozoico foi levantada e amostrada em detalhe na Amazônia Ocidental (Capítulos 3 e 4). A aquisição de dados em trabalho de campo foi realizada em agosto de 2019, em co-participação com uma equipe multidisciplinar de pesquisadores paleontólogos do *Institut des Sciences de l'Evolution de Montpellier, Universié Montpellier* - França (Laurent MARIVAUX, Pierre-Olivier ANTOINE), da Universidade Federal do Rio Grande do Sul - Brasil (Narla STUTZ), do *Consejo Nacional de Investigaciones Científicas y Técnicas* - Argentina (François PUJOS) e da *Universidad Nacional Mayor de San Marcos* - Peru (Aldo BENITES-PALOMINO), juntamente com a presença do orientador Martin RODDAZ da *Université de Toulouse, Géosciences-Environnement Toulouse* (Fig. 2.1B).

Denominada seção Juanjuí, localizada na Bacia de Huallaga, zona sub-Andina Peruana, porção leste da Cordilheira dos Andes, a mesma possui espessura aproximada de 1700 m. (Figuras 1.4; 3.2 e 3.4). O trabalho de campo realizado em 2019, focou nos afloramentos ao longo da estrada nacional 5N próxima ao rio Huallaga e as cidades de Juanjuí e Tarapoto (Peru), com áreas denominadas de Juanjuí, Abramachungo, Juan Guerra e Shapaja (Figuras 3.2 e 3.4; Dados suplementares Capítulo 3). A coleta de amostras foi realizada em diferentes níveis estratigráficos, visando um estudo sistemático da sequência.

Esta abordagem forneceu informações das distribuições de idades dos zircões detríticos e variações isotópicas ao longo da seção vertical, da base para o topo.



Figura 2. 2 Fotos representativas da área de estudo, equipe de trabalho e procedimentos de coleta e preparação de amostras realizados na região de Juanjuí, Bacia de Huallaga (Peru). A) Vista panorâmica do rio Huallaga; B) Equipe multidisciplinar que participou nas etapas de preparação, execução e finalização do trabalho de campo realizado em agosto de 2019 nos afloramentos da Bacia de Huallaga, nas regiões de Juanjuí e Tarapoto – Peru; C) Etapa de coleta de amostras e dados para análises paleontológicas e geológicas (petrográficas e geoquímica isotópica) em afloramento de carbonatos com camadas basculadas, da sequência sedimentar Maastrichtiano – Eoceno; D) Etapa de bateamento (preparação) de amostras para obtenção de concentrados de minerais pesados com auxílio da bateia.

2.1.2 Dados técnicos e amostras de poços

Na região de deposição do sistema AAMESA (Bacia da Foz do Amazonas) foi necessária a aquisição de poços exploratórios para acesso aos depósitos *offshore*. Os dados técnicos e amostras da Bacia da Foz do Amazonas (*offshore*) foram solicitados à Agência Nacional de Petróleo, Gás Natural e Biocombustíveis (ANP) e à Petrobras. Afim de

abranger todo o intervalo de tempo do Cenozoico, os parâmetros de aquisição das amostras foram baseados em suas posições no modelo de idade bioestratigráfico proposto por Figueiredo et al. (2007) (Poço 33E) e no modelo de idade proposto por Cruz et al. (2019) com base na correlação sísmica de superficies cronoestratigráficas. Critérios adicionais para a seleção das amostras, também foram levados em consideração, tais como: disponibilidade dos intervalos recuperados; quantidade suficiente da amostra; com exemplares da base, meio e topo da unidade. As amostras foram obtidas de cinco poços exploratórios localizados da plataforma interna à externa da Bacia da Foz do Amazonas, nos setores NW e Central. Com base nestes dados foram selecionados os poços e intervalos de interesse para amostragem. Os poços solicitados são identificados como: 1APS 0018AP; 1APS 0023AP; 1APS 0024AP; 1APS25AP e 1APS33EAP. A codificação dos poços (Figura 2.2) é definida pela Resolução ANP nº 699/2017.

O processo de solicitação seguiu as normas estabelecidas pela Resolução N° 71/2014 – ANP, o qual consiste em três grandes etapas: i) Cadastro de Usuario Externo ii) Solicitação de Dados Técnicos (SDT); iii) Solicitação de Acesso às Amostras (SAA) (Figura 2.2). A Solicitação de Dados Técnicos (SDT) necessita do registro como Usuário Externo junto ao Sistema Eletrônico de Informações (SEI) da ANP (10/2019) e da confirmação do cadastro (03/2020). Após a confirmação e autorização pela ANP, os seguintes Dados Técnicos são recebidos (10/2020): identificação do código do poço (ID), a profundidade da amostra (m), posição geográfica, descrição litológica, seções estratigráficas, respectivos relatórios e arquivos complementares.

A etapa seguinte consistiu no Cadastro de Solicitante (CSOL) (11/2020) e na Solicitação de Acesso às Amostras (SAA) (12/2020) (Figura 2.2). Devido a entraves burocráticos, logísticos e a crise sanitária COVID-19, esta etapa foi custosa e demorada, causando atraso nas análises. Esta etapa consistiu em novo registro junto ao setor de Amostras e Fluidos da ANP, denominado Cadastro de Solicitante (CSOL), sendo necessário cadastro somente do representante do Instituto de Geociências (IG/UnB) para validação via instituição de ensino e pesquisa. Após confirmação, um formulário de solicitação (SAA) com todos os dados referentes aos poços, tipos de amostras e intervalos de interesse foram encaminhados à ANP. Devido a entraves logísticos, não foi possível a aquisição de testemunhos (03/2021), amostras laterais e lâminas, sendo enviado nova solicitação somente com amostras de calhas. A Agência emite orçamento (12/2021), que é

direcionado ao setor financeiro da UnB que avalia e efetiva o pagamento (05/2022). Após confirmação do pagamento, a SAA permite somente o acesso às amostras (12/2022) com posterior retirada das amostras junto à Petrobras na unidade do Rio de Janeiro e encaminhadas à Brasília (12/2023). Para a realização de análises é necessário enviar a Solicitação de Análise Destrutiva (SAD) e obter a confirmação pela ANP e Petrobras (empresa depositária) (02/2023). Em seguida a confirmação da SAD, foi dado início aos procedimentos de preparação e análises das amostras (Sm-Nd, U-Pb) nos Laboratórios de Geoquímica – LAGEQ e de Estudos Geodinâmicos, Geocronológicos e Ambientais (LEGGA) (IG/UnB) (03/2023).

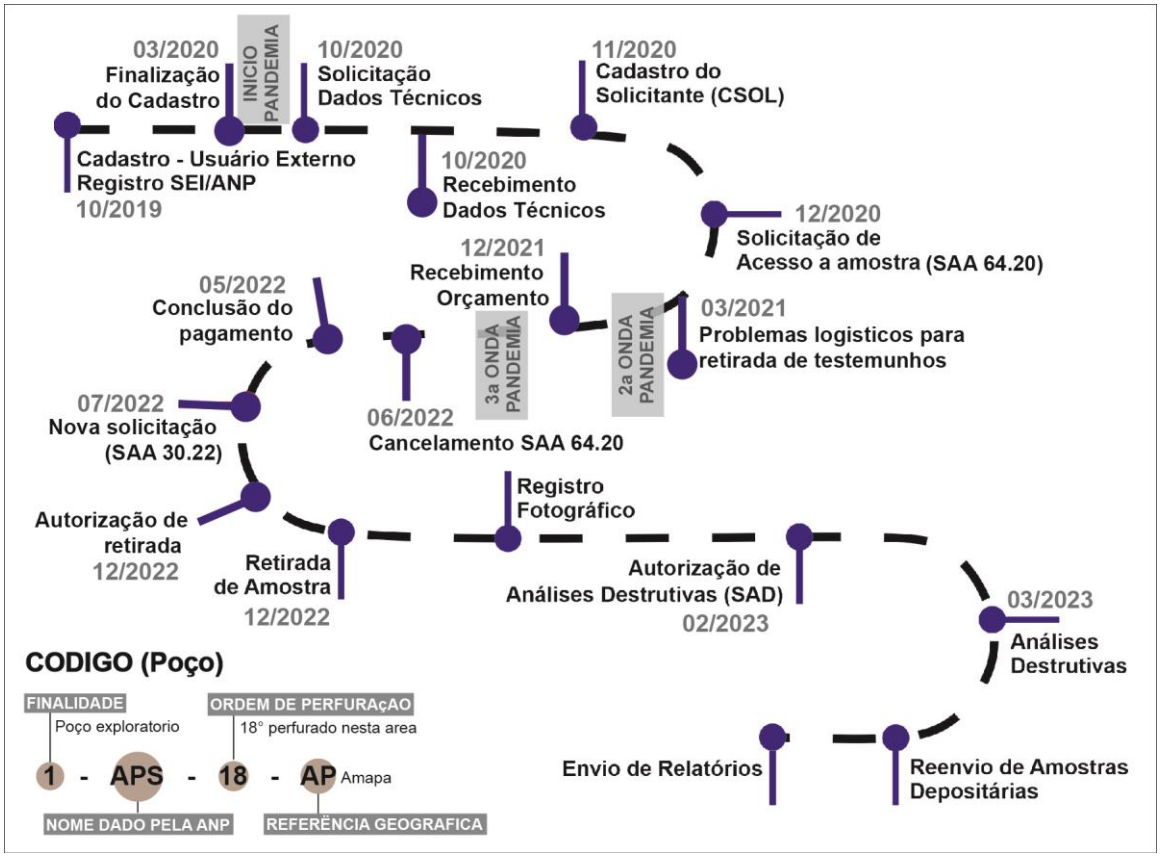


Figura 2. 2 Fluxograma dos processos de Solicitação de Acesso aos Dados Técnicos (SDT) e Solicitação de Acesso às Amostras (SAA) junto à Agência Nacional de Petróleo, Gás Natural e Biocombustíveis (ANP) e à Petrobras.

2.2 INTERPRETAÇÃO PALEOAMBIENTAL

2.2.1 Análise faciológica

Para entender melhor o ambiente deposicional, medimos e descrevemos vários afloramentos ao longo da seção Juanjuí. As fácies clásticas foram descritas em termos de sua litologia, geometria, estruturas sedimentares e conteúdo paleontológico (Miall (1977, 1996, 2006), com a interpretação dos processos sedimentares (p.e., Miall, 1978, 1996, 2006; Dalrymple e Choi, 2007; Nichols, 2009). As fácies químicas (microfácies) foram descritas utilizando a classificação de Dunham (1962), que considera as abundâncias de carbonatos, lama e grão. Esse esquema de classificação possibilita interpretar os processos de formação e/ou paleoambientais. Os critérios mais utilizados são a textura e fábrica deposicionais, bem como os dados de composição qualitativa e quantitativa (Flügel, 2010).

Dados de paleocorrentes foram obtidos com base em estratificações cruzadas e estratos inclinados de arenitos. As direções paleocorrentes foram corrigidas com base no plano de acamamento (estratos S0) utilizando o programa PALEOCOR versão 1.2 (Almeida, 2001). As fácies foram organizadas em associações de fácies, que permitiram a interpretação dos ambientes e sistemas deposicionais (Capítulos 3 e 4). As seções-delgadas de amostras de carbonato foram preparadas no Laboratório de Laminação (LABLAM) da Universidade de Brasília (UnB).

2.2.2 Análise de isótopos estáveis

A análise de fácies sedimentares foi realizada em conjunto com outras abordagens, como análise de isótopos e paleontologia, para obter uma cenário completo das condições ambientais durante o Cenozoico da Amazônia Ocidental. Foram utilizados os isótopos de Carbono ($\delta^{13}C$) e de Oxigênio ($\delta^{18}O$) para investigar variações ambientais no intervalo de tempo estudado. A razão entre os isótopos 12C e 13C (expressa como $\delta^{13}C$), pode identificar mudanças na vegetação e na disponibilidade de recursos. Enquanto que a razão dos isótopos ^{16}O e o ^{18}O (expressa como $\delta^{18}O$) permite reconstruir variações da temperatura da água por meio da proporção entre esses isótopos em sedimentos carbonáticos e carapaças de organismos.

Quarenta e seis amostras de calcários foram coletadas ao longo da seção estratigráfica de Juanjuí (Capitulo 3; Figura 3.4). As abreviaturas HUA (Huallaga) e JUA (Juanjuí) são utilizadas para amostras obtidas durante o trabalho de campo. A etapa de preparação das alíquotas consistiu na pulverização das amostras por meio do uso de uma broca (*drill*). As amostras foram analisadas no Laboratório de Estudos Geodinâmicos, Geocronológicos e Ambientais (LEGGA) (IG/UnB) no Espectrômetro de massa *Delta V Plus* conectado a um aparelho *Gas Bench II*. As amostras foram reagidas com H_3PO4 a uma temperatura de 72°C, em seguida, os tubos foram lavados com Hélio. Os resultados de isótopos estáveis são expressos em notação delta (δ), relativa ao padrão Vienna Pee Dee Belemnite (V-PDB), e calibrados em relação aos materiais de referência NBS 18 ($\delta^{13}C_{V\text{-}PDB}$ = −5.01‰ e $\delta^{18}O_{V\text{-}PDB}$ = −23.2‰) e NBS 19 ($\delta^{13}C_{V\text{-}PDB}$ = 1.95‰ and $\delta^{18}O_{V\text{-}PDB}$ = −2.20‰). Uma regressão linear dos resultados padronizados seguidos de correção dos dados amostrais, foram formados por viés instrumental. Para evitar vieses diagenéticos, selecionamos apenas amostras bem preservadas.

A composição isotópica de carbono e oxigênio em uma amostra foi expresso dividindo a razão isotópica (R) medida na amostra pela razão isotópica do padrão (V-PDB) usando a notação δ e expressa em partes por mil (‰). As composições isotopicas $\delta^{13}C$ e $\delta^{18}O$ foram obtidas pelo: $\delta^{13}C_{(amostra)} = [(R_{amostra}/R_{V\text{-}PDB}) - 1] * 10^3$; $\delta^{18}O_{(amostra)} = [(R_{amostra}/R_{V\text{-}PDB}) - 1] * 10^3$, respectivamente (Guiguer et al., 2003). Os resultados das composições isotópicas (C, O) das amostras analisadas são apresentadas nas Figs. 3.4 e 3.9 e no Material Suplementar (Capítulo 3).

Os dados de isótopos estáveis foram comparados com dados de isotopos estaveis em microfósseis do Mioceno da Amazônia (Alvim et al., 2021); rios *North American*, *Great Lakes*, *North Atlantic seawater*, e *San Francisco Bay estuary* (Varol, 2015; Logvina et al., 2004; Ingram et al., 1996; Keith et al., 1964). É importante enfatizar que, apesar de usar as composições de isotópos estáveis de locais modernos distintos de nossas localidades, os processos de fracionamento isotopicos nesses locais provavelmente ocorreram em ambientes sedimentares semelhantes (por exemplo, lagos, estuários ou mares).

2.2.3 Análise paleontológica

Dados de fósseis obtidos na área de estudo foram aplicados na interpretação paleoambiental, datação e correlação estratigráfica nas sequências cenozoicas da bacia da Amazônica Ocidental (Bacia de Huallaga). Na Bacia de Huallaga, os dados foram coletados em afloramentos da seção Juanjuí, compreendendo o intervalo do Meso-Cenozoico (Capítulo 3).

As amostras palinológicas foram preparadas na Universidade de Caldas (Colômbia), pelo pesquisador Carlos Jaramillo (co-autor) seguindo o método padrão de processamento palinológico proposto por Traverse (2007). Carbonatos e silicatos foram removidos por digestão das amostras em HCl e HF por 12 e 24 h, respectivamente. Depois da digestão ácida, as amostras foram neutralizadas através de diluição repetida com água destilada e decantação. O resíduo restante foi inicialmente peneirado com uma malha de 250 μm; este foi seguido de peneiramento através de uma malha de 10 μm. Este resíduo foi limpo em um equipamento ultrassônico por 15s e o resíduo orgânico foi concentrado por centrifugação, seguido da montagem de uma primeira lâmina de cobertura em uma solução de álcool polivinílico. Parte do resíduo foi oxidado em ácido nítrico por 2-3 minutos, e uma segunda lâmina foi montada. As lâminas foram seladas com bálsamo canadense. Uma *Nikon I80* foi usada para digitalizar o slides no Instituto de Pesquisa *Tropical Smithsonian*. O exame e descrição do material palinológico foram realizados utilizando-se uma imersão a óleo planapocromática com uma objetiva de 100x (Nikon). A identificação dos palinomorfos foi realizada através de uma comparação com fotografias e descrições de material polínico do Cretáceo e Paleoceno publicado no norte da América do Sul que são compilados numa base de dados *online* (Jaramillo e Rueda, 2021). A zonação palinológica de Jaramillo et al. (2011) e a análise gráfica biostratigráfica de Carvalho et al. (2021) e De La Parra et al. (2021) foram utilizadas para determinar a idade das amostras.

Demais espécimes de microfósseis foram preparados por meio da técnica de lavagem de telas, com malhas de 2 e 1 mm, totalizando aproximadamente 550 kg de sedimentos tratados. Os resíduos das peneiras foram examinados sob microscópios estéreo para coleta de microfósseis. Em seguida, foram fotografados usando microscópio eletrônico de varredura Hitachi S 4000 (MEV) no *Institut des Neurosciences de Montpellier* (INM), França. Tais metodologias foram realizadas em parceria e co-autoria com os pesquisadores Pierre-Olivier Antoine, Laurent Marivaux e Narla S. Stutz (co-

autores) (*Institut des Sciences de l'Evolution de Montpellier, Université Montpellier, CNRS, IRD*).

2.3 PROVENIÊNCIA SEDIMENTAR

2.3.1 Geoquímica elementar

O uso da geoquímica por meio do estudo de concentrações de elementos maiores e traços em sedimentos finos foi aplicado à analise de proveniência sedimentar para inferir suas fontes, histórico de transporte e processos de alteração (Nelson and De Paolo, 1988). Esses elementos ajudam a distinguir entre diferentes rochas geradoras (ígneas, metamórficas, sedimentares) e fornecem informações sobre a mineralogia das regiões geradoras. Elementos de Terras Raras (REEs) são usados como traçadores em estudos de proveniência pois possuem padrões distintos em diferentes tipos de rochas e são imóveis durante os processos sedimentares (McLennan et al., 1993; Li et al., 2021). As razões entre os elementos móveis e imóveis (Th/Sc, Cr/Th e Th/U), anomalias em Európio (Condie, 1993) e as composições isotópicas de Nd são consideradas como reflexos da composição da área-fonte (McLennan et al., 1993).

Doze (12) rochas sedimentares de grão fino foram coletadas nos afloramentos ao longo da seção estratigráfica de Juanjuí, Abra Machungo, Juan Guerra e Shapaja e analisadas quanto às concentrações de elementos maiores e traços. Concentrações maiores de óxidos e elementos-traço foram medidas no *Service d'Analyse des Roches et Minéraux* (SARM) em Nancy, França. As amostras de preparo, os procedimentos analíticos e o tratamento dos dados para determinação de elementos-traço seguiram as etapas propostas por (Carignan et al., 2001). Os principais elementos (Na, Mg, K, Ca, Sc, Ti, Mn, Fe, Al, Si e P) e os óxidos (SiO_2, Al_2O_3, Fe_2O_3, MnO, MgO, CaO, Na_2O, K_2O, TiO_2, P_2O_5) foram medidos e detectados por Plasma Indutivamente Acoplado – Espectometria de Emissão Optica (ICP-OES). Enquanto que, os elementos traços (Rb, Cs, Ba, Sr, Th, U, Y, Zr, Nb, Hf, Cr, V, Co, Cu, Ni, Zn, La, Ce, Pr, Nd, Sm, Eu, Gd, Tb, Dy, Ho, Ho, Ho, Ho, Co) foram medidos por Espectrometro de Massa (ICP-MS). Após a determinação, as concentrações de elementos principais e traços foram normalizadas para *Post Archean Australian Shales* (PAAS) (Taylor e McLennan, 1985; McLennan, 2001; Pourmand et al., 2012). Utilizamos o Índice Químico de Alteração (CIA) para avaliar o grau de intemperismo da área-fonte e

as condições paleoclimáticas dos sedimentos (Fedo et al., 1995; Nesbitt et al., 1996). Este índice mede a intensidade de intemperismo dos feldspatos em relação aos protólitos inalterados e é definido como: CIA = [Al_2O_3/(Al_2O_3 + CaO* + Na_2O + K_2O)] x 100 (em proporções molares), onde CaO* representa o conteúdo de CaO na fração silicato. Não temos dados de CO_2 para nossas análises e, portanto, não podemos corrigir o Ca em carbonatos para obter CaO*. Para calcular CaO*, assumimos o valor de CaO se CaO Na_2O, e CaO = Na_2O se CaO Na_2O (Bock et al., 1998). Para facilitar as comparações com sedimentos derivados de fontes básicas ou félsicas (Cullers, 2000) e o PAAS (Pourmand et al., 2012; Taylor e McLennan, 1985; McLennan, 2001), a anomalia Eu é calculada em relação aos condritos: Eu/Eu* = Eun/(smn dN)1/2 em que N se refere ao valor de concentração normalizado do condrito (Condie, 1993). A anomalia Cerium (ΩCe) normalizada com PAAS é calculada seguindo (De Baar et al., 1985): ΩCe = 2 × (Ceamostra/CePAAS) / [(Laamostra/LaPAAS) + (Pramostra/PrPAAS)], onde Xamostra é a concentração da amostra e XPAAS refere a concentração do padrão PAAS.

McLennan et al. (1993) definem cinco tipos de fontes susceptíveis de serem identificadas a partir das características geoquímicas dos sedimentos (Figura 2.3).

Tipos de Terrenos	εNd	Eu/Eu*	Th/Sc	Th/U	Outras características
Crosta Continental Superior antiga (OUC)	≤-10	~0.60-0.70	~1.0	>3.8 (folhelhos)	Composição de elementos maiores (por exemplo, alto Si/Al, CIA); altas abundâncias de LILE
Rochas Sedimentares Recicladas (RSR)	≤-10	~0.60-0.70	≥1.0		Concentração de minerais pesados de elementos-traços (Zr, Hf para zircão; ETRs para monazita);
Arco Indiferenciado Jovem (YUA)	≥+5	~1.0	<1.0	<3.0	Composições de elementos maiores (baixo Si/Al, CIA); baixas abundâncias de LILE;
Arco Diferenciado Jovem (YUA)	≥+5	~0.50-0.90	Variável	Variável	Composições de elementos maiores (alto Si/Al, CIA); altas abundâncias de LILE
Fontes exóticas	A assinatura química e/ou isotópica depende da natureza do componente; por exemplo, Mg, Cr, Ni, V e Cr/V muito altos seriam distintivos de fontes de ofiolito.				

Figura 2. 3 Características geoquímicas e isotópicas de distintas fontes definidos por McLennan et al., (1993)

A partir das características dos elementos-traços, Cullers (2000) distingue dois tipos de áreas-fonte: félsica e básica (Fig. 2.4).

	Sedimentos finos		Sedimentos grossos	
	Félsico	Básico	Félsico	Básico
Eu/Eu*	0.32-0.83	0.70-1.02	0.40-0.94	0.71-0.95
Th/Sc	0.64-18.1	0.05-0.4	0.84-20.5	0.05-0.22
Cr/Th	0.25-14.9	22.2-500	0.40-7.70	21.7-55.5

Figura 2. 4 Variações das razões Eu/Eu*, Th/Sc, Cr/Th para sedimentos finos e grossos de origem félsica e básica (Cullers, 2000).

2.3.2 Análise isotópica de Sm-Nd

Os isótopos de Nd podem ser usados como uma ferramenta de proveniência porque não são facilmente fracionados por processos sedimentares ou pós-deposicionais (McLennan et al., 1990). Isótopos como Sm-Nd e U-Pb fornecem a idade dos minerais detríticos nas rochas sedimentares. Estas idades são correlacionadas com assinaturas isotópicas conhecidas de potenciais rochas geradoras, permitindo restringir a área de proveniência dos sedimentos. Isso é possível devido as diferenças na razão isotópica do Neodímio (^{143}Nd / ^{144}Nd) em distintas fontes geológicas relacionadas a processos como a evolução crustal, diferenciação magmática e influência de fontes mantélicas (Nelson and De Paolo, 1988; Kessarkar et al., 2003; Wei et al., 2012; Rao et al., 2017; Cai et al., 2020). Outra característica que o torna um bom traçador geoquímico, é que as razões isotópicas do Nd são menos alteradas do que demais indicadores de proveniência, tais como tamanho dos grãos (Rao et al., 2017).

Para a análise isotópica de Sm-Nd, onze (11) rochas sedimentares representativas de grãos finos foram coletadas da sequência Meso-Cenozoica da Bacia do Huallaga, região proximal do sistema. Enquanto que na região distal do sistema, vinte e três (23) amostras foram selecionadas na sequência Cenozoica da Bacia da Foz do Amazonas, distribuídas ao longo dos cinco poços exploratórios. A preparação das amostras e procedimentos analíticos foram realizados no Laboratório de Geoquímica – LAGEQ e no Laboratório de Estudos Geodinâmicos, Geocronológicos e Ambientais (LEGGA) (IG/UnB).

A preparação das amostras compreendeu a trituração das alíquotas em pistilo de ágata. Em seguida, as amostras foram conduzidas ao procedimento de lixiviação sequencial

para a separação da fração carbonática, dos óxidos de Fe – Mn, do carbono orgânico e da fração detrítica dos sedimentos, visando a remoção das assinaturas marinhas (Fig. 2.5) (Bayon et al.; 2002). A capacitação para a realização deste procedimento foi realizada no *Institut Français de Recherche pour l'Exploitation de la Mer* (IFREMER) (Fig. 2.5).

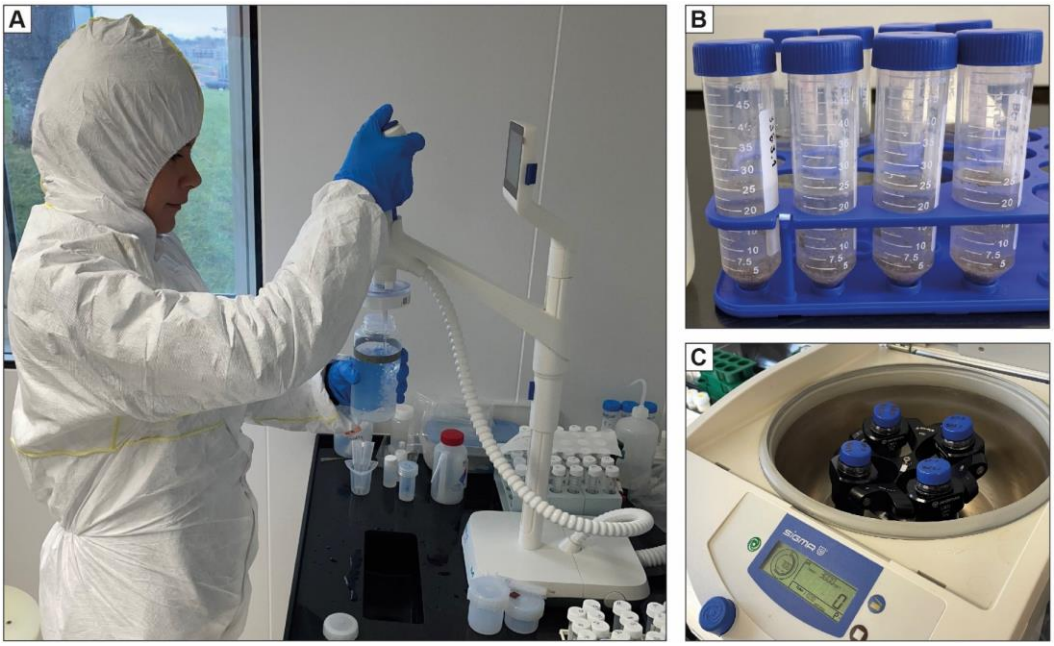


Figura 2. 5 Realização dos procedimentos métodologicos necessários na lixiviação sequencial para extração da fração carbonática, dos óxidos de Fe – Mn, do carbono orgânico e da fração detrítica dos sedimentos, realizados no IFREMER. A) Adição de água MiliQ (MQ H_2O) para condução do preparo das amostras; B) Tubos *falcon* de 50 ml contendo as frações sólidas das amostras em reação com ácido acético 10% para a separação da fração carbonática; C) Etapa de centrifugar as amostras com rotação de 3000 rpm / 2 minutos.

Esta etapa foi seguida por um procedimento de digestão da amostra, que compreende a separação dos elementos Terras Raras REEs, Sm e Nd utilizando colunas de cromatografia (Gioia e Pimentel, 2000). As razões isotópicas ($^{147}Sm/^{144}Nd$ e $^{143}Nd/^{144}Nd$) foram medidas usando o *Neptune XT™ High Resolution Multicollector ICP-MS*. A acurácia das medidas foi estimada pela análise repetida do padrão BHVO-2. A correção do sinal para o fracionamento de massa da razão $^{143}Nd/^{144}Nd$ foi feita pela normalização com $^{146}Nd/^{144}Nd = 0{,}7219$.

As medidas das razões $^{143}Nd/^{144}Nd_{sample}$ e $^{143}Sm/^{144}Nd_{sample}$ são exibidas em notação épsilon (Ɛ) (DePaolo, 1988). As razões $^{143}Nd/^{144}Nd$ medidas são apresentadas como o desvio fracionário em partes por 10^4 (unidades) de $^{143}Nd/^{144}Nd$ no Reservatório Uniforme Condrítico (CHUR), medido nos dias de hoje:

$$\varepsilon Nd(0) = [(^{143}Nd/^{144}Nd)S/ICHUR(0) - 1] * 104$$

onde ($^{143}Nd/^{144}Nd$)S é a relação atual medida na amostra, e ICHUR(0) é o $^{143}Nd/^{144}Nd$ no reservatório de referência CHUR no presente ICHUR(0) = 0,512638; (Jacobsen e Wasserburg, 1980).

2.3.3 Análise isotópica de U-Pb

A datação U-Pb aplicada à proveniência sedimentar envolveu a análise zircões detríticos presentes em arenitos da área-fonte e deposição do sistema AAMESA. Devido à sua resistência sob alterações físicas e químicas, os zircões podem fornecer informações valiosas sobre a idade e a fonte da rocha original da qual foram derivados (Morton e Hallsworth, 1999). Também são fundamentais para restringir idades máximas de deposição dos sedimentos, particularmente em unidades com controle bioestratigráfico escasso (Bahlburg and Berndt, 2016; Fedo et al., 2003). A datação U-Pb contudo, não é simples pois os zircões podem ser afetados por processos como metamorfismo, além de ser uma técnica que requer equipamentos especializados. Dessa forma, combinar várias análises geoquímicas (*multi-proxy*) é fundamental para mitigar vieses.

Para a análise isotópica de U-Pb, foram amostrados sete (7) arenitos da seção estratigráfica de Juanjuí; seis (6) arenitos e depósitos recentes arenosos dos afloramentos de Abra Machungo, Shapaja e Juan Guerra na Bacia de Huallaga. Enquanto que na Bacia da Foz do Amazonas, foram analisadas quatro (4) amostras de arenitos. A preparação e análises das amostras para datação U-Pb foram realizadas no Laboratório de Estudos Geodinâmicos, Geocronológicos e Ambientais (LEGGA) da Universidade de Brasília (UnB) e no *Géosciences Environnement Toulouse* (GET). Os métodos adotados na separação dos grãos de zircões detriticos foram distintos, sendo realizados de acordo com a quantidade, em peso, obtida para cada amostra.

Para amostras com alíquotas maiores (~ 5kg/amostra), a preparação compreendeu a britagem e peneiramento dos sedimentos, seguido pela concentração por método densimétrico com uso de bateia e por líquido denso (Fig. 2.6). Em seguida, o concentrado foi direcionado ao Separador Magnético Isodinâmico de Frantz (melhor recuperação dos grãos de zircões > 1,6A), onde a fração dos zircões foi separada dos minerais magnéticos (Fig. 2.5) (Stendal and Theobald, 1994). No entanto, as amostras de calhas com alíquotas

menores (~ 100g/amostra) recuperadas dos poços exploratorios da Bacia da Foz do Amazonas, seguiram os procedimentos de separação proposto por Oliveira et al. (2022). Este método usa uma combinação de separação física e dissolução química, através de uma série de digestões ácidas: aqua-regia, ácido fluorídrico, aqua-regia e finalmente ácido clorídrico. Este procedimento foi possível devido ao fato de que o zircão é um dos poucos minerais que podem sobreviver a este ataque de ácido na rocha (Oliveira et al., 2022). Os grãos de zircões concentrados foram separados (~120 grãos/amostra) no microscópio estereoscópico; montados em fita adesiva, colocados em um anel plástico de 9 mm de diâmetro fechado com resina epóxi (*mounts*). Finalmente, os grãos de zircão foram polidos para expor seus centros (Gehrels, 2014; Bühn et al., 2009; Gehrels et al., 2008). Para fornecer um mapa para registrar posições do ponto do laser, os *mounts* foram imageados por um Microscópio Eletrônico de Varredura (MEV).

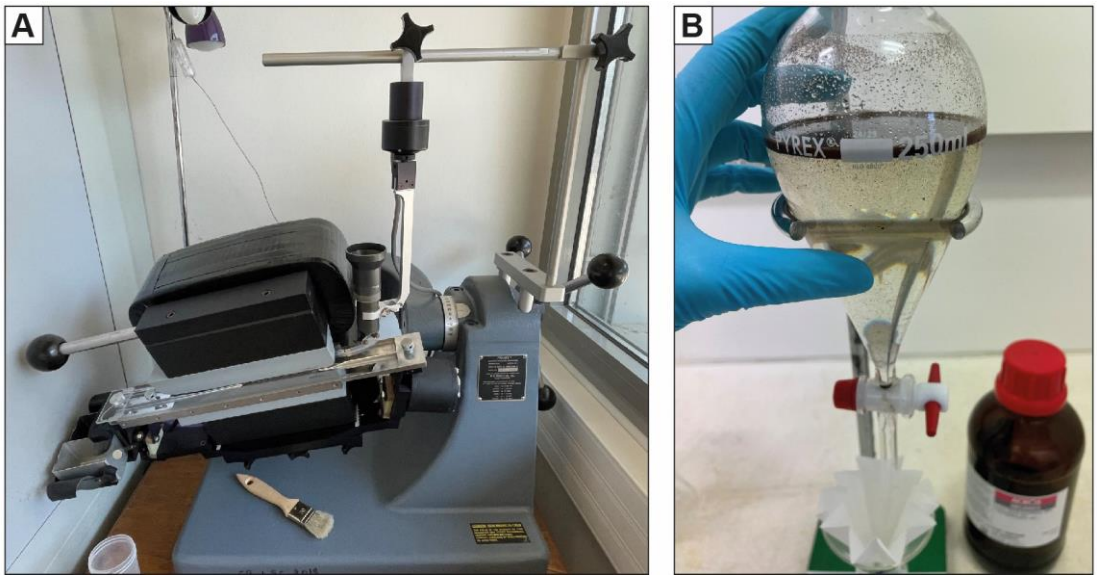


Figura 2. 6. Materiais e procedimentos realizados na concentração e separação dos cristais de zircões detríticos, realizados no laboratório *Géosciences Environnement Toulouse* (GET). A) Separador Magnético Isodinâmico de Frantz, utilizado na separação dos minerais magnéticos dos não-magnéticos. B) Separação dos zircões com método densimétrico utilizando líquido denso (Diiodomethane, 99+, d = 3.32 g/mL).

A aquisição analítica de dados de isótopos foi coletada usando Indutivamente Acoplado-Plasma Espectrometria de Massa (ICP-MS) *Finnigan Element XR*, acoplado a um sistema de ablação a *laser Iridia Excimer* (Arf) de 193 nm. As condições do laser incluíram um diâmetro do ponto de 25 µm, de 20 hertz, e de 2,0 J cm^{-2}. Os dados brutos

foram processados no *software Iolite 4.0* seguindo os procedimentos propostos por Paton et al., (2011) e a inspeção de sinais individuais foi realizada com auxílio do VizualAge (Petrus e Kamber, 2012). As idades efetivas de U-Pb foram de $^{206}Pb/^{238}U$ para grãos de zircões com idades de 1.5 Ga e $^{207}Pb/^{206}Pb$ para grãos com idades >1.5 Ga. Idades com graus de discordância >10% e amostras com poucos zircões (<35) não foram considerados devido à sua baixa representação estatística (Vermeesch, 2004). A normalização dos dados e o controle de qualidade foram feitos com base em três (3) materiais de referência diferentes: zircão GJ1 (Jackson et al., 2004), zircão 91500 (Widenbeck et al., 1995) e zircão Plešovice (Sláma et al., 2008).

Os grandes números de amostras e quantidades de dados de distribuição requerem métodos quantitativos e objetivos, como o escalonamento multidimensional (MDS), para analisá-los (Vermeesch, 2013; Vermeesch et al., 2016). Para aprimorar o método, aplicamos a estatística de Kolmogorov-Smirnov (KS), que é uma medida usada para comparar as distribuições das amostras. Uma distância KS menor e maior indica, respectivamente, uma maior ou menor dissimilaridade entre as distribuições (Vermeesch, 2013).

REFERÊNCIAS

Almeida, R. P. (2001). Evolução Tectono-sedimentar da Formação Santa Bárbara na Sub-Bacia Camaquã Ocidental. Dissertação (Mestrado). São Paulo: Instituto de Geociências – Universidade de São Paulo. 161p.

Alvim, A.M.V., Santos, R.V., Roddaz, M., Antoine, P.-O., Ramos, M.I.F., do Carmo, D.A., Linhares, A.P., Negri, F.R., 2021. Fossil isotopic constraints (C, O and 87Sr/86Sr) on Miocene shallow-marine incursions in Amazonia. Palaeogeography, Palaeoclimatology, Palaeoecology 573, 110422. https://doi.org/10.1016/j.palaeo.2021.110422

Bayon, G., German, C.R., Boella, R.M., Milton, J.A., Taylor, R.N., Nesbitt, R.W., 2002. An improved method for extracting marine sediment fractions and its application to Sr and Nd isotopic analysis. Chemical Geology 187, 179–199. https://doi.org/10.1016/S0009-2541(01)00416-8

Bahlburg, H., Berndt, J., 2016. Provenance from zircon U–Pb age distributions in crustally contaminated granitoids. Sedimentary Geology 336, 161–170. https://doi.org/10.1016/j.sedgeo.2015.08.006

Bock, B.; Mc Lennan, S.M.; Hanson, G.N. 1998. Geochemistry and provenance of theMiddle Ordovician Austin Glen Member (Normanskill Formation) and the TaconianOrogeny in New England. Sedimentology 1998, 45, 635–655.

Bühn, B., Pimentel, M.M., Matteini, M., Dantas, E.L., 2009. High spatial resolution analysis of Pb and U isotopes for geochronology by laser ablation multi-collector inductively coupled plasma mass spectrometry (LA-MC-ICP-MS). An. Acad. Bras. Ciênc. 81, 99–114. https://doi.org/10.1590/S0001-37652009000100011

Bruce K. Nelson (2), Donald J. DePa, 1988. Comparison of Isotopic and Petrographic Provenance Indicators in Sediments from Tertiary Continental Basins of New Mexico. SEPM JSR Vol. 58. https://doi.org/10.1306/212F8D91-2B24-11D7-8648000102C1865D

Cai, G., Li, S., Zhao, L., Zhong, L., Chen, H., 2020. Clay minerals, Sr-Nd isotopes and provenance of sediments in the northwestern South China Sea. Journal of Asian Earth Sciences 202, 104531. https://doi.org/10.1016/j.jseaes.2020.104531

Carignan, J., Hild, P., Mevelle, G., Morel, J., Yeghicheyan, D., 2001. Routine Analyses of Trace Elements in Geological Samples using Flow Injection and Low Pressure On-Line Liquid Chromatography Coupled to ICP-MS: A Study of Geochemical Reference Materials BR, DR-N, UB-N, AN-G and GH. Geostandards and Geoanalytical Research 25, 187–198. https://doi.org/10.1111/j.1751-908X.2001.tb00595.x

Carvalho, M.R., Jaramillo, C., de la Parra, F., Caballero-Rodríguez, D., Herrera, F., Wing, S., Turner, B.L., D'Apolito, C., Romero-Báez, M., Narváez, P., Martínez, C., Gutierrez, M., Labandeira, C., Bayona, G., Rueda, M., Paez-Reyes, M., Cárdenas, D., Duque, Á., Crowley, J.L., Santos, C., Silvestro, D., 2021. Extinction at the end-Cretaceous and the origin of modern Neotropical rainforests. Science 372, 63–68. https://doi.org/10.1126/science.abf1969

Cruz, A.M., Reis, A.T., Suc, J.P., Silva, C.G., Praeg, D., Granjeon, D., Rabineau, M., Popescu, S.M., Gorini, C., 2019. Neogene evolution and demise of the Amapá carbonate platform, Amazon continental margin, Brazil. Marine and Petroleum Geology 105, 185–203. https://doi.org/10.1016/j.marpetgeo.2019.04.009

Condie, K.C., 1993. Chemical composition and evolution of the upper continental crust: Contrasting results from surface samples and shales. Chemical Geology 104, 1–37. https://doi.org/10.1016/0009-2541(93)90140-E

Cullers, R.L., 2000. The geochemistry of shales, siltstones and sandstones of Pennsylvanian–Permian age, Colorado, USA: implications for provenance and metamorphic studies. Lithos 51, 181–203. https://doi.org/10.1016/S0024-4937(99)00063-8

Dalrymple, R.W., Choi, K., 2007. Morphologic and facies trends through the fluvial–marine transition in tide-dominated depositional systems: A schematic framework for environmental and sequence-stratigraphic interpretation. Earth-Science Reviews 81, 135–174. https://doi.org/10.1016/j.earscirev.2006.10.002

De La Parra, F., Pinzon, D., Mantilla-Duran, F., Rodriguez, G., Caballero, V., 2021. Marine-lacustrine systems during the Eocene in northern South America – Palynological evidence from Colombia. Journal of South American Earth Sciences 108, 103188. https://doi.org/10.1016/j.jsames.2021.103188

DePaolo, D.J., Wasserburg, G.J., 1976. Nd isotopic variations and petrogenetic models. Geophys. Res. Lett. 3, 249–252. https://doi.org/10.1029/GL003i005p00249

Dunham, R.J., 1962. Classification of carbonate rocks according to depositional texture. In: Ham, W.E. (Ed.), Classification of Carbonate Rocks. AAPG, Tulsa, pp. 108–121.

Fedo, C.M., Wayne Nesbitt, H., Young, G.M., 1995. Unraveling the effects of potassium metasomatism in sedimentary rocks and paleosols, with implications for paleoweathering conditions and provenance. Geol 23, 921. https://doi.org/10.1130/0091-7613(1995)023<0921:UTEOPM>2.3.CO;2

Fedo, C.M., Sircombe, K.N., Rainbird, R.H., 2003. Detrital Zircon Analysis of the Sedimentary Record. Reviews in Mineralogy and Geochemistry 53, 277–303. https://doi.org/10.2113/0530277

Figueiredo, J., Hoorn, C., van der Ven, P., Soares, E., 2009. Late Miocene onset of the Amazon River and the Amazon deep-sea fan: Evidence from the Foz do Amazonas Basin. Geology 37, 619–622. https://doi.org/10.1130/G25567A.1

Figueiredo, J.J.P., Zalán, P.V., Soares, E.F., 2007. Bacia Foz do Amazonas. Boletim de Geociências da Petrobras 15, 299–309.

Flügel, E., 2010. In: Munnecke, A. (Ed.), Microfacies of Carbonates Rocks - Analysis, Interpretation and Application, second ed. Springer. 10.1007/10.1007/978-3-642- 03796-2.

Gehrels, G.E., Valencia, V.A., Ruiz, J., 2008. Enhanced precision, accuracy, efficiency, and spatial resolution of U-Pb ages by laser ablation-multicollector-inductively coupled plasma-mass spectrometry: TECHNICAL BRIEF. Geochem. Geophys. Geosyst. 9, https://doi.org/10.1029/2007GC001805

Gehrels, G., 2014. Detrital Zircon U-Pb Geochronology Applied to Tectonics. Annu. Rev. Earth Planet. Sci. 42, 127–149. https://doi.org/10.1146/annurev-earth-050212-124012

Gioia, S.M.C.L., Pimentel, M.M., 2000. The Sm-Nd isotopic method in the geochronology laboratory of the University of Brasília. An. Acad. Bras. Ciênc. 72, 219–245. https://doi.org/10.1590/S0001-37652000000200009

Gorini, C., Haq, B.U., dos Reis, A.T., Silva, C.G., Cruz, A., Soares, E., Grangeon, D., 2014. Late Neogene sequence stratigraphic evolution of the Foz do Amazonas Basin, Brazil. Terra Nova 26, 179–185. https://doi.org/10.1111/ter.12083

Guiguer, K.R.R.A., Drimmie, R., Power, M., 2003. Validating methods for measuring?18O and?13C in otoliths from freshwater fish. Rapid Commun. Mass Spectrom. 17, 463–471. https://doi.org/10.1002/rcm.935

Hermoza, W., Brusset, S., Baby, P., Gil, W., Roddaz, M., Guerrero, N., Bolaños, R., 2005. The Huallaga foreland basin evolution: Thrust propagation in a deltaic environment, northern Peruvian Andes. Journal of South American Earth Sciences 19, 21–34. https://doi.org/10.1016/j.jsames.2004.06.005

Hoorn, C., Bogotá-A, G.R., Romero-Baez, M., Lammertsma, E.I., Flantua, S.G.A., Dantas, E.L., Dino, R., do Carmo, D.A., Chemale, F., 2017. The Amazon at sea: Onset and stages of the Amazon River from a marine record, with special reference to Neogene plant turnover in the drainage basin. Global and Planetary Change 153, 51–65. https://doi.org/10.1016/j.gloplacha.2017.02.005

Horton, B.K., 2018. Sedimentary record of Andean mountain building. Earth-Science Reviews 178, 279–309. https://doi.org/10.1016/j.earscirev.2017.11.025

Hurtado, C., Roddaz, M., Santos, R.V., Baby, P., Antoine, P.-O., Dantas, E.L., 2018. Cretaceous-early Paleocene drainage shift of Amazonian rivers driven by Equatorial Atlantic Ocean opening and Andean uplift as deduced from the provenance of northern Peruvian sedimentary rocks (Huallaga basin). Gondwana Research 63, 152–168. https://doi.org/10.1016/j.gr.2018.05.012

Ingram, B.L., Conrad, M.E., Ingle, J.C., 1996. Stable isotope and salinity systematics in estuarine waters and carbonates: San Francisco Bay. Geochimica et Cosmochimica Acta 60, 455–467. https://doi.org/10.1016/0016-7037(95)00398-3

Jackson, S.E., Pearson, N.J., Griffin, W.L., Belousova, E.A., 2004. The application of laser ablation-inductively coupled plasma-mass spectrometry to in situ U–Pb zircon geochronology. Chemical Geology 211, 47–69. https://doi.org/10.1016/j.chemgeo.2004.06.017

Jacobsen, S.B., Wasserburg, G.J., 1980. Sm-Nd isotopic evolution of chondrites. Earth and Planetary Science Letters 50, 139–155. https://doi.org/10.1016/0012-821X(80)90125-9

Jaramillo, C.A., Rueda, M., Torres, V., 2011. A palynological zonation for the Cenozoic of the Llanos and Llanos Foothills of Colombia. Palynology 35, 46–84. https://doi.org/10.1080/01916122.2010.515069

Jaramillo, C., Rueda, M., 2021. A Morphological Electronic Database of CretaceousTertiary Fossil Pollen and Spores from Northern South America V. 2012-2021. Smithsonian Tropical Research Institute. http://biogeodb.stri.si.edu/jaramillo/pal ynomorph/.

Keith, M.L., Anderson, G.M., Eichler, R., 1964. Carbon and oxygen isotopic composition of mollusk shells from marine and fresh-water environments. Geochimica et Cosmochimica Acta 28, 1757–1786. https://doi.org/10.1016/0016-7037(64)90021-3

Kessarkar, P.M., Rao, V.P., Ahmad, S.M., Babu, G.A., 2003. Clay minerals and Sr–Nd isotopes of the sediments along the western margin of India and their implication for sediment provenance. Marine Geology 202, 55–69. https://doi.org/10.1016/S0025-3227(03)00240-8

Kontak, D.J., Clark, A.H., Farrar, E., Archibald, D.A., Baadsgaard, H., 1990. Late Paleozoic-early Mesozoic magmatism in the Cordillera de Carabaya, Puno, southeastern Peru: Geochronology and petrochemistry. Journal of South American Earth Sciences 3, 213–230. https://doi.org/10.1016/0895-9811(90)90004-K

Li, Z., Chen, Q., Dong, S., Zhang, D., Yu, X., Zhang, C., 2021. Applicability of rare earth elements in eolian sands from desert as proxies for provenance: A case study in the Badain Jaran Desert, Northwestern China. CATENA 207, 105647. https://doi.org/10.1016/j.catena.2021.105647

Logvina, E., Mazurenko, L., Prasolov, E., 2004. Isotopic composition of carbon-13 and oxygen-18 from authigenic carbonates. In: Black Sea Region. AGU Spring Meeting Abstracts.

McLennan, S.M., Taylor, S.R., McCulloch, M.T., Maynard, J.B., 1990. Geochemical and Nd–Sr isotopic composition of deep-sea turbidites: crustal evolution and plate tectonic associations. Geochimica et Cosmochimica Acta 54 (7), 2015–2050. https://doi.org/10.1016/0016-7037(90)90269-Q

McLennan, S.M., Hemming, S., McDaniel, D.K., Hanson, G.N., 1993. Geochemical approaches to sedimentation, provenance, and tectonics, in: Geological Society of America Special Papers. Geological Society of America, pp. 21–40. https://doi.org/10.1130/SPE284-p21

McLennan, S.M. Relationship between the trace element composition of sedimentary rocks and upper continental crust. Geochem. Geophys. Geosysystem 2001, 2, 203–236.

Miall, A.D., 1978. Lithofacies types and vertical profile models in braided river deposits: a summary. Fluv. Sedimentol. 5, 597–600.

Miall, A.D., 1996. The Geology of Fluvial Deposits, Sedimentary Facies, Basin Analysis and Petroleum Geology. Sprin-ger, Berlin.

Miall, A.D., 2006. The Geology of Fluvial Deposits. Springer Berlin Heidelberg, Berlin, Heidelberg. https://doi.org/10.1007/978-3-662-03237-4

Morton, A.C., Hallsworth, C.R., 1999. Processes controlling the composition of heavy mineral assemblages in sandstones. Sedimentary Geology 124, 3–29. https://doi.org/10.1016/S0037-0738(98)00118-3

Nelson, B. K., DePaolo, D. J., 1988. Comparison of Isotopic and Petrographic Provenance Indicators in Sediments from Tertiary Continental Basins of New Mexico. SEPM JSR Vol. 58. https://doi.org/10.1306/212F8D91-2B24-11D7-8648000102C1865D

Nesbitt, H.W., Young, G.M., McLennan, S.M., Keays, R.R., 1996. Effects of Chemical Weathering and Sorting on the Petrogenesis of Siliciclastic Sediments, with Implications for Provenance Studies. The Journal of Geology 104, 525–542. https://doi.org/10.1086/629850

Nichols, G., 2010. Sedimentology and stratigraphy, 2. ed., [Nachdr.]. ed. Wiley-Blackwell, Chichester.

Nogueira, A.C.R., Silveira, R., Guimarães, J.T.F., 2013. Neogene–Quaternary sedimentary and paleovegetation history of the eastern Solimões Basin, central Amazon region. Journal of South American Earth Sciences 46, 89–99. https://doi.org/10.1016/j.jsames.2013.05.004

Oliveira, A.L., Schmitz, M.D., Wall, C.J., Hollanda, M.H.B.M., 2022. A bulk annealing and dissolution-based zircon concentration method for mafic rocks. Chemical Geology 597, 120817. https://doi.org/10.1016/j.chemgeo.2022.120817

Paton, C., Hellstrom, J., Paul, B., Woodhead, J., Hergt, J., 2011. Iolite: Freeware for the visualisation and processing of mass spectrometric data. J. Anal. At. Spectrom. 26, 2508. https://doi.org/10.1039/c1ja10172b

Petrus, J.A. and Kamber, B.S. 2012. VizualAge: A Novel Approach to Laser Ablation ICP-MS U-Pb Geochronology Data Reduction. Geostandards and Geoanalytical Research, 36: 247-270.

Pourmand, A., Dauphas, N., Ireland, T.J., 2012. A novel extraction chromatography and MC-ICP-MS technique for rapid analysis of REE, Sc and Y: Revising CI-chondrite and Post-Archean Australian Shale (PAAS) abundances. Chemical Geology 291, 38–54. https://doi.org/10.1016/j.chemgeo.2011.08.011

Rao, W., Mao, C., Wang, Y., Huang, H., Ji, J., 2017. Using Nd-Sr isotopes and rare earth elements to study sediment provenance of the modern radial sand ridges in the southwestern Yellow Sea. Applied Geochemistry 81, 23–35. https://doi.org/10.1016/j.apgeochem.2017.03.011

Sláma, J., Košler, J., Condon, D.J., Crowley, J.L., Gerdes, A., Hanchar, J.M., Horstwood, M.S.A., Morris, G.A., Nasdala, L., Norberg, N., Schaltegger, U., Schoene, B., Tubrett, M.N., Whitehouse, M.J., 2008. Plešovice zircon — A new natural reference material for U–Pb and Hf isotopic microanalysis. Chemical Geology 249, 1–35. https://doi.org/10.1016/j.chemgeo.2007.11.005

Stendal, H., Theobald, P.K., 1994. Heavy-Mineral Concentrates in Geochemical Exploration, in: Handbook of Exploration Geochemistry. Elsevier, pp. 185–225. https://doi.org/10.1016/B978-0-444-81854-6.50012-2

Stewart, J.A., Gutjahr, M., James, R.H., Anand, P., Wilson, P.A., 2016. Influence of the Amazon River on the Nd isotope composition of deep water in the western equatorial Atlantic during the Oligocene–Miocene transition. Earth and Planetary Science Letters 454, 132–141. https://doi.org/10.1016/j.epsl.2016.08.037

Taylor, S.R.; McLenana, S.M. The Continental Crust: Its Composition and Evolution; Oxford Blackwell: Oxford, UK, 1985; pp. 1–312

Traverse, A., 2007. Paleopalynology, second ed. Springer, Dordrecht, p. 813

van Soelen, E.E., Kim, J.-H., Santos, R.V., Dantas, E.L., Vasconcelos de Almeida, F., Pires, J.P., Roddaz, M., Sinninghe Damsté, J.S., 2017. A 30 Ma history of the Amazon River inferred from terrigenous sediments and organic matter on the Ceará Rise. Earth and Planetary Science Letters 474, 40–48. https://doi.org/10.1016/j.epsl.2017.06.025

Varol, B., 2015. Stable isotopes (d18O, d13C) of mollusk shells in environmental interpretations; an example from sinop Miocene succession (northern Turkey). Miner. Res Expl Bull 128, 49–60.

Vermeesch, P., 2013. Multi-sample comparison of detrital age distributions. Chemical Geology 341, 140–146. https://doi.org/10.1016/j.chemgeo.2013.01.010

Vermeesch, P., 2004. How many grains are needed for a provenance study? Earth Planet. Sci. Lett. 224, 441–451. https://doi.org/10.1016/j.epsl.2004.05.037.

Vermeesch, P., Resentini, A., Garzanti, E., 2016. An R package for statistical provenance analysis. Sedimentary Geology 336, 14–25. https://doi.org/10.1016/j.sedgeo.2016.01.009

Wei, G., Liu, Y., Ma, J., Xie, L., Chen, J., Deng, W., Tang, S., 2012. Nd, Sr isotopes and elemental geochemistry of surface sediments from the South China Sea: Implications for Provenance Tracing. Marine Geology 319–322, 21–34. https://doi.org/10.1016/j.margeo.2012.05.007

Widenbeck, M., All´e, P., Corfu, F., Griffin, W.L., Meier, M., Oberli, F., Quadt, A.V., Roddick, J.C., Spiegel, W., 1995. Three natural zircon standards for U-Th-Pb, Lu-Hf, trace element

and REE analyses. Geostand. Geoanalytical Res. 19, 1–23. https://doi.org/10.1111/j.1751-908X.1995.tb00147.x.

CAPÍTULO 3

RECONSTRUÇÕES PALEOAMBIENTAL E PALEOGEOGRÁFICA DO PALEÓGENO DA AMAZÔNIA OCIDENTAL

Nouvelles données paléogéographiques et biostratigraphiques sur le Paléogène de l'Amazonie occidentale

3. RECONSTRUÇÕES PALEOAMBIENTAL E PALEOGEOGRÁFICA DO PALEÓGENO DA AMAZÔNIA OCIDENTAL

RÉSUMÉ

Les résultats de ce chapitre sont exprimés sous la forme d'un article publié au Journal of South American Earth Sciences (Custodio et al., 2023, *New stratigraphic and paleoenvironmental constraints on the Paleogene paleogeography of Western Amazonia* https://doi.org/10.1016/j.jsames.2023.104256).

La croissance des Andes et la propagation associée du bassin d'avant-pays rétroarc amazonien au cours du Mésozoïque et du Cénozoïque ont façonné la paléogéographie et les paramètres paléoenvironnementaux de l'Amazonie occidentale. Une grande attention a été portée à l'évolution néogène du bassin amazonien occidental, mais peu d'études ont examiné en détail les paléoenvironnements Paléogènes de l'Amazonie occidentale. Nous présentons une étude multiparamétrique qui comprend de nouvelles données biostratigraphiques et paléontologiques, l'interprétation des environnements de dépôt et des données U-Pb sur les zircons de la séquence sédimentaire du Crétacé supérieur au Paléogène exposée dans le bassin de Huallaga (nord du Pérou). La datation biostratigraphique suggère que la partie inférieure de la séquence est d'âge maastrichtien. L'âge maximum de dépôt et l'âge le plus vraisemblable selon la datation U-Pb des zircons des roches sédimentaires du Paléogène indiquent des âges lutétiens à bartoniens (de 43.5 ± 0.64 Ma à 37.6 ± 0.85 Ma). Ces résultats révèlent une lacune dans l'enregistrement sédimentaire pendant le Paléocène que nous attribuons à un stage de quiescence tectonique. Deux systèmes de dépôt peuvent être distingués : un système lacustre composé de mudstones rouges intercalés de couches épaisses de grès et de lits de carbonates, et un système siliciclastique dominé par les marées, composé de grès fins à moyens associés à des couches de marées, des surfaces de réactivation et des stratifications hétérolithiques. Les valeurs isotopiques stables du carbone et de l'oxygène dans les carbonates tendent à caractériser un système d'eau douce, avec une transition vers des conditions saumâtres vers la partie supérieure de la section (bartonien), suggérant ainsi la présence d'un système estuarien. Enfin, nous suggérons que l'incursion marine peu profonde bartonienne enregistrée dans le bassin de Huallaga est survenue depuis le nord, à travers la mer des

Caraïbes, et qu'elle aurait pu jouer un rôle dans les schémas régionaux de biodiversité au Paléogène.

RESUMO

Os resultados deste capítulo são expressos sob forma de um artigo científico intitulado: "*New stratigraphic and paleoenvironmental constraints on the Paleogene paleogeography of Western Amazonia*", publicado na *Journal of South American Earth Sciences* (https://doi.org/10.1016/j.jsames.2023.104256). A partir de um estudo baseado em dados petrográficos, estratigráficos, paleontológicos, datações geocronológicas de U-Pb em zircões detríticos, composições isotópicas em carbono e oxigênio de rochas carbonáticas do final do Cretáceo ao Eoceno, foi possível reconstruir as variações paleoambiental e paleogeográfica associadas com o soerguimento dos Andes e propagação do sistema de bacia de retroarco de antepaís, durante o Paleógeno da Amazônia Ocidental.

O soerguimento dos Andes e a propagação associada da bacia do retroarco durante o Cenozóico Mesozóico no oeste da América do Sul moldaram a paleogeografia e os cenários paleoambientais da Amazônia Ocidental. Muita atenção tem sido dada à evolução neogênica da Bacia Amazônica, mas poucos estudos investigaram em detalhes os paleoambientes da Amazônia Ocidental durante o Paleogene. Apresentamos um estudo multi-proxy que inclui novos dados bioestratigráficos e paleontológicos, a interpretação de ambientes deposicionais e dados de zircão U-Pb da sequência sedimentar Cretáceo-Paleogênica Superior exposta na Bacia de Huallaga (norte do Peru). A datação bioestratigráfica sugere que a parte inferior da sequência é maastrichtiana em idade. A idade de deposição máxima e a idade de verossimilhança máxima de acordo com a datação em zircão U-Pb de rochas sedimentares Paleogênicas indicam idades Lutetianas a Bartonianas (de 43.5 ± 0.64 Ma a 37.6 ± 0.85 Ma). Estes resultados revelam um hiato no registro deposicional durante o Paleoceno. Dois sistemas deposicionais podem ser distinguidos: um sistema lacustre composto por mudrocks vermelhos entrelaçados com espessas camadas de arenito e leitos de carbonato, e um sistema siliciclástico dominado pela maré composto de arenitos finos a médios associados a feixes de maré, superfícies de reativação e estratificações heterolíticas. No entanto, os valores de isótopos estáveis de carbono e oxigênio em carbonatos tendem a caracterizar um sistema de água doce, com

uma transição para condições salobras em direção à parte superior da seção (Bartonian), sugerindo assim a presença de um sistema estuário. Finalmente, sugerimos que a incursão marinha rasa bartoniana registrada na Bacia de Huallaga ocorreu do norte através do Mar do Caribe, e que pode ter desempenhado um papel nos padrões regionais de biodiversidade no Paleogene.

NEW STRATIGRAPHIC AND PALEOENVIRONMENTAL CONSTRAINTS ON THE PALEOGENE PALEOGEOGRAPHY OF WESTERN AMAZONIA

Michele Andriolli Custódio[a,b,c], Martin Roddaz[a,c], Roberto Ventura Santos[a], Pierre-Olivier Antoine[d], Laurent Marivaux[d,h], Narla S. Stutz[d,e]; Elton Luiz Dantas[a], Carlos Jaramillo[f], Mélanie Louterbach[g], Christian Hurtado[h], Guilherme de Oliveira Gonçalves[a]

[a] Laboratório de Geocronologia, Instituto de Geociências, Universidade de Brasília, Brasília, DF 70910-000, Brazil

[b] Departamento de Geociências, Universidade Federal do Amazonas, CEP: 69.077-000, Manaus, AM, Brazil

[c] Géosciences-Environnement Toulouse, Université de Toulouse, UPS (SVT-OMP), CNRS, IRD, 14 Avenue Édouard Belin, 31400 Toulouse, France

[d] Institut des Sciences de l'Évolution de Montpellier, Univ Montpellier, CNRS, IRD, Place Eugène Bataillon, 34095, Montpellier, France

[e] Programa de Pós-Graduação em Geociências, Universidade Federal do Rio Grande do Sul (PPGGEO UFRGS). Av. Bento Gonçalves, 9500, 91501-970, Porto Alegre, Rio Grande do Sul, Brazil.

[f] Smithsonian Tropical Research Institute, Roosevelt Avenue, Building 401 Balboa, Ancon, Panama City, Panama

[g] Harvard Graduate School of Design, Department of Landscape Architecture, 48 Quincy Street, MA 02138 Cambridge, USA.

[h] Universidad Nacional Mayor de San Marcos, Av. Venezuela Cda. 34 s/n Lima-Cercado, Lima, Peru.

*Corresponding author

Email address: mi.andriolli@gmail.com (M.A. Custódio)

Published by Elsevier Ltd. – *Journal of South American Earth Sciences* (2023)

3.1 ABSTRACT

The rise of the Andes and the associated propagation of the retroarc foreland basin during the Mesozoic Cenozoic in western South America shaped the paleogeography and

paleoenvironmental settings of Western Amazonia. Much attention has been paid to the Neogene evolution of the Amazonian Basin, but few studies have investigated in detail the paleoenvironments of Western Amazonia during the Paleogene. We present a multi-proxy study that includes new biostratigraphic and paleontologic data, the interpretation of depositional environments and zircon U-Pb data from the Upper Cretaceous-Paleogene sedimentary sequence exposed in the Huallaga Basin (northern Peru). The biostratigraphic dating suggests that the lower part of the sequence is Maastrichtian in age. The maximum depositional age and maximum likelihood age according to the U-Pb zircon dating of Paleogene sedimentary rocks indicate Lutetian to Bartonian ages (from 43.5 ± 0.64 Ma to 37.6 ± 0.85 Ma). These results reveal a hiatus in the depositional record during Paleocene time. Two depositional systems can be distinguished: a lacustrine system composed of red mudrocks interbedded with thick sandstone layers and carbonate beds, and a siliciclastic tide-dominated system composed of fine- to medium-grained sandstones associated with tidal bundles, reactivation surfaces and heterolithic stratifications. However, the carbon and oxygen stable isotope values in carbonates tend to characterize a freshwater system, with a transition to brackish conditions toward the upper part of the section (Bartonian), thereby suggesting the presence of an estuary system. Finally, we suggest that the Bartonian shallow marine incursion recorded in the Huallaga Basin occurred from the north through the Caribbean Sea, and that it might have played a role in regional biodiversity patterns in the Paleogene.

Keywords: *zircon U-Pb dating, C and O isotopes, shallow marine deposits, northern Peru, paleogeography*

3.2 INTRODUCTION

Precise knowledge of the geological evolution of Amazonian landscapes and ecosystems is a prerequisite for understanding species diversification in this vast area today biodiversity seems to be deeply rooted in the pre-Quaternary (Hoorn et al., 2010b, and the references therein). The uplift of the Andes reconfigured drainage patterns, involved a vast influx of sediments into the Amazonian basins (Figure 3.1) (e.g. Roddaz et al., 2010, 2005a), and caused shallow marine incursions in Western Amazonia (Jaramillo et al., 2017; Boonstra et al., 2015; Hovikoski et al., 2010).

Recently, much attention has been paid to the Neogene paleogeographyof the Amazonian basins, especially to the timing of the modern transcontinental Amazon River (Hoorn et al., 2017; van Soelen et al., 2017; Eakin et al., 2014; Gorini et al., 2014; Sacek, 2014; Shephard et al., 2010; Figueiredo et al., 2009). Attention has also been given to the Neogene paleogeography of Western Amazonia (Carina Hoorn et al., 2010) and the number and nature of marine incursions that affected this area during the Miocene (i.e., the Pebas megawetland system) (Jaramillo et al., 2017; Antoine et al., 2016; Boonstra et al., 2015; Hovikoski et al., 2010; Hoorn, 1993). However, surface uplift driven by the tectonism and denudation of the present-day Amazonian Andes area started much earlier, as recorded in the Upper Maastrichtian-Paleocene deposits (Hurtado et al., 2018; Louterbach et al., 2018a).

In comparison with the Neogene period, the Paleogene paleoenvironmental changes of Western Amazonian basins have still a poorly documented and poorly dated stratigraphic record. Notable exceptions are the detailed studies of Antoine et al. (2016) and Louterbach et al., (2018b). In the Late Cretaceous (Middle Campanian and Late Maastrichtian), the sedimentary record of the Ecuadorian and northern Peruvian parts of the Western Amazonian Basin (i.e., the Marañón Basin) (Figure 3.1) indicates thick transgressive-regressive sequences alternating between fluvial-marine paleoenvironments controlled by eustatic processes (Zamora and Gil, 2018). It is unclear whether or not these conditions prevailed during the Paleogene and how the onset of the Andean uplift affected the landscape and paleoenvironment of Western Amazonia.

Two shallow marine transgressions that occurred during the Paleogene are currently documented in Western Amazonia. The oldest one is a Late Paleocene shallow marine transgression characterized by estuarine and bay paleoenvironments (Louterbach et al., 2014a). This latter event has only been documented in the southern part of the Amazonian retroarc foreland basin (Madre de Dios Basin, Peru) (Figure 3.1), and the entrance of this transgression remain unclear (Louterbach et al., 2014a). The second transgression is a Middle to Late Eocene shallow marine incursion known as the “Pozo” embayment or transgression, which flooded the northern part of the Amazonian retroarc foreland basins from the Gulf of Guayaquil or the Caribbean Sea (Roddaz et al., 2010; Santos et al., 2008; Christophoul et al., 2002; Antoine et al., 2016, 2021). However, the southwestern margin extension of this Pozo embayment needs to be better constrained. Hence, documenting

Paleogene paleoenvironments in other parts of the Western Amazonian Basin may contribute to resolving these issues.

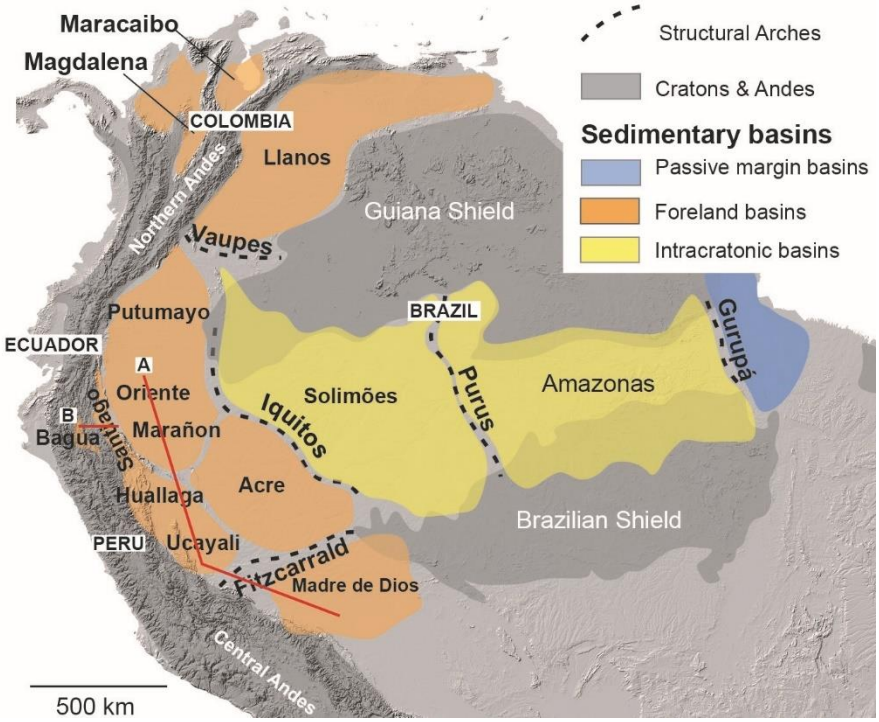


Figure 3. 1 Map of the geographic extent of the major morphotectonic provinces of the northern South Ameria, from west to east, the retroarc foreland basins (Colombia, Ecuador and Peru countries), the intracratonic and passive margin basins (Brazil), partially bounded by structural arches (dashed lines). Northern and Southern Amazon Craton are represented by the Guiana and Brazilian shields, respectively (modified and compiled from Albert et al., 2018; Moreno et al., 2020; Roddaz et al., 2010). The red lines indicate the location of figs 3 A and 3B.

Two shallow marine transgressions that occurred during the Paleogene are currently documented in Western Amazonia. The oldest one is a Late Paleocene shallow marine transgression characterized by estuarine and bay paleoenvironments (Louterbach et al., 2014a). This latter event has only been documented in the southern part of the Amazonian retroarc foreland basin (Madre de Dios Basin, Peru) (Figure 3.1), and the entrance of this transgression remain unclear (Louterbach et al., 2014a). The second transgression is a Middle to Late Eocene shallow marine incursion known as the “Pozo” embayment or transgression, which flooded the northern part of the Amazonian retroarc foreland basins from the Gulf of Guayaquil or the Caribbean Sea (Roddaz et al., 2010; Santos et al., 2008; Christophoul et al., 2002; Antoine et al., 2016). However, the southwestern margin extension of this Pozo embayment needs to be better constrained. Hence, documenting

Paleogene paleoenvironments in other parts of the Western Amazonian Basin may contribute to resolving these issues.

The Cretaceous–Cenozoic sedimentary infilling of the Huallaga Basin (Calderon et al., 2017a; Eude et al., 2015; Hermoza et al., 2005) has the unique potential to have recorded the Cretaceous–Paleogene paleoenvironmental evolution of the northern part of Western Amazonia as previous studies show major changes in the sedimentary provenance between the late Cretaceous and the Paleocene (Hurtado et al., 2018). The aim of this work is to characterize the paleoenvironmental evolution of the Huallaga Basin during the late Cretaceous-Paleogene time window, as a key element for unraveling the Andes – Amazon sedimentary evolution.

Our contribution comprises the first detailed stratigraphic analysis of the late Cretaceous–Paleogene sedimentary section, based on new multi-proxy analyses including sedimentological facies, biostratigraphy (palynostratigraphy and vertebrate biochronology), stable isotopes (C, O) in carbonates, and maximum depositional ages based on the U-Pb dating of detrital zircons.

3.3 GEOLOGICAL BACKGROUND

3.3.1 Tectonic setting and stratigraphy of the Huallaga Basin

The north-south trending Huallaga Basin (Figure 3.2) is currently 400 km long with a maximum width of 100 km (Hermoza et al., 2005), and it is part of the northern Peruvian Subandean Zone. It consists of the wedge-top depozone (DeCelles and Giles, 1996) of the North Amazonian retroarc foreland basin (Espurt et al., 2010, 2007; Roddaz et al., 2005b) that formed in response to the tectonic loading of the Andes (Roddaz et al., 2010). To the east, the Huallaga Basin is separated from the Marañón Basin by the Cushabatay High and Chazuta Thrust; the latter corresponds to the thrust front of the Subandean Zone (SAZ) (Figure 3.2) (Calderón et al., 2017a; Hermoza et al., 2005). To the west, the Huallaga Basin is delimited by the Eastern Cordillera (Figure 3.2). A sequential restoration based on low-temperature thermochronology and balanced cross-sections suggests that the Eastern Cordillera started to be uplifted between ca. 30 and 24 Ma, which caused thrusts to propagate over a regional detachment level located in the Upper Triassic evaporites (Carrillo et al, 2021; Calderón et al., 2017a, b; Eude et al., 2015). The Cretaceous tectonic

configuration of the Huallaga Basin is less constrained. The most recent model suggests that it could be part of a passive margin (Zamora and Gil, 2018) that received sediments from the Amazonian Craton (Hurtado et al., 2018).

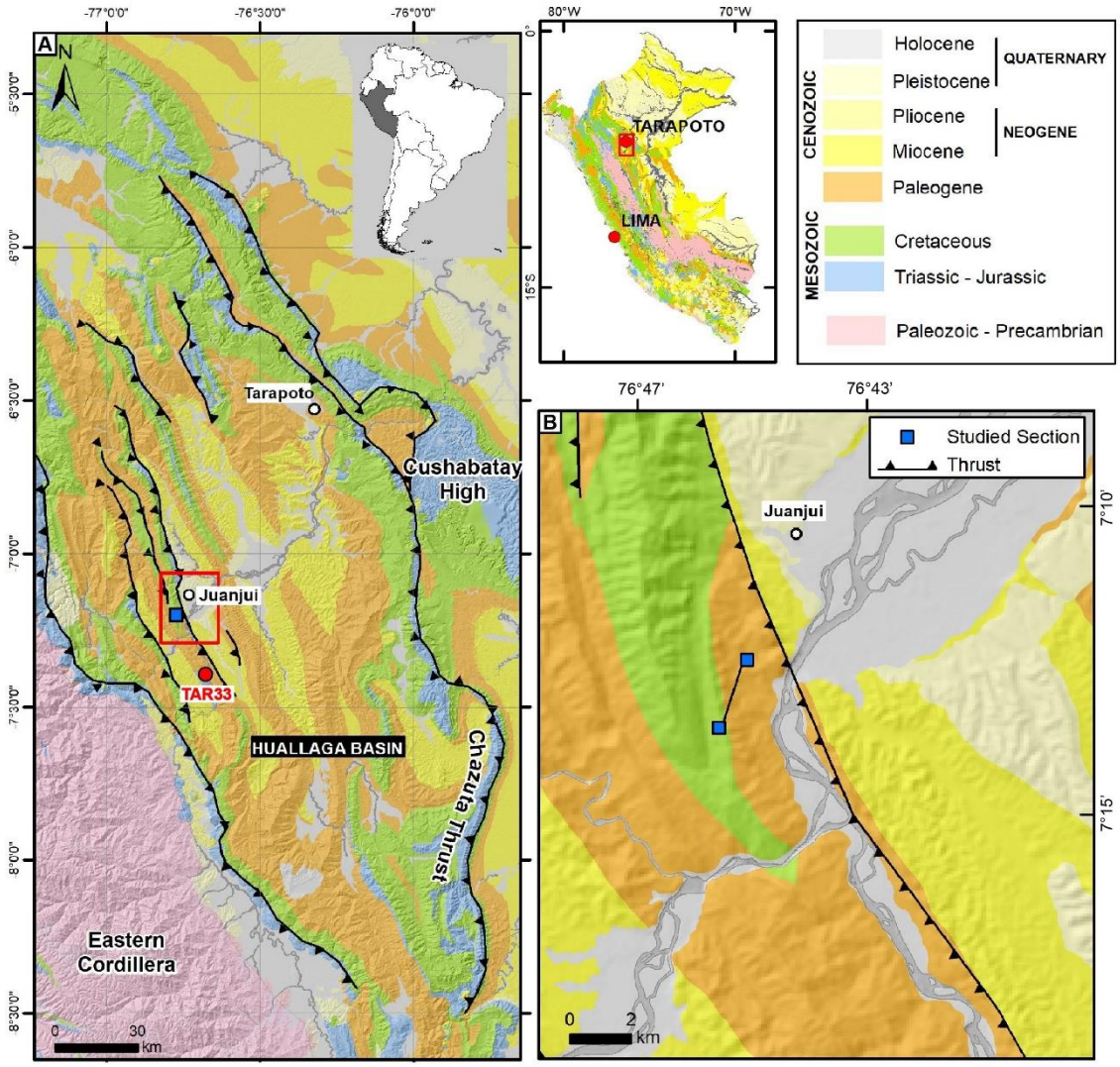


Figure 3. 2 Geological map of the studied area modified from the INGEMMET Geological Map of Peru available at http://geocatmin.ingemmet.gob.pe/geocatmin/. A) Regional geologic map of the Huallaga Basin, which is separated to the west from the Eastern Cordillera and limited, to east, from Marañón Basin by the Chazuta thrust and the Cushabatay High. The red rectangle indicate the location of the Juanjuí stratigraphic section. Location of the large dinosaur tracks is represented by TAR33; B) Detailed geological map showing the Mesozoic-Cenozoic geological contacts and the stratigraphic position of the Juanjui studied section.

The Cretaceous sequences of the Huallaga Basin comprise Albian to Maastrichtian fluvial to shallow marine successions of sandstones, shales and limestones (Cushabatay-Raya, Agua Caliente-Chonta, and Vivian-Cachiyacu-Huchpayacu formations) (Baby et al., 2018; Calderón et al., 2017a, b) (Figure 3.3). The Albian–Maastrichtian sedimentary rocks

of the Huallaga Basin have εNd(0) values (−16.8 to −18.6) consistent with a cratonic source, and a U-Pb zircon age distribution dominated by the easternmost Brazilian Shield terranes (Hurtado et al., 2018).

The Cenozoic stratigraphy of the Huallaga Basin still needs to be better constrained. Calderón et al. (2017) proposed that the Paleocene–lower Eocene sedimentary sequence started with the fluvial and tidal sandstones of the Casa Blanca Formation (Fm.), whereas other authors suggested that the Cenozoic sedimentary sequences started with the Paleogene fluvial sedimentary rocks of the Yahuarango Fm. (Hurtado et al., 2018; Roddaz et al., 2010; Hermoza et al., 2005; Gutierrez, 1982; Kummel, 1948). According to Hurtado et al. (2018), the Paleogene sedimentary rocks of the Yahuarango Fm. have an Andean provenance, with εNd(0) values ranging between -5.6 and -12.0, and up to 16% of U-Pb zircon ages are derived from the Andean volcanic arc.

3.3.2 Stratigraphy of other Western Amazonian basins

The Amazonian retroarc foreland basins experienced similar geological evolutions until the Pliocene uplift of the Fitzcarrald Arch (Figures 3.1 and 3.3) (Roddaz et al., 2010; Espurt et al., 2010). An extensional phase in a back-arc basin setting controlled the deposition of the mixed clastic and volcanic deposits of the Triassic Mitu group (George et al., 2019; Calderón et al., 2017), as recorded in the Bagua Basin, the Eastern Cordillera of Peru and the Santiago Basin (Figure 3.3). Farther southeast (Marañón-Huallaga-Ucayali basins), a regional extensional basin created due to post-extensional thermal subsidence drove the deposition of the Triassic-Jurassic eolian-fluvial deposits of the Lower Nia Fm. (Calderón et al., 2017a, b). These deposits grade laterally into the shallow marine carbonates of the post-rift Pucara Group and the Sarayaquillo fluvial sequence, as recorded in the Ecuadorian and Peruvian basins (George et al., 2019; Hurtado et al., 2018; Calderón et al., 2017) (Figure 3.3A; B). The Late Jurassic to Early Cretaceous are marked by a widespread sedimentary hiatus (145-120 Ma) (Hurtado et al., 2018; Calderón et al., 2017) (Figure 3.3A; B). Overlying this erosional unconformity, the Cretaceous sedimentary rocks comprised Albian to Maastrichtian fluvial to shallow marine deposits, mainly represented by the Goyallarisquizga, Cushabatay-Raya; Agua Caliente-Chonta, and Vivian-Cachiyacu-Huchpayacu formations (Figure 3.3A, B).

From the Late Cretaceous to the Early Paleogene, the Andean shortening started to control the configuration of the Western Amazonian basins (Horton et al., 2018; Hurtado et al., 2018; Louterbach et al., 2014; 2017; Calderón et al., 2017; Hermoza et al., 2005). The Cenozoic retroarc foreland infill comprises the fluvial and lacustrine siltstones/mudstones of the Paleogene Yahuarango Fm. (Marañon-Huallaga-Ucayali basins) (Hurtado et al., 2018; Roddaz et al., 2010; Hermoza et al., 2005; Gutierrez, 1982; Kummel, 1948), which can be correlated with the Tiyuyacu (Oriente Basin) (Baby et al., 2013) and Huayabamba formations (Madre de Dios Basin) (Louterbach et al., 2014).

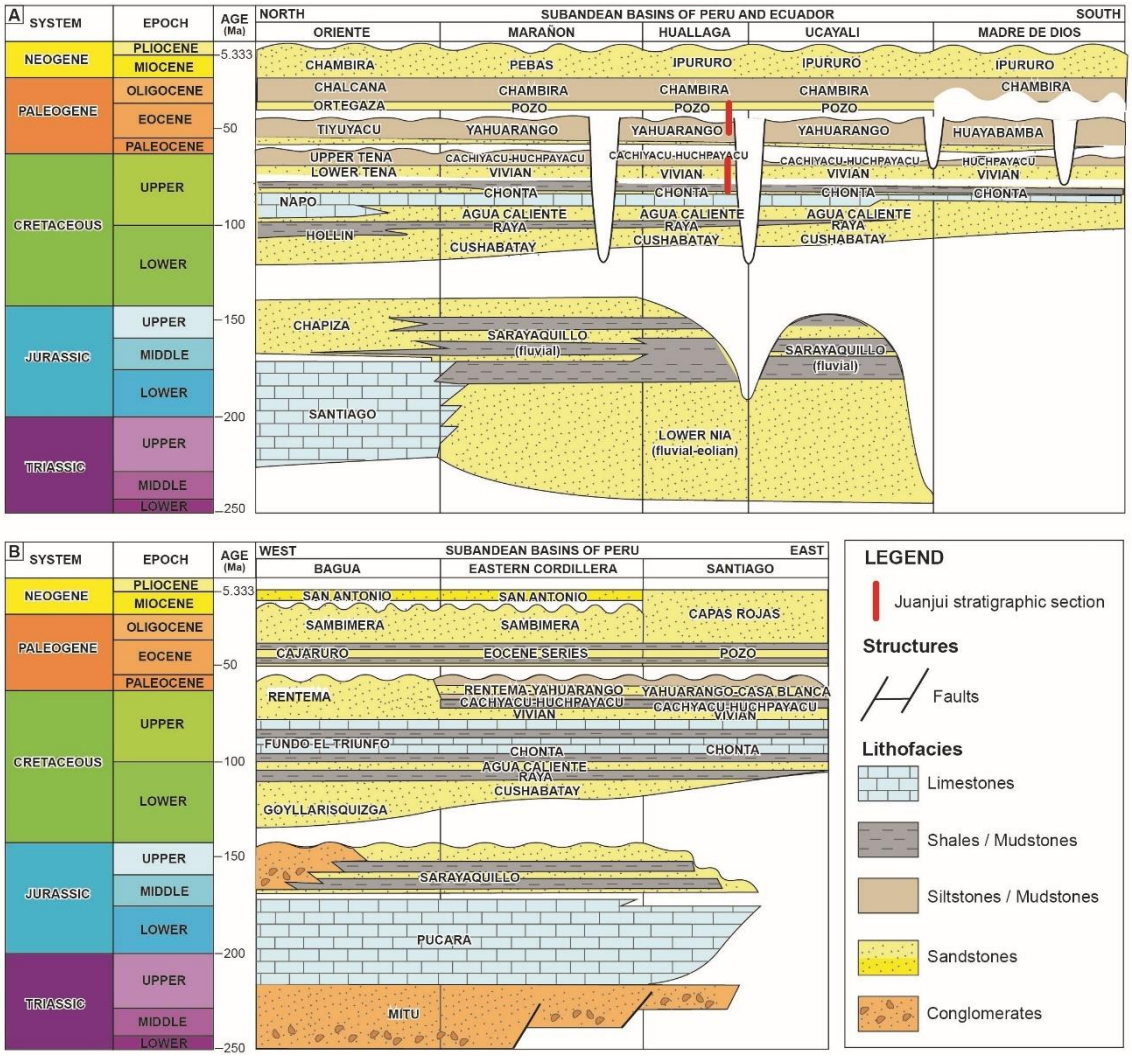


Figure 3. 3 Comparative chronostratigraphic diagram showing the stratigraphic nomenclature, age, lithology, tectonic setting, and stratigraphic discontinuities for (A) the Ecuadorian and Peruvian Subandean Amazonian basins and (B) Peruvian Amazonian foreland basins. The chronostratigraphic diagram (A) was constructed based on Baby et al. (2013); Calvès et al. (2018); Roddaz et al. (2010), Hurtado et al. (2018); Hermoza et al. (2005); Louterbach et al. (2014), and Calderón et al. (2017a, 2017b). The chronostratigraphic diagram (B) is based on Moreno et al. (2020; 2022) and George et al. (2019).

These formations can be correlated with the Paleocene-lower Eocene braided fluvial deposits of the Rentema Fm. in the Bagua Basin (Moreno et al., 2022; 2020) (Figure 3.3B). These formations are separated from the youngest formations by a middle Eocene regional unconformity recorded in the Ecuadorian and Peruvian retroarc foreland basins (Figure 3.3) (Roddaz et al., 2010; Christophoul et al., 2002;). The shallow marine deposits of the middle Eocene-Oligocene Pozo Fm. are recorded in the Santiago, Marañón, Huallaga and Ucayali basins. The Pozo Fm. can be correlated to the north with the Ortegaza Fm. (Oriente Basin) (Baby et al., 2013) and to the west with the Eocene Series (Eastern Cordillera) and the fluvio-lacustrine Cajaruro Fm. (Bagua basin) (Moreno et al., 2022; 2020) (Figure 3.3A, B). It is overlaid by the Upper Oligocene-Lower Miocene fluvial deposits of the Chambira Fm. in the Peruvian retroarc foreland basins (Antoine et al., 2016) and by the Chalcana Fm. in the Ecuadorian Oriente retroarc foreland basin (Baby et al., 2013). These formations can be correlated with the Upper Eocene-middle Miocene meandering deposits of the Sambimera Fm. in the Bagua Basin (Moreno et al., 2022, 2020) and Eastern Cordillera, and the Capas Rojas Fm. in the Santiago Basin (George et al., 2019) (Figure 3.3B). Finally, the Neogene sedimentary deposits are characterized by the fluvial deposits of the Ipururo, Chambira and San Antonio formations in the Bagua Basin, Eastern Cordillera, Huallaga, Ucayali, Madre de Dios basins (Moreno et al., 2022, 2020; George et al., 2019; Calderón et al., 2017; Hermoza et al., 2005) (Figure 3.3A, B). These deposits can be correlated with those of the Pebas Fm. that belong to the Pebas megawetland system (Hoorn et al., 2022; Jaramillo et al., 2017; Antoine et al., 2016; Boonstra et al., 2015; Hovikoski et al., 2010; Hoorn, 1993) in the Marañón Basin.

3.4 MATERIALS AND METHODS

3.4.1 Sedimentology

We studied in detail one Mesozoic–Cenozoic section, the Juanjuí section (Figure 3.4). The outcrops investigated in this study crop out along the 5N national road close to the Huallaga River and the city of Juanjuí (see Figure 3.2 for the location and Supplementary Material S1 for the coordinates). To better understand the depositional environment, we measured and described several outcrops along the Juanjuí stratigraphic section. We described the clastic facies in terms of their lithology, geometry, sedimentary structures and paleontological content (Miall, 2006; 1978). The chemical facies

(microfacies) were described using Dunham's (1962) classification, which considers the abundances of carbonates, mud and grains; this helps to better constrain the formation process and/or paleoenvironmental conditions. The most commonly used criteria are the depositional texture and fabric, as well as qualitative and quantitative compositional data (Flügel, 2010). As pointed out by Walker (1992), most classifications for carbonates were originally conceptualized for marine systems, but they have also been used for lacustrine deposits with some adjustments. The carbonate thin sections were prepared at the Laboratório de Laminação (LABLAM) of the Universidade de Brasília (UnB). Thirteen sedimentary facies have been identified (Tables 1).

3.4.2 Stable isotopes

Forty-six samples of limestones and sandstones in a carbonate matrix were collected along the Juanjuí stratigraphic section (Figure 3.4). The abbreviations HUA (Huallaga) and JUA (Juanjuí) are used to refer to the samples obtained during field work performed in September 2017 and August 2019, respectively. The carbon and oxygen isotopic compositions are shown in Supplementary Material Table S2.

The samples were analyzed at the Geochronology and Isotope Geochemistry Laboratory of the University of Brasília (LEGGA) on a Delta V Plus mass spectrometer connected to a Gas Bench II apparatus. The samples reacted with H_3PO_4 at a temperature of 72 °C after the flask was flushed with helium. Stable isotope results are reported in delta notation relative to the Vienna Pee Dee Belemnite (V-PDB) reference standard, and they were calibrated against the NBS 18 ($\delta^{13}C_{V\text{-}PDB} = -5.01‰$ and $\delta^{18}O_{V\text{-}PDB} = -23.2‰$) and NBS 19 ($\delta^{13}C_{V\text{-}PDB} = 1.95‰$ and $\delta^{18}O_{V\text{-}PDB} = -2.20‰$) reference materials. A linear regression of the standard results followed by correction of the sample data, were performed to account for instrumental bias. To avoid any diagenetic biases, we selected only well-preserved samples.

The isotopic composition of carbon and oxygen in a sample was expressed by dividing the isotopic ratio (R) measured in the sample by the isotopic ratio of a standard (V-PDB) using the δ notation; the isotopic composition is expressed in parts per thousand (‰). $\delta^{13}C$ and $\delta^{18}O$ were obtained as follows: $\delta^{13}C_{(sample)} = [(R_{sample}/R_{V\text{-}PDB}) - 1] * 10^3$, and $\delta^{18}O_{(sample)} = [(R_{sample}/R_{V\text{-}PDB}) - 1] * 10^3$, respectively (Guiguer et al., 2003).

3.4.3 Palynological analysis

The palynological samples were prepared at the Universidad de Caldas following the standard palynological processing method proposed by Traverse (2007). Carbonates and silicates were removed by digesting the samples in HCl and HF for 12 and 24 hours, respectively. After acid digestion, the samples were neutralized through repeated dilution with distilled water and decanting. The remaining residue was initially sieved with a 250 µm mesh; this was followed by sieving through a 10µm mesh. This residue was cleaned in an ultrasonic equipment for 15 seconds and the organic residue was concentrated by centrifugation, followed by the mounting of a first cover slide in a solution of polyvinyl alcohol. Part of the residue was oxidized in nitric acid for 2–3 minutes, and a second slide was mounted. The slides were sealed with Canadian balsam. A Nikon i80 at the Smithsonian Tropical Research Institute was used to scan the slides. The examination and description of the palynological material were carried out using a 100x Nikon oil immersion planapochromatic objective. The identification of the palynomorphs was performed through a comparison with photographs and descriptions of Cretaceous and Paleocene material published for northern South America that are compiled in an online database (Jaramillo and Rueda, 2021). The palynological zonation of Jaramillo et al. (2011) and the biostratigraphic analysis of Carvalho et al. (2021) and De La Parra et al. (2021) were used to assess the age of the samples.

3.4.4 U-Pb ages

Zircon grains were obtained from three samples of medium-grained sandstones collected along the Juanjuí section (JUA 8A/19, 11 and 14; Figures 2.4, S1 and S3–S5). For U-Pb analyses, each sample was prepared and analyzed at the Geochronology and Isotope Geochemistry Laboratory (LEGGA) of the University of Brasília (UnB). The sample preparation process included crushing rock samples, which was followed by heavy mineral separation by panning. Additionally, another separation was performed based on the magnetic properties of the minerals using the Frantz Isodynamic Magnetic Separator. A random selection of the zircon grains was handpicked (~150 grains per sample) under a stereomicroscope, mounted on adhesive tape, enclosed in a 9-mm-diameter plastic ring placed on the tape around the zircons and filled with epoxy resin. Finally, the zircon grains

were polished to expose their centers (Gehrels, 2014; Bühn et al., 2009; Gehrels et al., 2008). The mounts with zircon grains were imaged by a scanning electron microscope (SEM) and back-scattered electron (BSE) detector to identify morphological features and internal structures and to provide a base map for recording laser spot locations.

The masses of interest were measured on a Thermo Finningan Element XR high-resolution single-collector sector field Inductively Coupled Plasma Mass Spectrometry (ICP-MS) coupled to a 193 nm Iridia Excimer (ArF) laser ablation system. The laser ablation system is equipped with a cobalt dual-volume chamber. The mass spectrometer was tuned to improve U and Pb sensitivity while minimizing oxide production prior to each analytical session. Each analysis consisted of 10 s of background measurement followed by 20 s of sample acquisition. Each mass (202, 204, 206, 208, 232, 238) was measured using the triple detection mode (SEM + Faraday) by sweeping the electrostatic sector on each mass. Each sweep lasted 82 ms, resulting in over 800 scans for each ablation. Laser conditions included a spot diameter of 25 µm, 20 Hz and 2.0 J cm-2. The raw data were processed on Iolite 4.0 (Paton et al., 2011) as a time-resolved signal and individual signal inspection was done with the assistance of VizualAge (Petrus and Kamber, 2012). Data correction included blank subtraction, Laser Induced Elemental Fractionation (LIEF) correction using an exponential plus linear model and normalization using the GJ-1 zircon (Jackson et al., 2004) and 91500 zircon (Widenbeck et al., 1995). Excess variance on the primary calibrant was propagated on each analytical point. A systematic uncertainty of *ca.* 1% is propagated on each final age. No common lead correction was applied. The ages uncertainties are quoted at 2 sigma (2σ) confidence level.

The data reduction of the U-Pb isotopic results for detrital zircons was conducted using Iolite 4.0 and followed the procedures of Paton et al. (2011). Details regarding the LA-ICP-MS U-Th-Pb dating of the analyzed samples at the LEGGA can be found in Tables S3 to S6 (supplementary dataset).

For the three analyzed samples, we calculated a maximum depositional age using two different statistical methods, the “maximum depositional age’ (MDA) and “maximum likelihood age’ (MLA) (Table S6). The MDA was calculated as the weighted mean average of the overlapped analyses of the three youngest zircons and the associated 2σ uncertainty of this cluster (YC2σ[3+]; Sharman and Malkowski, 2020; Sharman et al., 2018; Dickinson and Gehrels, 2009) . The MLA is a statistical model that assumes that the zircon U-Pb ages

are defined as a two-component mixture in which a “fraction of the population is derived from a discrete minimum age peak and the remaining grains follow a (log)normal distribution” (Vermeesch, 2021; Gailbraith, 2005; Galbraith and Laslett, 1993). The MLA was calculated using IsoplotR (Vermeesch, 2021, 2018).

3.5 RESULTS

3.5.1 Sedimentary facies

The Juanjuí section is approximately 450 m thick and comprises nine siliciclastic facies and four carbonate microfacies, which are summarized in Table 1; Figure 3.4.

Table 3. 1 Summary of the descriptions and interpretations of each sedimentary silicilastic facies and carbonate microfacies.

Table 1
Summary of the descriptions and interpretations of each sedimentary siliciclastic facies and carbonate microfacies.

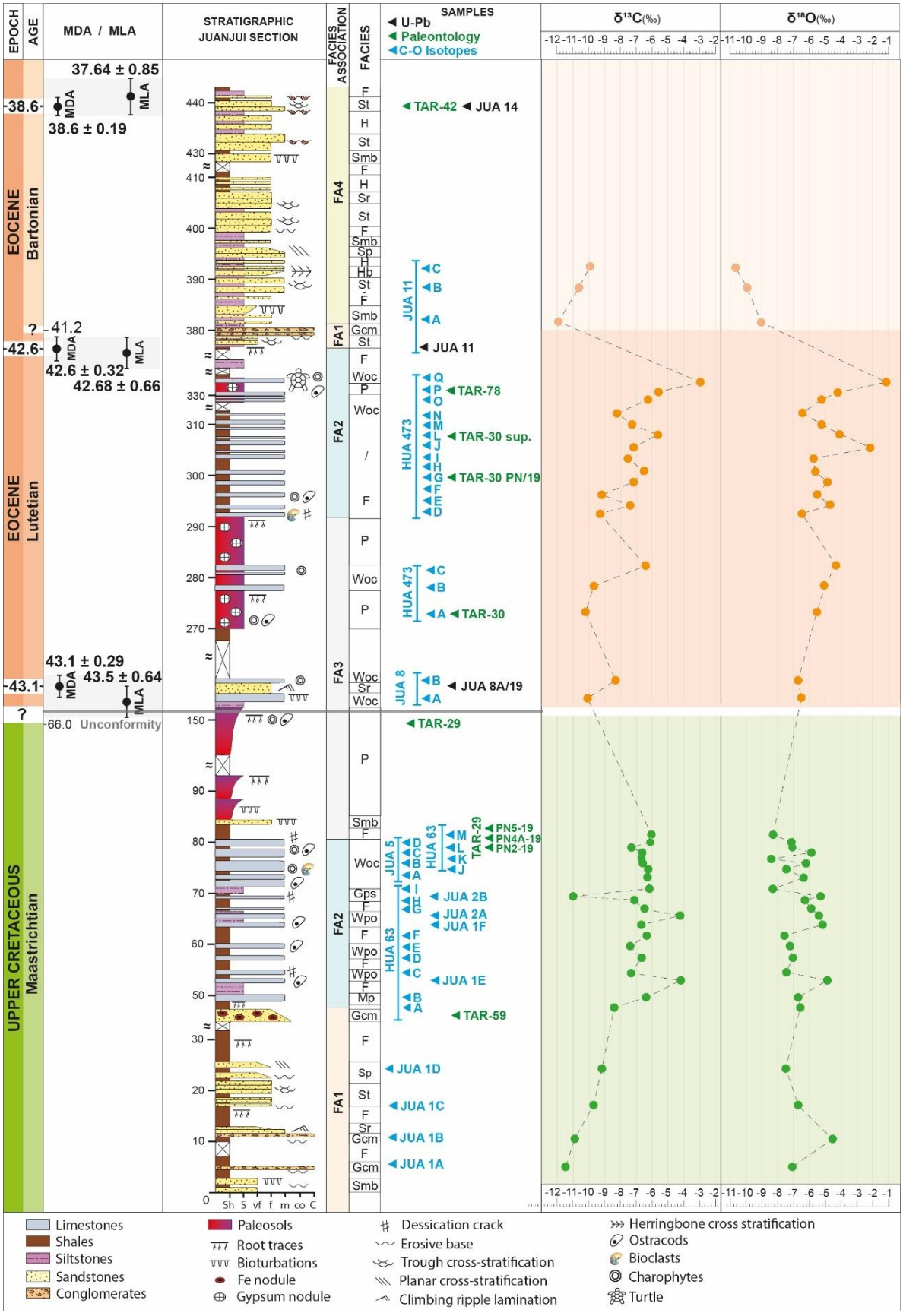
Facies/ Microfacies	Lithology and Texture	Sedimentary Structures	Paleontological content	Ichnology	Thickness (m)	Other characteristics/ Geometries	Interpretation
Siliciclastic facies							
Gcm Massive clast-supported conglomerate	Rounded- to sub-rounded mud-clasts (monomictic conglomerates), with cm-dm size (3–15 cm), scattered in the bed. Matrix composed by medium- to coarse-grained arkosik sandstones, with scattered subrounded granules and pebbles (milky quartz pebbles). Poorly-defined fining-upward trend; very poor sorting	Massive	No fossils	No trace fossils	0.3–0.5	Discontinuous and cuneiform beds, marked by concave-up bases	This deposits could be referred as filling of a channel lag deposits, under high sediment concentration and erosive event (Miall, 1978, 1996)
St Trough cross-stratified sandstone	Reddish and brownish, sub-rounded grains, well- to moderately-sorted, fine-to medium-grained arkosic sandstones, with thin mudstone layer drape on the foresets, regular thick-thin (0.1–0.5 cm) alternations in lamina thickeness. Foresets dipping at low angles (5–10°)	Trough cross-stratification	No fossils	No trace fossils	0.2–0.4	Dm-thick wedge-shaped beds. Reactivation surfaces delimiting the foresets.	Migration of subaqueous dunes (3D) by unidirectional flow in lower flow regime. Compound dune/tidal dune of channel infill. Variable energy flow (Miall, 1978, 1996)
Sp Planar cross-stratified sandstone	Sub-rounded grains, well- to moderate-sorted, medium-grained arkosic sandstones, organized in dm-thick	Planar cross-stratification	No fossils	No trace fossils	0.8	Tabular beds, typically flat on the top and concave-up base	Migration of 2D subaqueous dunes by unidirectional flow in lower flow regime (Miall, 1978, 1996)
Sr Climbing ripple cross-laminated sandstone	Rounded grains, well-sorted, very fine- to fine grained arkosic sandstones	Climbing ripple cross-lamination	No fossils	No trace fossils	0.25–0.4	Organized in cm-thick wedge-shaped beds, with flat base	Migration of supercritical climbing ripples by a lower regime unidirectional flow (Miall, 1978, 1996)
Smb Massive sandstone bioturbated	Reddish to brownish, sub-rounded to sub-angular grains, well- to moderate sorted, fine- to medium-grained arkosic sandstone, moderate to highly bioturbated	Massive	No fossils	Vertical and horizontal burrows	0.3–1.0	Tabular beds with flattered top and base. Obliteration of the primary sedimentary structure	Post-depositional modification by bioturbation (Miall, 1978, 1996)
H Heterolithic facies	Grey to beige, well-sorted, sub-rounded grains, very fine- to fine-grained arkosic sandstones with scattered flaser-bedding (mud drapes ~ 0.1 cm) interbedded with linsen and wavy-bedding (10–20 cm) mudstone layers. Mm- to dm-scale interlamination of thin mud-rich and sand-rich layers, arranged in dm- to m-thick beds	Linsen, wavy and flaser beddings	No fossils	No trace fossils	up to 1	Beds with tabular geometry, normally flattered top and base	They are deposits of shallow bodies of water, under variations in sediment supply and tidal velocity/energy flow (Dalrymple et al., 2003; Dalrymple and Choi, 2007)
Hb Herringbone cross-stratified sandstone	Well- to moderate-sorted, sub-rounded to rounded grains, medium-grained arkosic sandstones	Herringbone cross-stratification	No fossils	No trace fossils	0.3–0.4	Organized in dm-thick wedge-shaped beds. Reactivation surface in association with bidirectional flow evidence	Deposition under opposite-direction currents, dominated either by flood or ebb currents (Dalrymple and Choi, 2007)
F Fines	Red to purple mudstones and siltstones, moderately to highly bioturbated	Massive	Echimonocolpites protofranciscoi, Ulmoideipites krempii, Cricotriporites aff. Macroporus, Proxapertites psilatus, Momipites africanus; Araucariacites sp	Vertical and horizontal burrows	up to 5	Tabular beds	Decantation in subaqueous environment with very low or absent energy (Miall, 1978, 1996)
P Paleosol	Silty shales with mottled aspect; carbonate nodules (2–3 cm); root traces	Massive/ incipient lamination	No fossils	Root traces (undefined)	5 to 10	Tabular beds	Long periods of plants colonization, non-deposition or highly probable low rate of accumulation. Process of evaporation conducting to ions concentration and formation of carbonate nodules (Miall, 2006; Nichols, 2009)

Table 1 (*continued*)

Facies/ Microfacies	Lithology and Texture	Sedimentary Structures	Paleontological content	Ichnology	Thickness (m)	Other characteristics/ Geometries	Interpretation
Mp Peloidal Mudstone	Dark brown, fine-grained carbonatic mud matrix (micrite), with scattered peloids grains and minor fine siliciclastic grains	Massive	Peloids	No trace fossils	0.1–0.2	Tabular beds with flattered top and base. Peloids (20–200 μm in diameter) are spherical, ellipsoidal and irregular carbonate grains, with no internal structure, moderately-sorted	Organically induced precipitation (Flügel, 2010; Tucker and Wright, 1990)
Wpo Wackestone with peloids and ostracods	Dark-brown limestones, mud-supported carbonate rock, composed by ostracods and peloids grains (20–45%). Peloids have clotted textures and the ostracods are normally scattered but are occasionally found oriented parallel to stratigraphic bedding by disarticulated valves	Massive/ incipient lamination	Peloids and Ostracods (200–400 μm)	No trace fossils	0.2–0.4	Tabular bed with flattered top and base. Locally, peloids have dense packaging	Deposited under low-energy condition with some water agitations, indicating some transportation (disarticulated valves) (Flügel, 2010; Tucker and Wright, 1990)
Woc Wackestone with ostracods and charophytes	Mainly composed by micrite with scattered bioclasts (>10% grains) such as ostracods and charophyte gyrogonites	Massive	Peloids; ostracods (200 μm); charophyte gyrogonites (600–800 μm)	No trace fossils	0.2–0.5	Tabular beds with flat base and undulated top. Moldic porosity characterized by molds of ostracods and charophyte remains (both broken and intact)	Deposited under low- to medium-energy condition with some water agitations, indicating some transportation (disarticulated valves) (Flügel, 2010; Tucker and Wright, 1990)
Gps Pisolithic Grainstone	Grainstone fabric with dominant occurrence of pisoids. The matrix contain abundant angular to subrounded, moderate to poorly sorted terrigenous quartz grains. Sutured contacts (microstylolitic) and concave-convex contacts (pisoids - quartz grains)	Massive	Pisoids (>2 mm)	No trace fossils	0.1–0.2	Brown to red pisoids with dense or irregular laminations, sub-spherical to irregular, partially replaced by pyrite (?)	Biogenic processes or chemical precipitation. Sutured grains related to compaction and pressure dissolution (Flügel, 2010; Tucker and Wright, 1990)

Table 3. 2 Summary of the descriptions and interpretations of each sedimentary silicilastic facies and carbonate microfacies.

Figure 3. 4 Synthetic Juanjuí stratigraphic section through the late Cretaceous (Maastrichtian) to late middle Eocene (Bartonian) at the Huallaga Basin, constructed from field observations, with location of the analyzed samples for C-O isotopic compositions, paleontological content (biostratigraphic constraints) and U-Pb zircon dating. Siliciclastic facies: massive clast-supported conglomerate (Gcm); trough cross-stratified sandstone (St), planar cross-stratified sandstone (Sp), climbing ripple cross-laminated sandstone (Sr), bioturbated sandstone (Smb), heterolithic facies (H), herringbone cross-stratified sandstone (Hb), fines (F) and paleosol (P). Carbonate microfacies: peloidal mudstone (Mp); wackestone with peloids and ostracods (Wpo); wackestone with ostracods and charophytes (Woc); and pisolitic grainstone (Gps). FA= Facies association. See text and Table 1 for details.


EPOCH
AGE
MDA / MLA
STRATIGRAPHIC JUANJUI SECTION
FACIES ASSOCIATION
FACIES
SAMPLES
U-Pb
Paleontology
C-O Isotopes
δ13C(‰)
δ18O(‰)
EOCENE
Bartonian
EOCENE
Lutetian
UPPER CRETACEOUS
Maastrichtian
37.64 ± 0.85
MDA
MLA
38.6
38.6 ± 0.19
41.2
42.6
42.6 ± 0.32
42.68 ± 0.66
43.1 ± 0.29
43.5 ± 0.64
43.1
66.0 Unconformity
FA4
FA1
FA2
FA3
TAR-42
JUA 14
JUA 11
TAR-78
TAR-30 sup.
TAR-30 PN/19
TAR-30
JUA 8A/19
TAR-29
PN5-19
PN4A-19
PN2-19
JUA 2B
JUA 2A
JUA 1F
JUA 1E
TAR-59
JUA 1D
JUA 1C
JUA 1B
JUA 1A
HUA 473
HUA 63
JUA 5
JUA 8
Sh S vf f m co C
Limestones
Shales
Siltstones
Sandstones
Conglomerates
Paleosols
Root traces
Bioturbations
Fe nodule
Gypsum nodule
Dessication crack
Erosive base
Trough cross-stratification
Planar cross-stratification
Climbing ripple lamination
Herringbone cross stratification
Ostracods
Bioclasts
Charophytes
Turtle

3.5.1.1 Facies association 1 (FA1)

Description. Facies association 1 is made up of six facies: Gcm, St, Sp, Smb, Sr and F (Table 1, Figure 3.4). It vertical succession generally displays a fining- and thinning upward, and it typically has a m-scale thickness (5 m). It starts with the channelized bodies of the coarse-grained facies (Gcm) (Figure 3.5A, B), which grade to fine-to medium-grained arkosic sandstones with trough (St) (Figure 3.5C) and planar (Sp) cross-stratifications, and it ends with cm-scale-thick, very-fine- to fine, climbing-rippled sandstones (Sr) (Figure 3.5D) interbedded with the fines facies (F), which is marked by root traces. The channel bodies show discontinuous and cuneiform beds, and they laterally change into interbedded fine-to medium-grained arkosic sandstones. Locally, the fine-grained trough cross-bedded sandstones are arranged in wedge-shaped sets with mm-scale mudstone layers draped over the foresets (St facies) (Figure 3.5F), which are highlighted by reactivation surfaces. There are also dm-scale, very-fine-grained deposits with highly bioturbated sandstone (Smb) (Figure 3.5E) interbedded with the fines facies (F). FA1 is observed in the lower parts of the Juanjuí section (0 – 30 m) (Figure 3.4).

Interpretation. Channel body geometries, such as those observed in FA1, are common deposits in tidal and fluvial settings. In both systems, channels reveal an erosive base that internally comprises upward-fining and thinning-up strata that grade upwards into shales and siltstone beds. These fines beds at the top of the succession can characterize either tidal flat or fluvial floodplain deposits (Dalrymple and Choi, 2007).

The massive conglomerates (Gcm) or cross-bedded sandstones (St) with mud clasts at erosive basal surfaces can correspond to fluvial channel filling with reworking lag deposits (Miall, 1996). However, the mud clasts in the bottom channel deposits are also common in tide-influenced environments and can occur due to the erosion of thin, muddy tidal-flat deposits made by high-energy currents (Dalrymple and Choi, 2007). Additionally, the occurrence of thin mudstone layers on the foresets of cross-bedded sandstones (St) associated with reactivation surfaces could be used to infer variations in the current speed and may indicate tidal-flow reversals (Dalrymple and Choi, 2007; Mowbay and Visser, 1984); they suggest deposition in a tide-influenced environment. In conclusion, we interpret facies association 1 as channel deposits formed in the inner part (landward) of a fluvial-tidal transition zone during the early-stage of tide-influenced channel settlement.

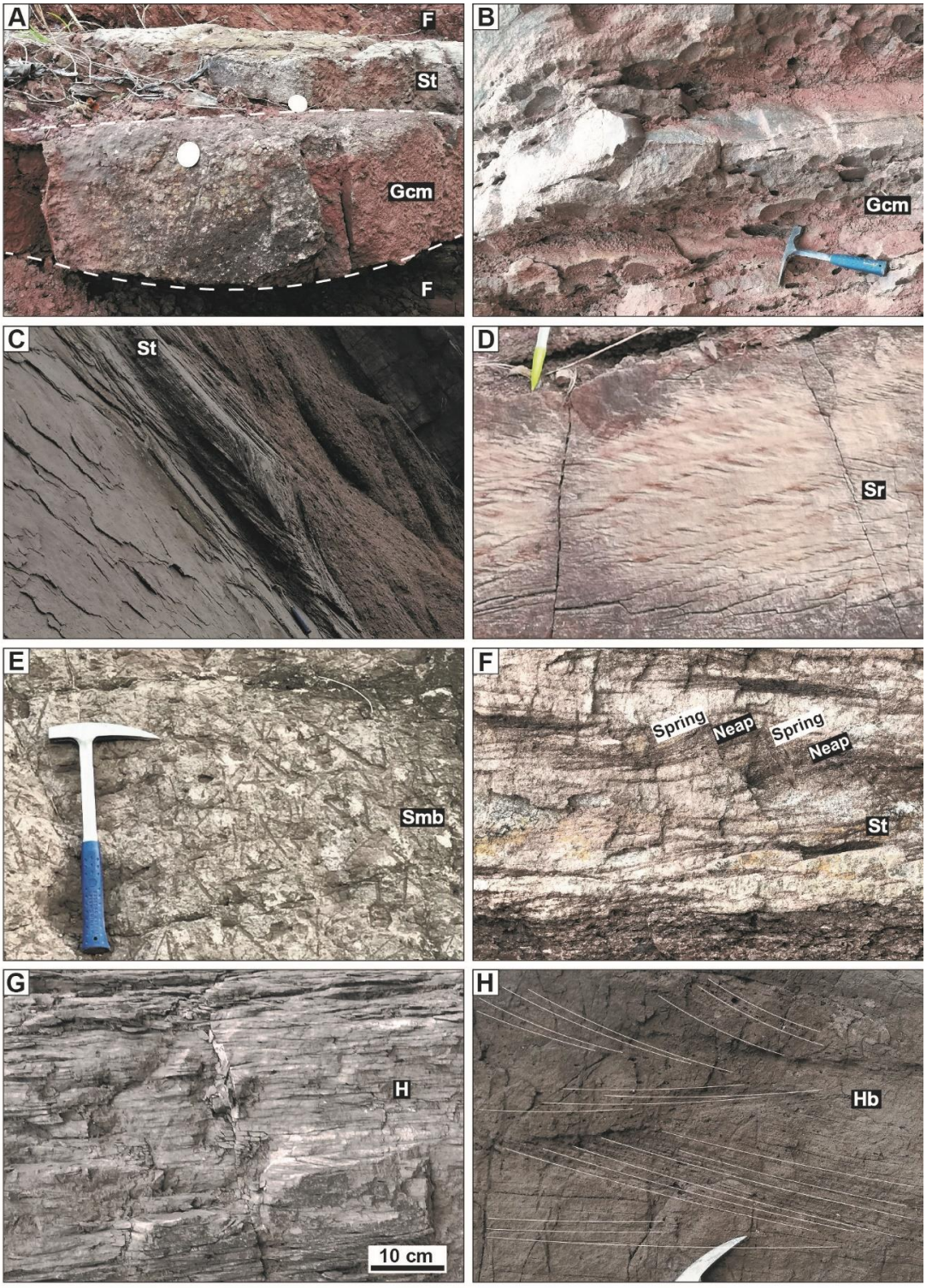


Figure 3. 5 Representative photographs of the siliciclastic facies. A) Massive clast-supported conglomerate (Gcm) with an erosive base, limited between fines with no structures (Fm) (below) and sandstones with through cross-stratification (St) (above); B) Massive conglomerates with scattered clasts (Gcm); C) Fine-grained sandstone with through cross-stratification; D) Fine-grained sandstone with climbing ripples; E) Highly bioturbated deposits (Smb) covering the primary structures in fines bodies; F) Thin mudstone layer drape on foresets of cross-bedded (St) fine-grained sandstones with regular variations (neap-spring influence); G) Heterolithic facies (H) with flaser bedding; H) Fine to medium-grained sandstones with bi-directional herringbone cross-stratification (Hb).

3.5.1.2 Facies association 2 (FA2)

Description. Facies association 2 is composed of five facies: Mp, Wpo, Woc, Gps and F (Table 1, Figure 3.4). Laterally, the facies association is represented by dm- to m-scale carbonate tabular beds (Figure 3.7A), which commonly occur with a flatten top and base, interbedded with m-scale, red to purple, fine-grained facies (F) (Figure 3.6A). It is characterized by cm-to-dm-thick beds of shelly carbonates composed of dispersed to dense microfossils (mainly ostracods and charophytes) and occasionally contains peloids and pisoids. Some beds are hybrid limestone composed of quartz grains and carbonate bioclasts (pisoids) (Gps). The vertical succession shows a coarsening-upward trend that starts with peloidal mudstones (Mp) (Figure 3.7B), which grade to the wackestones facies (Wpo; Woc) (Figure 3.7C–F) and then to the grainstone facies (Gps) (Figure 3.7G); generally, they are interbedded with mm-to-cm thick fine-grained structureless facies (F) (Figure 3.4). Poorly developed desiccation-crack surfaces are commonly present at the top of the carbonates and fine-grained beds. The fine-grained facies presented in this facies association contains numerous palynomorphs including *Echimonocolpites protofranciscoi*, *Ulmoideipites krempii*, *Cricotriporites* aff. *macroporus*, *Proxapertites psilatus*, *Momipites africanus* and *Araucariacites* sp. (Figure 3.6D–G) (Table 1). A microfacies analysis of thin sections made it possible to recognize the micritic matrix, which is mainly attributed to the mudstone facies (Mp) (Figure 3.7B), as well as the moldic porosity, which generally indicated molds of ostracod and charophyte remains (Figure 3.7F). FA2 has been observed approximately in two intervals of the Juanjuí stratigraphic section: 50 to 80 m and 292 to 335 m (Figure 3.4).

Interpretation. FA2 indicates minimum water agitation; sediments were deposited in lower-energy conditions (Flügel, 2010; Tucker and Wright, 1990), with some episodic water agitation attributed to the presence of fragmented ostracods (disarticulated valves) and sporadic terrigenous inflow due to an association with detrital quartz grains, suggesting low sedimentary transport or reworking. The peloid features may be organically induced precipitated features (Flügel, 2010). The charophyte-bearing carbonates are commonly attributed to freshwater environments, as they are ubiquitous in many ancient lake deposits (Tucker and Wright, 1990; Burne et al., 1980). The sedimentary succession presented

above is indicative of deposition in a shallow lacustrine environment with evaporation and decantation processes, episodic sediment supply events and subaerial exposition.

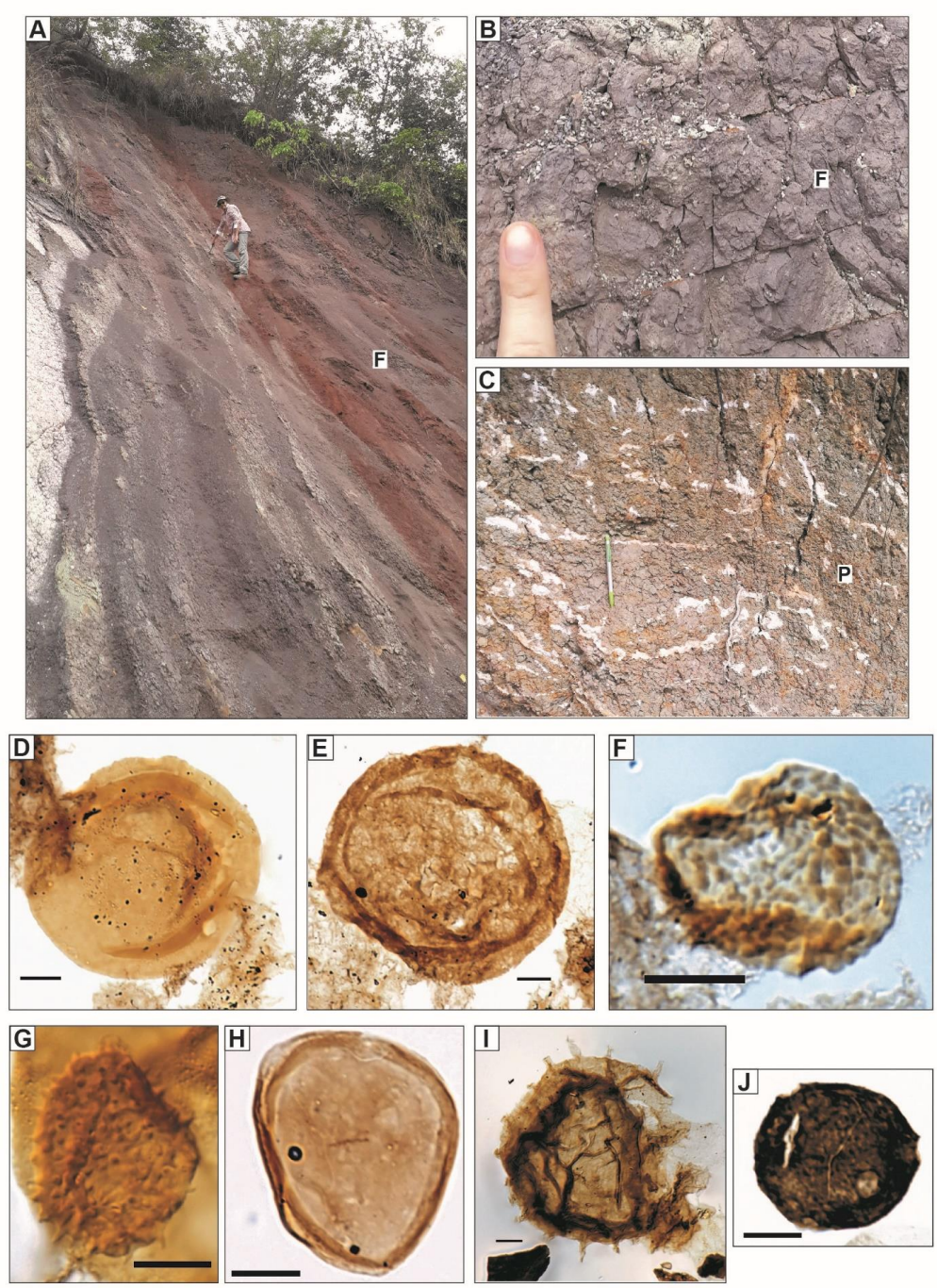


Figure 3. 6 Fine-grained facies; paleosols and palynological content. (A) Overall m-scale view of massive mudstones and siltstones, with red to purple colors, interbedded with cm-dm tabular carbonate beds. (B) Massive siltstones, presenting purple to green-grey colors, latter probably related to weathering processes. (C) Paleosols with incipient horizontal lamination, mottled horizons. (D) Cricotriporites aff. macroporus, slide 47176_A, England Finder (EF) W13; (E) Araucariacites sp., slide 47176_A, EF N12/2; (F) Ulmoideipites krempii, slide 47176_A, EF S8/4; (G) Echimonocolpites protofranciscoi, slide 47176_A, EF Q12/1; (H) Proxapertites psilatus, slide 47179_B, EF F15; (I) Balmeisporites minutus, slide 47179_B, EF S33/4; (J) Momipites africanus, slide 47179_B, EF M5/2. Scale bar= 10um.

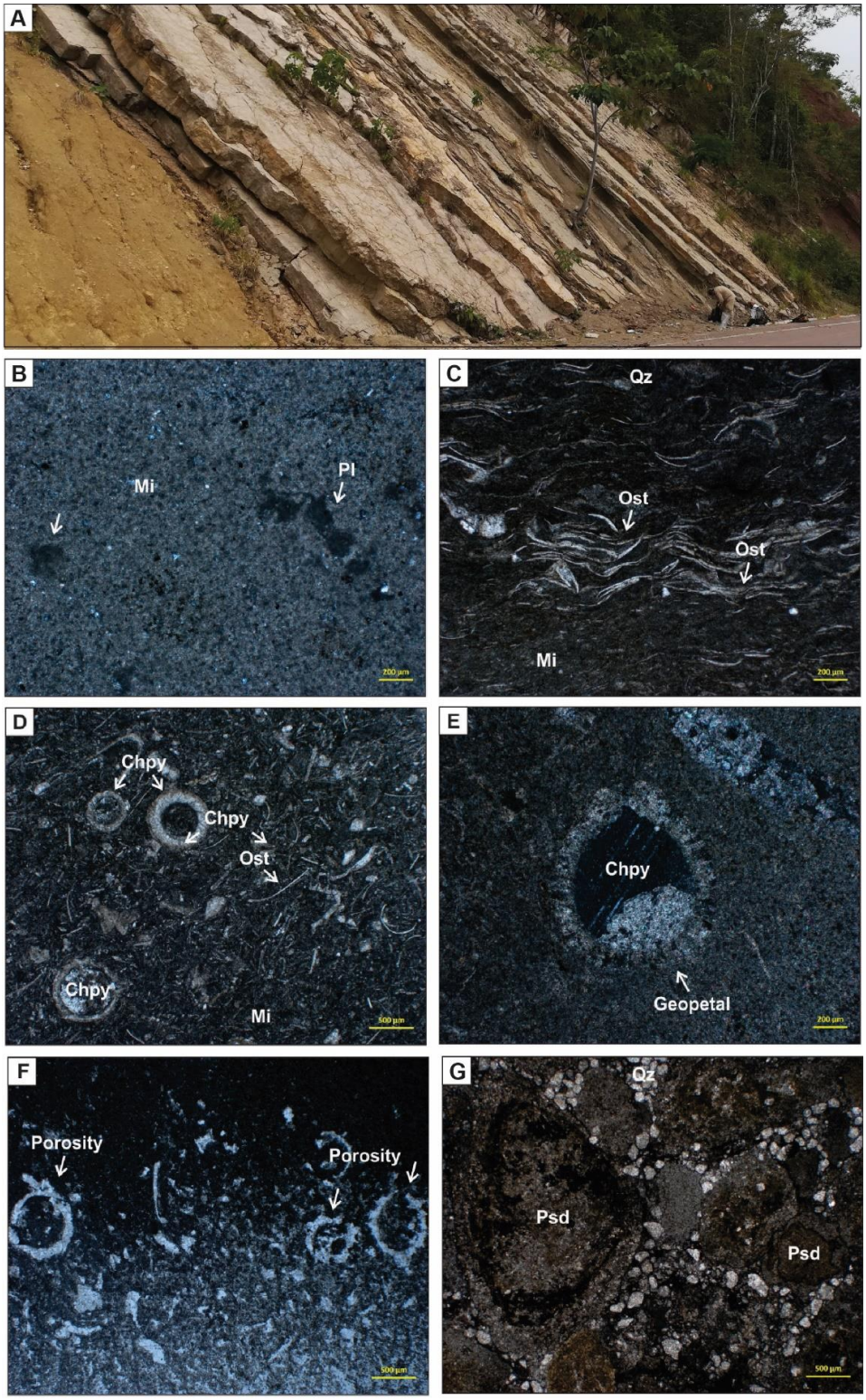


Figure 3. 7 Representative photographs of carbonate microfacies. A) General view of the carbonate outcrops; B) Mudstone deposits with scattered peloids (Mp) with clotted texture (HUA63B); C) Dark-brown wackestones with peloids and ostracods (Wpo) (HUA63C), characterized by disarticulated valves of ostracods oriented parallel to bedding of rock; D) Wackestone with scattered bioclasts as fragmented ostracods and charophytes (Woc) (JUA5A); E) Geopetal structure and recrystallized by spar marked in the inner part of charophytes (JUA5B); F) Moldic porosity is identified as secondary pores in charophytes (JUA5C); G) Fragments of pisoids partially replaced by pyrite (?) (JUA 2B). Mi= micrite; Pl= peloids; Ost= ostracod; Chpy= charophyte; Psd= pisoid.

3.5.1.3 Facies association 3 (FA3)

Description. Facies association 3 consists of four facies: P, Smb, Sr and Woc (Table 1, Figure 3.4). It is mainly composed of paleosols (P) horizons (Figure 3.6C) with scattered gypsum nodules in a very fine matrix, with less-common climbing-rippled sandstone beds (Sr), bioturbated sandstone deposits (Smb) and wackestone with ostracods and charophytes (Woc). The vertical and lateral relations of the facies reveal no significant changes; there are thick paleosol intervals with sparse dm-to-m thick carbonates and sandstones beds.

Interpretation. The carbonate nodules occurring in the paleosol intervals represent ions concentrations during processes of evaporation and capillary groundwater flow in arid periods (Nichols, 2009; Miall, 2006), indicating seasonal water fluctuations. Paleosols with root traces can indicate long periods of non-deposition and plant colonization or a low rate of accumulation.

3.5.1.4 Facies association 4 (FA4)

Description. Facies association 4 is composed of seven sedimentary facies: Smb, St, Sp, Sr, Hb, H and F (Table 1, Figure 3.4). The vertical facies association displays a coarsening and thickening upward into the section, which grades from very-fine- to medium-grained sandstones and cm-to-dm-thick to dm-to-m-thick beds. The section generally varies laterally; it is characterized by the dm-thick heterolithic facies (H) (Figure 3.5G) interbedded with fines (F) and fine- to medium grained cross-bedded (St) and climbing-rippled (Sr) sandstones. Occasionally, it shows herringbone cross-stratification (Hb) (Figure 3.5H) or planar cross-bedded (Sp) sandstones. The medium-grained cross-bedded (St) sandstones can present dm-thick wedge-shaped beds, with a concave-up base and mm-scale mudstone layers draped over the foresets (St facies), which are highlighted by reactivation surfaces, grading to climbing-rippled (Sr) sandstones. The highly bioturbated sandstones (Smb) are commonly interbedded with the fines (F) facies, showing no lateral variation. FA4 was recognized in the upper part of the present section, in the interval from about 380 to 442 m.

Interpretation. Heterolithic facies with flaser, wavy and linsen bedding, cross-bedded sandstones with thin mudstone drapes on the foresets, reactivation surfaces and

herringbone cross-bedded sandstones point to an environment influenced by tidal currents. The presence of reactivation surfaces might have been caused by tidal current reversals (Thomas et al., 1987; De Mowbray and Visser, 1984; Klein, 1970) although these surfaces could also be produced by river-discharge variations in fluvial settings (Dalrymple, 1984). Despite the fact that the H facies can be observed in river-dominated settings (Johnson and Dashtgard, 2014), the mud-sand-mud profile is not observed in bars further landward (Dashtgard and Gingras, 2012) and is more common in tide-dominated systems (Dalrymple and Choi, 2007; Dalrymple et al., 2003). Reactivation surfaces and mud layers might occur in fluvial point bar deposits (Collinson, 1996; Miall, 1996). The occurrence of bidirectional trough cross-bedding (Figure 3.5H) suggests a depositional area that received opposite-direction currents, which are characteristic of a tide-dominated environment (Longhitano et al., 2012) and can be either flood or ebb currents. The regular variations in the lamina thickness characterize rhythmic sedimentary structures, which are well documented in subtidal channels (Allen and Homewood, 1984; Visser 1980), and they could be interpreted as the influence of a neap-spring tidal cycle (Flemming, 2012; Dalrymple and Choi, 2007). In conclusion, we interpret facies association 4 as deposits formed in the distal part of a fluvial-tidal transition zone.

3.5.2 Depositional environments

The integration of the sedimentary facies association, paleontological content and stable isotopic compositions make it possible to characterize two depositional systems during the Maastrichtian-Bartonian: a tide-dominated depositional system and a lacustrine deposition system (Figures 3.4 and 3.10).

3.5.2.1 Tide-dominated environment: The fluvial-tidal transition zone

The tide-dominated depositional system was recognized in the Maastrichtian and late middle Bartonian (Figures 3.4 and 3.10A, C). This depositional system is composed of two facies associations: FA1 and FA4.

During the Maastrichtian (0 to 40 m along the section), FA1 generally prevails, and it is mainly composed of m-scale coarse-grained channelized shapes with upward-fining and thinning-up strata. The vertical stacking pattern and lateral changes of conglomerate facies to sandstone and finer facies were most probably related to a proximal area within a

fluvial-tidal transition zone (landward) that experienced a less-tide-dominated influence. These Maastrichtian tidal deposits can be correlated with those of the Vivian-Cachiyacu-Huchpayacu formations (Calvès et al., 2018; Hurtado et al., 2018; Louterbach et al., 2014). During the late-middle Bartonian (~350 to 450 m), FA4 is more abundant than FA1. The sedimentary stacking pattern reveals a tide-dominated environment, which is mainly represented by heterolithic facies interbedded with fines and climbing-rippled beds and also by typical tidal-current reversal deposits, such as herringbone cross-bedded sandstones. Reactivation surfaces and herringbone cross-bedding are more common in the distal area within a fluvial-tidal transition zone (seaward direction), where it is possible to recognize tidal bundles (Dalrymple and Choi, 2007). Compared with the Maastrichtian sedimentary rocks, these deposits are more deeply bioturbated. These Bartonian tide-influenced deposits can be correlated with the shallow marine deposits of the Pozo Fm. (see Roddaz et al., 2010, and the references therein).

3.5.2.2 Lacustrine environment

The lacustrine depositional system was recognized in the Maastrichtian and the Lutetian (Figures 3.4 and 3.10A, B). This depositional system is composed of two facies associations: FA2 and FA3.

The lacustrine setting starts with FA2. The sedimentary stacking pattern is mainly composed of continuous carbonate beds interbedded with shales and siltstone beds with a coarsening-upward trend; Gps and Woc are present at the top of the succession (Figure 3.4). This facies association occurs from approximately 50 to 80 m and from 292 to 350 m. This facies association was deposited under absent to low-energy hydrodynamic conditions, recording a shallowing-upward succession. The carbonates at the base of the sequence are mainly composed of the mudstone peloidal facies (Mp), which grades to the wackestones (Wpo, Woc) and grainstones (Gps) facies at the top. The sedimentary features observed in FA3 indicate a transition from ephemeral events under arid conditions to a period of low accumulation rates or long periods of non-deposition. The dominance of mudstone facies and the poor development of grainstone facies are interpreted to reflect lower wave energies and point to shallow lake environments (Platt and Wright, 1991). This is in agreement with the presence of charophytes, which are the dominant carbonate producers in low-energy and shallow freshwater settings (Platt and Wright, 1991). The

lacustrine carbonates / shelly strata represented by FA2 and FA3 can be correlated with the fluvial-lacustrine Yahuarango Fm. (Roddaz et al., 2010; Hermoza et al., 2005; Gutierrez, 1982; Kummel, 1948).

3.5.3 Oxygen and carbon stable isotopes

The results and variations of the stable isotopic compositions (C, O) of the analyzed samples are presented in Figures 3.4 and 3.9, and Table S2 (Supplementary Material). The analyzed stable isotopic data were compared with stable isotope values from Amazonian Miocene fossils (Alvim et al., 2021). North American rivers, the Great Lakes, North Atlantic seawater, the Black Sea and the San Francisco Bay estuary (Varol, 2015; Logvina et al., 2004; Ingram et al., 1996; Keith et al., 1964) (Figure 2.9). It is important to emphasize that, despite using the stable isotopic compositions of modern sites distinct from our localities, the isotopic fractionation processes at these sites are likely to have occurred in similar environments (e.g., lakes, estuaries or seas).

The succession exhibits significant variations in $\delta^{13}C$ and $\delta^{18}O$, as shown in Figure 3.4. In the first 53 m from the base to the top, the $\delta^{13}C$ values increase from -11.5 to -4.2‰ (JUA 1A-E) (Figure 3.4, Table S2). Between 53 and 82 m, most samples range from -7.3 to -6.0‰, except for the sample JUA 2B, which presents a strong negative carbon isotopic value (-11.1‰). Between 82 and 350 m (Lutetian), the $\delta^{13}C$ values increase slightly to between -10.0 and -2.8‰, and then they shift to low values (-11.9 to -10.0‰) in the upper part of the series (Bartonian).

The $\delta^{13}C$ and $\delta^{18}O$ values for the analyzed samples are negative, varying between -11.9 to -2.8‰ and from −10.2 to -1.1‰, respectively (Figures 3.4 and 2.9). The youngest samples (located between 382 and 392 m in Figure 3.4) are characterized by the most negative $\delta^{13}C$ values and plot within the North America river isotopic field. The isotopic compositions of the Lutetian samples are more scattered. Most of the samples have isotopic compositions similar to those of the Contamana Neogene fossils analyzed by Alvim et al. (2021) (dinoflagellate-, oyster- and foraminifer-yielding beds CTA-77 and CTA-58). Four samples are characterized by negative $\delta^{18}O$ values and plot between the Great Lakes and NA river fields (Figure 3.9). The four youngest samples that are associated with the TAR-78 fossil-bearing site have the highest $\delta^{18}O$ values and plot close to or within the isotopic field of the San Francisco Bay (Figure 3.9). The Lutetian samples plot mostly between the

NA river and Great Lakes fields, whereas the Maastrichtian and Bartonian samples have $\delta^{13}C$ and $\delta^{18}O$ values within or close to the NA river field (Figure 3.9).

Carbon and oxygen isotopic data exhibit isotopic values that indicate non-marine environmental conditions ($\delta^{13}C$ from -11.9 to -2.8‰ VPDB and $\delta^{18}O$ from -10.2 to -1.1‰ VPDB (Figures 3.4 and 3.9). According to the isotopic signatures, the deposits present a covariance of negative $\delta^{13}C$ and $\delta^{18}O$ isotopic compositions, which could support predominantly freshwater conditions (Vonhof et al., 1998). The $\delta^{13}C$ and $\delta^{18}O$ isotopic values of the upper part of this depositional system (samples HUA 473 N to Q, located from ~ 311 to 333 m; Figure 3.4) are much less negative ($\delta^{13}C$ ranging from -8.2 to -2.8‰ and $\delta^{18}O$ from -6.6 to -1.1‰) (Figures 3.4, 3.9 and S2), which could reflect a transition to brackish conditions in an estuarine depositional system (Figures 4 and 9) (Ingram et al., 1996). The fossil record is also in agreement with this paleoenvironmental transition, from freshwater to brackish conditions, which is indicated by the presence of i) marine, estuarine or brackish pycnodontiform ray-finned fish and myliobatiform selachians (*Potobatis* and *Ouledia*; Figure 3.8D) at TAR-30, and ii) pelomedusoid turtles, of brackish affinities at TAR-78.

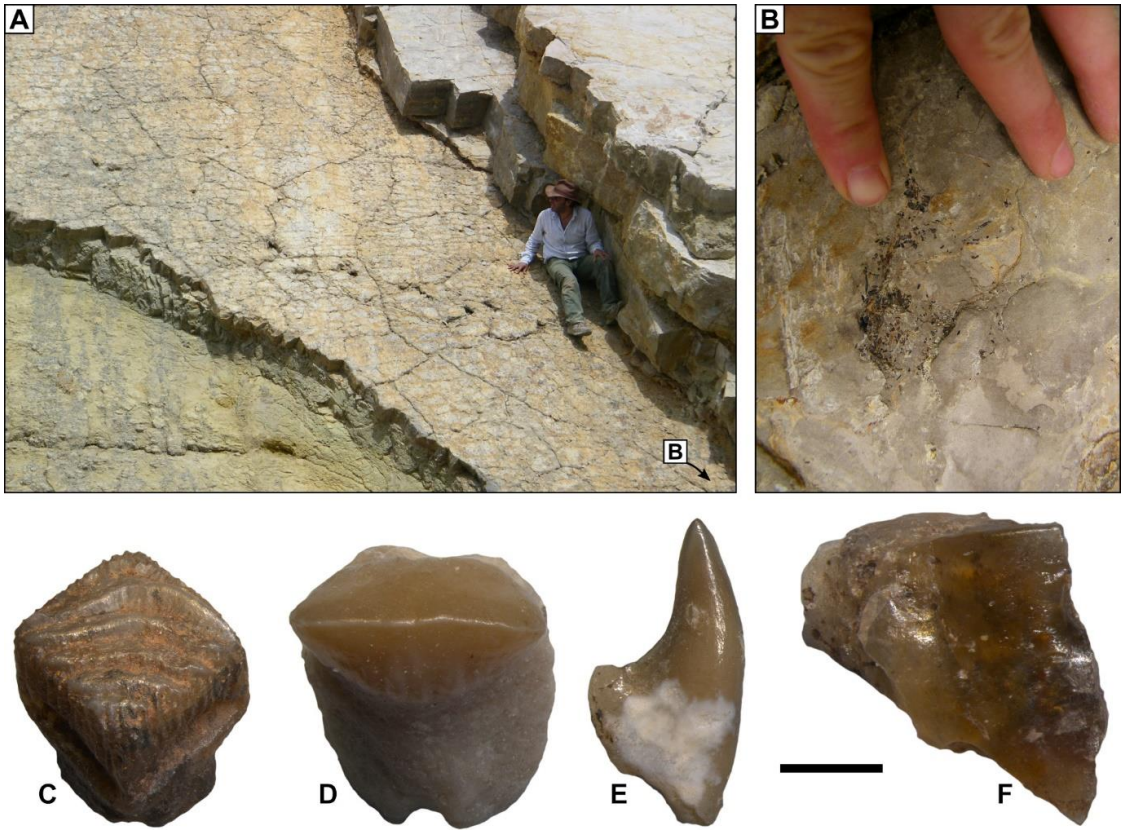


Figure 3. 8 Selected vertebrate-related findings and vertebrate fossils of interest from the Maastrichtian–Paleogene Juanjuí section, San Martín, Peru. A) Paddling-turtle track at TAR-29 (=HUA-63; Maastrichtian). The turtle was moving to the right. The same carbonated layer provided the regurgitation ball seen in B; B) Regurgitation ball (of an aquatic bird?), with fish bones and scales both gathered and split all around (TAR-29 = HUA-63; Maastrichtian); C) Pucapristis hoffstetteri, tooth in occlusal view (TAR-41, Maastrichtian); D) Ouledia sp., tooth in occlusal view (TAR-30 sup. = HUA-473; Lutetian); E) Stephanodus sp., pharyngeal tooth in lateral view (TAR-30 sup. = HUA-473; Lutetian); F) Polypterid polypteriform, fragmentary ganoin scale in external view (TAR-42 = JUA 14; Bartonian). Scale bar = 1 mm (C, E) and 0.5 mm (D, F).

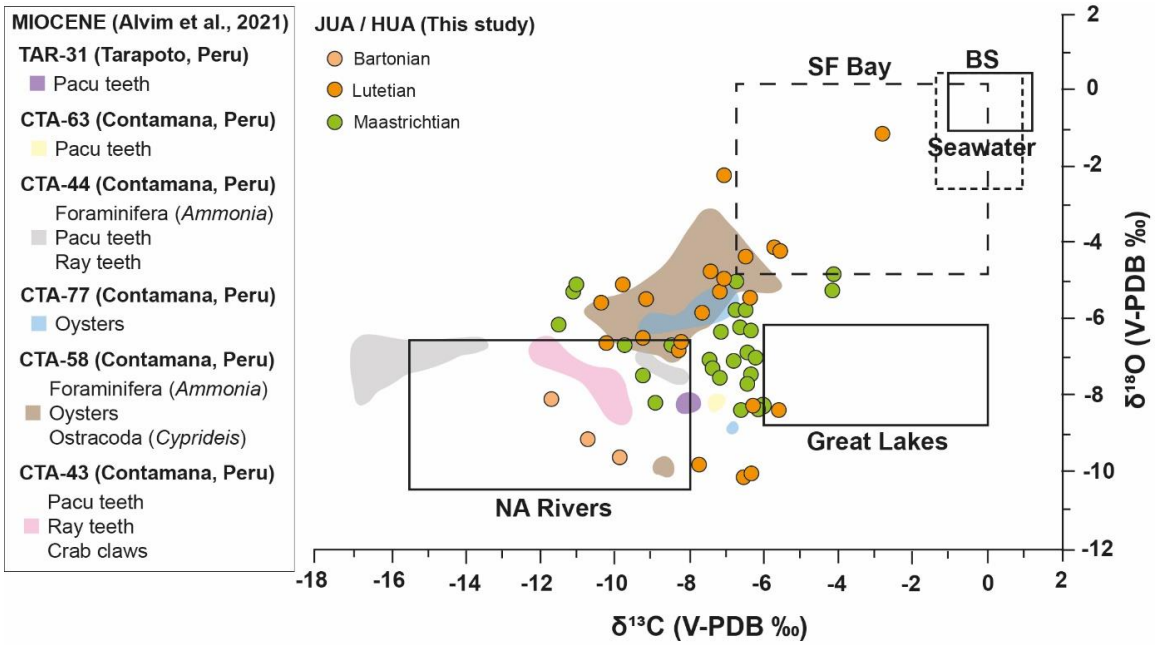


Figure 3. 9 Carbon versus oxygen isotopes cross plot of Miocene (Alvim et al., 2021a) and Eocene fossil and carbonates samples. Black boxes represent stable isotopes values of modern mollusks from North Atlantic seawater, Great Lakes, and North American rivers (Keith et al., 1964), the San Francisco Bay estuary (Ingram et al., 1996) and the Black Sea (Varol, 2015).

3.5.4 Biostratigraphic constraints: Paleontological content of the Juanjuí Maastrichtian–Eocene section

The TAR-59 sample (labeled in green in Figure 3.4) provided no macrofossil content, but crushed bone fragments, most likely documenting medium-sized dinosaurs, were retrieved from JUA 1B, 30 m below in the same section (Figure 3.4). Conversely, a palynological sample (TAR-PN-16-09) yielded an assemblage dominated by the freshwater algae *Pediastrum* (about 98% out of 300 grains counted) and other panchronic taxa, such as the fern spore *Laevigatosporites* sp., dinocysts assignable to *Batiacasphaera*, and reworked acritarchs.

The TAR-29 sample (labeled in green in Figure 3.4) has yielded charophyte oogonia by the thousands (unidentified), silicified plant cuticles, unidentified turriform gastropods, ostracods (under study), freshwater bony fish remains (pacu-like characiform teeth and loricariid siluriform iridescent dermal scutes), chelonian osteoderm fragments, a paddling-turtle trackway (collapsed in 2015; Figure 3.8A) and waterbirds regurgitated pellets (with numerous fish scales and spines; Figure 3.8B) in the uppermost levels of the exposure. Unfortunately, this assembly does not allow any precise biostratigraphic dating. Conversely, palynological samples TAR-29-PN2/19 (stratigraphic meter 79), TAR-29-

PN4A-19 (stratigraphic meter 81.4) and TAR-29-PN5-19 (stratigraphic meter 81.6) from the same sample point to a Maastrichtian age (based on the palynological zonation of Jaramillo et al. (2011) and De La Parra et al. (2021)). They are characterized by rich terrestrial organic matter and palynomorphs (Figure 3.6D–J), including abundant *Araucariacites* (gymnosperm), *Gnetaceaopollenites* (gymnosperm), *Pediastrum* (freshwater algae), *Echimonocolpites protofranciscoi* (angiosperm), *Ulmoideipites krempii* (angiosperm), *Longapertites* (angiosperm, palms), *Cricotriporites* aff. *macroporus* (angiosperm), *Echitriletes selaginelloides* (fern), *Racemonocolpites* (angiosperm, palm), abundant *Proxapertites psilatus* (gymnosperm Araceae), *Momipites africanus* (angiosperm), *Foveotriletes* aff. *margaritae* (fern) and *Balmeisporites minutus* (fern). The additional palynological samples TAR-29-PN1/19, TAR-29-PN3/19 and TAR-29-PN4/19 did not provide useful results.

Aside from unidentified charophyte oogonia and ostracods (under study), the TAR-30 sample (base + top) yielded a species-rich fish assemblage, with ray-finned taxa (characins: pacu- and piranha-like teeth; iridescent dermal scutes of loricariid siluriforms; *Stephanodus* pharyngeal teeth; Figure 3.8E), selachians (Myliobatiformes: the batoid *Ouledia* sp. (Figure 3.8D) and the dasyatoid *Potobatis*) and dipnoans (Ceratodontidae/Lepidosirenidae). *Ouledia* (Thanetian–Priabonian) and *Potobatis* (Danian–Thanetian) had also been recognized in shallow marine-influenced Thanetian deposits of the Madre de Dios Basin, in association with pycnodontiform pycnodontids (Louterbach et al., 2014). The TAR-30 fauna also include turriform gastropods, pelomedusoid turtle shell fragments, and crocodylomorph teeth. As a whole, the fauna point to a Thanetian biostratigraphic age, which is supported by close affinities with the Thanetian ichthyofauna of the Madre de Dios Basin (Louterbach et al., 2014), at least in the absence of younger strata yielding similar assemblages. The TAR-78 sample yielded charophyte oogonia and half a carapace of a pelomedusoid turtle, of brackish affinities (under study by Edwin Cadena).

At the top of the studied section, the TAR-42 sample yielded a ganoin scale of a polypterid polypteriform (*Latinopollia* or *Dagetella*; Figure 3.8F), as well as turtle shell fragments, a large crocodylomorph osteoderm, and a fragmentary lower molar of a tiny South American native ungulate (SANU), documenting a panperissodactyl (Notoungulata or Litopterna). The last appearance datum (LAD) of polypteriforms in South America is Paleocene in age (Gayet et al., 2002). The occlusal pattern and dimensions of the

panperissodactyl are in good agreement with a Thanetian–Ypresian biostratigraphic age and at odds with post-early Eocene SANUs.

3.5.5 U-Pb ages

Table 2 present the U-Pb zircon ages for the analyzed Cenozoic sedimentary rocks. Details on individual U-Pb zircon ages for each sample can be found in the supplementary material (Tables S2 to S6). The zircon population of the Cenozoic samples is dominated by grains from the Eocene Andean Arc (<0.065 Ga) (Table 2). The other dominant zircon populations are Grenville Sunsás (1.3–0.9 Ga) and to a lesser extent, Rondonia-San Ignacio (1.54–1.3 Ga) and Rio Negro-Jurena (1.82–1.54 Ga). The maximum depositional ages (MDAs), calculated as the weighted mean of YC2σ[+3] following Sharman and Malkowski (2020), are Eocene MDAs. The MDAs decrease up-section from ~43.1 ± 0.29 Ma (Lutetian, JUA 8A/19), to ~ 42.6 ± 0.32 Ma (Lutetian, JUA 11) and ~38.6 ± 0.19 Ma (Bartonian, JUA 14) in the upper part of the section (Figure 3.4, Table S2). The calculated maximum likelihood ages (MLAs) following Vermeesch (2021) are also Eocene ages. The MLAs range from ~43.5 ± 0.64 Ma (Lutetian, JUA 8A/19) to ~42.68 ±0.66 Ma (Lutetian, JUA 11) and ~37.64 ± 0.85 Ma (Bartonian - Priabonian, JUA 14) (Figure 3.4, Table S2). Overall, the MDAs and MLAs are quite similar, and they both decrease up-section.

Time (Ga)	Province / Event	EOCENE	Lutetian		Bartonian
			JUA 8A-19 **n** = 69/77 (%)	JUA 11 **n** = 102/120 (%)	JUA 14 **n** = 102/112 (%)
< 0.065	Cenozoic Andean Arc		14	28	38
0.145 - 0.065	Cretaceous Andean Arc		4	0	2
0.25 - 0.145	Triassic-Jurassic		0	1	7
0.4 - 0.26	Paleozoic Magmatic Arc		6	3	3
0.5 - 0.4	Famatinian		3	4	2
0.7 - 0.5	Brazilian		12	13	6
0.9 - 0.7			6	1	2
1.3 - 0.9	Greenville Sunsás		29	33	25
1.54 - 1.3	Rondonia - San Ignacio		3	7	8
1.82 - 1.54	Rio Negro - Jurena		10	6	7
2.0 - 1.82	Ventuari - Tapajós		6	1	0
2.2 - 2.0	Maroni - Itacaiunas		6	2	0
> 2.2	Central Amazon		1	1	0

Table 3. 3 Table showing the number and percentage U-Pb ages of zircons grains by distinct geochronological events in potential source areas on the Amazon craton and the northern central Andes. Temporal ranges of events according to Bahlburg et al. (2009), Chew et al. (2008) and Reimann et al. (2010). (n) is the number of samples analyzed for the time interval.

3.6 DISCUSSION

3.6.1 Age of the deposits

The first stratigraphic constraint regarding the studied sedimentary section is the biostratigraphic age of the TAR-59 sample. This locality yielded unambiguous dinosaur fossil remains. In addition, large dinosaur footprints were identified at the TAR33 outcrop that can be correlated with the TAR 59 sample (Supplementary Data S7); these footprints are consistent with the Maastrichtian interval (72.1–66.0 Ma) (Figure 4 and Supplementary Data S7). The TAR-59 sample has the same stratigraphic position as the HUA 63 sample (Figure 3.4), which was previously studied by Hurtado et al. (2018). Originally, a Danian age was assigned to HUA 63 (Hurtado et al., 2018) because it was mistakenly supposed to be intercalated between the TAR-29 fossil site, which yielded a rich charophyte assemblage with a composition similar to the Danian beds of the Ucayali Basin (Agua Caliente, CTA-54 locality; Antoine et al., 2016), and TAR30, which yielded a rich ichthyofauna, notably including the Danian dasyatid marker *Potobatis* sp. (Cappetta and Gayet, 2013). However, our revised fieldwork suggests that HUA 63 is located below the TAR29 sample, and is associated with the TAR-59 fossil site instead (Figure 3.4). The presence of several key biostratigraphic palynomorphs, including *Echimonocolpites protofranciscoi*, *Ulmoideipites krempii*, *Momipites africanus* and *Foveotriletes aff. margaritae*, which were found in the TAR-29 sample (PN2/19, PN4A-19, and PN5-19 located at 79, 81.4 and 81.6 m above the stratum level, respectively) also suggest a Maastrichtian age. Hence, the first 150 m of the Juanjuí sedimentary section as a whole may be ascribed to the Maastrichtian Cachiyacu Fm. Moreover, the contact between Maastrichtian and the overlying Cenozoic sedimentary rocks is located at ~ 150 m in the sedimentary section (Figure 3.4). Paleosol horizons are found above and below this contact (Figure 3.4). Paleosol horizons are found above and below this contact (Figure 3.4).

Above these paleosol horizons, the three analyzed Cenozoic sedimentary rocks presented MDAs that range from the Lutetian (JUA 8A/19, 43.1 ± 0.29 Ma, located at 170 m, and JUA 11, 42.6 ± 0.32 Ma, located at 375 m) to the Bartonian (JUA 14, 38.6 ± 0.19 Ma) located at 440 m (Figure 4). The MLAs of the analyzed samples show similar Lutetian (JUA 8A/19, 43.5 ± 0.64 Ma), and JUA 11, 42.7 ± 0.66 Ma) and Bartonian to Priabonian ages (JUA 14, 37.6 ± 0.85 Ma) (Table S6). These MDAs and MLAs are significantly younger than the biostratigraphic ages obtained from the fossil-rich outcrops TAR-30,

TAR-78 and TAR-42. The JUA 8/19A samples, which yield a Lutetian MDA (43.1 ± 0.29 Ma), are stratigraphically below the TAR-30 outcrop, which has a Thanetian biostratigraphical cachet, based on the co-occurrence of the selachians *Potobatis* and *Ouledia* (Paleocene and Thanetian–Priabonian ranges, respectively; Louterbach et al., 2014, and the references therein). Similarly, the Bartonian to Priabonian zircon MDAs and MLAs of sample JUA 14 are significantly younger than the Thanetian–Ypresian biostratigraphical age of TAR-42 (which yielded polypterid scales of presumed Maastrichtian–Paleocene age and a tiny early-diverging SANU of Paleocene–early Eocene hypothesized affinities), which is situated at the same stratigraphic level. In both cases, this temporal discrepancy may be related to unexpected longer stratigraphical ranges of remarkable fossil taxa, due to last appearances much younger than previously thought for *Potobatis* (world scale) or *Ouledia* and the polypterids (South American scale).

According to the MDAs and MLAs, the faunal content of the fossil site TAR-30 may not be Danian but Lutetian in age and the fossil sites TAR-78 and TAR-42 are Lutetian and Bartonian in age, respectively (Figure 3.4). These results suggest that i) the analyzed samples are part of the Eocene Pozo Fm. (Roddaz et al., 2010) and ii) contrary to what was published in Roddaz et al. (2010), the Paleocene Yahuarango Fm. may be absent in the Huallaga Basin.

3.6.2 Paleogeographic implications

Our multidisciplinary dataset provides new constraints on the paleoenvironmental evolution of Western Amazonia during the Maastrichtian – Bartonian (late middle Eocene).

Our data suggest that a tide-dominated system occupied the Huallaga Basin during the Maastrichtian. Previous paleogeographic reconstructions of the late Cretaceous configuration of Peruvian Western Amazonia also suggest that the Madre de Dios and Marañon basins were characterized by shallow marine deposits during the Campanian–Maastrichtian (Louterbach et al., 2018a; Zamora and Gil, 2018). In Ecuador, the Maastrichtian basal Tena sandstones of the Oriente Basin are also interpreted to represent tide-dominated deposits (Jaillard et al., 2005). The Upper Cretaceous units in neighboring basins (e.g., Vivian and Cachiyacu formations in the Santiago, Marañon and Madre de Dios basins) are also characterized by shallow marine paleoenvironments (Zamora and Gil, 2018, and the references therein). A coastal paleo-environment is also suggested in the

Bagua Basin (Moreno et al., 2020). As already emphasized by previous published studies (Hurtado et al., 2018; Zamora and Gil, 2018), this suggests that Western Amazonia basins were entirely flooded by an epicontinental sea at some point by the Maastrichtian.

At the Cretaceous–Paleogene boundary, a marine-to-continental transition was recorded in the northernmost part of the Andes, coeval with regional records for the onset of compressional deformation in the northern Andes (Central and Eastern Cordilleras) (Zapata et al., 2021; Bayona et al., 2021; George et al., 2019; Gutiérrez et al., 2019; Odoh et al., 2019; Horton, 2018). This transition from shallow marine/coastal to continental paleoenvironments is also recorded in the Huallaga Basin, but it occurred during the Maastrichtian, as indicated by the transition from a tide-dominated depositional system to a continental lacustrine depositional system.

Our new stratigraphic constraints suggest that the Paleocene-to-lower Eocene interval (66–47.8 Ma) may be documented by a 2-m-thick paleosol facies (Figure 3.4), indicating that a stratigraphic unconformity may separate the Maastrichtian from the Lutetian–Bartonian sedimentary sequences of the Huallaga Basin (Figures 3.4 and 3.10). A similar chronostratigraphic hiatus was observed to the north in the Oriente Basin (Ecuador) where the sedimentary deposits of the Lower Eocene Tiyuyacu Fm. unconformably overlie the Upper Cretaceous Tena Fm. (Gutiérrez et al., 2019). In Colombia, a regional unconformity was recognized on the eastern side of the Southern Llanos Basin (Colombia), which separates the pedogenized Cretaceous rocks from the overlying Middle or Upper Eocene rocks (Caballero et al., 2020). To the northwest, in the Bagua Basin (Peru) (Figure 3.11A), the Paleocene series are also absent, as shown by i) the absence of Paleocene MDAs obtained for U-Pb in zircons in the Upper Cretaceous to Miocene sedimentary rocks of the Bagua Basin (Moreno et al., 2020), and ii) the presence of a low-angle unconformity between the Campanian–Maastrichtian Fundo el Triunfo Fm. and the overlying Lower Eocene Rentema Fm. (54.2 ± 6.4 Ma) (Naeser et al., 1991). This regional unconformity could be generated by the presence of a migrating forebulge in response to Andean tectonic loading or tectonic quiescence (Horton, 2022). However, we believe that a forebulge unconformity is unlikely to have generated the Maastrichtian-to-Lutetian unconformity recorded in the Huallaga Basin, since an Andean provenance is recorded below and above this unconformity (HUA 63 in Hurtado et al. (2018) and JUA 8A/19 in this study). Following Horton (2022), we propose that a tectonic quiescence marked by a prolonged pause in crustal shortening and flexural loading may have promoted

isostatic rebound and the development of an unconformity. In this scenario, we suggest that the Paleocene corresponded to a stage of tectonic quiescence in the Huallaga Basin.

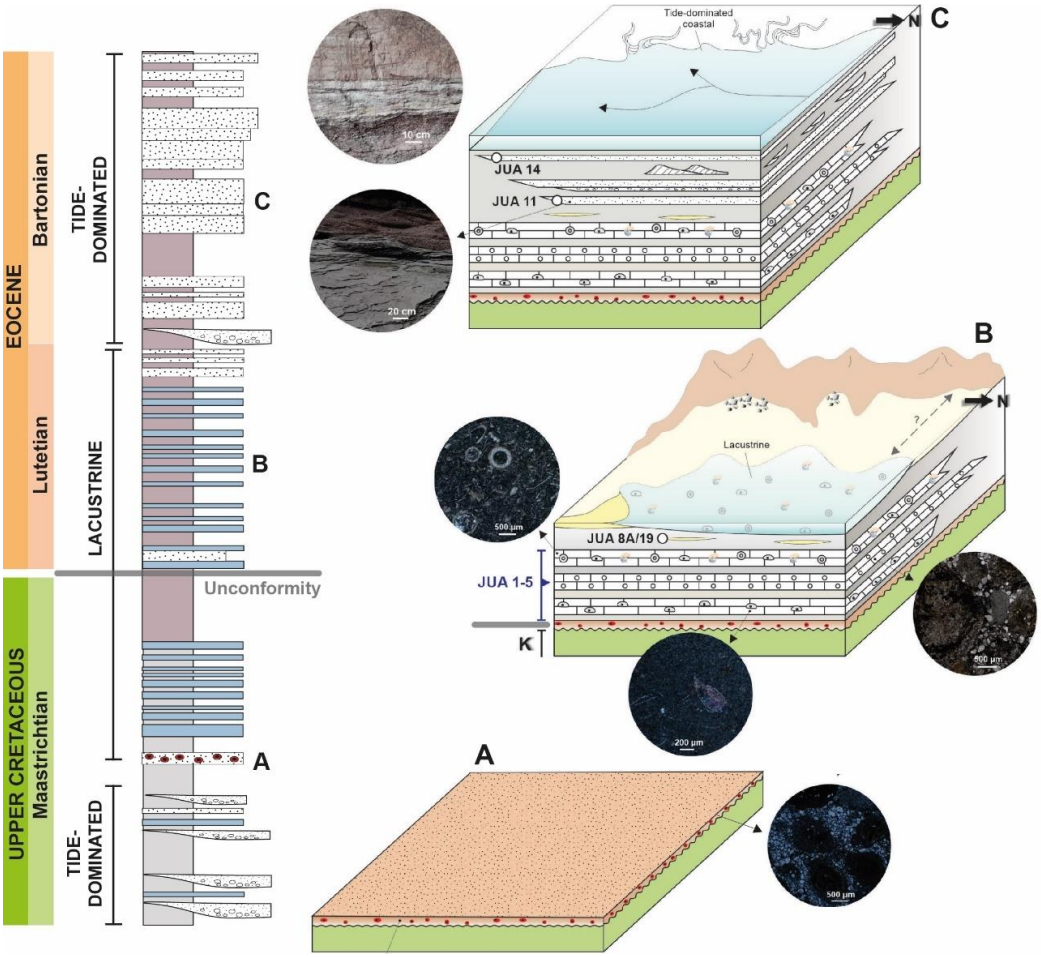


Figure 3. 10 Schematic composite section and 3D sketch representing the paleoenvironmental reconstruction of the (A) Maastrichtian – Paleogene stratigraphic unconformity, (B) Lutetian lacustrine setting, (C) The Bartonian transition from lacustrine system to the tide-dominated setting, represented by the distal part in a fluvial-tidal transition zone. See text for details.

In the Madre de Dios Basin, previous paleogeographic reconstructions suggest that a shallow marine transgression occurred during the late Paleocene (Louterbach et al., 2014a). At the time of the publication of this article, the entrance of this shallow marine transgression (Atlantic Ocean, Pacific Ocean or Caribbean Sea) was still unclear. Here, we suggest a southern connection with the Atlantic Ocean (Bolivia–Argentina) through the Parana Sea (Figure 3.11A), given the absence of Paleocene deposits in the Huallaga, Bagua and Llanos basins. In this scenario, the upper Paleocene shallow marine deposits of the Madre de Dios Basin may represent the northern end of the Paleocene Parana Sea, which

is also recorded by deeper marine deposits in the southern basins, such as the Potosí and Chaco basins (Cappetta and Gayet, 2013; Sempere et al., 1997).

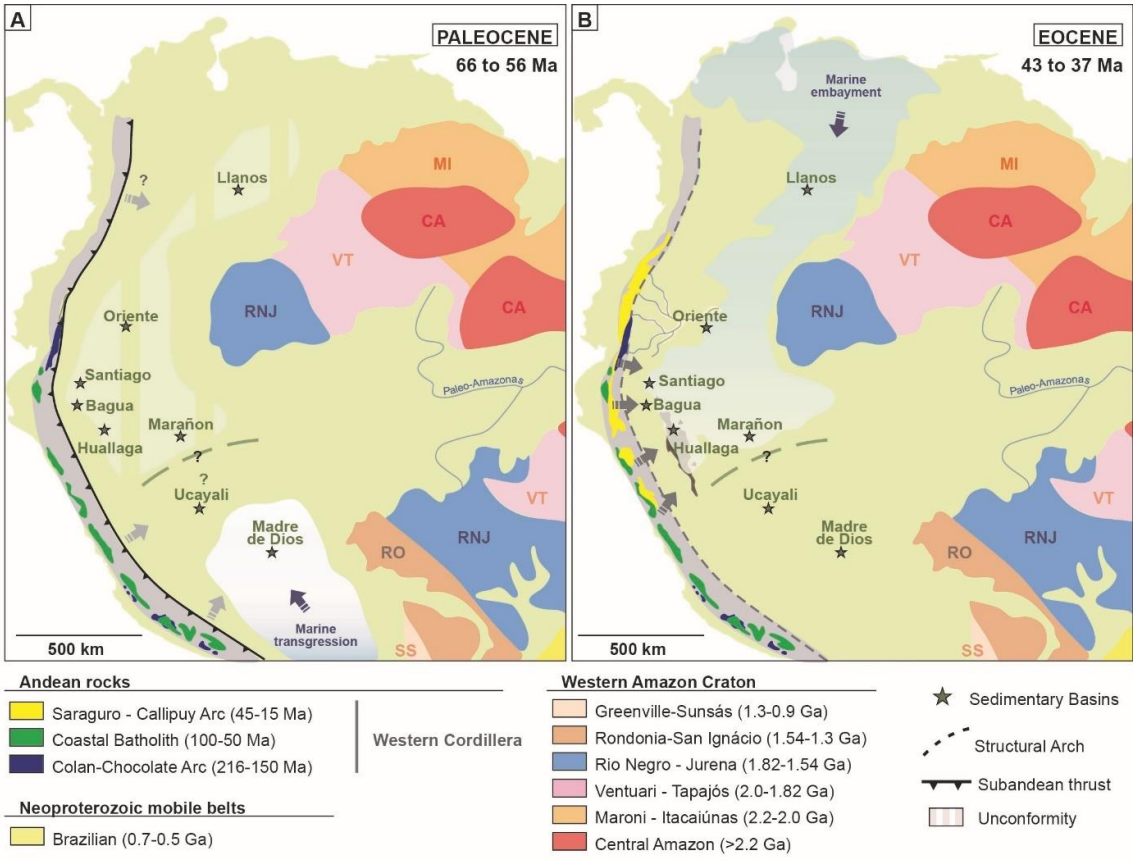


Figure 3. 11 Paleogeographic maps of Western Amazonia in Paleocene (A) Eocene (B) times. A) During the Paleocene, the northern part of the Western Amazonian basins are characterized by the presence of a regional unconformity while the southern part experienced shallow marine transgression (Louterbach et al., 2014). B) During the Eocene, the northern part likely experienced shallow marine embayment during short time-intervals through a connection with the Caribbean Sea while the southern part (the Madre de Dios Basin) is characterized by the absence of Eocene deposits (Louterbach, 2014).

Our data also recorded a shallow marine transgression that may have started during the Bartonian (Late middle Eocene), as indicated by the presence of a tide-dominated coastal depositional system (FA4) (from 42.6 to 38.6 Ma) that overlies the Lutetian lacustrine system (FA2 and FA3). In a tide-dominated estuarine setting, bidirectional currents are likely to be present in the meandering part of the tide-dominated estuary (Dalrymple and Choi, 2007; Dalrymple et al., 1992). This Bartonian shallow marine incursion could be correlated with the Eocene Pozo shallow marine transgression (Hoorn et al., 2010b; Roddaz et al., 2010) that affected the Marañón Basin, which is located east

of the studied area (Roddaz et al., 2010; Hermoza et al., 2005; Hermoza, 2004). Moreover, this shallow marine incursion was also recorded in the Santiago Basin (George et al., 2019), within the Pozo and Capas Rojas formations. Based on i) the absence of Eocene deposits in the southern Peruvian Madre de Dios and northern Bolivian Beni basins (Louterbach et al., 2018a; Louterbach, 2014; Roddaz et al., 2010; Hermoza, 2004), the presence of ii) Upper middle Eocene shallow marine sedimentary rocks (from 42 to 37 Ma) in the Colombian Llanos Basin (De La Parra et al., 2021) and iii) the presence of Eocene shallow marine deposits in the Ecuadorian Oriente Basin (Roddaz et al., 2010; Christophoul et al., 2002), a northern entrance through the Caribbean Sea is suggested for this Bartonian transgression (Figure 3.11B).

3.7 CONCLUSIONS

The multi-disciplinary study (biostratigraphy, sedimentological data, U-Pb zircon ages, and stable isotope composition) of the Upper Cretaceous-Paleogene sedimentary rocks documented in the Juanjuí stratigraphic section of the Huallaga Basin yields the following conclusions:

i) The maximum depositional U-Pb zircon ages of analyzed samples became younger up-section with peak MDAs at 43.1 ± 0.29 Ma, 42.6 ± 0.32 Ma and 38.6 ± 0.19 Ma, and MLAs at 43.5 ± 0.64 Ma, 42.7 ± 0.66 Ma and 37.6 ± 0.85 Ma. These data make it possible to refine the stratigraphic age of the studied section and reveal that the Maastrichtian sedimentary sequence is separated from the Lutetian–Bartonian sequence by a stratigraphic unconformity.

ii) The Upper Cretaceous-Eocene sedimentary rocks of the Huallaga Basin are characterized by two depositional systems: a tide-dominated system and a lacustrine system.

iii) Two marine transgressions occurred during the Maastrichtian and Bartonian epochs. They are dominated by brackish to freshwater tide-influenced siliciclastic sequences that indicate the presence of a regional embayment in northwestern South America during these time intervals.

iv) The middle Eocene interval (Lutetian) is characterized by the establishment of a lacustrine setting with contrasting seasons (wet and dry).

The presence of a shallow marine incursion in Western Amazonia during the Eocene might have involved biogeographical isolation, and as such, it may have promoted allopatric speciation for terrestrial organisms. This biogeographic context may have thus played a role in shaping the emergence of post-Paleogene regional biodiversity.

3.8 ACKNOWLEDGEMENTS

This work received financial and institutional support from the IRD (Institut pour la Recherche et le Développement). This study was also supported and funded by CAPES-COFECUB program Te 924/18/ 88881.143095/2017–01 "Paléo-Amazone: evolution Néogène de l'Amazonie Brésilienne/O PALEO AMAZONAS: evolução neogênica da Amazônia Brasileira", and CNPq (Proc. 312941/2018–8) "Neogene Evolution of Brazilian Amazon". This work was supported by an "Investissements d'Avenir" grant managed by the Agence Nationale de la Recherche (CEBA, ANR-10-LABX-25-01) and by the cooperative programs ECOS-FonCyT (A14-U01) and CoopIntEER CNRS-CONICET (n◦252540), in the frame of the ongoing cooperation agreement between the *Museo de Historia Natural de la Universidad Nacional Mayor San Marcos* (Lima, Peru) and the Institut des Sciences de l'Evolution-Université de Montpellier. We thank two anonymous reviewers as well as the editor Michelangelo Martini for valuable reviews that improved this contribution.

REFERENCES

Albert, J.S., Val, P., Hoorn, C., 2018. The changing course of the Amazon River in the Neogene: center stage for Neotropical diversification. Neotrop. Ichthyol. 16, 1–24. https://doi.org/10.1590/1982-0224-20180033.

Allen, P.A., Homewood, P., 1984. Evolution and mechanics of a Miocene tidal sandwave. Sedimentology 31, 63–81.

Alvim, A.M.V., Santos, R.V., Roddaz, M., Antoine, P.-O., Ramos, M.I.F., do Carmo, D.A., et al., 2021. Fossil isotopic constraints (C, O and 87Sr/86Sr) on Miocene shallowmarine incursions in Amazonia. Palaeogeogr. Palaeoclimatol. Palaeoecol. https://doi.org/10.1016/j.palaeo.2021.110422.

Antoine, P.-O., Abello, M.A., Adnet, S., Altamirano Sierra, A.J., Baby, P., Billet, G., et al., 2016. A 60-million-year Cenozoic history of western Amazonian ecosystems in Contamana, eastern Peru. Gondwana Res. 31, 30–59. https://doi.org/10.1016/j.gr.2015.11.001.

Baby, P., Rivadeneira, M., Barragan, R., Christophoul, F., 2013. Thick-skinned tectonics in the Oriente foreland basin of Ecuador. In: Nemˇcok, M., Mora, A., Cosgrove,

J.W. (Eds.), Thick-Skin-Dominated Orogens: from Initial Inversion to Full Accretion, vol. 377. Geological Society, London, Special Publications, pp. 59–76.
Baby, P., Calderon, ´ Y., Brusset, S., Roddaz, M., Brichau, S., Eude, A., et al., 2018. The Peruvian sub-Andean foreland Basin system: structural overview, geochronologic
constraints, and unexplored plays. AAPG Mem 117, 91–119. https://doi.org/ 10.1306/13622118M1173767.
Bahlburg, H., Vervoort, J.D., Du Frane, S.A., Bock, B., Augustsson, C., Reimann, C., 2009. Timing of crust formation and recycling in accretionary orogens: insights learned from the western margin of South America. Earth Science Reviews 97, 215–241. https://doi.org/10.1016/j.earscirev.2009.10.006.
Bayona, G., Baquero, M., Ramirez, C., Tabares, M., Salazar, A.F., Nova, G., Duarte, E., Pardo, A., Plata, A., Jaramillo, C., Rodriguez, G., Caballero, V., Cardona, A., Montes, C., Gomez-Marulanda, S., Cardenas-Rozo, A., 2021. Unraveling the widening of the earliest Andean northern orogen: Maastrichtian to early Eocene intra-basinal deformation in the northern Eastern Cordillera of Colombia. Basin Res. 33, 809–845.
Boonstra, M., Ramos, M.I.F., Lammertsma, E.I., Antoine, P.-O., Hoorn, C., 2015. Marine connections of Amazonia: evidence from foraminifera and dinoflagellate cysts (early to middle Miocene, Colombia/Peru). Palaeogeogr. Palaeoclimatol. Palaeoecol. 417, 176–194. https://doi.org/10.1016/j.palaeo.2014.10.032.
Bühn, B., Pimentel, M.M., Matteini, M., Dantas, E.L., 2009. High spatial resolution analysis of Pb and U isotopes for geochronology by laser ablation multi-collector inductively coupled plasma mass spectrometry (LA-MC-ICP-MS). An. Acad. Bras. Cienc. 81, 99–114. https://doi.org/10.1590/s0001-37652009000100011.
Burne, R.V., Bauld, J., De Deckker, P., 1980. Saline Lake Charophytes and Their Geological Significance. Journal of Sedimentary Petrology 50 (1), 281–293. https://doi.org/10.1306/212F79D2-2B24-11D7-8648000102C1865D.
Caballero, V.-M., Naranjo, J.-F., Rodriguez, G., Gomez, P.-D., Mora, A., Villamizar, C., Miller, F., G´elvez, J., 2020. Eocene facies successions and environments in the southern Llanos Basin, Colombia. Ciencia, Tecnologia y Futuro 10, 107–122. Num 1.
Calderón, Y., Baby, P., Hurtado, C., Brusset, S., 2017a. Thrust tectonics in the Andean retro-foreland Basin of northern Peru: permian inheritances and petroleum implications. Mar. Petrol. Geol. 82, 238–250. https://doi.org/10.1016/j.marpetgeo.2017.02.009.
Calderón, Y., Vela, Y., Hurtado, C., Bolaños, R., Baby, P., Eude, A., et al., 2017b. Petroleum systems restoration of the huallaga-marañon andean retroforeland basin, Peru. AAPG Mem 114, 95–116. https://doi.org/10.1306/13602026M1143702.
Calvès, G., Calderón, Y., Hurtado, C., Brusset, S., Santini, W., Baby, P. 2018. Mass Balance of Cenozoic Andes-Amazon Source to Sink System-Marañón Basin, Peru. Geosciences, MDPI, 8 (5). f10.3390/geosciences8050167ff. ffhal-01787548f

Cappetta, H., Gayet, M., 2013. A new elasmobranch genus (myliobatiformes, dasyatoidea) from the danian of Potosí (Bolivia). Neues Jahrbuch Geol. Palaontol.Abhand. 269, 285–290. https://doi.org/10.1127/0077-7749/2013/0351.
Carrillo, E., Barragan, R., Hurtado, C., Calderón, Y., Martín, G., Vázquez-Taset, Y., Parra, M., Rivera, A., Cadena, F.M., Sarmiento, L., 2021. Depositional sequences in northern Peru: new insights on the palaeogeographic and palaeotectonic

reconstruction of western Gondwana during late Permian and Triassic. J. Geol. Soc. 178 (6), jgs2020–j2186. https://doi.org/10.1144/jgs2020-186, 2021.
Carvalho, M.R., Jaramillo, C., De la Parra, F., Caballero-Rodriguez, D., Herrera, F., Wing, S., Turner, B.L., D'Apolito, C., Romero-Baez, M., Narvaez, P., Martinez, C., Gutierrez, M., Labandeira, C., Bayona, G., Rueda, M., Paez-Reyes, M., Cardenas, D.,
Duque, A., Crowley, J.L., Santos, C., Silvestro, D., 2021. Extinction at the end-Cretaceous and the origin of modern Neotropical rainforests. Science 372, 63–68.
Chew, D.M., Magna, T., Kirkland, C.L., Miskovic, A., Cardona, A., Spikings, R.,Schaltegger, U., 2008. Detrital zircon fingerprint of the Proto-Andes: evidence for a Neoproterozoic active margin? Precambrian Research 167, 186–200. https://doi.org/10.1016/j.precamres.2008.08.002.
Christophoul, F., Baby, P., D´avila, C., 2002. Stratigraphic responses to a major tectonic event in a foreland Basin: the Ecuadorian Oriente Basin from Eocene to Oligocene times. Tectonophysics 345, 281–298. https://doi.org/10.1016/S0040-1951(01) 00217-7.
Collinson, J.D., 1996. Alluvial sediments. In: Reading, H.G. (Ed.), Sedimentary Environments: Processes, Facies and Stratigraphy, third ed. Blackwell Science, Oxford, pp. 37–81.
Dalrymple, R.W., 1984. Morphology and internal structure of sand waves in the Bay of Fundy. Sedimentology 31, 365–382.
Dalrymple, R.W., Choi, K.S., 2003. Sediment transport by tidal currents. In: Middleton, G.V. (Ed.), Encyclopedia of Sediments and Sedimentary Rocks. Kluwer Academic.
Dalrymple, R.W., Choi, K.S., 2007. Morphologic and facies trends through the fluvialmarine transition in tide-dominated depositional systems: a schematic framework for environmental and sequence-stratigraphic interpretation. Earth Sci. Rev. 81, 135–174.
Dalrymple, R.W., Zaitlin, B.A., Boyd, R., 1992. Estuarine facies models: conceptual basis and stratigraphic implications. J. Sediment. Petrol. 62 (No. 6), 1130–1146.
Dashtgard, S.E., Gingras, M.K., 2012. Chapter 10: marine invertebrate neoichnology. In: Knaust, D., Bromley, R.G. (Eds.), Trace Fossils as Indicators of Sedimentary Environments. Elsevier, New York, pp. 273–295.
De La Parra, F., Pinzon, D., Mantilla-Duran, F., Rodriguez, G., Caballero, V., 2021. Marine-lacustrine systems during the Eocene in northern South America – palynological evidence from Colombia. J. South Am. Earth Sci. 108, 103188 https://doi.org/10.1016/j.jsames.2021.103188.
DeCelles, P.G., Giles, K.A., 1996. Foreland Basin systems. Basin Res. 8, 105–123. https://doi.org/10.1046/j.1365-2117.1996.01491.x.
Dickinson, W.R., Gehrels, G.E., 2009. Use of U-Pb ages of detrital zircons to infer maximum depositional ages of strata: a test against a Colorado Plateau Mesozoic database. Earth Planet Sci. Lett. 288, 115–125. https://doi.org/10.1016/j.epsl.2009.09.013.
Dunham, R.J., 1962. Classification of carbonate rocks according to depositional texture. In: Ham, W.E. (Ed.), Classification of Carbonate Rocks. AAPG, Tulsa, pp. 108–121.
Eakin, C.M., Lithgow-Bertelloni, C., D´avila, F.M., 2014. Influence of Peruvian flat-subduction dynamics on the evolution of western Amazonia. Earth Planet Sci. Lett. 404, 250–260. https://doi.org/10.1016/j.epsl.2014.07.027.

Espurt, N., Baby, P., Brusset, S., Roddaz, M., Hermoza, W., Regard, V., et al., 2007. How does the Nazca Ridge subduction influence the modern Amazonian foreland Basin? Geology 35, 515–518. https://doi.org/10.1130/G23237A.1.

Espurt, N., Baby, P., Brusset, S., Roddaz, M., Hermoza, W., Barbarand, J., 2010. The nazca ridge and uplift of the Fitzcarrald Arch: implications for regional geology in northern South America. Amazon. Landsc. Species Evol. Look Past 89–100. https://doi.org/10.1002/9781444306408.ch6.

Eude, A., Roddaz, M., Brichau, S., Brusset, S., Calderon, Y., Baby, P., et al., 2015. Controls on timing of exhumation and deformation in the northern Peruvian eastern Andean wedge as inferred from low-temperature thermochronology and balanced cross section. Tectonics 34, 715–730. https://doi.org/10.1002/2014TC003641.

Figueiredo, J., Hoorn, C., van der Ven, P., Soares, E., 2009. Late Miocene onset of the Amazon River and the Amazon deep-sea fan: evidence from the foz do amazonas basin. Geology 37, 619–622. https://doi.org/10.1130/G25567A.1.

Flemming, B.W., 2012. Siliciclastic back-barrier tidal flats. In: Davis Jr., R., Dalrymple, R. (Eds.), Principles of Tidal Sedimentology. Springer, Dordrecht. https://doi.org/10.1007/978-94-007-0123-6_10.

Flügel, E., 2010. In: Munnecke, A. (Ed.), Microfacies of Carbonates Rocks - Analysis, Interpretation and Application, second ed. Springer. 10.1007/10.1007/978-3-642-03796-2.

Galbraith, R.F., 2005. Statistics for Fission Track Analysis. CRC Press.

Galbraith, R., Laslett, G., 1993. Statistical models for mixed fission track ages. Nucl. Tracks Radiat. Meas. 21 (4), 459–470.

Gayet, M., Meunier, F.J., Werner, C., 2002. Diversification in polypteriformes and special comparison with the lepisosteiformes. Palaeontology 45 (2), 361–376.

Gehrels, G., 2014. Detrital zircon U-Pb geochronology applied to tectonics. Annu. Rev. Earth Planet Sci. 42, 127–149. https://doi.org/10.1146/annurev-earth-050212-124012.

Gehrels, G.E., Valencia, V.A., Ruiz, J., 2008. Enhanced precision, accuracy, efficiency, and spatial resolution of U-Pb ages by laser ablation-multicollector-inductively coupled plasma-mass spectrometry. G-cubed 9, 1–13. https://doi.org/10.1029/2007GC001805.

George, S.W.M., Horton, B.K., Jackson, L.J., Moreno, F., Carlotto, V., Garzione, C.N.,
2019. Sediment provenance variations during contrasting Mesozoic-early Cenozoic tectonic regimes of the northern Peruvian Andes and Santiago-Marañón foreland Basin. https://doi.org/10.1016/b978-0-12-816009-1.00012-5.

Gorini, C., Haq, B.U., dos Reis, A.T., Silva, C.G., Cruz, A., Soares, E., et al., 2014. Late Neogene sequence stratigraphic evolution of the foz do amazonas basin, Brazil. Terra. Nova 26, 179–185. https://doi.org/10.1111/ter.12083.

Guiguer, K.R.R.A., Drimmie, R., Power, M., 2003. Validating methods for measuring d18O and d13C in otoliths from freshwater fish. Rapid Commun. Mass Spectrom. 17, 463–471, 2003.

Gutierrez, M., 1982. Evaluación potential petrolífero cuencas Huallaga, Ucayali y Madre de Dios. Zonación bioestratigrafica del intervalo Cretáceo superior-Terciario inferior. Petroperú. Rapport interne inédit, Lima, p. 29.

Gutiérrez, E.G., Horton, B.K., Vallejo, C., Jackson, L.J., George, S.W.M., 2019. Provenance and geochronological insights into late cretaceous-cenozoic foreland basin development in the subandean zone and Oriente Basin of Ecuador. In: Horton,

B.K., Folguera, A. (Eds.), Andean Tectonics. Elsevier, pp. 237–268. https://doi.org/10.1016/B978-0-12-816009-1.00011-3.
Hermoza, W. 2004. Dynamique tectono-sédimentaire et restauration séquentielle du rétro-bassin d'avant-pays des Andes centrales. Available at: http://www.theses.fr/2004TOU30134 (Accessed 10 January 2022).
Hermoza, W., Brusset, S., Baby, P., Gil, W., Roddaz, M., Guerrero, N., et al., 2005. The Huallaga foreland Basin evolution: thrust propagation in a deltaic environment, northern Peruvian Andes. J. South Am. Earth Sci. 19, 21–34. https://doi.org/10.1016/j.jsames.2004.06.005.
Hoorn, C., 1993. Marine incursions and the influence of Andean tectonics on the Miocene depositional history of northwestern Amazonia: results of a palynostratigraphic study. Palaeogeogr. Palaeoclimatol. Palaeoecol. 105, 267–309. https://doi.org/10.1016/0031-0182(93)90087-Y.
Hoorn, C., Wesselingh, F.P., Hovikoski, J., Guerrero, J., 2010a. The development of the amazonian mega-wetland (Miocene; Brazil, Colombia, Peru, Bolivia). Amazon. Landsc. Species Evol. Look Past 123–142. https://doi.org/10.1002/9781444306408. ch8.
Hoorn, C., Wesselingh, F.P., Ter Steege, H., Bermudez, M.A., Mora, A., Sevink, J., et al., 2010b. Amazonia through time: Andean uplift, climate change, landscape evolution, and biodiversity. Science 330, 927–931. https://doi.org/10.1126/science.1194585.
Hoorn, C., Bogotá-A, G.R., Romero-Baez, M., Lammertsma, E.I., Flantua, S.G.A., Dantas, E.L., et al., 2017. The Amazon at sea: onset and stages of the Amazon River from a marine record, with special reference to Neogene plant turnover in the drainage Basin. Global Planet. Change 153, 51–65. https://doi.org/10.1016/j.gloplacha.2017.02.005.
Horton, B.K., 2018. Sedimentary record of Andean mountain building. Earth Sci. Rev.178, 279–309. https://doi.org/10.1016/j.earscirev.2017.11.025.
Horton, B.K., 2022. Unconformity development in retroarc foreland basins: implications for the geodynamics of Andean-type margins. J. Geol. Soc. 179.
Hovikoski, J., Wesselingh, F.P., Räsänen, M., Gingras, M., Vonhof, H.B., Marine influence in Amazonia: evidence from the geological record, 2010. In: Hoorn, C., Wesselingh, F.P. (Eds.), Amazonia, Landscape and Species Evolution. Blackwell Publishing), pp. 143–161.
Hurtado, C., Roddaz, M., Santos, R.V., Baby, P., Antoine, P.-O., Dantas, E.L., 2018. Cretaceous-early Paleocene drainage shift of Amazonian rivers driven by Equatorial Atlantic Ocean opening and Andean uplift as deduced from the provenance of northern Peruvian sedimentary rocks (Huallaga Basin). Gondwana Res. 63, 152–168. https://doi.org/10.1016/j.gr.2018.05.012.
Ingram, B.L., Conrad, M.E., Ingle, J.C., 1996. Stable isotope and salinity systematics in estuarine waters and carbonates: San Francisco Bay. Geochem. Cosmochim. Acta 60, 455–467. https://doi.org/10.1016/0016-7037(95)00398-3.
Jackson, S.E., Pearson, N.J., Griffin, W.L., Belousova, E., 2004. The application of laser ablation inductively coupled plasma mass spectrometry to in-situ U–Pb zircon geochronology. Chem. Geol. 211, 47–69.
Jaillard, E., Bengtson, P., Dhondt, A.V., 2005. Late Cretaceous marine transgressions in Ecuador and northern Peru: a refined stratigraphic framework. J. South Am. Earth Sci. 19, 307–323. https://doi.org/10.1016/j.jsames.2005.01.006.

Jaramillo, C., Rueda, M., 2021. A Morphological Electronic Database of Cretaceous-Tertiary Fossil Pollen and Spores from Northern South America V. 2012-2021. Smithsonian Tropical Research Institute. http://biogeodb.stri.si.edu/jaramillo/palynomorph/.

Jaramillo, C., Rueda, M., Torres, V., 2011. A palynological zonation for the cenozoic of the Llanos and Llanos foothills of Colombia. Palynology 35, 46–84.

Jaramillo, C., Romero, I., D'Apolito, C., Bayona, G., Duarte, E., Louwye, S., et al., 2017. Miocene flooding events of western Amazonia. Sci. Adv. 3, 1–12. https://doi.org/10.1126/sciadv.1601693.

Johnson, S.T., Dashtgard, S.E., 2014. Inclined heterolithic stratification in a mixed tidal–fluvial channel: differentiating tidal versus fluvial controls on sedimentation. Sediment. Geol. 301, 41–53.

Keith, M.L., Anderson, G.M., Eichler, R., 1964. Carbon and oxygen isotopic composition of mollusk shells from marine and fresh-water environments. Geochem. Cosmochim. Acta 28, 1757–1786. https://doi.org/10.1016/0016-7037(64)90021-3.

Klein, G. de V., 1970. Depositional and dispersal dynamics of intertidal sand bars. J. Sediment. Petrol. 40, 1095–1127.

Kummel, B., 1948. Geological reconnaissance of the Contamana region, Peru. Geol. Soc. Am. Bull. 12, 1217–1266. https://doi.org/10.1130/0016-7606, 1948)59.

Logvina, E., Mazurenko, L., Prasolov, E., 2004. Isotopic composition of carbon-13 and oxygen-18 from authigenic carbonates. In: Black Sea Region. AGU Spring Meeting Abstracts.

Longhitano, S.G., Mellere, D., Steel, R.J., Ainsworth, R.B., 2012. Tidal depositional systems in the rock record: a review and new insights. Sediment. Geol. 279, 2–22. https://doi.org/10.1016/j.sedgeo.2012.03.024.

Louterbach, M., Roddaz, M., Bailleul, J., Antoine, P.-O., Adnet, S., Kim, J.H., et al., 2014. Evidences for a Paleocene marine incursion in southern Amazonia (Madre de Dios sub-andean zone, Peru). Palaeogeogr. Palaeoclimatol. Palaeoecol. 414, 451–471. https://doi.org/10.1016/j.palaeo.2014.09.027.

Louterbach, M., Fernández, O., Sisinni, V., Gutierrez, M., Zamora, G., 2018a. Stratigraphy, structure, and hydrocarbon potential of the northern Bolivia subandean thrust belt (Beni basin). In: Petroleum Basins and Hydrocarbon Potential of the Andes of Peru and Bolivia AAPG Memoirs. AAPG), pp. 377–413.

Louterbach, M., Roddaz, M., Antoine, P.-O., Marivaux, L., Adnet, S., Bailleul, J., et al., 2018b. Provenance record of late maastrichtian–late palaeocene andean mountain building in the amazonian retroarc foreland basin (Madre de Dios basin, Peru). Terra. Nova 30, 17–23. https://doi.org/10.1111/ter.12303.

Miall, A.D., 1978. Lithofacies types and vertical profile models in braided river deposits: a summary. Fluv. Sedimentol. 5, 597–600.

Miall, A.D., 1996. The Geology of Fluvial Deposits, Sedimentary Facies, Basin Analysis and Petroleum Geology. Sprin-ger, Berlin.

Miall, A.D., 2006. The Geology of Fluvial Deposits. https://doi.org/10.1007/978-3-662-03237-4.

Moreno, F., Garzione, C.N., George, S.W.M., Horton, B.K., Williams, L., Jackson, L.J., et al., 2020. Coupled andean growth and foreland basin evolution, Campanian–Cenozoic Bagua Basin, northern Peru. Tectonics 39. https://doi.org/10.1029/2019TC005967.

Moreno, F., Garzione, C.N., George, S.W.M., Williams, L., Richter, F., Bandeian, A., 2022. Late cretaceous through cenozoic paleoenvironmental history of the Bagua

Basin, Peru: paleoelevation comparisons with the central andean plateau. Geosciences 12, 242. https://doi.org/10.3390/geosciences12060242.
Mowbray, T. and Visser, M. J. 1984. Reactivation surfaces in subtidal channel deposits, Oosterschelde, Southwest Netherlands. Journal of Sedimentary Research; 54 (3): 811–824. doi: https://doi.org/10.1306/212F8503-2B24-11D7-8648000102C1865D.
Naeser, C.W., Crochet, J.Y., Jaillard, E., Laubacher, G., Mourier, T., Sig´e, B., 1991. Tertiary fission-track ages from the Bagua syncline (northern Peru): stratigraphic and tectonic implications. J. South Am. Earth Sci. 4, 61–71. https://doi.org/10.1016/0895-9811(91)90018-G.
Nichols, G., 2009. Sedimentology and Stratigraphy, second ed. second ed. Wiley Blackwell.
Odoh, S., Saylor, J.E., Higuera, C., Copeland, P., Lapen, T.J., 2019. Chapter 6: discriminating mechanisms for coarse clastic progradation in the Colombian foreland Basin using detrital zircon double dating. In: Horton, B.K., Folguera, A. (Eds.), Andean Tectonics. Elsevier, pp. 133–171. https://doi.org/10.1016/B978-0-12-816009-1.00008-3.
Paton, C., Hellstrom, J., Paul, B., Woodhead, J., Hergt, J., 2011. Iolite: freeware for the visualisation and processing of mass spectrometric data. J. Anal. At. Spectrom. 26, 2508–2518. https://doi.org/10.1039/c1ja10172b.
Petrus, J.A., Kamber, B.S., 2012. VizualAge: a novel approach to laser ablation ICP-ms U-Pb geochronology data resolution. Geostand. Geoanal. Res. Volume36 (3), 247–270.
Platt, N.H., Wright, V.P., 1991. Lacustrine carbonates: facies models, facies distributions and hydrocarbon aspects. In: Anado´n, P., Cabrera, L., Kelts, K. (Eds.), Lacustrine Facies Analysis, vol. 13. International Association of Sedimentologists, Special Publication, pp. 57–74.
Reimann, C.R., Bahlburg, H., Kooijman, E., Berndt, J., Gerdes, A., Carlotto, V., Lopez, S., 2010. Geodynamic evolution of the early Paleozoic Western Gondwana margin 14°-17°S reflected by the detritus of the Devonian and Ordovician basins of southern Peru and northern Bolivia. Gondwana Research 18, 370–384.
Roddaz, M., Baby, P., Brusset, S., Hermoza, W., Darrozes, J.M., 2005a. Forebulge dynamics and environmental control in Western Amazonia: the case study of the Arc of Iquitos (Peru). Tectonophysics 399, 87–108. https://doi.org/10.1016/j.tecto.2004.12.017.
Roddaz, M., Viers, J., Brusset, S., Baby, P., H´erail, G., 2005b. Sediment provenances and drainage evolution of the Neogene Amazonian foreland Basin. Earth Planet Sci. Lett. 239, 57–78. https://doi.org/10.1016/j.epsl.2005.08.007.
Roddaz, M., Hermoza, W., Mora, A., Baby, P., Parra, M., Christophoul, F., et al., 2010. Cenozoic sedimentary evolution of the amazonian foreland basin system. Amazon. Landsc. Species Evol. Look Past 61–88. https://doi.org/10.1002/9781444306408.ch5.
Sacek, V., 2014. Drainage reversal of the Amazon River due to the coupling of surface and lithospheric processes. Earth Planet Sci. Lett. 401, 301–312. https://doi.org/10.1016/j.epsl.2014.06.022.
Santos, C., Jaramillo, C., Bayona, G., Rueda, M., Torres, V., 2008. Late Eocene marine incursion in north-western South America. Palaeogeogr. Palaeoclimatol. Palaeoecol. 264, 140–146. https://doi.org/10.1016/j.palaeo.2008.04.010.

Sempere, T., Butler, R.F., Richards, D.R., Marshall, L.G., Sharp, W., Swisher, C.C., 1997. Stratigraphy and chronology of upper cretaceous-lower Paleogene strata in Bolivia and northwest Argentina. Bull. Geol. Soc. Am. 109, 709–727. https://doi.org/10.1130/0016-7606.

Sharman, G.R., Malkowski, M.A., 2020. Needles in a haystack: detrital zircon U-Pb ages and the maximum depositional age of modern global sediment. Earth Sci. Rev. 203, 103–109. https://doi.org/10.1016/j.earscirev.2020.103109.

Sharman, G.R., Sharman, J.P., Sylvester, Z., 2018. detritalPy: a Python- based toolset for visualizing and analysing detrital geo-thermochronologic data. Depositional Rec 4, 202–215. https://doi.org/10.1002/dep2.45.

Shephard, G.E., Müller, R.D., Liu, L., Gurnis, M., 2010. Miocene drainage reversal of the Amazon River driven by plate-mantle interaction. Nat. Geosci. 3, 870–875. https://doi.org/10.1038/ngeo1017.

Thomas, R.G., Smith, D.G., Wood, J.M., Visser, J., Calverley-Range, E.A., Koster, E.H., 1987. Inclined heterolithic stratification-terminology, description, interpretation and significance. Sediment. Geol. 53, 123–179.

Traverse, A., 2007. Paleopalynology, second ed. Springer, Dordrecht, p. 813. Tucker, M.E., Wright, P.V., 1990. Carbonate Sedimentology. Blackwell Science.

van Soelen, E.E., Kim, J.H., Santos, R.V., Dantas, E.L., Vasconcelos de Almeida, F., Pires, J.P., et al., 2017. A 30 Ma history of the Amazon River inferred from terrigenous sediments and organic matter on the Ceará Rise. Earth Planet Sci. Lett. 474, 40–48. https://doi.org/10.1016/j.epsl.2017.06.025.

Varol, B., 2015. Stable isotopes (d18O, d13C) of mollusk shells in environmental interpretations; an example from sinop Miocene succession (northern Turkey). Miner. Res Expl Bull 128, 49–60. https://doi.org/10.19111/bmre.26386.

Vermeesch, P., 2018. IsoplotR: a free and open toolbox for geochronology. Geosci. Front. 9, 1479–1493.

Vermeesch, P., 2021. Maximum depositional age estimation revisited. Geosci. Front. 12, 843–850. https://doi.org/10.1016/j.gsf.2020.08.008.

Visser, M.J., 1980. Neap-spring cycles reflected in Holocene subtidal large-scale bedform deposits: a preliminary note. Geology 8, 543–546.

Vonhof, H.B., Wesselingh, F.P., Ganssen, G.M., 1998. Reconstruction of the Miocene
Western Amazonian aquatic system using moluscan isotopes signatures. Palaeogeogr. Palaeoclimatol. Palaeoecol. 141, 85–93.

Walker, R.G., 1992. Facies, facies models and modern stratigraphic concepts. In: Walker, R.G., James, N.P. (Eds.), Facies Models: Response to Sea-Level Change. Geological Association of Canada, Toronto, pp. 1–14.

Wiedenbeck, M., All´e, P., Corfu, F., Griffin, W.L., Meier, M., Oberli, F., Von Quadt, A., Roddick, J.C., Spiegel, W., 1995. Three natural zircon standards for U-Th-Pb.Lu-Hf, trace element and REE analyses. Geostandards 1950 Newsletter 19, 1–23.

Zamora, G., Gil, W., 2018. The Maran˜on ´ Basin: tectonic evolution and paleogeography. AAPG Mem 117, 121–143. https://doi.org/10.1306/13622119M1173768.

Zapata, S., Zapata-Henao, M., Cardona, A., Jaramillo, C., Silvestro, D., ObohIkuenobe, F., 2021. Long-term topographic growth and decay constrained by 3D thermo-kinematic modeling: tectonic evolution of the Antioquia Altiplano. Northern Andes Global and Planetary Change 203, 103553.

CAPÍTULO 4

HISTÓRIA EROSIVA DA REGIÃO NORTE DOS ANDES AMAZÔNICOS PERUANOS (MAASTRICHTIANO – CENOZOICO): IMPLICAÇÕES PARA EVOLUÇÃO DA CORDILHEIRA ORIENTAL

Histoire érosive maastrichtienne à actuelle de la partie nord des Andes Amazoniennes et implication sur la formation et l'érosion de la Cordillère Orientale

4. HISTORIA EROSIVA DA REGIAO NORTE DOS ANDES AMAZÖNICOS PERUANOS (MAASTRICHTIANO – CENOZOICO): IMPLICAÇOES PARA EVOLUÇAO DA CORDILHEIRA ORIENTAL

Os resultados deste capítulo são expressos na forma de artigo científico, intitulado: "*Maastrichtian-Cenozoic erosional history of the northern Peruvian Amazonian Andes: implications for the Eastern Cordillera evolution (Huallaga Basin, Northern Peru)*", submetido à revista *Gondwana Research*. Baseado nas concentrações de elementos principais e traços, composições isotópicas de Nd e datações geocronológicas U-Pb em grãos de zircões detríticos de depósitos sedimentares da Bacia de Huallaga, reconstruimos as principais mudanças de fontes sedimentares do final do Cretaceo ao longo de todo Cenozoico da Amazônia Peruana. Refinamos o *timing* erosivo da Cordilheira Oriental e a sua influência como barreira topográfica e na reorganização da rede de drenagem e a possível relação com o início do rio transcontinental paleo-Amazônico.

RÉSUMÉ

Les résultats de ce chapitre sont exprimées sous la forme d'un article intitulé «Maastrichtian-Cenozoic erosional history of the northern Peruvian Amazonian Andes: implications for the Eastern Cordillera evolution (Huallaga Basin, Northern Peru)" » qui est, lors de la soumission de ce manuscrit, en phase des dernières corrections pour être soumis à Gondwana Research. L'objectif de ce chapitre est de déterminer à partir de la provenance de l'enregistrement sédimentaire du bassin de Huallaga (nord Pérou) les différentes périodes d'érosion des cordillères andines.

La construction des Andes, du Crétacé supérieur au Cénozoïque, n'est pas un phénomène linéaire et a connu divers cycles orogéniques en réponse 1) aux variations de l'angle de subduction de la plaque de Nazca, 2) aux différents pulses magmatiques et 3) aux variations dans les taux de raccourcissement. En particulier, la chronologie de l'érosion de la Cordillère Orientale (CO) et la relation entre la construction des Andes et l'établissement de l'Amazone transcontinentale restent à préciser. L'histoire érosive des Andes Amazoniennes et la chronologie de ces événements orogéniques peuvent être déterminées en étudiant la provenance sédiments Crétacé supérieur à actuel du bassin d'avant-pays retroarc amazonien. Dans ce chapitre, nous avons déterminé la provenance des sédiments

des sédiments Maastrichtiens à actuel du bassin de Huallaga (nord Pérou) en se basant sur les concentrations en éléments majeurs et en éléments en trace, la composition isotopique Sm-Nd des roches sédimentaires à grain fin et la datation U-Pb des zircons. Nous avons aussi déterminé également l'environnement de dépôt des roches sédimentaires oligocènes et calculé les taux de sédimentation pour la succession sédimentaire du Paléogène. Nos résultats montrent que malgré la présence d'une lacune sédimentaire de 25 Ma entre le maastrichtien et l'Éocène, ces roches sédimentaires provenaient principalement des arcs magmatiques de la Cordillère Occidentale (COcc) et étaient déposées dans la partie distale de la zone de dépôt foredeep du bassin d'avant-pays retroarc amazonien. Les augmentations du % de zircons paléozoïques (0.4 à 0.26 Ma) et famatiniens (0.5 à 0.4 Ma) ainsi que le passage vers des valeurs plus négatives d'ƐNd(0) indiquent un changement de source avec une source prédominante de la Cordillère Orientale (COcc) pour l'Oligocène jusqu'au Miocène moyen. Ce changement source peut être daté du Rupélien, en se basant sur l'âge maximum vraisemblable (MLA) de JUA22 (29.70 ± 0.62 Ma), suggérant que la CO Péruvienne a commencé à agir comme une barrière topographique vers ~30 Ma. L'érosion de la COcc est accompagnée d'une augmentation des taux de sédimentation (50.1 à 99.4 m/Ma) et du développement d'un système fluvial méandriforme dans la formation Chambira, indiquant que le bassin de Huallaga faisait partie la zone de dépôt foredeep du bassin d'avant-pays retroarc amazonien entre l'Oligocène et le Miocène moyen. Enfin, une forte diminution de la contribution des zircons provenant des arcs andins crétacés et cénozoïques et une augmentation de la contribution des zircons de l'Arc Magmatique Paléozoïque pour les sédiments du Miocène supérieur à actuel indiquent des sources situées dans la CO et la SAZ et aucune contribution de la COcc. Nous suggérons que cette réorganisation du drainage pourrait être due à une propagation renouvelée/accélérée de la CO et de la SAZ, ce qui aurait pu provoquer la transcontientalisation de l'Amazone.

RESUMO

O Cretáceo superior - Cenozoic montanha andina pode ter experiências de vários ciclos orogênicos em resposta à variação em ângulo de imersão subducção, pulsos magmáticos distintos e taxas de encurtamento do Orógeno. Em detalhes, o momento da erosão da Cordilheira Oriental e a relação entre o edifício da montanha andina e o estabelecimento do rio Amazonas transcontinental continuam a ser especificados. A história erosiva dos Andes amazônicos e o tempo desses eventos orogênicos podem ser revelados através do

estudo da proveniência do registro sedimentar cretáceo-cenozóico superior da bacia amazônica retroarco. Neste estudo, investigamos a proveniência das rochas sedimentares Maastrichtianas-Cenozóicas da Bacia de Huallaga com base em concentrações de elementos principais e traços e composição isotópica Sm-Nd de rochas sedimentares de grão fino e datação por zircão U-Pb. Também refinamos o ambiente deposicional das rochas sedimentares Oligocenas e calculamos as taxas de sedimentação para a sucessão Paleógena. Nossos resultados mostram que, apesar da presença de um longo hiato sedimentar de 25 Myr entre o Maastrichtian e o Eoceno, essas rochas sedimentares foram principalmente originadas pelos arcos magmáticos da Cordilheira Ocidental e depositadas na zona de deposição distal *foredeep*. Aumentos nos grãos de zircão Paleozóico (0.4 – 0.26 Ga) e Famatiniano (0.5 – 0.4 Ga), bem como mudança para valores mais negativos de ƐNd(0) indicam fonte da Cordilheira Oriental dominante para o Oligoceno ao Mioceno médio. Esta mudança na área de proveniência pode ser estimada como sendo rupeliana em idade com base na Idade Máxima de Semelhança (MLA) de JUA22 (29.70 ± 0.62 Ma), sugerindo que a Cordilheira Oriental peruana começou a atuar como uma barreira topográfica em ~ 30 Ma. A erosão da Cordilheira Oriental é acompanhada por um aumento nas taxas de sedimentação (50.1 a 99.4 m/Ma) e o desenvolvimento de um sistema fluvial sinuoso no Chambira Fm. indicando que a bacia de Huallaga era parte do depozone foredeep durante o Oligocene-médio Miocene. Finalmente, a forte diminuição na contribuição de zircões originados dos arcos do Cretáceo e Cenozóico Andino e o aumento nos zircões do Arco Magmático Paleozoico para os sedimentos do Mioceno Superior até os dias atuais da Bacia de Huallaga indicam fontes localizadas na Cordilheira Oriental e Zona Sub-Andina e nenhuma contribuição da Cordilheira Ocidental. Sugerimos que essa reorganização da drenagem poderia ser causada pela elevação renovada/acelerada da EC e SAZ que poderia ter desencadeado o início do rio transcontinental paleo-amazônico.

MAASTRICHTIAN-CENOZOIC EROSIONAL HISTORY OF THE NORTHERN PERUVIAN AMAZONIAN ANDES: IMPLICATIONS FOR THE EASTERN CORDILLERA EVOLUTION (HUALLAGA BASIN, NORTHERN PERU)

Michele Andriolli Custódio[a,b,c], Martin Roddaz[a,c], Roberto Ventura Santos[a], Elton Luiz Dantas[a], Stéphane Brusset[c], Mélanie Louterbach[d], Christian Hurtado[e] Guilherme Oliveira Gonçalves[a]

[a] Laboratório de Geocronologia, Instituto de Geociências, Universidade de Brasília, Brasília, DF 70910-000, Brazil

[b] Departamento de Geociências, Universidade Federal do Amazonas, CEP: 69.077-000, Manaus, AM, Brazil

[c] Géosciences-Environnement Toulouse, Université de Toulouse, UPS (SVT-OMP), CNRS, IRD, 14 Avenue Édouard Belin, 31400 Toulouse, France

[d] Harvard Graduate School of Design, Department of Landscape Architecture, 48 Quincy Street, MA 02138 Cambridge, USA.

[e] Universidad Nacional Mayor de San Marcos, Av. Venezuela Cda. 34 s/n Lima-Cercado, Lima, Peru.

4.1 ABSTRACT

The late Cretaceous - Cenozoic Andean mountain building may have experiences various orogenic cycles in response to variation in dip angle subduction, distinct magmatic pulses and shortening rates of the orogen. In details, the timing of the Eastern Cordillera (EC) erosion and the relation between the Andean mountain building and the establishment of the transcontinental Amazon River remain to be specified. The erosional history of the Amazon Andes and the timing of these orogenic events may be revealed by studying the provenance of the late Cretaceous-Cenozoic sedimentary record of the Amazonian retroarc foreland basin. In this study, we investigate the provenance of the Maastrichtian-Cenozoic sedimentary rocks of the Huallaga Basin based on major and trace elements concentrations and Sm-Nd isotopic composition of fine-grained sedimentary rocks and U-Pb zircon dating. We also refine the depositional environment of the Oligocene sedimentary rocks and calculate sedimentations rates for the Paleogene succession. Our results show that despite the presence of a 25 Myr long sedimentary hiatus between the Maastrichtian and

Eocene, these sedimentary rocks were mainly sourced by the magmatic arcs of the Western Cordillera (WC) and deposited in the distal foredeep depozone. Increases in Paleozoic (0.4 – 0.26 Ga) and Famatinian (0.5 – 0.4 Ga) zircon grains a as well as shift toward more negative ℇNd(0) values indicate dominant EC source for the Oligocene to middle Miocene. This change in provenance area can be estimated to be Rupelian in age based on the Maximum Likehood Age (MLA) of JUA22 (29.70 ± 0.62 Ma) suggesting that the Peruvian EC started to act as a topographic barrier at ~30 Ma. The erosion of the EC is accompanied by an increase in sedimentation rates (50.1 to 99.4 m/Ma) and the development of a meandering fluvial system in the Chambira Fm. indicating that the Huallaga Basin was part of the foredeep depozone during the Oligocene-middle Miocene. Finally, strong decrease in contribution of zircons originated from the Cretaceous and Cenozoic Andean arcs and increase in Paleozoic Magmatic Arc zircons for the late Miocene to present day sediments of the Huallaga Basin indicate sources located in the EC and SAZ and no contribution of the WC. We suggest that this drainage reorganization could be caused by renewed/accelerated uplift of EC and SAZ that might have triggered the onset of the paleo-Amazon transcontinental river.

4.2 INTRODUCTION

The interplay between convergent oceanic-continental plates and the resulting deformation and uplift of the Earth's crust forms a wide and complex Cordilleran orogenic system characterized by multiple cycles of tectonic activity over millions of years (e.g. Mégard, 1984; DeCelles et al., 2009; Horton, 2018b). The modern Andean Cordilleran orogenic system is one of the most notable non-collisional orogenic belt that had been affected by several temporal and spatial variations of dip angle of the subducting slab, distinct magmatic pulses and shortening rates of the orogen (Boschman, 2021; Poblete et al., 2021; Sundell et al., 2019; Chen et al., 2019; Armijo et al., 2015; Beck and Zandt, 2002; Pfiffner and Gonzalez, 2013). The rise and erosion of the Andes built crossings and barriers for ecosystems, shaped river-drainage networks, affected the regional-scale climate by blocking zonal flows, wind patterns and controlled the sediment routing systems that jointly impacted on paleoenvironments and paleogeography evolution in the adjacent Amazon Basins through time (Zapata et al., 2021; Vallejo et al., 2021; García-Delgado et al., 2021; Albert et al., 2021; Serrano et al., 2021; Horton, 2018a; Hurtado et al., 2018; van Soelen et al., 2017; Louterbach et al., 2017; Roddaz et al., 2010; Insel et al., 2009; Potter,

1997; Lenters and Cook, 1995; Campetella and Vera, 2002; Espinoza et al., 2020). The tropical Andes and the adjacent Amazon Basin represent the richest hotspot of biodiversity worldwide (Rahbek et al., 2019; Hoorn et al., 2022). The current biodiversity patterns are deeply rooted in the pre-Quaternary and the Andean uplift was a major driver for the evolution of Amazonian landscapes and ecosystems (Hoorn et al., 2010) making the timing of the Andean uplift of particular interest to the wider scientific community including to biologists, paleontologists, and geoscientists.

Regarding the Andean uplift, it remains unclear if the timing and sequence of the subduction-related contractional orogeny was built over an uninterrupted interval (~50-100 Myr) or if is resulted from a multistage (<5-10 Myr) (i.e. Mégard, 1984; DeCelles and Horton, 2003; Barnes and Ehlers, 2009; Schellart, 2010; Horton, 2018a, b; Jara et al., 2021). Mountain building in the Andes is diachronous along strike (see Horton, 2018a,b; Boschman, 2021) but started in the late Cretaceous with the development of a retroarc foreland basin (e.g., DeCelles and Horton, 2003; Hurtado et al., 2018; Louterbach et al., 2018b; Vallejo et al., 2021) with initial tectonic loading probably related to the Maastrichtian (?) - Paleocene growth of the Western Cordillera in the Central and Northern Andes (Fig. 4.1) (DeCelles and Horton, 2003; Hurtado et al., 2018; Louterbach et al., 2017). Following this late Cretaceous-Paleocene period of mountain building and shortening, the retroarc foreland basins of the Central and Northern Andes experienced limited shortening or neutral to locally extensional conditions (Horton, 2018a) as recorded by the development of a regional unconformity or diminished accumulation in their sedimentary succession (see Horton, 2018a). This presence of neutral or extensional conditions in the retroarc hinterland is associated with a low degree of mechanical coupling along the subduction plate boundary and limited craton-ward propagation of the fold and thrust belt (Horton and Fuentes, 2016; Horton, 2018b, 2018a). However, some authors have suggested that the protracted exhumation of the Eastern Cordillera of Bolivia and Peru has been ongoing since 40–45 Ma (Benjamin et al., 1987; Farrar et al., 1988; Barnes et al., 2006; Gillis et al., 2006; Perez et al., 2016) or 50-55 Ma (Rak et al., 2017) and is likely linked to continued shortening. This Eocene timing has been disputed by other authors who have instead suggested an Oligocene-Miocene age for the exhumation and formation of the Eastern Cordillera (EC) based on thermochronology dating, balanced cross sections and sequential restoration (Eude et al., 2015) in response to the advance of craton-ward thrust front. One way to determine the timing of uplift of the Eastern Cordillera is to pinpoint in

the retroarc foreland basin sedimentary record the arrival of detritus sourced by the EC, as it has a distinct provenance when compared with other Andean terranes (Chew et al., 2016; Chew et al., 2008), providing that the retroarc foreland basin sedimentary record is well dated.

The Amazon River became transcontinental between 11.8 Ma and 8.7 Ma with the first arrival of Andean sediments in the Amazon fan (Figueiredo et al., 2009b; Hoorn et al., 2017b; van Soelen et al., 2017b) which have been related to acceleration of the denudation rates in the EC and forward propagation of eastern Andean Amazonian wedge (Subandean Zone (SAZ) and EC) (Mora et al., 2011). Before the late Miocene onset of transcontinental Amazon River, the western Amazon paleodrainage system was parallel to the Andes with a possible embouchure in the Maracaibo lake (Roddaz et al., 2010). This Paleogene to middle Miocene paleodrainage was perturbed by the Cenozoic shallow marine incursions that flooded western Amazonia (Alvim et al., 2021; Boonstra et al., 2015; Hoorn, 1993; Hoorn et al., 2010; Hovikoski et al., 2010; Jaramillo et al., 2017; Roddaz et al., 2010; Santos et al., 2008) and the existence of the early to middle Miocene Pebas megawetland (Hoorn et al., 2011). However, the relationship of the existence and establishments of these paleoenvironments with the Andean mountain building process are still unknown.

The goal of this study is to document the erosional history of the Amazonian Andes during the Maastricthian-Cenozoic and to unravel how and when it influenced on the onset of the transcontinental Amazon drainage system.

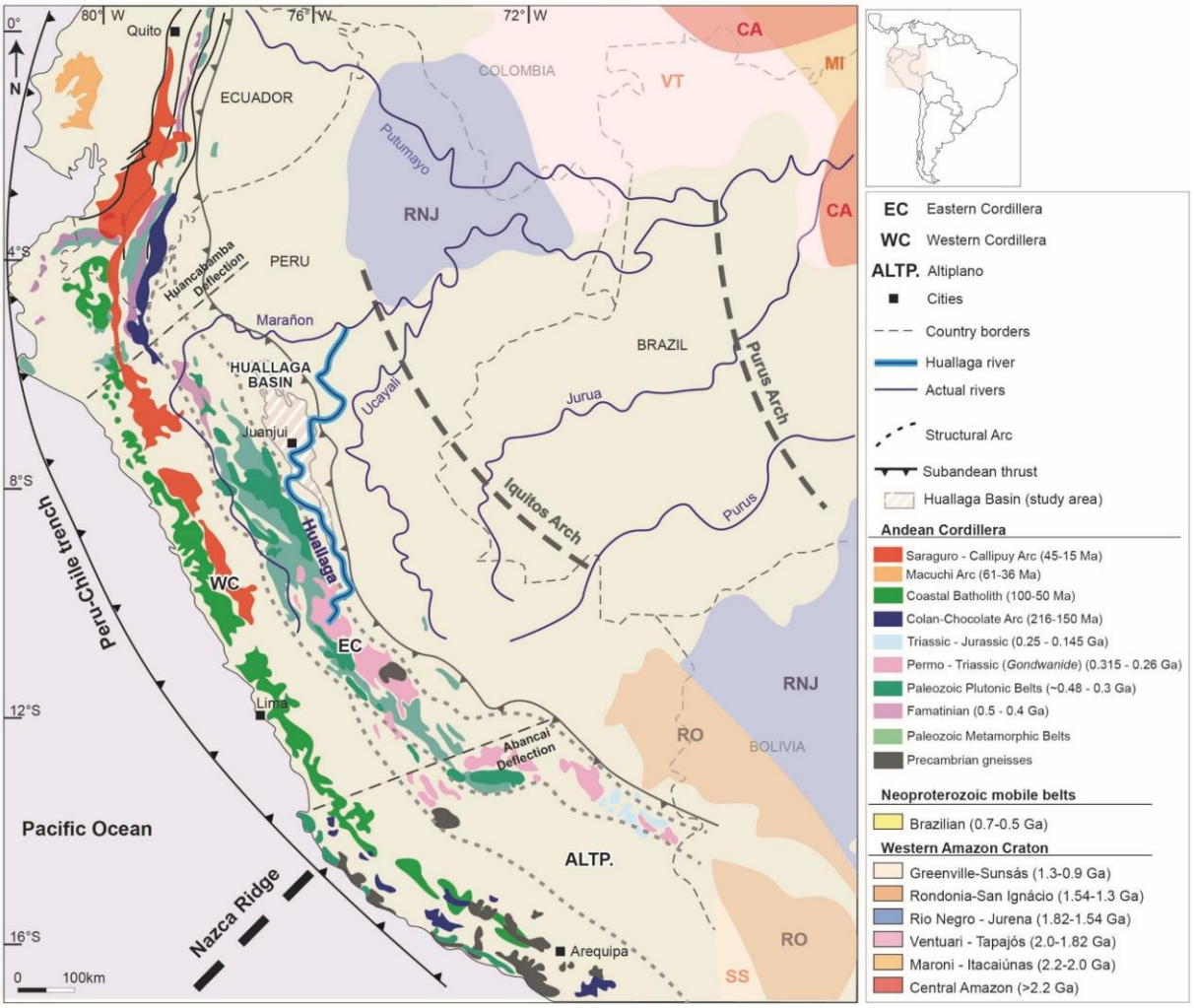


Figure 4. 1 Map of the geographic extent of the major potential source areas of the Western Amazonia, from the west to east, the Western Cordillera (Andean Magmatic Arch), Eastern Cordillera (retroarc fold-thrust belt) and Western Amazon Craton (Guyana and Brazilian shields). The actual Huallaga River is represented by the thicker blue line.

4.3 GEOLOGICAL SETTING

The Andean Amazonian retroarc foreland basins formed in response to the load exerted by the Andes (Western and Eastern cordilleras) onto the South American lithosphere (Horton, 2018b; Bayona et al., 2008; Horton and DeCelles, 1997; Jordan, 1995; Cooper et al., 1995). Since the Pliocene times (Espurt et al., 2007; Espurt et al., 2010) the Amazonian retroarc foreland basin was divided in two retroarc foreland basin systems (*sensu* DeCelles and Giles, 1996): the North and South Amazonian retroarc foreland basin systems, separated by the Fitzcarrald Arch (Roddaz et al., 2005). Before the Pliocene, the Amazonian retroarc foreland basin system formed an unique retroarc foreland basin system extending from northern Bolivia to Colombia (Roddaz et al., 2010). The initiation of the

Amazonian retroarc foreland basin system started during the late Cretaceous or early Paleocene times (DeCelles and Horton, 2003; Martin-Gombojav and Winkler, 2008; Roddaz et al., 2010; Hurtado et al., 2018; Louterbach et al., 2017), as a response to the onset shortening in the Andean belt (DeCelles et al., 2011; DeCelles and Horton, 2003; Horton et al., 2001; Louterbach et al., 2017; Nie et al., 2010; Parra et al., 2012; Roddaz et al., 2010; Sempere et al., 1997). The North Amazonian foreland basin system comprises the Colombian, Ecuadorian and Northern Peruvian foreland basins (Roddaz et al., 2010) with depozones experimenting either uplift or subsidence (Vallejo et al., 2021; Moreno et al., 2020; Gutiérrez et al., 2019; George et al., 2019; Odoh et al., 2019; Calvès et al., 2018; Zamora and Gil, 2018; Louterbach et al., 2017; Martin-Gombojav and Winkler, 2008; Christophoul et al., 2002; Hungerbühler et al., 2002).

4.3.1 Tectonic setting of the Huallaga Basin

The Huallaga Basin (Northern Peru) is part of the Huallaga – Moyabamba – Marañon Subandean retroforeland basin system situated at sub-Andean zone (SAZ) in the northern Central Andes (Espurt et al., 2007, 2011; Calderon et al., 2017). The Huallaga Basin defines the present-day wedge-top depozone and is separated to the east, from the foredeep depozone (Marañon Basin) by the sub-Andean thrust front (Roddaz et al., 2010; Hermoza et al., 2005) and to the west by the Eastern Cordillera (Fig. 4.1). It is N160E elongated and present 400 km length *vs* width of 100km, located between 76°–77°W and 6°–9°S (Fig. 4.2) (Hermoza et al., 2005).

The deformation of the sub-Andean zone is commonly associated with the propagation of the thrust wedge and the uplift of the Eastern Cordillera, which based on sequential restoration using low temperature thermochronology ages and balanced cross section started between 30 and 24 Ma (Eude et al., 2015). The further propagation of the wedge front was due to the reactivation of the preexisting basement structures (Eude et al., 2015), which allowed a total horizontal shortening from 70 to 76 km (Calderon et al., 2017).

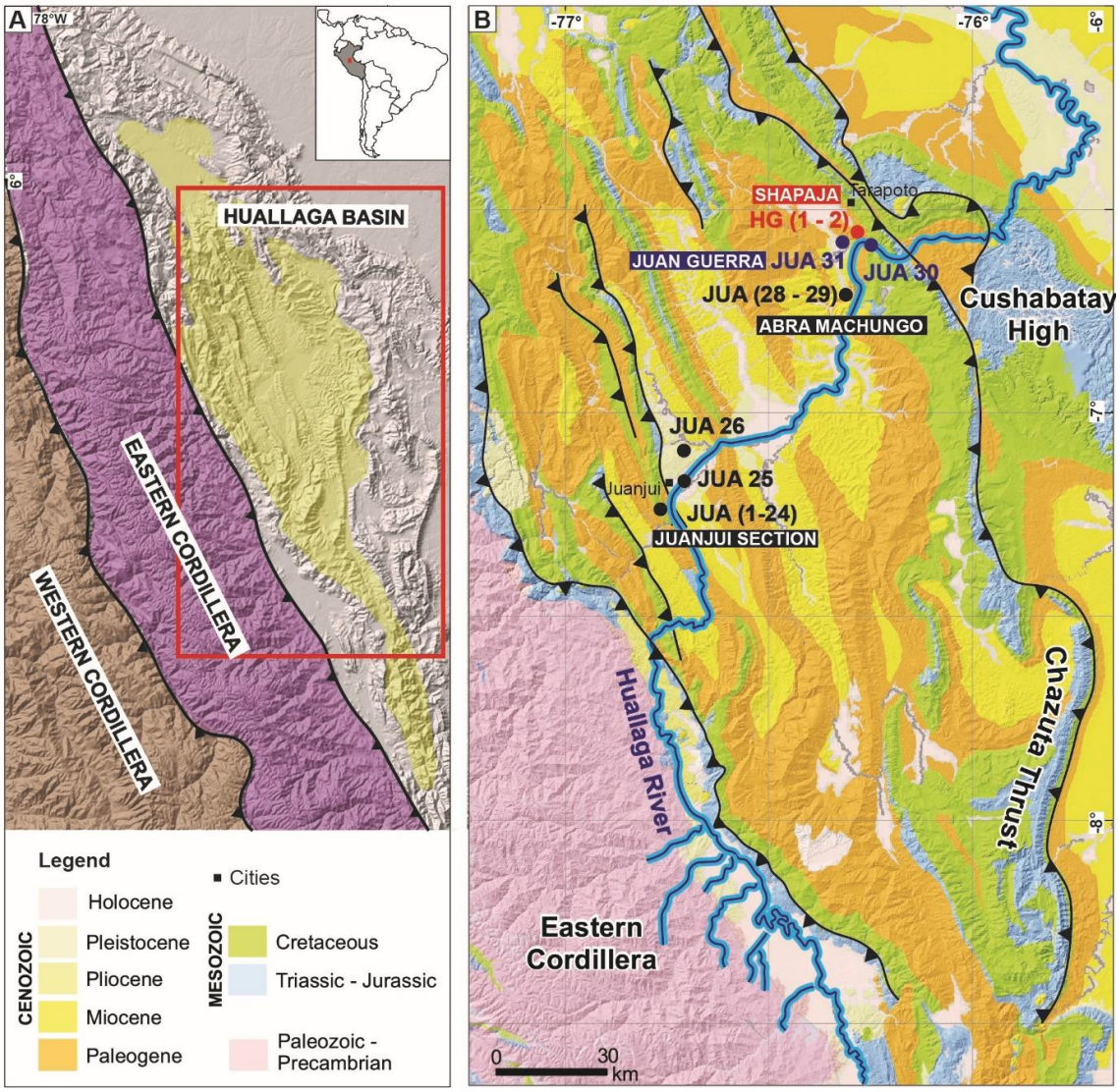


Figure 4. 2 Geologic map of the Huallaga foreland basin. Cenozoic sedimentary sections described in this study are localized along the Huallaga river (Juanjui Section). Additional set of data is localized near Tarapoto city, such as Abra Machungo, Juan Guerra and Shapaja areas. See details about cordinates position in Supplementary Data S1.

4.3.2 Stratigraphic framework

The late Cretaceous – Cenozoic sedimentary sequence of the Huallaga – Marañon retroarc foreland basin system comprises a shallow marine to continental foreland successions (Hermoza et al., 2005; Kummel, 1948; Roddaz et al., 2010).

The Cretaceous sequences of the Huallaga Basin comprise Albian to Maastrichtian fluvial to shallow marine successions of sandstones, shales and limestones represented by the Goyallarisquizga, Cushabatay-Raya; Agua Caliente-Chonta, and Vivian-Cachiyacu-Huchpayacu formations (Fig. 4.3) (Baby et al., 2018; Calderón et al., 2017a, 2017b;

Hermoza et al., 2005; Kummel, 1948) mainly sourced by the easternmost Brazilian Shield terranes (Fig. 4.1) (Hurtado et al., 2018).

The Paleogene sedimentary succession of the Huallaga Basin has been recently revised by Custódio et al. (2023). A chronostratigraphic hiatus separates the Maastrichtian series from the Lutetian-Bartonian sedimentary sequence (Fig. 4.3) (Custódio et al., 2023). This Paleocene- early Eocene hiatus is a regional unconformity also documented in other northern basins (Bagua, Oriente and Llanos basins) (Gutiérrez et al., 2019; Caballero et al., 2020; Moreno et al., 2020; Naeser et al., 1991). The Eocene sedimentary rocks overlaying this unconformity are represented by Lutetian carbonate – mud-rich lacustrine deposits of the Yahuarango Fm. (43.5 ± 0.64 Ma) succeed by Bartonian siliciclastic tide-influenced depositional system correlated to the Pozo Fm. (37.64 ± 0.85 Ma) (Custódio et al., 2023). The Yahuarango Fm. have a dominant Andean detritus (16%, < 0.12 Ga) and yields εNd (0) values ranging between − 5.6 and − 12.0, which is consistent with an Andean Arc provenance (Hurtado et al., 2018; Custódio et al., 2023). The Bartonian marine transgression might had been reached the Huallaga Basin from the north and is characterized by freshwater to brackish conditions as shown by carbon and oxygen stable isotope values, from − 11.9 to − 10.0‰ (Custódio et al., 2023).

Succeeding to the Pozo Fm, the Chambira Fm is Oligocene to Miocene in age with an inferred base age of 26.56 ± 0.07 Ma (Antoine et al., 2016) and characterized by fluvial deposits (Fig. 4.3) (Hermoza et al., 2005). It is overlaid by the Neogene (late Miocene–Pliocene ?) fluvial to deltaic deposits of the Ipururo Fm. (Fig. 4.3) (Hermoza et al., 2005). The younger and final sedimentary sequence is represented by the Pliocene-Pleistocene fluvial to alluvial fan deposits of the Juanjuí Fm. (Fig. 4.3) (Hermoza et al., 2005).

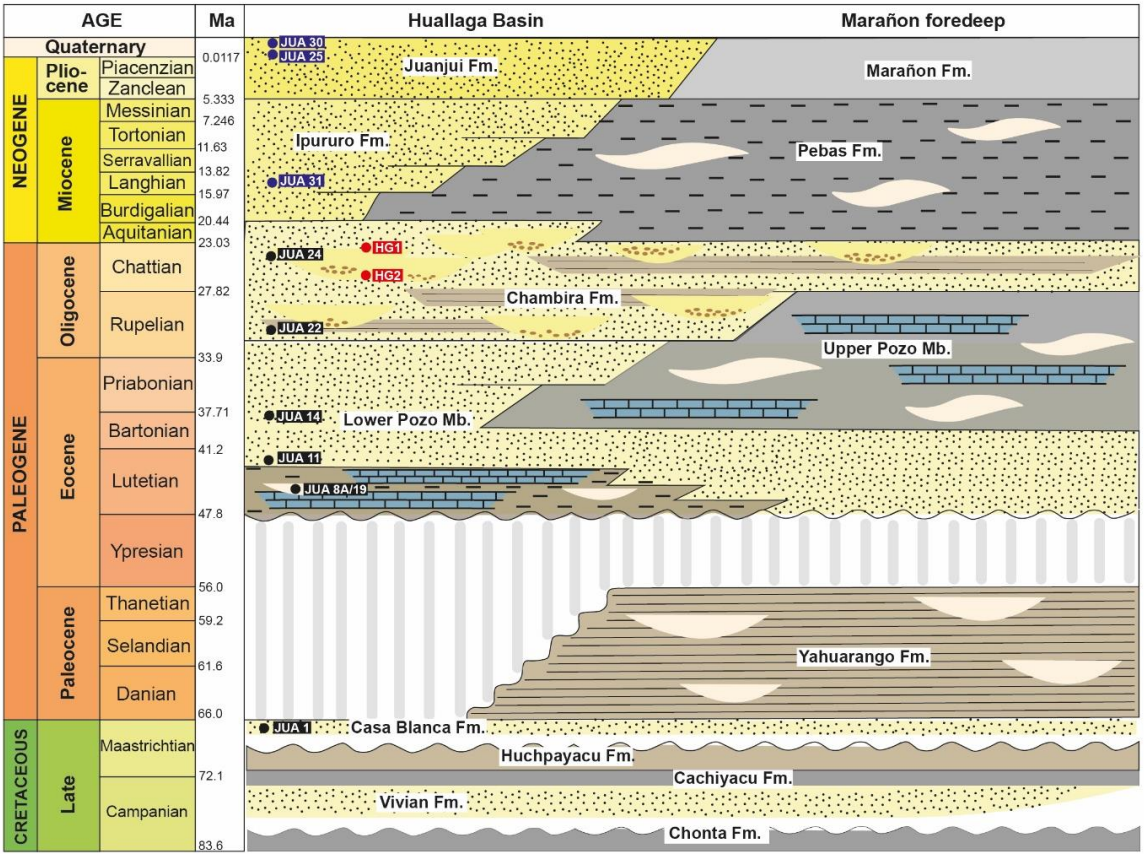


Figure 4. 3 Comparative chronostratigraphic diagram showing the stratigraphic nomenclature, age and stratigraphic discontinuities for the Huallaga and Marañón basins (modified from Roddaz et al., 2010). The circles indicate the stratigraphic position of the samples on the stratigraphic sections and the outcrops: black – Juanjuí section; red – Shapaja ; blue – Abra Machungo and Juan Guerra area.

4.4. MATERIALS AND METHODS

4.4.1 Sedimentology

We studied one Cenozoic section from the Huallaga Basin: the Juanjuí section (Fig. 4.4). The Maastrichtian to Bartonian sedimentary evolution of the Juanjui section has been published in Custódio et al. (2023). The sections and outcrops investigated here are located in Figure 4.2, and their geographic coordinates are given in Supplementary Data S1.

We described the sedimentary facies in terms of lithology, geometry, sedimentary structures and paleontological content (Miall, 1978; 2006). We also measured paleocurrent direction from cross-bedded sandstones in inclined strata. The paleocurrent directions were corrected based on their bedding plane (S0 strata) using the PALEOCOR program version

1.2 (Almeida, 2001). Based on the measurements and descriptions of the facies we defined seven facies associations and three depositional systems (Table 4.1).

4.4.2 Major and trace elements analyses

Twelve (12) fined-grained sedimentary rocks were collected from the outcrops along the Juanjuí stratigraphic section, Abra Machungo, Juan Guerra and Shapaja areas and were analyzed for major and trace element concentrations (Fig. 4.2; Table 4.2).

Major, oxides and trace elements concentrations were measured at the *Service d'Analyse des Roches et Minéraux* (SARM) in Nancy, France. The preparation samples, analytical procedures and treatment of data for trace element determinations followed the steps proposed by (Carignan et al., 2001). The major elements (Na, Mg, K, Ca, Sc, Ti, Mn, Fe, Al, Si and P) and the oxides (SiO_2, Al_2O_3, Fe_2O_3, MnO, MgO, CaO, Na_2O, K_2O, TiO_2, P_2O_5) were detected and measured by Inductively Coupled Plasma – Optical Emission Spectrometry (ICP-OES). Whereas, the trace elements (Rb, Cs, Ba, Sr, Th, U, Y, Zr, Nb, Hf, Cr, V, Co, Cu, Ni, Zn, La, Ce, Pr, Nd, Sm, Eu, Gd, Tb, Dy, Ho, Er, Tm, Yb, Lu and Ta) were measured by Inductively Coupled Plasma Mass Spectrometry (ICP-MS). After the determination, the major and trace element concentrations were normalized to Post Archean Australian Shales (PAAS) (Taylor and McLennan, 1985; McLennan, 2001; Pourmand et al., 2012).

We have used the Chemical Index of Alteration (CIA) to assess the degree of source-area weathering and the paleoweathering conditions of the sediments (Fedo et al., 1995; Nesbitt and Young, 1982). This index measures the weathering intensity of feldspars relative to unaltered protoliths, and is defined as: $CIA = [Al_2O_3/(Al_2O_3 + CaO^* + Na_2O + K_2O)] \times 100$ (in molar proportions), where CaO* represents the CaO content in the silicate fraction. We do not have CO_2 data for our analyses and thus we cannot correct for Ca in carbonates to obtain CaO*. To calculate CaO*, we have assumed the value of CaO if $CaO \leq Na_2O$, and $CaO = Na_2O$ if $CaO \geq Na_2O$ (Bock et al., 1998).

To facilitate comparisons with sediments derived from basic or felsic sources (Cullers, 2000) and the PAAS (Pourmand et al., 2012; Taylor and McLennan, 1985; McLennan, 2001), the Eu anomaly is calculated with respect to chondrites: Eu/Eu* = EuN/(SmN × GdN)1/2 where N refers to the chondrite- normalized concentration value (Condie, 1993). The Cerium anomaly (ΩCe) normalized to PAAS is calculated following

(De Baar et al., 1985): ΩCe = 2 × (Cesample/CePAAS) / [(Lasample/LaPAAS) + (Prsample/PrPAAS)], where Xsample is the concentration of samples and XPAAS refers to the concentrations of the PAAS standard.

4.4.3 Sm-Nd isotopes compositions

Eleven (JUA1, JUA5, JUA6, JUA15, JUA16, JUA22, JUA24, JUA28, JUA29, JUA31 HG2) representative fine-grained sedimentary rocks were collected from the Cretaceous – Cenozoic sequence of Huallaga Basin (Figures 4.2, 4.4; Table 4.3). The samples preparation and procedures for the analyses of Sm-Nd isotope composition were done at the Laboratório de Estudos Geodinâmicos, Geocronológicos e Ambientais (LEGGA) of the Universidade de Brasília (UnB). The $^{147}Sm/ ^{144}Nd$ and $^{143}Nd/ ^{144}Nd$ isotopic ratios were measured using the Neptune Series High Resolution Multicollector ICP-MS.

The samples preparation comprised the crush of the aliquots with a ball mill and followed the procedures of sample digestion, such as separation of REEs, Sm and Nd elements using chromatography columns, as described and proposed by Gioia and Pimentel (2000). To achieve the accuracy and quality of the measurements, repeated analysis were done on the BHVO-2 reference material (standard). The $^{143}Nd/ ^{144}Nd$ ratio was normalized using $^{146}Nd/ ^{144}Nd = 0.7219$ to correct the signal for mass fractionation.

The measured $^{143}Nd/ ^{144}Nd$ ratios are presented as the fractional deviation in parts per 10^4 (units) from $^{143}Nd/^{144}Nd$ in a Chondritic Uniform Reservoir (CHUR) as measured at the present-day:

$$\varepsilon Nd(0) = [(^{143}Nd/^{144}Nd)S/ICHUR(0) - 1] * 10^4$$

where ($^{143}Nd/ ^{144}Nd$) is the present-day ratio measured in the sample, and ICHUR(0) is the $^{143}Nd/ ^{144}Nd$ in the CHUR reference reservoir at the present ICHUR(0) = 0.512638 (Jacobsen and Wasserburg, 1980).

4.4.4 Zircon U-Pb dating

Seven sandstones (JUA1, JUA8A/19, JUA11, JUA14, JUA16, JUA22, JUA24) were analyzed from the Juanjuí stratigraphic section (Figures 4.2, 4.3, 4.4, Table 4.6, Supplementary Data S2). In addition, six sandstones and sands were collected (JUA25, JUA26, JUA30, JUA31, HG1, HG2) on Abra Machungo, Shapaja and Juan Guerra

outcrops for U-Pb dating (Figure 4.2; Table 4.6, Supplementary Data S2). The samples preparation and analyses for U-Pb dating were made at the Laboratório de Estudos Geodinâmicos, Geocronológicos e Ambientais (LEGGA) of the Universidade de Brasília (UnB).

The samples preparation comprised the crush, sieving of the aliquots and concentration heavy minerals by panning of about 5kg of each sample. Then, the zircon grains were separated from the concentrated fraction by magnetic susceptibilities of the minerals using the Frantz Isodynamic Magnetic Separator (best recovery of zircons grains > 1.6A) (Stendal and Theobald, 1994). Zircon grains recovered were randomly hand-picked (~150 grains for sample) under a stereoscopic microscope; mounted on adhesive tape, placed in a 9 mm diameter plastic ring enclosed with epoxy resin. To access the zircon core, the grains were polished to expose the centers. Zircon grains were imaged by a Scanning Electron Microscope (SEM) to obtain morphological features and internal structures.

The analytic acquisition of isotope data was collected using Inductively Coupled-Plasma Mass Spectrometry (ICP-MS) Finnigan Element XR, coupled to a 193 nm Iridia Excimer (ArF) laser ablation system. Laser conditions included a spot diameter of 25 μm, 20 Hz, and 2.0 J cm^{-2}. The raw data was processed on Iolite 4.0 following the procedures proposed by Paton et al., (2011) and, the individual signal inspection was done with assistance of the VizualAge (Petrus and Kamber, 2012). Data normalization and quality control were done by three different reference materials: GJ1 zircon (Jackson et al., 2004), 91500 zircon (Widenbeck et al., 1995) and Plešovice zircon (Sláma et al., 2008).

For each sample, we have reported the 'maximum depositional age' (MDA) and 'maximum likelihood age' (MLA) (Table 4.5, Supplementary Data S2). The MDA was calculated as the weighted mean average of the three youngest zircons overlapped analyses and associated 2σ uncertainty of this cluster (the YC2σ[3+]; Dickinson and Gehrels, 2009; Sharman et al., 2018; Sharman and Malkowski, 2020). The MLA is a statistical model that assumes that the zircon U-Pb ages defined a two component mixture, in which a "fraction of the population is derived from a discrete minimum age peak and the remaining grains follow a (log)normal distribution" (Galbraith, et al. 2005; Galbraith and Laslett, 1993; Vermeesch, 2021). The MLA was calculated using IsoplotR (Vermeesch, 2018; 2021).

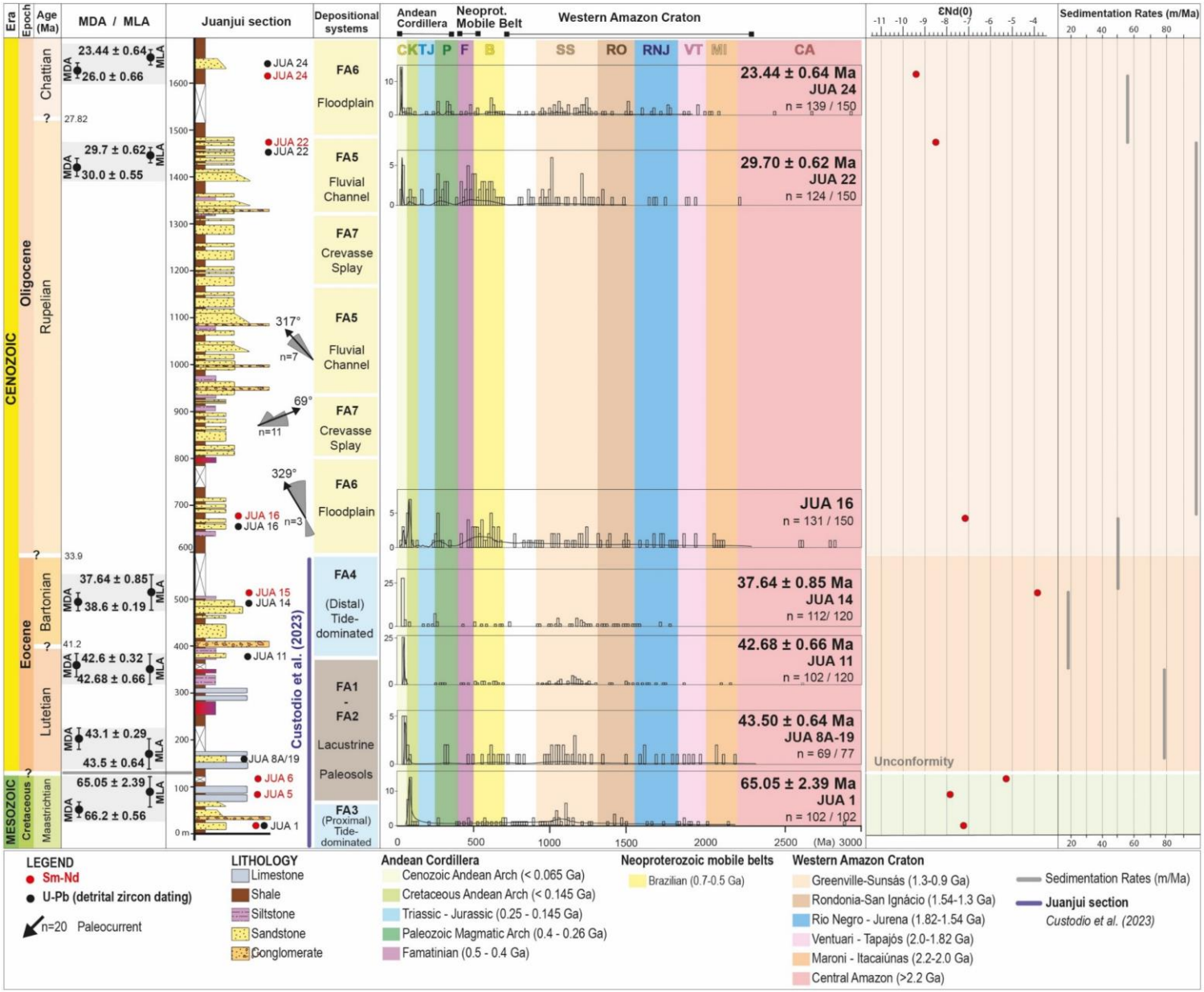
The large numbers of samples and amounts of distributional data requires quantitative and objective methods, such as multidimensional scaling (MDS) to analyze

them (Vermeesch, 2013; Vermeesch et al., 2016). To improve the method, we applied Kolmogorov–Smirnov (KS) statistic that is a measure used to compare samples distributions. A smaller and larger KS distance indicates more or less dissimilarity between the distributions, respectively (Vermeesch, 2013).

4.4.5 Sedimentation rates

We used the *GENEX* basin modeling software (*Institut Francais du Petrole* – IFP) to reconstruct the tectonic subsidence history of the Huallaga basin during the Cenozoic (see Figure 4.4; Table 4.4). To estimate the sedimentation rates, the program uses the back-stripping method. The measures of sedimentation rates consist of stratigraphic time-depth information (thicknesses, ages, lithologies and depositional water depths). The parameter of depositional water depths was settled based on theoretical scenario of the Cenozoic strata (50 meters maximum).

Figure 4. 4 Juanjuí stratigraphic section of the Huallaga Basin. The related chronostratigraphic ages, paleocurrents data, depositional systems, ƐNd values and measures of sedimentation rates obtained are indicated along the section. See text for more details.


Era
Epoch
Age (Ma)
MDA / MLA
Juanjui section
Depositional systems
Andean Cordillera
Neoprot. Mobile Belt
Western Amazon Craton
CK TJ P F B SS RO RNJ VT MI CA
εNd(0)
Sedimentation Rates (m/Ma)
CENOZOIC
MESOZOIC
Oligocene
Eocene
Cretaceous
Chattian
Rupelian
Bartonian
Lutetian
Maastrichtian
23.44 ± 0.64
26.0 ± 0.66
27.82
29.7 ± 0.62
30.0 ± 0.55
33.9
37.64 ± 0.85
38.6 ± 0.19
41.2
42.6 ± 0.32
42.68 ± 0.66
43.1 ± 0.29
43.5 ± 0.64
65.05 ± 2.39
66.2 ± 0.56
JUA 24
JUA 22
JUA 16
JUA 15
JUA 14
JUA 11
JUA 8A/19
JUA 6
JUA 5
JUA 1
317°
n=7
69°
n=11
329°
n=3
Custodio et al. (2023)
FA6 Floodplain
FA5 Fluvial Channel
FA7 Crevasse Splay
FA5 Fluvial Channel
FA7 Crevasse Splay
FA6 Floodplain
FA4 (Distal) Tide-dominated
FA1 - FA2 Lacustrine Paleosols
FA3 (Proximal) Tide-dominated
23.44 ± 0.64 Ma
JUA 24
n = 139 / 150
29.70 ± 0.62 Ma
JUA 22
n = 124 / 150
JUA 16
n = 131 / 150
37.64 ± 0.85 Ma
JUA 14
n = 112/ 120
42.68 ± 0.66 Ma
JUA 11
n = 102 / 120
43.50 ± 0.64 Ma
JUA 8A-19
n = 69 / 77
65.05 ± 2.39 Ma
JUA 1
n = 102 / 102
Unconformity
0 500 1000 1500 2000 2500 (Ma) 3000
LEGEND
Sm-Nd
U-Pb (detrital zircon dating)
n=20 Paleocurrent
LITHOLOGY
Limestone
Shale
Siltstone
Sandstone
Conglomerate
Andean Cordillera
Cenozoic Andean Arch (< 0.065 Ga)
Cretaceous Andean Arch (< 0.145 Ga)
Triassic - Jurassic (0.25 - 0.145 Ga)
Paleozoic Magmatic Arch (0.4 - 0.26 Ga)
Famatinian (0.5 - 0.4 Ga)
Neoproterozoic mobile belts
Brazilian (0.7-0.5 Ga)
Western Amazon Craton
Greenville-Sunsás (1.3-0.9 Ga)
Rondonia-San Ignácio (1.54-1.3 Ga)
Rio Negro - Jurena (1.82-1.54 Ga)
Ventuari - Tapajós (2.0-1.82 Ga)
Maroni - Itacaiúnas (2.2-2.0 Ga)
Central Amazon (>2.2 Ga)
Sedimentation Rates (m/Ma)
Juanjui section
Custodio et al. (2023)

4.5 RESULTS

4.5.1 Depositional systems from sedimentary analysis

Detailed facies sedimentary description of the Cenozoic sequence allowed the identification of sedimentary facies. These facies were grouped into seven genetic facies associations (Table 4.1): (1) Lake deposits; (2) Paleosols; (3) Proximal part of the fluvial-tidal transition zone; (4) distal part of the fluvial-tidal transition zone environment; (5) Channels; (6) Floodplain and; (7) Crevasse splay (Figure 4.4 and Table 4.1). The first four facies association characterized the Maastrichtian – Bartonian part of the Juanjuí section (Yahuarango and Pozo formations in Hermoza et al., 2002 and Roddaz et al., 2010). They have been described and interpreted in Custódio et al. (2023) and defined two depositional environments: The fluvial-tidal transition zone of a tide dominated environment and a lacustrine environment (Custódio et al., 2023). For details on these facies association and paleoenvironment, the reader is referred to this article (i.e. Custódio et al., 2023). The last three facies association defined the Oligocene part of the Juanjuí section that belong to the Chambira Formation (Roddaz et al., 2010).

Facies Association	Lithofacies	Description	Interpretation
FA5	Fm, Fs, P, Sr, Smb	Laminated red mudstones, abundant paleosol, carbonaceous streaks, plant rootles, scattered bioturbation and disiccation cracks are common	Floodplain
FA6	Ss, Sh, Sr, Fm, Fs	Very-fine to fine sandstones interlayered with shales and siltstones layers; flute casts are common, coarsening and thickening-upward succession	Crevasse Splay
F7	Gcm, St, Sp, Sh, Sm, Sr, Fs, Fm,	Fine to very coarse-grained sandstones and conglomerates with mud clasts, abundant basal erosional surfaces, lateral accretion macroforms	Fluvial Channel

Table 4. 1 Facies Association and Interpretation for the Cenozoic sequence of Western Amazonia (Huallaga basin, Peru). The FA1, FA2, FA3, FA4 were previously described and interpreted by Custódio et al. (2023).

4.5.1.1 Facies association 5: Channels deposits

Description - The FA5 comprises matrix-supported conglomerates (Gm), trough-cross-bedded sandstones (St), planar-cross-bedded sandstones (Sp), horizontally-bedded sandstones (Sh), massive sandstones (Sm), climbing-ripple cross-laminated sandstones

(Sr) and fines, such as, shales (Fm) and siltstones (Fs) (Table 4.1). The sandstones and conglomerates bodies present erosional concave-up base and flat top which configure a lateral wedge-out, ranging between 1-10 m thickness (T) and 10-80 m width (W) (Fig. 4.5A). Based on the width/thickness (W/T) ratio of the channels, these are classified as mobile channels (W/T: 8), exhibiting multistory channel bodies (Gibling, 2006; Friend et al., 1979). Internally, they are arranged in fining-upward beds composed at the base by medium- to coarse-grained sandstones (St, Sm facies) and conglomerates (Gm) with locally cm- to dm-rounded mud clasts, grading to Sp and Sr facies toward to the top (Figures 4.5C; 4.6). The sandstone bodies grades laterally into meter-thick successions of amalgamated sigmoidal clinoforms with foresets that show offlapped upper terminations and their lower terminations dips at a low angle, exhibiting tangential surface to the erosive bottomset, characterized as a lateral-accretion architectural element (Figure 4.5B). Vertically, the channel-fill grades to interbedded fine- to medium-grained rippled sandstones (Sr), siltstones (Fs) and mudstones (Fm), disposed in in thin (dm-thick) tabular beds (Figure 4.6).

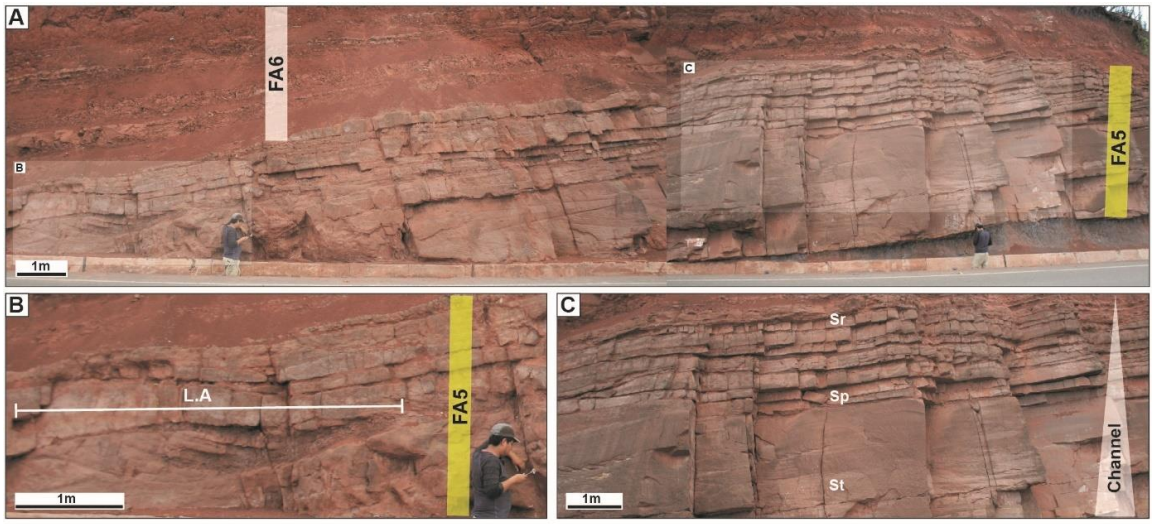


Figure 4. 5 Representative photographs of the Facies Associations of Channel deposits (FA5) and Floodplain deposits (FA6). A) General outcrop view along the road cutting, showing the vertical and lateral stacking pattern of the Facies Associations (FA5; FA6). B) Representative photograph of the FA5, represented by a m-scale amalgamated sigmoidal clinoform, showing internally tangential cross-beds, defined as a lateral-accretion architectural. C) View of the fining-upward beds, ranging from 3 to 0.2m, grading from coarse-grained sandstones trough cross-beds (St), passing to the top to planar (Sp) and climbing ripple (Sr) sandstones. Outcrop HUA 470.

Interpretation - A combination of extensive multistory channel bodies with prominent lateral-accretion macroforms are interpreted as meandering deposits (Gibling,

2006; Bridge, 2003; Miall, 1985). The juxtaposition of multiple channel-bodies and lateral accretion sets evidences a concomitant channel and point-bar migration (Gibling, 2006). The W/T channel-body's dimensions, erosional surface bases and fining-upward filling in channel-bodies reinforce the interpretation of meandering rivers formed in lateral migration (Gibling, 2006; Miall, 1985; Friend et al., 1979). The wide paleocurrent range, from NW to NE suggests a distributive fluvial system generated by the migration of the channel and accretion surfaces.

We estimated paleodischarge in cumecs (m^3/s) based on the parameters of surface exposures of the paleochannels, as proposed by Foix et al. (2012). The parameter taken in account were, in meters: mean depth (d_m= 5); width (W= 35) and velocity (v=0.75 m/s). The palaeohydrological estimations obtained a mean paleodischarge (Q) for the paleochannels with a mean of 131 m^3/s.

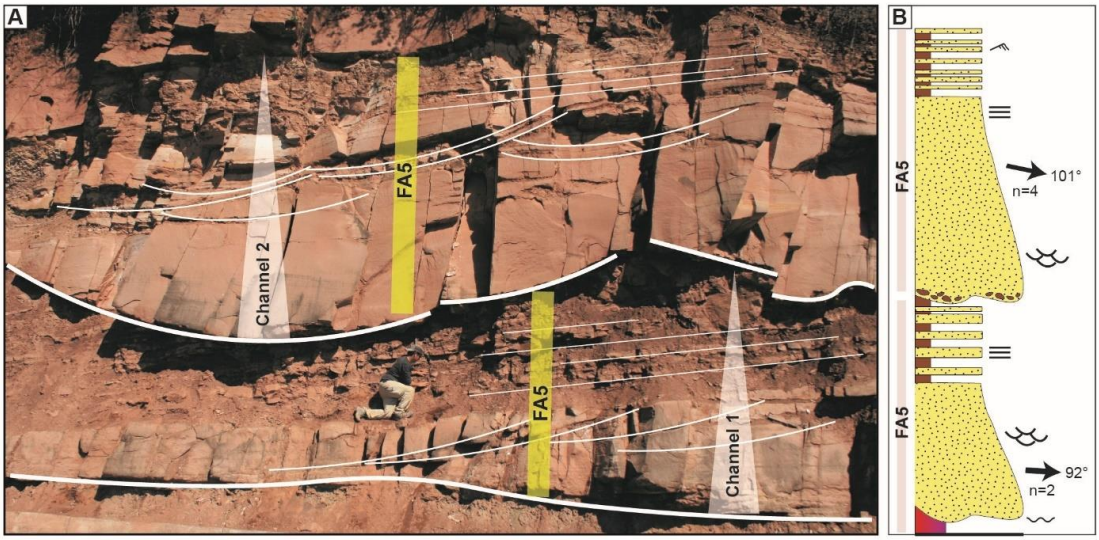


Figure 4. 6 A) General outcrop (JUA27) view along the road cutting, showing vertical fining upward beds and lateral variations of the sedimentary facies associated to archictetural channels. B) Sedimentary section with Facies Associations code (see Table 1 for details).

4.5.1.2 Facies association 6: Floodplain deposits

Description - This facies association consist of mainly fine deposits such as reddish to brown shales (Fm), paleosols (P) and, subordinately, siltstones (Fs), ripple cross-laminated sandstones (Sr) and massive sandstones (Sm) bioturbated, thus destroying internal laminae. The common features in shales (Fm) are plant rootles and desiccation cracks (Table 4.1). The paleosols (P) have reddish to purple color variations, mottled appearance, presence of scattered carbonate cements and nodules.

This Facies association 6 has been identified above the tide-dominated Facies association 4, which was described by Custódio et al. (2023); and also, in the upper part of the section (Figure 4.4). It generally starts with a metric accumulation of fine-grained deposits, such as, shales, siltstones and paleosols (meter-scale). Fossilized roots traces (Rhizoliths) and mud cracks are common on the top of the beds of the fine-grained deposits. The finer deposits are interrupted by thin layers of ripple cross-laminated sandstones and bioturbated sandstones. This facies has been observed above and as a lateral equivalent of the meandering channels (FA5).

Interpretation - The high occurrence and huge lateral extension of fine-grained deposits indicates deposition from suspension and are particularly important components of overbank flooding (Miall, 2006; Nanson and Croke, 1992). The recurrent presence of root traces and desiccation cracks suggest prolonged periods of subaerial exposure following suspension settling on subaqueous floodplains (Gulliford et al., 2017). Pedogenic carbonate nodules support an interpretation of moderate maturity paleosols (Nichols, 2009) and is a reliable indicator of seasonal precipitation (Tabor and Myers, 2015). The lateral and vertical correlation with Crevasse splay (FA7) and Fluvial Channels (FA5) indicates deposition in adjacent overbank successions and support the floodplain interpretation.

4.5.1.3 Facies association 7: Crevasse splay deposits

Description - The facies association 7 is mainly characterized by sandstones with distinct sedimentary structures, such as, scour-fill sandstones (Ss), horizontally-bedded sandstones (Sh) and climbing-ripple cross-laminated sandstones (Sr). Shales (Fm) and siltstones (Fs) interbedded with the sandstones deposits can occur (Figure 4.4; Table 4.1). The very-fine to fine-grained sandstones beds < 2 m thick, presenting finning-upward sequences, commonly grades from sandstone with horizontal lamination (Sh) to ripple cross-laminated sandstones (Sr), with this last facies being the most abundant (Figure 4.4). The sandstones are sheet-sandstones bodies, laterally extending over of 30 meters, with sharp tops and erosive basal contacts, which are interbedded in the top by cm-dm thick shales (Fm) and siltstones (Fs) beds. The paleocurrents data measured in the ripple cross-laminated sandstones (Sr) provides mean paleodirection towards the NE (Figure 4.4). The facies association 7 is thicker in the middle to upper part of the section (1085 – 1130m).

Interpretation - The sheet sandstones bodies, reaching 1-2 meters thick, dominated by Ss, Sh and Sr sedimentary facies are architectural elements interpreted as results of rapid deposition from unconfined flow across the alluvial plain, and therefore as crevasse splays deposits (Gulliford et al., 2017; Miall, 1985). The vertical sequence displaying fining-upward, topped by a transition from Sh to Sr, indicate a gradual abandonment caused by waning flow conditions, passing from upper flow regime to lower flow regime (Miall, 1985). The gradual decrease in flow velocity are feature characteristic of shallower water levels and can boost the deposition of fine-grained sediments, which is observed by the Fm and Fs facies. The coarse-grained scour-fills sandstones (Ss) are interpreted as indicative of deposition under upper flow regime (Fielding, 2006), in high-energy unconfined flow conditions, at the initial stages of flood event.

4.5.2 Major and trace element concentrations and Sm-Nd isotopes

Bulk chemical concentrations of major (wt%), trace (ppm) and rare earth elements (ppm) concentrations of analyzed samples were normalized to the Post Archean Australian Shales (PAAS) concentration (Taylor and McLennan, 1985; McLennan, 2001; Pourmand et al., 2012) and are reported in Table 4.2. Most of the analyzed samples are all depleted in SiO_2, Al_2O_3, K_2O, TiO_2, Rb, Cs, Th, Y, Cr, V, Co and Ni against PAAS (Table 4.2, Figure 4.7, Supplementary Data S3) with the exceptions of one late Cretaceous sample (JUA1) and late Oligocene (HG1), which are enriched in MnO with respect to PAAS (Table 4.2, Figure 4.7, Supplementary Data S4). The late Cretaceous samples (JUA1 and JUA5) are characterized by a strong depletion in Na_2O and Ba when compared with younger analyzed samples (Table 4.2, Figure 4.7, Supplementary Data S3).

Table 4. 2 Major and trace element concentrations of sedimentary rocks analyzed in Huallaga Basin, Peru.

Sample	JUA 1	JUA 5	JUA 6	JUA 15	JUA 16	JUA 22	HG 2	JUA 24	HG 1	JUA 28	JUA 29	JUA 31
Age	Upper Cretaceous			Eocene	Early Oligocene		Late Oligocene			Early Miocene		
	Maastrichtian			Bartonian	Rupelian		Chattian					
wt%												
SiO2	27.36	42.59	55.37	57.88	54.21	49.98	50.27	49.08	49.81	56.69	57.95	57.57
Al2O3	8.43	12.57	10.38	10.51	11.89	15.56	15.50	12.12	12.41	15.86	14.77	9.19
Fe2O3	3.59	3.52	3.69	4.67	4.61	7.20	4.80	4.65	4.92	6.17	6.79	2.72
MnO	0.13	0.039	0.053	0.065	0.063	0.045	0.055	0.068	0.120	0.033	0.038	0.082
MgO	1.75	1.98	1.32	1.15	2.40	2.74	2.65	1.58	2.13	2.79	2.54	1.21
CaO	27.72	15.37	11.40	9.39	9.06	5.88	7.98	11.85	10.15	2.49	3.07	11.66
Na2O	0.10	0.13	0.57	0.98	1.56	0.49	0.66	0.45	0.68	1.35	1.30	0.41
K2O	1.92	2.11	1.12	1.44	1.86	3.67	2.86	1.92	2.52	3.19	3.17	1.30
TiO2	0.36	0.57	0.67	0.67	0.58	0.69	0.76	0.64	0.65	0.81	0.73	0.45
P2O5	0.12	0.19	0.16	0.21	0.16	0.19	0.21	0.20	0.20	0.21	0.25	0.16
LOI	28.41	20.36	14.51	13.35	12.75	13.01	14.69	16.51	15.88	9.59	8.77	15.22
Total	99.89	99.43	99.24	100.32	99.14	99.45	100.44	99.04	99.46	99.19	99.37	99.96
Al/Si	0.35	0.33	0.21	0.21	0.25	0.35	0.35	0.28	0.28	0.32	0.29	0.18
CIA	80	84	82	76	49	61	57	46	48	69	66	41
ppm												
Sc	8.17	12.62	9.62	10.07	9.97	15.17	15.50	12.21	11.87	15.69	13.97	8.49
Rb	79.8	85.2	47.3	55.8	65.0	148.0	115.0	84.6	101.0	122.0	118.0	66.2
Cs	3.82	5.04	2.70	2.94	4.13	10.60	9.00	8.47	7.95	8.57	8.31	5.94
Ba	473	531	316	250	399	482	271	235	346	348	332	421
Sr	401	261	443	180	312	198	242	170	296	644	175	185
Th	5.48	8.86	7.79	6.65	6.70	11.70	12.00	9.85	10.30	12.00	10.20	7.81
U	1.19	2.26	2.58	2.03	1.81	2.55	5.66	2.37	3.37	2.92	2.51	2.72
Y	11.5	17.7	23.2	20.3	19.0	26.0	27.8	25.1	24.2	29.4	28.1	23.4
Zr	72.5	112.0	200.0	255.0	170.0	142.0	152.0	183.0	177.0	252.0	198.0	184.0
Nb	5.64	9.27	11.20	11.70	8.34	12.20	13.70	10.90	12.10	13.30	11.60	7.76
Hf	2.04	3.08	5.20	6.44	4.49	3.92	4.20	4.81	4.84	6.63	5.28	4.85
Cr	24.2	43.8	37.3	34.6	37.8	57.9	60.0	41.7	48.5	60.2	53.0	31.0
V	76.3	121.0	81.9	66.3	73.0	108.0	110.0	117.0	81.0	116.0	106.0	91.3
Co	5.1	10.1	8.1	12.5	10.8	12.1	17.5	11.0	14.9	14.4	12.0	19.4
Cu	14.3	28.5	41.8	9.7	29	21.5	47.1	15.9	153.0	58.8	41.9	24.4
Ni	12.2	24.1	17.5	11.8	17	28.2	45.4	21.3	24.3	29.5	24.7	16.7
Zn	45.1	56.9	64.2	68.7	78	113.0	97.5	93.0	94.5	113.0	109.0	70.1
La	15.2	27.2	23.7	23.8	21	35.1	36.2	29.2	29.3	35.6	31.9	25.1
Ce	29.7	54.3	47.2	45.6	42	70.7	72.1	58.7	58.9	70.1	65.6	53.9
Pr	3.52	6.37	5.66	5.40	5.14	8.45	8.60	7.05	7.07	8.35	7.99	6.37
Nd	13.1	24.0	21.8	20.8	20	32.4	32.5	27.1	26.7	32.0	31.4	24.9
Sm	2.62	4.61	4.51	4.19	4.16	6.44	6.42	5.42	5.38	6.40	6.40	5.23
Eu	0.55	0.96	1.03	1.08	0.989	1.37	1.34	1.13	1.14	1.39	1.44	1.16
Gd	2.22	3.55	3.99	3.64	3.53	5.29	5.35	4.57	4.59	5.41	5.47	4.51
Tb	0.34	0.54	0.65	0.58	0.557	0.81	0.832	0.721	0.716	0.855	0.85	0.688
Dy	2.07	3.31	4.06	3.60	3.44	4.79	4.96	4.41	4.32	5.22	5.10	4.11
Ho	0.43	0.7	0.86	0.77	0.716	1.00	1.03	0.92	0.905	1.10	1.04	0.842
Er	1.2	1.9	2.350	2.12	1.95	2.69	2.79	2.55	2.45	3.06	2.78	2.24
Tm	0.18	0.3	0.37	0.33	0.299	0.407	0.417	0.39	0.369	0.472	0.424	0.339
Yb	1.18	1.9	2.410	2.19	1.95	2.62	2.17	2.56	2.46	3.08	2.74	2.16
Lu	0.19	0.29	0.37	0.34	0.301	0.401	0.411	0.387	0.375	0.474	0.417	0.332
Ta	0.51	0.84	0.95	1.02	0.75	1.12	1.26	0.99	1.10	1.21	1.06	0.73
Sm/Nd	0.20	0.19	0.21	0.20	0.21	0.20	0.20	0.20	0.20	0.20	0.20	0.21
Eu/Eu*	0.70	0.72	0.74	0.85	0.79	0.72	0.70	0.69	0.70	0.72	0.74	0.73
ΩCe	0.98	0.99	0.98	0.97	0.970	0.99	0.98	0.99	0.99	0.98	0.99	1.03
Cr/Th	4.42	4.94	4.79	5.20	5.64	4.95	5.00	4.23	4.71	5.02	5.20	3.97
Th/Sc	0.67	0.70	0.81	0.66	0.67	0.77	0.77	0.81	0.87	0.76	0.73	0.92
Zr/Sc	8.87	8.87	20.79	25.32	17.050	9.36	9.81	14.99	14.91	16.06	14.17	21.67
LREE	1.04	1.88	1.67	1.62	1.516	2.488	2.53	2.076	2.07	2.479	2.344	1.86
HREE	1.22	1.97	2.45	2.23	1.996	2.686	2.76	2.597	2.49	3.149	2.800	2.23
MREE	1.14	1.81	2.15	1.93	1.856	2.685	2.75	2.394	2.37	2.836	2.818	2.29
MREE*	1.13	1.92	2.06	1.93	1.756	2.587	2.65	2.336	2.28	2.814	2.572	2.04

The calculated CIA values range from 41 to 84 (Table 4.2), showing an apparent trend of higher CIA values recorded in the older sedimentary rocks (late Cretaceous) (80 – 84), in which the lower CIA values are observed in the younger late Eocene to Miocene sedimentary rocks (41 – 69), with exception of JUA15 sample (76), that have CIA higher those of the PAAS (67, Taylor and McLennan, 1985). This trend is best observed along the Juanjuí stratigraphic section (Figure 4.4), where CIA values slightly decrease from the late Cretaceous (base) to the late Oligocene (Chattian). The Al/Si ratio ranges from 0.18 to 0.35 (Table 4.2), where the maximum values (0.35) are observed for the late Cretaceous (JUA1) and Oligocene (JUA22 and HG2) samples (Table 4.2). Whereas, the lowest value (0.18) is related to the middle Miocene (JUA31) sample (Table 4.2).

The Th/Sc ratios is a proxy of the composition of the source, while the Zr/Sc ratios may indicate zircon enrichments due to sedimentary recycling (McLennan et al., 1993). The Th/Sc ratios are relatively high and range from 0.66 to 1.0 (Table 4.2; Figure 4.4). The Zr/ Sc ratios range between 8.87 and 25.32 (Table 4.2; Figure 4.4). The analyzed samples have Cr/Th ratios relatively lower than PAAS standard (i.e., Cr/Th = 7.53), with a range from 3.97 to 6.0 (Table 4.2).

The samples have flat REE patterns and a positive Eu anomaly when normalized against PAAS (Figure 4.7). Overall, the samples show slight enrichment in Heavy REE (HREE) (Table 4.2; Figure 4.7). The late Cretaceous sample is less concentrated in REE than the other youngest samples. The Eu/Eu* ratios of the analyzed samples range between 0.70 and 0.85 and are higher than that of the PAAS standard (i.e., Eu/Eu* = 0.58) (Table 4.2; Figure 4.7).

The analyzed samples display no Ce anomalies with ΩCe values, ranging from 0.97 to 0.99, close to that of the PAAS (i.e., ΩCe = 1) (Figure 4.7). The Sm-Nd isotopic compositions of the late Cretaceous - Miocene sedimentary rocks of the Huallaga Basin are shown in Table 4.3. The εNd(0) values of the late Cretaceous samples range from -7.2 to -5.3. The εNd(0) values of the Cenozoic samples are between from -3.6 to -9.3. A strong decrease in εNd is observed between the Bartonian (Eocene) JUA15 sample (-3.6) to the Rupelian JUA16 (-7.1) (Figure 4.4; Table 4.3).

Table 4. 3 Sm-Nd isotopic compositions of sedimentary rocks analyzed in this study.

Age	Sample	Sm (ppm)	Nd (ppm)	Sm/Nd	$^{147}Sm/^{144}Nd$	fSm/Nd	$^{143}Nd/^{144}Nd$	± 2SE	εNd(0)	TDM (Ga)
Miocene	**JUA31**	5.5	25.7	0.21	0.128877	-0.345801	0.512211	13	-8.3	1.48
	JUA29	7.3	36.5	0.20	0.120356	-0.389057	0.512196	18	-8.6	1.37
	JUA28	8.1	41.3	0.20	0.119253	-0.394654	0.512183	11	-8.9	1.38
Oligocene (Rupelian - Chattian)	**JUA24**	6.4	32.2	0.20	0.120308	-0.389300	0.512163	11	-9.3	1.42
	HG2	7.2	37.6	0.19	0.116106	-0.410629	0.512172	19	-9.1	1.35
	JUA22	6.9	35.4	0.20	0.117915	-0.401444	0.512201	18	-8.5	1.33
	JUA16	4.6	22.9	0.20	0.121328	-0.384121	0.512274	18	-7.1	1.26
Eocene (Bartonian)	**JUA15**	4.4	22.3	0.20	0.119383	-0.393993	0.512455	19	-3.6	0.95
Late Cretaceous (Maastrichtian)	**JUA6**	4.6	22.9	0.20	0.120785	-0.386878	0.512365	65	-5.3	1.11
	JUA5	5.0	26.5	0.19	0.113131	-0.425729	0.512228	11	-8.0	1.23
	JUA1	2.9	15.1	0.19	0.116495	-0.408657	0.512267	12	-7.2	1.21

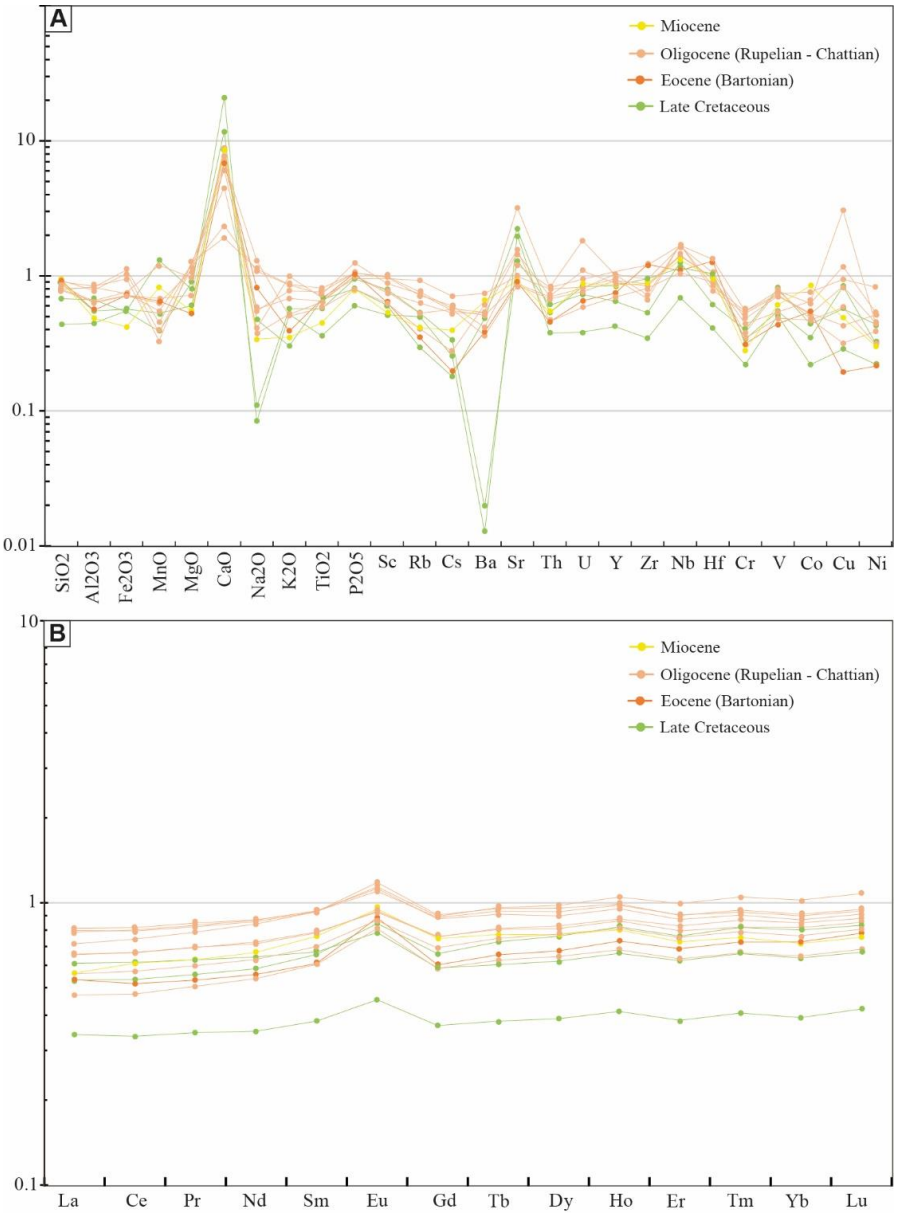


Figure 4. 7 Geochemical data. A) Major and selected trace element contents of analyzed samples normalized to PAAS (Taylor and McLennan, 1985; McLennan, 2001; Pourmand et al., 2012). From left to right on the diagram, these include the major elements (SiO_2, TiO_2, Al_2O_3, Fe_2O_3, MnO, MgO, CaO, Na_2O, K_2O and P_2O_5), LILE (Rb, Cs, Ba, Sr, Th and U), HFSE (Y, Zr, Nb, Hf), and TTE (Sc, Cr, Co, V and Ni). B) Rare Earth Element (REE) contents of studied samples normalized to PAAS (Taylor and McLennan, 1985; McLennan, 2001; Pourmand et al., 2012).

4.5.3 U-Pb ages

The distribution of U-Pb zircon ages and percentage of U-Pb ages of zircons grains by distinct geochronological events for the analyzed sedimentary rocks are shown in Table 4.3. Details on individual U-Pb zircon ages for each sample can be found in supplementary data (Supplementary Data S2).

The calculated 'maximum likehood age' (MLA) and 'maximum depositional age' (MDA), yield ages from Upper Cretaceous – Neogene (Figure 4.4). The MDAs of the analyzed samples show Maastrichtian (JUA1, 66.2 ± 0.56 Ma), and for the Lutetian – Bartonian samples, previously published by Custódio et al. (2023), yields ages from ~43.1 ± 0.29 Ma (Lutetian, JUA 8A/19), to ~ 42.6 ± 0.32 Ma (Lutetian, JUA 11) and ~38.6 ± 0.19 Ma (Bartonian, JUA 14). For the Oligocene to Recent, the MDAs exhibit ages from 30.0 ± 0.55 Ma (Rupelian, JUA22) to Chattian (HG2, 26.0 ± 0.66 Ma), (JUA24, 24.1 ± 0.39 Ma), (HG1, 23.2 ± 0.52 Ma). The Miocene deposits was represented by JUA31 that yields MDAs ages of 17.4 ± 0.25 Ma. Despite the obtained MDA ages for JUA26 showed 17.4 ± 0.25 Ma, the biostratigraphy age published by Stutz et al. (2022) attested ~13 Ma, a late middle Miocene age.

The MLAs of the analyzed samples show similar Maastrichtian (JUA1, 65.05 ± 2.39 Ma), to 43.5 ± 0.64 Ma (Lutetian, JUA8A/19), to 42.68 ± 0.66 Ma (Lutetian, JUA11), to 37.64 ± 0.19 Ma (Bartonian, JUA14), to 30.12 ± 1.39 Ma (Rupelian, JUA16), to 29.70 ± 0.62 Ma (Rupelian, JUA22), and reaching 23.44 ± 0.64 Ma (Chattian, JUA24) in the upper part of the section (Figure 4.4, Table 4.4; 4.6, Supplementary Data S2). These MLA ages are younger or equivalent to the expected stratigraphic age. The samples HG2 and HG1 have MLA of Chattian age (late Oligocene) (25.16 ± 1.22 Ma for HG2 and, 23.04 ± 0.83 Ma for HG1) (Table 4.4; 4.6; Supplementary Data S2). The Miocene samples (JUA26 and JUA31) (Supplementary Data S2) have MLA ages older than the expected stratigraphic age. The MLA age for JUA26 is 41.09 ± 1.01 Ma which is much older than the Miocene stratigraphic age of the Ipururo Formation (Hermoza et al., 2002; Roddaz et al., 2010). The calculated MLA age of JUA31 is 17.62 ± 0.82 Ma which is ~5 Ma older than the stratigraphic age obtained in TAR31, ~13 Ma (Late middle Miocene, Stutz et al. (2022)).

Sample	Age (Ma)	± 2σ	n
JUA30	Present day		126
JUA26	41.09	1.01	133
JUA25 (?)	209.7	10.6	138
HG1	23.04	0.83	100
JUA24	23.44	0.64	139
HG2	25.16	1.22	180
JUA22	29.70	0.62	124
JUA14	37.64	0.85	112
JUA11	42.68	0.66	102
JUA8A/19	43.50	0.64	69
JUA 1	65.05	2.39	102

Table 4. 4 Calculated ages of the samples using the 'Maximum Likelihood Age' (MLAs) method, following Vermeesch (2021).

Following Hurtado et al. (2018), potential sources of the detrital samples may comprise the Precambrian rocks of the Western Amazon Craton, the Neoproterozoic rocks of the Neoproterozoic mobile belts and Andean rocks including Famatinian and Paleozoic magmatic rocks, Permian volcanic rocks (Mitu) and Meso-Cenozoic volcanic rocks of the Andean Arc (Hollister and Sirvas, 1978; Cordani et al., 1999; Chew et al., 2008; Bahlburg et al., 2009).

The late Cretaceous (Maastrichtian) sample ~65.05 ± 2.39 Ma (JUA1) contain predominantly zircon ages of the Cretaceous Andean Arc (Western Cordillera), Brazilian and Greenville Sunsás age. The main peak ages of this sample occur at (0.065 – 0.145 Ga) (22%), 0.7-0.5 Ga (12 %) and 1.3-0.9 Ga (27 %) (Table 4.6). The Early Late Eocene (Lutetian – Bartonian) samples ~43.5 – 37.64 ± 0.19 Ma (JUA8A/19; JUA11 e JUA14) are dominated by zircons from the Cenozoic Andean Arc, Grenville Sunsás and Brazilian age. The dominant zircon peak ages of these samples occur at <0.065 Ga (14 – 38%), 0.7-0.5 Ga (6 – 13%) and 1.3-0.9 Ga (25 – 33%) (Table 4.6). In contrast, the Rupelian (early Oligocene) to early Miocene (~30.12 – 17.62 Ma) samples (JUA16; JUA22; JUA24; HG2; HG1; JUA31) have a different zircon U-Pb age distribution with main zircon populations from the Paleozoic Magmatic Arc (0.4-0.26 Ga, 8 – 16%), Famatinian (0.5-0.4 Ga, 4 – 15%), Brazilian (0.7-0.5 Ga, 9 – 22%) and Grenville Sunsás (1.3-0.9 Ga, 17 – 35%). The younger late Miocene to the present-day samples (JUA25, JUA26, JUA30), exhibited a sharp contrast in zircon U-Pb age distribution with almost exclusive contributions of the Paleozoic Magmatic Arc (0.4-0.26 Ga, 29 – 65%) and Grenville Sunsás (1.3-0.9 Ga, 28 – 43%) (Table 4.6).

4.5.4 Sedimentation Rates based on MLA ages

Based on JUA8A/19, JUA11, JUA14, JUA16, JUA22 and JUA24 MLA ages, we have calculated the sedimentation rates for the Juanjui section (Table 4.5; Supplementary Data S2). These MLA ages may not represent true depositional age in the case of the Oligocene part of the section (JUA 16, JUA 22 and JUA 24 samples) because, unlike as for the older Eocene samples (see Custódio et al., 2023), we have no paleontological constraints. Hence, the sedimentation rates calculated may represent maximum sedimentation rates and not true sedimentation rates.

The calculated sedimentation rates of the Lutetian part of the Juanjuí section range between 79.4 and 18.5 (m/Ma) (Figure 4.4; Table 4.5). Overall, the sedimentation rates are lower in the Eocene when compared with the Oligocene. The lowest sedimentation rates are found between the Lutetian to Bartonian (18.5 m/Ma). The sedimentation rates increase during the Eocene – Oligocene transition (Bartonian – Rupelian) (50.1 m/Ma) to reach its highest rate during the early Oligocene (Rupelian) (99.4 m/Ma). The late Oligocene (Chattian) sedimentation rate decrease when compared to that of the early Oligocene (Rupelian) but it is still about three fold higher than those of the middle Eocene (Bartonian) with a calculated value at ~ 57.6 m/Ma.

Period	Epoch	Age	Age (Ma)		Sedimentation rates
			Start	End	m/Ma
Oligocene	early - late Oligocene	Rupelian - Chattian	29.7	23.4	57.6
	early Oligocene	Rupelian	30.1	29.7	99.4
E - O	Eocene / Oligocene	Bartonian - Rupelian	37.6	30.1	50.1
Eocene	middle Eocene	Lutetian - Bartonian	42.7	37.6	18.5
	middle Eocene	Lutetian	43.5	42.7	79.4

Table 4. 5 Calculated sedimentation rates for the Cenozoic sequence of Huallaga Basin, northern Peruvian retroforeland basin. Maximum sedimentation rates calculated from GENEX 1D basin modelling software. Maximum sedimentation rates are based on stratigraphic thickness, time as well as compaction.

Time (Ga)	Province / Event	CRETACEO	Maastrichtian	EOCENE	Lutetian		Bartonian	OLIGOCEN	Rupelian		Chattian			MIOCENE	Burdigalian		QUATERNA	Quaternary	
			JUA 1		JUA 8A-19	JUA 11	JUA 14		JUA 16	JUA 22	HG2	JUA 24	HG1		JUA 26	JUA 31		JUA 25	JUA 30
			65.05 ± 2.39		43.5 ± 0.64	42.68 ± 0.66	37.64 ± 0.85		30.12 ± 1.39	29.70 ± 0.62	25.16 ± 1.22	23.44 ± 0.64	23.04 ± 0.83		41.09 ± 1.01	17.62 ± 0.82		209.7 ± 10.6	Present
			n = 102/102		n = 69/77	n = 102/120	n = 102/112		n = 131/150	n = 124/150	n = 180/198	n = 139/150	n = 100/120		n = 135/150	n = 104/120		n = 138/150	n = 126/150
			(%)		(%)	(%)	(%)		(%)	(%)	(%)	(%)	(%)		(%)	(%)		(%)	(%)
< 0.065	Cenozoic Andean Arc		1		14	28	38		5	6	4	13	4		3	10		0	1
0.145 - 0.065	Cretaceous Andean Arc		22		4	0	2		10	6	2	2	1		7	1		1	2
0.25 - 0.145	Triassic-Jurassic		2		0	1	7		1	2	3	3	4		1	0		1	2
0.4 - 0.26	Paleozoic Magmatic Arc		3		6	3	3		8	13	16	9	1		34	13		65	29
0.5 - 0.4	Famatinian		4		3	4	2		9	15	8	4	8		2	4		0	2
0.7 - 0.5	Brazilian		12		12	13	6		21	21	9	13	22		6	11		0	6
0.9 - 0.7			9		6	1	2		5	5	4	4	7		1	3		0	6
1.3 - 0.9	Greenville Sunsás		27		29	33	25		17	20	34	30	33		36	35		28	43
1.54 - 1.3	Rondonia - San Ignacio		7		3	7	8		6	5	13	6	7		4	11		1	6
1.82 - 1.54	Rio Negro - Jurena		6		10	6	7		9	3	2	8	5		4	6		4	1
2.0 - 1.82	Ventuari - Tapajós		5		6	1	0		3	2	1	4	5		0	5		0	2
2.2 - 2.0	Maroni - Itacaiunas		1		6	2	0		5	2	2	2	2		1	2		0	0
> 2.2	Central Amazon		2		1	1	0		3	1	1	2	1		0	2		0	0

Table 4. 6 Table showing the number and porcentage U-Pb ages of zircons grains by distinct geochronological events in potential source areas on the Amazon craton and the northern central Andes. Temporal ranges of events according to Bahlburg et al. (2009), Chew et al. (2008).

4.6 DISCUSSION

4.6.1 Interpretation of sedimentary provenance

The REE concentrations, Eu anomalies, elemental ratios (Cr/Th and Th/Sc) and Sm-Nd isotopic compositions of fine-grained sedimentary rocks may be used as tools for determining the provenance of sedimentary rocks (McLennan et al., 1993), to the condition that they are not affected by weathering, syndepositional clay authigenesis and mineral sorting (e.g. (Bouchez et al., 2011; McLennan et al., 1993; Roddaz et al., 2014) among many others). For instance, high Eu anomalies and Th/Sc and low Cr/Th are characteristic of felsic and more highly differentiated source rocks, whereas high Cr/Th and low Eu anomalies and Th/Sc suggest more mafic and less differentiated source rocks (Cullers, 2000; McLennan et al., 1993). In general, these ratios as well as the REE concentrations are not significantly affected by diagenesis or weathering (Cullers, 2000; Fedo et al., 1995; McLennan, 1990; McLennan et al., 1993). The effect of mineral sorting and chemical weathering can be evaluated by comparing the Al/Si ratios, which can be considered as a proxy for the sediment grain-size (Bouchez et al., 2011). The absence of any correlation (see Table 2) Al/Si with REE content, Eu/Eu*, Cr/Th, Th/Sc and εNd(0) suggests that chemical weathering and sedimentary sorting has not modified these provenance proxies.

In addition, relatively flat REE patterns with respect to PAAS and Ce anomalies (ΩCe) close to 1 also suggest that authigenesis did not affect the REE contents (Figure 7 and Table 2). We ascribed the enrichment in CaO and Sr to the presence of carbonate minerals (Figure 7) which in turn suggests a moderate Chemical weathering effect.

The analyzed samples have positive Eu anomalies (0.69 to 0.85) that are higher than those of the PAAS (0.58) (Figure 7 and Table 2) and typical of “basic” sediments (i.e., sediments derived from a basic source *sensu* Cullers (2000)), with Eu/Eu* >0.70). However other provenance ratios such as the Th/Sc and Cr/Th ratios do not indicate a dominant contribution from a basic source. We interpret the positive Eu anomalies of the analyzed samples as reflecting the contribution of a source rich in plagioclase (McLennan et al., 1993), most likely the Andean Arc.

Available studies based Nd isotopic compositions have distinguished cratonic-derived fine-grained river sediments transported by Amazonian cratonic rivers from Andean-derived fine grained sediments transported by Amazonian Andean rivers based on their Nd isotopic compositions (Allègre et al., 1996; Viers et al., 2008; Bouchez et al.,

2011; Rousseau et al., 2019). At geological timescale, past cratonic derived sedimentary rocks have εNd(0) values between -14.5 and -21 and Andean derived sediments have εNd(0) values > -13.8 (Roddaz et al., 2005, 2021; Horbe et al., 2013). In Colombia, the εNd(0) cutoff value of -12.7 have been used to distinguish between Andean and Cratonic derived sedimentary rocks (Nie et al., 2012).

The εNd(0) values measured in this study indicate a typical Andean provenance for all analyzed samples (εNd(0) -9.3 to -3.6) (Table 3) . Similar εNd(0) values were also measured in the late Paleocene sedimentary rocks of the Madre de Dios Basin (εNd(0) -10.7 to -6.2) (Louterbach et al., 2017). An Andean provenance is also attested by the U-Pb ages distribution of the analyzed sedimentary rocks (Table 6; Figures 4, 8). Despite the fact that all the analyzed Cenozoic sedimentary rocks are sourced by the Andes, differences in U-Pb zircon age distributions may help to characterize the contribution of the different Andean domains (Western and Eastern Cordillera).

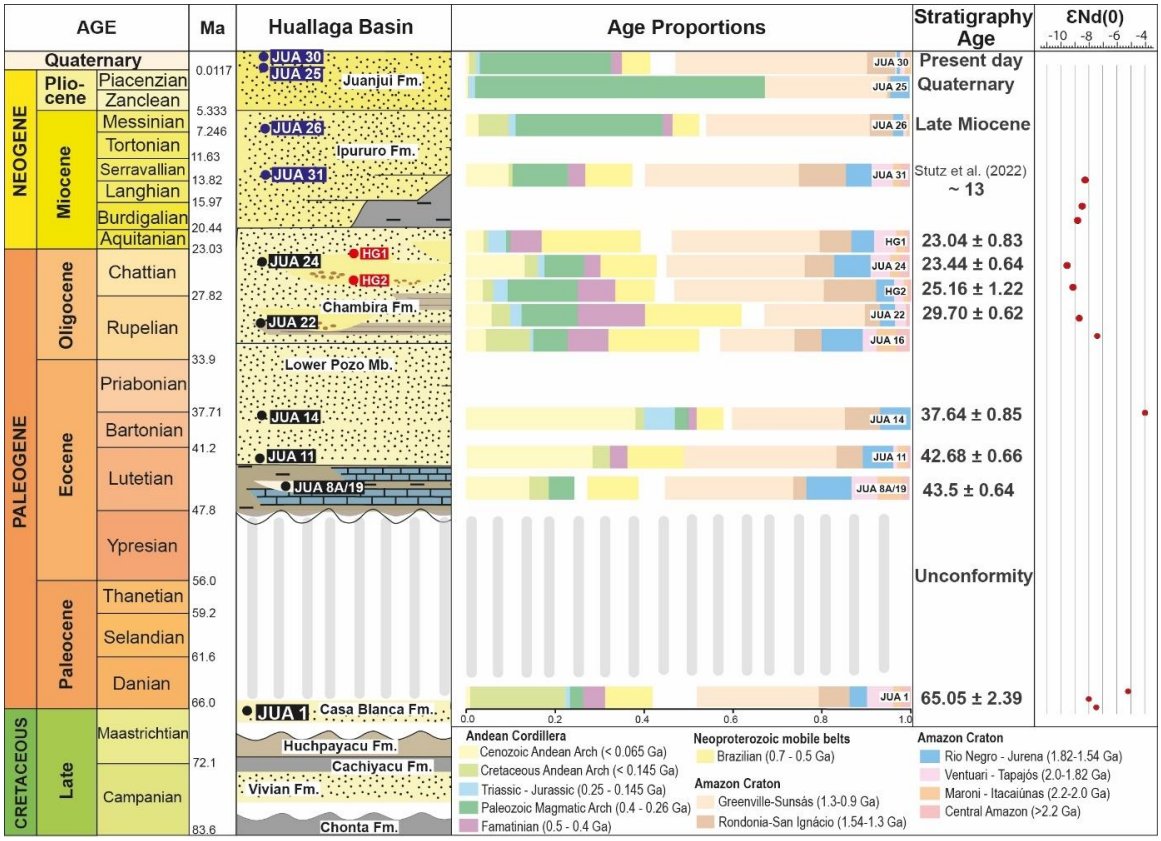


Figure 4. 8 Distribution of zircon U-Pb age proportions (bars) for the whole Cenozoic deposits of Huallaga Basin, Western Amazonia.

The late Cretaceous (Maastrichtian) sample (JUA1) is dominated by a contribution from the Cretaceous Andean Arc (< 0.145 Ga) (22%), Brazilian (0.7-0.5 Ga) (12%) and

Greenville Sunsas (1.3-0.9 Ga) (27%), with a predominant zircon population aged around 65.05 ± 2.39 Ma (Table 6; Figures 1, 4, 8). The Cretaceous zircon sources may comprise the Coastal Batholith (100-50 Ma) located in the Western Cordillera (Litty et al., 2017). While, the Eocene (Lutetian to Bartonian) samples (JUA8A/19; JUA11 and JUA14) are characterized by a strong contribution from the Cenozoic Andean Arc (Table 6; Figures 1, 4), with a dominant zircon population aged between ~37.6 – 43.5 Ma (14 – 38%). The sources for these Eocene zircons may include the magmatic arc intrusive rocks and related volcanic deposits of the Calipuy volcanic arc located in the Peruvian Western Cordillera (Navarro et al., 2010) or the Eocene Macuchi arc located in the Ecuadorian Western Cordillera (Chiaradia, 2009). Additionally, the fact that the calculated MLA ages may represent true depositional ages (Custódio et al., 2023) may indicate the presence of continuous volcanic eruption contemporaneous of the deposition of these sedimentary rocks suggest that the Eastern Cordillera was not a source for these Eocene rocks as the Eastern Cordillera can be mainly distinguished from other Andean terranes by the presence of Paleozoic and Famatinian rocks (see Chew et al., 2016; Hurtado et al., 2018 and references therein). Hence, we interpret these sedimentary rocks to be mainly source by the Western Cordillera.

The U-Pb age distribution of the Rupelian to middle Miocene sedimentary rocks of the Huallaga Basin (samples JUA16, JUA22, JUA24, JUA26, HG1 and HG2) indicate a change in sedimentary provenance. When compared with the older Eocene samples, the U-Pb age distributions of the Rupelian-middle Miocene samples are no more dominated by contributions of the Cenozoic volcanic Arc but by contributions of Paleozoic Magmatic Arc (400-260 Ma, 8-16%), Famatinian (500-400 Ma, 4-15%), Brazilian (700-500 Ma, 9-21%) zircons which we interpret to be sourced by the magmatic and metamorphic rocks of the Eastern Cordillera (Chew, et al., 2016). However, these samples have still partly sourced by the Western Cordillera because of the presence of zircons originated from the Cretaceous and Cenozoic Andean arcs (5-15%, Table 6). Finally, a change in provenance can also be seen for the three youngest late Miocene to present-day samples (JUA26, JUA25 and JUA30). The U-Pb zircon age distribution of these samples are characterized by a bimodal distribution composed of Paleozoic Magmatic Arc zircons (29-34%) and Grenville Sunsás (28-43%). Compared with older samples, the U-Pb zircon age distribution is marked by an increase in Paleozoic Magmatic Arc zircons and a strong decrease in contribution of zircons originated from the Cretaceous and Cenozoic Andean arcs. As the

present-day sands of the Huallaga River (JUA30) are mainly sourced by the Eastern Cordillera and the subandean zone (Fig. 2), and given that the U-Pb zircon age distributions of JUA25 and JUA26 are quite similar, we interpret that the three youngest late Miocene to present-day samples have similar provenance being sourced by the Eastern Cordillera and the Subandean zone.

The MDS map generated by using the KS statistic for the dataset from Late Cretaceous – Cenozoic samples of Huallaga Basin allows to infer that samples come from the four distinct underlying distribution (Figure 9). The Cretaceous nucleus might reveal a cratonic source dominance with a Cretaceous Andean Arc (Western Cordillera contribution). The Eocene samples keeps similarity with Cretaceous samples, however due to the higher zircon age population coming from the Cenozoic Andean Arc, it exhibits a distinct contribution. The third is represented by Oligocene samples, that seems to keep similarity with Eocene samples, however with a different pattern, possibly characterizing a different source represented by Eastern Cordillera detritus. The fourth is the most dissimilar field, where it could be related to the highest peaks of Eastern Cordillera detritus, where the WC becomes inexpressive.

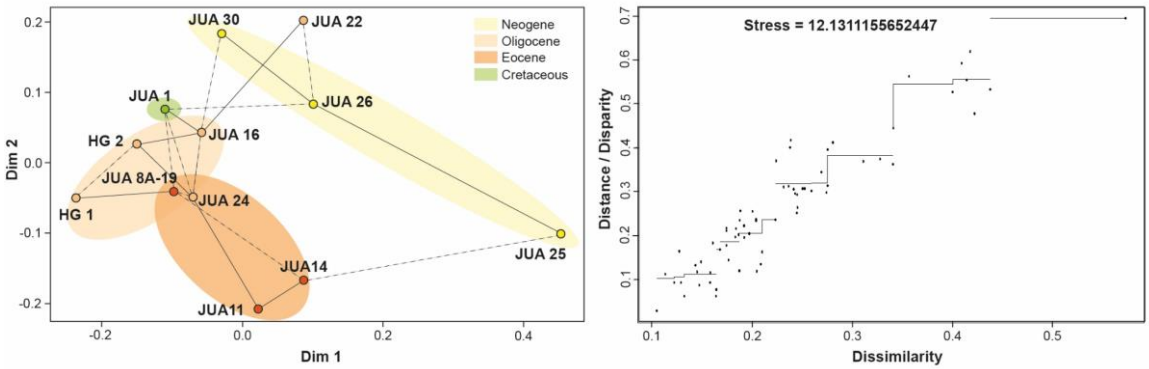


Figure 4. 9 Non-matrix metric multi-dimensional scaling (MDS) plot (Vermeesch, 2013) of detrital zircon ages from Cretaceous to Recent deposits in the studied area. The four groups indicate samples with similar detrital zircon age populations (see discussion in the text). The solid line connecting samples indicate the closest neighbors.

4.6.2 Erosional history of the Amazonian Andes during the late Cretaceous – Cenozoic

4.6.2.1 Maastrichtian Andean mountain building

During the Cenomanian-early Maastrichtian, the Huallaga Basin together with other Peruvian and Ecuadorian western Amazonian basins were sourced by a continent-

wide cratonic drainage developed probably in response to the uplift of the Purus Arch driven by a geodynamic process related to the post-rift opening of the Atlantic Equatorial Ocean (Rodrigues et al., 2023). Depending on the location of the basin, the shift from this continent-wide cratonic to an Andean dominated paleodrainage may occurred between the Campanian for basins now located in the Andes (e.g. Moreno et al., 2020) and the Maastrichtian (Louterbach et al., 2017; Hurtado et al., 2018). Our dataset suggests that the Maastrichtian sedimentary rocks of the Amazonian retroarc foreland basin were sourced by the Andean Western Cordillera (Figure 4.8). Previous published studies find similar Andean provenance for the late Cretaceous sedimentary rocks of the Ecuadorian (Vallejo et al., 2021) and Peruvian Bagua (Hurtado et al., 2018), Santiago (George et al., 2019), Huallaga (Hurtado et al., 2018), Madre de Dios (Louterbach et al., 2017) which were interpreted to have been deposited in the Andean-Amazonian retroarc foreland basins and represent a late Cretaceous period of Andean building (Ramos, 1999; Martin-Gombojav and Winkler 2008; Roddaz et al., 2010; Somoza and Ghidella, 2012; Horton, 2018; Hurtado et al., 2018; Louterbach et al., 2017; Rodrigues et al., 2023; Moreno et al., 2020). Hence, we suggest that the Huallaga Basin was part of the distal foredeep depozone of the Amazonian retroarc foreland basin during the Maastrichtian.

4.6.2.2 Paleocene-to-late Eocene: tectonic quiescence and erosion of the Western Cordillera

A major stratigraphic hiatus marked the Paleocene-to-early Eocene interval in Huallaga Basin. The Maastrichtian tide-dominated strata were unconformably overlain by Danian to Ypresian paleosols which represent a ~25 Ma sedimentary hiatus (Figure 4.3, 4.4, 4.8, 4.10) (Custódio et al., 2023). The interpretation we made is that the foreland flexural subsidence was possibly interrupted due to a long-period of tectonic quiescence, developing a regional unconformity across the retroarc foreland basins (Horton, 2018, 2022). This possible pause in Andean shortening could induce the erosion or bypass in the proximal foreland basin (Heller et al., 1988), which is in accordance with the unconformity observed during the Paleocene at Huallaga Basin (Custódio et al., 2023; Hermoza et al., 2005).

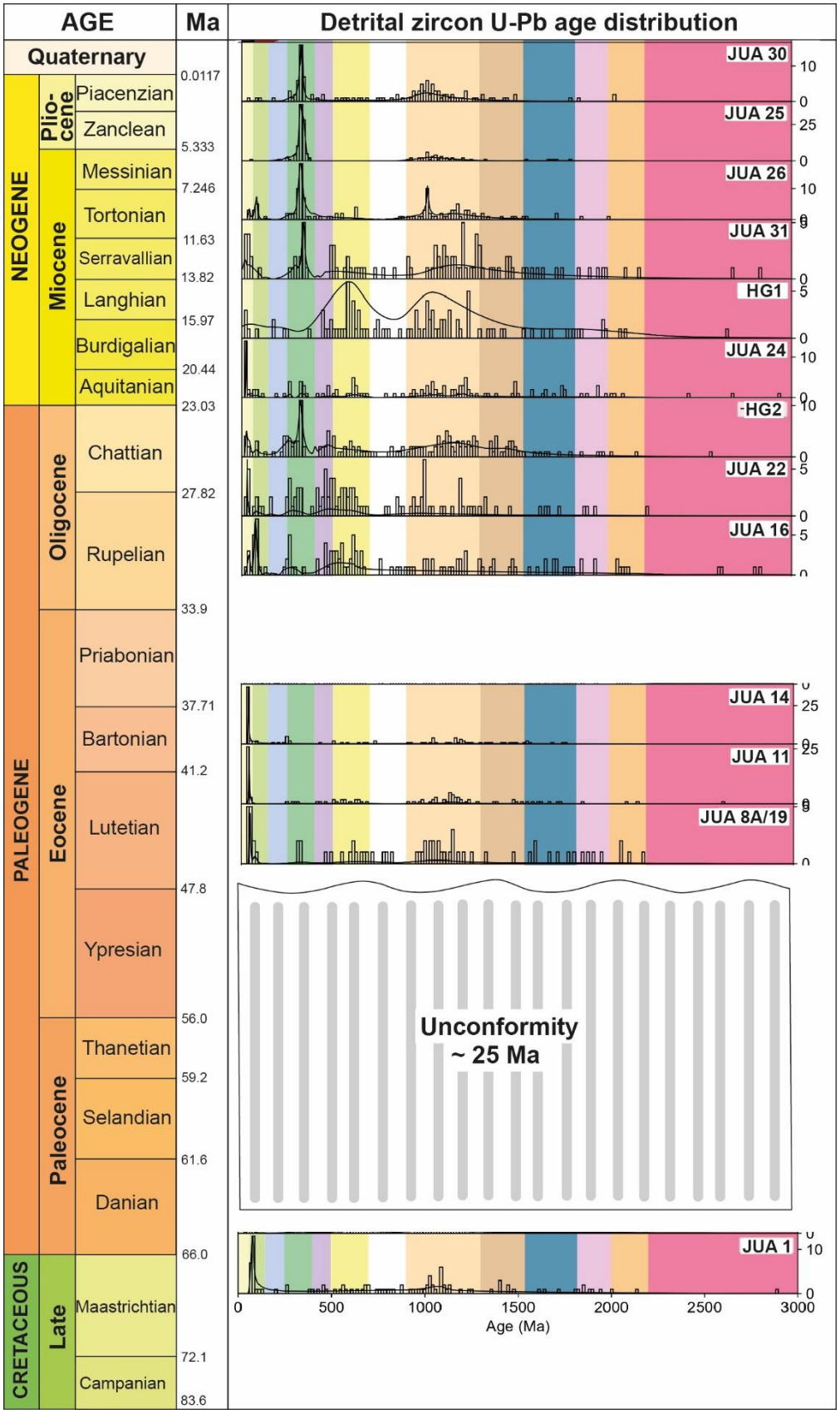


Figure 4. 10 Detrital-zircon age spectra of the late Cretaceous – Cenozoic samples from the Huallaga Basin.

Despite the ~25 Ma long sedimentary hiatus observed between the Paleocene and early Eocene (Custódio et al., 2023), no relevant source shift was observed between the Maastrichtian and the middle-late Eocene (Lutetian-Bartonian) sedimentary rocks. Indeed, the U-Pb age distributions of the four sedimentary rocks are dominated by young zircons from the Cretaceous-Eocene Andean magmatic Arc (Figures 4.4, 4.8, 4.10; Table 4.5). The Eocene zircons could be sourced by the Callipuy volcanic arc or the Macuchi volcanic arc, both located in the Western Cordillera (Pfiffner and Gonzalez, 2013; Navarro et al., 2010; Chiaradia, 2009). The Callipuy arc is composed of volcanoclastic and intrusive rocks (Pfiffner and Gonzalez, 2013), dated from ~45 to 16 Ma (Navarro et al., 2010). The Macuchi arc consists of early to late Eocene (~42-36 Ma) basaltic to andesitic pillow lavas (Chiaradia, 2009). With our dataset, we are unable to differentiate between zircons from the Callipuy or the Macuchi magmatic arcs and hence the Eocene zircons could be sourced by one of these arcs or a combination of these. In any case, the strong record of Eocene zircons grains from the Andean magmatic arcs of the Western Cordillera suggest that it acted as the dominant source area during the middle-late Eocene and that the Eastern Cordillera was not exposed and eroded at that time or was not high enough to act as a topographic barrier. This finding fits with the paleoelevation reconstruction of the central Andean plateau which indicated that the WC could be higher than EC during Eocene times (Boschman, 2021), with maximum paleoelevations reaching around 4000 m. (Poblete et al., 2021). It is also in agreement with thermochronological data that may indicate that the onset of growth of the Western-Central Cordillera system started in the middle Eocene (Villagómez and Spikings, 2013). In addition, an Andean deformation is mentioned during the Paleogene in the Huallaga-Marañon retroarc foreland basin system that was responsible for ~3 km of horizontal shortening (Figure 4.11) (Calves et al., 2018; Baby et al., 2018). The deformation and uplift of the WC could be related to a modification in convergence rate between the Farallon and South America tectonic plates (Jaillard and Soler, 1996). As pointed by Hermoza et al. (2005) and Roddaz et al., 2010, the middle Eocene sedimentary rocks of the Huallaga Basin were deposited in the distal foredeep depozone of the Amazonian retroarc foreland basin that extended from Bolivia to Colombia.

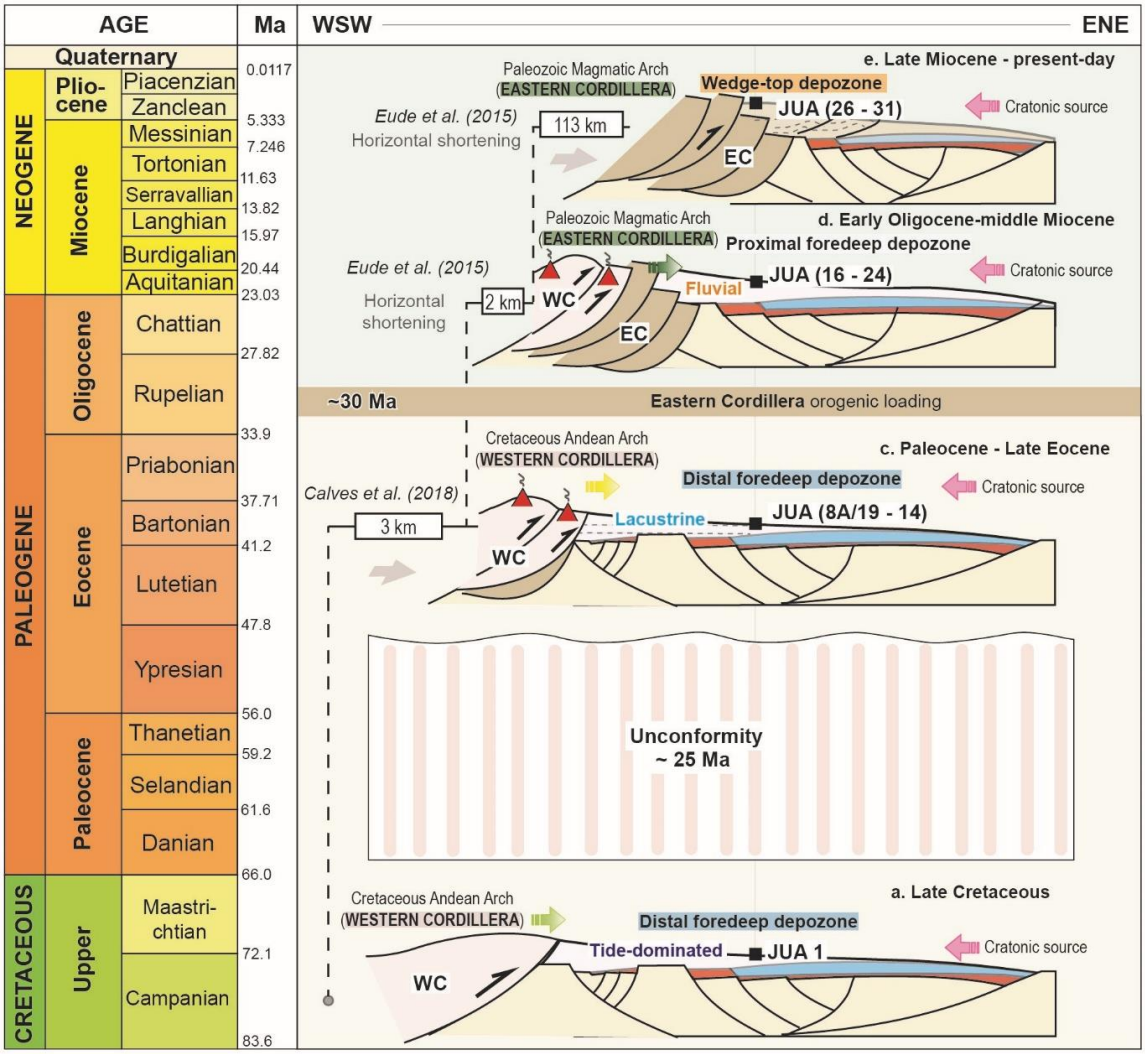


Figure 4. 11 Cross section of Huallaga Basin based on Calves et al., 2018 ; Eude et al., 2015 ; Hermoza et al., 2005. The cross-sections exhibits the Cretaceous – Cenozoic stages of tectonic loadings related to the eastward propagation of the orogenic wedge ; unconformity event ; basin morphology ; paleoenvironmental and paleogeographic changes due to the shifts in provenance areas.

4.6.2.3 Early Oligocene (Rupelian)-Middle Miocene: uplift and erosion of the Eastern Cordillera

An increase in Paleozoic (0.4 – 0.26 Ga) and Famatinian (0.5 – 0.4 Ga) zircon grains and a decrease of Cenozoic Andean magmatic Arc (< 0.0065 Ga) characterized the Oligocene (Rupelian to Chattian) to middle Miocene sedimentary rocks of Huallaga Basin (JUA16, JUA 22, JUA24, HG2, HG1 and JUA 31). We interpret these as indicating a change in the source area from a WC dominated source during the Eocene to a dominant EC source in the Oligocene. This shift in provenance area can be estimated to be Rupelian

in age based on the MLA Age of JUA22 (29.70 ± 0.62 Ma) (Figure 4.4, 4.8; Table 4.5). We interpret the increase of Paleozoic and Famatinian zircons in the Oligocene (~30 Ma) sedimentary record as recording the erosion of the EC because the Peruvian EC is Paleozoic in age and it mainly consists of an Ordovician magmatic and metamorphic event and Carboniferous arc magmatism (Chew et al., 2016; Cardona et al., 2009). A shift was also observed in the ƐNd(0) values, that are more negative in the Oligocene (-7.1 to -9.3) and Miocene (-8.3 to -8.9) times when compared with that of the Eocene (-3.6) (Table 4.3, Figure 4.4). We interpret this shift as reflecting contribution of the basement of the EC because the Eastern Peruvian Andes have ƐNd(0) values between -6.3 and -13.2 (Cardona et al., 2009). The change in provenance is also accompanied by changes of sediment geochemical compositions and depositional environments, from tide-dominated depositional system in the Bartonian Pozo Fm (Custódio et al., 2023) to a meandering fluvial system in the Chambira Fm. (Figures 4.4 and 4.11, Tables 4.1 and 4.2). This latter paleoenvironmental change coincides with the increase in sedimentation rates (50.1 to 99.4 m/Ma) (Table 4.4; Figure 4.4). We interpret these as indicating that the Huallaga Basin was part of the proximal foredeep depozone during the Oligocene-middle Miocene.

The onset of EC erosion at ~30 Ma recorded in the sedimentary record of the Huallaga Basin is in agreement with the results of the sequential restoration of Eude et al. (2015) that proposed that the onset of eastward propagation of the Eastern Cordillera occurred between 30 and 24 Ma based on the combined use of low temperature thermochronology and balanced cross section. However, some authors have suggested that the protracted exhumation of the Eastern Cordillera of Bolivia and southern Peru has been ongoing since 40–45 Ma (Benjamin et al., 1987; Farrar et al., 1988; Barnes et al., 2006; Gillis et al., 2006; Perez et al., 2016) or 50-55 Ma (Rak et al., 2017) and is likely linked to continued shortening. These may suggest that the onset of erosion and exhumation of the EC might be diachronous along strike, starting earlier in Bolivia and Southern Peru. During the Oligocene, the eastward migration of retroarc fold-thrust belt (the Eastern Cordillera and Subandean Zone) as a result of crustal thickening and tectonic uplift promoted widening of the orogeny, reactivation of preexisted Paleozoic thrust and normal faults (Figure 4.11) and Paleogene growth strata in the Huallaga Basin (Boschman, 2021; Horton, 2018a; Eude et al., 2015; Roddaz et al., 2010; Hermoza et al., 2005; Baby et al., 2018). We thus suggest that the Peruvian EC started to act as a topographic barrier at ~30 Ma.

We also suggest that the EC promoted tectonic loading and flexural subsidence in the adjacent Amazonian retroarc foreland basins as recorded in the Huallaga Basin by increase in sedimentation rate during the Oligocene (99.4 m/Ma) and north paleocurrent direction of the fluvial channel of the Chambira Fm. Hence, following Roddaz et al., (2010), we suggest that the Huallaga Basin was part of the foredeep depozone of Amazonian retroarc foreland basin from the Oligocene to the middle Miocene.

4.6.2.4 Late Miocene to present-day accelerated exhumation of the EC, drainage reorganization and the onset of the transcontinental Amazon River

Our U-Pb zircon data indicate that the provenances of the late Miocene Ipururo Fm (JUA 26), the Plio-Pleistocene Juanjui Fm (JUA 25) and the present-day sands of the Huallaga River are quite similar and originated from the EC and SAZ with no contribution of the WC. We interpret these as indicating a drainage reorganization when compared with the Oligocene-middle Miocene times with a drainage of the Huallaga Basin restricted to the EC and SAZ. Focused erosion of the EC and SAZ could be caused by focused rainfall due to climatic change between the middle and late Miocene. However, we believe that this hypothesis is unlikely because recent published studies have shown that both the middle and late Miocene paleogeographies in the Huallaga Basin were characterized by similar lowland forest developed in humid and warm tropical conditions (Stutz et al., 2022; Tcheumeleu et al., 2020). Alternatively, the drainage reorganization could be caused by renewed/accelerated uplift of EC and SAZ. Late Miocene renewed/accelerated exhumation of the northern Peruvian EC is attested by studies using apatite and zircon (U-Th)/He thermochronology (Laubacher and Naeser, 1994; Michalak et al., 2016). Deformation in the SAZ was also active since the Miocene with 93 km of shortening accommodated by SAZ thrusts at an average shortening rate of ~5.5 $mm.yr^{-1}$ (Eude et al., 2015). Hence, we conclude that the latter provenance shift and the associated drainage capture may be driven by renewed/increasing uplift of the EC.

4.6.3 Comparison with the sedimentary record of the Amazon Fan

A recent published study based on U-Pb crystallization ages and U-Th/He (ZHe) cooling ages of Pleistocene zircons of the Amazon Fan suggest the occurrence of a strong

72 Myr magmatic event in the Andes and two period of crustal cooling at 92 and 57 Myrs (Mason et al., 2022). Additionally, a late Cretaceous-Paleogene and a Miocene "phases" of the Andean orogenesis were recorded by the youngest ZHe ages (Mason et al., 2022). The magmatic event at ca 72 Ma may have been recorded by the Maastrichtian sedimentary rocks of Western Amazonian basins because they as they are mainly derived from the Andean Cretaceous Magmatic Arcs (Western Cordillera) (this study; Rodrigues et al., 2023; Vallejo et al., 2021; Horton et al., 2018a; Hurtado et al., 2018; George et al., 2019; Louterbach et al., 2017). The occurrence of this Maastrichtian magmatic event is coeval with the onset of Amazonian Andean erosion ascribed to a late Maastrichtian–late Palaeocene period of Andean mountain building (Louterbach et al., 2017) which may corroborated the model of DeCelles et al. (2009) where period of high magmatic flux are associated with tectonic growth of the fold and thrust belt, and enhanced erosion rates caused by delamination of a dense mafic orogenic root (DeCelles et al., 2009). The period of crustal cooling at ca 57 Ma is not recorded in the Huallaga Basin because a long-lived stratigraphic hiatus (~25 Ma) occurred between the Maastrichtian and the Lutetian (Custódio et al., 2023) ascribed to a period of tectonic quiescence (Custódio et al., 2023). Alternatively, the period of crustal cooling at ca 57 Ma could be related with the Andean Cordillera loading that caused the Thanetian shallow marine transgression in the Madre de Dios Basin (Louterbach et al., 2014b). In this scenario, the Pleistocene sediments of the Amazon fan only recorded the erosion of the southern part of the Amazonian Andes.

The onset of the erosion of the EC at ca 30 Ma which we interpret to record a period Andean mountain building and forward propagation of the Amazonian orogenic wedge (EC+SAZ, e.g. Eude et al., 2015). This Oligocene erosional event is not registered by the ZHe ages of the Pleistocene Amazon fan sediments (Mason et al., 2022) because no transcontinental Andean Amazon River existed during the Oligocene as the Oligocene sedimentary rocks of the Ceará Rise, which is located relatively close to the Amazon River mouth Amazon are cratonic in provenance (van Soelen et al., 2017). It follows that the Pleistocene Amazon fan sedimentary record is unlikely to capture the complete erosional history of the Amazonian Andes.

Interestingly, the late Miocene timing of increasing/renewed uplift of the northern Peruvian EC and provenance shift in the Huallaga Basin also recorded by ZHe crustal cooling ages (~12 Ma) in the Pleistocene deposits of the Amazon fan (Mason et al., 2022) is broadly coeval with the timing onset where the transcontinental Amazon River took

place as shown by the earliest arrival of Andean derived detritus in the Amazon fan that occurred between 11. 8 Ma and 8.7 Ma (Figueiredo et al., 2009b; Hoorn et al., 2017b; van Soelen et al., 2017b) and the arrival of high-altitude palynological taxa such as *Podocarpus, Hedyosmum, Jamesonia, or Polylepis* in the Amazon Fan (Hoorn et al., 2017). However, more work is needed to fully assess the potential links between the uplift of the northern Peruvian EC and the associated provenance shift and the onset of the transcontinental Amazon River.

4.7 CONCLUSIONS

The multi-proxy study (sedimentology, geochemistry, Sm-Nd isotopes and U-Pb zircon dating) of the Maastrichtian – Neogene sedimentary rocks of the Huallaga Basin yield the following conclusions:

- Similar to other western Amazonian basins, the Maastrichtian sedimentary rocks were Andean in Provenance, sourced by the WC and deposited in the distal part of the foredeep of the Amazonian retroarc foreland basin;
- Despite the ~25 Ma long sedimentary hiatus between the Paleocene and early Eocene, no relevant source shift was observed between the Maastrichtian and the middle-late Eocene (Lutetian-Bartonian) sedimentary rocks. The middle-late Eocene sedimentary are mainly sourced by the magmatic arcs of the WC and were deposited in the distal part of foredeep of the Amazonian retroarc foreland basin;
- Increases in Paleozoic (0.4 – 0.26 Ga) and Famatinian (0.5 – 0.4 Ga) zircon grains and a decrease of Cenozoic Andean magmatic Arc (< 0.0065 Ga) as well as shift toward more negative ƐNd(0) values shift indicate dominant EC source for the Oligocene (Rupelian to Chattian) to middle Miocene sedimentary rocks of Huallaga Basin. This shift in provenance area can be estimated to be Rupelian in age based on the MLA Age of JUA22 (29.70 ± 0.62 Ma) suggesting that the Peruvian EC started to act as a topographic barrier at ~30 Ma.
- This change in provenance for the Oligocene (Rupelian to Chattian) to middle Miocene sedimentary rocks of Huallaga Basin is also accompanied by an increase in sedimentation rates (50.1 to 99.4 m/Ma) and the development of a meandering fluvial system in the Chambira Fm. indicating that the Huallaga Basin was part of the foredeep depozone during the Oligocene-middle Miocene.

- A last change in provenance is indicated by our U-Pb zircon ages for the late Miocene to present day sediments of the Huallaga Basin with sources located in the EC and SAZ and no contribution of the WC. We suggest that this drainage reorganization could be caused by renewed/accelerated uplift of EC and SAZ.

Finally, when compared with the Pleistocene Amazon fan sediments which was suspected to register cycles of Andean Mountain building (Mason et al., 2022), the Oligocene erosion of the EC is only recorded in the Huallaga Basin suggesting that the Pleistocene Amazon fan achieves might not completely capture the erosional history of the Amazonian Andes.

ACKNOWLEDGMENT

This work received financial and institutional support from the IRD (Institut pour la Recherche et le Développement). This study was also supported and funded by CAPES-COFECUB program Te 924/18/ 88881.143095/2017–01 "Paléo-Amazone: evolution Néogène de l'Amazonie Brésilienne/O PALEO AMAZONAS: evolução neogênica da Amazônia Brasileira", and CNPq (Proc. 312941/2018–8) "Neogene Evolution of Brazilian Amazon".

REFERENCES

Albert, J.S., Bernt, M.J., Fronk, A.H., Fontenelle, J.P., Kuznar, S.L., Lovejoy, N.R., 2021. Late Neogene megariver captures and the Great Amazonian Biotic Interchange. Global and Planetary Change 205, 103554. https://doi.org/10.1016/j.gloplacha.2021.103554

Allègre, C.J., Dupré, B., Négrel, P., Gaillardet, J., 1996. Sr-Nd-Pb isotope systematics in Amazon and Congo River systems: constraints about erosion processes. Chemical Geology 131, 93–112. https://doi.org/10.1016/0009-2541(96)00028-9

Alvim, A.M.V., Santos, R.V., Roddaz, M., Antoine, P.-O., Ramos, M.I.F., do Carmo, D.A., Linhares, A.P., Negri, F.R., 2021. Fossil isotopic constraints (C, O and 87Sr/86Sr) on Miocene shallow-marine incursions in Amazonia. Palaeogeography, Palaeoclimatology, Palaeoecology 573, 110422. https://doi.org/10.1016/j.palaeo.2021.110422

Antoine, P.-O., Salas-Gismondi, R., Pujos, F., Ganerød, M., Marivaux, L., 2017. Western Amazonia as a Hotspot of Mammalian Biodiversity Throughout the Cenozoic. J Mammal Evol 24, 5–17. https://doi.org/10.1007/s10914-016-9333-1

Armijo, R., Lacassin, R., Coudurier-Curveur, A., Carrizo, D., 2015. Coupled tectonic evolution of Andean orogeny and global climate. Earth-Science Reviews 143, 1–35. https://doi.org/10.1016/j.earscirev.2015.01.005

Almeida, R. P. (2001). Evolução Tectono-sedimentar da Formação Santa Bárbara na Sub-Bacia Camaquã Ocidental. Dissertação (Mestrado). São Paulo: Instituto de Geociências – Universidade de São Paulo. 161p.

Baby, P., Calderon, Y., Brusset, S., Roddaz, M., Brichau, S., Eude, A., et al., 2018. The Peruvian sub-Andean foreland Basin system: structural overview, geochronologic constraints, and unexplored plays. AAPG Mem 117, 91–119. https://doi.org/10.1306/13622118M1173767.

Bahlburg, H., Vervoort, J.D., Du Frane, S.A., Bock, B., Augustsson, C., Reimann, C., 2009. Timing of crust formation and recycling in accretionary orogens: Insights learned from the western margin of South America. Earth-Science Reviews 97, 215–241. https://doi.org/10.1016/j.earscirev.2009.10.006

Barnes, J.B., Ehlers, T.A., 2009. End member models for Andean Plateau uplift. Earth-Science Reviews 97, 105–132. https://doi.org/10.1016/j.earscirev.2009.08.003

Barnes, J.B., Ehlers, T.A., McQuarrie, N., O'Sullivan, P.B., Pelletier, J.D., 2006. Eocene to recent variations in erosion across the central Andean fold-thrust belt, northern Bolivia: Implications for plateau evolution. Earth and Planetary Science Letters 248, 118–133. https://doi.org/10.1016/j.epsl.2006.05.018

Bayona, G., Cortes, M., Jaramillo, C., Ojeda, G., Aristizabal, J.J., Reyes-Harker, A., 2008. An integrated analysis of an orogen-sedimentary basin pair: Latest Cretaceous-Cenozoic evolution of the linked Eastern Cordillera orogen and the Llanos foreland basin of Colombia. Geological Society of America Bulletin 120, 1171–1197. https://doi.org/10.1130/B26187.1

Beck, S.L., Zandt, G., 2002. The nature of orogenic crust in the central Andes: nature of orogenic crust. J. Geophys. Res. 107, ESE 7-1-ESE 7-16. https://doi.org/10.1029/2000JB000124

Benjamin, M.T., Johnson, N.M., Naeser, C.W., 1987. Recent rapid uplift in the Bolivian Andes: Evidence from fission-track dating. Geol 15, 680. https://doi.org/10.1130/0091-7613(1987)15<680:RRUITB>2.0.CO;2

Bock, B., McLennan, S. M., & Hanson, G. N. 1998. Geochemistry and provenance of the middle Ordovician Austin Glen member (Normanskill formation) and the Taconian orogeny in New England. Sedimentology, 45(4), 635-655.

Boonstra, M., Ramos, M.I.F., Lammertsma, E.I., Antoine, P.-O., Hoorn, C., 2015. Marine connections of Amazonia: Evidence from foraminifera and dinoflagellate cysts (early to middle Miocene, Colombia/Peru). Palaeogeography, Palaeoclimatology, Palaeoecology 417, 176–194. https://doi.org/10.1016/j.palaeo.2014.10.032

Boschman, L.M., 2021. Andean mountain building since the Late Cretaceous: A paleoelevation reconstruction. Earth-Science Reviews 220, 103640. https://doi.org/10.1016/j.earscirev.2021.103640

Bouchez, J., Gaillardet, J., France-Lanord, C., Maurice, L., Dutra-Maia, P., 2011. Grain size control of river suspended sediment geochemistry: Clues from Amazon River depth profiles: RIVER SEDIMENTS GRAIN SIZE AND CHEMISTRY. Geochem. Geophys. Geosyst. 12, n/a-n/a. https://doi.org/10.1029/2010GC003380

Bridge, J. S. 2003. Rivers and floodplains: forms, processes, and sedimentary record. John Wiley & Sons.

Caballero, V.M., Naranjo Vesga, J.F., Gómez Gutiérrez, P.D., Rodriguez Forero, G., Mora Bohorquez, A.R., Franco Castro, W.M., Gelvez Llanez, J.R., Villamizar Villamizar, C.A., 2020. Eocene facies successions and environments in the Southern Llanos basin, Colombia. CT&F Cienc. Tecnol. Futuro 10, 107–122. https://doi.org/10.29047/01225383.141

Calderon, Y., Baby, P., Hurtado, C., Brusset, S., 2017a. Thrust tectonics in the Andean retro-foreland basin of northern Peru: Permian inheritances and petroleum implications. Marine and Petroleum Geology 82, 238–250. https://doi.org/10.1016/j.marpetgeo.2017.02.009

Calderon, Y., Baby, P., Vela, Y., Hurtado, C., Eude, A., Roddaz, M., Brusset, S., Calvès, G., Bolaños, R., 2017b. Petroleum systems restoration of the Huallaga-Marañon Andean retroforeland basin, Peru, in: Petroleum Systems Analysis—Case Studies, AAPG Memoir 114.

Calvès, G., Calderón, Y., Hurtado Enriquez, C., Brusset, S., Santini, W., Baby, P., 2018. Mass Balance of Cenozoic Andes-Amazon Source to Sink System—Marañón Basin, Peru. Geosciences 8, 167. https://doi.org/10.3390/geosciences8050167

Campetella, C.M., Vera, C.S., 2002. The influence of the Andes mountains on the South American low-level flow. Geophys. Res. Lett. 29, 7-1-7–4. https://doi.org/10.1029/2002GL015451

Cardona, A., Cordani, U.G., Ruiz, J., Valencia, V.A., Armstrong, R., Chew, D., Nutman, A., Sanchez, A.W., 2009. U-Pb Zircon Geochronology and Nd Isotopic Signatures of the Pre-Mesozoic Metamorphic Basement of the Eastern Peruvian Andes: Growth and Provenance of a Late Neoproterozoic to Carboniferous Accretionary Orogen on the Northwest Margin of Gondwana. The Journal of Geology 117, 285–305. https://doi.org/10.1086/597472

Chen, Y.-W., Wu, J., Suppe, J., 2019. Southward propagation of Nazca subduction along the Andes. Nature 565, 441–447. https://doi.org/10.1038/s41586-018-0860-1

Chew, D., Magna, T., Kirkland, C., Miskovic, A., Cardona, A., Spikings, R., Schaltegger, U., 2008. Detrital zircon fingerprint of the Proto-Andes: Evidence for a Neoproterozoic active margin? Precambrian Research 167, 186–200. https://doi.org/10.1016/j.precamres.2008.08.002

Chew, D.M., Pedemonte, G., Corbett, E., 2016. Proto-Andean evolution of the Eastern Cordillera of Peru. Gondwana Research 35, 59–78. https://doi.org/10.1016/j.gr.2016.03.016

Chiaradia, M., 2009. Adakite-like magmas from fractional crystallization and melting-assimilation of mafic lower crust (Eocene Macuchi arc, Western Cordillera, Ecuador). Chemical Geology 265, 468–487. https://doi.org/10.1016/j.chemgeo.2009.05.014

Christophoul, F., Baby, P., Dávila, C., 2002. Stratigraphic responses to a major tectonic event in a foreland basin: the Ecuadorian Oriente Basin from Eocene to Oligocene times. Tectonophysics 345, 281–298. https://doi.org/10.1016/S0040-1951(01)00217-7

Condie, K.C., 1993. Chemical composition and evolution of the upper continental crust: Contrasting results from surface samples and shales. Chemical Geology 104, 1–37. https://doi.org/10.1016/0009-2541(93)90140-E

Cooper, M. A., Addison, F. T., Alvarez, R., Coral, M., Graham, R. H., Hayward, A. B., ... & Taborda, A. (1995). Basin development and tectonic history of the Llanos basin, Eastern Cordillera, and Middle Magdalena Valley, Colombia. AAPG bulletin, 79(10), 1421-1442.

Cordani, U.G., 1999. Crustal evolution of the South American.pdf. pp. 167–173.

Cullers, R.L., 2000. The geochemistry of shales, siltstones and sandstones of Pennsylvanian–Permian age, Colorado, USA: implications for provenance and metamorphic studies. Lithos 51, 181–203. https://doi.org/10.1016/S0024-4937(99)00063-8

Custódio, M.A., Roddaz, M., Santos, R.V., Antoine, P.-O., Marivaux, L., Stutz, N.S., Dantas, E.L., Jaramillo, C., Louterbach, M., Hurtado, C., Oliveira Gonçalves, G., 2023. New stratigraphic and paleoenvironmental constraints on the Paleogene paleogeography of Western Amazonia. Journal of South American Earth Sciences 124, 104256. https://doi.org/10.1016/j.jsames.2023.104256

De Baar, H.J.W., Bacon, M.P., Brewer, P.G., Bruland, K.W., 1985. Rare earth elements in the Pacific and Atlantic Oceans. Geochimica et Cosmochimica Acta 49, 1943–1959. https://doi.org/10.1016/0016-7037(85)90089-4

DeCelles, P.G., Carrapa, B., Horton, B.K., Gehrels, G.E., 2011. Cenozoic foreland basin system in the central Andes of northwestern Argentina: Implications for Andean geodynamics and modes of deformation: ANDEAN FORELAND BASIN. Tectonics 30, n/a-n/a. https://doi.org/10.1029/2011TC002948

DeCelles, P.G., Ducea, M.N., Kapp, P., Zandt, G., 2009. Cyclicity in Cordilleran orogenic systems. Nature Geosci 2, 251–257. https://doi.org/10.1038/ngeo469

DeCelles, P.G., Giles, K.A., 1996. Foreland basin systems. Basin Research 8, 105–123. https://doi.org/10.1046/j.1365-2117.1996.01491.x

DeCelles, P.G., Horton, B.K., 2003. Early to middle Tertiary foreland basin development and the history of Andean crustal shortening in Bolivia. Geological Society of America Bulletin 115, 58–77. https://doi.org/10.1130/0016-7606(2003)115<0058:ETMTFB>2.0.CO;2

Dickinson, W.R., Gehrels, G.E., 2009. Use of U–Pb ages of detrital zircons to infer maximum depositional ages of strata: A test against a Colorado Plateau Mesozoic database. Earth and Planetary Science Letters 288, 115–125. https://doi.org/10.1016/j.epsl.2009.09.013

Espinoza JC, Garreaud R, Poveda G, et al. 2020. Hydroclimate of the Andes Part I: Main Climatic Features. Front Earth Sci 8.

Espurt, N., Baby, P., Brusset, S., Roddaz, M., Hermoza, W., Barbarand, J., 2011. The Nazca Ridge and Uplift of the Fitzcarrald Arch: Implications for Regional Geology in Northern South America, in: Hoorn, C., Wesselingh, F.P. (Eds.), Amazonia: Landscape and Species Evolution. Wiley-Blackwell Publishing Ltd., Oxford, UK, pp. 89–100. https://doi.org/10.1002/9781444306408.ch6

Espurt, N., Baby, P., Brusset, S., Roddaz, M., Hermoza, W., Regard, V., Antoine, P.-O., Salas-Gismondi, R., Bolaños, R., 2007. How does the Nazca Ridge subduction influence the modern Amazonian foreland basin? Geol 35, 515. https://doi.org/10.1130/G23237A.1

Eude, A., Roddaz, M., Brichau, S., Brusset, S., Calderon, Y., Baby, P., Soula, J.-C., 2015. Controls on timing of exhumation and deformation in the northern Peruvian eastern Andean wedge as inferred from low-temperature thermochronology and balanced cross section: EXHUMATION AND DEFORMATION OF NORTH PERU. Tectonics 34, 715–730. https://doi.org/10.1002/2014TC003641

Farrar E, Clark AH, Kontak DJ, Archibald DA. 1988. Zongo-San Gabon zone: Eocene foreland boundary of Central Andean orogen, northwest Bolivia and southeast Peru. Geology 16:55–58

Fedo, C.M., Wayne Nesbitt, H., Young, G.M., 1995. Unraveling the effects of potassium metasomatism in sedimentary rocks and paleosols, with implications for paleoweathering conditions and provenance. Geol 23, 921. https://doi.org/10.1130/0091-7613(1995)023<0921:UTEOPM>2.3.CO;2

Fielding, C.R., 2006. Upper flow regime sheets, lenses and scour fills: Extending the range of architectural elements for fluvial sediment bodies. Sedimentary Geology 190, 227–240. https://doi.org/10.1016/j.sedgeo.2006.05.009

Figueiredo, J., Hoorn, C., van der Ven, P., Soares, E., 2009. Late Miocene onset of the Amazon River and the Amazon deep-sea fan: Evidence from the Foz do Amazonas Basin. Geology 37, 619–622. https://doi.org/10.1130/G25567A.1

Foix, N., Allard, J.O., Paredes, J.M., Giacosa, R.E., 2012. Fluvial styles, palaeohydrology and modern analogues of an exhumed, Cretaceous fluvial system: Cerro Barcino Formation, Cañadón Asfalto Basin, Argentina. Cretaceous Research 34, 298–307. https://doi.org/10.1016/j.cretres.2011.11.010

Friend, P. F., Slater, M. J., & Williams, R. C. 1979. Vertical and lateral building of river sandstone bodies, Ebro Basin, Spain. Journal of the Geological Society, 136(1), 39-46.

Galbraith, R.F., Roberts, R.G., Yoshida, H., 2005. Error variation in OSL palaeodose estimates from single aliquots of quartz: a factorial experiment. Radiation Measurements 39, 289–307. https://doi.org/10.1016/j.radmeas.2004.03.023

Galbraith, R., Laslett, G. 1993. Statistical models for mixed fission track ages. Nucl. Tracks Radiat. Meas. 21 (4), 459–470.

García-Delgado, H., Villamizar-Escalante, N., Bermúdez, M.A., Bernet, M., Velandia, F., 2021. Climate or tectonics? What controls the spatial-temporal variations in erosion rates across the Eastern Cordillera of Colombia? Global and Planetary Change 203, 103541. https://doi.org/10.1016/j.gloplacha.2021.103541

George, S.W.M., Horton, B.K., Jackson, L.J., Moreno, F., Carlotto, V., Garzione, C.N., 2019. Sediment provenance variations during contrasting Mesozoic-early Cenozoic tectonic regimes of the northern Peruvian Andes and Santiago-Marañón foreland basin, in: Andean Tectonics. Elsevier, pp. 269–296. https://doi.org/10.1016/B978-0-12-816009-1.00012-5

Gibling, M.R., 2006. Width and Thickness of Fluvial Channel Bodies and Valley Fills in the Geological Record: A Literature Compilation and Classification. Journal of Sedimentary Research 76, 731–770. https://doi.org/10.2110/jsr.2006.060

Gillis, R.J., Horton, B.K., Grove, M., 2006. Thermochronology, geochronology, and upper crustal structure of the Cordillera Real: Implications for Cenozoic exhumation of the central Andean plateau: EXHUMATION OF THE CENTRAL ANDEAN PLATEAU. Tectonics 25, n/a-n/a. https://doi.org/10.1029/2005TC001887

Gioia, S.M.C.L., Pimentel, M.M., 2000. The Sm-Nd isotopic method in the geochronology laboratory of the University of Brasília. An. Acad. Bras. Ciênc. 72, 219–245. https://doi.org/10.1590/S0001-37652000000200009

Gulliford, A.R., Flint, S.S., Hodgson, D.M., 2017. Crevasse splay processes and deposits in an ancient distributive fluvial system: The lower Beaufort Group, South Africa. Sedimentary Geology 358, 1–18. https://doi.org/10.1016/j.sedgeo.2017.06.005

Gutiérrez, E.G., Horton, B.K., Vallejo, C., Jackson, L.J., George, S.W.M., 2019. Provenance and geochronological insights into Late Cretaceous-Cenozoic foreland basin development in the Subandean Zone and Oriente Basin of Ecuador, in: Andean Tectonics. Elsevier, pp. 237–268. https://doi.org/10.1016/B978-0-12-816009-1.00011-3

Heller, P. L., Angevine, C. L., Winslow, N. S., Paola, C. 1988. Two-phase stratigraphic model of foreland-basin sequences. Geology, 16(6), 501-504.

Hermoza, W., Baby, P., Brusset, S., Christophoul, F., Gil, W.G., n.d. Foreland basin system evolution of the Peruvian Andes : new insights from mass balance computation.

Hermoza, W., Brusset, S., Baby, P., Gil, W., Roddaz, M., Guerrero, N., Bolaños, R., 2005. The Huallaga foreland basin evolution: Thrust propagation in a deltaic environment, northern Peruvian Andes. Journal of South American Earth Sciences 19, 21–34. https://doi.org/10.1016/j.jsames.2004.06.005

Hollister, V.F., Sirvas, E.B., 1978. The Calipuy Formation of Northern Peru, and its relation to volcanism in the Northern Andes. Journal of Volcanology and Geothermal Research 4, 89–98. https://doi.org/10.1016/0377-0273(78)90030-6

Hoorn, C. ; Palazzesi, L. ; Silvestro, D. 2021. Exploring the impact of Andean uplift and climate on life evolution and landscape modification: From Amazonia to Patagonia, Global and Planetary Change (2021), https://doi.org/10.1016/j.gloplacha.2022.103759

Hoorn, C., 1993. Marine incursions and the influence of Andean tectonics on the Miocene depositional history of northwestern Amazonia: results of a palynostratigraphic study. Palaeogeography, Palaeoclimatology, Palaeoecology 105, 267–309. https://doi.org/10.1016/0031-0182(93)90087-Y

Hoorn, C., Bogotá-A, G.R., Romero-Baez, M., Lammertsma, E.I., Flantua, S.G.A., Dantas, E.L., Dino, R., do Carmo, D.A., Chemale, F., 2017. The Amazon at sea: Onset and stages of the Amazon River from a marine record, with special reference to Neogene plant turnover in the drainage basin. Global and Planetary Change 153, 51–65. https://doi.org/10.1016/j.gloplacha.2017.02.005

Hoorn, C., Boschman, L.M., Kukla, T., Sciumbata, M., Val, P., 2022. The Miocene wetland of western Amazonia and its role in Neotropical biogeography. Botanical Journal of the Linnean Society 199, 25–35. https://doi.org/10.1093/botlinnean/boab098

Hoorn, C., Wesselingh, F.P., ter Steege, H., Bermudez, M.A., Mora, A., Sevink, J., Sanmartín, I., Sanchez-Meseguer, A., Anderson, C.L., Figueiredo, J.P., Jaramillo, C., Riff, D., Negri, F.R., Hooghiemstra, H., Lundberg, J., Stadler, T., Särkinen, T., Antonelli, A., 2010. Amazonia Through Time: Andean Uplift, Climate Change, Landscape Evolution, and Biodiversity. Science 330, 927–931. https://doi.org/10.1126/science.1194585

Horbe, A.M.C., Motta, M.B., de Almeida, C.M., Dantas, E.L., Vieira, L.C., 2013. Provenance of Pliocene and recent sedimentary deposits in western Amazônia, Brazil: Consequences for the paleodrainage of the Solimões-Amazonas River. Sedimentary Geology 296, 9–20. https://doi.org/10.1016/j.sedgeo.2013.07.007

Horton, B. K. and DeCelles, P. G. 2001. Modern and ancient fluvial megafans in the foreland basin system of the central Andes, southern Bolivia: Implications for drainage network evolution in fold-thrust belts. Basin research, 13(1), 43-63.

Horton, B.K., 2022. Unconformity development in retroarc foreland basins: implications for the geodynamics of Andean-type margins. JGS 179, jgs2020-263. https://doi.org/10.1144/jgs2020-263

Horton, B.K., 2018a. Tectonic Regimes of the Central and Southern Andes: Responses to Variations in Plate Coupling During Subduction. Tectonics 37, 402–429. https://doi.org/10.1002/2017TC004624

Horton, B.K., 2018b. Sedimentary record of Andean mountain building. Earth-Science Reviews 178, 279–309. https://doi.org/10.1016/j.earscirev.2017.11.025

Horton, B.K., DeCelles, P.G., 1997. The modern foreland basin system adjacent to the Central Andes. Geol 25, 895. https://doi.org/10.1130/0091-7613(1997)025<0895:TMFBSA>2.3.CO;2

Horton, B.K., Fuentes, F., 2016. Sedimentary record of plate coupling and decoupling during growth of the Andes. Geology 44, 647–650. https://doi.org/10.1130/G37918.1

Hovikoski, J. ; Weselingh, F.P. ; Räsänen, M. ; Gingras, M. ; Vonhof, H.B. 2010. Marine influence in Amazonia: evidence from the geological record. In. Amazonia, Landscape and Species Evolution, 1st edition. Edited by C. Hoorn and F.P. Wesselingh. Blackwell Publishing, p. 143-161.

Hungerbühler, D., Steinmann, M., Winkler, W., Seward, D., Egüez, A., Peterson, D.E., Helg, U., Hammer, C., 2002. Neogene stratigraphy and Andean geodynamics of southern Ecuador. Earth-Science Reviews 57, 75–124. https://doi.org/10.1016/S0012-8252(01)00071-X

Hurtado, C., Roddaz, M., Santos, R.V., Baby, P., Antoine, P.-O., Dantas, E.L., 2018. Cretaceous-early Paleocene drainage shift of Amazonian rivers driven by Equatorial Atlantic Ocean opening and Andean uplift as deduced from the provenance of northern Peruvian sedimentary rocks (Huallaga basin). Gondwana Research 63, 152–168. https://doi.org/10.1016/j.gr.2018.05.012

Insel, N., Poulsen, C.J., Ehlers, T.A., 2010. Influence of the Andes Mountains on South American moisture transport, convection, and precipitation. Clim Dyn 35, 1477–1492. https://doi.org/10.1007/s00382-009-0637-1

Jackson, S.E., Pearson, N.J., Griffin, W.L., Belousova, E.A., 2004. The application of laser ablation-inductively coupled plasma-mass spectrometry to in situ U–Pb zircon geochronology. Chemical Geology 211, 47–69. https://doi.org/10.1016/j.chemgeo.2004.06.017

Jacobsen, S.B., Wasserburg, G.J., 1980. Sm-Nd isotopic evolution of chondrites. Earth and Planetary Science Letters 50, 139–155. https://doi.org/10.1016/0012-821X(80)90125-9

Jaillard, E., Soler, P., 1996. Cretaceous to early Paleogene tectonic evolution of the northern Central Andes (0–18°S) and its relations to geodynamics. Tectonophysics 259, 41–53. https://doi.org/10.1016/0040-1951(95)00107-7

Jara, J.J., Barra, F., Reich, M., Leisen, M., Romero, R., Morata, D., 2021. Episodic construction of the early Andean Cordillera unravelled by zircon petrochronology. Nat Commun 12, 4930. https://doi.org/10.1038/s41467-021-25232-z

Jaramillo, C., Romero, I., D'Apolito, C., Bayona, G., Duarte, E., Louwye, S., Escobar, J., Luque, J., Carrillo-Briceño, J.D., Zapata, V., Mora, A., Schouten, S., Zavada, M., Harrington, G., Ortiz, J., Wesselingh, F.P., 2017. Miocene flooding events of western Amazonia. Sci. Adv. 3, e1601693. https://doi.org/10.1126/sciadv.1601693

Jordan, T. E. 1995. Retroarc foreland and related basins. Tectonics of Sedimentary Basins. Blackwell Scientific: Cambridge, 331-362.

Kummel, B., 1948. Geological reconnaissance of the Contamana region, Peru. Geol Soc America Bull 59, 1217. https://doi.org/10.1130/0016-7606(1948)59[1217:GROTCR]2.0.CO;2

Laubacher, G., & Naeser, C. W. 1994. Fission-track dating of granitic rocks from the Eastern Cordillera of Peru: Evidence for Late Jurassic and Cenozoic cooling. Journal of the Geological Society, 151(3), 473-483.

Lenters, J.D., Cook, K.H., 1995. Simulation and Diagnosis of the Regional Summertime Precipitation Climatology of South America. J. Climate 8, 2988–3005. https://doi.org/10.1175/1520-0442(1995)008<2988:SADOTR>2.0.CO;2

Louterbach, M., Roddaz, M., Antoine, P.-O., Marivaux, L., Adnet, S., Bailleul, J., Dantas, E., Santos, R.V., Chemale, F., Baby, P., Sanchez, C., Calderon, Y., 2017. Provenance record of late Maastrichtian-late Palaeocene Andean Mountain building in the Amazonian retroarc foreland basin (Madre de Dios basin, Peru). Terra Nova 30, 17–23. https://doi.org/10.1111/ter.12303

Martin-Gombojav, N., Winkler, W., 2008. Recycling of Proterozoic crust in the Andean Amazon foreland of Ecuador: implications for orogenic development of the Northern Andes: Multiple recycling of Proterozoic crust in the Northern Andes. Terra Nova 20, 22–31. https://doi.org/10.1111/j.1365-3121.2007.00782.x

Mason, C.C., Romans, B.W., Patterson, M.O., Stockli, D.F., Fildani, A., 2022. Cycles of Andean mountain building archived in the Amazon Fan. Nat Commun 13, 6983. https://doi.org/10.1038/s41467-022-34561-6

McLennan, S.M., Hemming, S., McDaniel, D.K., Hanson, G.N., 1993. Geochemical approaches to sedimentation, provenance, and tectonics, in: Geological Society of America Special Papers. Geological Society of America, pp. 21–40. https://doi.org/10.1130/SPE284-p21

McLennan, S.M. 2001. Relationship between the trace element composition of sedimentary rocks and upper continental crust. Geochem. Geophys. Geosysystem, 2, 203–236.

Mégard, F., 1984. The Andean orogenic period and its major structures in central and northern Peru. JGS 141, 893–900. https://doi.org/10.1144/gsjgs.141.5.0893

Miall, A.D., 2006. The Geology of Fluvial Deposits. Springer Berlin Heidelberg, Berlin, Heidelberg. https://doi.org/10.1007/978-3-662-03237-4

Miall, A.D., 1978. Lithofacies types and vertical profiles models, in: Summary of Braided River Deposits. Calgary, Alberta, pp. 597–604.

Miall, A.D., n.d. Architectural-Element Analysis: A New Method of Facies Analysis Applied to Fluvial Deposits. Earth-Science Reviews 22, 261–308.

Michalak, M.J., Hall, S.R., Farber, D.L., Audin, L., Hourigan, J.K., 2016. (U-Th)/He thermochronology records late Miocene accelerated cooling in the north-central Peruvian Andes. Lithosphere 8, 103–115. https://doi.org/10.1130/L485.1

Mora, A., Baby, P., Roddaz, M., Parra, M., Brusset, S., Hermoza, W., Espurt, N., 2011. Tectonic History of the Andes and Sub-Andean Zones: Implications for the Development of the Amazon Drainage Basin, in: Hoorn, C., Wesselingh, F.P. (Eds.), Amazonia: Landscape and Species Evolution. Wiley-Blackwell Publishing Ltd., Oxford, UK, pp. 38–60. https://doi.org/10.1002/9781444306408.ch4

Moreno, F., Garzione, C.N., George, S.W.M., Horton, B.K., Williams, L., Jackson, L.J., Carlotto, V., Richter, F., Bandeian, A., 2020. Coupled Andean Growth and Foreland Basin Evolution, Campanian–Cenozoic Bagua Basin, Northern Peru. Tectonics 39. https://doi.org/10.1029/2019TC005967

Naeser, C.W., Crochet, J.-Y., Jaillard, E., Laubacher, G., Mourier, T., Sigé, B., 1991. Tertiary fission-track ages from the Bagua syncline (northern Peru): Stratigraphic and tectonic implications. Journal of South American Earth Sciences 4, 61–71. https://doi.org/10.1016/0895-9811(91)90018-G

Nanson, G.C., Croke, J.C., 1992. A genetic classification of floodplains. Geomorphology 4, 459–486. https://doi.org/10.1016/0169-555X(92)90039-Q

Nesbitt, H.W. and Young, G.M. 1982. Early Proterozoic climatesand plate motions inferred from major element chemistry of lu-tites. – Nature, 299: 715–717, London (Macmillan).

Nichols, G., 2010. Sedimentology and stratigraphy, 2. ed., [Nachdr.]. ed. Wiley-Blackwell, Chichester.

Nie, J., Horton, B.K., Mora, A., Saylor, J.E., Housh, T.B., Rubiano, J., Naranjo, J., 2010. Tracking exhumation of Andean ranges bounding the Middle Magdalena Valley Basin, Colombia. Geology 38, 451–454. https://doi.org/10.1130/G30775.1

Nie, J., Horton, B.K., Saylor, J.E., Mora, A., Mange, M., Garzione, C.N., Basu, A., Moreno, C.J., Caballero, V., Parra, M., 2012. Integrated provenance analysis of a convergent retroarc foreland system: U–Pb ages, heavy minerals, Nd isotopes, and sandstone compositions of the Middle Magdalena Valley basin, northern Andes, Colombia. Earth-Science Reviews 110, 111–126. https://doi.org/10.1016/j.earscirev.2011.11.002

Odoh, S., Saylor, J.E., Higuera, C., Copeland, P., Lapen, T.J., 2019. Discriminating mechanisms for coarse clastic progradation in the Colombian foreland basin using detrital zircon double dating, in: Andean Tectonics. Elsevier, pp. 133–171. https://doi.org/10.1016/B978-0-12-816009-1.00008-3

Parra, M., Mora, A., Lopez, C., Ernesto Rojas, L., Horton, B.K., 2012. Detecting earliest shortening and deformation advance in thrust belt hinterlands: Example from the Colombian Andes. Geology 40, 175–178. https://doi.org/10.1130/G32519.1

Paton, C., Hellstrom, J., Paul, B., Woodhead, J., Hergt, J., 2011. Iolite: Freeware for the visualisation and processing of mass spectrometric data. J. Anal. At. Spectrom. 26, 2508. https://doi.org/10.1039/c1ja10172b

Perez, N.D., Horton, B.K., McQUARRIE, N., Stübner, K., Ehlers, T.A., 2016. Andean shortening, inversion and exhumation associated with thin- and thick-skinned deformation in southern Peru. Geol. Mag. 153, 1013–1041. https://doi.org/10.1017/S0016756816000121

Petrus, J.A. and Kamber, B.S. 2012. VizualAge: A Novel Approach to Laser Ablation ICP-MS U-Pb Geochronology Data Reduction. Geostandards and Geoanalytical Research, 36: 247-270.

Pfiffner, O., Gonzalez, L., 2013. Mesozoic–Cenozoic Evolution of the Western Margin of South America: Case Study of the Peruvian Andes. Geosciences 3, 262–310. https://doi.org/10.3390/geosciences3020262

Poblete, F., Dupont-Nivet, G., Licht, A., van Hinsbergen, D.J.J., Roperch, P., Mihalynuk, M.G., Johnston, S.T., Guillocheau, F., Baby, G., Fluteau, F., Robin, C., van der Linden, T.J.M., Ruiz, D., Baatsen, M.L.J., 2021. Towards interactive global paleogeographic maps, new reconstructions at 60, 40 and 20 Ma. Earth-Science Reviews 214, 103508. https://doi.org/10.1016/j.earscirev.2021.103508

Potter, P.E., 1997. The Mesozoic and Cenozoic paleodrainage of South America: a natural history. Journal of South American Earth Sciences 10, 331–344. https://doi.org/10.1016/S0895-9811(97)00031-X

Pourmand, A., Dauphas, N., Ireland, T.J., 2012. A novel extraction chromatography and MC-ICP-MS technique for rapid analysis of REE, Sc and Y: Revising CI-chondrite and Post-Archean Australian Shale (PAAS) abundances. Chemical Geology 291, 38–54. https://doi.org/10.1016/j.chemgeo.2011.08.011

Rahbek, C., Borregaard, M.K., Antonelli, A., Colwell, R.K., Holt, B.G., Nogues-Bravo, D., Rasmussen, C.M.Ø., Richardson, K., Rosing, M.T., Whittaker, R.J., Fjeldså, J., 2019. Building mountain biodiversity: Geological and evolutionary processes. Science 365, 1114–1119. https://doi.org/10.1126/science.aax0151

Rak, A.J., McQuarrie, N., Ehlers, T.A., 2017. Kinematics, Exhumation, and Sedimentation of the North Central Andes (Bolivia): An Integrated Thermochronometer and Thermokinematic Modeling Approach. Tectonics 36, 2524–2554. https://doi.org/10.1002/2016TC004440

Ramos, V.A., 1999. Plate tectonic setting of the Andean Cordillera. Episodes 22, 183–190. https://doi.org/10.18814/epiiugs/1999/v22i3/005

Roddaz, M., Baby, P., Brusset, S., Hermoza, W., Maria Darrozes, J., 2005. Forebulge dynamics and environmental control in Western Amazonia: The case study of the Arch of Iquitos (Peru). Tectonophysics 399, 87–108. https://doi.org/10.1016/j.tecto.2004.12.017

Roddaz, M., Hermoza, W., Mora, A., Baby, P., Parra, M., Christophoul, F., Brusset, S., Espurt, N., 2010. Cenozoic Sedimentary Evolution of the Amazonian Foreland Basin System, in: Hoorn, C., Wesselingh, F.P. (Eds.), Amazonia: Landscape and Species Evolution. Wiley-Blackwell Publishing Ltd., Oxford, UK, pp. 61–88. https://doi.org/10.1002/9781444306408.ch5

Roddaz, M., Viers, J., Moreira-Turcq, P., Blondel, C., Sondag, F., Guyot, J.-L., Moreira, L., 2014. Evidence for the control of the geochemistry of Amazonian floodplain sediments by stratification of suspended sediments in the Amazon. Chemical Geology 387, 101–110. https://doi.org/10.1016/j.chemgeo.2014.07.022

Rodrigues, M. de A., Roddaz, M., Santos, R.V., Louterbach, M., D'Apolito, C., Brusset, S., Dantas, E.L., Negri, F.R., 2023. New insights into the Cretaceous evolution of the Western Amazonian paleodrainage system. Sedimentary Geology 453, 106434. https://doi.org/10.1016/j.sedgeo.2023.106434

Rousseau, T.C.C., 2019. Controls on the geochemistry of suspended sediments from large tropical South American rivers (Amazon, Orinoco and Maroni). Chemical Geology.

Santos, C., Jaramillo, C., Bayona, G., Rueda, M., Torres, V., 2008. Late Eocene marine incursion in north-western South America. Palaeogeography, Palaeoclimatology, Palaeoecology 264, 140–146. https://doi.org/10.1016/j.palaeo.2008.04.010

Schellart, W.P., 2017. Andean mountain building and magmatic arc migration driven by subduction-induced whole mantle flow. Nat Commun 8, 2010. https://doi.org/10.1038/s41467-017-01847-z

Sempere, T., Butler, R.F., Richards, D.R., Marshall, L.G., Sharp, W., Swisher, C.C., 1997. Stratigraphy and chronology of Upper Cretaceous–lower Paleogene strata in Bolivia and northwest Argentina. Geological Society of America Bulletin 109, 709–727. https://doi.org/10.1130/0016-7606(1997)109<0709:SACOUC>2.3.CO;2

Serrano, J., Richardson, J.E., Milne, R.I., Mondragon, G.A., Hawkins, J.A., Bartish, I.V., Gonzalez, M., Chave, J., Madriñán, S., Cárdenas, D., Sanchez, S.D., Cortés-B, R., Pennington, R.T., 2021. Andean orogeny and the diversification of lowland neotropical rain forest trees: A case study in Sapotaceae. Global and Planetary Change 201, 103481. https://doi.org/10.1016/j.gloplacha.2021.103481

Sharman, G.R., Malkowski, M.A., 2020. Needles in a haystack: Detrital zircon U Pb ages and the maximum depositional age of modern global sediment. Earth-Science Reviews 203, 103109. https://doi.org/10.1016/j.earscirev.2020.103109

Sharman, G.R., Sharman, J.P., Sylvester, Z., 2018. detritalPy: A Python-based toolset for visualizing and analysing detrital geo-thermochronologic data. Depositional Rec 4, 202–215. https://doi.org/10.1002/dep2.45

Sláma, J., Košler, J., Condon, D.J., Crowley, J.L., Gerdes, A., Hanchar, J.M., Horstwood, M.S.A., Morris, G.A., Nasdala, L., Norberg, N., Schaltegger, U., Schoene, B., Tubrett, M.N., Whitehouse, M.J., 2008. Plešovice zircon — A new natural reference material for U–Pb and Hf isotopic microanalysis. Chemical Geology 249, 1–35. https://doi.org/10.1016/j.chemgeo.2007.11.005

Somoza, R., Ghidella, M.E., 2012. Late Cretaceous to recent plate motions in western South America revisited. Earth and Planetary Science Letters 331–332, 152–163. https://doi.org/10.1016/j.epsl.2012.03.003

Stendal, H., Theobald, P.K., 1994. Heavy-Mineral Concentrates in Geochemical Exploration, in: Handbook of Exploration Geochemistry. Elsevier, pp. 185–225. https://doi.org/10.1016/B978-0-444-81854-6.50012-2

Stutz, N.S., Abello, M.A., Marivaux, L., Boivin, M., Pujos, F., Benites-Palomino, A.M., Salas-Gismondi, R., Tejada-Lara, J.V., Custódio, M.A., Roddaz, M., Santos, R.V., Ribeiro, A.M., Antoine, P.-O., 2022. Late middle Miocene Metatheria (Mammalia: Didelphimorphia and Paucituberculata) from Juan Guerra, San Martín Department, Peruvian Amazonia. Journal of South American Earth Sciences 118, 103902. https://doi.org/10.1016/j.jsames.2022.103902

Sundell, K.E., Saylor, J.E., Lapen, T.J., Styron, R.H., Villarreal, D.P., Usnayo, P., Cárdenas, J., 2018. Peruvian Altiplano Stratigraphy Highlights Along-Strike Variability in Foreland Basin Evolution of the Cenozoic Central Andes. Tectonics 37, 1876–1904. https://doi.org/10.1029/2017TC004775

Tabor, N.J., Myers, T.S., 2015. Paleosols as Indicators of Paleoenvironment and Paleoclimate. Annu. Rev. Earth Planet. Sci. 43, 333–361. https://doi.org/10.1146/annurev-earth-060614-105355

Taylor, S.R.; McLenana, S.M. 1985. The Continental Crust: Its Composition and Evolution; Oxford Blackwell: Oxford, UK, p. 1–312

Tcheumeleu, A.F., Fauquette, S., Castillo, A.A., Martinez, C., Moreno, F., Navarrete, R.E., Parra, F., Wesselingh, F.P., Salas-Gismondi, R., Varas-Malca, R., Roddaz, M., Antoine, P.-O., 2020. Depositional environments and landscapes of the upper Miocene Ipururo Formation at Shumanza, Subandean Zone, northern Peru. Palaeobio Palaeoenv 100, 719–735. https://doi.org/10.1007/s12549-019-00400-8

Vallejo, C., Romero, C., Horton, B.K., Spikings, R.A., Gaibor, J., Winkler, W., Esteban, J.J., Thomsen, T.B., Mariño, E., 2021. Jurassic to Early Paleogene sedimentation in the Amazon

region of Ecuador: Implications for the paleogeographic evolution of northwestern South America. Global and Planetary Change 204, 103555. https://doi.org/10.1016/j.gloplacha.2021.103555

van Soelen, E.E., Kim, J.-H., Santos, R.V., Dantas, E.L., Vasconcelos de Almeida, F., Pires, J.P., Roddaz, M., Sinninghe Damsté, J.S., 2017. A 30 Ma history of the Amazon River inferred from terrigenous sediments and organic matter on the Ceará Rise. Earth and Planetary Science Letters 474, 40–48. https://doi.org/10.1016/j.epsl.2017.06.025

Vermeesch, P., 2021. Maximum depositional age estimation revisited. Geoscience Frontiers 12, 843–850. https://doi.org/10.1016/j.gsf.2020.08.008

Vermeesch, P., 2018. Dissimilarity measures in detrital geochronology. Earth-Science Reviews 178, 310–321. https://doi.org/10.1016/j.earscirev.2017.11.027

Vermeesch, P., 2013. Multi-sample comparison of detrital age distributions. Chemical Geology 341, 140–146. https://doi.org/10.1016/j.chemgeo.2013.01.010

Vermeesch, P., Resentini, A., Garzanti, E., 2016. An R package for statistical provenance analysis. Sedimentary Geology 336, 14–25. https://doi.org/10.1016/j.sedgeo.2016.01.009

Viers, J., Roddaz, M., Filizola, N., Guyot, J.-L., Sondag, F., Brunet, P., Zouiten, C., Boucayrand, C., Martin, F., Boaventura, G.R., 2008. Seasonal and provenance controls on Nd–Sr isotopic compositions of Amazon rivers suspended sediments and implications for Nd and Sr fluxes exported to the Atlantic Ocean. Earth and Planetary Science Letters.

Widenbeck, M., Allé, P., Corfu, F., Griffin, W.L., Meier, M., Oberli, F., Quadt, A.V., Roddick, J.C., Spiegel, W., 1995. Three natural zircon standards for U-Th-Pb, Lu-Hf, trace element and REE analyses. Geostand. Geoanalytical Res. 19, 1–23. https://doi.org/10.1111/j.1751-908X.1995.tb00147.x.

Zamora, G., Gil, W., 2018. The Marañón basin: Tectonic evolution and paleogeography. AAPG Memoir 117, 121–143. https://doi.org/10.1306/13622119M1173768

Zapata, S., Zapata-Henao, M., Cardona, A., Jaramillo, C., Silvestro, D., Oboh-Ikuenobe, F., 2021. Long-term topographic growth and decay constrained by 3D thermo-kinematic modeling: Tectonic evolution of the Antioquia Altiplano, Northern Andes. Global and Planetary Change 203, 103553. https://doi.org/10.1016/j.gloplacha.2021.103553

CAPÍTULO 5

PROVENIÊNCIA SEDIMENTAR DA BACIA DA FOZ DO AMAZONAS: IMPLICAÇÕES PARA O SISTEMA FONTE – DEPOSIÇÃO NO NOROESTE DA MARGEM EQUATORIAL BRASILEIRA

Reconstitution du paleo réseau de drainage amazonien paléogène oriental à partir de la provenance des sédiments du bassin Foz de Amazonas

5. PROVENIÊNCIA SEDIMENTAR DA BACIA DA FOZ DO AMAZONAS: IMPLICAÇÕES PARA O SISTEMA FONTE – DEPOSIÇÃO NO NOROESTE DA MARGEM EQUATORIAL BRASILEIRA

Neste capítulo utilizamos dados das composições isotópicas de Nd e datações geocronológicas U-Pb em grãos de zircões detríticos de depósitos sedimentares Cenozoicos da Bacia da Foz do Amazonas para obter mais informações sobre as variações geodinâmicas ocorridas ao norte da Plataforma Sul-Americana (NW da Margem Equatorial Brasileira) e suas influências na construção do sistema área-fonte – deposição AMEESA. Mostramos que a Bacia da Foz do Amazonas registra as fases de maior aporte sedimentar associadas com a mudança de área-fonte e eventos de reativações e soerguimentos ocorridos ao norte da Plataforma Sul-Americana.

RÉSUMÉ

Les résultats de ce chapitre sont exprimés sous la forme d'un article en préparation qui est, lors de la soumission de ce manuscrit, en attente de résultats complémenaires, notamment de datations U-Pb sur zircons avant d'être finalisé et soumis. L'objectif de ce chapitre est de reconstituer le paléo réseau de drainage amazonien cénozoïque oriental à partir de la provenance de sediments de cuttings provenant de puits du bassin Foz de Amazonas. Cette étude préliminaire est la première étude à présenter des âges U-Pb sur zircons dans les sédiments pré quaternaire du bassin Foz de Amazonas. L'âge des sédiments analyés a été déterminé grâce au modèle stratigraphique établi par les travaux d'Alberto Cruz (Cruz, 2018 et Cruz et al., 2019) sur les puits échantillonnés. D'un point de vue méthodologique, une séparation chimique a été faite afin de maximiser la récupération de zircons. Les roches sédimentaires paléogènes du bassin Foz de Amazonas se caractérisent par une provenance cratonique avec des valeurs très faibles d'ƐNd(0) (de -20.1 à -19.1) et l'absence de zircons plus jeunes que 500 Ma. Les contributions dominantes des âges de zircons Ventuari-Tapajo (2.0 – 1.85 Ga) et Maroni-Itacaiunas (2.2 – 2.0 Ga) indique des sources soit localisées dans le craton amazonien soit dans la ceinture de Gurupi. La presence de zircons stonien (~1 Ga) et Brasiliano (panafricain) inidque une contribution de la province de Borborema. Les roches sedimentaires analysées ont enregistré la transcontinentalisation de l'Amazone qui se marque par le passage de valeurs d'ƐNd(0) caractéristiques de réseau de drainage

cratonique (-20.2 to -14.3) à des valeurs caractéristiques de réseaux andins (-14.2 to -11.4). Ce passage est daté du miocène moyen à au miocène supérieur (11.93 to 10.8 Ma) dans la partie centrale du bassin. Il est enregistré dans des sédiments plus jeune (fin du Miocène supérieur) dans la partie plus septentrionale. La distribution des âges U-Pb sur zircons confirme une provenance andine avec la présence de zircons paléozoïques, crétacés et cénozoïques. Les valeurs d'ƐNd(0) des sédiments pleistocènes (-11.7 à-10.1) suggèrent une source andine. Cependant, cette source andine n'est pas confirmée par la distribution des âges U-Pb puisque aucun zircon plus jeune que 500 Ma n'a été détecté. Cependant, une source andine ne peut être exclue à cause du faible nombre de zircons analysés (n=42). Finalement, nos données encore préliminaires de provenance permettent de montrer i) le contrôle du bouclier amazonien sur l'export des sédiments dans le bassin Foz de Amazonas au cours du Paléogène, et ii) de contraindre la transcontinentalisation de l'Amazone au miocène moyen-supérieur.

RESUMO

Os resultados deste capítulo são expressos na forma de um artigo em preparação que, no momento da submissão deste manuscrito, está aguardando resultados adicionais, em particular a datação U-Pb em zircões, antes de ser finalizado e submetido. O objetivo deste capítulo é reconstruir a rede de paleodrenagem do leste da Amazônia Cenozoica a partir da proveniência de sedimentos de calhas de poços na bacia da Foz do Amazonas. Esse estudo preliminar é o primeiro a apresentar idades U-Pb em zircões em sedimentos pré-Quaternários da bacia da Foz do Amazonas. A idade dos sedimentos analisados foi determinada usando o modelo estratigráfico estabelecido pelo trabalho de Alberto Cruz (Cruz, 2018 e Cruz et al., 2019) nos poços amostrados. Do ponto de vista metodológico, a separação química foi realizada para maximizar a recuperação do zircão. As rochas sedimentares paleogênicas da bacia da Foz do Amazonas são caracterizadas por uma proveniência cratônica com valores muito baixos de ƐNd(0) (de -20.1 a -19.1) e a ausência de zircões mais jovens que 500 Ma. As contribuições dominantes das idades de zircão Ventuari-Tapajó (2.0 - 1.85 Ga) e Maroni-Itacaiunas (2.2 - 2.0 Ga) indicam fontes localizadas no cráton amazônico ou no cinturão Gurupi. A presença de zircões Stonianos (~1 Ga) e Brasilianos (Pan-Africanos) sugere uma contribuição da província Borborema. As rochas sedimentares analisadas registraram a transcontinentalização da Amazônia,

marcada pela transição de valores de ƐNd(0) característicos de redes de drenagem cratônicas (-20.2 a -14.3) para valores característicos de redes andinas (-14.2 a -11.4). Essa transição é datada do Mioceno médio a superior (11.93 a 10.8 Ma) na parte central da bacia. Ela é registrada em sedimentos mais jovens (Mioceno Superior tardio) na parte mais ao norte. A distribuição das idades U-Pb nos zircões confirma uma proveniência andina com a presença de zircões paleozóicos, cretáceos e cenozóicos. Os valores de ƐNd(0) nos sedimentos do Pleistoceno (-11.7 a -10.1) sugerem uma fonte andina. No entanto, essa fonte andina não é confirmada pela distribuição de idade U-Pb, pois não foi detectado nenhum zircão com menos de 500 Ma. Entretanto, uma fonte andina não pode ser descartada devido ao pequeno número de zircões analisados (n=42). Por fim, nossos dados de proveniência ainda preliminares demonstram i) o controle do escudo amazônico sobre a contribuição de sedimentos na bacia da Foz do Amazonas durante o Paleógeno e ii) restringem a transcontinentalização da Amazônia durante o Mioceno Médio-Superior.

5.1 ABSTRACT

The results of this chapter are expressed in the form of an article in preparation which is, at the time of submission of this manuscript, awaiting further results, notably U-Pb dating on zircons before being finalized and submitted. The aim of this chapter is to reconstruct the eastern Cenozoic Amazonian paleo-drainage network from the provenance of cuttings sediments from wells in the Foz de Amazonas basin. This preliminary study is the first to present U-Pb ages on zircons in pre-Quaternary sediments from the Foz de Amazonas Basin. The age of the analyzed sediments was determined using the stratigraphic model established by Alberto Cruz's work (Cruz, 2019 and Cruz et al., 2019) on the sampled wells. From a methodological standpoint, chemical separation was performed to maximize zircon recovery. Paleogenic sedimentary rocks from the Foz de Amazonas basin are characterized by a cratonic provenance with very low ƐNd(0) values (from -20.1 to -19.1) and the absence of zircons younger than 500 Ma. The dominant contributions of Ventuari-Tapajo (2.0 - 1.85 Ga) and Maroni-Itacaiunas (2.2 - 2.0 Ga) zircon ages indicate sources either located in the Amazon craton or in the Gurupi belt. The presence of Stonian (~1 Ga) and Brasiliano (Pan-African) zircons suggests a contribution from the Borborema province. The sedimentary rocks analyzed recorded the transcontinentalization of the Amazon, marked by the transition from ƐNd(0) values characteristic of cratonic drainage networks (-20.2 to -14.3) to values characteristic of Andean networks (-14.2 to -11.4). This transition is dated

from Middle to Upper Miocene (11.93 to 10.8 Ma) in the central part of the basin. It is recorded in younger sediments (late Upper Miocene) in the more northerly part. The distribution of U-Pb ages on zircons confirms an Andean provenance with the presence of Paleozoic, Cretaceous and Cenozoic zircons. ƐNd(0) values in Pleistocene sediments (-11.7 to-10.1) suggest an Andean source. However, this Andean source is not confirmed by the U-Pb age distribution since no zircon younger than 500 Ma was detected. However, an Andean source cannot be ruled out due to the small number of zircons analyzed (n=42). Finally, our still preliminary provenance data demonstrate i) the control of the Amazonian shield on sediment export in the Foz de Amazonas basin during the Paleogene, and ii) constrain the transcontinentalization of the Amazon during the Middle-Upper Miocene.

5.2 INTRODUCTION

Reconstructing the temporal evolution of the source-to-sink system (S2S) may contribute to our understanding of the origin, shaping and evolution of landscapes, which in turn may help to better understand and discuss the respective role of climate and tectonics on erosional fluxes (e.g. Caracciolo et al., 2020; Chew et al., 2020). The Andes – Amazon – Brazilian Equatorial Margin (AAEM) source-to-sink system (S2S) is one of the largest S2S of the world (Callède et al., 2004; Gaillardet et al., 2007; Filizola and Guyot, 2004). The AAEM hosts the impressive Amazon River which ranks number one in terms of global mass transfer from the continents to the oceans. Indeed, the Amazon River supplies about 20% of the water (Callède et al., 2004), ~10% of the dissolved load (Gaillardet et al., 2007) and ~3% of the suspended load (Milliman and Syvitski, 1992) to the world's oceans. More than 95 % of the mean annual suspended sediment flux delivered by the Amazon River is contributed by Andean tributaries (2/3 and 1/3 from the Solimões and Madeira rivers, respectively; Filizola and Guyot, 2004). The sediment contributions of other large cratonic tributaries such as the Negro, Trombetas, Tapajos and Xingu rivers are negligible, and account for less than 5%. The AAEM S2S connect the Andes, the western Amazonian retroarc foreland basins, the Brazilian intracratonic basins and the Amazon Craton (Brazilian and Guiana Shields), to the Foz do Amazonas Basin (Fig. 5.1). The geological history of the AAEM S2S is strongly linked to the geological history of the Amazonian Andes (see Mora et al., 2010; Eude et al., 2015), Amazonian retroarc foreland basins (see Horton, 2018, Roddaz et 2010), the Amazonian intracratonic basins (see Horbe et al., 2019;

Caputo and Soares, 2016; Nogueira et al., 2013; Hoorn, 1994) and the Foz de Amazonas basin (Cruz et al., 2019 ; Mason et al., 2019, 2022 ; Rouby et al., 2023 ; Figueiredo et al., 2009 ; Hoorn et al., 2017, 2010). It is also linked to the geological history of the Amazon River which experienced several directional shifts during the Meso-Cenozoic (Hurtado et al., 2018; Rodrigues et al., 2023; Caputo e Soares, 2016; Sacek, 2014; Shephard, et al., 2010; Potter, 1997).

The most remarkable geomorphic change in the South America platform during the Cenozoic is the uplift of the Andes produced by the shortening associated to the Late Cretaceous-Cenozoic Andean orogeny (e.g. Armijo et al, 2015; Martínez et al., 2023; Faccenna et al., 2017; Horton and Fuentes, 2016; Eakin et al., 2014; Hoorn et al., 2010; Schellart, 2010; Ramos, 1999). The uplift of the Andes plays a crucial role in the topographical variations of South America, shifting the hinterland drainage pathways fromEast directed paleo drainage in the Cretaceous with a source located in the Amazon Craton to a W directed paleo drainage during the Cenozoic (e.g. Potter, 1997; Hurtado et al., 2018; Rodrigues et al., 2023). Later, during the Neogene, the uplift of the Andes is thought to be the mechanism responsible of the existence of a transcontinental Amazon River (Figueiredo et al., 2009; Hoorn et al., 2010; 2017; Mora et al., 2010; van Soelen et al., 2017). However, the timing of the onset and development of the transcontinental Amazon River-fan system is still a matter of controversy ranging between the early Miocene (18.3 Ma) (van Soelen et al., 2017), late Miocene (11.8 to 11.3 Ma) (Figueiredo et al., 2009), (9.4 to 9.0 Ma) (Hoorn et al., 2017), and late Pliocene (ca. 2.5 Ma) (Campbell, 2010). In addition to this controversy, the post transcontinental paleogeography of the Amazon Basin is virtually unknown. Also little is known about the Paleogene configuration of the AAEM, the paleodrainage of the western and eastern Amazonian basins, and the sources that feeded the the Foz de Amazon Basin. This is because the sedimentary record of intracratonic basin of these period is difficult to access and lack of precise biostratigraphic dating. This is not the case for the Foz de Amazonas Basin where the entire Cenozoic sequence is well conserved. Hence, as a major zone of sedimentation in the source-to-sink AAEM system, access to the Cenozoic sedimentary record of the Foz do Amazonas Basin is crucial for reconstructing the Paleogeography of eastern Amazonia before the existence of a transcontinental Amazon River. Provenance studies involving Sm-Nd-Sr isotopic composition of fine grained sedimentary rocks as well as U-Pb zircons have been proven to be useful for reconstructing paleo drainage network and geodynamic

evolution of the Amazon Basin during the Meso-Cenozoic (i.e. Figueiredo et al., 2009; Hoorn et al., 2017; Horbe et al., 2019, 2014; Hurtado et al., 2018; Louterbach et al., 2017; Roddaz et al., 2005b; Rodrigues et al., 2023; van Soelen et al., 2017). However, despite the existence of provenance studies using Sm-Nd isotopic compositions of Neogene sediments from the Foz de Amazonas Basin (Figueiredo et al., 2009; Hoorn et al., 2017; van Soelen et al., 2017), to date there is no provenance study regarding pre Pleistocene sediments of the Foz de Amazonas Basin that use U-Pb zircon detrital ages.

In this work, we analyze the provenance of the the Paleogene - Pleistocene sedimentary record of the Foz de Amazonas Basin by measuring the Sm-Nd isotopic composition of leached clay material and U-Pb zircon ages. This unique dataset allow us to propose new paloegeographic maps during the Paleogene that will help to better constrain the geological history of the biggest S2S on earth.

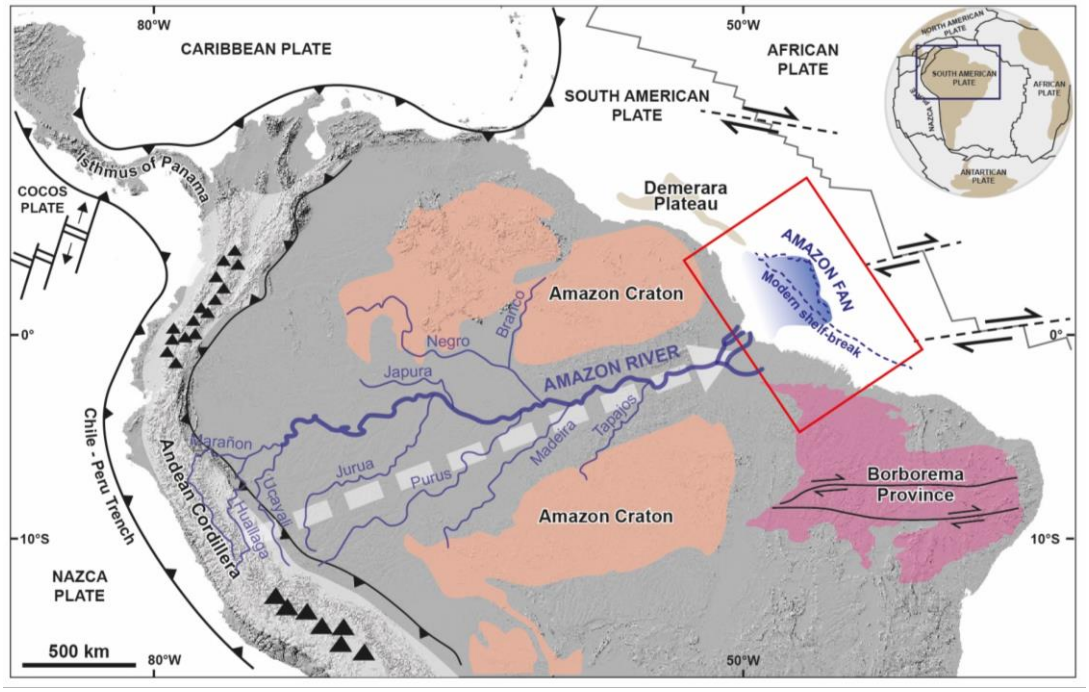


Figure 5. 1 Simplified geologic map of the northern South American plate showing main geotectonic units. From source-to-sink is exhibited the Andes mountain chain, intracratonis basins, Amazon Craton, Borborema Province (NE Brazil) and the Brazilian Equatorial Margin. The red box, in detail, indicates the geographic location of the Foz do Amazonas Basin (study area).

5.3 GEOLOGICAL SETTING

The Foz do Amazonas Basin is an offshore basin situated in the northwesternmost part of the Brazilian Equatorial Atlantic Margin, and it covers an area of about 360.000

km^2 (Figure 5.2) (Silva et al., 1998). A distinct feature of this basin is the presence of the largest river-fed mud-rich submarine fan system in the world (Damuth et al., 1988) and therefore, this basin provides a unique record of the geological history of the Amazon River and the surrounding region.

The geologic evolution of the Brazilian Equatorial Margin was intrinsically related to the fragmentation of Gondwana and the opening of the Atlantic Ocean (Darros de Matos, 2000). Such tectonic setting was mainly formed by two phases: the first started during the Triassic-Jurassic (225-145 Ma) and, the later one was marked by the major rifting event dated as Early Cretaceous (~120-105 Ma), when transtensional conditions prevailed (Darros de Matos, 2000).

The stratigraphic filling of the Foz do Amazonas Basin comprises three main stages : Pre-Rift, Rift and Drift (Fig. 5.3) (Figueiredo et al., 2007). The Pre-Rift encompasses to the Triassic-Jurassic vulcanossiliciclastic succession represented by the Calçoene Fm., characterized by the intercalation of red-brown sandstones and basaltic lavas (235 – 194 Ma), which was related to the central North Atlantic Ocean caused by rifting and magmatism events (CAMP - Central Atlantic Magmatic Province) (Fig. 5.3) (Marzoli et al., 2018; Peyve, 2013; Figueiredo et al., 2007; Darros de Matos, 2000; McHone, 2000; Baksi and Archibald, 1997). The Rift phase is marked by a predominance of distensive regime and generation of basins, promoting the stablishment of normal faults that spaned the Early Cretaceous epoch (Cassiporé Fm.) (Fig. 5.3) (Figueiredo et al., 2007). The Drift stage is related to the sea spreading, which spans from the Late Cretaceous (Fm. Limoeiro) through Cenozoic (Paleogene – Neogene, Marajó / Travosas Fms) and, the first appearance of a carbonate platform (Amapá Fm.) (Fig. 5.3) (Figueiredo et al., 2007). The top of the Amapá carbonates was positionated at 10.5 Ma by Figueiredo et al. (2007), mainly based on biostratigraphic zonations, however more recent studies have proposed ages varying between 11.8 and 8.3 Ma (e.g. Cruz et al., 2019; Hoorn et al., 2017; van Soelen et al., 2017; Stewart et al., 2016; Nogueira et al., 2013; Gorini et al., 2014; Figueiredo et al., 2009; 2010).

The Foz do Amazonas Basin recorded a sharp shift from predominantly carbonate contribution to siliciclastic sedimentation in the Late Miocene (Cruz et al., 2019; Hoorn et al., 2017; van Soelen et al., 2017; Stewart et al., 2016; Nogueira et al., 2013, 2021; Gorini et al., 2014; Figueiredo et al., 2009; 2010). As a consequence, the Amapá carbonate platform was demised by an expressive siliciclastic input, from the Late Miocene to the

present, depicted by Orange, Pirarucu and Tucunaré Fms. (Pará Group), which stablish the Amazon Fan (Fig. 5.3) (Figueiredo et al., 2007).

5.3.1 Cenozoic sequence of the Foz do Amazonas Basin

The overall Cenozoic sedimentary sequence was mainly related to the seafloor spreading and the establishment of the Amazon fan domain, which allowed a mixed shelf carbonate-siliciclastic deposition in the Drift phase (Fig. 5.2). Despite the Drift phase began in Late Albian, it prevailed during the Cenozoic, from Paleocene onwards (Figueiredo et al., 2007).

The Drift phase is characterized by transgressions and regressions events and it encompasses three sedimentary successions: siliciclastic marine deposition (Late Albian to Early Paleocene – Limoeiro Formation), mixed carbonate-siliciclastic sequence (Middle Paleocene to Middle Miocene – Amapá, Marajó and Travosas Formations), and a huge terrigenous input (Late Miocene to Holocene – Pará Group) (Fig. 5.2) (da Cruz et al., 2021 ; Figueiredo et al., 2007).

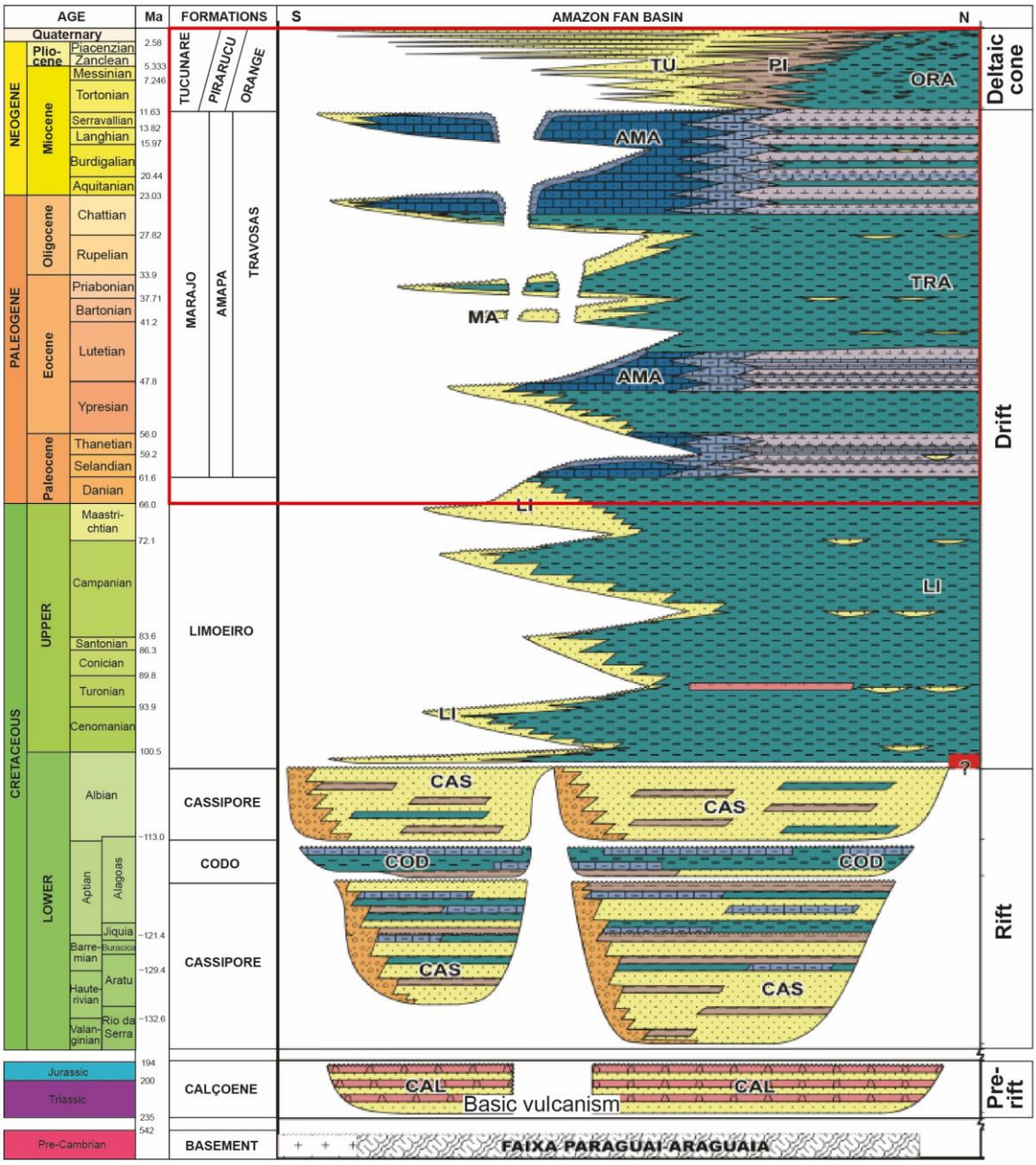


Figure 5. 2 Stratigraphic chart of the Foz do Amazonas Basin (simplified from Figueiredo et al., 2007). The red box indicates the geologic time interval investigated in this study.

The Limoeiro Fm. started with late Albian (~102 Ma) open-marine clastic deposition and is characterized by the interdigitation of deep-water mudstones / siltstones and sandstones, that lasted until the Paleocene (~59 Ma), and is capped by Amapá carbonate layers (Figueiredo et al., 2007).

The late Paleocene to middle Miocene Amapá Fm. is composed by a stable carbonate shelf deposited in shallow water zone, where platform calcilutites and calcarenites prevailed (da Cruz et al., 2021 ; Figueiredo et al., 2007). The Marajó Fm. is

mainly composed by muddy deltaic sediments, deposited on the inner continental shelf in a passive margin context (Boulila et al., 2020; Cruz et al., 2019; Figueiredo et al., 2007; Pasley et al., 2005). The mixed carbonate-siliciclastic platform (Marajó and Amapá Fms.) was laterally equivalent to the Travosas Fm. (Fig. 5.2) (Brandão and Feijó, 1994 ; Figueiredo et al., 2007). As pointed by Pasley et al. (2005), the significant clastic material from Travosas Fm. was probably delivered into the basin during a event of sea-level lowstand occurred in Oligocene.

The Amazon carbonate shelf had been affected by the transition from carbonate to terrigenous sedimentation driven by changes in Amazon River drainage pathway, which favoured the huge influx of sediment into the Foz do Amazonas Basin and the stablishment of the expressive Amazon fan sedimentation (Cruz et al., 2019; Gorini et al., 2014; Flood and Piper, 1997; Reis et al., 2010). Such setting culminated in the deposition of deep-water mud facies (Orange Fm.), continental slope fine sand and clay facies (Pirarucu Fm.), interdigited with the shoreline facies (Tucunaré Fm.) (Fig. 5.2) (Brandão and Feijó, 1994 ; Figueiredo et al., 2007). Additionally, gravity-driven slope processes created a load-induced flexure that affected the entire marine sequences of the Foz do Amazonas Basin, including the topmost Amazon Fan (Reis et al., 2010 ; Perovano et al., 2009).

5.3.2 Potential sources

Detrital zircon U-Pb ages have widely been used in provenance studies in the AAEM basins to reconstruct the main contributions during of the Andean and cratonic sources the Cretaceous – Cenozoic (Rodrigues et al., 2023; Moizinho et al., 2022; Moreno et al., 2022; 2020; George et al., 2019; Mason et al., 2019; 2022; Horton, 2018; Hurtado et al., 2018; Louterbach et al., 2017; Pepper et al., 2016; Horton et al., 2010; Mapes et al., 2005). The potential source-areas of sediments to Cenozoic deposits in the Foz do Amazonas Basin have complex evolution and composition, with different types of terranes and ages (Fig. 5.3). Precambrian zircon U-Pb ages (> 900 Ma) can be found in three distinct areas: the Amazon Craton (Guiana and Brazilian shields), the São Luís Craton and the Borborema Province (Fig. 5.3) (Caxito et al., 2020; Dantas et al., 2013; Van Schmus et al., 2003, 2008, 2011; Bettencourt et al., 2010; Cordani and Teixeira, 2007; Klein et al., 2005; Dantas et al., 2004; Brito Neves et al., 1995, 2001, 2003; Santos et al., 2000; Tassinari and Macambira, 1999). The rocks related to Transamazonic Orogenic cycle (Amazon and São

Luís cratons as well as the Gurupi Belt) can also source Foz do Amazonas Basin (Costa, 2000; Palheta et al., 2009; Klein et al., 2020a, b).

Zircon U-Pb ages between 900-500 Ma may be associated with rocks originated from the fold and thrust belts that emerged during the assembly of the supercontinent Gondwana, which were affected by the Brazilian Event (Brito Neves, 2003), and by magmatic events linked to orogenic cycles that occured in western Gondwana (Chew et al., 2008, 2016) (Fig. 5.3) or recycling from the Paleozoic Parnaíba Basin (Hollanda et al., 2018).

Younger detrital zircon U-Pb ages (< 500 Ma) are mainly related to an Andean signature. As showed by Chew et al. (2016), contributions of Famatinian (500-400 Ma), Paleozoic Magmatic Arc (400-260 Ma) zircons population are interpreted to be sourced by magmatic and metamorphic rocks of the Eastern Cordillera. While, the Western Cordillera is mainly attributed to Cretaceous (< 145 Ma) (Litty et al., 2017) and Cenozoic (< 65 Ma) (Navarro et al., 2010; Chiaradia, 2009) zircon population.

Additionally, source contributions are also defined by Nd isotopes, which are not easily fractionated by sedimentary or post-depositional processes (McLennan et al., 1990). The lowest ƐNd(0) values (-14.5 to -20) are mainly attributed to Cratonic-derived river sediments, while Andean-derived sediments have εNd(0) values > −13.8 (Figueiredo et al., 2009; Horbe et al., 2014; Roddaz et al., 2005b).

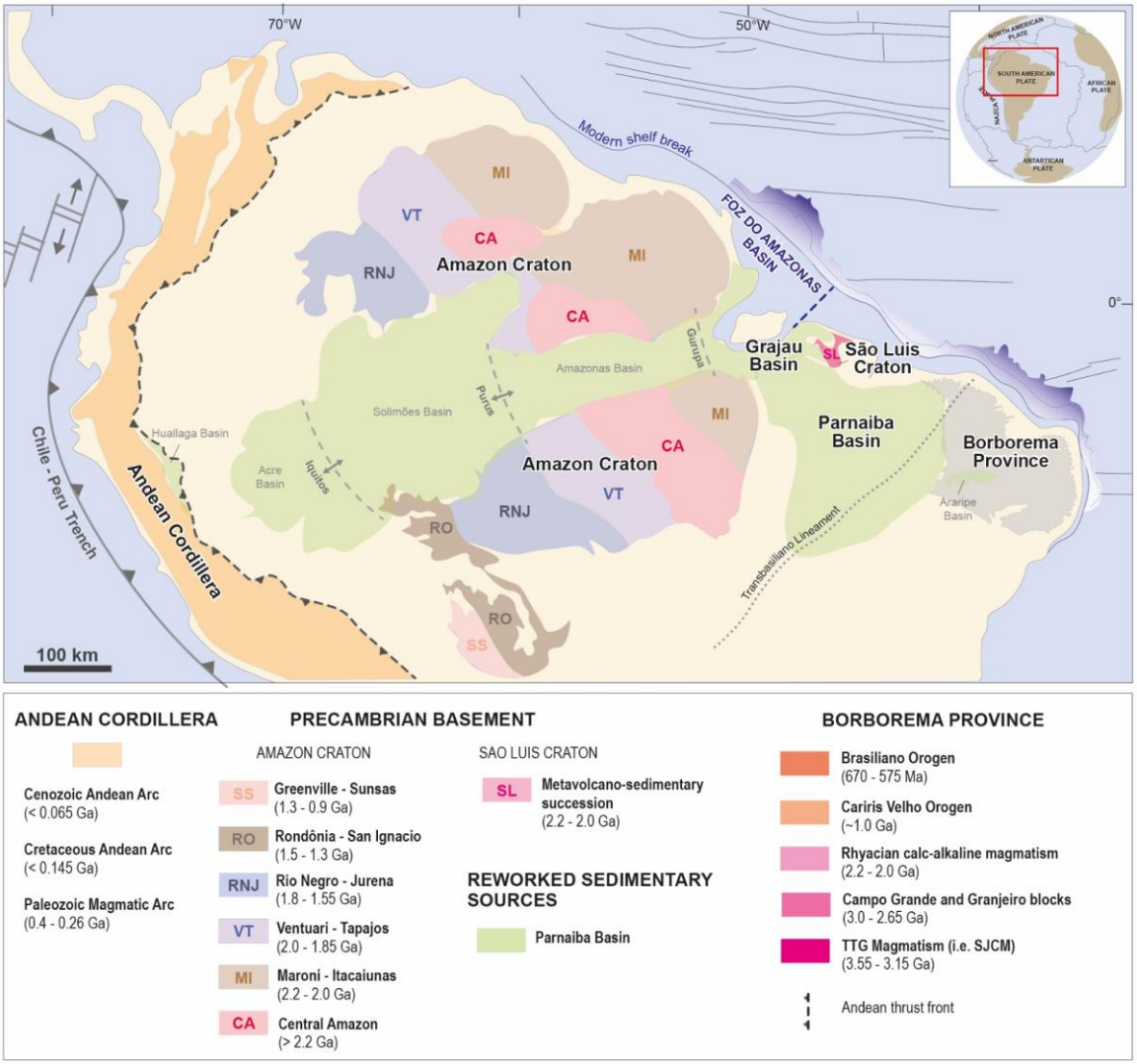


Figure 5. 3 The potential source-areas to source-to-sink Andes – Amazon – Brazilian Equatorial Margin system located in northern South American plate (Caxito et al., 2020; Dantas et al., 2004, 2013; Cordani and Teixeira, 2007; Klein et al., 2005; Brito Neves et al., 1995, 2003; Van Schumus et al., 2003; Santos et al., 2000; Tassinari and Macambira, 1999; Hollanda et al., 2018; Rodrigues et al., 2023; Moizinho et al., 2022; Hurtado et al., 2018; Costa, 2000; Palheta et al., 2009; Klein et al., 2020a, b; Litty et al., 2017; Navarro et al., 2010; Bettencourt et al., 2010; Chiaradia, 2009).

5.4 MATERIALS AND METHODS

5.4.1 Data acquisition

The samples were obtained from five exploratory wells located from inner to outer shelf of the Foz do Amazonas Basin, in the NW and Central sectors (Fig. 5.4). The requested wells are identified as : 1APS 0018AP ; 1APS 0023AP ; 1APS 0024AP ; 1APS25AP and 1APS33EAP. Downhole information comprises the well code identification (ID), sample depth (m) and geographic position (Table 5.1). The acquisition

of technical data and lithological cores were requested to the Brazilian National Agency of Petroleum, Natural Gas and Biofuels (ANP) and Petrobras. In order to encompass all the Cenozoic time interval, all analyzed samples were chosen based on their chronostratigraphic position, based on an age model from biostratigraphic data (well 33E, Figueiredo et al., 2007) and on refined biostratigraphic framework from correlations of seismically-defined stratigraphic units (Cruz et al., 2019). Additional criterious to the selection of the samples, such as: availability of the cores recovered; sample sufficient amount; chronostratigraphic position, with exemplars from base, middle and top of the unit were also taken in account.

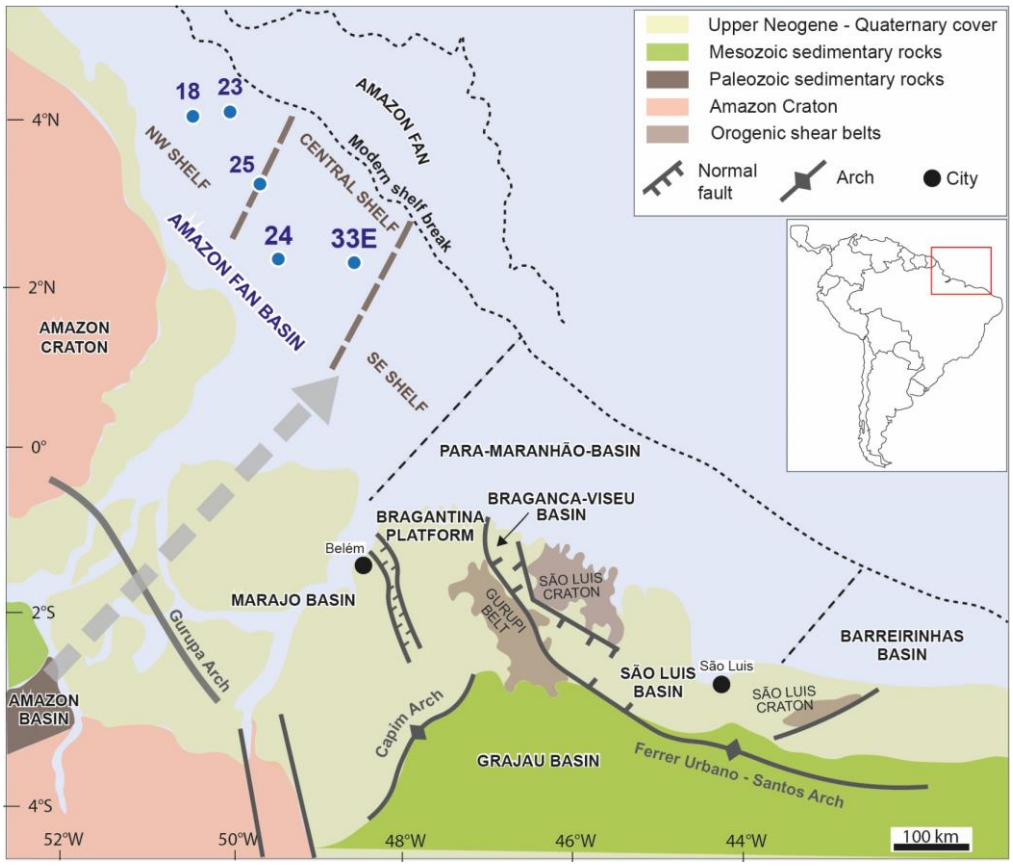


Figure 5. 4 Geological map of study area and adjacent basins, indicating the geographic location of the five (5) studied cores (blue circles), exhibiting simplified codes. Small dashed lines show the modern shelf break. The onshore and offshore basins are bounded by large dashed lines, while the strutures zones are limited by dark solid lines. (18) 1APS0018AP; (23) 1APS0023AP; (24) 1APS0024AP; (25) 1APS25AP and (33E) 1APS33EAP.

5.4.2 Whole-rock Sm-Nd isotopes

For the Sm-Nd isotopic analysis, twenty-three (23) samples of fine-grained sedimentary rocks were selected (Table 5.1; Figure 5.5). Before the chemical techniques,

all the selected samples were crushed in an agate mortar. Thereafter, they were conducted to a sequential leaching procedure, realized at the Laboratório de Geoquímica e Água (LAGEQ/UnB), in order to separate the Fe – Mn oxides and the detrital fraction from marine sediments (Bayon et al.; 2002). This stage was followed by a sample digestion procedure, which comprises the separation of REEs, Sm and Nd elements using chromatography columns (Gioia and Pimentel, 2000), that it was conducted at the Laboratório de Estudos Geodinâmicos, Geocronológicos e Ambientais (LEGGA) of the Universidade de Brasília (UnB). The isotopic ratios ($^{147}Sm/ ^{144}Nd$ and $^{143}Nd/ ^{144}Nd$) were measured using the Neptune Series High Resolution Multicollector ICP-MS. The accuracy of the measurements was estimated by repeated analysis of the BHVO-2 standard. The correction of the signal for the mass fractionation of $^{143}Nd/ ^{144}Nd$ ratio was done by the normalization with $^{146}Nd/ ^{144}Nd = 0.7219$. The measurements of $^{143}Nd/ ^{144}Nd_{sample}$ and $^{143}Sm/ ^{144}Nd_{sample}$ ratios are exhibited in epsilon notation (DePaolo, 1988) and express the fractional deviation in parts per 10^4 unit from the Chondritic Uniform Reservoir (CHUR) (Jacobsen and Wasserburg, 1980).

5.4.3 Detrital zircon geochronology

Zircon geochronology is widely applied as a sedimentary provenance signature to precisely and accurately date rocks via U-Pb decay. LA-ICP-MS U-Pb analysis of detrital zircons from five distinct core samples (1APS 0018AP ; 1APS 0023AP ; 1APS 0024AP ; 1APS25AP and 1APS33EAP). We analyzed zircon grains from 4 selected sandstones exemplars (Figure 5.5; 5.6), in order to cover the source-areas from all the Cenozoic stratigraphic units of Foz do Amazonas Basin. Samples were performed at the Laboratório de Estudos Geodinâmicos, Geocronológicos e Ambientais (LEGGA/UnB).

The concentration of almost pure zircon aliquot was obtained based on an efficient procedure developed and proposed by Oliveira et al. (2022). This method uses a combination of physical separation and chemical dissolution, through a series of acid digestions: aqua-regia, hydrofluoric acid, aqua-regia and finally hydrochloric acid. This procedure was possible due the fact that zircon is one of the few minerals that can survive this bulk rock acid attack (Oliveira et al., 2022).

A random selection of the zircon grains (~120 grains per sample) was done under stereomicroscope and mounted on adhesive tape over a thin-section; then they were

enclosed in a 9-mm-diameter plastic ring placed on the tape around the zircons and filled with epoxy resin. Finally, the zircon grains were polished to expose their centers (Gehrels, 2014; Bühn et al., 2009; Gehrels et al., 2008). To provide a base map for recording laser spot positions and to identify morphological features of the zircon grains, the mounts were imaged by a Scanning Electron Microscope (SEM).

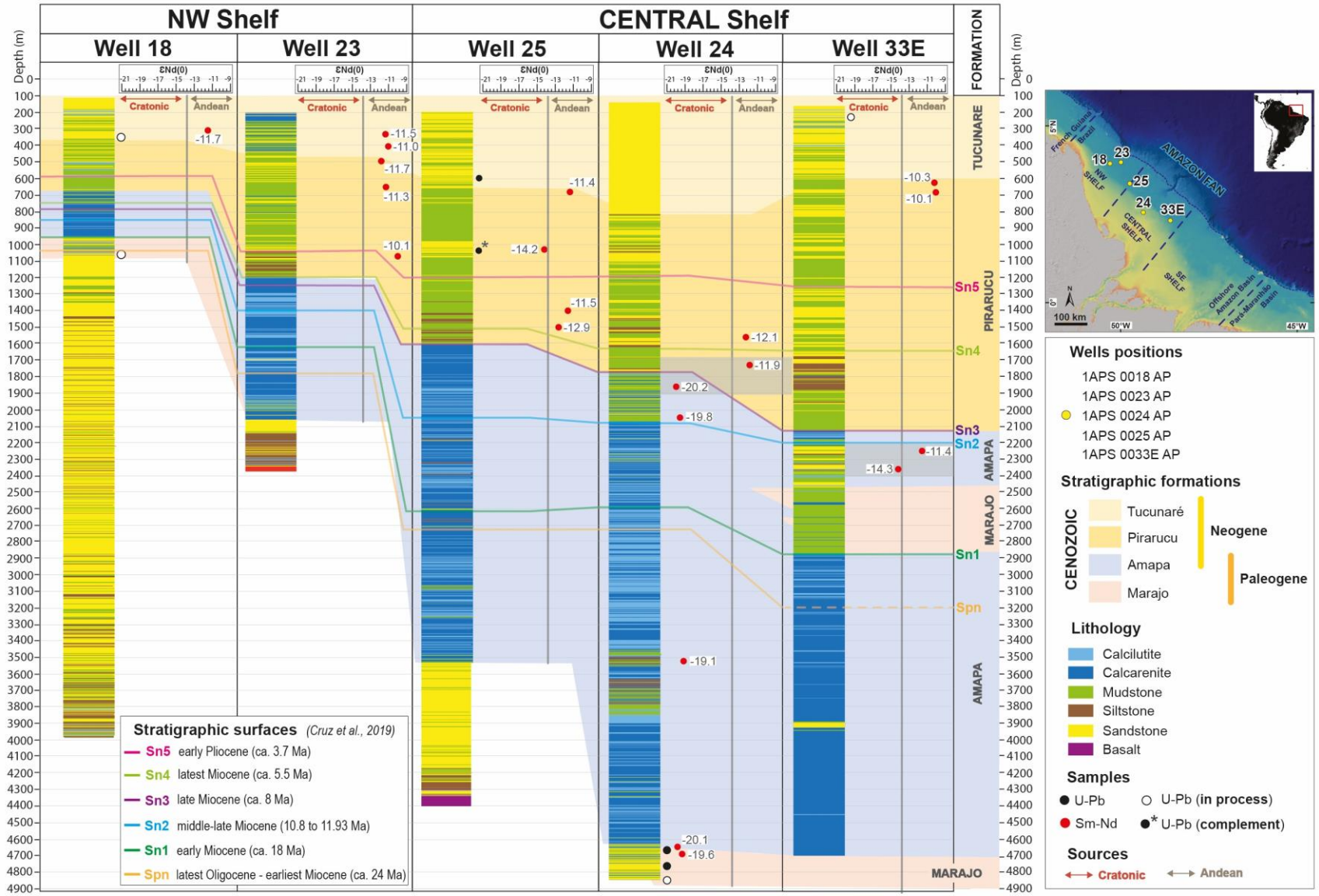
The masses of interest were measured on a Thermo Finningan Element XR high-resolution single-collector sector field Inductively Coupled Plasma Mass Spectrometry (ICP-MS) coupled to a 193 nm Iridia Excimer (ArF) laser ablation system. Each analysis consisted of 10 s of background measurement followed by 20 s of sample acquisition. The raw data were processed on Iolite 4.0 (Paton et al., 2011) as a time-resolved signal and individual signal inspection was done with the assistance of VizualAge (Petrus and Kamber, 2012). Data correction included blank subtraction, Laser Induced Elemental Fractionation (LIEF) correction using an exponential plus linear model and normalization using the GJ-1 zircon (Jackson et al., 2004) and 91500 zircon (Wiedenbeck et al., 1995). A systematic uncertainty of ca. 1% is propagated on each final age. No common lead correction was applied. The ages uncertainties are quoted at 2 sigma (2σ) confidence level.

The large numbers of samples and amounts of distributional data requires quantitative and objective methods, such as multidimensional scaling (MDS) to analyze them (Vermeesch, 2013; Vermeesch et al., 2016). To improve the method, we applied Kolmogorov–Smirnov (KS) statistic that is a measure used to compare samples distributions. A smaller and larger KS distance indicates more or less dissimilarity between the distributions, respectively (Vermeesch, 2013).

5.5 RESULTS

The preliminary dataset presented in this draft include the localization of cutting samples on the selected wells with the biostratigraphic scheme proposed by Cruz et al. (2019), the variation of Sm-Nd isotopic compotions and the U-Pb age distributions of detrital zircons of the analyzed samples (Fig. 5.5).

Figure 5. 5 Regional Central-NW cross-section displaying all five wells studied in the Foz do Amazonas Basin. In detail, litotratigraphic units (Figureiredo et al., 2007); stratigraphic surfaces; cuttings locations (U-Pb, Sm-Nd); distribution of the ƐNd(0) isotopic compositions along the interval. The colored lines indicate the stratigraphic surfaces (surfaces Spn and Sn1 to Sn5) proposed by Cruz et al. (2019). Well 33E after Figueiredo et al. (2009).


NW Shelf
CENTRAL Shelf
Well 18
Well 23
Well 25
Well 24
Well 33E
FORMATION
Depth (m)
εNd(0)
Cratonic
Andean
TUCUNARE
PIRARUCU
AMAPA
MARAJO
Sn5
Sn4
Sn3
Sn2
Sn1
Spn
Stratigraphic surfaces (Cruz et al., 2019)
Sn5 early Pliocene (ca. 3.7 Ma)
Sn4 latest Miocene (ca. 5.5 Ma)
Sn3 late Miocene (ca. 8 Ma)
Sn2 middle-late Miocene (10.8 to 11.93 Ma)
Sn1 early Miocene (ca. 18 Ma)
Spn latest Oligocene - earliest Miocene (ca. 24 Ma)
AMAZON FAN
NW SHELF
CENTRAL SHELF
SE SHELF
Offshore Amazon Basin
Pará-Maranhão Basin
100 km
Wells positions
1APS 0018 AP
1APS 0023 AP
1APS 0024 AP
1APS 0025 AP
1APS 0033E AP
Stratigraphic formations
CENOZOIC
Tucunaré
Pirarucu
Amapa
Marajo
Neogene
Paleogene
Lithology
Calcilutite
Calcarenite
Mudstone
Siltstone
Sandstone
Basalt
Samples
U-Pb
U-Pb (in process)
Sm-Nd
U-Pb (complement)
Sources
Cratonic
Andean

5.5.1 Sm-Nd isotopes

The Sm-Nd isotopic compositions of the Cenozoic sedimentary rocks of the Amazon Fan Basin are shown in Table 5.1 and Figure 5.5. The ƐNd(0) values of the analyzed samples ranges from -10.1 to -20.2 (Table 5.1; Fig. 5.5). The Paleogene to latest Oligocene samples yields the lowest ƐNd(0) values (-20.1 to -19.1) (Table 5.1; Fig. 5.5). The middle-late to late Miocene samples of the APS24 well (APS24_2049-1851) are also characterized by negative ƐNd(0) values ranging from -20.2 to 19.8 (Table 5.1; Fig. 5.5). However, the middle-late Miocene sample core APS33E (2390-2250m), have less negative ƐNd(0) values (ƐNd(0) -14.3 to -11.4) (Table 5.1; Fig. 5.5). The ƐNd(0) values becomes less negative for the youngest late Miocene to recent samples (from – 12.9 to -10.1) with the exception of one early Pliocene sample (APS_25 1005) which has a more negative ƐNd(0) value (-14.2).

Age	Sample	Sm (ppm)	Nd (ppm)	Sm/Nd	$^{147}Sm/^{144}Nd$	$^{143}Nd/^{144}Nd$	± 2SE	ƐNd(0)	TDM (Ga)
Early Pliocene to Recent (ca. 3.7 to Recent)	APS18_306	8.008	44.342	0.181	0.109	0.512041	3	**-11.7**	1.45
	APS23_381	2.956	45.259	0.065	0.0395	0.512048	9	**-11.5**	0.87
	APS23_459	2.575	42.384	0.061	0.0367	0.512073	14	**-11.0**	0.84
	APS23_489	2.819	39.068	0.072	0.0436	0.512038	8	**-11.7**	0.90
	APS33E_620	9.947	44.175	0.225	0.1361	0.512108	20	**-10.3**	1.82
	APS23_651	2.633	38.162	0.069	0.0417	0.512060	18	**-11.3**	0.87
	APS25_669	9.700	44.270	0.219	0.1324	0.512056	4	**-11.4**	1.84
	APS33E_680	12.326	48.297	0.255	0.1543	0.512119	12	**-10.1**	2.36
	APS25_1005	4.891	37.452	0.131	0.0789	0.511910	49	**-14.2**	1.27
	APS23_1080	3.409	37.293	0.091	0.0553	0.512118	15	**-10.1**	0.89
Latest Miocene to early Pliocene (ca. 5.5 - 3.7 Ma)	APS25_1401	7.906	53.118	0.149	0.0900	0.512050	41	**-11.5**	1.22
	APS25_1500	28.705	45.432	0.632	0.3819	0.511978	39	**-12.9**	1.05
	APS24_1575	2.732	41.696	0.066	0.0396	0.512019	11	**-12.1**	0.90
Late Miocene to latest Miocene (ca. 8 - 5.5 Ma)	APS24_1701	3.019	42.579	0.071	0.0429	0.512029	7	**-11.9**	0.91
Middle-late to Late Miocene (10.8 - 8.0 Ma)	APS24_1851	10.143	36.760	0.276	0.1668	0.511602	6	**-20.2**	5.12
	APS24_2049	4.405	47.426	0.093	0.0561	0.511622	6	**-19.8**	1.37
Middle-late Miocene (11.93 - 10.8 Ma)	APS33E_2250	13.812	36.490	0.379	0.2288	0.512052	12	**-11.4**	
	APS33E_2390	3.713	46.518	0.080	0.0483	0.511907	5	**-14.3**	1.04
Paleogene - latest Oligocene (56 to 24 Ma)	APS24_3519	3.173	27.364	0.116	0.0701	0.511657	25	**-19.1**	1.46
	APS24_4659	3.638	43.212	0.084	0.0509	0.511608	10	**-20.1**	1.34
	APS24_4671	7.212	59.452	0.121	0.0733	0.511633	4	**-19.6**	1.52

Table 5. 1 Sm-Nd isotopic compositions of sedimentary rocks analyzed accross the Cenozoic of the Foz do Amazonas Basin.

5.5.2 U-Pb zircon ages

The U-Pb zircons ages of the analyzed Cenozoic samples of the Foz do Amazonas Basin can be found in the Supplementary data file and are shown in Figure 5.6.

5.5.2.1 Paleogene

A total of 205 spot analyses distributed in two samples (APS24_4770-4665) from the Paleogene Marajo Fm. were performed. However, of the 205 analyses, only 97 yield concordant values (Supplementary data and Fig. 5.6). The U-Pb age distribution of the analyzed samples shows a multimodal pattern and show zircons older than 500 Ma. The U-Pb age distribution is dominated by two main population between Ventuari-Tapajos (2.0 – 1.85 Ga, 22%) and Maroni-Itacaiunas (2.2 – 2.0 Ga, 15 %). Other subordinate populations include Grenville/Sunsas and/or Cariris Velho (at ~1.0 Ga, 7%) and Brasiliano (670 – 575 Ma 7%) and Rondonia-San Ignácio (1.5 – 1.3 Ga, 10%) (Fig. 5.6).

5.5.2.2 Neogene (Middle – late Miocene to early Pliocene)

A total of 100 spot analyses were performed in the APS25_1011 sample from the Neogene Pirarucu Fm. with only 63 concordant U-Pb ages (Supplementary data and Fig. 5.6). The U-Pb ages distribution present dominant peaks at 1.0 Ga (Grenville/Sunsas and/or Cariris Velho, 30%) and 2.0 – 1.85 Ga (Venturari-Tapajos, 17%), respectively (Fig. 5.6). Subordinate population include Brasiliano (670 – 575 Ma, 7%) and Rondonia-San Ignácio (1.5 – 1.3 Ga, 4%) zircon ages. This sample contain zircon ages younger than 500 Ma with Paleozoic (n= 5), Cretaceous (n= 2) and Cenozoic (n= 2) zircons

5.5.2.3 Quaternary (Pleistone to Recent)

The younger sample analyzed in the Cenozoic succession was collected in the Pleistocene to Recent Tucunaré Fm. A range of 120 U-Pb zircon ages were measured and, 42 yield concordant values (APS25_600) (Supplementary data and Fig. 5.6). Such huge discordance allowed to identy few clusters. U-Pb detrital zircon ages younger than 500 Ma were not observed in this sample but their presence cannot be excluded. The dominant zircon age populations include Maroni-Itacaiunas (2.2 – 2.0 Ga, 17 %), and Rio Negro Jurena (1.8 – 1.55 Ga, 19%) zircon ages (Fig. 5.6). Subordinate population include Grenville/Sunsas and/or Cariris Velho (0.9 – 1.3 Ga, 11%) and Brasiliano (670 – 575 Ma, 9%) (Fig. 5.6).

5.6 DISCUSSION

New detrital zircon U-Pb age spectra and Nd isotopic compositions help shed light on the sedimentary evolution of the Foz do Amazonas Basin and the paleogeographic reconstruction of the adjacent catchments areas, in northern Brazilian Equatorial Margin during the Cenozoic (Fig. 5.5; 5.6).

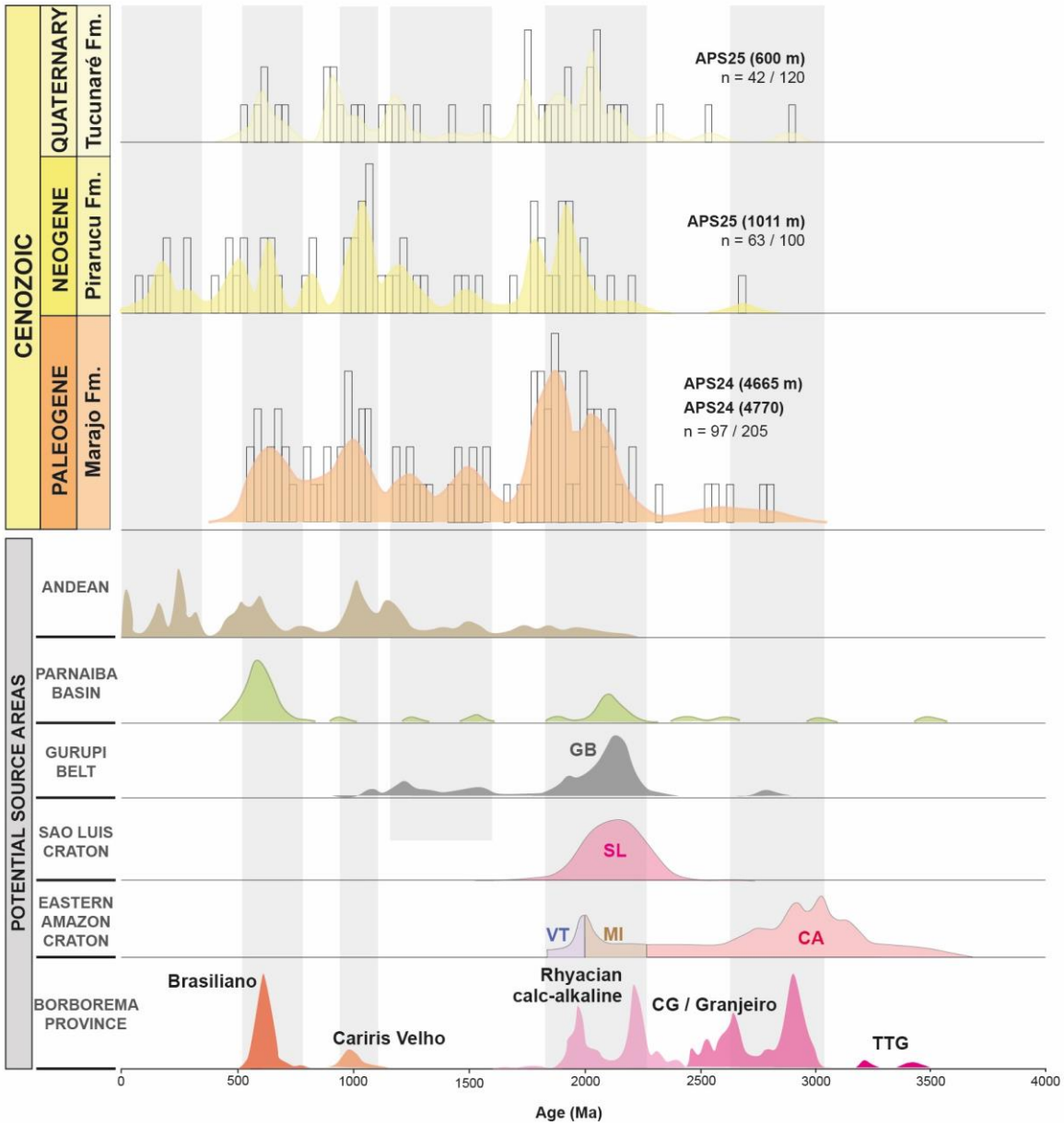


Figure 5. 6 Histograms of the zircon ages distribution displayed as Kernel density estimate plots (KDE) of each sample analyzed in this study correlated with potetial sources.

5.6.1 Interpretation of provenance

5.6.1.1. Paleogene

The analyzed Paleogene sedimentary rocks are characterized by negative ƐNd(0) values (-20.1 to -19.1) which tipify cratonic-derived sedimentary rocks (Table 5.1; Fig. 5.5) (Figueiredo et al., 2009; Horbe et al., 2014; Moizinho et al., 2022; Roddaz et al., 2005b). These ƐNd(0) values are similar to those of the late Cretaceous Ipixuna Fm and Pirabas Fm (Moizinho et al., 2022), and to those of Tapajos and Maroni Suspended Particular Matters (SPM) (Allègre et al., 1996; Rousseau et al., 2019) suggesting that the analyzed Paleogene sedimentary rocks are sourced by the Amazon craton. A cratonic origin for the Paleogene sedimentary rocks is also confirmed by the U-Pb zircon age distribution because there is no zircon younger than 500 Ma that characterized Andean rocks (Fig. 5.6) (Hurtado et al., 2018). Additionally, the dominance of Ventuari-Tapajo (2.0 – 1.85 Ga) and Maroni-Itacaiunas (2.2 – 2.0 Ga) zircons ages indicate sources that may be located i) in the Amazon Craton (Tassinari et al., 2000; Tassinari and Macambira, 1999) and in the Purus Arch (Rodrigues et al., 2023), ii) in the Gurupi Belt because they contain theTromaí Intrusive Suite (2168–2147 Ma), the Tracuateua Suite (2086–2091 Ma), the Negra Velha Granite (2056–2076 Ma) and the Japiim Granite (2116–2072 Ma) (Klein et al., 2020a) and iii) the Borborema Province - Alto Moxoto Terrane (2.0 - 2.2 Ga) (Caxito et al., 2020; Van Schumus et al., 2008; 2011; Brito Neves et al., 2001). However, the presence of subordinate Grenville/Sunsas stonian (at ~1.0 Ga,) and Brasiliano zircon ages further suggest that the Borborema province sourced the Paleogene sedimentary rocks because of the presence of the Cariris Velhos suite in Borborema Province, that is characterized by U-Pb zircon ages of 1.1 – 0.95 Ma and the presence of extensive Brasiliano rocks (Van Schmus et al., 2008, 2011; Brito Neves et al., 1995, 2003, 2005). In the MDS graph (Fig. 5.7) which is used to represent statistically the degree of similarity in U–Pb zircon age distribution between analyzed samples (Vermeesch, 2013, 2018), the Paleogene sedimentary rocks are connected by solid lines (closest neighbors) with the Quaternary sample and the Middle Miocene sedimentary rocks of the Bragantina platform analyzed in Moizinho et al., 2022 which suggest a shared source. These latter were interpreted to be sourced by the Gurupi belt and the São Luís craton (Moizinho et al., 2022). To conclude, we suggest that the Paleogene sedimentary rocks were potentially sourced by the Amazon craton (Purus Arch), the Sao Luis craton, Gurupi belt and the Borborema province.

5.6.1.2. Neogene

The analyzed Neogene sedimentary rocks are represented by two distinct range of ƐNd(0) values. The passage from negative ƐNd(0) values (-20.2 to -14.3) to a lower ƐNd(0) values (-14.2 to -11.4) marks a transition between cratonic-derived to Andean-derived sedimentary rocks (Table 5.1; Fig. 5.5) (Figueiredo et al., 2009; Horbe et al., 2014; Moizinho et al., 2022; Roddaz et al., 2005b). The cratonic-derived ƐNd(0) values are comparable to those of the late Cretaceous Ipixuna Fm and Pirabas Fm (Moizinho et al., 2022), and to those of Tapajos and Maroni Suspended Particular Matters (SPM) (Allègre et al., 1996; Rousseau et al., 2019), while the Andean-derived ƐNd(0) values matches with those of the Solimões and Madeira rivers (Viers et al., 2008), the Solimões Fm. (Horbe et al., 2019), Madre de Dios Fm. and Iñapari Fm. (Roddaz et al., 2005b). An Andean origin for the Neogene sedimentary rocks is also corroborated by the U-Pb zircon age distribution because there are Paleozoic, Cretaceous and Cenozoic zircons are sourced by Andean Rocks (Fig. 5.6) (Hurtado et al., 2018). In addition, the dominance of Ventuari – Tapajos (2.0 – 1.85 Ga) and Greenville / Sunsas and Cariris Velho (at ~1.0 Ga) suggest that the Paleogene sedimentary rocks sources were also located: i) in the Purus Arch (Rodrigues et al., 2023) and ii) the Borborema Province that is characterized by U-Pb zircon ages of 1.1 – 0.95 Ma from Cariris Velhos suite (Fig. 5.6) (Van Schmus et al., 2011; Brito Neves et al., 1995). The Borborema province contribution is reinforced by the presence of a subordinate population from the Brasiliano belt (670 – 575 Ma) (Van Schmus et al., 2011; Brito Neves et al., 1995). While, the contribution of the Amazon Craton is also suggested by the presence of subordinate Rondonia-San Ignácio (1.5 – 1.3 Ga) zircons population (Bettencourt et al., 2010; Tassinari and Macambira, 1999). In the MDS graph (Fig. 5.7), the Neogene sedimentary rocks are connected by solid lines (closest neighbors) with the Amazon Craton (Negro River) (Mapes et al., 2005) and Northern and Central Andes (Mapes et al., 2005; Pepper et al., 2016) samples and also has similarity with the Holocene sedimentary rocks of the Foz do Amazonas Basin (Mason et al., 2019) which were interpreted to be sourced by the Andes (Mason et al., 2019, 2022). These suggest that they shared a common Andean source could suggest a shared source. To conclude, we suggest that the Neogene sedimentary rocks were sourced by the Amazon craton (Purus Arch), the Borborema province (Cariris Velhos and Brasiliano) and by the Northern and Central Andes.

5.6.1.3. Quaternary

The analyzed Quaternary sedimentary rocks are characterized by less negative ƐNd(0) values (-14.2 to -10.1), which tipify an Andean source (Table 5.1; Fig. 5.5) (Viers et al., 2008; Horbe et al., 2019; Roddaz et al., 2005b; van Soelen et al., 2017). These ƐNd(0) values are similar to those of the Solimões and Madeira rivers (Viers et al., 2008), the Solimões Fm. (Horbe et al., 2019) and the Madre de Dios Fm. and the Iñapari Fm. (Roddaz et al., 2005b), which indicate that the Neogene sedimentary rocks were sourced by the Andes. However, our U-Pb zircon ages did not indicate an Andean contribution because no zircon younger than 500 Ma was found in the Pleistocene sediment (Fig. 5.6). We attributed this discrepancy to the number of concordant zircons analyzed (n=42) that did not allow to statistically identify all the zircon populations (Vermeesch, 2004). Additionaly, the dominance of Maroni-Itacaiunas (2.2 – 2.0 Ga) and Rio Negro Jurena (1.8 – 1.55 Ga) indicate sources mainly located in i) the Amazon Craton (Fig. 5.6) (Tassinari et al., 2000; Tassinari and Macambira, 1999), ii) the Gurupi Belt because they contain the Tromaí Intrusive Suite (2168–2147 Ma), the Tracuateua Suite (2086–2091 Ma), the Negra Velha Granite (2056–2076 Ma) and the Japiim Granite (2116–2072 Ma) (Klein et al., 2020a), São Luís Craton (2.2 – 2.0 Ga) (Klein et al., 2005, 2020b) and, iii) the Borborema Province - Alto Moxoto Terrane (2.0 - 2.2 Ga) (Caxito et al., 2020; Van Schumus et al., 2008; 2011; Brito Neves et al., 2001). The presence of subordinate Grenville/Sunsas stonian (at ~1.0 Ga,) and Brasiliano zircon ages further suggest that the Borborema province sourced the Quaternary sedimentary rocks because of the presence of the Cariris Velhos suite in Borborema Province, that is characterized by U-Pb zircon ages of 1.1 – 0.95 Ma and the presence of Brasiliano rocks (Van Schmus et al., 2011; Brito Neves et al., 1995). In the MDS graph (Fig. 5.7), the Quaternary sedimentary rocks are connected by solid (closest neighbors) with the Paleogene samples from this study, and by dashed lines with the Bragantina Platform (Moizinho et al., 2022), which suggest a shared source. These latter were interpreted to be sourced by the Gurupi belt and the Sao Luís craton (Moizinho et al., 2022). To conclude, we infer that the Quaternary sedimentary rocks were potentially sourced by the Amazon Craton (Maroni-Itacaiunas, Grenville/Sunsas and Rio Negro Jurena), the São Luís Craton, Gurupi belt, Borborema province and even by the Andes.

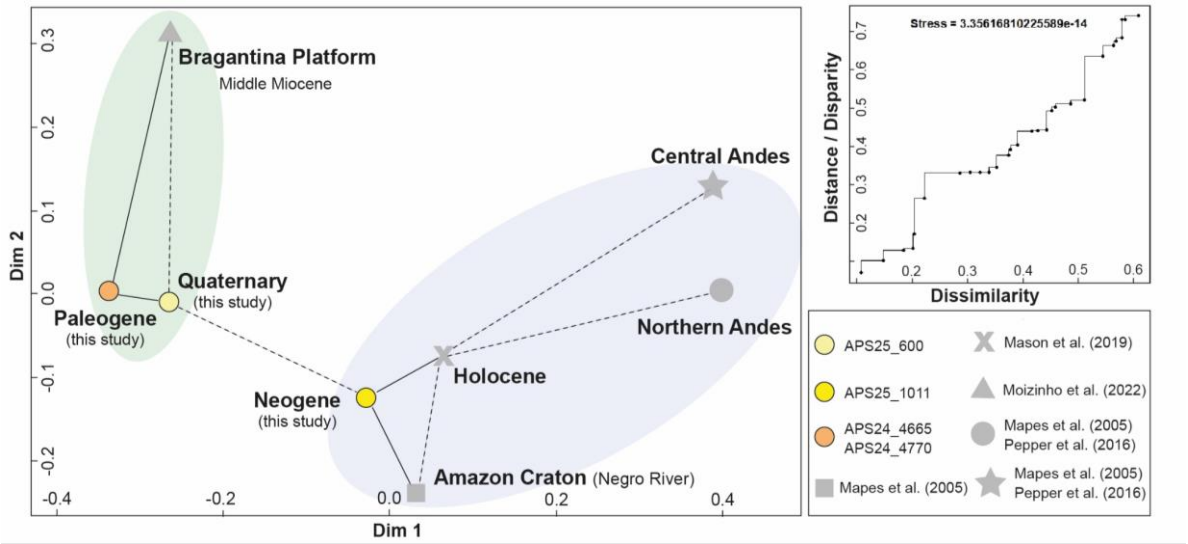


Figure 5. 7 Multidimensional scaling (MDS) (Vermeesch, 2013) map for U–Pb ages of detrital zircons in the Foz do Amazonas Basin and catchment areas from Paleocene to Holocene. Sedimentary units of Bragantina Platform (Moizinho et al., 2022), Northern and Central Andes (Pepper et al., 2016; Mappes, 2009); Amazon Craton (Mapes et al., 2005) and the Holocene of Foz do Amazonas Basin studied by Mason et al. (2019, 2022). The green and blue circles indicate similar detrital zircon age populations (see discussion in the tex and supplementary data). The solid line connecting samples indicate the closest neighbors. The stress values of the configuration indicate a fair goodness of fit (Vermeesch, 2013).

5.6.2 Paleogeographic implications

5.6.2.1 Paleogene (66 to 23 Ma)

Previous published studies have suggested that during the Oligocene to Miocene, the Amazon Basin consisted of two catchments areas divided by the Purus Arch: i) a=the western Amazonian catchment that was draining the Andean Amazonian retroarc foreland basins wich hosted the by Pebas megawetlands (Hoorn et al., 2010; Hoorn et al., 2011) with an overall Andean provenance (Horbe et al., 2019; Roddaz et al., 2012, 2006, 2005b) and, ii) an eastern Amazonian catchment that was sourcing the Foz de Amazonas Basin with an overall cratonic provenance (Figueiredo et al., 2009b; Hoorn et al., 2017; Stewart et al., 2016; van Soelen et al., 2017). This Oligocene to middle Miocene divide of the Amazonian drainage into two subdrainage basins might have been disturbed by an episode of transcontinental connection at 18.3 Ma (van Soelen et al., 2017). We do not see any Andean contribution in the early Miocene sedimentary rocks analyzed in this study. Rather, the results obtained in our dataset for the Paleogene sedimentary rocks of the Foz do Amazonas Basin are consistent with the findings of Stewart et al. (2016). The low ƐNd

values observed for Paleogene to latest Oligocene sedimentary rocks (-20.1 to -19.1) tipify a cratonic-derived source (Table 5.1; Fig. 5.5). A cratonic-source is also supported by the U-Pb zircon ages distribution where no zircon younger thant 500 Ma was found (Fig. 5.6; Supplementary data), which we interpret to suggest that no Andean contribution was arriving to the Atlantic Ocean because the Purus Arch was probably acting as a topographic barrier, although care must be taken because of the relatively low sampling resolution of the Paleogene interval. An alternative to the Purus Arch as a source or complementary sources may include the Borborema Province, the Amazon and São Luís cratons and recycled sedimentary rocks from the Paleozoic Parnaíba Basin as they have similar U-Pb age characteristics.

Indeed, the Boborema province might be uplifting during the Paleogene as it may have experienced crustal reactivations, regional tectonomagmatic events and drainage reorganizations from the late Cretaceous to the Neogene (Fellin et al., 2023; Souza et al., 2022; Oliveira et al., 2023; Klöcking et al., 2020; Souza et al., 2013). In turn, these crustal reactivations might have affected the adjacent Gurupi and São Luis cratons and could explain their potential contributions to the Paleogene Foz de Amazonas sedimentary rocks. Hence, the potential sources of the Paleogene sedimentary rocks of the Foz de Amazonas Basin could be located in the Ii) Eastern Amazon Basin (Guiana Shield and Purus Arch) and, ii) the NE South American plate (Gurupi belt, São Luis craton and Borborema Province).

5.6.2.2 Neogene (~23 to 2.58 Ma)

Previous studies have reported dramatic changes in the configuration of the Amazon drainage system during the Neogene, of which the biggest change is the transcontinental connection of the Amazon River recorded in the Foz de Amazonas Basin by the provenance shift from cratonic-derived to Andean-derived sediments (Figueiredo et al., 2009; van Soelen et al., 2017; Hoorn et al., 2017). The timing of the onset and development of the transcontinental Amazon river is a matter of some controversy, between a temporal transcontinental connection in the early Miocene (18.3 Ma) (van Soelen et al., 2017) and a definive transcontinental connection in the late Miocene (11.8 to 11.3 Ma) (Figueiredo et al., 2009), (9.4 to 9.0 Ma) (Hoorn et al., 2017), late Pliocene (ca. 2.5 Ma) (Campbell, 2010). Additionnally, some drainage changes occurred in the intracontinental basins during the late Miocene-Pliocene in response to the uplift of the

Iquitos Arch (Horbe et al., 2014; Roddaz et al., 2005b). Our provenance dataset which samples were dated based on their relative position with thestratigraphic surfaces ages proposed by Cruz et al. (2019) indicate that an Andean provenance started to be recorded in the in the well 33 of the Foz do Amazonas Basin during the middle-late Miocene (11.93 to 10.8 Ma), which agrees with the findings of Figueiredo et al. (2009) (11.8 to 11.3 Ma). The Andean provenance is recorded latter in the late Miocene (ca. 8Ma) with an ƐNd(0) value of -11.9 in the well 24 (Table 5.1; Fig. 5.5). This change in provenance is accompanied by a change in the depositional environment from the limestones of the carbonates platform of the Amapa Fm. to the siliciclastic deposits of the Pirarucu Fm. (Nogueira et al., 2021; Gorini et al., 2014; Cruz et al., 2019). We do not see the early Miocene (18.3 Ma) temporal transcontinental connection of the Amazon River (van Soelen et al., 2017) in our provenance dataset. Rather, the analyzed samples older than the stratigraphic surface Sn 1 of Cruz et al. (2019) have tipical Cratonic signatures with very low negative ƐNd values (-20.1 to -19.1) (Table 5.1; Fig. 5.5). These reinforce the idea that this early Miocene transcontinental connection was an episodic phenomenon. Our dataset also provides additional constraints regarding the development of the transcontinental Amazon River: the transcontinental Amazon River is recored by younger deposits in the northern part (well 18; latest Miocene 8 to 5.5 Ma) than in the southern part (well 33 middle to late Miocene 11.93 to 10.8 Ma). These might have a relationship with the establishement of the north Brazilian current during the Neogene (Heinrich and Zonneveld, 2013; Nace et al., 2014; Alves et al., 2023) but more work is needed to assess its potential role.

A recent study demonstrated that the Andes was not the only source to the Amazonian Equatorial margin and the Miocene Bragantina platform was sourced by the adjacent craton (Fig. 5.7) (Moizinho et al., 2022). Our dataset indicate that the middle-late Miocene deposits analyzed in the offshore Foz do Amazonas Basin were Andean in provenance whereas the middle-Miocene siliciclatic deposits in the onshore part of the, as in Marajó Basin and Bragantina Platform were fed mainly by reworked autochthonous Cretaceous sedimentary rocks and by Neoproterozoic granites from the Gurupi Belt and São Luís Craton, and reworked sedimentary rocks from the Parnaíba and Grajaú basins (Moizinho et al., 2022). These suggest a compartimentaliaztion of the onshore area represented by the Bragantina platform and the Marajo Basin with the offshore Foz de Amazonas Basin. We believe that this compartimentalization is caused by the Neogene epeirogenic uplift of the Borborema Province as a consequence of Oligocene to Miocene

volcanism, (ca. 27 to 12 Ma ($^{40}Ar/^{39}Ar$) (Souza et al., 2013), with topographic growth since the last 30 Ma (Souza et al., 2022; Klöcking et al., 2020). This crustal uplift of the Borborema province may have promoted basement denudation, fluvial systems rearrangements, such as drainage reversal and radial drainage patterns (domes) (Souza et al., 2022; Klöcking et al., 2020). A local uplift and transpressive and transtensive deformations were also noticed in the onshore compartments of the Bragantina Platform (Moizinho et al., 2022) and Marajo Island (Rossetti et al., 2012), respectively, which may control the sedimentation patherns in the Pleistocene Post-Barreiras unit. Finally, our provenance dataset allow us to conclude that the onset of the transcontinental Amazon River started during midde-late Miocene at 11.93 to 10.8 Ma and is recorded in the northern part in younger deposits (latest Miocene from ca. 8 to 5.5 Ma).

5.6.2.3 Quaternary (2.58 Ma to Recent)

Despite that the Amazon River became transcontiental during the middle-late Miocene, no Andean sediments were recorded on the Pleistocene Post-Barreiras unit and modern coastal sands of the onshore compartiments in the eastern Amazônia Coast (Moizinho et al., 2022), However, our ƐNd values rather attest of the presence of Andean sources and then we cannot use the preliminary zircon U-Pb dataset to exclude an Andean source given the low number of zircon analyzed (n=42, well 25). In addition, an Andean provenance has been attested by Mason et al. (2019, 2022) who showed that the late Pleistocene Amazon Fan recorded several cycles of Andean mountain building.

5.7 CONCLUSIONS

The provenance study of the Paleogene to Pleistocene sedimentary rocks of the Foz de Amazonas Basin based on zircon U–Pb ages and Nd isotopic composition yield the following conclusions.

i) The Paleogene to middle-late Miocene carbonate-siliciclastic deposits of the offshore the Foz do Amazonas Basin have typical Cratonic provenance with very negative ƐNd(0) isotopic values (from -20.2 to -14.3) and U-Pb ages detrital zircon ages older than 500 Ma (> 500 Ma). Two main sources are suggested: the Eastern Amazon craton (Guiana Shield and Purus Arch) and the NE part of the South American plate (São Luís Craton and Borborema Province);

ii) The onset of the transcontinental Amazon River started during the midde-late Miocene at 11.93 to 10.8 Ma and is recorded in younger deposits in the northern part of the Foz de Amazonas basin (from ca. 8 to 5.5 Ma).

iii) The Early Pleistocene to recent U-Pb detrital zircon ages show no Andean zircon but this may be due to the low number of zricon analyzed. However an Andean provenance is attested by Nd isotopic composition (ƐNd(0) -11.7 to -10.1).

REFERENCES

Allègre, C.J., Dupré, B., Négrel, P., Gaillardet, J., 1996. Sr-Nd-Pb isotope systematics in Amazon and Congo River systems: constraints about erosion processes. Chemical Geology 131, 93–112. https://doi.org/10.1016/0009-2541(96)00028-9

Alves, D.P.V., Maselli, V., Iacopini, D., Viana, A.R., Jovane, L. 2023. Oceanographic exchanges between the Southern and Northern Atlantic during the Cenozoic inferred from mixed contourite-turbidite systems in the Brazilian Equatorial Margin. Marine Geology, vol. 456, 20 p. https://doi.org/10.1016/j.margeo.2022.106975

Armijo, R., Lacassin, R., Coudurier-Curveur, A., Carrizo, D., 2015. Coupled tectonic evolution of Andean orogeny and global climate. Earth-Science Reviews 143, 1–35. https://doi.org/10.1016/j.earscirev.2015.01.005

Baksi, A.K., Archibald, D.A. 1997. Mesozoic igneous activity in the Maranhão province, northern Brazil, 40Ar/39Ar evidence for separate episodes of basaltic magmatism. Ear Planet Sci Lett 151:139–153

Bayon, G., German, C.R., Boella, R.M., Milton, J.A., Taylor, R.N., Nesbitt, R.W., 2002. An improved method for extracting marine sediment fractions and its application to Sr and Nd isotopic analysis. Chemical Geology 187, 179–199. https://doi.org/10.1016/S0009-2541(01)00416-8

Bettencourt, J.S.; Leite Jr, W.; Payolla, B.; Ruiz, A.S.; Matos, R.S.; Tosdal, R.M. 2010. The Rondonian-San Ignacio Province in the SW Amazonian Craton: an overview J. S. Am. Earth Sci., 29 (2010), pp. 28-46. doi:10.1016/j.jsames.2009.08.006

Boulila, S., Brange, C., Cruz, A.M., Laskar, J., Gorini, C., Dos Reis, T., Silva, C.G. 2020. Astronomical pacing of Late Cretaceous third- and second-order sea-level sequences in the Foz do Amazonas Basin. Marine and Petroleum Geology, vol. 117. 16 p. https://doi.org/10.1016/j.marpetgeo.2020.104382.

Brandão, J.A.S.L., Feijo, F.J., 1994. Bacia da Foz do Amazonas. Boletim de Geociências da Petrobras 8, 91–100.

Brito Neves, B.B. de, Schmus, W.R.V., Santos, E.J.D., Campos Neto, M.C., Kozuch, M., 1995. O evento Cariris Velhos na Provincia Borborema: integração de dados, implicações e perspectivas. RBG 25, 279–296. https://doi.org/10.25249/0375-7536.1995279296

Brito Neves, B. B., Campos Neto, M. C., Van Schmus, W. R., Fernandez, T. M. G. and Souza, S. L. 2001. O terreno Alto Moxoto´ no leste da Paraiba (Maciço Caldas Brandão). Revista Brasileira de Geociências, 31, 185–194

Brito Neves, B.B. de, Passarelli, C.R., Basei, M.A.S., Santos, E.J. dos, 2003. Idades U-Pb em zircão de alguns granitos clássicos da Província Borborema. Geol. USP, Sér. cient. 3, 25–38. https://doi.org/10.5327/S1519-874X2003000100003

Bühn, B., Pimentel, M.M., Matteini, M., Dantas, E.L., 2009. High spatial resolution analysis of Pb and U isotopes for geochronology by laser ablation multi-collector inductively coupled plasma mass spectrometry (LA-MC-ICP-MS). An. Acad. Bras. Ciênc. 81, 99–114. https://doi.org/10.1590/S0001-37652009000100011

Callède, J., Guyot, J.-L., Ronchail, J., L'Hote, Y., Niel, H., de Oliveira, E., 2004. Evolution du debit de l'Amazonea Obidos de 1902 a 1999. Hydrol. Sci. J. 49, 85–97. https://doi.org/10.1623/hysj.49.1.85.53992

Campbell, K.E., 2010. Late Miocene onset of the Amazon River and the Amazon deep-sea fan: Evidence from the Foz do Amazonas Basin: COMMENT. Geology 38, e212–e212. https://doi.org/10.1130/G30633C.1

Caracciolo, L., Chew, D., Andò, S., 2020. Sediment Generation and Sediment Routing Systems. Earth-Science Reviews 207, 103221. https://doi.org/10.1016/j.earscirev.2020.103221

Caxito, F. de A., Santos, L.C.M. de L., Ganade, C.E., Bendaoud, A., Fettous, E.-H., Bouyo, M.H., 2020. Toward an integrated model of geological evolution for NE Brazil-NW Africa: The Borborema Province and its connections to the Trans-Saharan (Benino-Nigerian and Tuareg shields) and Central African orogens. Braz. J. Geol. 50, e20190122. https://doi.org/10.1590/2317-4889202020190122

Caputo, M.V., Soares, E.A.A., 2016. Eustatic and tectonic change effects in the reversion of the transcontinental Amazon River drainage system. Braz. J. Geol. 46, 301–328. https://doi.org/10.1590/2317-4889201620160066

Chew, D., Magna, T., Kirkland, C., Miskovic, A., Cardona, A., Spikings, R., Schaltegger, U., 2008. Detrital zircon fingerprint of the Proto-Andes: Evidence for a Neoproterozoic active margin? Precambrian Research 167, 186–200. https://doi.org/10.1016/j.precamres.2008.08.002

Chew, D.M., Pedemonte, G., Corbett, E., 2016. Proto-Andean evolution of the Eastern Cordillera of Peru. Gondwana Research 35, 59–78. https://doi.org/10.1016/j.gr.2016.03.016

Chew, D., O'Sullivan, G., Caracciolo, L., Mark, C., Tyrrell, S., 2020. Sourcing the sand: Accessory mineral fertility, analytical and other biases in detrital U-Pb provenance analysis. Earth-Science Reviews 202, 103093. https://doi.org/10.1016/j.earscirev.2020.103093

Chiaradia, M., 2009. Adakite-like magmas from fractional crystallization and melting-assimilation of mafic lower crust (Eocene Macuchi arc, Western Cordillera, Ecuador). Chemical Geology 265, 468–487. https://doi.org/10.1016/j.chemgeo.2009.05.014

Cordani, U.G., Teixeira, W., 2007. Proterozoic accretionary belts in the Amazonian Craton. Geological Society of America Memoirs. vol. 200. Geological Society of America, pp. 297–320. https://doi.org/10.1130/2007.1200(14).

Costa, J.L., 2000. Programa Levantamentos Geologicos Basicos Do Brasil. Programa Grande Carajas. Castanhal, Folha SA. 23-V-C. Estado Do Para. Belem, CPRM (CDROM)

Cruz, A.M. 2018. Integrated geological and geophysical studies applied to understanding the evolution of the Offshore Amazon Basin. Thèse de doctorat en Géologie. Sorbonne Université, Ecole doctorale Géosciences Ressources Naturelles et Environnement, 223 p.

Cruz, A.M., Reis, A.T., Suc, J.P., Silva, C.G., Praeg, D., Granjeon, D., Rabineau, M., Popescu, S.M., Gorini, C., 2019. Neogene evolution and demise of the Amapá carbonate platform, Amazon continental margin, Brazil. Marine and Petroleum Geology 105, 185–203. https://doi.org/10.1016/j.marpetgeo.2019.04.009

da Cruz, C.A., Severiano Ribeiro, H.J.P., da Silva, E.B., 2021. Exploratory plays of the Foz do Amazonas Basin, NW portion, in deep and ultra-deep waters, Brazilian Equatorial Margin. Journal of South American Earth Sciences 111, 103475. https://doi.org/10.1016/j.jsames.2021.103475

Damuth J.E., Flood R.D., Kowsmann R.O., Belderson R.H. ; Gorini M.A. 1988. Anatomy and growth pattern of Amazon deep-sea fan as revealed by long-range side-scan sonar (GLORIA) and high resolution seismic studies. AAPG Bulletin, 72: 885–911.

Dantas, E.L., de Souza, Z.S., Wernick, E., Hackspacher, P.C., Martin, H., Xiaodong, D., Li, J.-W., 2013. Crustal growth in the 3.4–2.7Ga São José de Campestre Massif, Borborema Province, NE Brazil. Precambrian Research 227, 120–156. https://doi.org/10.1016/j.precamres.2012.08.006

Dantas, E.L., Van Schmus, W.R., Hackspacher, P.C., Fetter, A.H., de Brito Neves, B.B., Cordani, U., Nutman, A.P., Williams, I.S., 2004. The 3.4–3.5 Ga São José do Campestre massif, NE Brazil: remnants of the oldest crust in South America. Precambrian Research 130, 113–137. https://doi.org/10.1016/j.precamres.2003.11.002

Darros de Matos, R.M., 2000. Tectonic evolution of the equatorial South Atlantic, in: Mohriak, W., Taiwani, M. (Eds.), Geophysical Monograph Series. American Geophysical Union, Washington, D. C., pp. 331–354. https://doi.org/10.1029/GM115p0331

DePaolo, D.J., 1988. Neodymium Isotope Geochemistry: An Introduction. Springer, Berlin, Heidelberg.

Eakin, C.M., Lithgow-Bertelloni, C., Dávila, F.M., 2014. Influence of Peruvian flat-subduction dynamics on the evolution of western Amazonia. Earth and Planetary Science Letters 404, 250–260. https://doi.org/10.1016/j.epsl.2014.07.027

Eude, A., Roddaz, M., Brichau, S., Brusset, S., Calderon, Y., Baby, P., Soula, J.-C., 2015. Controls on timing of exhumation and deformation in the northern Peruvian eastern Andean wedge as inferred from low-temperature thermochronology and balanced cross section: Exhumation And Deformation of North Peru. Tectonics 34, 715–730. https://doi.org/10.1002/2014TC003641

Faccenna, C., Oncken, O., Holt, A.F., Becker, T.W., 2017. Initiation of the Andean orogeny by lower mantle subduction. Earth and Planetary Science Letters 463, 189–201. https://doi.org/10.1016/j.epsl.2017.01.041

Filizola, N., Guyot, J.L., 2004. The use of Doppler technology for suspended sediment discharge determination in the River Amazon / L'utilisation des techniques Doppler pour la détermination du transport solide de l'Amazone. Hydrol. Sci. J. 49, 143–153. https://doi.org/10.1623/hysj.49.1.143.53990

Figueiredo, J., Hoorn, C., van der Ven, P., Soares, E., 2009. Late Miocene onset of the Amazon River and the Amazon deep-sea fan: Evidence from the Foz do Amazonas Basin. Geology 37, 619–622. https://doi.org/10.1130/G25567A.1

Figueiredo, J.J.P., Zalán, P.V., Soares, E.F., 2007. Bacia Foz do Amazonas. Boletim de Geociências da Petrobras 15, 299–309.

Figueiredo, J., Hoorn, C., van der Ven, P., Soares, E., 2010. Late Miocene onset of the Amazon River and the Amazon deep-sea fan: Evidence from the Foz do Amazonas Basin: Reply. Geology 38, e213–e213. https://doi.org/10.1130/G31057Y.1

Fellin, M.G., Zattin, M., Zuffa, G.G., De Ros, L.F., Cupertino, J.A., De Souza, R.S., Morais Neto, J.M., Dalmonte, C. 2023. New detrital petrographic and thermochronologic constraints on the Late Cretaceous–Neogene erosional history of the equatorial margin of Brazil: Implications for the surface evolution of a complex rift margin. Basin Research. 2023;00:1–27. DOI: 10.1111/bre.12808.

Flood, R.D., Piper, D.J.W., Klaus, A., Peterson, L.C. (Eds.), 1997. Proceedings of the Ocean Drilling Program, 155 Scientific Results, Proceedings of the Ocean Drilling Program. Ocean Drilling Program. https://doi.org/10.2973/odp.proc.sr.155.1997

Gaillardet, J., Viers, J., Dupré, B., 2007. Trace element in river waters, in: J.I. Drever (Ed), Surface and Ground Water, Weathering, and soils, vol. 5, in: Holland, H.D., Turekian, K.K. (Eds), Treatise on Geochemistry, Pergamon, 225-272

Gehrels, G., 2014. Detrital Zircon U-Pb Geochronology Applied to Tectonics. Annu. Rev. Earth Planet. Sci. 42, 127–149. https://doi.org/10.1146/annurev-earth-050212-124012

Gehrels, G.E., Valencia, V.A., Ruiz, J., 2008. Enhanced precision, accuracy, efficiency, and spatial resolution of U-Pb ages by laser ablation-multicollector-inductively coupled plasma-mass spectrometry: TECHNICAL BRIEF. Geochem. Geophys. Geosyst. 9, n/a-n/a. https://doi.org/10.1029/2007GC001805

George, S.W.M., Horton, B.K., Jackson, L.J., Moreno, F., Carlotto, V., Garzione, C.N., 2019. Sediment provenance variations during contrasting Mesozoic-early Cenozoic tectonic regimes of the northern Peruvian Andes and Santiago-Marañón foreland basin, in: Andean Tectonics. Elsevier, pp. 269–296. https://doi.org/10.1016/B978-0-12-816009-1.00012-5

Gioia, S.M.C.L., Pimentel, M.M., 2000. The Sm-Nd isotopic method in the geochronology laboratory of the University of Brasília. An. Acad. Bras. Ciênc. 72, 219–245. https://doi.org/10.1590/S0001-37652000000200009

Gorini, C., Haq, B.U., dos Reis, A.T., Silva, C.G., Cruz, A., Soares, E., Grangeon, D., 2014. Late Neogene sequence stratigraphic evolution of the Foz do Amazonas Basin, Brazil. Terra Nova 26, 179–185. https://doi.org/10.1111/ter.12083

Heinrich, S. and Zonneveld, K.A.F. 2013. Influence of the Amazon River development and constriction of the Central American Seaway on Middle/Late Miocene oceanic conditions at the Ceara Rise. Palaeogeography, Palaeoclimatology, Palaeoecology, vol. 386, 599-606. http://dx.doi.org/10.1016/j.palaeo.2013.06.026

Hollanda, M.H.B.M., Goes, A.M., Negri, F.A., 2018. Provenance of sandstones in the Parnaíba Basin through detrital zircon geochronology. Geol. Soc. Lond. Spec. Publ. 472, 181–197. https://doi.org/10.1144/SP472.16.

Horbe, A.M.C., da Trindade, I.R., Dantas, E.L., Santos, R.V., Roddaz, M., 2014. Provenance of quaternary and modern alluvial deposits of the Amazonian floodplain (Brazil) inferred from major and trace elements and Pb–Nd–Sr isotopes. Palaeogeogr. Palaeoclimatol. Palaeoecol. 411, 144–154. https://doi.org/10.1016/j.palaeo.2014.06.019

Horbe, A.M.C., Roddaz, M., Gomes, L.B., Castro, R.T., Dantas, E.L., do Carmo, D.A., 2019. Provenance of the Neogene sediments from the Solimões Formation (Solimões and Acre Basins), Brazil, Journal of South American Earth Sciences, Volume 93. https://doi.org/10.1016/j.jsames.2019.05.004.

Hoorn, C., 1994. An environmental reconstruction of the paleo-Amazon River system (Middle-late Miocene, NW Amazonia). Palaeogeogr. Palaeoclimatol. Palaeoecol. 112, 187–238

Hoorn, C., Bogotá-A, G.R., Romero-Baez, M., Lammertsma, E.I., Flantua, S.G.A., Dantas, E.L., Dino, R., do Carmo, D.A., Chemale, F., 2017. The Amazon at sea: Onset and stages of the Amazon River from a marine record, with special reference to Neogene plant turnover in the drainage basin. Global and Planetary Change 153, 51–65. https://doi.org/10.1016/j.gloplacha.2017.02.005

Hoorn, C., Roddaz, M., Dino, R., Soares, E., Uba, C., Ochoa-Lozano, D., & Mapes, R. 2010. The Amazonian Craton and its influence on past fluvial systems (Mesozoic-Cenozoic, Amazonia). Amazonia: Landscape and Species Evolution: A look into the past, 103-122.

Horton, B.K., Saylor, J.E., Nie, J., Mora, A., Parra, M., Reyes-Harker, A., Stockli, D.F., 2010. Linking sedimentation in the northern Andes to basement configuration, Mesozoic extension, and Cenozoic shortening: Evidence from detrital zircon U-Pb ages, Eastern Cordillera, Colombia. Geological Society of America Bulletin 122, 1423–1442. https://doi.org/10.1130/B30118.1

Horton, B.K., 2018. Sedimentary record of Andean mountain building. Earth-Science Reviews 178, 279–309. https://doi.org/10.1016/j.earscirev.2017.11.025

Horton, B.K., Fuentes, F., 2016. Sedimentary record of plate coupling and decoupling during growth of the Andes. Geology 44, 647–650. https://doi.org/10.1130/G37918.1

Hurtado, C., Roddaz, M., Santos, R.V., Baby, P., Antoine, P.-O., Dantas, E.L., 2018. Cretaceous-early Paleocene drainage shift of Amazonian rivers driven by Equatorial Atlantic Ocean opening and Andean uplift as deduced from the provenance of northern Peruvian sedimentary rocks (Huallaga basin). Gondwana Research 63, 152–168. https://doi.org/10.1016/j.gr.2018.05.012

Jackson, S.E., Pearson, N.J., Griffin, W.L., Belousova, E.A., 2004. The application of laser ablation-inductively coupled plasma-mass spectrometry to in situ U–Pb zircon geochronology. Chemical Geology 211, 47–69. https://doi.org/10.1016/j.chemgeo.2004.06.017

Jacobsen, S.B., Wasserburg, G.J., 1980. Sm–Nd isotopic evolution of chondrites. Earth and Planetary Science Letters 50 (1), 139–155. https://doi.org/10.1016/0012-821X(80)90125-9

Klein, E.L., Moura, C.A.V., Pinheiro, B.L.S., 2005. Paleoproterozoic Crustal Evolution of the Sao Luís Craton, Brazil: evidence from Zircon Geochronology and Sm-Nd Isotopes. Gondwana Res. 8, 177–186. https://doi.org/10.1016/S1342-937X(05)71116-3.

Klein, E.L., Lopes, E.C.S., Rodrigues, J.B., Souza-Gaia, S.M., Cordani, U.G., 2020a. Rhyacian and Neoproterozoic magmatic associations of the Gurupi Belt, Brazil: Implications for the tectonic evolution, and regional correlations. Geosci. Front. 11, 2243–2269. https://doi.org/10.1016/j.gsf.2020.02.016.

Klein, E.L., Rodrigues, J.B., Lopes, E.C.S., Gusmão de Oliveira, R., Souza-Gaia, S.M., de Oliveira, L.B.T., 2020b. Age, provenance and tectonic setting of metasedimentary sequences of the Gurupi Belt and Sao Luís cratonic fragment, northern Brazil: Broadening the understanding of the Proterozoic-early Cambrian tectonic evolution. Precambrian Res. 351, 105950 https://doi.org/10.1016/j.precamres.2020.105950.

Klöcking, M., Hoggard, M.J., Rodríguez Tribaldos, V., Richards, F.D., Guimarães, A.R., Maclennan, J., White, N.J. 2020. A tale of two domes: Neogene to recent volcanism and dynamic uplift of northeast Brazil and southwest Africa. Earth and Planetary Science Letters 547, https://doi.org/10.1016/j.epsl.2020.116464.

Litty, C., Lanari, P., Burn, M., Schlunegger, F., 2017. Climate-controlled shifts in sediment provenance inferred from detrital zircon ages, western Peruvian Andes 45.

Louterbach, M., Roddaz, M., Antoine, P.-O., Marivaux, L., Adnet, S., Bailleul, J., Dantas, E., Santos, R.V., Chemale, F., Baby, P., Sanchez, C., Calderon, Y., 2017. Provenance record of late Maastrichtian-late Palaeocene Andean Mountain building in the Amazonian retroarc foreland basin (Madre de Dios basin, Peru). Terra Nova 30, 17–23. https://doi.org/10.1111/ter.12303

Mapes, R.W., Coleman, D.S., and Nogueira, A.C.R. 2005. Understanding zircon transport in the modern Amazon River: Geological Society of America Abstracts with Programs, v. 37, no. 4, p. 86.

Martínez, F., López, C., Torres, C., González, R., Peña, M. 2023. Understanding the initial upper plate architecture and shortening distribution in subduction-related orogens: Insights from the Central Andean forearc. Tectonophysics 863 (2023) 230001. https://doi.org/10.1016/j.tecto.2023.230001

Mason, C.C., Romans, B.W., Patterson, M.O., Stockli, D.F., Fildani, A., 2022. Cycles of Andean mountain building archived in the Amazon Fan. Nat Commun 13, 6983. https://doi.org/10.1038/s41467-022-34561-6

Mason, C.C., Romans, B.W., Stockli, D.F., Mapes, R.W., Fildani, A., 2019. Detrital zircons reveal sea-level and hydroclimate controls on Amazon River to deep-sea fan sediment transfer. Geology 47, 563–567. https://doi.org/10.1130/G45852.1

Marzoli, A., Callegaro, S., Dal Corso, J., Davies, J.H.F.L., Chiaradia, M., Youbi, N., Bertrand, H., Reisberg, L., Merle, R., Jourdan, F., 2018. The Central Atlantic Magmatic Province (CAMP): A Review, in: The Late Triassic World, Topics in Geobiology. Springer International Publishing, Cham, pp. 91–125. https://doi.org/10.1007/978-3-319-68009-5_4

McHone, J.G., 2000. Non-plume magmatism and rifting during the opening of the central Atlantic Ocean. Tectonophysics 316, 287–296. https://doi.org/10.1016/S0040-1951(99)00260-7

McLennan, S.M., Taylor, S.R., McCulloch, M.T., Maynard, J.B., 1990. Geochemical and Nd–Sr isotopic composition of deep-sea turbidites: crustal evolution and plate tectonic associations. Geochimica et Cosmochimica Acta 54 (7), 2015–2050. https://doi.org/10.1016/0016-7037(90)90269-Q

Milliman, J.D., Syvitski, J.P.M., 1992. Geomorphyc/tectonic control of sediment discharge to the ocean: the importance of small mountainous rivers. J. Geol. 100, 525–544.

Moizinho, G.R., Vieira, L.C., Santos, R.V., Nogueira, A.C.R., Dantas, E.L., Roddaz, M., 2022. Provenance of Miocene-Pleistocene siliciclastic deposits in the Eastern Amazonia coast (Brazil) and paleogeographic implications. Palaeogeography, Palaeoclimatology, Palaeoecology 587, 110799. https://doi.org/10.1016/j.palaeo.2021.110799

Mora, A., Baby, P., Roddaz, M., Parra, M., Brusset, S., Hermoza, W., Espurt, N., 2010. Tectonic History of the Andes and Sub-Andean Zones: Implications for the Development of the Amazon Drainage Basin, in: Hoorn, C., Wesselingh, F.P. (Eds.), Amazonia: Landscape and Species Evolution. Wiley-Blackwell Publishing Ltd., Oxford, UK, pp. 38–60. https://doi.org/10.1002/9781444306408.ch4

Moreno, F., Garzione, C.N., George, S.W.M., Horton, B.K., Williams, L., Jackson, L.J., Carlotto, V., Richter, F., Bandeian, A., 2020. Coupled Andean Growth and Foreland Basin Evolution, Campanian–Cenozoic Bagua Basin, Northern Peru. Tectonics 39. https://doi.org/10.1029/2019TC005967

Moreno, F., Garzione, C.N., George, S.W.M., Williams, L., Richter, F., Bandeian, A., 2022. Late Cretaceous through Cenozoic Paleoenvironmental History of the Bagua Basin, Peru: Paleoelevation Comparisons with the Central Andean Plateau. Geosciences 12, 242. https://doi.org/10.3390/geosciences12060242

Nace, T.E., Baker, P.A., Dwyer, G.S., Silva, C.G., Rigsby, C.A., Burns, S.J., Giosan, L., Otto-Bliesner, B., Liu, Z., Zhu, J. 2014. The role of North Brazil Current transport in the paleoclimate of the Brazilian Nordeste margin and paleoceanography of the western tropical Atlantic during the late Quaternary. Palaeogeography, Palaeoclimatology, Palaeoecology, vol. 415, 3-13. http://dx.doi.org/10.1016/j.palaeo.2014.05.030

Navarro, C., Alexis, P., Rivera Porras, M. A., Monge Miguel, R. W. 2010. Geología y metalogenia del Grupo Calipuy (Volcanismo Cenozoico) segmento Santiago de Chuco, norte del Perú - [Boletín D 28]. Instituto Geológico, Minero y Metalúrgico – INGEMMET, 192p.

Nogueira, A.C.R., Silveira, R., Guimarães, J.T.F., 2013. Neogene–Quaternary sedimentary and paleovegetation history of the eastern Solimões Basin, central Amazon region. Journal of South American Earth Sciences 46, 89–99. https://doi.org/10.1016/j.jsames.2013.05.004

Nogueira, A.C.R., Amorim, K.B., Góes, A.M., Truckenbrodt, W., Petri, S., Nogueira, A.A.E., Bandeira, J., Soares, J.L., Baía, L.B., Imbiriba Júnior, M., Bezerra, I.S., Ribas, C.C., Cracraft, J., 2021. Upper Oligocene-Miocene deposits of Eastern Amazonia: Implications for the collapse of Neogene carbonate platforms along the coast of northern Brazil. Palaeogeography, Palaeoclimatology, Palaeoecology 563, 110178. https://doi.org/10.1016/j.palaeo.2020.110178

Oliveira, A.L., Schmitz, M.D., Wall, C.J., Hollanda, M.H.B.M. 2022. A bulk annealing and dissolution-based zircon concentration method for mafic rocks. Chemical Geology 597, 120817. https://doi.org/10.1016/j.chemgeo.2022.120817

Oliveira, G.P., Côrrea, A.C. de B., Tavares, B.A.C., Monteiro, K.A. 2023. The influence of Cenozoic magmatism on drainage rearrangement processes of the northeast sector of the Borborema Highlands, northeastern Brazil. Journal of South American Earth Sciences 121, 104124. https://doi.org/10.1016/j.jsames.2022.104124

Palheta, E.S., Abreu, F., Moura, C.A.V., 2009. Granitoides proterozoicos como marcadores da evolução geotectonica da regiao nordeste do Para, Brasil. Rev. Bras. Geociencias 39, 647–657. https://doi.org/10.25249/0375-7536.2009394647657.

Paton, C., Hellstrom, J., Paul, B., Woodhead, J., Hergt, J., 2011. Iolite: Freeware for the visualisation and processing of mass spectrometric data. J. Anal. At. Spectrom. 26, 2508. https://doi.org/10.1039/c1ja10172b

Pazley, M.A. ; Shepherd, D.B. ; Pocknall, D.T. ; Boyd, K.P. ; Andrade, V. ; Figueiredo, J.P. 2005. Sequence stratigraphy and basin evolution of the Foz do Amazonas Basin, Brazil. In : AAPG International Conference and Exhibition. Extended Abstract Volume. American Association of Petroleum Geologists, p.12.

Pepper, M., Gehrels, G., Pullen, A., Ibanez-Mejia, M., Ward, K.M., Kapp, P., 2016. Magmatic history and crustal genesis of western South America: Constraints from U-Pb ages and Hf isotopes of detrital zircons in modern rivers. Geosphere 12, 1532–1555. https://doi.org/10.1130/GES01315.1

Perovano, R., Reis, A.T. dos, Silva, C.G., Vendeville, B.C., Gorini, C., Oliveira, V. de, Araújo, É.F. da S., 2009. O processo de colapso gravitacional da seção marinha da bacia da foz do Amazonas - margem equatorial brasileira. Rev. Bras. Geof. 27, 459–484. https://doi.org/10.1590/S0102-261X2009000300012

Petrus, J.A. and Kamber, B.S. 2012. VizualAge: A Novel Approach to Laser Ablation ICP-MS U-Pb Geochronology Data Reduction. Geostandards and Geoanalytical Research, 36: 247-270.

Peyve, A.A., 2013. Central Atlantic Igneous Province: Origin and mechanisms of formation. Geotecton. 47, 431–438. https://doi.org/10.1134/S0016852113060046

Potter, P.E., 1997. The Mesozoic and Cenozoic paleodrainage of South America: a natural history. Journal of South American Earth Sciences 10, 331–344. https://doi.org/10.1016/S0895-9811(97)00031-X

Ramos, V.A., 1999. Plate tectonic setting of the Andean Cordillera. Episodes 22, 183–190. https://doi.org/10.18814/epiiugs/1999/v22i3/005

Reis, A.T., Perovano, R., Silva, C.G., Vendeville, B.C., Araújo, E., Gorini, C., Oliveira, V., 2010. Two-scale gravitational collapse in the Amazon Fan: a coupled system of gravity tectonics and mass-transport processes. JGS 167, 593–604. https://doi.org/10.1144/0016-76492009-035

Roddaz, M., Viers, J., Brusset, S., Baby, P., Hérail, G., 2005b. Sediment provenances and drainage evolution of the Neogene Amazonian foreland basin. Earth Planet. Sci. Lett. 239, 57–78. https://doi.org/10.1016/j.epsl.2005.08.007.

Rodrigues, M. de A., Roddaz, M., Santos, R.V., Louterbach, M., D'Apolito, C., Brusset, S., Dantas, E.L., Negri, F.R., 2023. New insights into the Cretaceous evolution of the Western Amazonian paleodrainage system. Sedimentary Geology 453, 106434. https://doi.org/10.1016/j.sedgeo.2023.106434

Rossetti, D.F., Souza, L.S.B., Elis, V.R., 2012. Neotectonics in the Northern Equatorial Brazilian margin. J. S. Am. Earth Sci. 37, 175–190. https://doi.org/10.1016/j. jsames.2012.03.004.

Rouby, D., Loparev, A., Chardon, D., Bajolet, F., Dall'Asta, M., Paquet, F., Fillon, C., Roig, J.-Y., Ye, J. 2023. Sediment routing systems to the Atlantic rifted margin of the Guiana Shield. Geosphere. https://doi.org/10.1130/GES02561.1

Rousseau, T.C.C., 2019. Controls on the geochemistry of suspended sediments from large tropical South American rivers (Amazon, Orinoco and Maroni). Chemical Geology.

Sacek, V., 2014. Drainage reversal of the Amazon River due to the coupling of surface and lithospheric processes. Earth and Planetary Science Letters 401, 301–312. https://doi.org/10.1016/j.epsl.2014.06.022

Santos, J.O.S., Hartmann, L.A., Gaudette, H.E., Groves, D.I., Mcnaughton, N.J., Fletcher, I.R., 2000. A new understanding of the provinces of the Amazon Craton based on integration of field mapping and U–Pb and Sm–Nd geochronology. Gondwana Research 3 (4), 453–488. https://doi.org/10.1016/S1342-937X(05)70755-3.

Schellart, W.P., 2010. Andean mountain building and magmatic arc migration driven by subduction-induced whole mantle flow. Nat Commun 8, 2010. https://doi.org/10.1038/s41467-017-01847-z

Silva, S.R.P., Maciel, R.R., Severino, M.C.G., 1998. Cenozoic tectonics of Amazon Mouth Basin. Geo-Marine Letters 18, 256–262. https://doi.org/10.1007/s003670050077

Shephard, G.E., Müller, R.D., Liu, L., Gurnis, M., 2010. Miocene drainage reversal of the Amazon River driven by plate–mantle interaction. Nature Geosci 3, 870–875. https://doi.org/10.1038/ngeo1017

Souza, C.M.P., Lima, C.C.U. de, Costa, L.M., Veloso, G.V., Gomes, R.L., Leite, M.E., Fernandes-Filho, E.I., 2022. Geomorphic indices, machine learning and osl-palynology chronology to assess neotectonic deformation in the continental margin – Northeastern Brazil. Journal of South American Earth Sciences 118, 103931. https://doi.org/10.1016/j.jsames.2022.103931

Souza, Z.S., Vasconcelos, P.M., Knesel, K.M., da Silveira Dias, L.G., Roesner, E.H., Cordeiro de Farias, P.R., de Morais Neto, J.M., 2013. The tectonic evolution of Cenozoic extensional basins, northeast Brazil: Geochronological constraints from continental basalt 40Ar/39Ar ages. Journal of South American Earth Sciences 48, 159–172. https://doi.org/10.1016/j.jsames.2013.09.008

Stewart, J.A., Gutjahr, M., James, R.H., Anand, P., Wilson, P.A., 2016. Influence of the Amazon River on the Nd isotope composition of deep water in the western equatorial Atlantic during the Oligocene–Miocene transition. Earth and Planetary Science Letters 454, 132–141. https://doi.org/10.1016/j.epsl.2016.08.037

Tassinari, C.C.G., Macambira, M.J.B., 1999. Geochronological provinces of the Amazonian Craton. Episodes 22, 174–182. https://doi.org/10.18814/epiiugs/1999/v22i3/004.

Tassinari, C.C.G., Bettencourt, J.S., Geraldes, M.C., Macambira, M.J.B., Lafon, J.M., 2000. The Amazon Craton. In: Cordani, U.G., Milani, E.J., Thomaz Filho, A.M, Campos, D.A. (Eds.), Tectonic evolution of South America: 31st International Geological Congress, Rio de Janeiro, pp. 41–95.

Van Schmus, W.R., de Brito Neves, B.B., Williams, I.S., Hackspacher, P.C., Fetter, A.H., Dantas, E.L., Babinski, M., 2003. The Seridó Group of NE Brazil, a late Neoproterozoic pre- to syn-collisional basin in West Gondwana: insights from SHRIMP U–Pb detrital zircon ages and Sm–Nd crustal residence (TDM) ages. Precambrian Research 127, 287–327. https://doi.org/10.1016/S0301-9268(03)00197-9

Van Schmus, W.R., Oliveira, E.P., da Silva Filho, A.F., Toteu, S.F., Penaye, J., Guimarães, I.P., 2008. Proterozoic links between the Borborema Province, NE Brazil, and the Central African Fold Belt. SP 294, 69–99. https://doi.org/10.1144/SP294.5

Van Schmus, W.R., Kozuch, M., de Brito Neves, B.B., 2011. Precambrian history of the Zona Transversal of the Borborema Province, NE Brazil: Insights from Sm–Nd and U–Pb geochronology. Journal of South American Earth Sciences 31, 227–252. https://doi.org/10.1016/j.jsames.2011.02.010

van Soelen, E.E., Kim, J.-H., Santos, R.V., Dantas, E.L., Vasconcelos de Almeida, F., Pires, J.P., Roddaz, M., Sinninghe Damsté, J.S., 2017. A 30 Ma history of the Amazon River inferred from terrigenous sediments and organic matter on the Ceará Rise. Earth and Planetary Science Letters 474, 40–48. https://doi.org/10.1016/j.epsl.2017.06.025

Vermeesch, P., 2004. How many grains are needed for a provenance study? Earth and Planetary Science Letters 224 (3–4), 441–451. https://doi.org/10.1016/j.epsl.2004.05.037

Vermeesch, P., 2013. Multi-sample comparison of detrital age distributions. Chem. Geol. 341, 140–146. https://doi.org/10.1016/j.chemgeo.2013.01.010.

Vermeesch, P., Resentini, A., Garzanti, E., 2016. An R package for statistical provenance analysis. Sedimentary Geology 336, 14–25. https://doi.org/10.1016/j.sedgeo.2016.01.009

Viers, J., Roddaz, M., Filizola, N., Guyot, J.-L., Sondag, F., Brunet, P., Zouiten, C., Boucayrand, C., Martin, F., Boaventura, G.R., 2008. Seasonal and provenance controls on Nd-Sr isotopic compositions of Amazon rivers suspended sediments and implications for Nd and Sr fluxes exported to the Atlantic Ocean. Earth Planetary Science Letters. 274, 511–523.

Widenbeck, M., Allé, P., Corfu, F., Griffin, W.L., Meier, M., Oberli, F., Quadt, A.V., Roddick, J.C., Spiegel, W., 1995. Three natural zircon standards for U-Th-Pb, Lu-Hf, trace element and REE analyses. Geostand. Geoanalytical Res. 19, 1–23. https://doi.org/10.1111/j.1751-908X.1995.tb00147.x.

CAPÍTULO 6

SÍNTESE E DISCUSSÃO

6. SÍNTESE E DISCUSSÃO

RÉSUMÉ

Ce chapitre intègre les principaux résultats de cette thèse et discute comment les principaux événements géologiques survenus au cours du Cénozoïque dans les régions occidentales et septentrionales de la plaque sud-américaine ont influencé l'origine et l'évolution du système Andes-Amazone-Marge Équatoriale Sud-Américaine (AAMESA). La paléogéographie de l'Amazonie Occidentale du Paléocène à l'Éocène inférieur (66 – 43.5 Ma) diffère de la configuration présentée au Maastrichtien (Rodrigues et al., 2023; Moreno et al., 2022; George et al., 2019; Hurtado et al., 2018; Zamora and Gil, 2018; Louterbach et al., 2017; Mourier et al., 1988), en raison de l'absence de soulèvement andin (épisode de quiescence tectonique dans la Cordillère occidentale) et de l'arrêt consécutif de la sédimentation dans les bassins d'avant-pays retroarc amazoniens. Le hiatus stratigraphique identifié par une discordance régionale enregistré dans les bassins de l'Amazonie occidentale marque un arrêt du soulèvement crustali (~ 25 Ma) (Horton, 2022; Custódio et al., 2023; Gutiérrez et al., 2019; Caballero et al., 2020; Moreno et al., 2020; Naeser et al., 1991; Roddaz et al., 2010). Au cours de la même période, la région nord-ouest de la marge équatoriale de l'Atlantique se caractérise par de faibles taux de sédimentation (Rouby et al., 2023) et a reçu des apports continus des zones cratoniquesdu Craton amazonien occidental (provenant principalement du bouclier guyanais) (Roddaz et al., 2021) et du craton de São Luís, de la ceinture de Gurupi et de la province de Borborema. Au Paléocène, le bouclier guyanais (craton amazonien) a connu des épisodes de latéritisation avec la formation de paléosurfaces bauxitiques et ferrugineuses liées au cycle de latéritisation "Sul-Americano" (Théveniaut e Freyssinet, 2002; Rossetti, 2004; Gautheron et al., 2022). La coïncidence temporelle, au cours du Paléocène, entre les événements de latéralisation qui ont eu lieu dans les régions de l'Amazonie occidentale et de l'Amazonie orientale (Rossetti, 2004; Théveniaut e Freyssinet, 2002) et le hiatus straigraphique enregistré dans les bassins d'avant-pays retroarc andino-amazoniens pourrait suggérer qu'il existe une relation entre l'absence de soulèvement Andin et l'arrêt de la sédimentation dans les d'avant-pays retroarc andino-amazonien avecla latéralisation, les faibles apports sédimentaires et le développement consécutif de la plate-forme carbonatée dans le bassin de Foz do Amazonas.

Après un long hiatus sédimentaire observé du Paléocène à l'Éocène inférieur, un système d'arc magmatique andin s'est développé dans la région de la Cordillère Occidentale, et ils consitutent la source principale des roches sédimentaires du bassin d'avant-pays retroarc amazonien nord péruvien au cours de l'Éocène moyen à supérieur (Lutétien - Bartonien) (43.5 – 37.6 Ma).. Durant cette période de temps, la sedimentation dans les bassins d'avant-pays retroarc se caractérise par une une augmentation du taux de sédimentation (18.5 – 50.1 m/Ma) alors que dans le même temps, de très faibles taux d'accumulation sont observé sur la marge équatoriale (bassin de Foz do Amazonas), favorisant l'établissement et le maintien d'une plate-forme carbonatée.

C'est au début de l'Oligocène et au milieu du Miocène que les bassins d'avant-pays retroarc amazonien ont enregistré un changement dans la zone d'apport avec l'arrivée des premiers sédiments en provenance de la Cordillère Orientale. Ce changement est lié au soulèvement et à l'érosion de la Cordillère orientale (~30 Ma) en relation avec la propoagation du prisme orogénique est amazonien , (~30 - 24 Ma Eude et al., 2015)). Le soulèvement de la Cordillère Orientale peut avoir contribué à la création de nouveaux habitats, favorisant l'isolement et la diversification biotique (Pérez-Escobar et al., 2022 ; Hoorn et al., 2018 ; Perrigo et al., 2019). Le début de la formation d'une barrière topographique causée par le soulèvement de la Cordillère orientale peut avoir eu un impact sur les conditions de circulation atmosphérique locales, et régionales (Poulsen et al., 2010), ainsi que sur l'intensification de l'altération et le développement de surfaces latéritiques en Amazonie centrale (Gautheron et al., 2022) et sur la réorganisation du réseau de drainage, avec l'établissement d'un réseau de drainage méandriformeen Amazonie Occidentale.

Au cours du Miocène supérieur, la transcontientalisation de l'Amazone a commencé à relier les bassins d'avant-pays retroarc amazonien aux bassins de la marge l équatoriale atlantique. Nos résultats confirment un âge miocène moyen à supérieur, à partir de 11.93 Ma et jusqu'à 8.0 Ma pour le début de cette transcontinentalisation avec des valeurs d' ƐNd(0) devenant moins négative. Ces résultats sont en accord avec ceux publiés dans de précédentes études (van Soelen et al., 2017 ; Hoorn et al., 2017 ; Figueiredo et al., 2009). En revanche, en comparant nos données avec celles de van Soelen et al. (2017), nous n'avons pas pu identifier la présence dede sédiments d'origine andine au Miocène inférieur (18.3 Ma). Cela peut être liée à la faible résolution de l'échantillonnage ou à la présence de barrières topographiques entre le Ceara Rise et les puits analysés. , seulement des signatures ƐNd typiquement cratoniques (-20.1 à 19.1). Il n'est donc pas correct de

parler d'un apport andin dominant au cours du Miocène inférieur. Toutefois, cette divergence peut être attribuée à la faible résolution de l'échantillonnage ou au fait que le Purus était encore actif au milieu de 18 Ma. Nous attribuons la transcontinentalisationde l'Amazone à une accélération du du soulèvement de la Cordillère Orientale qui a entraîné une augmentation considérable de l'apport sédimentaire dans les bassinsd'avant-pays retroarc amazoniens, une réorganisation du réseau de drainage amazonien et la suralimentation de ces bassins permettant la transcontinentalisation de l'Amazone (Roddaz et al., 2010 ; Sacek, 2014) (Fig. 6.5) (Potter, 1997).

Il convient de noter que la transcontinentalisation de l'Amazone précède l'augmentation des taux de sédimentation dans le bassin Foz de Amazonas (Figueiredo et al., 2009).

6.1 EVOLUÇÃO ESPAÇO-TEMPORAL DO SISTEMA ANDES-AMAZÖNIA-MARGEM EQUATORIAL SUL-AMERICANA

6.1.1 Paleoceno ao Eoceno inferior (Daniano – Ypresiano) (66 – 47.8 Ma)

Quiescência tectônica dos Andes e aporte sedimentar à margem Equatorial Atlântica

A paleogeografia na Amazônia Ocidental durante o Paleoceno ao Eoceno inferior distingue da configuração presente no Maastrichtiano (Rodrigues et al., 2023; Moreno et al., 2022; George et al., 2019; Hurtado et al., 2018; Zamora and Gil, 2018; Louterbach et al., 2017; Mourier et al., 1988), pela ausência do soerguimento Andino (Cordilheira Ocidental) e consequente cessação da sedimentação nas bacias Amazônicas de retroarco antepaís (Horton, 2022, 2018; Custódio et al., 2023). O hiato estratigráfico registrado nas bacias Amazônicas Ocidentais, marca uma parada no soerguimento crustal, identificada por uma discordância regional (~ 25 Ma) (Fig. 6.1) (Horton, 2022; Custódio et al., 2023; Gutiérrez et al., 2019; Caballero et al., 2020; Moreno et al., 2020; Naeser et al., 1991; Roddaz et al., 2010). Durante o Paleoceno, esta região deve ter estado isolada das bacias ao sul (Madre de Dios, Potosi e Chaco), dada as evidências da ingressão marinha (Louterbach et al., 2014; Cappetta and Gayet, 2013; Sempère et al., 1997). No mesmo intervalo de tempo, a região noroeste da Margem Equatorial Atlântica recebia aporte contínuo das áreas cratônicas e orogênicas: Cráton Amazônico Ocidental (principalmente do Escudo das Guianas) (Roddaz et al., 2021), ainda que com baixas taxas de sedimentação

(Rouby et al., 2023) e fonte do NE da placa Sul-Americana, devido ao soerguimento da Provinica Borborema desde o Cretaceo superior ao Recente, representado pelos Cráton São Luís, Cinturão Gurupi, Província Borborema e subordinalmente sedimentos retrabalhos na Bacia do Parnaíba.

Ao longo de todo Cenozoico, o Escudo das Guianas (Cráton do Amazonas), tem experimentado episódios de laterização com formações de paleosuperfícies bauxíticas e ferruginosas relacionadas ao ciclo de lateritização "Sul Americano" (Théveniaut e Freyssinet, 2002). Adicionalmente, também foram reconhecidas à nordeste da Amazônia cinco (S1-S5) paleosuperficies de laterização, com desenvolvimento desde o Cretaceo superior ao Quaternario (Rossetti, 2004). O evento de laterização mais antigo datado do Cretaceo superior ao Paleoceno (~60 - 50 Ma) (S1 - sucessão Ipixuna/Cujupe) (Rossetti, 2004) e depósito de bauxita *Bakhuis Mountain* (Théveniaut e Freyssinet, 2002), coincide com o período de quiescência tectônica Andina ocorrido na Cordilheira Ocidental (Fig. 7.1) (Horton, 2022; Custódio et al., 2023; Gutiérrez et al., 2019; Caballero et al., 2020; Moreno et al., 2020; Naeser et al., 1991; Roddaz et al., 2010) e, com as baixas taxas de acumulações siliciclásticas registradas na Bacia da Foz do Amazonas (Rouby et al., 2023). A coincidência temporal durante o Paleoceno entre os eventos de laterização ocorridos nas regiões da Amazônia Ocidental e Oriental, poderia sugerir que houve uma relação entre a ausência de soeguimento dos Andes e cessação da sedimentação nas bacias Amazônicas de retroarco antepaís com o evento de laterização, baixos aportes sedimentares e consequentemente desenvolvimento da plataforma carbonática na Bacia da Foz do Amazonas. Desse modo, o extenso período de intemperismo laterítico bauxítico ocorrido ao norte da placa da América do Sul durante o Paleoceno deve ter sido controlado pelas variações climáticas ocorridas durante o período de *Greenhouse*, favorecendo o intemperismo químico continental sobre o intemperismo físico (erosão mecânica) (Prasad, 1983) e desenvolvimento das superfícies lateríticas no sistema *source-to-sink* AAMESA. Como identificado por (Tardy and Roquin, 1998), as condições paleoclimaticas no Escudo das Guianas foram quentes e umidas do Cretaceo superior ao Oligoceno inferior, que infere um controle paleoclimatico sobre a sedimentação e laterização na Amazônia Oriental e da Bacia da Foz do Amazonas. As baixas taxas de aporte oriundos das regiões cratônicas (Escudo das Guianas, Cráton São Luís, Província Borborema) favoreceram o desenvolvimento da plataforma carbonática.

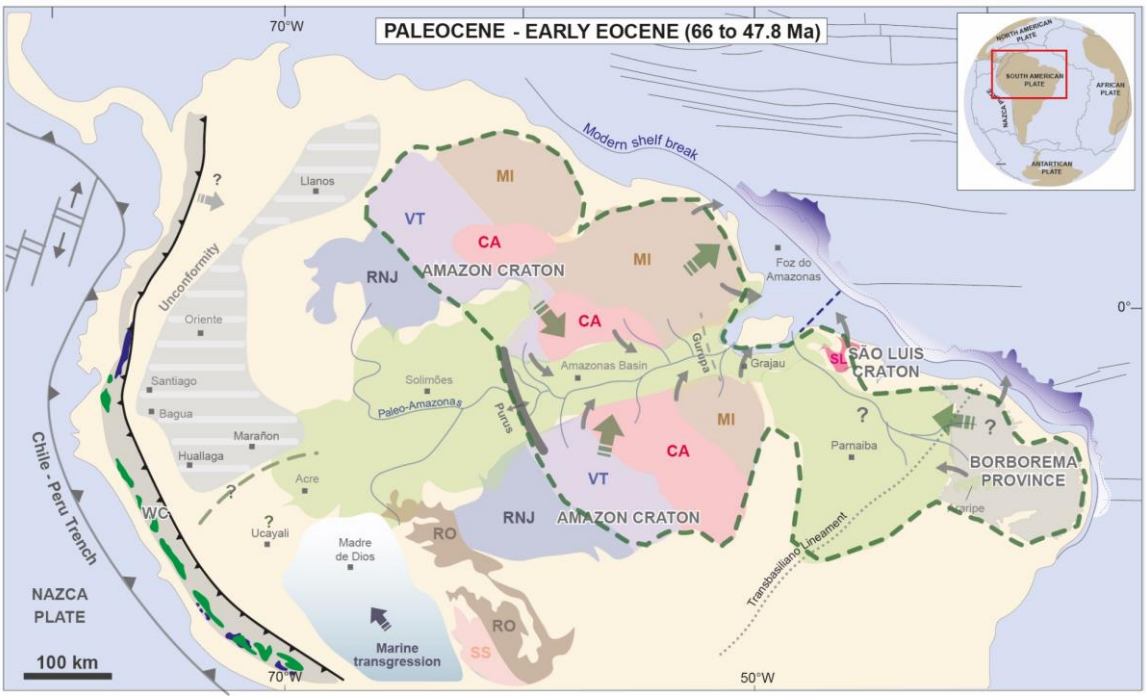


Figura 6. 1 Mapa da reconstrução paleogeográfica da porção norte da América do Sul, detalhes das areas source-to-sink durante o Paleoceno ao Eoceno inferior (66 – 47.8 Ma).

6.1.2 Eoceno médio a superior (Lutetiano – Bartoniano) (43.5 – 37.6 Ma)

Erosão da Cordilheira Ocidental e instauração da plataforma carbonática

Após longo hiato sedimentar (~ 25 Ma) observado entre o Paleoceno ao Eoceno inferior (Roddaz et al., 2010; Horton, 2022; Custódio et al., 2023; Gutiérrez et al., 2019; Caballero et al., 2020; Moreno et al., 2020; Naeser et al., 1991), sedimentos derivados da Cordilheira Ocidental foram trapeados nas bacias de antepaís de retroarco, preenchendo a zona distal *foredeep* Peruana (Bacia de Huallaga) durante o Eoceno médio a superior (Lutetiano – Bartoniano) (43.5 – 37.6 Ma) na Amazônia Ocidental (Fig. 6.2). Um sistema de arco magmático Andino se desenvolveu na região da Cordilheira Ocidental, onde a maioria dos arcos vulcânicos forneceram crucial aporte sedimentar às bacias subandinas, registrados por picos de idades U-Pb de zircões de ~45 a 16 Ma (Arco Callipuy, Pfiffner and Gonzalez, 2013; Navarro et al., 2010) e lavas basálticas à andesíticas datadas de ~42 a 36 Ma (Arco Macuchi, Chiaradia, 2009). O registro sedimentar destes grãos de zircões Eocenos originados de arcos magmáticos Cretáceo – Eoceno da Cordilheira Ocidental sugerem que esta atuou como dominante área-fonte de sedimentos na Amazônia Ocidental

durante o Eoceno médio a superior, sem expressiva contribuição da Cordilheira Oriental até este momento (Fig. 6.2).

Esta configuração paleogeográfica atesta que não houve mudança significativa da área-fonte desde o Cretáceo ao Eoceno superior. O substancial processo de elevação da Cordilheira Ocidental durante o Eoceno deve estar associado às alterações na taxa de convergência entre as placas de Farallon e Sul-Americana. (Jaillard e Soler, 1996).

Com a propagação, a zona de deposição *foredeep* distal recebeu principalmente sedimentos clásticos não-marinhos (lacustres) com esporádicas incursões marinhas nas bacias de Huallaga, Marañon, Santiago e Oriente, indicada por uma ingressão vinda do norte, do mar do Caribe (Fig. 6.2) (Custódio et al., 2023; De La Parra et al., 2021; George et al., 2019; Louterbach et al., 2017; Hoorn et al., 2010; Roddaz et al., 2010; Hermoza et al., 2005; Hermoza, 2004; Christophoul et al., 2002). A transição paleoambiental ocorrida com a passagem de um ambiente continental isolado lacustre para ambiente costeiro com esporádicas ingressões marinhas, pode ter ampliado as interações da flora e fauna, contribuindo para a evolução da biodiversidade. A associação com as variações na paisagens devido ao soerguimento e a erosão da Cordilheira Ocidental resultantes de erupções vulcânicas, podem ter desempenhado papel fundamental no aumento da conectividade da cadeia de montanhas por elevação e preenchimento de vale, condicionando o padrão de distribuição biodiversidade em todo o norte dos Andes (Sanín et al., 2022).

Caracterizada por aumento na taxa de sedimentação (18.5 – 50.1 m/Ma), as bacias antepaís de retroarco se opõem às baixas taxas de acumulação observadas na região noroeste da margem Equatorial Atlântica (Bacia da Foz do Amazonas), favorecendo o estabelecimento e manutenção de uma plataforma carbonática (Rouby et al., 2023). O baixo aporte sedimentar trapeado neste região deriva principalmente de regiões cratônicas, tais como o Escudo das Guianas (Roddaz et al., 2021), Craton São Luís e Provincia Borbormea, evidenciados pela distribuição de idades de graõs de zircões detriticos > 500 Ma (2.2 – 2.0 Ga); (2.0 – 1.8 Ga); (~1.0 Ga) e valores mais radiogênicos para as composições isotópicas de Nd (ƐNd(0) -20.1 to -19.1). Em termos de sistema fonte-deposição (source-to-sink), durante o Paleogene ao Miocene inferior a médio, os dominios cratônicos (Guiana Shield) registraram baixas taxas de acumulação siliciclastica (Rouby et al., 2023), o que favorece a instauração da plataforma carbonatica na região da Bacia da Foz do Amazonas.

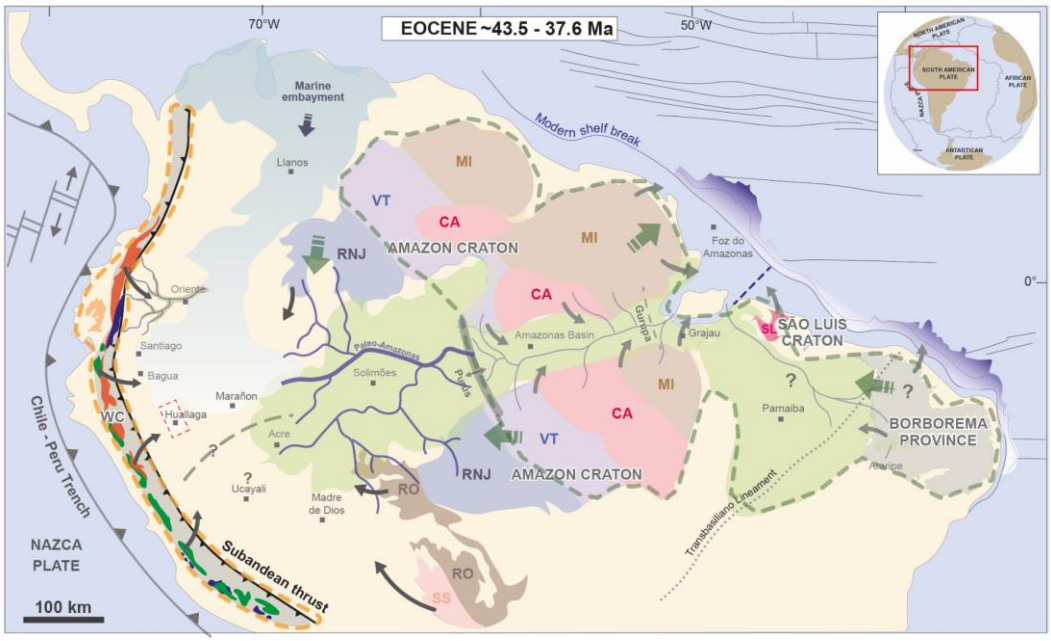


Figura 6. 2 Mapa da reconstrução paleogeográfica da porção norte da América do Sul, detalhes das areas source-to-sink durante o Eoceno médio a superior (43.5 – 37.6 Ma).

6.1.3 Oligoceno inferior (Rupeliano) a Mioceno médio (~30 – 12 Ma)

Soerguimento e erosão da Cordilheira Oriental e reativações tectonomagmáticas no NE da placa Sul-Americana

Foi no início do Oligoceno ao Mioceno médio que a Amazônia Ocidental passa a registrar forte mudança da área-fonte de sedimentos. Atrelado aos eventos de soerguimento e erosão da Cordilheira Oriental (~ 30 Ma), propagação do *front* orogênico e encurtamento horizontal (Bayona et al., 2008; Eude et al., 2015; Pfiffner and Gonzalez, 2013), o aumento significativo de sedimentos Paleozoicos (0.4 – 0.26 Ga) e Famatinianos (0.5 – 0.4 Ga) no registro sedimentar das bacias Amazônicas retroarco de antepaís sugere que a Cordilheira Oriental passa a ser dominante como area-fonte (Fig. 6.3). A mudança na proveniência também é acompanhada por mudanças de composições geoquímicas sedimentares e ambientes deposicionais, do sistema deposicional dominado por maré no Bartoniano Pozo Fm (Custódio et al., 2023) a um sistema fluvial sinuoso no Chambira Fm (Fig. 6.3). Esta última alteração paleoambiental coincide com o aumento das taxas de sedimentação (50.1 a 99.4 m/Ma). Interpretamos estes como indicativos de deposição na zona proximal do

foredeep durante o Oligoceno ao Mioceno médio, provavelmente atrelado ao encurtamento horizontal (Eude et al., 2015).

O intenso soerguimento da Cordilheira Oriental, a cerca de 30 - 12 Ma, pode ter contribuído para a geração de novos habitats, promovendo o isolamento e a divesificação biótica (Pérez-Escobar et al., 2022; Hoorn et al., 2018; Perrigo et al., 2019). Como consequência, o inicio da formação de uma barreira topográfica causada pelo soerguimento da Cordilheira Oriental pode ter impactado nas condições da circulação atmosférica local e regional, a médio e longo prazo (Poulsen et al., 2010), bem como na reorganização e ampliação da rede de drenagem, com instauração de uma padrão de sistemas fluviais meandrantes na Amazônia Ocidental (Fig. 6.3), implicando na extensão das áreas de drenagens aos domínios internos dos cratons. A atuação como barreira na distribuição de sedimentos é uma consequência deste processo de soerguimento da Cordilheira Oriental, atestado pela redução brusca de grãos de zircões oriundos dos arcos magmáticos Cretáceo-Cenozoico (Cordilheira Ocidental) (Fig. 6.3). A substancial elevação da Cordilheira Oriental pode ter impactado inclusive na intensificação do intemperismo e no desenvolvimento de terrenos elevados duradouros na Amazônia Central. Como identificado por Gautheron et al. (2022), o desenvolvimento de perfis de intemperismo laterítico na Amazônia Central permitiu definir ao menos dois principais períodos de fases intempéricas durante o Cenozoico. A fase mais antiga foi iniciada no Eoceno, sendo datada em torno de 42 Ma, que foi intensificada entre 30 e 18 Ma, e uma fase mais jovem bem registrada de ~8 a 1 Ma. Os eventos de soerguimentos das Cordilheiras Ocidental e Oriental, observados no presente estudo, datados do Eoceno (43.5 – 37.6 Ma) e Oligoceno ao Mioceno (~30 – 12 Ma) corroboram com os eventos intempéricos registrados por Gautheron et al. (2022) na Amazônia Central. A formação da segunda planície laterítica pode estar relacionada com o ciclo de laterização ‘Late Velhas surface’ de idade Miocênica (Théveniaut e Freyssinet, 2002) e as superficies S3-S4 que ocorre no Oligoceno superior ao Mioceno médio (Formações Pirabas e Barreiras) na Amazônia Oriental (Rossetti, 2004). Tais eventos intempéricos permitem inferir que os soerguimentos registrados inicialmente da Cordilheira Ocidental no Eoceno e, posteriormente da Cordilheira Oriental no Oligoceno condicionaram na mudança das condições atmosféricas atuantes na Amazônia Ocidental e Central, com impactos a médio e longo prazo. Dessa forma, a gênese desses depositos lateriticos formados na Amazônia Central e Oriental neste periodo pode ter sido

controlada pela interação complexa do intenso soerguimento da Cordilheira Oriental (tectônica), clima (chuvas orograficas), aumento das taxas de erosão.

Apesar do estabelecimento de um pungente sistema fluvial na região da Amazônia Ocidental, durante o Oligoceno ao Mioceno médio, o mesmo não permitiu a conexão com a Amazônia Oriental, permanecendo domínio da sedimentação Cratônica na Bacia da Foz do Amazonas (Moizinho et al., 2022), corroborado no presente estudo pelos valores mais negativos das composições isotópicas de Nd (ƐNd(0) -20.1 a -19.1) e sem a evidência de contribuição Andina nos grãos de zircões detríticos (Fig. 6.4).

Os processos de reorganização da rede de drenagem também são registrados na região nordeste da placa Sul-Americana (Oliveira et al., 2023), por vezes obdecendo padrões radiais, típicos de domos vulcânicos (Fig. 6.4) (Klöcking et al., 2020). Produtos de reativações tectonomagmáticas, estes sistemas de drenagens passam atuar como fornecedores de sedimentos da Província Borborema à margem Equatorial do Oceano Atlântico (Fig. 6.4). Tais configuraçoes neotectônicas sugerem que as reativações de zonas de cisalhamentos (Souza et al., 2022) e eventos magmáticos Cenozoicos (Oliveira et al., 2023; Klöcking et al., 2020; Souza et al., 2013), levaram ao soerguimento da crosta na região nordeste placa Sul-Americana e contribuiram ao registro sedimentar da Bacia da Foz do Amazonas (Fig. 6.4; 7.1).

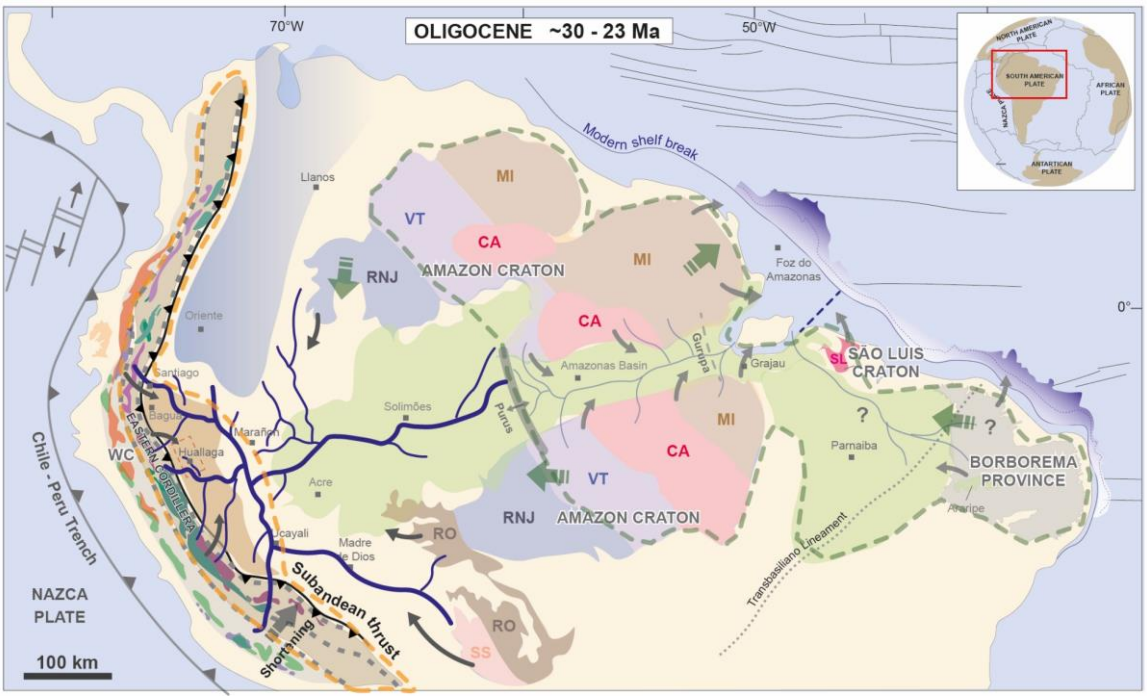


Figura 6. 3 Mapa da reconstrução paleogeográfica da porção norte da América do Sul, detalhes das áreas source-to-sink durante o Oligoceno (~30 – 23 Ma).

Em termos do sistema area-fonte e deposição (*source-to-sink*), o intenso evento de soerguimento da Cordilheira Oriental, aumentou o aporte sedimentar para as bacias de retroarco antepaís, para as quais foi o principal contribuinte. Enquanto que, os eventos neotectonicos de reativações e magmatismo Cenozoico (27 to 12 Ma) (Souza et al., 2013) ocorridos no nordeste da placa Sul-Americana, atuaram como dominante area fonte de sedimentos para a região noroeste da margem Equatorial do Oceano Atlântico. Para ambos, estariam atuando como consequencias ao movimento da placa sul-Americana em sentido a oeste, apos a fragmentação do Gondwana.

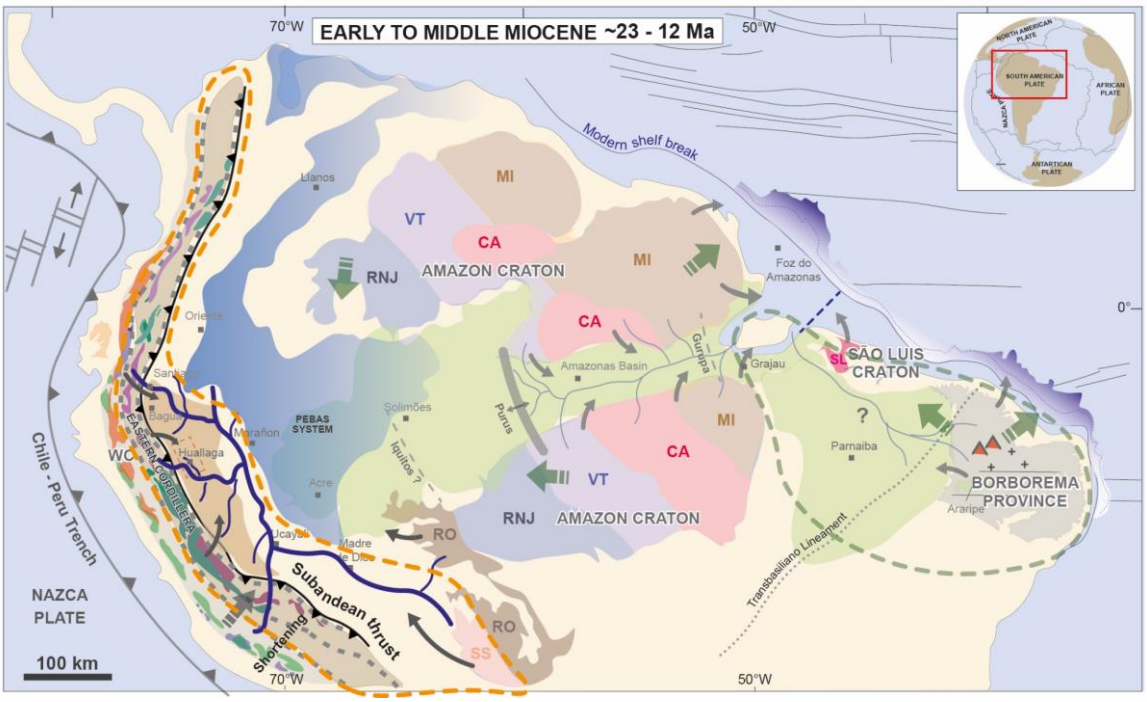


Figura 6. 4 Mapa da reconstrução paleogeográfica da porção norte da América do Sul, detalhes das areas source-to-sink durante o Mioceno inferior a médio (23 – 12 Ma).

6.1.4 Mioceno médio - superior ao Recente (~12 Ma – Recente)

Exumação acelerada da Cordilheira Oriental, reorganização de drenagens e início do rio transcontinental do Amazonas

Durante o Mioceno superior, o estabelecimento do atual curso do rio transcontinental do Amazonas passa a conectar as bacias de Amazônicas de antepaís retroarco e as bacias da margem Equatorial Atlântica (Hoorn et al., 2010), indicado pelos primeiros detritus Andinos na Bacia da Foz do Amazonas 8.3 e 11.8 Ma atrás (Mioceno superior) (van Soelen et al., 2017; Hoorn et al., 2017; Figueiredo et al., 2009). A mudança de fonte na margem Equatorial esta em concordância com as variações dos valores das composições isotopicas de Nd, onde sinalizam que a partir de 11.93 Ma – 8.0 Ma, os valores de ƐNd(0) se tornam menos radiogênicos, com valores da ordem de -11.4. De fato, a aceleração do soerguimento da Cordilheira Oriental resultou em um aumento consideravel do aporte sedimentar nas bacias de retroarco-antepais, reorganização das drenagens, resultando no *overfilled* destas bacias (Roddaz et al., 2010; Sacek, 2014) e inversão do PaleoAmazonas para leste (Fig. 6.5) (Potter, 1997). A construção da Cordilheira Oriental como barreira topográfica, pode ter causado aumento da sua erosão e

da Zona Sub-Andina por precipitações concentradas devido às mudanças climáticas entre o Mioceno médio e o Mioceno superior. Em resposta, o sistema de drenagem na região *retro-foreland* expandiu-se para leste na Bacia do Amazonas, sobrepassando o Arco do Purus e, por fim, conectando com um vale fluvial costeiro para dar origem ao moderno Rio Amazonas (Fig. 6.5).

Na Amazônia Oriental, em particular nas bacias onshore e plataformas, registraram um aumento maciço de aporte siliciclastico durante o Mioceno médio (Mabesoone et al., 1972; Bigarella, 1975; Arai, 2006; Rossetti et al., 2013). A acumulação de rochas sedimentares Miocênicas na costa da Amazônia Oriental teria sido governada por atividades Neotectônicas post-rift (Bezerra et al., 2001; Rossetti e Goes, 2004; Rossetti, 2006; Nobrega et al., 2005; Rossetti et al., 2013), que condicionaram inclusive a deposição de sedimentos Pleistocënicos – Holocênicos na porção norte da margem Equatorial Brasileira (Rossetti et al., 2012).

Ressalta-se que a transcontinentalização do Amazonas River antecede ao aumento das taxas de sedimentação na Bacia da Foz do Amazonas (Figueiredo et al., 2009), reforçado pela mudança dos valores de ƐNd registradas inicialmente no topo da Formação Amapa (11.93 – 10.8 Ma). Comparando nossos dados com o de van Soelen et al. (2017) não conseguimos identificar um episódico pulso de sedimentos de origem Andina no Mioceno inferior (18.3 Ma), somente assinaturas tipicamente cratônicas ƐNd (-20,1 a 19). Portanto, se referir a uma entrada dominantemente Andina durante o Mioceno inferior não é correto. No entanto, à esta discrepância, podemos atribuir à baixa resolução de amostragem ou que Purus ainda estava ativo em meados de 18 Ma.

As complexas interações de atividades neotectônicas, variações climaticas e de taxas de sedimentação e erosão teriam controlado a formação da mais recente superficie lateritica (S5) datada do Plio-Pleistoceno (Post-Barreiras 1) (Rossetti, 2004).

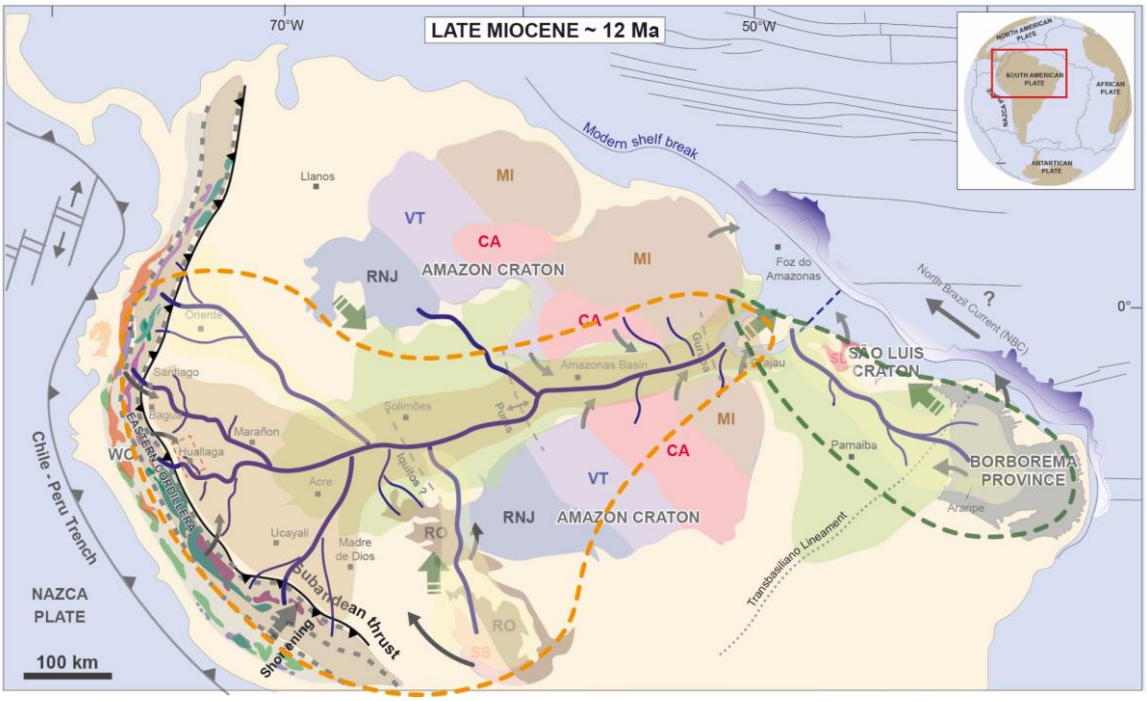


Figura 6. 5 Mapa da reconstrução paleogeográfica da porção norte da América do Sul, detalhes das areas source-to-sink durante o Miocene superior (~ 12 Ma).

REFERÊNCIAS

Bayona, G., Cortes, M., Jaramillo, C., Ojeda, G., Aristizabal, J.J., Reyes-Harker, A., 2008. An integrated analysis of an orogen-sedimentary basin pair: Latest Cretaceous-Cenozoic evolution of the linked Eastern Cordillera orogen and the Llanos foreland basin of Colombia. Geological Society of America Bulletin 120, 1171–1197. https://doi.org/10.1130/B26187.1

Bezerra, F.H.R., Amaro, V.E., Vitafinzi, C., Saadi, A., 2001. Pliocene–Quaternary fault control of sedimentation and coastal plain morphology in NE Brazil. J. S. Am. Earth Sci. 14, 61–75.

Caballero, V.M., Naranjo Vesga, J.F., Gómez Gutiérrez, P.D., Rodriguez Forero, G., Mora Bohorquez, A.R., Franco Castro, W.M., Gelvez Llanez, J.R., Villamizar Villamizar, C.A., 2020. Eocene facies successions and environments in the Southern Llanos basin, Colombia. CT&F Cienc. Tecnol. Futuro 10, 107–122. https://doi.org/10.29047/01225383.141

Chiaradia, M., 2009. Adakite-like magmas from fractional crystallization and melting-assimilation of mafic lower crust (Eocene Macuchi arc, Western Cordillera, Ecuador). Chemical Geology 265, 468–487. https://doi.org/10.1016/j.chemgeo.2009.05.014

Christophoul, F., Baby, P., Dávila, C., 2002. Stratigraphic responses to a major tectonic event in a foreland basin: the Ecuadorian Oriente Basin from Eocene to Oligocene times. Tectonophysics 345, 281–298. https://doi.org/10.1016/S0040-1951(01)00217-7

Custódio, M.A., Roddaz, M., Santos, R.V., Antoine, P.-O., Marivaux, L., Stutz, N.S., Dantas, E.L., Jaramillo, C., Louterbach, M., Hurtado, C., Oliveira Gonçalves, G., 2023. New stratigraphic and paleoenvironmental constraints on the Paleogene paleogeography of Western Amazonia. Journal of South American Earth Sciences 124, 104256. https://doi.org/10.1016/j.jsames.2023.104256

De La Parra, F., Pinzon, D., Mantilla-Duran, F., Rodriguez, G., Caballero, V., 2021. Marine-lacustrine systems during the Eocene in northern South America – Palynological evidence from Colombia. Journal of South American Earth Sciences 108, 103188. https://doi.org/10.1016/j.jsames.2021.103188

Eude, A., Roddaz, M., Brichau, S., Brusset, S., Calderon, Y., Baby, P., Soula, J.-C., 2015. Controls on timing of exhumation and deformation in the northern Peruvian eastern Andean wedge as inferred from low-temperature thermochronology and balanced cross section: Exhumation and Deformation of North Peru. Tectonics 34, 715–730. https://doi.org/10.1002/2014TC003641

Figueiredo, J., Hoorn, C., van der Ven, P., Soares, E., 2009. Late Miocene onset of the Amazon River and the Amazon deep-sea fan: Evidence from the Foz do Amazonas Basin. Geology 37, 619–622. https://doi.org/10.1130/G25567A.1

Gautheron, C., Sawakuchi, A.O., Albuquerque, M. F. S., Cabriolu, C., Parra, M., Ribas, C.C., Pupim, F.N., Schwartz, S., Kern, A.K., Gómez, S., Almeida, R.P., Horbe, A.M.C., Haurine, F., Miska, S., Nouet, J., Findling, N., Riffel, S.B., Pinna-Jamme, R. 2022. Cenozoic weathering of fluvial terraces and emergence of biogeographic boundaries in Central Amazonia, Global and Planetary Change, Volume 212.

George, S.W.M., Horton, B.K., Jackson, L.J., Moreno, F., Carlotto, V., Garzione, C.N., 2019. Sediment provenance variations during contrasting Mesozoic-early Cenozoic tectonic regimes of the northern Peruvian Andes and Santiago-Marañón foreland basin, in: Andean Tectonics. Elsevier, pp. 269–296. https://doi.org/10.1016/B978-0-12-816009-1.00012-5

Gorini, C., Haq, B.U., dos Reis, A.T., Silva, C.G., Cruz, A., Soares, E., Grangeon, D., 2014. Late Neogene sequence stratigraphic evolution of the Foz do Amazonas Basin, Brazil. Terra Nova 26, 179–185. https://doi.org/10.1111/ter.12083

Gutiérrez, E.G., Horton, B.K., Vallejo, C., Jackson, L.J., George, S.W.M., 2019. Provenance and geochronological insights into Late Cretaceous-Cenozoic foreland basin development in the Subandean Zone and Oriente Basin of Ecuador, in: Andean Tectonics. Elsevier, pp. 237–268. https://doi.org/10.1016/B978-0-12-816009-1.00011-3

Hermoza, W., Brusset, S., Baby, P., Gil, W., Roddaz, M., Guerrero, N., Bolaños, R., 2005. The Huallaga foreland basin evolution: Thrust propagation in a deltaic environment, northern Peruvian Andes. Journal of South American Earth Sciences 19, 21–34. https://doi.org/10.1016/j.jsames.2004.06.005

Hermoza, W., 2004. Dynamique tectono-s´edimentaire et restauration s´equentielle du r´etro-bassin d'avant-pays des Andes centrales. Available at: http://www.theses.fr. (Accessed 10 January 2022) http://www.theses.fr/2004TOU30134. Accessed.

Hoorn, C., Bogotá-A, G.R., Romero-Baez, M., Lammertsma, E.I., Flantua, S.G.A., Dantas, E.L., Dino, R., do Carmo, D.A., Chemale, F., 2017. The Amazon at sea: Onset and stages of the Amazon River from a marine record, with special reference to Neogene plant turnover in the drainage basin. Global and Planetary Change 153, 51–65. https://doi.org/10.1016/j.gloplacha.2017.02.005

Hoorn, C., Wesselingh, F.P., ter Steege, H., Bermudez, M.A., Mora, A., Sevink, J., Sanmartín, I., Sanchez-Meseguer, A., Anderson, C.L., Figueiredo, J.P., Jaramillo, C., Riff, D., Negri, F.R., Hooghiemstra, H., Lundberg, J., Stadler, T., Särkinen, T., Antonelli, A., 2010. Amazonia Through Time: Andean Uplift, Climate Change, Landscape Evolution, and Biodiversity. Science 330, 927–931. https://doi.org/10.1126/science.1194585

Hoorn, C., Perrigo, A., Antonelli, A., 2018. Introduction: Mountains, Climate and Biodiversity. In: Mountains, Climate and Biodiversity, Hoorn, C., Perrigo, A., & Antonelli, A. (Eds.). (2018). John Wiley & Sons.

Horton, B.K., 2018. Sedimentary record of Andean mountain building. Earth-Science Reviews 178, 279–309. https://doi.org/10.1016/j.earscirev.2017.11.025

Horton, B.K., 2022. Unconformity development in retroarc foreland basins: implications for the geodynamics of Andean-type margins. JGS 179, jgs2020-263. https://doi.org/10.1144/jgs2020-263

Hurtado, C., Roddaz, M., Santos, R.V., Baby, P., Antoine, P.-O., Dantas, E.L., 2018. Cretaceous-early Paleocene drainage shift of Amazonian rivers driven by Equatorial Atlantic Ocean opening and Andean uplift as deduced from the provenance of northern Peruvian sedimentary rocks (Huallaga basin). Gondwana Research 63, 152–168. https://doi.org/10.1016/j.gr.2018.05.012

Jaillard, E., Soler, P., 1996. Cretaceous to early Paleogene tectonic evolution of the northern Central Andes (0–18°S) and its relations to geodynamics. Tectonophysics 259, 41–53. https://doi.org/10.1016/0040-1951(95)00107-7

Klöcking, M., Hoggard, M.J., Rodríguez Tribaldos, V., Richards, F.D., Guimarães, A.R., Maclennan, J., White, N.J., 2020. A tale of two domes: Neogene to recent volcanism and dynamic uplift of northeast Brazil and southwest Africa. Earth and Planetary Science Letters 547, 116464. https://doi.org/10.1016/j.epsl.2020.116464

Louterbach, M., Roddaz, M., Antoine, P.-O., Marivaux, L., Adnet, S., Bailleul, J., Dantas, E., Santos, R.V., Chemale, F., Baby, P., Sanchez, C., Calderon, Y., 2017. Provenance record of late Maastrichtian-late Palaeocene Andean Mountain building in the Amazonian retroarc foreland basin (Madre de Dios basin, Peru). Terra Nova 30, 17–23. https://doi.org/10.1111/ter.12303

Louterbach, M., Roddaz, M., Bailleul, J., Antoine, P.-O., Adnet, S., Kim, J.H., van Soelen, E., Parra, F., Gérard, J., Calderon, Y., Gagnaison, C., Sinninghe Damsté, J.S., Baby, P., 2014. Evidences for a Paleocene marine incursion in southern Amazonia (Madre de Dios Sub-Andean Zone, Peru). Palaeogeography, Palaeoclimatology, Palaeoecology 414, 451–471. https://doi.org/10.1016/j.palaeo.2014.09.027

Moizinho, G.R., Vieira, L.C., Santos, R.V., Nogueira, A.C.R., Dantas, E.L., Roddaz, M., 2022. Provenance of Miocene-Pleistocene siliciclastic deposits in the Eastern Amazonia coast (Brazil) and paleogeographic implications. Palaeogeography, Palaeoclimatology, Palaeoecology 587, 110799. https://doi.org/10.1016/j.palaeo.2021.110799

Moreno, F., Garzione, C.N., George, S.W.M., Horton, B.K., Williams, L., Jackson, L.J., Carlotto, V., Richter, F., Bandeian, A., 2020. Coupled Andean Growth and Foreland Basin Evolution, Campanian–Cenozoic Bagua Basin, Northern Peru. Tectonics 39. https://doi.org/10.1029/2019TC005967

Moreno, F., Garzione, C.N., George, S.W.M., Williams, L., Richter, F., Bandeian, A., 2022. Late Cretaceous through Cenozoic Paleoenvironmental History of the Bagua Basin, Peru: Paleoelevation Comparisons with the Central Andean Plateau. Geosciences 12, 242. https://doi.org/10.3390/geosciences12060242

Mourier, T., Bengtson, P., Bonhomme, M., Buge, E., Cappettta, H., Crochet, J.-Y., Feist, M., Hirsch, K.F., Jaillard, E., Laubacher, G., Lefranc, J.P., Moullade, M., Noblet, C., Pons, D., Rey, J., Sigé, B., Tambareau, Y., Taquet, P., 1988. The Upper Cretaceous - Lower Tertiary marine to continental transition in the Bagua basin, northern Peru - Paleontology, biostratigraphy, radiometry, correlations. nos 19, 143–177. https://doi.org/10.1127/nos/19/1988/143

Navarro, C., Alexis, P., Rivera Porras, M. A., Monge Miguel, R. W. 2010. Geología y metalogenia del Grupo Calipuy (Volcanismo Cenozoico) segmento Santiago de Chuco, norte del Perú - [Boletín D 28]. Instituto Geológico, Minero y Metalúrgico – INGEMMET, 192p.

Naeser, C.W., Crochet, J.-Y., Jaillard, E., Laubacher, G., Mourier, T., Sigé, B., 1991. Tertiary fission-track ages from the Bagua syncline (northern Peru): Stratigraphic and tectonic implications. Journal of South American Earth Sciences 4, 61–71. https://doi.org/10.1016/0895-9811(91)90018-G

Oliveira, G.P., Carlos de Barros Corrêa, A., de Azevedo Cavalcanti Tavares, B., de Araujo Monteiro, K., 2023. The influence of cenozoic magmatism on drainage rearrangement processes of the northeast sector of the Borborema Highlands, northeastern Brazil. Journal of South American Earth Sciences 121, 104124. https://doi.org/10.1016/j.jsames.2022.104124

Pérez-Escobar OA, Zizka A, Bermúdez MA, Meseguer AS, Condamine FL, Hoorn C, Hooghiemstra H, Pu Y, Bogarín D, Boschman LM, Pennington RT, Antonelli A, Chomicki G. The Andes through time: evolution and distribution of Andean floras. Trends Plant Sci. 2022 Apr;27(4):364-378. doi: 10.1016/j.tplants.2021.09.010. Epub 2022 Jan 6. PMID: 35000859.

Perrigo, A., Hoorn, C., & Antonelli, A. 2019. Why mountains matter for biodiversity. Journal of Biogeography, 47(2), 315-325.

Pfiffner, O., Gonzalez, L., 2013. Mesozoic–Cenozoic Evolution of the Western Margin of South America: Case Study of the Peruvian Andes. Geosciences 3, 262–310. https://doi.org/10.3390/geosciences3020262

Prasad, G. 1983. A review of the early Tertiary bauxite event in South America, Africa and India. J. Afr. Earth Sci. 1, 305–313.

Potter, P.E., 1997. The Mesozoic and Cenozoic paleodrainage of South America: a natural history. Journal of South American Earth Sciences 10, 331–344. https://doi.org/10.1016/S0895-9811(97)00031-X

Poulsen, C.J., Ehlers, T.A., and Insel, N. 2010. Onset of convective rainfall during gradual late Miocene rise of the central Andes. Science, 328(5977), 490-493.

Roddaz, M., Hermoza, W., Mora, A., Baby, P., Parra, M., Christophoul, F., Brusset, S., Espurt, N., 2010. Cenozoic Sedimentary Evolution of the Amazonian Foreland Basin System, in: Hoorn, C., Wesselingh, F.P. (Eds.), Amazonia: Landscape and Species Evolution. Wiley-Blackwell Publishing Ltd., Oxford, UK, pp. 61–88. https://doi.org/10.1002/9781444306408.ch5

Roddaz, M., Viers, J., Brusset, S., Baby, P., Boucayrand, C., Hérail, G., 2006. Controls on weathering and provenance in the Amazonian foreland basin: Insights from major and trace element geochemistry of Neogene Amazonian sediments. Chemical Geology 226, 31–65. https://doi.org/10.1016/j.chemgeo.2005.08.010

Roddaz, M., Dera, G., Mourlot, Y., Calvès, G., Kim, J.-H., Chaboureau, A.-C., Mounic, S., Raisson, F., 2021. Provenance constraints on the Cretaceous-Paleocene erosional history of the Guiana Shield as determined from the geochemistry of clay-size fraction of sediments from the Arapaima-1 well (Guyana-Suriname basin). Marine Geology 434, 106433. https://doi.org/10.1016/j.margeo.2021.106433

Rodrigues, M. de A., Roddaz, M., Santos, R.V., Louterbach, M., D'Apolito, C., Brusset, S., Dantas, E.L., Negri, F.R., 2023. New insights into the Cretaceous evolution of the Western Amazonian paleodrainage system. Sedimentary Geology 453, 106434. https://doi.org/10.1016/j.sedgeo.2023.106434

Rossetti, D.F., 2004. Paleosurfaces from northeastern Amazonia as a key for Reconstructing Paleolandscapes and Understanding weathering Products. Sedimentary Geology, Holanda 169 (3–4), 151–174. https://doi.org/10.1016/j.sedgeo.2004.05.003

Rossetti, D.F., 2006. Evoluçao Sedimentar Miocˆenica nos Estados do Para e Maranhao. Rev. do Inst. Geociencias, USP 6 (2), 7–18. https://doi.org/10.5327/S1519874X2006000300003.

Rossetti, D.F., Bezerra, F.H.R., Dominguez, J.M.L., 2013. Late Oligocene–Miocene transgressions along the equatorial and eastern margins of Brazil. Earth-Sci. Rev. 123, 87–112. https://doi.org/10.1016/j.earscirev.2013.04.005.

Rossetti, D.F., Souza, L.S.B., Elis, V.R., 2012. Neotectonics in the Northern Equatorial Brazilian margin. J. S. Am. Earth Sci. 37, 175–190. https://doi.org/10.1016/j. jsames.2012.03.004.

Rossetti, D.F., Goes, A.M., 2004. Geologia. In: Rossetti; Goes. (Org.). O Neogeno da Amazonia Oriental. 1ed. Bel´em: Editora Museu Goeldi, 1, pp. 13–52.

Rouby, D., Loparev, A., Chardon, D., Bajolet, F., Dall'Asta, M., Paquet, F., Fillon, C., Roig, J.-Y., Ye, J., 2023. Sediment routing systems to the Atlantic rifted margin of the Guiana Shield. Geosphere. https://doi.org/10.1130/GES02561.1

Sacek, V., 2014. Drainage reversal of the Amazon River due to the coupling of surface and lithospheric processes. Earth and Planetary Science Letters 401, 301–312. https://doi.org/10.1016/j.epsl.2014.06.022

Sanín, M.J., Cardona, A, Valencia-Montoya, W.A., Jiménez, M.F.T., Carvalho-Madrigal, S., Gómez, A.C., Bacon, C.D., Tangarife, T.R., Jaramillo, J.S., Zapata, S., Valencia, V., Valencia, J.W.A., Vargas, V., Paris, M. 2022. Volcanic events coincide with plant dispersal across the Northern Andes, Global and Planetary Change, Volume 210.

Souza, C.M.P., Lima, C.C.U. de, Costa, L.M., Veloso, G.V., Gomes, R.L., Leite, M.E., Fernandes-Filho, E.I., 2022. Geomorphic indices, machine learning and osl-palynology chronology to

assess neotectonic deformation in the continental margin – Northeastern Brazil. Journal of South American Earth Sciences 118, 103931. https://doi.org/10.1016/j.jsames.2022.103931

Souza, Z.S., Vasconcelos, P.M., Knesel, K.M., da Silveira Dias, L.G., Roesner, E.H., Cordeiro de Farias, P.R., de Morais Neto, J.M., 2013. The tectonic evolution of Cenozoic extensional basins, northeast Brazil: Geochronological constraints from continental basalt 40Ar/39Ar ages. Journal of South American Earth Sciences 48, 159–172. https://doi.org/10.1016/j.jsames.2013.09.008

Tardy, Y.;C. Roquin. 1998. Dérive des continents paléoclimats et altérations tropicales: 1-473. BRGM, Orléans.

Théveniaut, H., Freyssinet, Ph. 2002. Timing of lateritization on the Guiana Shield: synthesis of paleomagnetic results from French Guiana and Suriname. Palaeogeography, Palaeoclimatology, Palaeoecology 178 (2002) 91-117

van Soelen, E.E., Kim, J.-H., Santos, R.V., Dantas, E.L., Vasconcelos de Almeida, F., Pires, J.P., Roddaz, M., Sinninghe Damsté, J.S., 2017. A 30 Ma history of the Amazon River inferred from terrigenous sediments and organic matter on the Ceará Rise. Earth and Planetary Science Letters 474, 40–48. https://doi.org/10.1016/j.epsl.2017.06.025

Zamora, G., Gil, W., 2018. The Marañon Basin: tectonic evolution and paleogeography. AAPG Mem 117, 121–143. https://doi.org/10.1306/13622119M1173768.

CAPÍTULO 7

CONCLUSÃO E PERSPECTIVAS

7. CONCLUSÃO E PERSPECTIVAS

Les résultats de cette thèse ont pu montrer que du Paléocène à l'Éocène inférieur (Danien - Yprésien) (66 – 43.5 Ma), un hiatus de dépôt s'est développé dans les bassins d'avant retroarc amazonien lié à un épisode de quiescence tectonique dans les Andes. Cette quiescence tectonique est contemporaine de la formation des surfaces latéritiques "sul-americano" en Amazonie centrale et aux faibles taux de sédimentation dans le bassin de Foz do Amazonas (Fig. 7.1). En Amazonie orientale, les faibles taux d'apport des régions cratoniques peuvent avoir favorisé le développement de la plate-forme carbonatée au nord-ouest de la marge équatoriale sud-américaine. La présence de cette quiescence dans la tectonique andine au Paléocène suggère que la première phase de de latérisation "sul-americano" a probablement été contrôlée par des facteurs climatiques. La reprise du soulèvement et de l'érosion des Andes péruviennes à l'Éocène moyen ou tardif (Lutétien - Bartonien) (43.5 – 37.6 Ma) a été enregistrée dans la sédimentation du bassin d'avant-pays retroarc amazonien par la présence de détritus provenant des arcs magmatiques de la Cordillère Occidentale et par une transgression au Bartonien marquée par la présence de dépôts tidaux sur des dépôts continentaux lacustres. Le début du soulèvement de la Cordillère Orientale est enregistré dans les sédiments du d'avant-pays retroarc amazonien (bassin de Huallaga) il y a 30 Ma, au Rupélien (Fig. 7.1). Du Rupélien au Miocène moyen, la Cordillère Orientale continue à se soulever, créant un relief topographique capable de jouer le rôle de barrière orographique aux flux atmosphérique en provenance de l'Océan Atlantique. Ce soulèvement continue peut avoir provoquer la présence de climats plus humides en Amazonie occidentale ce qui pourrait avoir favoriser la formation de surfaces latéritiques en Amazonie centrale entre l'Oligocène et le Miocène inférieur,en relation avec la phase intense d'altération ayant eu lieue entre 30 et 18 Ma (Fig. 7.1). Nos données de provenance enregistrent une nouvelle période d'exhumation de la Cordillère Orientale du Miocène supérieur à l'actuel. Cette période se marque dans l'enregistrement sédimentaire du bassin d'avant-pays retroarc amazonien par des detritus provenant exclusivement de la Cordillère Orientale.Cette période de réjuvenation du relief de la Cordillère orientale est liée à une période de propagation du prisme orogénique amazonien en direction du craton. Elle induit une réorganisation du réseau de drainage amazonien et constitue probablement un des moteurs de la transcontinentalisation de l'Amazone au miocène moyen-supérieur. Finalement, le système AAMESA n'existe en termes de "source-to-sink" (S2S) qu'à partir

du Miocène supérieur, avec l'établissement transcontinental du fleuve Amazone. La période précédente est marquée par la domination de deux systèmes différents, représentés par le craton amazonien oriental et la région NE de l'Amérique du Sud (province de Borborema, craton de São Luis, ceinture de Gurupi). Pour améliorer la connaissance géologique de ces systèmes, il serait intéressant de travailler dans le futur à l'intégration des données sismiques 2D et 3D des bassins intracratoniques brésiliens avec celles de la marge équatoriale. La connaissance de la partie orientale du système pourrait être améliorée en s'intéressant aux paramètres climatiques et paleoenvironnementaux qui ont contrôlé l'établissement de la plate forme carbonatée de la formation Amapa en pratiquant un échantillonnage serré et systématique pour mesurer les compositions isotopiques en Sr, C et O. Enfin, l'effet des courants océaniques sur le déplacement des sédiments sur la marge équatoriale au cours du Paléogène mériterait d'être investigué.

7.1 CONCLUSÃO

Os resultados desta tese mostraram que, do Paleoceno ao Eoceno Inferior (Daniano - Ypresiano) (66 - 43.5 Ma), desenvolveu-se um hiato deposicional nas bacias do *foreland* do retroarco amazônico ligado a um episódio de quiescência tectônica nos Andes. Essa quiescência tectônica foi contemporânea à formação das superfícies lateríticas "sul-americanas" na Amazônia Central e às baixas taxas de sedimentação na bacia da Foz do Amazonas (Fig. 7.1). No leste da Amazônia, as baixas taxas de entrada das cargas sedimentares das regiões cratônicas podem ter favorecido o desenvolvimento da plataforma carbonática a noroeste da margem equatorial da América do Sul. A presença dessa quiescência na tectônica andina durante o Paleoceno sugere que a primeira fase da laterização "sul-americana" foi provavelmente controlada por fatores climáticos.

A retomada do soerguimento e da erosão dos Andes peruanos no Eoceno médio ou tardio (Luteciano - Bartoniano) (43.5 - 37.6 Ma) foi registrada na sedimentação da bacia do *foreland* do retroarco amazônico pela presença de detritos dos arcos magmáticos da Cordilheira Ocidental e por uma transgressão no Bartoniano marcada pela presença de depósitos de maré em depósitos lacustres continentais. O início do soerguimento da Cordilheira Oriental é registrado nos sedimentos do *foreland* do retroarco amazônico (bacia Huallaga) há 30 Ma, no Rupeliano (Fig. 7.1). Do Rupeliano ao Mioceno Médio, a

Cordilheira Oriental continuou a se elevar, criando um relevo topográfico capaz de atuar como uma barreira orográfica aos fluxos atmosféricos do Oceano Atlântico. Essa elevação contínua pode ter levado à presença de climas mais úmidos no oeste da Amazônia, o que poderia ter favorecido a formação de superfícies lateríticas na Amazônia central entre o Oligoceno e o Mioceno Inferior, em relação à intensa fase de alteração que ocorreu entre 30 e 18 Ma (Fig. 7.1).

Nossos dados de proveniência registram um novo período de exumação da Cordilheira Oriental desde o Mioceno Superior até os dias atuais. Esse período é marcado no registro sedimentar da bacia do foreland do retroarco amazônico por detritos originários exclusivamente da Cordilheira Oriental. Esse período de rejuvenescimento do relevo da Cordilheira Oriental está ligado a um período de propagação do prisma orogênico amazônico em direção ao cráton. Isso levou a uma reorganização da rede de drenagem amazônica e é provavelmente uma das forças motrizes por trás da transcontinentalização da Amazônia no Mioceno Médio-Superior.

Por fim, o sistema AAMESA não existia em termos de "source-to-sink" (S2S) até o Mioceno tardio, com o estabelecimento transcontinental do rio Amazonas. O período anterior foi marcado pelo domínio de dois sistemas diferentes, representados pelo cráton amazônico oriental e pela região NE da América do Sul (província Borborema, cráton São Luis, cinturão Gurupi).

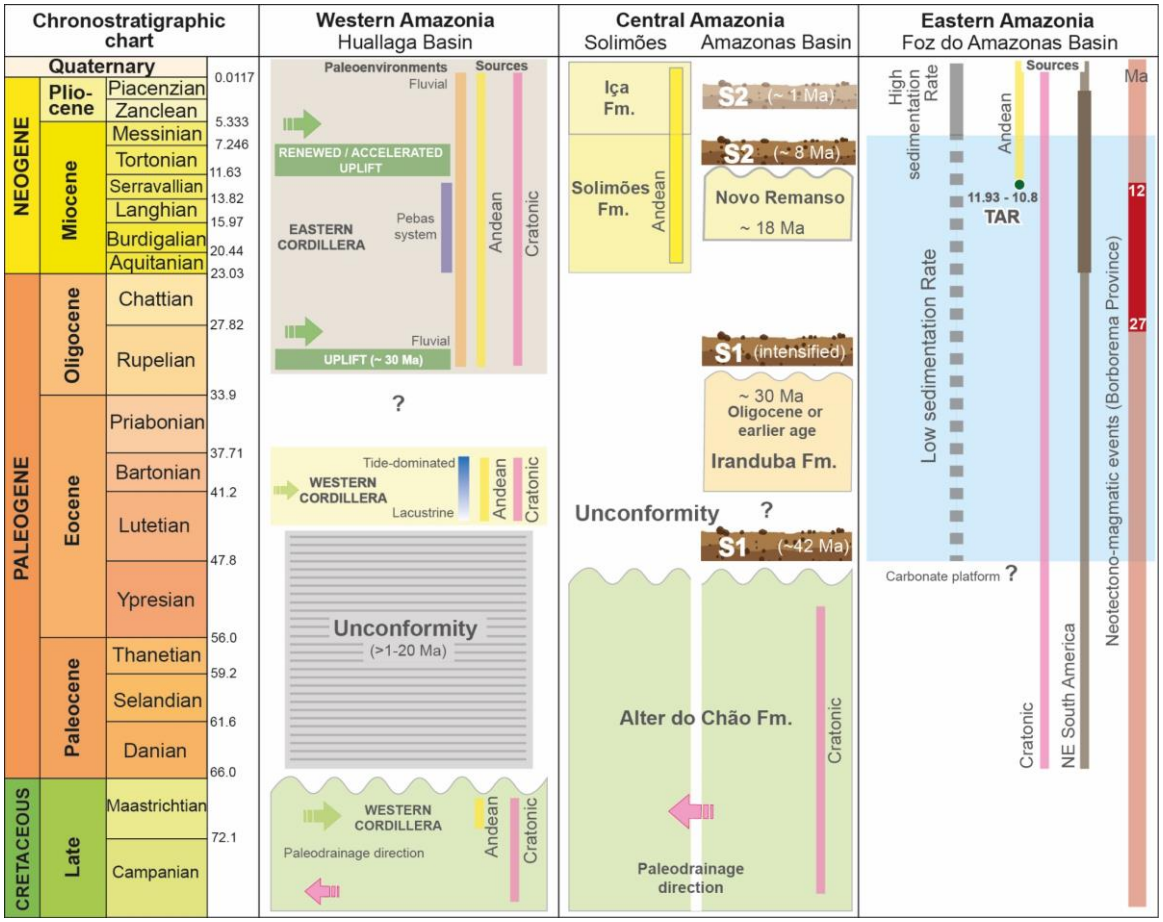


Figura 7. 1 Esboço esquemático dos principais eventos geológicos ocorridos espaço-temporalmente no sistema fonte-sedimentação Andes-Amazônia-Margem Equatorial Sul-Americana ao longo do Cenozoico. Os dados representam as principais mudanças de áreas-fontes; variações paleoambientais; reorganização do padrão de drenagens Amazônico; eventos de discordância regional; eventos erosivos das Cordilheiras Oriental e Ocidental; início do estabelecimento do rio Amazonas transcontinental (*Transcontinental Amazon River* - TAR); formação de superfícies lateríticas na Amazônia Central (S1-S2) (Gautheron et al., 2022); variações nas taxas de sedimentação (Rouby et al., 2023); áreas-fontes da sequência Miocênica da Bacia do Solimões (Horbe et al., 2019; 2013); eventos neotectono-magmáticos ocorridos na Província Borborema (Souza et al., 2013; Oliveira et al., 2023; Klöcking et al., 2020; Souza et al., 2013).

7.2 PERSPECTIVAS

Considerando a dimensão espaço-temporal e a complexidade de variáveis envolvidas no sistema fonte-sedimentação Andes – Amazônia – Margem Equatorial Sul-Americana (AAMESA) é necessário ter em conta que a presente pesquisa é um passo em direção a um entendimento mais profundo do tópico. Apesar da pesquisa ter avançado no conhecimento da lacuna de eventos ocorridos antes do estabelecimento do atual rio transcontinental do Amazonas durante o Paleogeno nas Amazônias Ocidental e Oriental,

tais entendimentos podem ser aprofundados ou expandidos. Nesse sentido, podendo envolver estudos de seguimento com diferentes abordagens ou uma ampliação da amostragem.

No estudo da evolução sedimentar do sistema AAMESA, maior disponibilidade de dados (dados sísmicos 2D e 3D, perfurações, amostras), principalmente na zona central do sistema (bacias intracratônicas brasileiras) integrados com dados da zona de sedimentação (margem equatorial) permitiria melhorar o conhecimento geológico desse sistema.

Os resultados deste projeto trazem novas restrições ao contexto sedimentar (paleogeografia, rede de drenagem, precisão estratigráfica) que podem ser implementados em modelos digitais regionais que associam clima-oceano-estratigrafia, bem como a modelagem do aporte sedimentar desde a área-fonte à zona de sedimentação.

A relação dos principais eventos tectono-climáticos governam a origem e desenvolvimento de sistemas fonte-sedimentação. Neste âmbito, aprofundar e integrar o conhecimento acerca das variações climáticas ocorridas ao longo do Cenozoico na plataforma Sul-Americana com dados de variações paleoambientais, modelos digitais seriam de suma importância no entendimento da evolução do sistema. Uma amostragem sistemática e de precisão ao longo da extensão espaço-tempo da plataforma carbonática (isótopos de Sr; C e O; datação bioestratigráfica de detalhe), desenvolvida na Bacia da Foz do Amazonas na margem equatorial do Oceano Atlântico correlacionando com dados de variações ocorridas nas regiões cratônicas (Craton do Amazonas, São Luís e Província Borborema) permitiria reconstituir as variações climáticas e identificar as fases intempéricas registradas nos três setores do sistema (Ocidental, Central e Oriental), integrando com dados prévios da literatura, abordando sobre possiveis impactos na evolução sedimentar do sistema.

A quebra e fragmentação do supercontinente Gondwana afetou tanto a região interna da placa quanto ao sistema de correntes oceânicas nas margens sul e equatorial. Desta forma, entender como as variações no padrão de correntes oceânicas e variações do nivel do mar afetaram o clima e a dispobilidade de aporte sedimentar à Bacia da Foz do Amazonas pode contribuir na reconstituição paleogeografica e paleoambiental do sistema.

ANEXOS CAPITULO 3

Anexo 1. Geographic coordinates of all samples collected for paleontological and geochemical analysis along the Juanjuí stratigraphic section. JUA= Juanjuí ; HUA= Huallaga ; TAR= Tarapoto.

Sample	Latitude	Longitude
JUA 1	-7.245171	-76.742373
JUA 2	-7.236322	-76.745668
JUA 5	-7.234625	-76.746375
JUA 8	-7.231972	-76.746428
JUA 11	-7.228194	-76.744375
JUA 14	-7.222988	-76.74583
HUA 63	-7.234715	-76.746284
TAR 29	-7.234625	-76.746375
TAR 30	-7.230800	-76.745533
TAR 42	-7.222988	-76.74583
TAR 78	-7.230268	-76.745291

Anexo 2. Carbon and oxygen isotope data from upper Cretaceous to early Eocene sequence. JUA= Juanjuí ; HUA= Huallaga

Sample	δ13C (‰)	δ18O (‰)	Position (m)
JUA 1A	-11.50	-6.08	5
JUA 1B	-10.96	-4.58	11
JUA 1C	-9.73	-6.71	17
JUA 1D	-9.24	-7.50	24
JUA 1E	-4.16	-4.91	53
JUA 1F	-6.71	-5.08	64
JUA 2A	-4.24	-5.38	66
JUA 2B	-11.07	-5.35	69
JUA 5A	-6.35	-6.24	73
JUA 5B	-6.66	-6.05	75
JUA 5C	-6.62	-5.95	77
JUA 5D	-6.06	-7.02	80
JUA 8A	-10.09	-6.66	154
JUA 8B	-8.28	-6.83	155
JUA 11A	-11.88	-8.06	382
JUA 11B	-10.70	-9.09	388
JUA 11C	-9.97	-9.67	392
HUA 63 A	-8.45	-6.62	47
HUA 63 B	-6.41	-6.96	50
HUA 63 C	-7.28	-7.55	54
HUA 63 D	-6.89	-7.09	57
HUA 63 E	-7.47	-7.27	60
HUA 63 F	-6.41	-7.63	63
HUA 63 G	-6.48	-5.89	67
HUA 63 H	-7.15	-6.30	68
HUA 63 I	-6.07	-8.32	71
HUA 63 J	-6.27	-7.42	74
HUA 63 K	-6.61	-8.41	76
HUA 63 L	-7.37	-7.06	79
HUA 63 M	-6.04	-8.32	82
HUA 473 A	-10.34	-5.65	273
HUA 473 B	-9.86	-5.02	278
HUA 473 C	-6.55	-4.42	281
HUA 473 D	-9.26	-6.50	292
HUA 473 E	-7.43	-4.84	295
HUA 473 F	-9.10	-5.51	298
HUA 473 G	-7.09	-4.95	300
HUA 473 H	-6.50	-5.76	301
HUA 473 I	-7.63	-5.86	303
HUA 473 J	-7.09	-2.16	305
HUA 473 L	-5.85	-4.05	307
HUA 473 M	-7.19	-5.29	310
HUA 473 N	-8.20	-6.57	311
HUA 473 O	-6.39	-5.39	329
HUA 473 P	-5.63	-4.28	331
HUA 473 Q	-2.84	-1.12	333

Anexo 3. U-Pb data from sample JUA8A-19.

Instituto de Geociencias, Universidade de Brasilia								ta for Tera-Wasserburg p				Data for Wetherill plot					Dates									%	%	Idade	2s
Identifier	pot Numbe	f206c	206Pb	Uppm	Th/U	206Pb/204Pb	1s%	38U/206P	1s%	07Pb/206P	1s%	207Pb/235U	1s%	206Pb/238U	1s%	Rho	207Pb/206Pb	2s (abs)	2ssys (abs)	206Pb/238U	2s (abs)	2ssys (abs)	207Pb/235U	2s (abs)	2ssys	conc3	conc4	Preferida[7]	abs
JUA8A-19 (	Spot6	0.268809793	28497	563	1.2	6279.726906	56.22602032	150.55	0.6	0.04887	0.81	0.0446	1.2	0.00664	0.6	0.8	140	38	40	43	1	1	44	1	1	30.5	96	43	1
JUA8A-19 (	Spot 65	1.776498042	3127	88	1.6	254.4300381	53.33377752	223.42	2.7	0.05550	6.00	0.0345	7.4	0.00450	2.4	0.64	448	251	251	29	1	2	34	5	5	6.5	84	29	1
JUA8A-19 (	Spot9	0	7295	176	2.3	171.7896898	241.7459912	183.88	1.0	0.04296	2.55	0.0322	3.0	0.00544	0.9	0.6				35	1	1	32	2	2		109	35	1
JUA8A-19 (	Spot 52	12.35423494	30871	323	2.6	151.4356049	0.584366764	175.33	1.2	0.05591	8.63	0.0440	7.4	0.00571	1.2	0.9	426	369	369	37	1	1	44	6	6	8.6	84	37	1
JUA8A-19 (	Spot 93	1.953878676	18469	446	1.0	21221.01403	84.39412228	151.66	2.2	0.05127	1.79	0.0463	2.7	0.00662	2.2	0.75	248	84	85	43	2	2	46	2	3	17.1	92	43	2
JUA8A-19 (	Spot 47	2.151609152	67364	662	1.5	6254.600237	52.19529911	150.07	0.5	0.05261	1.60	0.0488	2.0	0.00668	0.5	0.5	377	67	67	43	0	1	48	2	2	11.4	89	43	0
JUA8A-19 (	Spot 80	1.075784853	46183	998	1.4	2266.822795	19.91966736	144.55	0.8	0.05126	2.52	0.0486	3.2	0.00692	0.8	0.97	247	114	114	44	1	2	48	3	4	18.0	92	44	1
JUA8A-19 (	Spot 49	6.448976036	43273	405	1.1	1556.521738	52.02844205	144.78	0.5	0.06679	1.78	0.0647	2.3	0.00693	0.5	0.8	781	63	63	45	0	1	64	3	3	5.7	70	45	0
JUA8A-19 (	Spot34	1.049579783	18302	388	1.7	7248.325249	110.9619911	143.32	0.6	0.04746	1.49	0.0457	1.7	0.00698	0.6	0.6	114	59	60	45	1	1	45	2	2	39.3	99	45	1
JUA8A-19 (	Spot50	0.892104829	25846	544	2.2	961858788.5	91.28708681	136.50	0.9	0.04748	0.87	0.0479	1.6	0.00733	0.9	0.9	72	42	44	47	1	1	48	1	2	65.8	99	47	1
JUA8A-19 (	Spot41	3.075285865	10587	212	1.5	620.645056	28.02364395	135.22	1.3	0.04569	1.06	0.0466	1.6	0.00741	1.3	0.8	95	31	32	48	1	1	46	1	2	50.2	103	48	1
JUA8A-19 (	Spot 50	4.605220127	75768	657	1.3	433.3787006	34.21977707	134.44	0.6	0.06644	4.61	0.0745	7.9	0.00751	0.9	1.0	665	111	111	48	1	1	68	7	8	7.3	71	48	1
JUA8A-19 (	Spot 46	13.21219255	26181	237	1.0	188.8311655	9.913872011	133.03	1.9	0.07054	7.10	0.0727	6.3	0.00755	2.0	0.2	926	267	267	49	2	2	71	9	9	5.2	68	49	2
JUA8A-19 (	Spot 51	4.645816783	55373	474	1.1	535.1037435	50.50459036	131.84	0.6	0.05308	1.68	0.0562	2.5	0.00762	0.7	0.9	358	64	64	49	1	1	55	3	3	13.7	88	49	1
JUA8A-19 (	Spot23	1.661446121	12295	239	1.3	1789.998187	29.65802572	129.67	1.3	0.04682	0.84	0.0497	1.6	0.00772	1.3	0.9	56	28	29	50	1	1	49	2	2	88.5	101	50	1
JUA8A-19 (	Spot 48	3.049859467	65459	518	1.8	887.0476686	48.41854637	128.36	0.3	0.05345	0.88	0.0575	1.0	0.00780	0.3	0.5	378	35	35	50	0	1	57	1	2	13.3	88	50	0
JUA8A-19 (	Spot33	1.356380531	13705	190	1.1	100.0069232	561.2550305	92.21	0.6	0.04774	2.27	0.0713	2.3	0.01085	0.6	0.1	160	112	112	70	1	1	70	3	3	43.5	99	70	1
JUA8A-19 (	Spot 73	0.129292593	63017	750	2.4	6406.571876	58.97821678	86.10	0.7	0.04820	0.51	0.0769	1.0	0.01162	0.8	0.89	108	24	25	74	1	3	75	1	3	69.1	99	74	1
JUA8A-19 (	Spot 87	0.583413914	56527	714	0.8	6170.195681	38.52515893	81.94	1.0	0.04870	1.46	0.0814	2.1	0.01221	1.0	0.81	130	67	67	78	2	3	79	3	5	60.2	99	78	2
JUA8A-19 (	Spot 53	32.98353197	10695	37	3.0	30.44112795	0.037148526	48.35	2.6	0.50487	9.50	1.4406	12.1	0.02070	2.6	1.0	4248	281	281	132	7	7	903	145	145	3.1	15	132	7
JUA8A-19 (	Spot36	0.167688331	122667	393	0.8	266.2487756	1539.547019	20.76	0.7	0.05260	0.27	0.3486	0.8	0.04817	0.7	1.0	311	12	18	303	4	6	304	4	8	97.6	100	303	4
JUA8A-19 (	Spot37	0.003197888	141339	426	0.8	11143.62457	98.3227819	20.26	0.4	0.05289	0.47	0.3597	0.5	0.04936	0.4	0.3	323	21	25	311	3	5	312	3	7	96.2	100	311	3
JUA8A-19 (	Spot28	0.203201351	10294	30	1.1	145.3626505	673.5205989	19.30	0.6	0.05281	1.56	0.3770	1.9	0.05183	0.6	0.7	317	72	74	326	4	6	325	10	12	102.8	100	326	4
JUA8A-19 (	Spot12	0.213682342	41123	117	2.1	7301.420831	69.20715103	19.23	0.9	0.05423	0.59	0.3864	1.0	0.05202	0.9	0.8	379	26	30	327	6	7	332	6	9	86.1	99	327	6
JUA8A-19 (	Spot 66	4.949515284	12711	29	1.3	521.0403408	24.95324823	17.36	1.5	0.09253	6.03	0.7381	6.9	0.05772	1.5	0.67	1439	229	229	362	10	16	557	59	62	25.1	65	362	10
JUA8A-19 (	Spot10	0.884409786	32765	63	1.4	857.4386286	232.0129788	13.71	0.7	0.05639	0.62	0.5647	1.0	0.07299	0.7	0.8	466	28	31	454	7	9	455	7	11	97.4	100	454	7
JUA8A-19 (	Spot5	0.586170175	225151	375	2.2	3565.179817	17.4250607	12.97	2.9	0.06461	0.49	0.6857	2.5	0.07734	2.9	1.0	761	21	24	480	26	27	530	21	23	63.1	91	480	26
JUA8A-19 (	Spot 72	0.040107088	201689	301	0.4	101576.832	82.53823324	11.23	0.5	0.05890	0.51	0.7208	0.6	0.08908	0.4	0.54	562	22	23	550	5	18	551	5	18	97.9	100	550	5
JUA8A-19 (	Spot35	0.505398153	17309	28	0.7	1924.043975	74.31611324	10.31	1.1	0.05911	1.03	0.7883	0.9	0.09704	1.1	0.5	569	46	48	597	13	16	590	8	13	104.9	101	597	13
JUA8A-19 (	Spot38	0.010443777	324955	529	0.1	27010.91443	135.7359396	10.21	0.6	0.06020	0.25	0.8095	0.8	0.09796	0.6	1.0	610	11	17	602	7	12	602	7	13	98.8	100	602	7
JUA8A-19 (	Spot47	0.364929648	41478	64	1.4	4576.295746	58.68518389	10.20	0.9	0.06006	0.79	0.8112	1.4	0.09807	0.9	0.9	604	35	37	603	10	13	603	13	17	99.8	100	603	10
JUA8A-19 (	Spot8	0.22577133	313017	438	0.0	9398.603454	19.81378842	9.97	0.5	0.06434	0.77	0.8833	0.9	0.10026	0.5	0.7	752	33	35	616	5	10	643	9	14	82.0	96	616	5
JUA8A-19 (	Spot48	0.100295861	170415	243	1.0	230.5360871	7472.412461	9.30	2.1	0.06983	2.61	1.0367	4.9	0.10765	2.2	1.0	920	105	105	659	27	29	721	50	51	71.6	91	659	27
JUA8A-19 (	Spot24	0.106035325	144139	203	1.6	5646.077223	148.7830593	9.10	0.8	0.06167	0.23	0.9320	0.8	0.10992	0.8	0.9	662	10	16	672	10	14	669	8	14	101.6	101	672	10
JUA8A-19 (	Spot 79	0.059887659	75278	96	1.2	377.552958	2843.882182	8.95	0.8	0.06489	0.45	0.9960	1.2	0.11185	0.8	0.99	770	19	20	683	10	24	702	12	24	88.8	97	683	10
JUA8A-19 (	Spot 86	0.008069555	107610	143	1.2	19396.46763	103.8725389	9.07	7.0	0.07071	0.63	1.1302	6.7	0.11618	6.1	1.00	947	26	27	707	83	86	760	74	78	74.6	93	707	83
JUA8A-19 (	Spot 67	0.358520371	195070	213	1.1	5523.510304	14.03246883	7.81	0.7	0.06978	0.44	1.2267	0.7	0.12807	0.7	0.83	921	18	19	777	11	27	813	7	24	84.4	96	777	11
JUA8A-19 (	Spot22	0.471994801	289861	358	1.3	20427.69588	65.57566074	7.88	6.2	0.07379	1.58	1.2991	4.5	0.12877	6.1	1.0	1034	64	65	780	89	90	844	52	53	75.5	92	780	89
JUA8A-19 (	Spot39	0.26464982	149094	173	0.6	7014.030582	10.57600137	7.42	1.0	0.07333	0.49	1.3589	1.3	0.13483	1.0	0.9	1022	20	23	815	15	19	871	16	21	79.8	94	815	15
JUA8A-19 (	Spot11	0.006292066	461257	410	1.0	41459.54021	65.09385339	6.29	0.5	0.07125	0.24	1.5544	0.5	0.15900	0.5	0.9	964	10	15	951	9	17	952	6	16	98.7	100	951	9
JUA8A-19 (	Spot 97	0.174538143	421016	401	1.4	11909.48401	14.28290796	6.13	1.1	0.07834	0.13	1.7472	1.0	0.16310	1.1	0.99	1155	5	8	974	19	36	1026	13	30	84.3	95	974	19
JUA8A-19 (	Spot 70	0.212904278	159289	126	1.0	10474.39438	107.1048341	6.05	1.5	0.07490	0.77	1.7064	1.7	0.16557	1.4	0.90	1064	30	31	988	26	41	1010	22	35	92.8	98	988	26
JUA8A-19 (	Spot53	0.343760494	30841	29	1.5	3347.906017	60.01165825	6.02	0.5	0.07356	0.82	1.6832	0.8	0.16613	0.5	0.4	1028	33	35	991	9	17	1002	10	18	96.4	99	991	9
JUA8A-19 (	Spot 68	0.535344401	54678	44	0.4	1894.882841	122.7908403	6.00	0.7	0.07241	0.39	1.6593	0.8	0.16671	0.7	0.88	996	16	17	994	13	34	993	11	28	99.8	100	994	13
JUA8A-19 (	Spot21	0.138230252	202809	180	2.9	13861.72442	10.77815333	5.86	0.3	0.07387	0.28	1.7346	0.4	0.17075	0.3	0.9	1037	11	17	1016	5	15	1021	6	16	98.0	99	1021	6
JUA8A-19 (	Spot 88	0.020718125	85282	76	0.0	800721990.3	95.34834154	5.81	1.9	0.07367	1.08	1.7462	2.8	0.17284	1.9	0.95	1030	44	44	1027	36	48	1024	36	45	99.8	100	1024	36
JUA8A-19 (	Spot 94	0.057238943	216814	194	0.6	18694.86974	139.8329075	5.72	0.4	0.07426	0.21	1.7763	0.3	0.17485	0.4	0.84	1047	8	10	1039	8	33	1037	4	27	99.2	100	1037	4
JUA8A-19 (	Spot51	0.062560226	304446	283	0.7	20179.28181	109.5902567	5.88	0.5	0.07652	0.96	1.7893	1.3	0.16996	0.5	0.9	1107	38	40	1012	10	17	1041	18	23	91.4	97	1041	18
JUA8A-19 (	Spot14	0.029405176	624529	509	0.3	68115.01956	140.8933302	5.65	0.6	0.07690	0.48	1.8703	0.4	0.17718	0.6	0.4	1117	19	23	1052	11	19	1071	6	17	94.1	98	1071	6
JUA8A-19 (	Spot 81	0.055298963	300137	246	0.2	8479.637689	317.5894408	5.50	1.3	0.07593	0.23	1.8959	1.3	0.18211	1.3	0.99	1092	9	11	1078	26	42	1079	17	32	98.7	100	1079	17
JUA8A-19 (	Spot25	0.007434588	95592	79	1.5	486.5917073	1744.751001	5.34	0.3	0.07524	0.69	1.9371	0.7	0.18732	0.3	0.2	1074	28	30	1107	7	17	1094	9	18	103.1	101	1094	9
JUA8A-19 (	Spot20	0.208265007	36467	30	0.7	2679.493172	60.96748932	5.45	0.6	0.07700	0.97	1.9415	1.2	0.18338	0.6	0.6	1120	38	40	1085	12	19	1095	16	22	96.9	99	1095	16
JUA8A-19 (	Spot 95	0.278068146	199053	175	0.7	8255.172198	20.91052924	5.39	1.9	0.08001	0.42	2.0374	2.3	0.18614	1.9	0.99	1196	17	18	1100	38	51	1127	31	42	92.0	98	1127	31
JUA8A-19 (	Spot7	0.043508714	325489	229	0.5	1951266945	93.54208817	5.17	0.9	0.07835	0.77	2.0799	1.5	0.19355	0.9	0.9	1154	31	33	1141	18	24	1142	20	26	98.8	100	1142	20
JUA8A-19 (	Spot26	0.037687768	210935	166	0.6	0	0	5.09	0.3	0.07733	0.17	2.0904	0.3	0.19661	0.3	0.9	1129	7	14	1157	6	18	1146	5	17	102.5	101	1146	5
JUA8A-19 (	Spot55	0.474379461	30510	25	1.0	20012.90725	65.33204007	5.19	0.9	0.07901	1.15	2.0963	1.2	0.19265	0.9	0.4	1170	46	48	1136	18	24	1147	17	23	97.0	99	1147	17
JUA8A-19 (	Spot 84	0.031868933	423675	310	1.0	14774.26939	103.639925	5.01	0.7	0.07987	0.14	2.1848	0.9	0.19966	0.7	0.98	1193	5	8	1173	15	39	1176	12	31	98.4	100	1176	12
JUA8A-19 (	Spot54	0.002982412	263167	197	0.9	8267.781575	186.3442947	4.85	0.4	0.08081	0.43	2.2958	0.3	0.20619	0.4	0.6	1216	17	20	1208	10	20	1211	5	17	99.4	100	1211	5
JUA8A-19 (	Spot42	0.350893286	76604	53	0.9	8938.263852	37.30545026	4.56	0.4	0.08126	0.38	2.4526	0.6	0.21930	0.4	0.7	1227	15	19	1278	10	21	1258	8	19	104.2	102	1258	8
JUA8A-19 (	Spot 82	0.293492219	65296	42	1.9	4623.710999	36.58389535	4.36	0.7	0.08545	0.50	2.6843	0.7	0.22935	0.7	0.76	1325	19	20	1331	16	44	1324	11	33	100.5	101	1324	11
JUA8A-19 (	Spot 71	0.152076241	74186	40	0.6	518.1471552	1349.578652	3.89	0.5	0.09208	0.19	3.2538	0.5	0.25737	0.5	0.90	1468	7	9	1476	13	46	1470	8	33	100.6	100	1470	8

JUA8A-19 (Spot19	0.227055483	163694	91	0.9	8675.41766	40.31546625	3.62	0.8	0.09760	0.58	3.6998	1.0	0.27613	0.8	0.8	1578	22	24	1572	21	30	1571	16	24	99.6	100	1571	16
~~JUA8A-19 (Spot 102~~	~~3.103606794~~	~~289998~~	~~217~~	~~0.6~~	~~579.5553492~~	~~15.61127076~~	~~4.55~~	~~2.9~~	~~0.12377~~	~~3.06~~	~~3.7164~~	~~1.2~~	~~0.22095~~	~~3.1~~	~~0.09~~	~~2005~~	~~109~~	~~109~~	~~1286~~	~~71~~	~~81~~	~~1575~~	~~19~~	~~38~~	~~64.1~~	~~82~~	~~1575~~	~~19~~
JUA8A-19 (Spot40	0.157383351	282782	159	0.6	24647.29894	39.53301973	3.55	1.1	0.09925	0.28	3.8363	0.9	0.28152	1.0	1.0	1609	11	15	1599	30	37	1600	14	24	99.4	100	1600	14
JUA8A-19 (Spot52	0.841189208	311731	190	1.6	3283.540249	37.86199978	3.90	3.1	0.10911	3.06	3.8678	6.0	0.25699	3.1	1.0	1781	110	111	1474	81	84	1604	96	98	82.8	92	1604	96
JUA8A-19 (Spot13	0.4491633	290721	152	1.3	4497.702196	15.65721397	3.50	1.0	0.10699	0.70	4.1973	1.4	0.28623	1.0	0.9	1748	26	28	1623	29	36	1673	23	30	92.8	97	1673	23
JUA8A-19 (Spot49	0.216868112	285250	161	2.8	9570.263201	27.30925726	3.54	1.7	0.11450	0.33	4.4501	1.8	0.28280	1.7	1.0	1871	12	16	1605	49	54	1721	29	35	85.8	93	1721	29
JUA8A-19 (Spot 98	0.224574458	258060	138	1.3	9380.730996	17.69018616	3.32	2.7	0.11586	0.35	4.7922	2.8	0.30261	2.7	0.99	1892	13	14	1703	80	94	1782	47	59	90.0	96	1782	47
JUA8A-19 (Spot 74	0.107426305	164685	71	1.2	9977.819138	51.43135813	2.98	0.5	0.10660	0.38	4.9059	0.6	0.33559	0.5	0.80	1741	14	15	1865	16	56	1803	9	36	107.1	103	1803	9
JUA8A-19 (Spot56	0.051308365	288694	140	2.9	158775.9616	90.44896261	3.05	0.7	0.11489	0.21	5.1814	0.8	0.32750	0.7	1.0	1877	8	13	1826	21	32	1849	13	24	97.3	99	1849	13
JUA8A-19 (Spot 100	0.01081361	658863	323	1.1	6577.943856	373.2356614	2.99	0.5	0.11719	0.38	5.3508	0.8	0.33443	0.5	0.92	1913	14	15	1860	18	57	1877	13	38	97.2	99	1877	13
JUA8A-19 (Spot 83	0.006906213	476206	210	1.0	7204.036164	380.11854	2.89	0.8	0.11745	0.15	5.5615	0.8	0.34612	0.8	0.98	1917	5	8	1916	26	62	1910	14	39	100.0	100	1910	14
JUA8A-19 (Spot 101	0.017776509	382970	179	0.7	85929.04452	124.5721175	2.82	0.4	0.12096	0.24	5.8602	0.4	0.35511	0.4	0.77	1970	9	10	1959	14	59	1955	7	37	99.5	100	1955	7
JUA8A-19 (Spot27	0.061663601	365109	147	0.6	163399.1701	84.02813436	2.75	0.7	0.13108	0.24	6.5812	0.8	0.36421	0.7	1.0	2112	8	13	2002	25	37	2057	15	25	94.8	97	2057	15
JUA8A-19 (Spot 85	0.329773186	188081	74	1.5	5299.62493	12.350275	2.70	0.3	0.12975	0.31	6.5888	0.4	0.37059	0.3	0.74	2094	11	12	2032	9	59	2058	8	37	97.1	99	2058	8
JUA8A-19 (Spot 99	0.296843013	97086	42	2.7	31617.36793	77.92110214	2.64	0.8	0.13373	0.26	6.9289	0.8	0.37962	0.8	0.96	2147	9	10	2074	30	67	2102	15	40	96.6	99	2102	15
JUA8A-19 (Spot 69	0.332158361	26831	9	2.0	1594.681681	98.18034534	2.46	2.1	0.13490	1.15	7.5800	2.5	0.40901	2.1	0.88	2161	40	40	2209	77	100	2180	45	59	102.3	101	2180	45
JUA8A-19 (Spot 96	0.161593868	120337	32	0.8	48408.79256	105.2383351	1.74	1.0	0.24082	0.41	18.9343	1.3	0.57477	1.0	0.99	3125	13	14	2927	49	93	3038	25	47	93.7	96	3038	25

Anexo 4. U-Pb data from sample JUA11.

Instituto de Geociencias, Universidade de Brasilia								Data for Tera-Wasserburg plot				Data for Wetherill plot					Dates									
Identifier	Spot Number	f206c	206Pb	Uppm	Th/U	206Pb/ 204Pb	1s%	238U/20 6Pb	1s%	207Pb/2 06Pb	1s%	207Pb/ 235U	1s%	206Pb/ 238U	1s%	Rho	207Pb/ 206Pb	2s (abs)	206Pb/ 238U	2s (abs)	207Pb /235U	2s (abs)	% conc3	% conc 4	**Idade Preferida[7]**	**2s abs**
JUA11	Z-53	67.09315456	621	170	1.4	3.029	147	176.70	3.3	0.05168	14.39	0.0389	13.9	0.00594	3.3	-0.03	1546	413	38	2	38	11	2	100	38	2
JUA11	Z-105	25.72085752	751	202	1.3	2.602	226	166.76	2.4	0.04951	13.45	0.0399	12.7	0.00611	2.3	-0.13	1438	333	39	2	39	10	3	100	39	2
JUA11	Z-41	15.09871834	1813	458	0.7	24.51	69.4	158.65	2.0	0.05329	6.63	0.0461	6.4	0.00638	2.4	0.09	859	164	41	2	46	6	5	90	41	2
JUA11	Z-23	1.254962229	1748	432	0.6	13.44	109	160.45	2.3	0.04854	6.99	0.0416	6.8	0.00639	2.1	0.54	776	177	41	2	41	6	5	100	41	2
JUA11	Z-15	7.221384363	2597	640	0.9	38.95	59.8	157.69	1.6	0.04318	6.01	0.0386	6.0	0.00643	1.7	0.19	584	187	41	1	38	5	7	108	41	1
JUA11	Z-79	0.400533416	6358	1638	5.1	94.3	131	155.90	1.3	0.04902	3.66	0.0434	3.7	0.00646	1.3	0.37	452	115	42	1	43	3	9	96	42	1
JUA11	Z-87	5.271928341	984	254	1.7	62.18	64	160.71	2.9	0.05193	11.68	0.0420	10.6	0.00647	2.7	0.00	1120	307	42	2	41	9	4	101	42	2
~~**JUA11**~~	~~Z-80~~	~~36.65519579~~	~~1567~~	~~392~~	~~0.6~~	~~0.744~~	~~2177~~	~~159.72~~	~~2.9~~	~~0.03137~~	~~11.26~~	~~0.0287~~	~~10.6~~	~~0.00649~~	~~2.6~~	~~0.03~~	~~851~~	~~319~~	~~42~~	~~2~~	~~28~~	~~6~~	~~5~~	~~146~~	~~42~~	~~2~~
JUA11	Z-54	48.15781851	731	181	1.5	16.18	125	161.19	3.8	0.05304	15.20	0.0455	14.1	0.00652	3.7	-0.07	1181	381	42	3	44	12	4	94	42	3
JUA11	Z-102	22.06493716	1972	504	0.6	3.5	490	154.21	2.1	0.05405	7.95	0.0472	6.9	0.00653	2.4	-0.13	909	255	42	2	47	6	5	90	42	2
JUA11	Z-69	1.672023937	4014	1012	2.0	28.32	128	154.94	1.6	0.05082	4.78	0.0453	4.4	0.00653	1.6	-0.07	649	159	42	1	45	4	6	94	42	1
~~**JUA11**~~	~~Z-83~~	~~90.99036906~~	~~1260~~	~~316~~	~~1.6~~	~~4.41~~	~~200~~	~~158.66~~	~~2.9~~	~~0.06347~~	~~8.86~~	~~0.0579~~	~~9.0~~	~~0.00655~~	~~2.9~~	~~0.20~~	~~1117~~	~~230~~	~~42~~	~~2~~	~~57~~	~~10~~	~~4~~	~~74~~	~~42~~	~~2~~
JUA11	Z-30	20.04012119	1205	301	3.6	98.15	50.5	155.29	1.9	0.05136	11.94	0.0435	11.3	0.00655	1.8	-0.16	1343	336	42	2	43	10	3	99	42	2
JUA11	Z-40	43.39803571	579	142	1.5	9.299	105	155.04	2.6	0.05266	14.62	0.0496	14.6	0.00657	2.8	-0.12	1377	326	42	2	48	14	3	88	42	2
~~**JUA11**~~	~~Z-77~~	~~8.453977313~~	~~2307~~	~~582~~	~~2.1~~	~~80.17~~	~~49.3~~	~~155.01~~	~~2.1~~	~~0.06068~~	~~5.59~~	~~0.0548~~	~~6.4~~	~~0.00658~~	~~2.1~~	~~-0.06~~	~~821~~	~~161~~	~~42~~	~~2~~	~~54~~	~~7~~	~~5~~	~~78~~	~~42~~	~~2~~
~~**JUA11**~~	~~Z-73~~	~~29.89146721~~	~~2803~~	~~696~~	~~1.2~~	~~27.94~~	~~93.3~~	~~154.32~~	~~1.7~~	~~0.02333~~	~~12.06~~	~~0.0203~~	~~12.4~~	~~0.00658~~	~~1.8~~	~~0.10~~	~~795~~	~~924~~	~~42~~	~~2~~	~~20~~	~~5~~	~~5~~	~~209~~	~~42~~	~~2~~
JUA11	Z-39	113.3766688	437	111	1.7	5.18	69.5	162.25	4.1	0.04993	29.20	0.0464	28.5	0.00661	4.3	0.21	1851	443	42	4	42	25	2	101	42	4
JUA11	Z-68	24.78632781	2484	621	1.4	4.088	642	152.46	1.8	0.05230	7.03	0.0475	6.7	0.00664	1.8	0.00	914	357	43	2	47	6	5	91	43	2
~~**JUA11**~~	~~Z-75~~	~~16.94145226~~	~~2083~~	~~521~~	~~1.0~~	~~28.4~~	~~83.6~~	~~152.44~~	~~1.5~~	~~0.04343~~	~~6.87~~	~~0.0391~~	~~6.8~~	~~0.00664~~	~~1.5~~	~~0.31~~	~~538~~	~~173~~	~~43~~	~~1~~	~~39~~	~~5~~	~~8~~	~~110~~	~~43~~	~~1~~
JUA11	Z-67	100.5537053	539	130	2.1	8.027	146	156.90	3.7	0.04311	22.05	0.0403	23.6	0.00665	3.5	0.17	1432	359	43	3	42	17	3	101	43	3
~~**JUA11**~~	~~Z-16~~	~~268.2089951~~	~~255~~	~~60~~	~~0.9~~	~~0.995~~	~~186~~	~~181.84~~	~~7.6~~	~~0.03724~~	~~70.51~~	~~0.0049~~	~~408.5~~	~~0.00666~~	~~6.7~~	~~-0.14~~	~~2585~~	~~494~~	~~43~~	~~6~~	~~-5~~	~~41~~	~~2~~	~~-916~~	~~43~~	~~6~~
JUA11	Z-88	4.486839603	1473	367	1.8	44.76	49.1	152.98	3.0	0.04640	9.30	0.0418	9.3	0.00667	2.8	-0.11	837	274	43	2	41	7	5	104	43	2
JUA11	Z-117	54.52327814	1333	343	2.0	20.12	76.6	151.54	2.0	0.04745	8.17	0.0436	8.2	0.00673	2.0	0.28	768	222	43	2	43	7	6	100	43	2
JUA11	Z-13	12.92408774	1883	451	0.8	13.54	63.1	153.28	2.7	0.05887	8.25	0.0506	6.6	0.00673	2.7	0.02	887	277	43	2	50	7	5	87	43	2
JUA11	Z-7	4.114805686	5310	1221	2.8	48.99	163	148.85	1.3	0.04473	3.38	0.0416	3.1	0.00673	1.2	-0.01	329	95	43	1	41	3	13	105	43	1
~~**JUA11**~~	~~Z-17~~	~~47.32417871~~	~~490~~	~~116~~	~~0.2~~	~~12.34~~	~~53.6~~	~~158.74~~	~~4.4~~	~~0.06772~~	~~20.94~~	~~0.0540~~	~~18.7~~	~~0.00676~~	~~4.7~~	~~0.01~~	~~1861~~	~~342~~	~~43~~	~~4~~	~~51~~	~~19~~	~~2~~	~~85~~	~~43~~	~~4~~
JUA11	Z-120	17.84453178	2647	676	2.1	71.3	76.3	149.63	1.7	0.05554	5.45	0.0503	5.0	0.00677	1.6	0.11	685	179	44	1	50	5	6	88	44	1
JUA11	Z-62	1.791847169	4059	964	0.6	52.08	52.9	148.25	1.6	0.04779	5.30	0.0442	4.8	0.00678	1.6	0.00	671	195	44	1	44	4	6	100	44	1
JUA11	Z-81	13.88347878	960	242	1.4	5.724	131	150.91	2.5	0.04469	13.13	0.0440	13.9	0.00679	2.6	-0.02	1080	303	44	2	43	12	4	101	44	2
JUA11	Z-11	10.58017281	1497	350	0.9	72.33	54.3	149.75	2.2	0.04649	8.63	0.0439	8.5	0.00682	2.2	0.08	822	268	44	2	43	7	5	101	44	2
JUA11	Z-114	32.30577263	977	247	3.2	170.6	68.8	151.93	3.0	0.05348	7.88	0.0505	8.1	0.00683	2.9	0.39	929	236	44	3	50	8	5	88	44	3
JUA11	Z-38	3.855559863	3234	762	1.3	12.09	213	147.34	1.6	0.04811	6.14	0.0452	6.1	0.00688	1.6	0.11	677	227	44	1	45	5	7	99	44	1
JUA11	Z-22	105.1597504	949	219	1.0	133.7	56.1	150.40	2.9	0.04910	13.16	0.0472	12.4	0.00693	3.2	0.11	1308	348	45	3	46	11	3	97	45	3
~~**JUA11**~~	~~Z-95~~	~~64.07329335~~	~~625~~	~~149~~	~~2.2~~	~~2.746~~	~~272~~	~~148.08~~	~~2.9~~	~~0.02453~~	~~22.97~~	~~0.0228~~	~~23.3~~	~~0.00706~~	~~3.2~~	~~-0.05~~	~~1000~~	~~433~~	~~45~~	~~3~~	~~22~~	~~10~~	~~5~~	~~204~~	~~45~~	~~3~~
JUA11	Z-116	59.21888127	1183	298	1.7	5.608	212	144.80	3.0	0.04929	12.37	0.0469	12.9	0.00712	2.8	-0.06	1063	285	46	3	46	12	4	99	46	3
JUA11	Z-55	45.83704129	1923	453	0.8	21.88	96.6	142.09	3.0	0.04921	8.07	0.0507	8.9	0.00721	3.1	-0.19	817	258	46	3	50	9	6	93	46	3

Instituto de Geociencias, Universidade de Brasilia								Data for Tera-Wasserburg plot				Data for Wetherill plot					Dates									
Identifier	Spot Number	f206c	206Pb	Uppm	Th/U	206Pb/ 204Pb	1s%	238U/20 6Pb	1s%	207Pb/2 06Pb	1s%	207Pb/ 235U	1s%	206Pb/ 238U	1s%	Rho	207Pb/ 206Pb	2s (abs)	206Pb/ 238U	2s (abs)	207Pb /235U	2s (abs)	% conc3	% conc 4	**Idade Preferida**[7]	**2s abs**
JUA11	Z-1	0.347909028	1478	320	0.9	18.67	43.6	143.16	2.6	0.04736	8.66	0.0490	9.3	0.00719	2.5	0.05	975	312	46	2	48	9	5	96	46	2
~~**JUA11**~~	~~Z-106~~	~~27.60634476~~	~~1894~~	~~411~~	~~1.0~~	~~39.82~~	~~72~~	~~131.32~~	~~1.9~~	~~0.04449~~	~~8.81~~	~~0.0464~~	~~8.4~~	~~0.00769~~	~~1.8~~	~~-0.14~~	~~810~~	~~200~~	~~49~~	~~2~~	~~46~~	~~8~~	~~6~~	~~108~~	~~49~~	~~2~~
~~**JUA11**~~	~~Z-104~~	~~17.68479434~~	~~2002~~	~~451~~	~~1.3~~	~~8.595~~	~~238~~	~~131.58~~	~~2.4~~	~~0.04414~~	~~9.15~~	~~0.0464~~	~~8.6~~	~~0.00776~~	~~2.5~~	~~0.18~~	~~835~~	~~288~~	~~50~~	~~2~~	~~46~~	~~8~~	~~6~~	~~109~~	~~50~~	~~2~~
~~**JUA11**~~	~~Z-92~~	~~32.4164306~~	~~945~~	~~210~~	~~2.1~~	~~5.258~~	~~241~~	~~131.54~~	~~2.5~~	~~0.00396~~	~~####~~	~~0.0029~~	~~218.7~~	~~0.00784~~	~~2.6~~	~~-0.18~~	~~662~~	~~263~~	~~50~~	~~3~~	~~2~~	~~13~~	~~8~~	~~2577~~	~~50~~	~~3~~
~~**JUA11**~~	~~Z-91~~	~~43.84711482~~	~~1347~~	~~95~~	~~1.8~~	~~10454~~	~~142~~	~~43.88~~	~~2.5~~	~~0.01200~~	~~29.75~~	~~0.0372~~	~~30.6~~	~~0.02348~~	~~2.4~~	~~0.00~~	~~1610~~	~~1401~~	~~150~~	~~7~~	~~34~~	~~22~~	~~9~~	~~439~~	~~150~~	~~7~~
JUA11	Z-103	33.3320292	2893	121	2.3	8274	83.8	25.47	1.8	0.05693	4.64	0.3089	4.3	0.03979	1.7	0.01	739	144	251	8	271	21	34	93	251	8
JUA11	Z-36	9.674378864	5093	193	2.6	91.27	141	22.75	1.7	0.05503	3.70	0.3448	4.4	0.04458	1.7	0.24	613	161	281	9	298	22	46	94	281	9
JUA11	Z-32	3.125540904	7300	255	1.5	5.639	686	21.95	1.0	0.05546	2.61	0.3477	2.4	0.04577	1.0	0.10	527	98	288	6	302	13	55	95	288	6
~~**JUA11**~~	~~Z-84~~	~~5.489745794~~	~~3979~~	~~146~~	~~4.4~~	~~4.064~~	~~601~~	~~22.05~~	~~1.5~~	~~0.04910~~	~~4.81~~	~~0.3099~~	~~4.8~~	~~0.04587~~	~~1.5~~	~~0.07~~	~~507~~	~~162~~	~~289~~	~~9~~	~~271~~	~~23~~	~~57~~	~~107~~	~~289~~	~~9~~
JUA11	Z-42	17.89859836	2925	95	2.9	6.837	331	20.37	1.5	0.05342	8.59	0.3642	8.7	0.04965	1.5	-0.13	919	278	312	9	304	42	34	103	312	9
JUA11	Z-47	8.141377083	6824	167	2.5	77.12	44.5	15.15	1.2	0.05486	3.33	0.5041	3.6	0.06608	1.1	0.36	590	98	412	9	411	25	70	100	412	9
JUA11	Z-29	2.892321229	9720	244	2.0	791	55.7	14.86	1.2	0.05598	2.94	0.5157	2.8	0.06776	1.2	0.25	565	99	423	10	420	19	75	101	423	10
JUA11	Z-56	10.99945344	8320	189	1.4	31926	69.4	13.75	1.4	0.05440	3.46	0.5354	2.7	0.07334	1.4	0.06	544	130	456	12	439	23	84	104	456	12
JUA11	Z-20	8.552298467	5507	108	2.7	71.36	57.5	12.57	1.6	0.05711	3.87	0.6309	3.7	0.08062	1.6	0.12	691	124	500	16	492	29	72	102	500	16
JUA11	Z-85	2.849688036	10807	229	2.0	296.9	47.1	12.34	1.3	0.05968	4.78	0.6688	4.7	0.08144	1.4	0.15	633	176	505	14	515	37	80	98	505	14
JUA11	Z-59	1.320517394	20679	444	1.1	254.2	46.6	12.31	1.8	0.05906	1.69	0.6694	2.2	0.08243	1.7	0.55	548	73	510	17	518	18	93	98	510	17
JUA11	Z-66	10.12996848	6671	123	1.5	106.1	45.3	11.35	1.2	0.05899	3.09	0.7220	3.2	0.08869	1.2	0.24	637	110	548	12	547	27	86	100	548	12
JUA11	Z-8	2.367034124	29735	521	0.2	2162	105	11.19	0.9	0.05923	1.44	0.7346	1.6	0.08971	0.9	0.47	571	60	554	10	558	14	97	99	554	10
JUA11	Z-44	1.407559627	27943	494	0.2	8582	46.7	11.02	0.9	0.05911	1.51	0.7433	1.5	0.09111	1.0	0.37	555	63	562	10	563	13	101	100	562	10
JUA11	Z-60	9.459078885	8765	161	0.7	112.1	72.8	10.88	1.1	0.05709	5.01	0.7004	4.5	0.09199	1.2	-0.18	671	155	567	13	548	39	84	103	567	13
JUA11	Z-78	5.215827452	3406	57	3.0	7.546	1012	10.38	1.7	0.07035	3.97	0.9528	3.9	0.09697	1.8	0.18	996	147	596	20	680	36	60	88	596	20
JUA11	Z-49	7.287229741	5204	82	1.0	58.35	132	9.99	1.9	0.06166	3.53	0.8535	3.0	0.10151	2.0	0.10	726	162	623	23	623	28	86	100	623	23
JUA11	Z-71	1.83429713	4971	79	2.8	32.6	108	9.84	1.4	0.05517	3.33	0.7763	3.0	0.10265	1.4	0.24	571	128	630	17	586	29	110	107	630	17
JUA11	Z-25	3.909117656	8786	135	2.1	225.4	51.2	9.65	1.3	0.06118	2.39	0.8784	2.1	0.10448	1.3	0.17	635	97	640	16	638	20	101	100	640	16
JUA11	Z-61	2.035344356	8040	130	0.6	187.4	65.2	9.57	1.2	0.06174	2.43	0.8932	2.3	0.10518	1.2	0.15	650	99	645	15	645	21	99	100	645	15
JUA11	Z-63	3.203260234	15220	229	1.0	63.16	212	9.72	2.2	0.06286	1.95	0.9347	3.3	0.10544	2.2	0.65	689	81	646	27	664	32	94	97	646	27
~~**JUA11**~~	~~Z-43~~	~~7.825232027~~	~~3552~~	~~55~~	~~1.6~~	~~170.6~~	~~50.5~~	~~9.55~~	~~2.0~~	~~0.10851~~	~~5.56~~	~~1.6001~~	~~6.0~~	~~0.10667~~	~~2.0~~	~~0.35~~	~~1617~~	~~197~~	~~653~~	~~25~~	~~940~~	~~70~~	~~40~~	~~69~~	~~653~~	~~25~~
JUA11	Z-118	5.908922797	6025	91	2.1	511.3	68.1	9.04	1.3	0.06052	2.73	0.9268	2.6	0.11141	1.2	0.19	617	106	681	16	662	25	110	103	681	16
JUA11	Z-21	5.017634304	4697	50	1.5	47.42	143	6.72	1.6	0.07164	3.45	1.4837	3.5	0.15044	1.5	0.12	978	130	903	26	914	43	92	99	903	26

JUA11	Z-107	0.025203017	19500	196	1.1	38.56	290	6.48	1.1	0.07539	1.28	1.6162	1.7	0.15526	1.1	0.65	1067	51	930	20	974	21	87	95	930	20
JUA11	Z-98	16.3661813	5421	56	1.5	82.9	36.4	6.25	1.3	0.06753	3.09	1.4915	2.8	0.16119	1.3	-0.04	835	118	963	23	920	34	115	105	963	23
JUA11	Z-33	5.447959437	8430	86	1.2	1226	70.7	6.13	1.3	0.07381	2.68	1.6677	2.6	0.16446	1.2	0.25	989	110	981	23	990	33	99	99	981	23
JUA11	Z-46	7.352647711	5118	51	1.0	192.4	71.8	6.12	1.5	0.07558	3.04	1.7148	3.0	0.16483	1.5	0.29	1093	111	983	27	1006	41	90	98	983	27
JUA11	Z-5	0.124816228	16007	153	0.8	142.8	279	5.85	1.3	0.07275	1.79	1.7304	1.9	0.17254	1.3	0.31	984	75	1026	24	1016	24	104	101	1026	24
JUA11	Z-101	2.212365994	15693	151	1.3	105.4	113	5.75	1.1	0.07695	1.58	1.8523	1.8	0.17484	1.1	0.49	1123	70	1038	20	1062	23	92	98	1038	20
JUA11	Z-19	1.01172713	25481	233	0.8	347.4	139	5.72	1.3	0.07423	1.68	1.7866	1.4	0.17607	1.2	0.33	1031	68	1045	24	1043	21	101	100	1045	24
JUA11	Z-24	1.752921712	11529	103	1.7	732.6	49.9	5.65	1.2	0.07436	2.18	1.8075	1.9	0.17822	1.2	0.17	1021	88	1057	24	1050	27	103	101	1057	24
JUA11	Z-96	3.728204502	5535	54	1.2	25.8	141	5.65	1.7	0.07277	2.83	1.7887	2.7	0.17942	1.6	0.12	992	107	1063	32	1034	35	107	103	1063	32
JUA11	Z-94	0.85296831	29760	280	1.2	105.9	169	5.59	0.6	0.07265	1.41	1.7981	1.4	0.17937	0.6	0.21	990	58	1063	12	1043	18	107	102	1063	12
JUA11	Z-110	2.333700139	28937	262	1.0	475.6	78.7	5.34	0.8	0.07326	1.45	1.8876	1.2	0.18724	0.9	0.07	1006	59	1106	18	1075	16	110	103	1106	18
JUA11	Z-112	4.34827895	14602	133	1.2	52.72	179	5.35	0.8	0.07429	1.82	1.9236	2.1	0.18747	0.8	0.43	1042	84	1107	17	1091	30	106	102	1107	17
JUA11	Z-10	7.240278505	8695	74	1.8	39.41	156	5.26	1.2	0.07741	2.70	2.0439	2.8	0.18976	1.1	0.30	1089	118	1120	22	1123	40	103	100	1120	22
JUA11	Z-52	4.187223677	15994	135	1.0	175.1	205	5.24	1.0	0.08000	1.57	2.1175	1.6	0.19100	1.0	0.35	1182	61	1126	20	1152	21	95	98	1126	20
JUA11	Z-65	9.119572894	4412	37	1.2	135.3	34.7	5.27	1.5	0.08183	2.98	2.1501	2.8	0.19170	1.5	0.10	1182	128	1130	31	1156	39	96	98	1130	31
JUA11	Z-93	2.690338917	12969	114	3.6	3369	57	5.23	0.8	0.07886	2.05	2.0743	1.9	0.19183	0.8	0.08	1143	83	1131	16	1136	27	99	100	1131	16
JUA11	Z-89	28.56235043	1490	13	1.4	16.18	46.4	5.29	2.5	0.08229	6.50	2.2026	6.3	0.19281	2.4	0.06	1448	196	1134	51	1134	90	78	100	1134	51
JUA11	Z-74	6.427801835	20410	178	1.0	451	45	5.21	0.6	0.07740	1.30	2.0634	1.2	0.19251	0.6	0.16	1120	54	1135	13	1139	15	101	100	1135	13
JUA11	Z-51	22.70872208	2011	16	0.7	14.81	87.2	5.29	2.8	0.08260	6.06	2.1893	6.3	0.19394	2.4	-0.02	1301	203	1141	52	1141	91	88	100	1141	52
JUA11	Z-18	0.740473233	5963	50	0.2	411.1	36	5.18	1.9	0.08012	3.53	2.1953	3.7	0.19483	1.7	0.09	1181	142	1146	36	1164	51	97	98	1146	36
JUA11	Z-14	0.34231392	35671	290	0.6	195.3	237	5.15	0.9	0.08111	1.19	2.1999	1.5	0.19509	0.9	0.57	1214	48	1149	19	1178	21	95	97	1149	19
JUA11	Z-12	6.359977441	8368	68	1.3	90.21	84.6	5.13	1.5	0.07622	2.57	2.0647	2.5	0.19555	1.4	0.21	1061	106	1151	30	1131	33	108	102	1151	30
JUA11	Z-108	0.432609047	24955	212	0.7	210.5	107	5.11	0.9	0.08046	1.04	2.1789	1.1	0.19629	0.9	0.41	1201	40	1155	19	1173	16	96	98	1155	19
JUA11	Z-28	30.73532074	3930	32	2.2	7.881	223	5.09	1.4	0.08052	2.66	2.2198	3.1	0.19720	1.3	0.02	1209	96	1159	28	1175	45	96	99	1159	28
JUA11	Z-64	3.841744153	5192	44	1.0	64.01	81.4	5.10	1.4	0.08288	3.27	2.2443	2.8	0.19826	1.5	-0.09	1203	127	1165	33	1186	39	97	98	1165	33
JUA11	Z-27	9.606717575	5983	49	2.0	86.57	83.4	5.05	1.4	0.08414	3.50	2.3058	3.6	0.19975	1.4	0.41	1271	157	1173	30	1201	50	92	98	1173	30
JUA11	Z-119	5.210034314	13684	116	2.5	105.7	65.5	5.02	0.8	0.07916	1.99	2.1774	1.8	0.19988	0.8	-0.06	1150	82	1174	17	1170	25	102	100	1174	17
~~**JUA11**~~	~~Z-82~~	~~6.486201532~~	~~4128~~	~~35~~	~~1.8~~	~~328~~	~~43.3~~	~~5.03~~	~~1.6~~	~~0.07455~~	~~4.33~~	~~2.0626~~	~~4.2~~	~~0.20114~~	~~1.6~~	~~-0.17~~	~~1136~~	~~150~~	~~1180~~	~~35~~	~~1117~~	~~62~~	~~104~~	~~106~~	~~1180~~	~~35~~
JUA11	Z-100	8.185924939	5507	46	0.9	726.2	51.6	5.01	1.3	0.07915	2.69	2.1869	2.7	0.20115	1.3	0.18	1171	100	1181	28	1168	38	101	101	1181	28
JUA11	Z-97	2.091137402	14108	118	0.4	479.1	78.3	4.97	1.3	0.07920	2.03	2.2068	1.9	0.20277	1.3	0.20	1154	80	1189	29	1180	26	103	101	1189	29
JUA11	Z-57	2.582869215	16531	132	0.9	1219	53.3	4.90	0.8	0.08073	1.88	2.2898	1.8	0.20381	0.7	0.16	1192	75	1196	16	1205	25	100	99	1196	16
JUA11	Z-86	6.621485829	5467	44	0.9	354.6	47.7	4.80	1.3	0.07763	2.80	2.2298	2.8	0.20886	1.3	0.24	1082	123	1222	30	1181	41	113	103	1222	30
JUA11	Z-4	3.649678004	16769	127	1.1	85.38	291	4.75	0.8	0.08094	1.90	2.3602	1.8	0.21126	0.8	0.11	1198	75	1235	19	1227	26	103	101	1235	19
JUA11	Z-45	0.838892134	19187	146	0.6	160.4	74	4.72	1.1	0.08140	1.58	2.4108	1.9	0.21290	1.1	0.40	1229	66	1244	25	1242	26	101	100	1244	25
JUA11	Z-113	0.628459916	18198	140	0.9	473.4	39	4.58	0.8	0.08022	1.33	2.4237	1.3	0.21917	0.8	0.24	1190	54	1277	19	1247	19	107	102	1277	19
JUA11	Z-9	1.522600731	13738	96	1.6	8.298	1275	4.23	1.3	0.08977	1.66	2.9411	1.5	0.23837	1.3	0.25	1403	64	1377	33	1389	22	98	99	1377	33
~~**JUA11**~~	~~Z-99~~	~~0.594427285~~	~~32331~~	~~241~~	~~1.3~~	~~462.5~~	~~59.3~~	~~4.54~~	~~2.7~~	~~0.12364~~	~~1.58~~	~~3.8648~~	~~2.5~~	~~0.22712~~	~~2.3~~	~~0.78~~	~~2009~~	~~51~~	~~1316~~	~~56~~	~~1596~~	~~43~~	~~66~~	~~82~~	~~1316~~	~~56~~
JUA11	Z-26	1.0257488	18007	118	2.8	235.2	75.9	4.16	1.1	0.09433	1.59	3.1258	1.5	0.24071	1.0	0.38	1498	61	1390	25	1441	25	93	96	1390	25
JUA11	Z-48	1.320576015	11758	74	4.0	1842	37	3.90	0.9	0.09502	2.08	3.3561	1.9	0.25646	1.0	-0.05	1502	78	1471	26	1489	29	98	99	1471	26
JUA11	Z-111	3.372402836	4046	27	2.3	47.24	118	3.94	1.9	0.08611	3.32	3.0141	2.6	0.25836	1.9	-0.03	1330	111	1479	50	1411	37	111	105	1479	50
JUA11	Z-115	2.050305011	37191	249	0.5	228.2	154	3.83	0.7	0.09196	1.45	3.3163	1.4	0.26141	0.7	0.19	1459	55	1497	18	1483	22	103	101	1497	18
JUA11	Z-6	4.032967236	19667	117	2.0	194.1	72.1	3.74	1.0	0.09564	1.54	3.5299	1.3	0.26793	1.1	0.24	1527	57	1529	31	1531	21	100	100	1527	57
JUA11	Z-58	0.459123915	36374	228	1.5	648.1	80.6	3.82	0.8	0.09645	1.15	3.4925	1.0	0.26249	0.8	0.17	1549	44	1502	21	1524	16	97	99	1549	44
JUA11	Z-34	0.609237535	46312	256	0.2	380.8	219	3.45	0.8	0.09813	0.94	3.9415	1.0	0.29078	0.7	0.42	1583	35	1645	22	1621	15	104	101	1583	35
~~**JUA11**~~	~~Z-2~~	~~0.758694301~~	~~17139~~	~~82~~	~~1.5~~	~~44.63~~	~~222~~	~~3.19~~	~~1.1~~	~~0.09885~~	~~1.93~~	~~4.3039~~	~~2.0~~	~~0.31496~~	~~1.0~~	~~0.34~~	~~1588~~	~~73~~	~~1764~~	~~32~~	~~1690~~	~~33~~	~~111~~	~~104~~	~~1588~~	~~73~~
JUA11	Z-50	0.728120391	35380	213	1.6	591.5	49.9	3.72	0.9	0.09984	1.12	3.7218	1.1	0.27022	0.9	0.41	1613	42	1541	25	1574	18	96	98	1613	42
JUA11	Z-3	0.947267212	21798	122	1.3	538.7	39.1	3.42	1.1	0.10084	1.18	4.0599	1.5	0.29129	1.2	0.64	1631	44	1647	35	1648	23	101	100	1631	44
JUA11	Z-76	0.575445963	19477	110	1.8	1051	53.3	3.48	1.0	0.10281	1.33	4.1186	1.2	0.28885	0.9	0.36	1677	45	1635	27	1656	19	97	99	1677	45
JUA11	Z-37	3.692766375	9693	53	1.8	127.3	74.7	3.43	1.0	0.10620	2.02	4.2800	1.8	0.29271	1.0	-0.01	1713	73	1654	30	1685	28	97	98	1713	73
JUA11	Z-31	0.777727073	38899	195	2.3	319	77.6	3.12	0.8	0.10592	1.00	4.7287	1.0	0.32178	0.8	0.26	1732	40	1798	25	1771	17	104	102	1732	40
JUA11	Z-90	1.695337991	22950	115	2.2	188.3	106	3.04	0.6	0.11376	1.06	5.1381	1.1	0.32914	0.6	0.14	1854	38	1834	18	1845	18	99	99	1854	38
JUA11	Z-72	0.224212036	44757	208	2.4	2733	54.8	2.82	0.8	0.12956	0.86	6.3756	1.1	0.35618	0.8	0.66	2087	30	1963	27	2027	20	94	97	2087	30
JUA11	Z-109	2.940054563	24547	105	3.2	243.5	98.2	2.56	0.7	0.13411	1.16	7.2383	1.1	0.39126	0.7	0.17	2145	40	2128	25	2139	19	99	99	2145	40
~~**JUA11**~~	~~Z-35~~	~~3.423023984~~	~~7135~~	~~33~~	~~2.4~~	~~10611~~	~~232~~	~~2.89~~	~~1.6~~	~~0.14086~~	~~2.09~~	~~6.8159~~	~~2.2~~	~~0.34829~~	~~1.6~~	~~0.39~~	~~2216~~	~~71~~	~~1937~~	~~59~~	~~2098~~	~~40~~	~~87~~	~~92~~	~~2216~~	~~71~~
JUA11	Z-70	0.216035947	52097	179	1.6	981.1	70.4	2.10	0.8	0.17683	0.61	######	1.0	0.47657	0.8	0.73	2621	20	2511	32	2575	18	96	98	2621	20

Anexo 5. U-Pb data from sample JUA14.

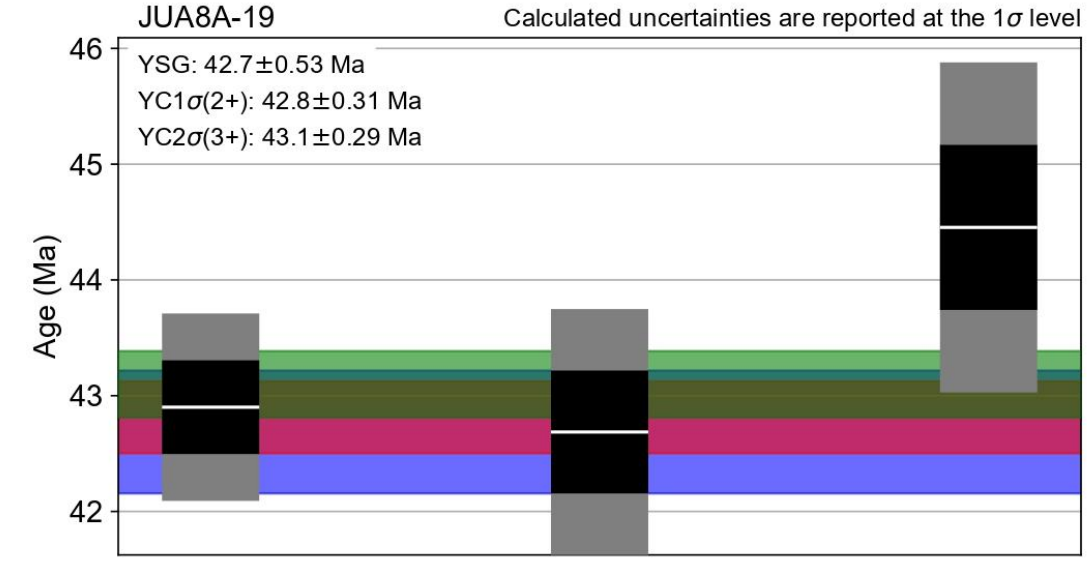
nstituto de Geociencias, Universidade de Brasilia								for Tera-Wasserbur				Data for Wetherill plot					Dates									
Identifier	Spot	f206c	206Pb	Upp m	Th/ U	206Pb/ 204Pb	1s%	238U/ 206Pb	1s %	207Pb/ 206Pb	1s%	207Pb/ 235U	1s%	206Pb/ 238U	1s%	Rho	207Pb/ 206Pb	2s (abs)	206Pb/ 238U	2s (abs)	207Pb/ 235U	2s (abs)	% conc	% conc4	Idade Preferida	2s abs
~~JUA14~~	~~spot45~~	~~10.135~~	~~38184~~	~~449~~	~~2.7~~	~~183.61~~	~~0.198~~	~~174.69~~	~~2.0~~	~~0.05453~~	~~4.38~~	~~0.0429~~	~~2.4~~	~~0.00573~~	~~2.0~~	~~1.00~~	~~389~~	~~197~~	~~37~~	~~1~~	~~43~~	~~2~~	~~9.5~~	~~86~~	~~37~~	~~1~~
JUA14	spot8	0.7364	14299	307	2.9	24430	89.34	172.57	0.2	0.04698	1.99	0.0375	1.9	0.00579	0.2	0.5	80	71	37	0	37	1	46.4	100	37	0
JUA14	spot11	1.9813	68603	622	1.8	1585.4	45.94	169.28	0.4	0.05111	0.72	0.0416	0.7	0.00593	0.4	0.33	314	28	38	0	41	1	12.2	92	38	0
JUA14	spot73	1.1763	7671	171	1.6	280.04	187.4	167.50	0.6	0.04643	3.04	0.0382	3.0	0.00597	0.5	0.1	158	165	38	0	38	2	24.3	101	38	0
JUA14	spot125	1.2328	9771	234	2.0	61.018	1548	166.96	0.4	0.04631	1.08	0.0382	1.2	0.00599	0.4	0.5	51	38	38	0	38	1	76.1	101	38	0
JUA14	spot26	14.62	15573	158	1.5	361.72	19.03	168.52	1.0	0.04930	1.81	0.0401	1.5	0.00599	1.0	0.09	368	73	39	1	40	1	10.5	96	39	1
JUA14	spot13	6.7983	25810	237	1.4	128.58	82.7	166.68	0.4	0.04825	0.71	0.0399	0.6	0.00602	0.4	0.06	262	28	39	0	40	0	14.8	97	39	0
~~JUA14~~	~~spot108~~	~~3.8517~~	~~7193~~	~~170~~	~~2.1~~	~~45.288~~	~~1247~~	~~165.48~~	~~0.8~~	~~0.06216~~	~~2.26~~	~~0.0518~~	~~2.2~~	~~0.00605~~	~~0.8~~	~~0.1~~	~~673~~	~~96~~	~~39~~	~~1~~	~~51~~	~~2~~	~~5.8~~	~~76~~	~~39~~	~~1~~
JUA14	spot12	14.701	12724	127	1.8	238.43	76.49	166.48	1.2	0.05227	1.99	0.0426	1.5	0.00607	1.2	0.08	479	72	39	1	42	1	8.1	92	39	1
JUA14	spot100	3.7492	3269	74	1.6	22.305	2046	164.11	1.1	0.04784	4.50	0.0402	4.3	0.00610	1.1	0.1	205	161	39	1	40	3	19.1	98	39	1
JUA14	spot14	22.625	10463	97	1.3	168.76	49.2	167.31	1.5	0.04981	2.37	0.0409	1.7	0.00610	1.4	0.05	449	93	39	1	41	1	8.7	96	39	1
JUA14	spot122	2.9079	4151	98	2.3	905.02	76.49	163.16	0.5	0.04699	1.98	0.0397	2.1	0.00613	0.5	0.4	77	73	39	0	40	2	51.0	100	39	0
JUA14	spot30	3.9545	59608	574	0.7	450.11	52.45	162.77	0.2	0.04742	0.42	0.0402	0.4	0.00615	0.2	0.33	146	17	40	0	40	0	27.0	99	40	0
JUA14	spot126	2.4401	3229	76	1.7	267.38	41.74	162.60	0.9	0.04736	4.57	0.0402	4.7	0.00615	0.9	0.2	279	177	40	1	40	4	14.2	99	40	1
JUA14	spot17	9.3244	20310	205	1.2	1794.5	36.49	163.52	1.6	0.05020	2.36	0.0423	2.1	0.00616	1.4	0.19	340	74	40	1	42	2	11.7	94	40	1
JUA14	spot35	2.6449	52093	536	1.2	480.48	32.05	162.18	0.3	0.04776	0.81	0.0405	0.9	0.00617	0.3	0.32	177	33	40	0	40	1	22.4	98	40	0
JUA14	spot15	5.3311	28915	258	1.2	150.15	73.43	161.48	0.4	0.04898	0.83	0.0416	0.7	0.00620	0.5	0.02	289	29	40	0	41	1	13.8	96	40	0
JUA14	spot41	1.4743	11634	245	1.7	351.78	281.2	161.14	0.5	0.04757	2.33	0.0407	2.2	0.00621	0.5	0.0	172	64	40	0	40	2	23.2	99	40	0
JUA14	spot34	10.685	27669	279	0.6	187.51	20.35	161.85	1.7	0.05085	2.49	0.0433	2.3	0.00621	1.7	0.29	295	109	40	1	43	2	13.5	93	40	1
JUA14	spot29	2.3215	67133	620	0.6	561.53	45.37	160.45	0.2	0.04727	0.41	0.0407	0.4	0.00623	0.2	0.11	149	15	40	0	40	0	26.8	99	40	0
JUA14	spot127	1.8075	16145	365	1.4	3821.4	98.52	159.38	0.6	0.04684	1.27	0.0405	1.3	0.00628	0.6	0.3	78	45	40	0	40	1	51.6	100	40	0
JUA14	spot46	0.1214	49823	1008	1.0	611.75	646.2	159.27	0.6	0.04750	0.60	0.0411	0.6	0.00628	0.6	0.4	73	29	40	1	41	0	55.2	99	40	1
~~JUA14~~	~~spot37~~	~~5.4585~~	~~5941~~	~~123~~	~~1.9~~	~~346.69~~	~~172.8~~	~~159.09~~	~~1.1~~	~~0.07591~~	~~###~~	~~0.0663~~	~~14.0~~	~~0.00629~~	~~1.1~~	~~0.9~~	~~947~~	~~557~~	~~40~~	~~1~~	~~65~~	~~18~~	~~4.3~~	~~62~~	~~40~~	~~1~~
JUA14	spot79	0.0216	22625	494	1.1	9497.5	92.45	158.12	0.5	0.04708	1.51	0.0410	1.3	0.00633	0.5	0.2	88	63	41	0	41	1	46.1	100	41	0
JUA14	spot115	4.3268	11244	254	1.8	4159.3	72.92	157.54	0.5	0.04696	1.63	0.0411	1.5	0.00635	0.5	0.1	112	59	41	0	41	1	36.3	100	41	0
JUA14	spot38	2.2021	8172	163	1.0	941.14	54.43	157.37	0.8	0.04550	3.96	0.0399	4.2	0.00636	0.8	0.5	198	83	41	1	40	3	20.7	103	41	1
JUA14	spot27	4.7913	57216	534	0.7	107.01	160.9	156.43	0.3	0.04929	1.21	0.0434	1.2	0.00640	0.3	0.10	398	82	41	0	43	1	10.3	95	41	0
~~JUA14~~	~~spot28~~	~~7.0611~~	~~22544~~	~~212~~	~~1.1~~	~~276.89~~	~~61.07~~	~~155.66~~	~~0.8~~	~~0.05416~~	~~1.21~~	~~0.0481~~	~~1.1~~	~~0.00643~~	~~0.7~~	~~0.12~~	~~418~~	~~46~~	~~41~~	~~1~~	~~48~~	~~1~~	~~9.9~~	~~87~~	~~41~~	~~1~~
JUA14	spot95	0.2069	20089	437	1.1	374.13	232.6	155.39	0.3	0.04707	1.69	0.0418	1.8	0.00644	0.3	0.4	111	81	41	0	42	1	37.1	100	41	0
JUA14	spot10	1.4858	68163	577	0.5	2991.1	31.25	155.48	0.2	0.04783	0.37	0.0424	0.3	0.00644	0.2	0.12	152	15	41	0	42	0	27.2	98	41	0
JUA14	spot82	0.1272	38182	827	0.5	5538.1	280.9	154.57	0.6	0.04720	1.00	0.0421	1.0	0.00647	0.6	0.3	74	40	42	1	42	1	56.2	99	42	1
JUA14	spot102	1.5313	20338	445	1.0	2067.8	49.08	154.38	0.2	0.04612	1.52	0.0412	1.5	0.00648	0.2	0.0	80	55	42	0	41	1	52.3	102	42	0
JUA14	spot17	1.2756	6707	130	2.8	65.896	270.4	154.15	0.5	0.04628	1.21	0.0414	1.2	0.00649	0.4	0.2	117	29	42	0	41	1	35.7	101	42	0
JUA14	spot16	11.751	19730	174	1.4	131.87	61.42	153.89	1.0	0.05082	1.60	0.0450	1.1	0.00652	1.1	0.01	355	58	42	1	45	1	11.8	94	42	1
JUA14	spot60	1.6112	1634	33	0.9	252.45	152.4	151.95	1.5	0.04173	9.39	0.0378	8.8	0.00659	1.4	0.3	455	0	42	1	38	6	9.3	112	42	1
JUA14	spot128	1.1896	24293	527	0.8	4311.2	38.78	151.71	0.4	0.04753	1.31	0.0432	1.5	0.00659	0.4	0.7	90	57	42	0	43	1	47.1	99	42	0
~~JUA14~~	~~spot110~~	~~8.4341~~	~~4067~~	~~91~~	~~1.5~~	~~3E+07~~	~~89.44~~	~~152.12~~	~~2.1~~	~~0.08294~~	~~###~~	~~0.0781~~	~~24.0~~	~~0.00660~~	~~2.2~~	~~1.0~~	~~1164~~	~~839~~	~~42~~	~~2~~	~~75~~	~~34~~	~~3.6~~	~~56~~	~~42~~	~~2~~
JUA14	spot129	1.5877	21279	463	0.6	5899.1	83.58	151.52	0.6	0.05410	2.16	0.0493	2.6	0.00660	0.6	0.9	369	97	42	0	49	3	11.5	87	42	0
JUA14	spot31	0.7579	187108	1663	0.4	1160.2	73.22	151.10	0.6	0.04760	0.44	0.0433	0.4	0.00662	0.7	0.79	153	21	43	1	43	0	27.8	99	43	1
JUA14	spot43	4.0114	49827	488	0.3	110.65	150.7	150.91	0.5	0.05424	0.84	0.0495	0.9	0.00665	0.5	0.28	379	35	43	0	49	1	11.3	87	43	0
JUA14	spot114	1.4966	5942	129	1.9	1.4602	17817	149.87	0.7	0.04707	2.82	0.0433	2.9	0.00667	0.7	0.2	232	177	43	1	43	2	18.5	100	43	1
JUA14	spot9	1.5033	85933	717	0.3	335.17	91.48	149.70	0.3	0.04853	0.34	0.0448	0.5	0.00670	0.3	0.62	164	13	43	0	45	0	26.2	97	43	0
JUA14	spot109	15.299	1842	37	1.2	178.75	111.3	137.21	1.0	0.04905	9.56	0.0492	9.3	0.00729	1.0	0.2	393	368	47	1	49	9	11.9	96	47	1
~~JUA14~~	~~spot98~~	~~17.563~~	~~3771~~	~~69~~	~~1.6~~	~~102.91~~	~~21.4~~	~~129.83~~	~~1.5~~	~~0.14768~~	~~4.84~~	~~0.1570~~	~~5.0~~	~~0.00771~~	~~1.6~~	~~0.3~~	~~2304~~	~~173~~	~~50~~	~~2~~	~~148~~	~~14~~	~~2.2~~	~~33~~	~~50~~	~~2~~
JUA14	spot71	8.7737	5436	90	1.7	1787	61.33	123.20	0.6	0.04669	1.33	0.0522	1.2	0.00812	0.6	0.0	99	66	52	1	52	1	52.7	101	52	1
~~JUA14~~	~~spot33~~	~~28.288~~	~~8853~~	~~65~~	~~1.1~~	~~621.15~~	~~33.87~~	~~115.52~~	~~2.6~~	~~0.21187~~	~~5.75~~	~~0.2520~~	~~4.7~~	~~0.00893~~	~~2.4~~	~~0.30~~	~~2784~~	~~175~~	~~57~~	~~3~~	~~226~~	~~18~~	~~2.1~~	~~25~~	~~57~~	~~3~~

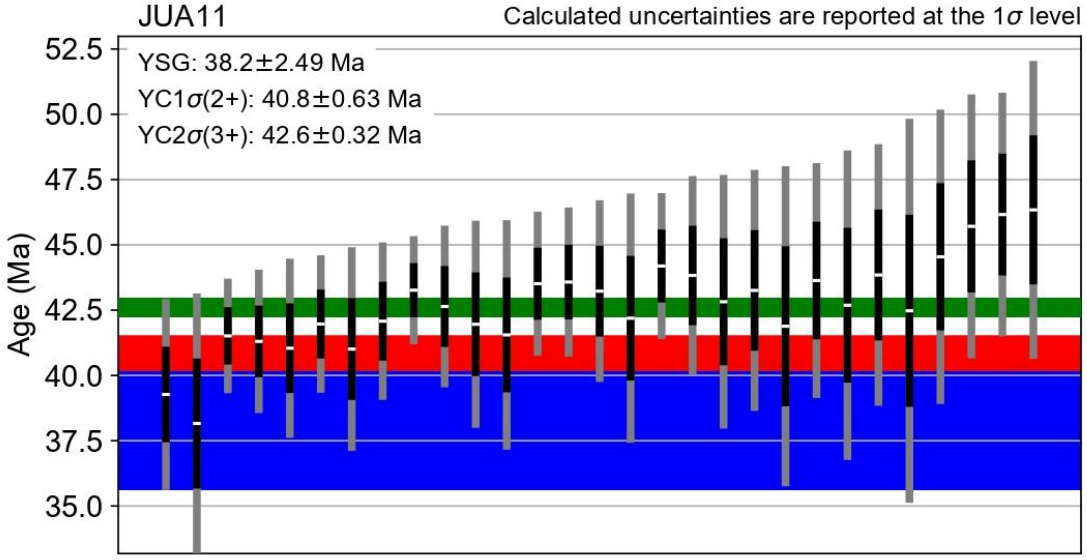
JUA14	spot32	21.472	16681	102	1.3	91.038	75.23	114.55	4.2	0.28043	8.76	0.4075	12.5	0.01023	5.4	0.82	2842	232	66	7	338	72	2.3	19	66	7
JUA14	spot29	1.6563	13538	137	1.6	237.19	245.5	80.79	1.7	0.04753	1.46	0.0813	2.4	0.01241	1.9	0.8	114	56	79	3	79	4	69.8	100	79	3
JUA14	spot26	0.3941	50242	487	1.7	5337.9	56.89	76.73	0.5	0.04899	1.25	0.0881	1.5	0.01303	0.5	0.6	145	58	83	1	86	3	57.7	97	83	1
JUA14	spot69	1.5181	10018	48	3.0	10071	74.19	35.93	0.6	0.04814	1.56	0.1848	1.5	0.02784	0.6	0.1	151	45	177	2	172	5	117.2	103	177	2
JUA14	spot39	1.2401	15986	65	1.9	445.2	204.2	31.04	0.7	0.05000	1.47	0.2220	1.1	0.03223	0.7	0.2	191	70	204	3	204	4	107.0	100	204	3
JUA14	spot65	1.0734	27988	99	4.9	4855.8	44.54	26.86	0.4	0.05035	1.39	0.2584	1.2	0.03723	0.4	0.3	208	64	236	2	233	5	113.2	101	236	2
JUA14	spot16	0.3286	29507	98	1.4	5098.1	110.4	26.36	0.5	0.05116	0.90	0.2676	0.8	0.03795	0.5	0.2	246	42	240	2	241	4	97.7	100	240	2
JUA14	spot14	0.4973	62385	199	2.9	2772.6	125.8	25.99	0.6	0.05125	0.83	0.2720	0.7	0.03849	0.5	0.2	250	38	243	3	244	3	97.3	100	243	3
JUA14	spot87	0.7693	37208	132	3.3	2591.4	128.9	25.87	0.4	0.05287	0.90	0.2819	1.1	0.03866	0.4	0.6	321	41	245	2	252	5	76.1	97	245	2
JUA14	spot24	0.2396	38986	125	2.2	9718.4	100.5	25.41	0.8	0.05108	0.74	0.2774	1.2	0.03938	0.8	0.8	243	34	249	4	249	5	102.4	100	249	4
JUA14	spot86	1.9584	28912	99	2.4	10027	89.19	25.14	0.7	0.06306	4.43	0.3467	5.0	0.03979	0.7	0.8	690	185	252	4	302	26	36.4	83	252	4
JUA14	spot30	0.0598	18772	61	3.3	3688.4	52.27	25.12	0.4	0.05177	1.24	0.2841	1.2	0.03982	0.4	0.0	272	57	252	2	254	5	92.4	99	252	2
JUA14	spot121	1.0531	14854	52	1.3	919.79	119.5	24.63	0.6	0.05077	1.31	0.2842	1.2	0.04062	0.6	0.0	227	59	257	3	254	5	113.0	101	257	3
JUA14	spot85	0.0563	71098	238	1.6	1369.9	609.2	23.91	0.3	0.05180	0.54	0.2986	0.5	0.04182	0.3	0.1	275	25	264	1	265	2	96.0	100	264	1
JUA14	spot11	1.4583	93009	173	1.9	3170.2	36.96	14.61	0.8	0.06376	3.50	0.6023	3.7	0.06849	0.8	0.4	721	144	427	6	478	28	59.2	89	427	6
JUA14	spot53	0.216	46520	76	3.6	1090.4	117.9	12.41	0.2	0.05667	0.37	0.6294	0.4	0.08057	0.2	0.4	478	16	500	2	496	3	104.6	101	500	2
JUA14	spot88	0.9524	19992	34	7.9	20440	91.66	12.27	0.5	0.05770	1.50	0.6484	1.5	0.08153	0.5	0.1	515	68	505	5	507	12	98.1	100	505	5
JUA14	spot80	0.1739	314562	505	1.0	849.62	792.6	11.50	4.7	0.06140	1.62	0.7389	3.2	0.08751	4.6	1.0	651	68	541	48	561	27	83.0	96	541	48
JUA14	spot112	0.3095	72704	112	3.9	11558	63.82	10.71	0.2	0.05880	0.55	0.7564	0.4	0.09334	0.2	0.6	558	24	575	2	572	4	103.0	101	575	2
JUA14	spot55	0.3674	43040	55	2.5	10464	106.4	9.66	0.5	0.05992	1.00	0.8551	1.3	0.10351	0.4	0.8	599	44	635	5	627	12	106.0	101	635	5
JUA14	spot130	0.0124	400005	527	1.1	425943	87.83	9.12	0.3	0.06231	0.27	0.9421	0.3	0.10966	0.3	0.7	684	12	671	4	674	3	98.1	100	671	4
JUA14	spot27	0.0984	98454	111	1.3	24332	47.93	9.03	0.3	0.06460	0.70	0.9867	0.5	0.11077	0.3	0.4	760	29	677	4	697	5	89.1	97	677	4
JUA14	spot124	0.2149	90960	111	0.8	9196.2	80.81	8.34	0.3	0.06302	0.67	1.0413	0.8	0.11984	0.3	0.8	708	29	730	4	724	9	103.1	101	730	4
JUA14	spot31	0.0211	434847	472	0.1	24192	130.9	8.31	2.7	0.06789	0.80	1.1291	3.5	0.12061	2.7	1.0	864	33	734	37	767	37	84.9	96	734	37
JUA14	spot107	0.2608	80940	76	0.2	7274.1	40.86	6.59	0.5	0.06963	0.53	1.4567	0.9	0.15177	0.5	0.9	916	22	911	9	913	11	99.4	100	911	9
JUA14	spot99	0.0495	373088	331	1.4	1799	1844	6.47	1.0	0.07107	0.52	1.5168	1.4	0.15473	1.0	1.0	958	21	927	18	937	18	96.8	99	927	18
JUA14	spot101	0.2893	144029	122	3.4	11104	26.23	6.06	0.3	0.07172	0.25	1.6313	0.3	0.16496	0.3	0.6	977	10	984	6	982	3	100.8	100	984	6
JUA14	spot51	0.1361	34455	27	1.8	3793.7	44.31	5.99	0.3	0.07132	0.70	1.6419	0.7	0.16694	0.3	0.1	965	28	995	5	986	9	103.1	101	995	5
JUA14	spot9	0.3229	118708	85	1.4	2778.9	162.3	5.76	0.6	0.07330	0.46	1.7559	0.7	0.17373	0.6	0.8	1021	19	1033	11	1029	9	101.1	100	1029	9
JUA14	spot70	0.2664	31876	25	2.4	33867	70.6	5.66	0.8	0.07285	0.98	1.7744	1.3	0.17673	0.8	0.6	1008	39	1049	16	1036	17	104.1	101	1036	17
JUA14	spot84	0.2094	83758	66	1.2	10843	234.1	5.75	0.9	0.07422	0.81	1.7814	1.6	0.17402	0.9	0.9	1046	33	1034	17	1038	20	98.9	100	1038	20
JUA14	spot67	0.0017	300064	229	0.9	29236	123.8	5.72	0.7	0.07434	0.32	1.7921	0.7	0.17479	0.7	0.9	1050	13	1038	14	1042	9	98.9	100	1042	9
JUA14	spot15	0.1043	115288	81	1.9	46236	128.9	5.69	0.5	0.07439	0.50	1.8041	0.8	0.17582	0.5	0.8	1051	20	1044	9	1047	11	99.3	100	1047	11
JUA14	spot66	0.9354	54667	43	2.1	2556.5	24.26	5.87	0.2	0.07837	0.98	1.8396	1.1	0.17024	0.2	0.5	1155	39	1013	5	1060	15	87.8	96	1060	15
JUA14	spot54	0.3446	276603	194	0.8	917.96	764.9	5.37	0.9	0.07819	0.32	2.0094	1.0	0.18636	0.9	1.0	1151	13	1102	18	1119	14	95.7	98	1119	14
JUA14	spot93	0.2917	100823	73	0.6	7083.5	19.45	5.28	0.6	0.07817	0.78	2.0416	0.7	0.18941	0.6	0.3	1150	31	1118	12	1129	9	97.2	99	1129	9
JUA14	spot22	0.2509	93071	62	2.0	1206	432.3	5.29	1.1	0.08226	0.75	2.1449	1.6	0.18904	1.1	0.9	1250	29	1116	22	1163	23	89.3	96	1163	23
JUA14	spot12	0.0769	117794	75	1.6	4960.4	126.3	5.09	0.4	0.07916	0.39	2.1454	0.8	0.19651	0.4	0.9	1175	16	1157	9	1163	10	98.4	99	1163	10
JUA14	spot113	0.1605	91579	67	1.9	14661	109.5	5.09	0.4	0.07941	0.34	2.1489	0.3	0.19634	0.4	0.5	1181	13	1156	8	1165	4	97.8	99	1165	4
JUA14	spot25	0.1793	159649	105	1.1	2E+09	94.28	5.08	0.7	0.07945	0.29	2.1578	0.7	0.19699	0.7	0.9	1182	12	1159	16	1167	10	98.0	99	1167	10
JUA14	spot81	0.1481	116289	83	0.9	4456.5	199.1	4.95	0.7	0.07880	0.34	2.1930	0.9	0.20196	0.7	0.9	1166	14	1186	15	1179	12	101.7	101	1179	12
JUA14	spot97	0.333	46082	32	2.2	4E+10	93.54	5.00	0.5	0.08070	0.57	2.2240	0.8	0.19988	0.5	0.7	1213	22	1175	10	1189	12	96.8	99	1189	12
JUA14	spot83	0.3694	91857	63	1.3	3083	124	4.83	0.9	0.07822	0.49	2.2326	1.0	0.20711	0.9	0.9	1151	19	1213	20	1191	14	105.4	102	1191	14
JUA14	spot43	0.1622	147608	96	1.9	2601.8	220.2	4.94	0.5	0.08025	0.82	2.2416	1.0	0.20263	0.5	0.5	1202	32	1189	11	1194	14	99.0	100	1194	14
JUA14	spot72	0.0742	78636	50	1.0	41251	51.06	4.72	1.0	0.07884	0.52	2.3045	1.4	0.21196	0.9	1.0	1167	20	1239	21	1213	20	106.2	102	1213	20
JUA14	spot96	0.0245	310797	213	1.1	19320	66.88	4.86	0.2	0.08115	0.22	2.3037	0.3	0.20594	0.2	0.7	1224	9	1207	4	1213	4	98.6	99	1213	4
JUA14	spot94	0.032	174114	118	1.1	9687.9	112.8	4.77	0.3	0.08156	0.18	2.3566	0.2	0.20967	0.3	0.7	1234	7	1227	6	1230	2	99.4	100	1230	2
JUA14	spot40	0.0043	64276	39	1.2	32810	64.28	4.77	0.5	0.08175	0.32	2.3626	0.6	0.20960	0.5	0.9	1239	13	1227	10	1231	9	99.0	100	1231	9
JUA14	spot116	0.1754	80862	53	0.9	8666.5	77.18	4.54	0.6	0.07993	0.57	2.4298	0.8	0.22055	0.6	0.7	1194	23	1285	13	1251	12	107.6	103	1251	12
JUA14	spot52	0.0997	73423	44	1.4	22067	51.62	4.56	1.0	0.08593	0.49	2.5975	0.8	0.21924	1.0	0.9	1336	19	1278	23	1300	11	95.7	98	1300	11

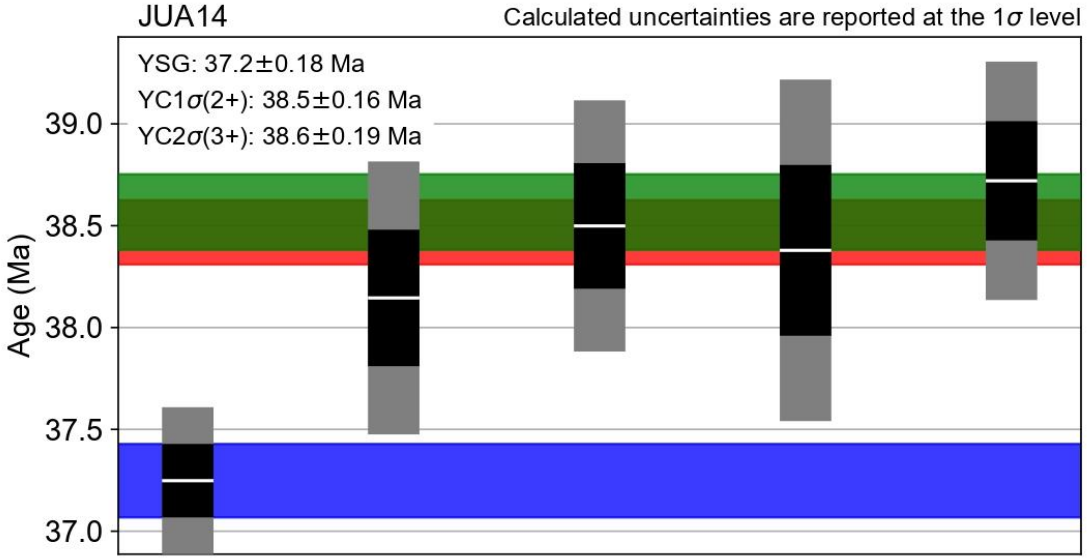
JUA14	spot68	0.0546	72378	42	1.5	16630	48.94	4.42	0.5	0.08699	0.50	2.7172	0.8	0.22652	0.5	0.8	1359	20	1316	11	1333	11	96.8	99	1333	11
JUA14	spot32	0.1282	125952	70	2.1	3952.6	180	4.37	0.5	0.08648	0.38	2.7262	0.6	0.22863	0.5	0.8	1348	15	1327	13	1336	10	98.5	99	1336	10
JUA14	spot56	0.0492	125260	71	2.1	4286.9	146.6	4.23	0.6	0.08671	0.35	2.8273	0.8	0.23658	0.6	0.9	1353	13	1369	14	1363	12	101.2	100	1363	12
~~JUA14~~	~~spot45~~	~~0.1473~~	~~1203219~~	~~828~~	~~1.2~~	~~12164~~	~~9.49~~	~~5.07~~	~~6.1~~	~~0.10725~~	~~1.69~~	~~2.9728~~	~~4.6~~	~~0.20252~~	~~6.2~~	~~1.0~~	~~1750~~	~~62~~	~~1186~~	~~135~~	~~1397~~	~~70~~	~~67.8~~	~~85~~	~~1397~~	~~70~~
JUA14	spot57	0.1145	144368	79	1.4	20562	286.4	4.17	1.8	0.09164	0.71	3.0373	2.4	0.24026	1.8	1.0	1459	27	1388	45	1416	36	95.1	98	1416	36
JUA14	spot10	0.072	175694	91	1.1	342601	60.63	4.16	0.5	0.09270	0.41	3.0739	0.6	0.24046	0.4	0.7	1481	16	1389	11	1426	9	93.8	97	1426	9
JUA14	spot13	0.0692	114847	60	3.5	20209	65.37	4.14	1.3	0.09712	0.64	3.2428	1.9	0.24207	1.3	1.0	1568	24	1397	33	1467	28	89.1	95	1467	28
JUA14	spot59	0.1716	91103	47	1.8	10004	137.4	3.96	0.2	0.09373	0.31	3.2666	0.5	0.25271	0.2	0.9	1502	12	1452	6	1473	8	96.7	99	1473	8
JUA14	spot44	0.227	49553	25	2.8	2448.7	143.6	3.83	0.6	0.09384	0.67	3.3811	0.9	0.26137	0.6	0.6	1504	25	1497	15	1500	13	99.5	100	1500	13
JUA14	spot23	0.0761	150942	73	2.2	20414	66.75	3.77	0.5	0.09578	0.33	3.5060	0.3	0.26549	0.5	0.8	1543	13	1518	13	1529	5	98.4	99	1543	13
JUA14	spot28	0.0684	410450	199	0.5	18827	37.74	3.78	0.3	0.09709	0.31	3.5426	0.4	0.26464	0.3	0.6	1568	12	1514	7	1537	6	96.5	98	1568	12
JUA14	spot58	0.0338	411999	204	1.8	59873	188.8	3.71	0.4	0.09658	0.30	3.5847	0.5	0.26928	0.4	0.8	1558	11	1537	11	1546	7	98.7	99	1558	11
JUA14	spot111	0.0038	343615	180	1.2	50458	57.77	3.64	0.3	0.09652	0.21	3.6522	0.5	0.27451	0.3	0.9	1557	8	1564	9	1561	7	100.4	100	1557	8
JUA14	spot74	0.0309	194375	86	0.9	445.61	6491	3.29	0.8	0.10357	0.26	4.3356	1.0	0.30366	0.8	1.0	1688	9	1709	23	1700	16	101.3	101	1688	9
JUA14	spot123	0.0834	346309	170	3.8	13578	254.1	3.40	2.0	0.10767	0.59	4.3778	2.1	0.29497	1.9	1.0	1759	22	1666	57	1707	35	94.7	98	1759	22
JUA14	spot42	0.081	236604	97	2.0	106675	51.86	3.18	0.6	0.10720	0.33	4.6436	0.6	0.31418	0.6	0.9	1751	12	1761	17	1757	11	100.6	100	1751	12

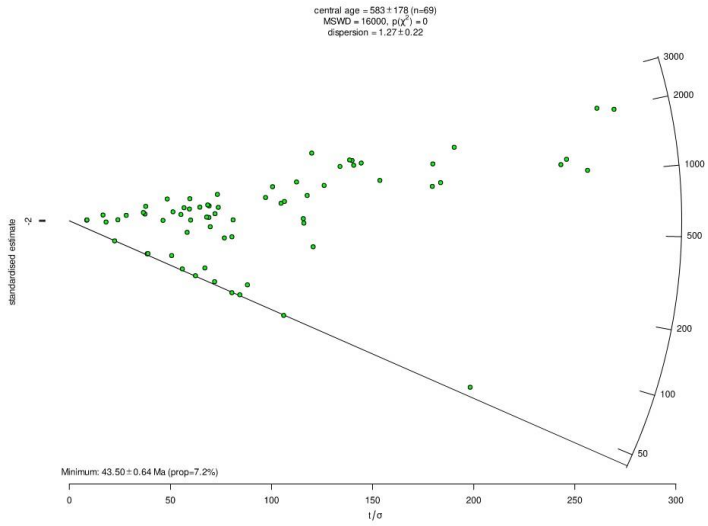
Anexo 6. Data from the statistic methods from 'Maximum Depositional Age' and 'Maximum Likehood Age' (MDA – MLA)

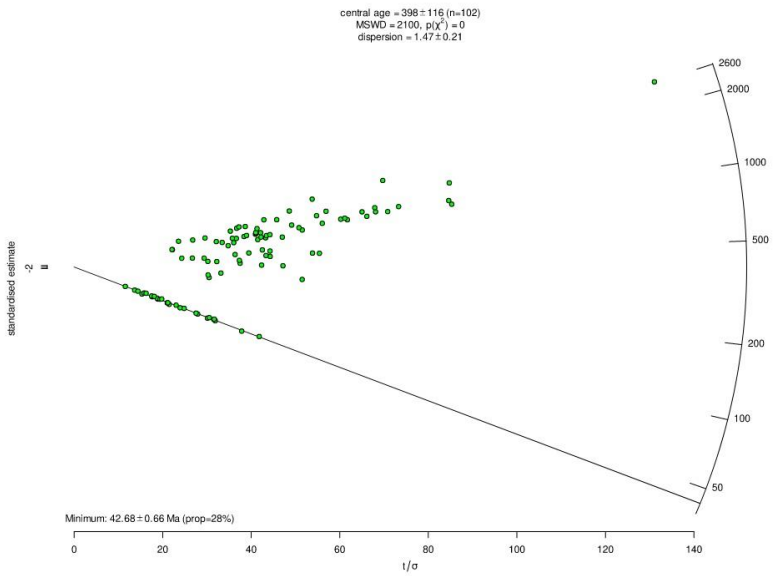
Sample	MDA	MLA
	YC2σ(3+)	
JUA 14	38.6 ± 0.19 Ma	37.64 ± 0.85 Ma
JUA 11	42.6 ± 0.32 Ma	42.68 ± 0.66 Ma
JUA 8A/19	43.1 ± 0.29 Ma	43.50 ± 0.64 Ma

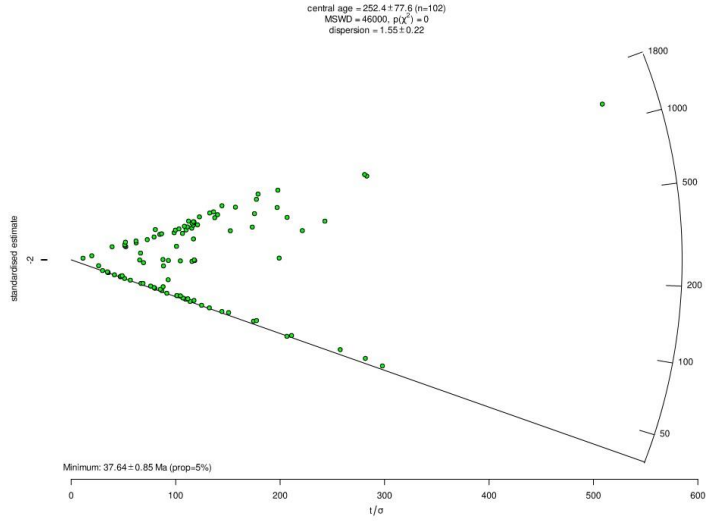

JUA8A-19
Calculated uncertainties are reported at the 1σ level
YSG: 42.7±0.53 Ma
YC1σ(2+): 42.8±0.31 Ma
YC2σ(3+): 43.1±0.29 Ma
Age (Ma)
46
45
44
43
42


JUA11
Calculated uncertainties are reported at the 1σ level
YSG: 38.2±2.49 Ma
YC1σ(2+): 40.8±0.63 Ma
YC2σ(3+): 42.6±0.32 Ma
Age (Ma)
52.5
50.0
47.5
45.0
42.5
40.0
37.5
35.0


JUA14
Calculated uncertainties are reported at the 1σ level
YSG: 37.2±0.18 Ma
YC1σ(2+): 38.5±0.16 Ma
YC2σ(3+): 38.6±0.19 Ma
Age (Ma)
39.0
38.5
38.0
37.5
37.0


central age = 583 ± 178 (n=69)
MSWD = 16000, p(χ²) = 0
dispersion = 1.27 ± 0.22
standardised estimate
-2
0
2
3000
2000
1000
500
200
100
50
Minimum: 43.50 ± 0.64 Ma (prop=7.2%)
0
50
100
150
200
250
300
t/σ


central age = 398 ± 116 (n=102)
MSWD = 2100, p(χ²) = 0
dispersion = 1.47 ± 0.21
standardised estimate
-2
0
2
2600
2000
1000
500
200
100
50
Minimum: 42.68 ± 0.66 Ma (prop=28%)
0
20
40
60
80
100
120
140
t/σ


central age = 252.4 ± 77.6 (n=102)
MSWD = 46000, p(χ²) = 0
dispersion = 1.55 ± 0.22
standardised estimate
-2
0
2
1800
1000
500
200
100
50
Minimum: 37.64 ± 0.85 Ma (prop=5%)
0
100
200
300
400
500
600
t/σ

ANEXOS CAPITULO 4

Anexo 1. General data of all analyzed samples, concerning geographical location, type of rock, method, results from MDA, MLA, and ƐNd.

Location	Sample	Code Lab	Latitude	Longitude	Rock Type	Method	MDA (YC2σ) (Ma)	MLA (Ma)	Maximum Stratigraphic Age	Age	ƐNd(0)
Juan Guerra (Stutz et al., 2022)	JUA 31	LAB4043 LAB4043XR	-6.587692	-76.305833	Sandstone	U-Pb	17.4 ± 0.25	17.62 ± 0.82	Early Miocene		-8.3
Shapaja	HG 1	LABXR030	-6.5818	-76.28155	Sandstone	U-Pb	23.2 ± 0.52	23.04 ± 0.83	Late Oligocene	Chattian	< LOD
	HG 2	LABXR002_1 LABXR002_2 LABXR030-31	-6.583033	-76.281433	Sandstone	U-Pb	26.0 ± 0.66	25.16 ± 1.22	Late Oligocene	Chattian	-9.1
Abra Machungo	JUA 30	LABXR_0118	-6.58311	-76.264138	Sands	U-Pb	Present	Present	Present Day		
	JUA 29		-6.706217	-76.286845	Shale	Sm-Nd					-8.6
	JUA 28		-6.706217	-76.286845	Shale	Sm-Nd					-8.9
Juanjuí	JUA 26	LABXR_0114	-7.073454	-76.695866	Sandstone	U-Pb	41.1 ± 0.82	41.09 ± 1.01			
	JUA 25	LABXR_0117	-7.161301	-76.734366	Sandstone	U-Pb			Quaternary		
	JUA 24	LABXR_0113	-7.208325	-76.738268	Sandstone	U-Pb	24.1 ± 0.39	23.44 ± 0.64	Late Oligocene	Chattian	-9.3
	JUA 22	LABXR_0115	-7.214056	-76.740167	Sandstone	U-Pb	30.0 ± 0.55	29.70 ± 0.62	Early Oligocene	Rupelian	-8.5
	JUA 16	LABXR_0116	-7.219375	-76.744922	Sandstone	U-Pb	41.0 ± 1.69	30.12 ± 1.39	Early Oligocene	Rupelian	-7.1
	JUA 15		-7.186641	-76.526121	Shale	Sm-Nd					-3.6
	JUA 14	LABXR_0161	-7.222988	-76.745826	Sandstone	U-Pb	38.6 ± 0.19	37.64 ± 0.85	Late Eocene	Bartonian	
	JUA 11C										
	JUA 11B										
	JUA 11A										
	JUA 11	LABXR_018	-7.22836	-76.744399	Sandstone	U-Pb	42.6 ± 0.32	42.68 ± 0.66	Middle Eocene	Lutetian	
	JUA 8A-19	LAB4042-1 LAB4042-2 LABXT0011	-7.231972	-76.746427	Sandstone	U-Pb	43.1 ± 0.29	43.50 ± 0.64	Middle Eocene	Lutetian	
	JUA 6		-7.234064	-76.746436	Shale	Sm-Nd					-5.3
	JUA 5		-7.234625	-76.746375	Shale	Sm-Nd					-8.0
	JUA 1	LABXR_0160	-7.245171	-76.74237	Sandstone	U-Pb	66.2 ± 0.56	65.05 ± 2.39	Upper Cretaceous	Maastrichtian	-7.2

Anexo 2. U-Pb data from JUA 16.

31 October 2022, Instituto de Geociências, Unive	Data for Tera-Wasserburg plot										Data for Wetherill plot							Dates							
Identifier	f206c	206Pb	Uppm	Th/U	206Pb/204Pb	1s%	238U/206Pb	1s%	207Pb/206Pb	1s%	207Pb/235U	1s%	206Pb/238U	1s%	Rho	207Pb/206Pb	2s (abs)	206Pb/238U	2s (abs)	207Pb/235U	2s (abs)	Conc (%) 6/8 -7/6	Conc (%) 6/8 -7/5	Idade Preferida	2s abs
JUA16-9	-0.518	8306	849	1.6	-407.4	-5.1	218.95	1.9	0.04775	6.52	0.0309	6.0	0.00463	1.8	-0.17	-228	350	30	1	31	4	-13	97	30	1
JUA16-6	24.92	3647	355	1.2	-1781	-12	232.23	7.8	0.10703	17.30	0.0434	15.6	0.00522	8.1	-0.10	976	671	34	5	42	13	3	79	34	5
JUA16-1	19.07	1004	91	0.9	-26189	-573	229.47	6.3	0.10802	12.34	0.0623	9.0	0.00544	4.2	-0.01	802	444	35	3	60	10	4	58	35	3
JUA16-1	12.49	5475	520	1.8	5247.5	24.4	193.86	4.3	0.05867	9.13	0.0366	11.4	0.00561	3.7	-0.04	249	360	36	3	36	8	14	100	36	3
JUA16-1	-8.059	1164	102	1.2	-73.26	-11	254.11	9.8	0.20649	16.32	0.1082	11.4	0.00568	7.1	-0.01	1772	514	37	5	100	22	2	37	37	5
JUA16-6	39.97	1718	133	1.0	427.7	7.81	185.93	4.3	0.19493	7.83	0.1397	6.7	0.00616	3.9	-0.13	2326	262	40	3	129	16	2	31	40	3
JUA16-9	4.737	16539	1419	3.7	17928	16.2	164.77	3.2	0.06254	7.74	0.0402	12.6	0.00624	3.1	-0.19	406	391	40	2	40	10	10	101	40	2
JUA16-1	36.89	1097	83	1.7	-173.8	-6.4	183.47	3.8	0.06215	13.81	0.0426	11.2	0.00632	3.6	-0.10	666	427	41	3	41	9	6	100	41	3
JUA16-1	17.38	1724	136	1.6	-316.6	-7.1	167.64	4.9	0.15778	20.93	0.1012	16.4	0.00658	4.5	-0.04	1291	507	42	4	92	28	3	46	42	4
JUA16-6	42.98	3536	303	1.5	-1658	-121	173.57	106.0	0.07275	#####	0.1870	41.7	0.00681	11.2	0.97	2689	1025	44	10	80	88	2	55	44	10
JUA16-9	0.569	8098	625	1.2	-915.5	-8.7	154.72	5.1	0.05137	11.07	0.0459	9.3	0.00701	5.1	-0.01	-234	636	45	5	45	8	-19	99	45	5
JUA16-1	3.633	13903	710	1.3	27378	6.87	105.35	2.3	0.05153	4.68	0.0645	7.3	0.00978	2.4	-0.10	131	209	63	3	63	10	48	100	63	3
JUA16-2	3.677	14790	664	1.2	-3754	-10	93.13	1.8	0.05889	4.12	0.0905	4.5	0.01102	1.8	0.13	334	205	71	2	87	7	21	81	71	2
JUA16-7	10.05	12720	538	1.9	-3301	-5.4	91.57	1.7	0.04766	5.82	0.0727	5.8	0.01106	1.7	0.06	164	222	71	2	70	8	43	101	71	2
JUA16-4	4.235	13573	630	1.4	19360	8.91	94.19	3.8	0.05166	7.70	0.0755	7.1	0.01121	3.7	-0.04	88	459	72	5	73	10	82	98	72	5
JUA16-9	3.951	10647	466	1.5	6193.8	5.31	91.66	3.2	0.04964	7.27	0.0758	6.5	0.01138	2.9	-0.18	-312	417	73	4	74	9	-23	99	73	4
JUA16-2	9.216	4265	196	1.5	-2437	-12	95.49	6.0	0.05457	12.22	0.0771	14.2	0.01145	6.1	0.13	71	673	73	9	74	20	103	100	73	9
JUA16-9	8.452	7087	281	2.1	6745.7	93	86.28	2.1	0.05142	5.56	0.0808	5.4	0.01171	2.3	-0.05	-243	355	75	3	78	8	-31	96	75	3
JUA16-1	8.113	9248	390	1.4	-1266	-5.8	88.78	2.5	0.05284	6.35	0.0805	5.4	0.01175	2.4	-0.03	-4	348	75	4	78	8	-1707	96	75	4
JUA16-1	9.416	53155	2120	1.2	-4236	-21	87.43	1.8	0.13046	5.29	0.2282	5.8	0.01189	1.8	0.40	1694	181	76	3	200	21	4	38	76	3
JUA16-7	5.581	12455	542	0.9	2445.1	6.51	89.00	3.3	0.05029	6.44	0.0776	6.8	0.01190	3.4	-0.15	-112	356	76	5	75	10	-68	101	76	5
JUA16-3	0.371	23252	1010	1.5	-2696	-6.3	85.93	3.5	0.05324	5.82	0.0794	7.3	0.01201	3.0	0.07	76	315	77	5	77	11	101	100	77	5
JUA16-8	0.074	16511	707	0.9	30938	8.48	85.61	4.2	0.06083	6.55	0.0829	10.3	0.01240	4.4	0.25	402	314	79	7	80	16	20	100	79	7
JUA16-4	0.436	6203	254	1.0	4525.5	4.72	83.00	4.0	0.05286	9.71	0.0831	7.8	0.01242	3.5	0.03	17	438	80	6	80	12	456	99	80	6
JUA16-9	7.1	6129	256	1.3	3937.8	5.78	86.58	3.3	0.08417	6.27	0.1280	5.2	0.01248	3.6	-0.27	1007	271	80	6	121	12	8	66	80	6
JUA16-1	11.91	19985	807	0.9	-1E+06	-14	82.43	2.2	0.16052	5.61	0.2869	6.3	0.01268	2.1	0.35	2066	240	81	3	245	28	4	33	81	3
JUA16-1	-6.326	4320	164	1.1	-139.4	-4.3	80.40	1.8	0.04906	5.87	0.0859	5.4	0.01292	1.9	0.02	-25	266	83	3	82	9	-327	101	83	3
JUA16-9	14.89	1148	38	1.2	-755	-31	97.76	4.2	0.05432	25.88	0.0519	25.6	0.01445	8.6	-0.01	1232	453	86	11	38	23	7	230	86	11
JUA16-5	12.86	5265	183	0.9	1196.3	11.1	76.05	3.8	0.05341	9.25	0.0953	8.5	0.01420	4.5	0.08	39	460	91	8	90	15	231	100	91	8
JUA16-3	10.89	12498	312	1.2	-70005	-19	106.42	8.7	0.07936	6.36	0.1550	11.0	0.01681	9.3	0.14	956	295	107	20	139	29	11	77	107	20
JUA16-3	1.932	13776	391	1.0	-1415	-12	57.71	4.4	0.07607	6.15	0.1745	6.8	0.01818	4.9	0.03	925	286	116	11	161	21	13	72	116	11
JUA16-1	0.125	35716	924	1.1	-5257	-5.5	50.09	4.7	0.06050	6.12	0.1590	9.1	0.02100	4.3	-0.05	475	280	134	12	148	26	28	91	134	12

~~JUA16-1~~	~~10.73~~	~~4783~~	~~103~~	~~2.8~~	~~992.38~~	~~8.44~~	~~43.86~~	~~2.7~~	~~0.07690~~	~~6.34~~	~~0.2332~~	~~6.2~~	~~0.02418~~	~~2.7~~	~~-0.05~~	~~791~~	~~295~~	~~154~~	~~8~~	~~210~~	~~25~~	~~19~~	~~73~~	~~154~~	~~8~~
JUA16-5	6.403	14267	200	1.9	-44206	-8	27.71	3.9	0.07346	8.33	0.2890	13.7	0.03746	3.8	0.20	871	344	237	18	245	66	27	97	237	18
JUA16-4	0.886	53084	645	2.0	-7209	-3.9	25.59	1.4	0.05293	2.68	0.2883	2.2	0.03972	1.4	-0.07	189	130	251	7	256	10	133	98	251	7
JUA16-1	4.765	14375	167	1.8	-2392	-4.6	25.12	1.7	0.05428	5.20	0.2892	4.7	0.04013	1.7	0.29	91	271	254	8	253	20	279	100	254	8
JUA16-6	-1.651	10253	128	0.8	-568.2	-13	26.37	5.2	0.05782	7.24	0.2921	6.4	0.04108	6.2	0.01	450	278	259	31	256	31	57	101	259	31
JUA16-1	0.921	34864	418	2.4	-25091	-11	24.38	1.4	0.05354	2.61	0.3040	2.4	0.04160	1.3	-0.12	225	125	263	7	269	12	117	98	263	7
JUA16-9	1.402	24080	291	0.9	-22415	-587	24.59	2.3	0.05769	5.50	0.3192	4.8	0.04191	2.3	-0.09	268	244	265	12	278	22	99	95	265	12
JUA16-2	1.096	40855	482	1.3	-3406	-6.4	24.27	2.0	0.05039	3.28	0.2900	2.7	0.04194	1.9	0.11	88	157	265	10	257	12	301	103	265	10
JUA16-1	6.671	16816	193	1.6	-18105	-12	24.14	1.2	0.04924	3.75	0.2830	3.2	0.04264	1.4	0.54	-136	162	269	7	246	13	-198	109	269	7
~~JUA16-1~~	~~6.334~~	~~44725~~	~~506~~	~~1.3~~	~~13117~~	~~7.29~~	~~23.30~~	~~1.4~~	~~0.09899~~	~~3.65~~	~~0.5834~~	~~4.1~~	~~0.04384~~	~~1.4~~	~~0.17~~	~~1398~~	~~142~~	~~276~~	~~7~~	~~454~~	~~29~~	~~20~~	~~61~~	~~276~~	~~7~~
JUA16-9	0.563	36715	427	1.6	-2336	-5.4	23.39	2.9	0.05401	4.69	0.3194	3.7	0.04440	2.6	-0.01	183	230	280	14	279	18	153	100	280	14
JUA16-6	0.838	25808	279	1.1	-5E+06	-453	22.31	2.1	0.05399	4.46	0.3426	3.8	0.04599	2.0	-0.06	247	193	290	11	296	19	117	98	290	11
JUA16-1	1.13	56582	520	1.3	5432	3.17	18.86	1.6	0.05405	3.07	0.3864	2.3	0.05376	1.6	0.07	241	128	339	10	333	12	141	102	339	10
JUA16-1	1.873	9028	63	1.5	3059	3.11	15.40	1.9	0.05841	4.89	0.5261	4.6	0.06579	2.2	-0.04	394	265	410	17	422	33	104	97	410	17
JUA16-1	1.495	28415	216	2.8	14407	4.41	15.15	1.6	0.05921	3.75	0.5148	4.1	0.06632	1.6	-0.15	383	175	414	13	412	30	108	100	414	13
JUA16-1	1.467	45642	320	1.5	5092	5.61	14.11	2.1	0.06410	4.01	0.6015	3.8	0.07317	2.1	-0.01	562	191	455	18	479	26	81	95	455	18
JUA16-8	0.913	#####	788	0.7	-27430	-7.1	14.01	2.1	0.06560	3.24	0.5826	4.8	0.07353	2.2	-0.25	697	138	457	19	463	39	66	99	457	19
JUA16-2	0.946	27087	174	1.7	-4204	-6	13.76	1.4	0.05647	2.85	0.5674	2.3	0.07421	1.3	-0.01	384	127	461	12	458	17	120	101	461	12
JUA16-3	1.337	37754	234	2.0	-7114	-7.3	13.57	1.7	0.05747	4.27	0.5919	3.8	0.07478	1.6	-0.04	363	193	465	15	467	28	128	100	465	15
JUA16-8	39.6	13002	87	1.4	-23194	-5.2	13.34	2.6	0.06655	5.83	0.6354	6.8	0.07720	2.6	0.04	575	254	479	24	477	57	83	100	479	24
JUA16-2	2.173	34370	212	1.3	-71947	-8.3	13.07	1.0	0.05779	1.89	0.6149	1.6	0.07753	1.0	-0.01	434	87	481	9	483	12	111	100	481	9
JUA16-1	1.272	37159	231	1.4	-6515	-8.8	12.94	1.3	0.05843	2.85	0.6259	2.4	0.07882	1.3	-0.06	418	117	489	12	488	18	117	100	489	12
JUA16-7	1.654	#####	1251	0.2	43138	6.21	12.86	1.0	0.07086	2.03	0.7890	2.6	0.07914	1.0	0.18	872	73	491	10	581	20	56	84	491	10
JUA16-1	2.23	30376	197	0.9	15639	5.58	12.80	2.0	0.06606	3.48	0.6552	5.0	0.07948	2.1	0.23	695	148	496	18	506	42	71	98	496	18
JUA16-1	0.736	27557	176	1.6	-13379	-6.3	12.83	2.6	0.06003	3.65	0.6466	3.0	0.08012	2.5	0.14	515	161	496	24	502	24	96	99	496	24

JUA16-(	0.535	36721	216	0.7	-2666	-3.9	12.49	1.4	0.05975	2.49	0.6628	2.3	0.08155	1.3	0.07	503	112	505	13	512	19	100	99	505	13
JUA16-1	0.963	30208	186	1.2	-5E+05	-6.9	12.43	3.9	0.06589	6.15	0.7026	4.4	0.08328	3.6	0.46	590	265	515	35	546	43	87	94	515	35
JUA16-(	1.54	27192	151	0.5	-2097	-8	12.26	2.2	0.05920	4.32	0.6847	3.7	0.08346	2.2	-0.11	473	200	516	21	524	31	109	99	516	21
JUA16-9	0.598	#####	796	1.2	-2E+06	-97	12.06	2.1	0.05872	3.52	0.6719	2.7	0.08460	2.0	-0.04	462	163	523	21	519	22	113	101	523	21
JUA16-5	0.386	59540	341	0.8	-13557	-212	11.83	2.0	0.06059	3.17	0.7011	2.4	0.08581	2.0	0.05	537	128	530	21	535	20	99	99	530	21
JUA16-(	2.713	26535	160	0.9	-22428	-12	11.84	3.1	0.08749	6.73	0.9337	9.9	0.08692	2.9	0.28	1187	271	537	30	627	111	45	86	537	30
JUA16-(	0.031	46431	271	0.4	-4749	-7	11.88	2.9	0.06284	4.70	0.7368	3.8	0.08795	2.8	-0.20	531	204	542	29	546	26	102	99	542	29
JUA16-1	1.885	25364	155	1.3	-4079	-6.9	11.97	3.5	0.06644	6.58	0.7063	7.6	0.08804	3.8	0.17	683	318	543	39	519	72	79	105	543	39
JUA16-1	1.603	14282	79	1.2	-2005	-4.3	11.71	2.2	0.06106	4.20	0.7228	3.5	0.08879	2.1	0.10	417	208	548	22	543	30	131	101	548	22
JUA16-(	1.779	36558	208	0.2	-3E+05	-7.5	11.55	2.7	0.06128	4.68	0.7326	3.6	0.08951	2.5	-0.09	495	204	552	27	553	30	111	100	552	27
JUA16-2	0.875	53073	288	0.4	55044	6.5	11.30	2.2	0.06212	3.73	0.7229	4.6	0.09029	1.9	-0.16	582	170	557	21	556	38	96	100	557	21
JUA16-1	2.16	39432	210	2.8	-2657	-5.8	11.03	1.7	0.06149	3.41	0.7751	2.8	0.09288	1.6	-0.14	524	152	572	18	575	24	109	99	572	18
JUA16-1	4.342	13562	68	1.5	-1786	-10	10.84	2.3	0.06288	5.16	0.8068	4.2	0.09579	2.4	-0.03	476	239	588	27	586	38	124	100	588	27
JUA16-1	0.3	69783	362	0.4	-24000	-7.5	10.55	1.4	0.06113	2.63	0.8015	2.1	0.09620	1.5	0.08	553	115	592	17	594	19	107	100	592	17
JUA16-1	1.58	29910	150	1.5	-30609	-14	10.43	1.3	0.06119	2.57	0.8206	2.2	0.09791	1.3	-0.01	560	110	602	15	602	20	107	100	602	15
JUA16-7	0.489	63713	308	1.5	-4616	-3.4	10.35	1.3	0.06114	2.25	0.8283	2.0	0.09870	1.3	0.17	551	103	606	15	607	19	110	100	606	15
JUA16-4	5.631	16293	81	1.4	1723.3	5.38	10.41	2.0	0.06020	3.84	0.8153	3.1	0.09908	1.9	-0.09	460	173	608	22	598	28	132	102	608	22
JUA16-1	2.481	23392	116	2.1	-5E+05	-7.1	10.32	1.4	0.06201	2.77	0.8405	2.4	0.09927	1.3	0.05	522	130	609	16	610	22	117	100	609	16
JUA16-3	1.48	26068	125	1.5	-1E+05	-4.6	10.28	1.6	0.06024	3.14	0.8264	2.7	0.09958	1.6	-0.05	498	138	611	18	603	25	123	101	611	18
JUA16-1	0.834	78816	412	0.7	-16667	-7.7	10.05	2.6	0.06565	4.22	0.8775	5.1	0.10077	2.8	0.32	707	179	618	33	650	36	87	95	618	33
JUA16-7	0.936	55480	274	1.0	-40205	-10	10.15	2.0	0.06158	2.83	0.8438	2.6	0.10122	1.7	0.24	584	123	621	20	620	22	106	100	621	20
JUA16-1	2.864	13019	64	1.9	-1446	-5.8	10.17	2.2	0.06340	4.88	0.8897	4.9	0.10157	2.2	0.03	542	230	623	27	629	45	115	99	623	27
~~JUA16-9~~	~~2.34~~	~~#####~~	~~634~~	~~0.5~~	~~145254~~	~~13.3~~	~~9.69~~	~~1.5~~	~~0.07535~~	~~2.45~~	~~1.0791~~	~~1.9~~	~~0.10427~~	~~1.6~~	~~0.00~~	~~1005~~	~~99~~	~~639~~	~~19~~	~~737~~	~~21~~	~~64~~	~~87~~	~~639~~	~~19~~
JUA16-5	0.876	63957	305	0.2	-20996	-5.9	9.89	2.4	0.06353	3.70	0.8811	2.6	0.10468	2.3	-0.01	602	164	641	29	642	26	106	100	641	29
JUA16-1	4.414	13406	64	1.1	-52675	-8.2	9.59	2.1	0.06223	4.41	0.9292	4.7	0.10619	2.0	0.21	580	219	650	25	656	46	112	99	650	25
JUA16-1	1.663	50018	243	1.2	-7666	-7.3	9.54	2.4	0.06818	4.47	0.9283	4.8	0.10659	2.6	-0.21	745	198	652	33	689	33	88	95	652	33
JUA16-1	0.837	18819	82	0.9	-2978	-5.5	9.51	1.2	0.06381	2.41	0.9304	2.1	0.10734	1.2	0.09	596	103	656	15	660	21	110	99	656	15
JUA16-2	1.253	53948	238	2.0	-15614	-6.8	9.30	1.3	0.06249	2.09	0.9379	1.7	0.10978	1.2	-0.03	622	90	671	16	668	17	108	100	671	16
JUA16-1	0.792	45067	179	0.8	-3382	-4.6	8.27	2.3	0.06889	3.96	1.1547	3.0	0.12571	2.4	-0.09	731	176	762	34	770	32	104	99	762	34
JUA16-5	-0.276	17478	71	0.7	-1813	-4.1	8.21	3.0	0.06855	5.18	1.1667	4.9	0.12635	3.1	0.20	666	234	765	45	767	52	115	100	765	45
JUA16-3	0.004	68256	238	0.7	-16231	-7.5	7.51	2.4	0.07261	3.24	1.3384	2.7	0.13557	2.4	0.33	955	135	819	36	859	31	86	95	819	36
JUA16-1	0.923	27780	97	1.0	-8E+06	-9.7	7.45	1.9	0.06870	2.80	1.2936	2.6	0.13957	1.6	0.08	747	123	841	25	827	31	113	102	841	25
JUA16-3	0.454	#####	336	0.6	-2E+05	-17	7.08	1.1	0.06863	1.78	1.3471	1.3	0.14364	1.1	-0.09	813	76	864	17	863	15	106	100	864	17
JUA16-1	32.93	#####	587	0.4	-20487	-6	6.96	2.4	0.07498	3.89	1.5007	3.1	0.14799	2.4	-0.22	956	168	888	39	921	38	93	96	888	39

JUA16-1	3.61129	19360	66	1.0	-1E+06	-7.6	6.81	2.8	0.08400	4.56	1.6306	5.5	0.15246	3.0	0.11	1168	200	912	50	964	72	78	95	912	50
JUA16-1	0.39515	154738	515	0.7	-80394	-8.2	6.70	3.3	0.07894	4.89	1.5987	5.7	0.15468	3.3	0.17	1071	192	925	57	982	52	86	94	925	57
JUA16-3	1.76715	18606	59	0.9	-3568.2	-8	6.49	1.7	0.07198	3.06	1.5161	2.8	0.15652	1.7	0.17	862	148	936	30	928	36	109	101	936	30
JUA16-2	0.17779	135266	401	0.2	-1E+06	-4.5	6.08	1.9	0.07326	3.02	1.6764	2.8	0.16824	1.9	-0.26	964	129	1001	35	1006	27	104	99	1001	35
JUA16-8	0.95883	113368	326	0.4	-25848	-7.1	5.98	1.0	0.07446	1.82	1.7334	1.5	0.16867	1.0	-0.03	1015	76	1004	18	1017	19	99	99	1004	18
JUA16-5	0.79957	64481	180	0.5	-61416	-3.9	5.96	0.9	0.07328	1.69	1.6969	1.3	0.16973	1.0	-0.02	948	68	1009	18	1001	16	106	101	1009	18
JUA16-1	2.10387	27239	77	6.2	12226	11.8	5.97	1.3	0.07583	2.43	1.7459	2.0	0.17025	1.2	-0.02	980	97	1011	23	1015	27	103	100	1011	23
JUA16-4	0.7404	63614	177	4.7	11259	99.8	5.81	1.1	0.07580	1.90	1.8256	1.5	0.17459	1.1	-0.02	1032	79	1036	21	1048	20	100	99	1036	21
JUA16-4	2.20829	54008	148	1.0	19053	10.7	5.80	1.5	0.08336	2.94	1.9925	2.4	0.17612	1.5	0.00	1174	118	1044	30	1098	32	89	95	1044	30
JUA16-8	0.46667	125388	343	0.2	4E+06	6.72	5.50	1.9	0.07875	3.23	1.9573	2.0	0.18442	2.0	-0.27	1088	129	1089	39	1096	26	100	99	1089	39
JUA16-1	0.41568	195439	526	1.2	-9051.8	-5.3	5.41	1.2	0.07708	1.75	1.9711	1.3	0.18766	1.2	0.12	1073	68	1107	25	1103	18	103	100	1107	25
JUA16-1	0.47148	104275	278	0.8	-8518.3	-6.6	5.31	2.1	0.08737	3.68	2.2652	2.6	0.19335	2.1	-0.19	1263	145	1137	43	1191	37	90	95	1137	43
JUA16-2	0.68833	41666	93	1.9	-78598	-6.4	5.17	1.4	0.08015	2.55	2.1657	2.4	0.19634	1.5	0.10	1122	104	1154	31	1157	34	103	100	1154	31
JUA16-1	-0.0726	86862	218	0.9	-6073.1	-3.6	5.03	1.8	0.08214	3.14	2.2464	2.4	0.20160	1.8	-0.12	1190	121	1182	39	1186	34	99	100	1182	39
JUA16-5	0.11694	286761	716	0.1	-158152	-11	5.17	2.5	0.08292	3.65	2.2488	4.5	0.20220	2.7	0.31	1168	131	1183	58	1186	51	101	100	1183	58
JUA16-8	0.93331	110727	276	0.7	-27896	-11	5.06	1.9	0.08254	2.67	2.2354	2.6	0.20331	1.8	-0.07	1197	108	1191	39	1196	28	100	100	1191	39
JUA16-4	0.06511	60280	147	2.0	-3397.9	-3.9	5.03	2.0	0.08226	2.96	2.2786	2.4	0.20505	2.2	0.19	1158	116	1199	47	1193	34	104	100	1199	47
JUA16-3	1.05527	67980	156	1.5	666528	99.8	4.87	0.9	0.08315	1.59	2.3464	1.4	0.20784	0.9	-0.09	1213	64	1216	20	1226	18	100	99	1216	20
JUA16-1	0.44825	214698	508	0.3	-164689	-116	4.88	1.4	0.08769	2.44	2.4925	1.6	0.20846	1.4	0.01	1302	91	1219	31	1263	23	94	96	1219	31
JUA16-1	0.56797	39934	92	1.5	-7250	-11	4.90	1.5	0.08003	2.21	2.2921	1.8	0.20865	1.5	0.13	1138	89	1219	34	1203	26	107	101	1219	34
~~JUA16-7~~	~~0.37403~~	~~142585~~	~~351~~	~~0.7~~	~~-165569~~	~~-6~~	~~4.92~~	~~2.8~~	~~0.13985~~	~~3.84~~	~~3.7494~~	~~4.5~~	~~0.21120~~	~~2.6~~	~~-0.11~~	~~2142~~	~~135~~	~~1232~~	~~59~~	~~1619~~	~~44~~	~~58~~	~~76~~	~~1232~~	~~59~~
JUA16-3	-0.2517	36547	74	1.1	-1124.3	-5.7	4.54	1.2	0.08684	2.24	2.6495	2.0	0.22186	1.2	0.06	1313	87	1290	27	1311	29	98	98	1290	27
JUA16-1	0.21316	114994	252	1.0	-12743	-3.4	4.54	1.2	0.09003	2.00	2.7519	1.5	0.22333	1.1	-0.09	1374	79	1298	27	1340	23	94	97	1298	27
JUA16-1	0.71224	51012	108	1.6	-3090	-3.9	4.46	1.1	0.08592	1.95	2.7098	1.7	0.22677	1.1	0.02	1298	79	1316	25	1323	26	101	99	1316	25
JUA16-5	0.27493	69199	138	2.1	-8129.3	-7.5	4.30	1.1	0.08742	1.70	2.8227	1.3	0.23625	1.1	0.05	1309	65	1365	26	1356	19	104	101	1365	26
JUA16-3	0.22225	137662	289	0.3	-29929	-5.1	4.30	2.0	0.09225	3.60	2.9783	2.7	0.23747	2.0	-0.09	1399	132	1371	49	1392	40	98	99	1371	49
JUA16-2	1.08216	54455	107	1.7	-94358	-7.2	4.24	1.0	0.09109	1.69	2.9644	1.3	0.23911	1.0	0.01	1388	65	1380	24	1389	19	99	99	1380	24
JUA16-1	0.45892	95443	175	2.0	188999	9.28	3.97	1.1	0.09241	1.77	3.2664	1.4	0.25430	1.2	-0.11	1460	72	1459	30	1469	21	100	99	1459	30
JUA16-8	0.28775	124766	242	0.9	-19063	-6.1	3.93	1.6	0.09642	2.69	3.4173	2.0	0.25837	1.6	-0.22	1481	103	1479	41	1498	32	100	99	1479	41
JUA16-1	0.77779	159697	310	1.3	-141594	-6.4	3.94	1.7	0.10389	2.40	3.6783	1.8	0.25943	1.7	0.10	1642	88	1484	44	1558	29	90	95	1484	44

JUA16-(	0.66595	91994	169	0.4	86605	7.82	3.85	1.3	0.09694	2.27	3.4749	1.7	0.26277	1.4	-0.06	1492	84	1501	36	1511	26	101	99	1492	84
JUA16-2	0.37648	89101	151	1.4	-16529	-10	3.69	1.4	0.09964	1.44	3.8739	1.7	0.28085	1.4	0.15	1574	56	1590	38	1589	28	101	100	1574	56
JUA16-7	0.29202	180852	327	1.3	-15900	-7.2	3.67	2.5	0.10354	3.88	3.9125	2.5	0.28153	2.8	-0.12	1612	140	1594	77	1607	39	99	99	1612	140
JUA16-1	0.91779	137133	262	1.8	36895	9.74	3.73	2.2	0.10639	3.65	3.9400	2.9	0.27407	2.1	0.00	1662	136	1558	59	1609	47	94	97	1662	136
JUA16-1	0.44913	74530	123	2.1	51827	10.1	3.31	3.1	0.10396	3.41	4.2415	3.9	0.30792	2.8	0.07	1663	118	1720	90	1684	63	103	102	1663	118
JUA16-1	0.28898	77919	126	2.6	-18894	-10	3.32	1.5	0.10744	2.38	4.4931	1.8	0.30698	1.5	0.03	1697	84	1722	46	1720	29	101	100	1697	84
JUA16-4	0.49928	63407	108	2.5	-27081	-8	3.51	2.6	0.10930	3.90	4.3064	2.6	0.29399	2.6	-0.14	1703	141	1656	75	1684	42	97	98	1703	141
JUA16-7	0.33684	104497	185	3.1	-8534	-4.7	3.52	2.1	0.10974	3.76	4.2856	2.3	0.28699	2.1	-0.24	1714	128	1623	60	1681	37	95	97	1714	128
JUA16-5	0.56664	90118	154	2.0	411708	4.74	3.51	2.1	0.10978	3.05	4.3423	2.5	0.29231	2.2	0.18	1722	110	1647	64	1687	40	96	98	1722	110
JUA16-4	0.59435	76443	107	1.7	17691	16.2	3.01	0.9	0.11042	1.42	5.0600	1.1	0.33378	0.9	0.06	1764	53	1856	30	1822	20	105	102	1764	53
JUA16-4	0.7045	42188	65	1.4	9785.1	3.01	3.20	2.3	0.11491	3.50	5.0183	2.6	0.32151	2.1	0.10	1784	125	1791	66	1805	44	100	99	1784	125
JUA16-7	0.95831	58918	96	1.1	-7113.8	-4.9	3.35	2.2	0.11239	2.96	4.8395	2.7	0.30952	2.1	0.22	1796	115	1732	64	1783	43	96	97	1796	115
JUA16-1	0.27263	65605	96	1.8	-16268	-8	2.91	2.2	0.11667	3.55	5.4966	2.5	0.35259	2.1	-0.08	1809	126	1940	71	1884	42	107	103	1809	126
JUA16-1	1.83843	187669	308	2.2	20498	12.2	3.26	2.2	0.11820	3.61	5.0148	2.7	0.31547	2.3	-0.08	1853	132	1763	70	1809	45	95	97	1853	132
JUA16-1	0.41274	125354	169	1.6	76385	4.78	2.93	1.0	0.11510	1.39	5.4962	1.1	0.34398	1.0	0.13	1859	53	1904	34	1899	19	102	100	1859	53
JUA16-8	0.27165	156641	252	0.7	-31913	-8.7	3.25	1.7	0.12177	2.50	5.0569	3.5	0.31366	1.7	0.16	1928	88	1764	56	1865	48	91	95	1928	88
JUA16-5	0.19627	428343	684	0.8	431119	10	3.26	2.1	0.12296	3.00	4.9054	3.7	0.31497	2.0	0.09	1929	102	1759	63	1751	104	91	100	1929	102
~~JUA16-(~~	~~0.61927~~	~~78651~~	~~127~~	~~0.9~~	~~-17040~~	~~-3.5~~	~~3.56~~	~~1.2~~	~~0.12224~~	~~1.48~~	~~4.8540~~	~~1.4~~	~~0.28576~~	~~1.1~~	~~0.35~~	~~1961~~	~~52~~	~~1617~~	~~32~~	~~1782~~	~~25~~	~~82~~	~~91~~	~~1961~~	~~52~~
JUA16-1	0.24912	121198	167	1.2	-9432.7	-4.8	2.77	1.7	0.13002	2.69	6.4827	1.9	0.36708	1.7	-0.07	2044	94	2011	59	2034	32	98	99	2044	94
JUA16-1	0.23666	113942	157	2.4	14023	5.01	2.73	1.5	0.12982	2.54	6.5953	1.9	0.37167	1.5	-0.10	2052	89	2034	53	2050	34	99	99	2052	89
JUA16-1	1.41563	12246	17	0.2	-12661	-5.4	2.79	4.9	0.13611	5.07	6.7653	5.5	0.38712	4.2	0.14	2066	196	2087	152	2062	83	101	101	2066	196
JUA16-1	0.17463	126621	168	0.3	-14393	-5.1	2.63	1.9	0.13290	3.39	6.9846	2.6	0.38732	1.9	-0.07	2074	117	2106	67	2096	45	102	100	2074	117
JUA16-4	1.41845	49052	62	1.3	4514.8	4.38	2.62	1.4	0.13345	2.23	7.1054	1.8	0.38493	1.4	0.04	2099	81	2103	47	2111	33	100	100	2099	81
JUA16-7	0.00632	328453	432	0.8	-46288	-3	2.72	1.7	0.13376	2.34	6.8704	1.6	0.37433	1.7	0.14	2101	81	2044	62	2087	28	97	98	2101	81
JUA16-(	0.11392	481927	493	0.1	-3E+06	-102	2.12	1.7	0.17931	2.21	11.8376	1.5	0.47997	1.6	0.12	2607	73	2520	68	2583	29	97	98	2607	73
JUA16-1	0.28679	150574	142	1.0	1E+06	5.48	1.95	2.1	0.18239	3.12	13.0173	2.0	0.52550	2.0	-0.20	2620	104	2714	88	2671	38	104	102	2620	104
~~JUA16-(~~	~~-176.24~~	~~-15~~	~~0~~	~~0.2~~	~~162.86~~	~~96~~	~~-4.59~~	~~-66.8~~	~~-0.01114~~	~~#####~~	~~81.8356~~	~~###~~	~~######~~	~~22.1~~	~~-0.05~~	~~2631~~	~~466~~	~~18565~~	~~1930~~	~~6345~~	~~446~~	~~706~~	~~293~~	~~2631~~	~~466~~
JUA16-5	0.30852	137810	119	1.3	-29979	-4.4	1.82	1.2	0.19904	1.94	15.2295	1.4	0.55326	1.2	-0.14	2792	64	2835	55	2824	26	102	100	2792	64
JUA16-7	1.65013	111952	103	1.3	14501	6.04	1.86	1.2	0.20631	1.59	15.5207	1.3	0.55303	1.0	0.25	2830	52	2829	48	2835	25	100	100	2830	52

U-Pb data from JUA 22.

University of Brasilia							Data for Tera-Wasserburg plot				Data for Wetherill plot					Dates								
Identifier	f206c	206Pb	Uppm	Th/U	206Pb/ 204Pb	1s%	238U/ 206Pb	1s%	207Pb/20 6Pb	1s%	207Pb/ 235U	1s%	206Pb/ 238U	1s%	Rho	207Pb/ 206Pb	2s (abs)	206Pb/ 238U	2s (abs)	207Pb/ 235U	2s (abs)	Conc (%) 6/8 -7/6	Conc (%) 6/8 -7/5	Idade Preferida	2s abs
~~JUA22-19.F~~	~~3.89~~	~~1342~~	~~127~~	~~2.2~~	~~-129.3~~	~~-6~~	~~250.58~~	~~3.0~~	~~0.06189~~	~~9.76~~	~~0.0350~~	~~9.2~~	~~0.00451~~	~~2.8~~	~~0.11~~	~~841~~	~~321~~	~~29~~	~~2~~	~~34~~	~~6~~	~~3~~	~~85~~	~~29~~	~~2~~
JUA22-38.F	0.28	5647	527	2.7	-374.9	-5	226.60	1.6	0.05116	4.48	0.0318	4.2	0.00459	1.8	0.13	-34	217	29	1	32	3	-87	93	29	1
JUA22-36.F	-1.77	1964	185	2.0	-116.5	-4	236.92	2.7	0.06895	12.48	0.0351	8.9	0.00466	2.6	-0.03	435	328	30	2	34	6	7	88	30	2
~~JUA22-11.F~~	~~7.53~~	~~1517~~	~~143~~	~~1.9~~	~~-63.29~~	~~-8~~	~~246.19~~	~~3.3~~	~~0.06876~~	~~8.25~~	~~0.0414~~	~~7.5~~	~~0.00468~~	~~2.9~~	~~-0.04~~	~~876~~	~~304~~	~~30~~	~~2~~	~~40~~	~~6~~	~~3~~	~~75~~	~~30~~	~~2~~
JUA22-56.F	42.2	2057	198	2.0	-660	-9	243.37	2.9	0.05447	9.09	0.0313	7.9	0.00469	2.9	-0.01	695	278	30	2	31	5	4	98	30	2
JUA22-129.	3.53	4995	510	2.0	-203.1	-5	224.94	2.0	0.05036	5.53	0.0313	4.7	0.00470	1.9	-0.03	-50	231	30	1	31	3	-60	97	30	1
JUA22-138.	-1.41	4433	453	1.9	-223	-4	221.97	2.0	0.04694	5.23	0.0303	4.9	0.00473	1.9	0.25	-81	243	30	1	30	3	-37	101	30	1
~~JUA22-42.F~~	~~-1.7~~	~~3986~~	~~371~~	~~2.2~~	~~-156.9~~	~~-5~~	~~217.87~~	~~2.0~~	~~0.05548~~	~~6.10~~	~~0.0362~~	~~5.9~~	~~0.00483~~	~~1.9~~	~~-0.03~~	~~237~~	~~257~~	~~31~~	~~1~~	~~36~~	~~4~~	~~13~~	~~87~~	~~31~~	~~1~~
~~JUA22-123.~~	~~-7.31~~	~~6951~~	~~743~~	~~2.5~~	~~-356.2~~	~~-6~~	~~214.75~~	~~2.6~~	~~0.06161~~	~~7.77~~	~~0.0403~~	~~7.1~~	~~0.00484~~	~~2.4~~	~~-0.04~~	~~538~~	~~278~~	~~31~~	~~1~~	~~40~~	~~6~~	~~6~~	~~78~~	~~31~~	~~1~~
~~JUA22-95.F~~	~~8.56~~	~~2945~~	~~291~~	~~1.7~~	~~-173.6~~	~~-6~~	~~219.84~~	~~2.4~~	~~0.09402~~	~~8.03~~	~~0.0589~~	~~7.3~~	~~0.00486~~	~~2.3~~	~~0.06~~	~~1225~~	~~302~~	~~31~~	~~1~~	~~57~~	~~8~~	~~3~~	~~55~~	~~31~~	~~1~~
~~JUA22-139.~~	~~-0.47~~	~~5440~~	~~553~~	~~2.5~~	~~-1098~~	~~-78~~	~~213.83~~	~~1.6~~	~~0.05962~~	~~5.47~~	~~0.0380~~	~~4.9~~	~~0.00490~~	~~1.9~~	~~0.00~~	~~185~~	~~222~~	~~32~~	~~1~~	~~38~~	~~4~~	~~17~~	~~84~~	~~32~~	~~1~~
~~JUA22-136.~~	~~-56.3~~	~~600~~	~~65~~	~~2.1~~	~~-28.05~~	~~-11~~	~~286.63~~	~~7.9~~	~~0.11435~~	~~24.62~~	~~0.0500~~	~~20.6~~	~~0.00502~~	~~7.1~~	~~0.24~~	~~1176~~	~~688~~	~~32~~	~~5~~	~~46~~	~~19~~	~~3~~	~~71~~	~~32~~	~~5~~
~~JUA22-144.~~	~~9.94~~	~~892~~	~~92~~	~~1.2~~	~~-171.7~~	~~-10~~	~~221.09~~	~~13.5~~	~~0.10239~~	~~21.89~~	~~0.0440~~	~~16.1~~	~~0.00508~~	~~6.2~~	~~0.05~~	~~1223~~	~~351~~	~~33~~	~~4~~	~~40~~	~~13~~	~~3~~	~~82~~	~~33~~	~~4~~
~~JUA22-62.F~~	~~14.3~~	~~2988~~	~~258~~	~~2.2~~	~~5655.6~~	~~23~~	~~214.56~~	~~5.2~~	~~0.07538~~	~~12.44~~	~~0.0560~~	~~13.1~~	~~0.00542~~	~~5.9~~	~~-0.03~~	~~713~~	~~430~~	~~35~~	~~4~~	~~54~~	~~13~~	~~5~~	~~65~~	~~35~~	~~4~~
JUA22-82.F	-5.86	2167	189	1.7	-126.2	-5	196.01	2.4	0.05907	7.63	0.0401	6.9	0.00550	2.3	0.03	636	280	35	2	39	5	6	90	35	2
JUA22-64.F	1.34	1730	154	1.8	-154.6	-5	202.35	3.0	0.06074	13.31	0.0432	10.4	0.00561	2.7	0.01	541	324	36	2	41	8	7	88	36	2
~~JUA22-117.~~	~~-12.5~~	~~880~~	~~70~~	~~2.2~~	~~-43.55~~	~~-11~~	~~191.44~~	~~13.0~~	~~0.10968~~	~~29.27~~	~~0.0620~~	~~13.7~~	~~0.00594~~	~~6.2~~	~~-0.13~~	~~1176~~	~~518~~	~~38~~	~~5~~	~~57~~	~~16~~	~~3~~	~~66~~	~~38~~	~~5~~
JUA22-16.F	5.19	7114	287	2.5	-380.4	-5	94.15	1.7	0.05773	4.43	0.0867	4.0	0.01094	1.7	0.01	206	224	70	2	84	6	34	84	70	2
JUA22-141.	0.94	3399	131	1.5	-211.7	-3	84.16	1.8	0.05919	5.59	0.0953	5.3	0.01251	2.0	-0.02	411	231	80	3	90	9	19	89	80	3
JUA22-4.FI	0.14	3239	110	1.3	-499.9	-4	82.33	1.8	0.05004	6.80	0.0873	6.2	0.01251	1.8	0.04	74	276	80	3	81	9	108	99	80	3
~~JUA22-74.F~~	~~14.4~~	~~2150~~	~~82~~	~~2.5~~	~~-267~~	~~-7~~	~~82.12~~	~~3.8~~	~~0.19534~~	~~17.14~~	~~0.3100~~	~~13.2~~	~~0.01445~~	~~4.5~~	~~0.04~~	~~1308~~	~~341~~	~~92~~	~~8~~	~~236~~	~~46~~	~~7~~	~~39~~	~~92~~	~~8~~
JUA22-52.F	-1.15	16002	525	1.3	-678.6	-4	77.53	3.9	0.05571	2.66	0.1188	4.1	0.01565	3.4	0.77	353	124	100	7	112	9	28	89	100	7
JUA22-131.	0.92	8090	233	0.9	-572.1	-4	62.33	1.3	0.05349	3.75	0.1221	3.6	0.01661	1.3	-0.02	160	184	106	3	115	8	66	92	106	3
~~JUA22-10.F~~	~~0.63~~	~~4737~~	~~102~~	~~3.0~~	~~-346.8~~	~~-7~~	~~50.46~~	~~3.0~~	~~0.10128~~	~~8.68~~	~~0.2713~~	~~7.8~~	~~0.02120~~	~~2.8~~	~~-0.17~~	~~1019~~	~~345~~	~~135~~	~~7~~	~~231~~	~~31~~	~~13~~	~~58~~	~~135~~	~~7~~
JUA22-89.F	5.78	11245	180	2.4	-896.7	-8	93.89	10.5	0.07374	11.54	0.2257	6.0	0.02483	5.0	0.75	892	223	157	16	197	23	18	80	157	16
JUA22-41.F	0.04	25388	438	1.2	-1044	-5	44.72	3.6	0.05411	2.43	0.1840	2.9	0.02487	2.4	0.61	252	120	158	8	170	9	63	93	158	8
JUA22-20.F	11.7	9924	113	3.6	-700.2	-5	26.39	1.4	0.06138	3.60	0.3318	3.5	0.03877	1.4	0.39	592	158	245	7	285	18	41	86	245	7
JUA22-50.F	0.54	45876	509	1.2	-2318	-3	25.47	0.8	0.05522	1.57	0.2984	1.6	0.03967	0.8	0.26	352	75	251	4	264	7	71	95	251	4
JUA22-92.F	2.11	15270	188	1.0	-1615	-5	25.06	1.6	0.05895	3.37	0.3305	3.3	0.04114	1.7	0.17	407	154	260	9	286	16	64	91	260	9
JUA22-114.	0.15	19515	224	2.3	-1262	-3	24.59	1.0	0.05668	2.30	0.3207	2.2	0.04129	1.0	0.11	361	107	261	5	281	11	72	93	261	5
~~JUA22-44.F~~	~~1.96~~	~~7154~~	~~80~~	~~1.5~~	~~-417.8~~	~~-5~~	~~24.77~~	~~2.0~~	~~0.06497~~	~~4.76~~	~~0.3636~~	~~4.4~~	~~0.04144~~	~~2.0~~	~~-0.02~~	~~553~~	~~222~~	~~262~~	~~10~~	~~308~~	~~23~~	~~47~~	~~85~~	~~262~~	~~10~~
JUA22-76.F	1.44	35016	420	1.3	-2601	-7	23.88	1.0	0.05740	2.08	0.3364	2.1	0.04247	0.9	0.10	392	94	268	5	292	11	68	92	268	5
JUA22-14.F	1.14	13744	141	1.3	-609	-5	23.82	1.1	0.05799	2.87	0.3399	2.7	0.04262	1.2	0.07	320	138	269	6	292	14	84	92	269	6
JUA22-93.F	1.62	28809	322	1.5	-2936	-4	23.41	0.9	0.05357	2.01	0.3208	1.9	0.04331	0.9	0.08	252	98	273	5	281	9	108	97	273	5
~~JUA22-34.F~~	~~2.1~~	~~11636~~	~~110~~	~~4.7~~	~~-1007~~	~~-5~~	~~23.31~~	~~1.7~~	~~0.07517~~	~~3.13~~	~~0.4560~~	~~2.9~~	~~0.04458~~	~~1.5~~	~~0.05~~	~~850~~	~~129~~	~~281~~	~~8~~	~~375~~	~~18~~	~~33~~	~~75~~	~~281~~	~~8~~
JUA22-118.	-0.3	26476	272	1.8	-1120	-4	22.10	0.9	0.06386	2.40	0.4026	2.4	0.04549	1.0	0.21	608	107	287	6	341	14	47	84	287	6
JUA22-67.F	1.84	16146	166	4.3	-2457	-5	22.37	1.4	0.06360	2.65	0.3957	2.4	0.04566	1.4	-0.02	583	122	288	8	334	14	49	86	288	8
~~JUA22-53.F~~	~~1.65~~	~~79889~~	~~795~~	~~1.2~~	~~-2145~~	~~-6~~	~~22.15~~	~~0.8~~	~~0.07305~~	~~2.04~~	~~0.4584~~	~~1.9~~	~~0.04569~~	~~0.9~~	~~-0.02~~	~~954~~	~~81~~	~~288~~	~~5~~	~~380~~	~~12~~	~~30~~	~~76~~	~~288~~	~~5~~
JUA22-3.FI	1.49	22148	201	2.1	-5842	-3	21.21	1.0	0.05706	2.22	0.3831	2.2	0.04784	1.0	0.07	376	105	301	6	325	12	80	93	301	6
JUA22-79.F	1.61	26161	256	1.6	-1870	-3	20.59	0.8	0.05446	1.98	0.3669	1.9	0.04906	0.8	0.20	304	93	309	5	316	10	101	98	309	5
~~JUA22-103.~~	~~5.15~~	~~18683~~	~~184~~	~~1.3~~	~~-2494~~	~~-5~~	~~23.14~~	~~4.5~~	~~0.07026~~	~~4.33~~	~~0.4227~~	~~2.2~~	~~0.04970~~	~~2.4~~	~~0.09~~	~~659~~	~~154~~	~~312~~	~~15~~	~~354~~	~~14~~	~~47~~	~~88~~	~~312~~	~~15~~
JUA22-86.F	1.11	13758	134	2.3	-636.1	-5	20.41	1.4	0.06291	3.55	0.4174	3.1	0.04967	1.3	-0.09	503	161	312	8	347	18	62	90	312	8
JUA22-146.	1.73	27002	260	3.3	-11165	-3	20.20	1.0	0.05283	2.09	0.3663	2.0	0.05021	0.9	0.12	232	106	316	6	316	11	136	100	316	6
JUA22-97.F	-0.51	22276	216	3.6	-1028	-3	19.91	0.9	0.05216	2.31	0.3587	2.1	0.05092	0.9	0.12	133	109	321	6	308	11	241	104	321	6
~~JUA22-73.F~~	~~1.51~~	~~98156~~	~~1027~~	~~3.3~~	~~-8279~~	~~-6~~	~~20.19~~	~~1.6~~	~~0.06614~~	~~1.40~~	~~0.4698~~	~~2.0~~	~~0.05145~~	~~1.6~~	~~0.63~~	~~799~~	~~62~~	~~323~~	~~10~~	~~388~~	~~12~~	~~40~~	~~83~~	~~323~~	~~10~~
JUA22-26.F	0.16	24053	198	0.7	-1026	-6	19.42	1.0	0.05660	2.35	0.4058	2.3	0.05232	1.0	0.01	408	105	329	7	342	13	80	96	329	7
~~JUA22-66.F~~	~~3.65~~	~~19258~~	~~151~~	~~1.2~~	~~-2622~~	~~-7~~	~~19.88~~	~~1.8~~	~~0.06822~~	~~3.03~~	~~0.5008~~	~~3.1~~	~~0.05371~~	~~1.7~~	~~0.33~~	~~681~~	~~144~~	~~337~~	~~11~~	~~406~~	~~22~~	~~49~~	~~83~~	~~337~~	~~11~~
~~JUA22-24.F~~	~~3.26~~	~~17514~~	~~124~~	~~2.8~~	~~-1917~~	~~-4~~	~~18.22~~	~~2.3~~	~~0.07075~~	~~2.26~~	~~0.5613~~	~~2.2~~	~~0.06023~~	~~2.0~~	~~0.41~~	~~839~~	~~97~~	~~376~~	~~15~~	~~447~~	~~16~~	~~45~~	~~84~~	~~376~~	~~15~~
JUA22-137.	-0.42	8270	65	2.9	-378.1	-3	16.92	1.3	0.05412	3.29	0.4532	3.1	0.06047	1.2	0.14	183	165	378	9	369	20	207	102	378	9

JUA22-124.	-8.82	9080	64	3.0	-342.4	-5	18.14	6.1	0.06721	5.62	0.5583	4.1	0.06621	2.3	0.16	546	196	412	19	434	30	76	95	412	19
JUA22-122.	1.42	54541	424	1.6	-4689	-5	15.63	2.0	0.06795	1.73	0.6165	1.6	0.06664	1.8	0.50	817	74	415	14	485	12	51	86	415	14
JUA22-27.F	0.61	50104	346	0.5	-1987	-8	16.45	3.0	0.06519	1.92	0.5885	2.4	0.06719	2.2	0.61	707	85	418	18	463	18	59	90	418	18
JUA22-112.	1.52	21026	152	2.0	-1493	-4	16.51	3.3	0.06454	2.50	0.5818	2.5	0.06842	2.4	0.40	612	104	425	20	458	19	69	93	425	20
~~JUA22-5.FI~~	~~7.46~~	~~13664~~	~~84~~	~~2.7~~	~~-1437~~	~~-5~~	~~15.25~~	~~1.8~~	~~0.11985~~	~~5.08~~	~~1.2022~~	~~6.1~~	~~0.06866~~	~~1.7~~	~~0.49~~	~~1412~~	~~194~~	~~427~~	~~14~~	~~723~~	~~61~~	~~30~~	~~59~~	~~427~~	~~14~~
JUA22-116.	-0.19	73187	493	0.1	-3503	-3	14.11	0.8	0.05668	1.23	0.5590	1.2	0.07141	0.8	0.26	442	58	445	7	449	8	101	99	445	7
JUA22-145.	0.75	47210	316	0.5	-8333	-5	14.05	1.0	0.05970	2.02	0.5898	1.7	0.07220	1.0	-0.03	528	85	449	9	469	12	85	96	449	9
JUA22-17.F	-0.27	12676	76	1.3	-810.4	-4	14.03	1.3	0.06299	2.80	0.6306	2.5	0.07273	1.3	0.06	540	135	452	12	490	20	84	92	452	12
JUA22-90.F	13.5	3369	23	1.3	-2507	-4	16.57	3.7	0.06278	4.94	0.5899	5.0	0.07311	2.9	0.27	500	223	452	25	442	38	90	102	452	25
JUA22-30.F	1.18	33998	192	1.6	-2418	-4	14.09	1.4	0.06323	2.29	0.6304	2.2	0.07284	1.4	0.11	593	99	454	12	492	17	77	92	454	12
JUA22-113.	0.81	18058	115	1.8	-1226	-3	13.64	1.1	0.05603	2.18	0.5690	2.1	0.07461	1.0	0.17	318	104	464	9	454	16	146	102	464	9
JUA22-104.	2.31	12846	85	2.7	-1693	-5	13.80	1.8	0.06318	3.16	0.6440	2.7	0.07481	1.6	0.06	576	142	464	14	497	22	81	94	464	14
JUA22-111.	0.47	71338	453	0.5	-5760	-4	13.36	0.8	0.06276	1.52	0.6572	1.3	0.07550	0.8	-0.03	657	62	469	7	511	11	71	92	469	7
~~JUA22-6.FI~~	~~2.05~~	~~56572~~	~~337~~	~~2.1~~	~~-2901~~	~~-6~~	~~13.56~~	~~1.3~~	~~0.06930~~	~~3.45~~	~~0.7902~~	~~5.5~~	~~0.07593~~	~~1.5~~	~~0.52~~	~~781~~	~~130~~	~~471~~	~~14~~	~~558~~	~~37~~	~~60~~	~~84~~	~~471~~	~~14~~
JUA22-60.F	0.78	#####	840	1.7	-4950	-4	16.60	3.6	0.06575	1.12	0.6780	2.6	0.07656	2.9	0.92	765	48	473	27	513	22	62	92	473	27
JUA22-150.	0.09	36923	223	2.9	-2510	-3	13.02	0.8	0.05883	1.70	0.6299	1.6	0.07759	0.8	0.10	485	76	482	7	495	12	99	97	482	7
JUA22-80.F	1.12	54842	334	0.5	-4324	-4	12.99	0.8	0.06049	1.69	0.6476	1.7	0.07778	0.8	0.38	538	71	483	7	503	13	90	96	483	7
JUA22-120.	0.27	45643	286	1.7	-2434	-4	12.85	0.8	0.05758	1.72	0.6199	1.5	0.07860	0.8	0.03	440	73	488	7	488	11	111	100	488	7
JUA22-22.F	4.4	8824	49	2.0	-2759	-3	13.23	1.7	0.06386	3.16	0.6723	3.0	0.07913	1.5	0.20	546	147	490	14	511	25	90	96	490	14
JUA22-58.F	3.25	13623	77	1.8	-16371	-7	12.74	1.3	0.05633	2.96	0.6290	2.8	0.08039	1.2	0.11	300	143	498	12	493	23	166	101	498	12
JUA22-65.F	0.88	39523	233	2.4	-2498	-5	12.40	0.8	0.06198	1.77	0.6809	1.5	0.08118	0.8	-0.01	597	77	503	8	524	12	84	96	503	8
JUA22-49.F	1.16	11574	66	10.9	-531.7	-6	12.57	1.7	0.06479	4.17	0.7060	3.7	0.08149	1.7	-0.01	611	193	504	17	529	32	83	95	504	17
JUA22-46.F	0.08	25410	143	1.8	-956.9	-5	12.50	1.4	0.06016	2.39	0.6669	2.2	0.08178	1.4	0.21	532	104	506	13	513	18	95	99	506	13
JUA22-87.F	0.52	51732	295	1.6	-2388	-3	12.04	0.7	0.05822	1.58	0.6671	1.4	0.08346	0.7	-0.04	462	71	517	7	516	11	112	100	517	7
JUA22-127.	1.04	59451	359	1.6	-4085	-4	11.88	1.2	0.06287	1.56	0.7417	1.6	0.08619	1.1	0.30	647	67	532	11	559	13	82	95	532	11
JUA22-39.F	0.89	11820	59	0.2	-830.9	-4	11.74	1.4	0.06284	3.35	0.7319	2.8	0.08721	1.3	-0.06	548	130	538	14	552	24	98	98	538	14
JUA22-85.F	-0.57	27045	146	1.7	-913.8	-5	11.58	1.1	0.05818	2.31	0.7056	2.4	0.08787	1.1	0.20	460	110	543	11	535	20	118	101	543	11
JUA22-40.F	0.54	63671	329	1.1	-6334	-4	11.41	0.7	0.05941	1.50	0.7215	1.3	0.08785	0.7	0.00	527	67	543	8	549	11	103	99	543	8
JUA22-106.	0.69	55898	295	1.4	-5082	-3	11.50	0.8	0.06329	1.33	0.7713	1.2	0.08817	0.8	0.14	670	57	544	9	578	11	81	94	544	9
JUA22-133.	0.44	76796	414	2.2	-2825	-5	11.03	0.7	0.06391	1.36	0.8081	1.1	0.09135	0.8	0.07	703	56	563	8	599	10	80	94	563	8
JUA22-25.F	-0.1	34736	166	2.0	-2217	-6	11.01	0.9	0.06328	2.09	0.7838	2.0	0.09187	0.9	0.16	627	92	566	10	584	18	90	97	566	10
JUA22-135.	0.86	68298	366	2.3	-1835	-6	10.95	0.7	0.06712	1.49	0.8652	1.3	0.09211	0.7	-0.02	807	65	568	8	629	12	70	90	568	8
JUA22-15.F	0.29	16514	78	2.0	-788.8	-10	11.02	1.8	0.06528	5.22	0.8162	3.7	0.09264	1.6	0.00	602	154	570	18	595	32	95	96	570	18
JUA22-31.F	0.33	14926	67	4.5	-1130	-9	10.79	1.0	0.06102	2.30	0.7890	2.1	0.09441	1.1	0.00	515	102	581	12	583	19	113	100	581	12
JUA22-47.F	1.07	92467	438	2.0	-3105	-4	10.60	0.7	0.06663	2.47	0.9181	4.4	0.09512	0.7	0.77	707	58	585	8	615	16	83	95	585	8
JUA22-108.	1.3	58281	283	0.7	-2331	-4	10.55	1.2	0.07201	2.54	0.9796	3.3	0.09652	1.2	0.66	891	93	593	14	685	31	67	87	593	14
JUA22-78.F	1.82	29666	147	2.5	-1758	-6	10.35	1.1	0.05914	2.05	0.7959	1.8	0.09763	1.0	-0.02	478	90	600	12	588	16	126	102	600	12
JUA22-59.F	0.7	45309	214	1.5	-3672	-4	10.25	0.9	0.06069	1.55	0.8307	1.6	0.09877	0.8	0.30	566	68	607	10	610	14	107	100	607	10
JUA22-54.F	4.15	10262	55	3.0	-843.7	-8	10.60	2.5	0.07460	3.76	1.0272	7.1	0.10631	6.4	-0.67	917	161	612	33	675	43	67	91	612	33
JUA22-29.F	0.62	21390	94	1.2	-1010	-5	10.17	1.6	0.06664	3.11	0.9116	2.7	0.10017	1.5	0.00	742	117	615	17	650	25	83	95	615	17
JUA22-8.FI	0.85	32423	153	3.0	-2452	-4	10.15	1.3	0.06796	2.34	0.9478	2.3	0.10025	1.2	0.27	796	101	615	14	671	22	77	92	615	14
JUA22-75.F	0.39	68354	328	1.7	-9802	-4	10.06	0.9	0.06067	1.29	0.8434	1.3	0.10091	0.8	0.37	592	57	619	10	617	12	105	100	619	10
JUA22-43.F	0.01	75646	340	1.8	-3639	-3	9.71	0.8	0.06085	1.45	0.8587	1.3	0.10334	0.9	0.15	603	62	634	10	629	12	105	101	634	10
JUA22-121.	0.43	#####	657	0.7	-25620	-7	11.82	4.2	0.07986	1.71	1.2698	4.9	0.10822	3.7	0.96	1159	66	656	47	776	54	57	85	656	47
JUA22-147.	1.47	15768	73	1.7	-16622	-6	9.85	2.4	0.06346	2.67	0.9263	2.6	0.10820	1.1	0.17	524	120	661	14	650	25	126	102	661	14
JUA22-132.	0.43	77460	331	0.3	-3640	-5	9.10	1.3	0.06660	1.40	1.0362	1.4	0.11211	1.2	0.34	790	60	684	15	718	15	87	95	684	15
JUA22-109.	-1.15	14204	60	1.4	-887.2	-3	8.71	3.6	0.07211	2.70	1.3046	3.3	0.13030	2.6	0.03	842	112	790	40	818	39	94	96	790	40
JUA22-7.FI	0.56	31472	104	1.8	-1969	-3	7.68	0.9	0.06844	1.62	1.2553	1.5	0.13226	0.9	0.06	821	70	800	14	819	17	97	98	800	14
~~JUA22-45.F~~	~~2.36~~	~~48081~~	~~160~~	~~1.1~~	~~-2252~~	~~-7~~	~~8.15~~	~~2.8~~	~~0.10495~~	~~2.44~~	~~1.8935~~	~~2.5~~	~~0.13838~~	~~3.1~~	~~0.58~~	~~1630~~	~~95~~	~~829~~	~~48~~	~~1061~~	~~33~~	~~51~~	~~78~~	~~829~~	~~48~~
JUA22-18.F	0.71	#####	387	0.6	-7476	-6	7.29	1.9	0.08813	1.66	1.7552	2.6	0.14113	2.0	0.73	1364	65	849	31	1017	32	62	83	849	31
JUA22-134.	-0.31	55853	184	1.2	-2238	-3	7.38	1.6	0.07295	1.24	1.4593	2.1	0.14169	1.6	0.26	1000	47	852	25	898	25	85	95	852	25
JUA22-55.F	0.63	68368	218	1.8	-25824	-4	7.01	0.9	0.07292	1.16	1.4684	1.2	0.14416	0.8	0.33	989	49	867	13	912	15	88	95	867	13
JUA22-115.	0.78	27613	96	0.7	-1490	-6	6.89	1.4	0.07987	2.52	1.6133	2.4	0.14685	1.4	0.25	1109	106	882	23	967	30	80	91	882	23

JUA22-37.F	0.29	59357	185	1.0	-3428	-4	6.77	1.7	0.07273	1.40	1.5541	2.0	0.15347	1.5	0.45	972	56	918	27	940	24	94	98	918	27
JUA22-148.	0.06	#####	370	0.4	-12336	-3	6.39	0.5	0.07049	0.82	1.5354	0.7	0.15730	0.5	0.19	923	33	941	9	943	9	102	100	941	9
JUA22-2.FI	5.96	11110	32	2.3	25736	6.1	7.65	15.1	0.10280	10.90	1.6470	8.4	0.16103	4.1	0.17	1249	162	944	70	1019	61	76	93	944	70
JUA22-71.F	6.04	19636	56	6.1	-1663	-10	6.45	2.0	0.07993	4.88	1.7175	3.8	0.16010	1.9	0.01	968	152	953	35	964	50	98	99	953	35
JUA22-110.	0.47	74753	227	0.4	-12773	-4	6.26	1.5	0.07446	1.81	1.6820	1.6	0.16262	1.5	0.31	1034	70	970	27	997	21	94	97	970	27
JUA22-48.F	0.2	60962	163	1.7	-2498	-3	6.18	0.9	0.07487	1.20	1.6836	1.3	0.16357	0.9	0.38	1045	51	976	16	997	16	93	98	976	16
JUA22-105.	0.92	37022	107	1.1	-5583	-3	6.20	1.0	0.07632	1.59	1.7229	1.4	0.16442	0.9	0.07	1054	70	980	17	1009	18	93	97	980	17
JUA22-32.F	0.9	54882	150	1.3	-4323	-5	6.08	1.0	0.08540	1.68	1.9778	1.7	0.16622	1.0	0.17	1286	62	990	19	1100	21	77	90	990	19
JUA22-96.F	0.18	9001	26	1.0	-451.7	-4	6.18	1.3	0.07880	3.44	1.7605	3.0	0.16654	1.3	-0.02	902	140	991	24	996	37	110	100	991	24
JUA22-125.	3.16	9099	26	1.1	-387.7	-19	6.23	1.5	0.09506	3.50	2.1426	3.1	0.16696	1.6	-0.03	1339	138	992	29	1134	43	74	87	992	29
JUA22-72.F	0.8	57464	168	1.8	-5648	-4	6.03	0.9	0.08028	1.27	1.8421	1.2	0.16759	0.8	0.05	1173	51	998	16	1058	16	85	94	998	16
JUA22-102.	0.55	35954	101	2.2	-3225	-2	6.05	0.9	0.07223	1.65	1.6640	1.3	0.16782	0.8	0.12	946	66	999	16	990	17	106	101	999	16
JUA22-94.F	1.15	45282	134	0.8	-3432	-4	5.83	1.0	0.07461	1.69	1.7617	1.5	0.17393	0.9	0.19	1018	67	1033	18	1030	18	101	100	1033	18
JUA22-128.	1.14	7325	20	1.5	-390.7	-4	5.73	1.8	0.07659	3.12	1.8684	2.9	0.18516	1.7	0.11	896	150	1091	33	1031	42	122	106	1091	33
JUA22-81.F	0.07	#####	312	1.9	-11675	-2	5.73	0.7	0.07680	0.93	1.8775	0.8	0.17621	0.7	0.25	1101	37	1046	13	1072	11	95	98	1046	13
JUA22-88.F	-0.14	27161	69	2.4	-1486	-2	5.41	0.9	0.07604	1.71	1.9251	1.6	0.18726	0.9	0.25	1026	68	1107	19	1080	22	108	103	1107	19
JUA22-13.F	1.02	60693	153	1.1	-2216	-6	6.13	1.6	0.08801	1.37	2.0714	1.3	0.16873	1.4	0.40	1354	52	1003	26	1132	18	74	89	1003	26
JUA22-9.FI	1.65	47928	115	4.2	-4946	-6	5.20	0.9	0.07841	1.65	2.1386	1.5	0.19444	0.8	0.23	1136	67	1146	17	1152	22	101	99	1146	17
JUA22-51.F	-0.25	37477	84	1.9	-1706	-4	4.96	0.9	0.08238	1.72	2.2932	1.6	0.20346	0.9	0.07	1193	67	1192	19	1198	22	100	100	1192	19
JUA22-68.F	0.62	38308	89	0.4	-3068	-4	4.75	1.3	0.07703	1.51	2.2603	1.7	0.21138	1.3	0.32	1092	61	1237	28	1198	21	113	103	1237	28
JUA22-63.F	1.98	20942	49	1.7	-11543	-5	4.99	1.0	0.08232	1.64	2.2885	1.5	0.20361	0.9	0.23	1203	64	1195	21	1200	21	99	100	1195	21
JUA22-33.F	0.25	31253	65	1.4	-3376	-3	4.94	0.8	0.08158	1.42	2.3193	1.3	0.20416	0.8	0.23	1193	56	1196	17	1209	19	100	99	1196	17
JUA22-140.	-0.01	#####	397	1.4	-5373	-5	4.87	0.9	0.08291	1.51	2.3309	1.1	0.20740	0.9	0.02	1229	59	1214	20	1220	15	99	99	1214	20
JUA22-126.	0.51	94489	239	1.0	-5438	-5	4.95	1.0	0.09031	1.21	2.5055	1.3	0.20352	1.0	0.47	1395	46	1192	22	1271	19	85	94	1192	22
JUA22-21.F	0.16	#####	334	0.7	-16147	-3	4.60	0.7	0.08259	0.74	2.5132	0.8	0.21882	0.7	0.50	1248	30	1275	16	1272	12	102	100	1275	16
~~JUA22-83.F~~	~~-0.28~~	~~16700~~	~~40~~	~~4.6~~	~~-633.3~~	~~-8~~	~~5.52~~	~~3.0~~	~~0.10144~~	~~2.92~~	~~2.7007~~	~~2.9~~	~~0.19556~~	~~3.0~~	~~0.49~~	~~1628~~	~~120~~	~~1142~~	~~62~~	~~1319~~	~~43~~	~~70~~	~~87~~	~~1142~~	~~62~~
JUA22-77.F	0.16	37350	78	0.5	-2358	-4	4.41	1.0	0.08581	1.50	2.7014	1.3	0.22874	1.0	0.03	1288	59	1325	25	1322	19	103	100	1325	25
JUA22-107.	0.77	29208	63	1.6	-1510	-4	4.71	1.5	0.09173	1.75	2.7559	2.0	0.21643	1.3	0.41	1404	65	1259	31	1325	30	90	95	1259	31
JUA22-84.F	0.56	#####	237	0.9	-3207	-5	4.52	1.0	0.09030	1.23	2.7327	0.9	0.22361	0.9	0.30	1400	46	1299	21	1333	14	93	97	1299	21
JUA22-143.	0.59	#####	227	0.8	-14119	-7	4.43	1.5	0.09754	1.14	3.1466	1.8	0.23015	1.5	0.80	1570	43	1332	36	1431	29	85	93	1332	36
JUA22-35.F	0.09	#####	185	3.1	-7068	-4	4.22	0.9	0.09663	0.90	3.2501	1.1	0.24023	0.9	0.71	1543	34	1386	23	1463	18	90	95	1386	23
~~JUA22-100.~~	~~2.72~~	~~36141~~	~~84~~	~~2.7~~	~~-7737~~	~~-76~~	~~4.62~~	~~1.6~~	~~0.11581~~	~~2.30~~	~~3.4844~~	~~2.5~~	~~0.22215~~	~~1.7~~	~~-0.06~~	~~1833~~	~~81~~	~~1289~~	~~39~~	~~1512~~	~~40~~	~~70~~	~~85~~	~~1289~~	~~39~~
JUA22-98.F	0.08	#####	240	1.0	-5113	-6	3.97	1.0	0.10822	1.22	3.8182	1.6	0.25497	1.0	0.49	1746	44	1466	27	1586	24	84	92	1466	27
JUA22-61.F	0.61	60977	104	3.0	-13567	-4	3.63	1.2	0.10168	1.50	3.9952	2.0	0.28171	1.5	0.53	1620	57	1583	35	1609	31	98	98	1620	57
JUA22-57.F	0.36	69886	104	1.4	-36803	-2	3.30	0.6	0.10254	1.07	4.3672	1.0	0.30441	0.7	0.18	1654	40	1712	20	1701	16	103	101	1654	40
JUA22-91.F	0.61	81699	145	1.7	-5522	-4	3.71	1.5	0.10371	1.15	3.9552	1.6	0.27563	1.3	0.70	1673	44	1564	36	1616	26	94	97	1673	44
~~JUA22-23.F~~	~~0.36~~	~~#####~~	~~250~~	~~1.6~~	~~-2E+05~~	~~-7~~	~~3.84~~	~~1.3~~	~~0.10653~~	~~0.70~~	~~3.9547~~	~~1.5~~	~~0.26795~~	~~1.2~~	~~0.86~~	~~1734~~	~~25~~	~~1526~~	~~34~~	~~1615~~	~~23~~	~~88~~	~~94~~	~~1734~~	~~25~~
JUA22-101.	0.28	#####	188	2.6	-6768	-4	3.28	0.6	0.10772	0.95	4.5555	0.9	0.30740	0.7	0.10	1740	35	1726	20	1736	15	99	99	1740	35
JUA22-99.F	0.75	50452	81	2.3	-2548	-5	3.23	0.8	0.11631	1.30	4.9997	1.2	0.31196	0.9	0.25	1871	47	1748	27	1814	20	93	96	1871	47
JUA22-130.	-0	92551	136	1.1	-3859	-4	3.03	0.7	0.11625	1.00	5.3381	0.8	0.33182	0.7	0.00	1887	33	1845	22	1870	15	98	99	1887	33
JUA22-149.	0.13	#####	180	2.1	-7698	-5	3.34	1.1	0.11961	0.92	5.0674	1.1	0.30567	1.0	0.65	1934	33	1715	32	1821	19	89	94	1934	33
~~JUA22-69.F~~	~~0.12~~	~~#####~~	~~231~~	~~0.7~~	~~-8794~~	~~-6~~	~~3.25~~	~~1.4~~	~~0.13311~~	~~1.00~~	~~5.7478~~	~~1.3~~	~~0.31874~~	~~1.4~~	~~0.71~~	~~2116~~	~~36~~	~~1776~~	~~42~~	~~1933~~	~~24~~	~~84~~	~~92~~	~~2116~~	~~36~~
~~JUA22-12.F~~	~~-0.06~~	~~#####~~	~~169~~	~~0.4~~	~~-4339~~	~~-4~~	~~4.24~~	~~4.5~~	~~0.13847~~	~~1.80~~	~~6.2590~~	~~3.3~~	~~0.30234~~	~~2.7~~	~~0.95~~	~~2150~~	~~75~~	~~1676~~	~~82~~	~~1881~~	~~81~~	~~78~~	~~89~~	~~2150~~	~~75~~
JUA22-119.	-0.02	#####	126	1.6	-4376	-3	2.61	0.7	0.13980	0.89	7.5059	0.9	0.38763	0.7	0.57	2210	31	2109	24	2169	17	95	97	2210	31
~~JUA22-70.F~~	~~2.43~~	~~705~~	~~2~~	~~2.4~~	~~-31.4~~	~~-11~~	~~4.60~~	~~11.1~~	~~0.27027~~	~~22.39~~	~~7.5166~~	~~33.5~~	~~0.39506~~	~~23.9~~	~~-1.00~~	~~2377~~	~~483~~	~~1708~~	~~515~~	~~1909~~	~~317~~	~~72~~	~~89~~	~~2377~~	~~483~~
~~JUA22-28.F~~	~~0.29~~	~~#####~~	~~184~~	~~1.7~~	~~-5924~~	~~-5~~	~~2.71~~	~~2.6~~	~~0.17801~~	~~0.90~~	~~10.0215~~	~~2.0~~	~~0.40621~~	~~1.8~~	~~0.89~~	~~2618~~	~~29~~	~~2179~~	~~68~~	~~2398~~	~~43~~	~~83~~	~~91~~	~~2618~~	~~29~~
~~JUA22-142.~~	~~0.09~~	~~#####~~	~~203~~	~~1.5~~	~~-23507~~	~~-3~~	~~2.26~~	~~0.7~~	~~0.19926~~	~~0.71~~	~~12.2743~~	~~0.9~~	~~0.44571~~	~~0.7~~	~~0.52~~	~~2815~~	~~24~~	~~2373~~	~~29~~	~~2620~~	~~16~~	~~84~~	~~91~~	~~2815~~	~~24~~
~~JUA22-1.FI~~	~~0.95~~	~~95354~~	~~131~~	~~0.7~~	~~-12472~~	~~-3~~	~~3.53~~	~~6.4~~	~~0.20249~~	~~1.09~~	~~11.7555~~	~~3.5~~	~~0.39910~~	~~3.2~~	~~0.97~~	~~2831~~	~~37~~	~~2106~~	~~127~~	~~2400~~	~~102~~	~~74~~	~~88~~	~~2831~~	~~37~~

U-Pb data from JUA 24.

Universidade de Brasília							Data for Tera-Wasserburg plot					Data for Wetherill plot						Dates							
Identifier	f206c	206Pb	Uppm	Th/U	206Pb/ 204Pb	1s%	238U/ 206Pb	1s%	207Pb/2 06Pb	1s%	207Pb/ 235U	1s%	206Pb/ 238U	1s%	Rho	207Pb/ 206Pb	2s (abs)	206Pb/ 238U	2s (abs)	207Pb/ 235U	2s (abs)	Conc (%) 6/8 -7/6	Conc (%) 6/8 -7/5	Idade Preferida	2s abs
83-JUA24-5	-31	998	125	1.1	-61.34	-6.72638	329.46	5.3	0.04727	23.49	0.0219	20.0	0.00339	4.7	0.11	1510	569	22	2	21	9	1	102	22	2
139-JUA24	-2.95	2905	340	0.7	-130.1	-3.64942	300.13	2.3	0.04971	6.53	0.0245	6.2	0.00360	2.2	0.03	187	275	23	1	24	3	12	95	23	1
107-JUA24	7.225	2562	294	0.8	-141.6	-3.69045	295.92	2.2	0.04920	6.27	0.0238	5.9	0.00360	2.1	0.02	323	241	23	1	24	3	7	98	23	1
147-JUA24	-12.7	1548	176	1.5	-65.94	-4.93504	317.88	3.9	0.06263	18.64	0.0232	10.5	0.00364	2.8	-0.07	468	371	23	1	23	5	5	103	23	1
176-JUA24	-2.31	1742	204	1.2	-71	-5.85744	301.70	2.9	0.05218	9.75	0.0249	8.3	0.00367	2.6	-0.05	646	306	24	1	24	4	4	98	24	1
21-JUA24-1	-2.9	3126	356	0.6	-147.8	-5.59216	283.61	3.7	0.04403	10.64	0.0239	10.6	0.00373	3.2	0.10	75	454	24	2	24	5	32	101	24	2
142-JUA24	-6.46	2672	303	0.8	-118.9	-12.4711	285.29	2.8	0.04594	9.95	0.0233	9.1	0.00384	3.0	-0.04	398	353	25	1	23	4	6	107	25	1
163-JUA24	14.74	2121	229	1.0	-122.5	-7.5136	287.07	2.9	0.05712	10.41	0.0254	8.8	0.00386	3.2	0.65	447	323	25	2	25	4	6	99	25	2
87-JUA24-(	54.36	1718	188	0.7	-83.08	-9.96672	277.94	4.5	0.05313	16.38	0.0250	14.9	0.00391	4.7	-0.13	562	597	25	2	25	7	4	102	25	2
193-JUA24	-6.42	2794	325	0.8	-152.6	-12.1549	284.94	2.8	0.05404	8.97	0.0271	8.2	0.00394	3.5	-0.07	437	331	25	2	26	4	6	97	25	2
210-JUA24	-3.24	1596	181	1.0	-141.2	-26.6563	287.95	2.8	0.05230	10.15	0.0259	9.6	0.00395	3.5	-0.01	741	373	25	2	25	5	3	100	25	2
179-JUA24	10.44	2336	277	0.8	-91.44	-14.0808	280.01	5.8	0.06062	19.38	0.0281	22.1	0.00400	6.5	0.03	978	606	26	3	27	12	3	94	26	3
64-JUA24-4	6.391	1512	145	1.0	-84.52	-6.09924	267.04	3.6	0.05676	10.82	0.0292	10.2	0.00405	3.3	-0.03	918	335	26	2	29	6	3	91	26	2
92-JUA24-(	-20.6	1570	161	0.6	-73.84	-5.1588	268.41	4.7	0.05598	18.44	0.0278	15.7	0.00422	3.8	-0.02	817	600	27	2	27	8	3	100	27	2
50-JUA24-3	26.79	2269	163	0.9	-103.6	-6.08692	186.45	3.1	0.05144	10.43	0.0378	8.7	0.00577	2.9	0.09	368	364	37	2	37	6	10	100	37	2
112-JUA24	3.225	7435	493	0.8	-483.2	-5.03679	156.86	1.9	0.04696	6.07	0.0419	5.7	0.00652	2.0	-0.03	-345	402	42	2	41	5	-12	101	42	2
125-JUA24	66.23	4798	278	1.1	9297.7	3.970134	137.60	2.1	0.05073	6.71	0.0503	5.6	0.00754	2.1	0.16	-32	288	48	2	49	5	-151	98	48	2
11-JUA24-5	2	9610	394	1.2	-578.9	-3.74166	102.72	1.3	0.04923	4.04	0.0660	3.6	0.00988	1.3	-0.12	-84	207	63	2	65	5	-76	97	63	2
155-JUA24	0.361	17514	706	0.8	-812	-3.49649	98.63	1.0	0.04481	2.96	0.0636	2.9	0.01025	1.1	0.03	-192	150	66	1	62	3	-34	105	66	1
72-JUA24-4	-2.95	6233	211	1.3	-329.5	-6.71909	80.68	1.9	0.05151	5.87	0.0861	5.3	0.01288	1.8	0.04	279	215	82	3	82	8	30	100	82	3
28-JUA24-1	0.749	14708	453	1.2	-628.2	-3.51463	78.01	1.1	0.04888	2.73	0.0886	2.5	0.01308	1.1	0.07	-80	148	84	2	86	4	-104	98	84	2
10-JUA24-4	5.451	9399	226	1.2	-577.5	-4.60806	59.97	2.2	0.05331	4.92	0.1262	4.4	0.01742	2.2	0.14	186	204	111	5	120	10	60	93	111	5
52-JUA24-3	0.611	27567	384	1.7	-1284	-4.43247	33.57	1.4	0.05122	2.83	0.2119	2.5	0.03032	1.4	-0.10	116	148	192	5	194	9	166	99	192	5
~~36-JUA24-2~~	~~6.523~~	~~107071~~	~~1303~~	~~0.7~~	~~-514.4~~	~~-48.3227~~	~~32.69~~	~~1.5~~	~~0.13424~~	~~1.85~~	~~0.5793~~	~~1.9~~	~~0.03102~~	~~1.5~~	~~0.46~~	~~2132~~	~~63~~	~~197~~	~~6~~	~~462~~	~~14~~	~~9~~	~~43~~	~~197~~	~~6~~
115-JUA24	1.011	8419	87	1.0	-765.3	-4.1331	27.32	1.9	0.05281	6.06	0.2727	5.9	0.03756	1.9	-0.05	-52	333	238	9	239	25	-456	99	238	9
7-JUA24-1.	1.185	33725	347	1.2	-2112	-4.73144	24.89	1.5	0.05151	3.20	0.2902	2.6	0.04098	1.5	-0.11	108	156	259	7	257	12	240	101	259	7
191-JUA24	-0.78	27456	291	1.5	-1141	-2.19954	24.57	0.9	0.05316	1.88	0.3016	1.8	0.04111	0.9	0.14	254	89	260	5	267	9	102	97	260	5
198-JUA24	0.478	6760	69	2.7	-399.3	-5.41647	25.00	2.6	0.05046	5.56	0.2857	5.8	0.04196	2.4	0.22	-209	378	265	12	249	26	-127	106	265	12
120-JUA24	0.455	110919	1136	1.3	-32343	-2.78586	23.78	1.0	0.05206	1.77	0.3041	1.4	0.04216	1.0	-0.15	224	87	266	5	269	6	119	99	266	5
43-JUA24-2	0.659	40532	348	1.2	-1639	-5.01024	19.98	2.1	0.05483	3.85	0.3879	3.3	0.05068	2.1	-0.08	341	184	318	13	333	20	93	96	318	13
171-JUA24	0.285	28542	243	1.5	-1253	-4.49923	19.61	0.9	0.05477	2.00	0.3878	1.9	0.05132	0.9	0.08	292	98	322	6	330	11	110	98	322	6
79-JUA24-5	1.6	10865	87	1.4	-609.7	-3.16015	19.92	1.2	0.05425	3.03	0.3867	2.9	0.05133	1.2	-0.03	200	164	322	8	325	16	161	99	322	8
197-JUA24	-0.6	17469	153	1.2	-1031	-4.48369	19.43	1.5	0.05421	4.44	0.3895	3.9	0.05234	1.5	-0.29	245	200	329	10	328	22	134	100	329	10
58-JUA24-3	-0.34	17819	136	2.6	-928.4	-4.33848	19.42	1.1	0.05342	2.39	0.3868	2.2	0.05256	1.1	0.06	232	113	330	7	330	13	142	100	330	7
38-JUA24-2	1.387	30185	247	0.9	-1201	-5.6976	19.23	1.9	0.05610	3.70	0.4056	2.9	0.05265	1.9	-0.15	308	182	331	12	343	17	107	96	331	12
196-JUA24	0.424	39733	340	0.7	-2122	-4.50315	18.75	1.7	0.05386	2.74	0.4051	2.9	0.05418	1.7	0.38	291	134	340	11	343	17	117	99	340	11
119-JUA24	0.817	38574	308	4.3	-7363	-5.12644	18.30	1.7	0.05487	3.10	0.4146	2.6	0.05520	1.6	0.12	292	146	346	11	350	15	119	99	346	11

100-JUA24	-0.43	29701	198	2.0	-1383	-5.31193	15.24	1.9	0.05717	3.74	0.5402	3.6	0.06671	1.7	-0.06	390	171	416	14	433	25	107	96	416	14
165-JUA24	0.932	30892	193	1.3	-1598	-3.71826	14.26	1.4	0.06517	2.22	0.6431	2.1	0.07168	1.4	0.26	685	95	446	12	499	17	65	89	446	12
141-JUA24	-0.11	18285	106	1.4	-725.6	-3.75544	13.31	1.4	0.05518	3.29	0.5685	2.9	0.07592	1.5	0.07	254	156	471	13	450	21	186	105	471	13
111-JUA24	0.863	22650	126	1.0	-1356	-4.06696	13.21	1.0	0.05719	2.70	0.5960	2.3	0.07642	1.0	-0.09	410	120	474	9	475	19	116	100	474	9
162-JUA24	0.475	60782	358	1.6	-3168	-6.39759	13.11	1.0	0.05825	2.09	0.6125	1.9	0.07663	1.0	0.10	519	94	476	10	486	15	92	98	476	10
70-JUA24-4	0.482	26589	126	2.3	-1397	-3.94068	12.31	1.2	0.05970	2.67	0.6745	2.5	0.08219	1.2	0.08	478	123	509	12	518	20	107	98	509	12
85-JUA24-5	1.073	27577	143	0.7	-1364	-6.98278	12.23	1.0	0.06062	2.49	0.6786	2.2	0.08285	1.2	-0.11	514	107	513	11	522	17	100	98	513	11
56-JUA24-3	-0.15	23800	114	1.7	-1212	-3.70898	11.99	0.9	0.05882	2.24	0.6790	2.0	0.08451	1.0	0.04	425	101	523	10	522	16	123	100	523	10
67-JUA24-4	0.022	54838	242	0.9	-2958	-3.31112	10.59	1.0	0.06071	2.26	0.7842	1.9	0.09484	1.1	-0.13	550	102	584	12	586	17	106	100	584	12
65-JUA24-4	0.355	28677	124	1.9	-1496	-3.8607	10.40	1.3	0.06062	3.13	0.8041	2.8	0.09738	1.3	-0.09	503	149	599	15	592	24	119	101	599	15
129-JUA24	0.19	79728	339	1.2	-13113	-4.74416	10.25	1.3	0.06207	2.41	0.8305	1.9	0.09780	1.4	0.03	659	105	601	16	612	18	91	98	601	16
95-JUA24-6	0.065	40091	171	1.5	-1790	-3.62362	10.27	0.8	0.05952	1.52	0.8140	1.3	0.09820	0.8	-0.03	560	71	604	9	601	12	108	100	604	9
199-JUA24	0.285	33651	146	1.6	-2197	-4.06873	10.28	0.9	0.05901	2.18	0.7963	1.8	0.09828	0.9	-0.08	479	101	604	11	592	17	126	102	604	11
183-JUA24	-3.24	6414	29	1.4	-222.2	-4.06398	10.65	2.3	0.06405	5.36	0.8536	5.2	0.09870	2.2	0.10	525	246	605	26	604	50	115	100	605	26
57-JUA24-3	0.227	44533	181	1.3	-2346	-2.73695	10.08	0.9	0.06151	1.69	0.8418	1.4	0.09984	0.9	0.08	579	75	613	10	616	13	106	99	613	10
213-JUA24	0.095	118116	537	0.7	-6532	-4.50217	10.12	1.1	0.06019	1.41	0.8367	1.4	0.10028	1.1	0.33	589	66	616	13	617	13	104	100	616	13
99-JUA24-6	-0.07	39976	168	1.3	-1940	-2.59981	10.08	0.9	0.06105	2.15	0.8323	1.7	0.10045	0.9	-0.09	570	91	617	11	613	16	108	101	617	11
86-JUA24-5	1.277	8383	33	3.1	-428.8	-6.2268	10.11	1.8	0.06492	5.30	0.8949	4.8	0.10159	1.8	0.01	588	194	623	21	629	44	106	99	623	21
~~175-JUA24~~	~~0.331~~	~~539688~~	~~2337~~	~~0.5~~	~~-11904~~	~~-12.8068~~	~~9.76~~	~~1.0~~	~~0.08612~~	~~1.32~~	~~1.2325~~	~~1.3~~	~~0.10337~~	~~1.1~~	~~0.37~~	~~1323~~	~~51~~	~~634~~	~~13~~	~~813~~	~~15~~	~~48~~	~~78~~	~~634~~	~~13~~
94-JUA24-6	-0.49	20581	79	1.3	-907	-3.00571	9.79	1.1	0.06034	2.21	0.8583	2.0	0.10324	1.0	0.04	513	100	635	13	622	18	124	102	635	13
212-JUA24	0.529	32794	136	0.9	-1915	-4.34336	9.61	1.0	0.06200	1.91	0.9016	1.8	0.10592	0.9	0.24	578	88	648	12	647	18	112	100	648	12
22-JUA24-1	-0.05	186319	736	0.3	-8282	-4.19234	9.28	1.5	0.06146	2.51	0.9117	1.6	0.10819	1.6	-0.06	594	108	662	21	656	15	111	101	662	21
135-JUA24	0.78	58103	230	0.7	-2769	-5.73605	9.11	1.0	0.06380	2.15	0.9637	1.7	0.11110	1.1	-0.16	676	92	679	14	684	17	100	99	679	14
~~78-JUA24-5~~	~~6.831~~	~~9622~~	~~32~~	~~2.4~~	~~-465.8~~	~~-6.30319~~	~~8.30~~	~~2.2~~	~~0.14190~~	~~5.01~~	~~2.4023~~	~~5.0~~	~~0.12425~~	~~2.0~~	~~0.24~~	~~2005~~	~~204~~	~~754~~	~~28~~	~~1185~~	~~76~~	~~38~~	~~64~~	~~754~~	~~28~~
136-JUA24	0.411	11045	35	1.2	-566	-3.43593	7.84	1.2	0.06674	2.93	1.1947	3.0	0.12895	1.3	0.15	745	136	781	18	785	35	105	100	781	18
~~69-JUA24-4~~	~~0.434~~	~~467479~~	~~1397~~	~~0.3~~	~~-14718~~	~~-10.1617~~	~~7.46~~	~~0.9~~	~~0.08517~~	~~1.26~~	~~1.5800~~	~~1.0~~	~~0.13498~~	~~0.8~~	~~-0.01~~	~~1300~~	~~50~~	~~816~~	~~13~~	~~961~~	~~12~~	~~63~~	~~85~~	~~816~~	~~13~~
35-JUA24-2	0.038	46066	142	0.8	-1918	-5.58705	7.37	1.8	0.06936	3.57	1.2978	2.9	0.13754	1.8	-0.12	794	158	830	29	836	33	104	99	830	29
~~51-JUA24-3~~	~~27.46~~	~~1347~~	~~4~~	~~7.6~~	~~-56.37~~	~~-17.3581~~	~~8.08~~	~~6.9~~	~~0.87376~~	~~6.58~~	~~16.1804~~	~~4.9~~	~~0.13966~~	~~6.4~~	~~0.32~~	~~4327~~	~~211~~	~~834~~	~~101~~	~~2830~~	~~108~~	~~19~~	~~29~~	~~834~~	~~101~~
164-JUA24	1.66	6802	20	0.9	-362.4	-3.93441	7.06	2.1	0.07543	4.76	1.4855	4.5	0.14686	2.1	0.15	881	195	881	34	894	55	100	99	881	34
128-JUA24	0.439	74415	204	0.3	-19984	-3.54706	6.57	0.8	0.07121	1.37	1.5129	1.1	0.15416	0.8	0.00	919	59	923	14	931	14	100	99	923	14
93-JUA24-6	0.267	75676	195	0.3	-3405	-2.97187	6.45	0.8	0.07276	1.63	1.5674	1.5	0.15646	0.8	0.08	964	66	937	15	953	18	97	98	937	15
184-JUA24	-2.06	8043	22	1.9	-276.4	-4.06365	6.56	1.9	0.07254	3.30	1.5537	3.1	0.15727	1.5	0.05	835	143	943	25	932	40	113	101	943	25
185-JUA24	-1.12	32569	93	1.2	-1187	-2.87686	6.36	1.4	0.07511	2.76	1.6415	2.5	0.15938	1.4	0.07	999	114	953	24	978	31	95	97	953	24
140-JUA24	-0.16	58303	164	0.8	-2662	-10.9601	6.23	2.2	0.07547	3.44	1.7072	3.2	0.16439	2.4	0.15	1026	137	979	43	1005	42	95	97	979	43
170-JUA24	-0.24	65551	170	0.9	-3112	-3.7538	6.12	0.8	0.07173	1.46	1.6314	1.3	0.16546	0.8	0.15	940	59	986	14	980	16	105	101	986	14
195-JUA24	0.308	86465	234	1.0	-4320	-3.33295	6.07	1.0	0.07255	1.68	1.6565	1.3	0.16651	0.9	-0.06	965	69	992	17	992	16	103	100	992	17
71-JUA24-4	-0.22	84316	202	0.4	-4634	-3.71971	5.92	0.8	0.07301	1.24	1.7228	1.1	0.17069	0.8	0.16	980	52	1015	15	1012	14	104	100	1015	15
204-JUA24	0.061	44175	119	0.6	-3458	-4.11671	5.90	1.4	0.07172	2.62	1.6732	2.3	0.17103	1.4	0.17	910	109	1017	27	996	30	112	102	1017	27
169-JUA24	0.086	100214	249	0.5	-4772	-3.3604	5.89	0.7	0.07464	1.25	1.7547	1.1	0.17093	0.7	0.10	1033	53	1017	12	1024	15	98	99	1017	12
209-JUA24	0.419	53159	135	0.8	-3482	-2.72014	5.90	0.9	0.07380	1.44	1.7491	1.2	0.17164	0.8	-0.04	998	60	1020	16	1021	15	102	100	1020	16
177-JUA24	0.359	69979	187	1.4	-2600	-6.12595	5.77	1.2	0.07568	2.04	1.8329	1.9	0.17554	1.2	0.12	1048	81	1042	22	1051	24	99	99	1042	22
126-JUA24	1.349	31760	79	1.1	-2E+05	-6.68226	5.77	1.3	0.07054	2.22	1.7366	1.9	0.17605	1.4	0.11	891	94	1044	26	1017	25	117	103	1044	26
25-JUA24-1	0.114	39496	93	0.2	-1607	-4.48515	5.71	1.0	0.07483	2.06	1.8208	1.8	0.17660	1.0	-0.09	1025	80	1047	20	1044	23	102	100	1047	20
55-JUA24-3	0.03	85575	199	0.9	-4253	-3.6523	5.70	1.0	0.07729	1.69	1.8692	1.4	0.17692	1.0	0.07	1088	67	1049	19	1066	18	96	98	1049	19
189-JUA24	-0.04	72333	178	1.2	-2737	-7.39025	5.72	0.9	0.07496	1.41	1.8278	1.3	0.17723	0.9	0.00	1022	56	1051	17	1052	16	103	100	1051	17
17-JUA24-1	0.538	65229	156	1.1	-3066	-5.98555	5.71	1.8	0.07614	2.52	1.8816	2.0	0.17835	1.7	-0.07	1064	108	1057	33	1069	26	99	99	1057	33
81-JUA24-5	0.551	37559	92	0.6	-2018	-5.61111	5.79	2.8	0.08100	3.80	1.9378	2.8	0.18047	2.6	0.08	1082	157	1066	51	1081	39	99	99	1066	51

168-JUA24	-0.44	40915	98	0.8	-2080	-3.82366	5.50	1.3	0.08005	2.25	2.0171	2.1	0.18393	1.3	0.17	1151	92	1087	27	1114	30	94	98	1087	27
207-JUA24	0.454	60526	141	0.6	-4235	-2.99849	5.45	0.9	0.07712	1.40	1.9654	1.2	0.18597	0.9	0.14	1086	56	1098	18	1097	17	101	100	1098	18
153-JUA24	0.035	70654	173	0.8	-3121	-4.55237	5.46	2.2	0.08120	3.63	2.0503	2.5	0.18668	2.1	-0.08	1161	131	1101	44	1124	35	95	98	1101	44
101-JUA24	0.041	337053	784	0.4	-16272	-3.92694	5.40	1.2	0.07994	1.52	2.0648	1.2	0.18669	1.2	0.17	1179	64	1102	25	1135	17	94	97	1102	25
205-JUA24	0.826	35332	75	0.7	-2530	-4.77385	5.21	1.4	0.08353	2.72	2.2465	2.2	0.19442	1.4	-0.02	1226	108	1144	30	1188	32	93	96	1144	30
24-JUA24-1	0.046	44237	91	0.7	-1900	-2.99315	5.17	0.9	0.07765	1.58	2.1062	1.4	0.19549	0.9	0.09	1079	66	1152	19	1142	19	107	101	1152	19
30-JUA24-1	0.306	31051	66	1.3	-1383	-3.07352	5.16	1.3	0.08225	2.36	2.1887	2.0	0.19688	1.3	0.18	1174	89	1156	29	1165	28	99	99	1156	29
49-JUA24-3	0.356	56507	113	0.7	-2585	-4.13204	5.10	0.9	0.07862	1.60	2.1540	1.4	0.19827	0.9	0.03	1127	66	1165	20	1161	19	103	100	1165	20
151-JUA24	-0.07	52075	111	0.6	-2193	-4.29387	5.00	0.7	0.07940	1.41	2.2253	1.2	0.20193	0.8	0.06	1143	54	1185	17	1183	16	104	100	1185	17
14-JUA24-7	1.184	33571	67	1.0	-1783	-3.97123	4.97	1.1	0.08060	1.79	2.2462	1.6	0.20357	1.1	0.15	1159	74	1193	24	1192	23	103	100	1193	24
182-JUA24	-0.06	90314	194	0.5	-3080	-4.95178	4.94	0.8	0.08023	1.30	2.2593	1.0	0.20426	0.7	-0.04	1164	52	1197	16	1196	15	103	100	1197	16
77-JUA24-5	-0.16	56886	118	1.0	-3306	-3.05922	4.94	1.3	0.08233	2.10	2.2835	1.8	0.20373	1.2	0.21	1218	80	1200	29	1202	25	98	100	1200	29
66-JUA24-4	0.025	34863	65	0.9	-1858	-3.61464	4.92	1.4	0.07933	2.14	2.2590	1.8	0.20547	1.3	0.14	1124	85	1203	28	1192	25	107	101	1203	28
123-JUA24	0.614	75449	158	0.7	329180	4.200682	4.90	0.7	0.07840	1.38	2.2377	1.0	0.20562	0.8	-0.06	1116	54	1204	17	1189	14	108	101	1204	17
73-JUA24-5	-0.07	63079	130	1.3	-3461	-2.63563	4.91	1.1	0.08020	1.62	2.2785	1.3	0.20589	1.1	0.01	1166	66	1205	25	1204	19	103	100	1205	25
108-JUA24	0.473	15626	31	0.8	-851.9	-3.13519	4.90	1.2	0.08129	2.18	2.3229	2.0	0.20808	1.1	0.09	1151	88	1216	24	1205	29	106	101	1216	24
41-JUA24-2	0.347	39832	78	0.5	-1660	-3.67495	4.93	1.3	0.08175	1.67	2.3223	1.4	0.20821	1.2	0.23	1188	70	1217	27	1215	21	102	100	1217	27
114-JUA24	0.006	21010	43	0.5	-1652	-2.94311	4.88	1.3	0.08213	2.64	2.3216	2.3	0.20766	1.4	0.01	1152	109	1219	29	1203	33	106	101	1219	29
8-JUA24-2.	0.025	239725	483	0.5	-15843	-3.68599	4.81	1.0	0.08001	1.65	2.3146	1.3	0.20864	1.2	0.03	1165	65	1220	26	1216	19	105	100	1220	26
161-JUA24	0.578	61714	135	0.7	-3162	-5.38904	4.82	1.5	0.08479	2.33	2.4563	1.9	0.20875	1.6	0.00	1276	94	1220	35	1257	28	96	97	1220	35
15-JUA24-8	0.032	133857	269	0.7	-7528	-3.57567	4.81	1.4	0.08118	2.33	2.3308	1.7	0.21074	1.4	-0.13	1175	95	1231	31	1221	25	105	101	1231	31
13-JUA24-6	0.099	26348	51	0.8	-1545	-3.13057	4.82	1.3	0.08347	2.25	2.4311	2.2	0.21165	1.3	0.22	1200	94	1235	29	1236	32	103	100	1235	29
37-JUA24-2	0.14	48859	98	0.9	-2008	-4.26078	4.72	1.3	0.08036	2.13	2.3992	1.7	0.21408	1.3	-0.16	1177	87	1249	29	1236	23	106	101	1249	29
106-JUA24	0.695	52287	100	0.9	-2540	-4.54439	4.62	1.2	0.08115	1.92	2.4300	1.5	0.22003	1.2	0.09	1173	77	1280	28	1248	22	109	103	1280	28
121-JUA24	0.833	93183	181	0.8	-44772	-4.85638	4.40	1.1	0.08617	1.98	2.7370	1.8	0.22825	1.1	0.06	1322	78	1324	27	1333	26	100	99	1324	27
31-JUA24-2	0.018	91779	158	0.7	-3967	-4.38361	4.34	0.9	0.08612	1.55	2.7443	1.2	0.23306	0.9	-0.03	1300	61	1349	22	1338	17	104	101	1349	22
149-JUA24	0.064	242877	426	1.2	-9202	-3.16389	4.22	0.8	0.10221	0.90	3.3871	0.9	0.23905	0.8	0.42	1647	33	1380	20	1497	14	84	92	1380	20

53-JUA24-3	0.137	45134	69	1.7	-2215	-3.00997	3.77	0.9	0.09523	1.60	3.4962	1.3	0.26698	0.9	0.01	1480	59	1523	25	1517	20	103	100	1480	59
148-JUA24	0.274	253995	418	0.1	-8949	-5.82153	3.77	1.1	0.09415	1.55	3.4946	1.2	0.26791	1.1	0.27	1488	60	1533	30	1525	19	103	101	1488	60
133-JUA24	0.11	90063	141	0.8	-6191	-2.58651	3.72	0.8	0.09435	1.28	3.5147	1.0	0.27020	0.7	0.37	1488	48	1543	20	1524	16	104	101	1488	48
23-JUA24-1	-0.06	226290	348	0.6	-9805	-3.95726	3.71	1.0	0.09472	1.57	3.5155	1.0	0.27166	1.0	-0.17	1490	58	1548	27	1530	16	104	101	1490	58
167-JUA24	0.362	30513	49	1.9	-1554	-3.56389	3.80	1.1	0.09718	1.95	3.5587	1.6	0.26701	1.1	0.15	1500	74	1522	31	1526	26	102	100	1500	74
9-JUA24-3.	0.141	282885	425	0.8	-17603	-3.60861	3.73	0.7	0.09444	0.99	3.5208	0.8	0.26956	0.8	0.09	1500	38	1537	21	1530	12	102	100	1500	38
27-JUA24-1	0.349	119683	174	1.2	-5075	-4.02682	3.60	1.3	0.09962	1.81	3.8697	1.6	0.28328	1.2	0.19	1582	71	1605	35	1598	25	101	100	1582	71
109-JUA24	0.098	60846	83	1.6	-3403	-4.36098	3.57	1.2	0.10001	2.10	3.9344	1.9	0.28225	1.1	0.11	1588	80	1601	32	1613	31	101	99	1588	80
122-JUA24	0.55	122299	164	1.3	-2E+05	-4.73064	3.32	0.8	0.10224	1.43	4.2864	1.1	0.30243	0.8	-0.03	1647	53	1703	23	1688	19	103	101	1647	53
192-JUA24	-0.05	89818	133	1.2	-3613	-3.70576	3.38	0.8	0.10347	1.47	4.2483	1.3	0.29757	0.8	0.06	1653	56	1677	24	1678	20	101	100	1653	56
203-JUA24	0.353	171078	270	1.4	-12198	-7.20679	3.55	0.8	0.10307	1.51	3.9983	1.3	0.28308	0.9	-0.01	1658	56	1606	24	1630	20	97	99	1658	56
45-JUA24-3	-0.18	61426	87	1.2	-2586	-3.95982	3.41	1.7	0.10863	2.60	4.4428	2.0	0.30145	1.7	0.02	1705	96	1694	51	1713	34	99	99	1705	96
105-JUA24	0.277	122767	167	1.4	-5930	-4.2406	3.23	0.8	0.10878	1.37	4.6386	1.0	0.31107	0.8	-0.10	1744	50	1747	26	1753	16	100	100	1744	50
29-JUA24-1	0.403	130569	170	1.2	-5069	-5.22202	3.10	1.3	0.10737	1.79	4.9084	1.4	0.32723	1.3	-0.01	1746	73	1821	41	1796	24	104	101	1746	73
113-JUA24	0.049	19435	25	2.9	-1390	-2.61159	3.09	1.4	0.11052	2.15	4.9378	2.0	0.32852	1.4	0.24	1753	82	1832	44	1798	33	105	102	1753	82
44-JUA24-2	-0.1	39738	48	1.5	-1707	-3.2298	3.08	1.0	0.10847	1.62	4.8792	1.3	0.32590	1.0	0.02	1755	62	1816	32	1796	23	103	101	1755	62
178-JUA24	-0.15	49352	73	1.6	-1881	-3.9357	3.27	1.3	0.11000	1.82	4.6735	1.6	0.31059	1.2	0.19	1765	68	1740	38	1753	26	99	99	1765	68
97-JUA24-6	0.3	64582	77	1.5	-2893	-3.09153	2.90	0.9	0.11508	1.26	5.5424	1.0	0.34795	0.9	0.15	1854	48	1922	28	1902	18	104	101	1854	48
63-JUA24-4	-0	82321	94	1.1	-4332	-3.37327	2.95	1.1	0.11680	1.52	5.5198	1.3	0.34225	1.0	0.18	1880	56	1895	34	1897	22	101	100	1880	56
16-JUA24-9	0.386	46011	48	1.2	-2418	-3.13885	2.67	0.9	0.12158	1.44	6.3346	1.2	0.37761	0.8	0.00	1938	53	2062	29	2015	21	106	102	1938	53
181-JUA24	0.116	101784	129	1.5	-3368	-4.6611	2.85	1.2	0.12129	2.07	5.8558	1.6	0.35415	1.3	0.03	1944	73	1951	43	1955	28	100	100	1944	73
211-JUA24	0.098	160418	199	1.0	-9441	-3.55765	2.81	0.6	0.12010	0.94	5.9459	0.7	0.35641	0.6	0.07	1945	34	1968	21	1964	12	101	100	1945	34
154-JUA24	0.311	129150	161	0.7	-5105	-7.51201	2.76	1.9	0.12504	3.05	6.4265	2.3	0.36771	2.1	-0.01	1995	110	2013	72	2025	41	101	99	1995	110
91-JUA24-6	0.193	287864	376	2.4	-11686	-6.05381	2.98	1.5	0.12538	2.02	5.9270	1.5	0.33937	1.5	0.01	2013	76	1880	49	1959	26	93	96	2013	76
84-JUA24-5	0.238	137478	155	0.9	-6919	-4.5289	2.78	1.1	0.12739	1.65	6.3246	1.2	0.36262	1.1	-0.02	2039	58	1993	37	2021	20	98	99	2039	58
190-JUA24	0.084	109741	128	0.7	-4120	-4.58397	2.64	0.8	0.12985	1.02	6.8655	0.9	0.38405	0.8	0.14	2073	36	2092	28	2089	15	101	100	2073	36
80-JUA24-5	0.044	383519	335	0.6	-21665	-3.09543	2.15	0.7	0.15994	1.11	10.2709	0.8	0.46847	0.7	-0.07	2435	38	2474	28	2455	14	102	101	2435	38
98-JUA24-6	-0	249190	217	1.6	-11750	-4.29697	2.01	1.3	0.18519	1.83	12.9216	1.5	0.50347	1.3	0.13	2680	62	2625	58	2668	29	98	98	2680	62
156-JUA24	0.233	99148	73	0.8	-4653	-2.99967	1.74	0.9	0.21647	1.23	17.2600	1.0	0.57573	0.9	0.21	2926	40	2939	39	2943	19	100	100	2926	40

U-Pb data from JUA 25

University of Brasilia							Data for Tera-Wasserburg plot				Data for Wetherill plot								Dates						Best Age	2s abs
Identifier	f206c	206Pb	Uppm	Th/U	206Pb/ 204Pb	1s%	238U/ 206Pb	1s%	207Pb/2 06Pb	1s%	207Pb/ 235U	1s%	206Pb/2 38U	1s%	Rho	207Pb/2 06Pb	2s (abs)	206Pb/2 38U	2s (abs)	207Pb/2 35U	2s (abs)	Conc (%) 6/8 -7/6	Conc (%) 6/8 -7/5		
~~JUA25-71.FIN~~	~~-6.7543~~	~~1973~~	~~181~~	~~1.5~~	~~-126.3~~	~~-8.43~~	~~277.31~~	~~3.2~~	~~0.09156~~	~~15.59~~	~~0.0495~~	~~16.5~~	~~0.00453~~	~~6.3~~	~~0.76~~	~~862~~	~~317~~	~~29~~	~~4~~	~~41~~	~~11~~	~~3~~	~~71~~	~~29~~	~~4~~
JUA25-14.FIN	2.51137	4909	269	1.0	-424.3	-3.09	139.96	1.6	0.05212	4.66	0.0513	4.3	0.00742	1.6	-0.08	-6	221	48	1	51	4	-843	94	48	1
JUA25-113.FI	1.02896	50821	637	1.0	-1933	-4.79	30.67	0.9	0.06418	2.11	0.2871	1.8	0.03294	0.9	0.12	655	90	209	4	256	8	32	82	209	4
JUA25-7.FIN2	1.80506	21113	222	2.9	-1202	-3.56	26.29	1.0	0.05867	2.35	0.3137	2.1	0.03862	1.0	-0.03	450	112	244	5	276	10	54	89	244	5
JUA25-107.FI	0.82783	41991	430	1.3	-10681	-2.46	25.16	1.0	0.05332	1.78	0.2935	1.4	0.04022	1.0	-0.14	270	83	254	5	260	6	94	98	254	5
JUA25-77.FIN	1.41664	15393	153	0.7	-1043	-4.04	24.78	1.1	0.05263	2.91	0.2981	2.7	0.04109	1.1	0.19	80	151	259	6	261	12	326	99	259	6
JUA25-65.FIN	1.86297	16929	150	2.0	-1144	-7.07	22.47	1.2	0.05548	3.26	0.3431	3.2	0.04557	1.2	0.04	199	143	287	7	290	13	145	99	287	7
JUA25-146.FI	1.3661	22601	202	2.4	-994.5	-3.56	22.03	1.3	0.06305	2.34	0.4008	2.2	0.04672	1.4	0.19	587	104	294	8	338	13	50	87	294	8
JUA25-1.FIN2	0.04082	52711	453	0.8	-3181	-3.61	21.70	1.1	0.05271	1.70	0.3459	1.6	0.04709	1.1	0.24	242	79	296	6	300	8	123	99	296	6
JUA25-131.FI	0.78621	22690	210	0.5	-1288	-5.24	21.67	1.1	0.05415	2.80	0.3483	2.6	0.04727	1.2	0.32	184	143	298	7	302	13	162	99	298	7
JUA25-85.FIN	1.07446	21099	180	2.6	-1151	-4.96	21.43	1.3	0.05614	2.56	0.3632	2.2	0.04772	1.2	0.10	312	117	300	7	314	12	96	96	300	7
JUA25-37.FIN	3.54513	18007	154	1.5	-12497	-2.79	20.97	1.2	0.05694	2.86	0.3741	2.3	0.04826	1.2	0.93	272	121	304	7	319	12	112	95	304	7
JUA25-127.FI	1.77469	51970	449	1.6	-2365	-4.88	20.71	0.8	0.06554	1.72	0.4370	1.5	0.04888	0.8	0.08	711	73	308	5	366	9	43	84	308	5
JUA25-51.FIN	0.23946	22943	184	2.3	-1091	-2.92	20.90	1.1	0.05448	2.14	0.3679	2.1	0.04900	1.0	0.19	252	102	308	6	315	11	122	98	308	6
JUA25-121.FI	1.91376	15763	134	2.6	-1732	-3.89	20.74	1.1	0.05904	2.70	0.3938	2.5	0.04901	1.1	0.02	395	128	308	7	334	14	78	92	308	7
JUA25-141.FI	2.04152	13978	120	1.2	-702.5	-4.09	20.60	1.3	0.05694	2.92	0.3816	2.7	0.04935	1.3	0.06	302	144	310	8	323	15	103	96	310	8
JUA25-147.FI	0.41576	10480	91	2.4	-493.2	-3.5	20.68	1.3	0.05639	3.53	0.3818	3.8	0.04948	1.2	0.22	117	171	311	7	318	20	265	98	311	7
JUA25-2.FIN2	1.26808	37487	304	1.9	-4980	-3.65	20.37	0.9	0.05457	1.73	0.3766	1.5	0.04973	0.8	0.07	325	78	313	5	323	9	96	97	313	5
JUA25-88.FIN	2.88884	10858	94	1.5	-1078	-4.42	21.07	1.6	0.05459	4.11	0.3877	6.1	0.04997	1.7	0.02	79	167	314	10	309	20	400	102	314	10
JUA25-136.FI	-1.0388	11558	100	2.0	-672.7	-5.45	20.66	1.3	0.05430	3.44	0.3717	3.5	0.05003	1.5	0.56	123	153	314	9	312	18	255	101	314	9
~~JUA25-89.FIN~~	~~2.40037~~	~~31576~~	~~263~~	~~0.9~~	~~-2090~~	~~-63.2~~	~~20.16~~	~~1.5~~	~~0.06531~~	~~2.76~~	~~0.4667~~	~~3.1~~	~~0.05095~~	~~1.4~~	~~0.21~~	~~699~~	~~116~~	~~315~~	~~9~~	~~382~~	~~20~~	~~45~~	~~82~~	~~315~~	~~9~~
JUA25-31.FIN	0.52325	24925	207	2.7	-1643	-3.5	20.27	1.0	0.05588	2.45	0.3847	2.1	0.05011	1.0	0.02	303	104	315	6	327	12	104	96	315	6
JUA25-125.FI	0.53639	48795	418	1.6	-3475	-3.6	20.11	0.9	0.05424	1.69	0.3748	1.5	0.05018	0.9	0.04	321	79	315	5	322	8	98	98	315	5
JUA25-138.FI	0.54688	5198	44	1.5	-290.5	-3.77	20.80	1.9	0.05784	4.27	0.3820	4.0	0.05031	1.8	-0.02	257	204	316	11	319	22	123	99	316	11
JUA25-47.FIN	-0.7515	14180	113	1.5	-1006	-4.84	20.33	1.6	0.05367	3.13	0.3704	2.8	0.05027	1.3	0.34	127	139	316	8	314	15	248	101	316	8
JUA25-4.FIN2	0.71782	53765	449	2.1	-3337	-5.2	20.14	0.8	0.05484	1.76	0.3806	1.6	0.05032	0.9	0.06	342	82	316	5	327	9	92	97	316	5
JUA25-110.FI	0.46809	32786	266	0.9	-1986	-3.64	20.27	1.0	0.05651	2.23	0.3947	2.0	0.05040	1.0	0.10	361	101	317	6	335	11	88	95	317	6
JUA25-90.FIN	1.12923	45575	404	1.0	-4363	-8.51	20.25	1.1	0.05441	2.71	0.3689	2.2	0.05045	1.2	-0.06	241	109	317	7	315	12	132	101	317	7
JUA25-35.FIN	-0.59	3934	32	1.5	-229.9	-3.11	20.91	1.9	0.05072	5.18	0.3399	5.2	0.05051	1.9	0.07	41	251	317	12	280	26	769	113	317	12
JUA25-52.FIN	-1.455	34723	257	1.2	-2543	-37.8	20.63	1.0	0.05864	3.34	0.4070	3.4	0.05050	1.7	0.01	329	128	317	10	338	18	96	94	317	10
JUA25-122.FI	2.07148	11971	98	1.8	-1028	-3.58	20.08	1.1	0.05504	3.01	0.3867	2.9	0.05050	1.1	0.02	166	145	317	7	325	16	191	98	317	7
JUA25-130.FI	0.67473	26184	221	1.5	-1322	-3.26	20.10	1.1	0.05631	2.34	0.3830	2.0	0.05070	1.1	0.00	308	110	319	7	329	11	103	97	319	7
JUA25-109.FI	0.80885	24085	206	2.0	-1916	-5.05	20.11	1.3	0.05437	3.52	0.3783	3.0	0.05071	1.5	-0.25	242	148	319	9	326	18	132	98	319	9
JUA25-104.FI	2.68578	11867	100	2.0	-904.1	-3.24	20.36	1.4	0.05984	3.04	0.4090	2.9	0.05074	1.3	0.06	305	158	319	8	342	17	104	93	319	8
JUA25-112.FI	0.23998	18515	148	1.8	-793.8	-2.8	20.11	1.1	0.05335	2.59	0.3675	2.2	0.05074	1.1	-0.07	150	122	319	7	314	12	213	101	319	7
JUA25-119.FI	1.43281	15016	120	2.5	-1070	-3.67	19.94	1.1	0.05347	2.45	0.3768	2.3	0.05095	1.1	0.06	226	116	320	7	321	13	141	100	320	7
JUA25-27.FIN	0.22602	44706	367	1.7	-2530	-2.97	19.74	0.9	0.05212	1.84	0.3662	1.6	0.05108	0.9	0.05	180	88	321	6	315	9	179	102	321	6
JUA25-116.FI	0.61885	43574	355	1.0	-2662	-4.28	19.70	1.0	0.05137	2.07	0.3610	1.7	0.05111	1.0	0.00	148	97	321	6	311	9	217	103	321	6
JUA25-149.FI	2.24079	9635	79	1.4	-598.4	-2.75	19.96	1.3	0.05512	3.19	0.3814	2.8	0.05115	1.3	0.03	101	161	321	8	322	16	319	100	321	8
JUA25-118.FI	0.2701	14734	117	1.7	-894	-2.38	19.94	1.0	0.05405	2.64	0.3754	2.4	0.05118	1.1	0.03	147	135	322	7	320	14	219	100	322	7
JUA25-145.FI	2.22942	8907	73	1.3	-505.7	-4.11	20.00	1.5	0.05873	4.48	0.4040	4.3	0.05121	1.4	0.06	272	173	322	9	327	20	118	98	322	9
JUA25-74.FIN	5.22025	8477	70	1.4	-635.5	-3.09	20.20	1.5	0.05810	3.79	0.4013	3.7	0.05129	1.4	-0.11	204	181	322	9	332	20	158	97	322	9
JUA25-30.FIN	3.57026	13291	108	1.1	-1140	-6.27	19.98	1.3	0.05345	3.38	0.3744	3.2	0.05129	1.4	0.17	96	170	322	9	317	18	336	102	322	9
JUA25-101.FI	5.76754	10843	91	1.2	-1229	-4.5	20.18	1.8	0.05715	3.24	0.4051	3.3	0.05142	1.5	0.09	294	151	323	9	336	19	110	96	323	9
JUA25-80.FIN	0.43598	29149	231	2.0	-1550	-2.97	19.85	1.0	0.05386	2.05	0.3813	1.8	0.05144	1.0	0.11	263	95	323	6	325	10	123	99	323	6
JUA25-16.FIN	1.56175	13255	108	2.6	-1135	-4.7	19.98	1.4	0.05737	3.31	0.3982	3.1	0.05149	1.2	0.34	355	171	323	8	332	18	91	97	323	8
JUA25-105.FI	1.45612	18872	151	2.2	-1579	-2.86	19.80	1.1	0.05488	3.17	0.3863	3.1	0.05153	1.0	-0.08	155	132	324	7	325	16	208	100	324	7
JUA25-10.FIN	-0.3637	22936	183	1.8	-1247	-2.93	19.67	0.9	0.05122	2.02	0.3666	1.8	0.05153	0.9	-0.04	158	101	324	6	316	10	205	103	324	6
JUA25-70.FIN	1.36929	15403	127	1.6	-993.9	-5.95	19.66	1.3	0.05142	2.56	0.3626	2.3	0.05158	1.2	0.15	73	131	324	8	310	12	446	104	324	8
JUA25-95.FIN	0.47197	32628	263	2.3	-5233	-2.55	19.68	1.0	0.05243	2.11	0.3727	1.8	0.05169	0.9	-0.06	212	102	325	6	320	10	153	101	325	6
JUA25-86.FIN	0.67984	14870	119	0.9	-1010	-5.15	19.63	1.3	0.05430	2.65	0.3877	2.4	0.05174	1.2	0.06	259	130	325	8	328	14	126	99	325	8
JUA25-63.FIN	0.90157	50217	392	1.0	-3121	-5.36	19.49	0.8	0.05444	1.71	0.3893	1.5	0.05186	0.8	0.04	314	80	326	5	333	9	104	98	326	5
JUA25-106.FI	1.24889	24790	203	1.6	-4863	-2.7	19.56	0.9	0.05424	2.09	0.3906	2.3	0.05192	1.0	0.70	258	94	326	6	328	10	126	99	326	6
JUA25-43.FIN	0.38301	19158	146	1.8	-1115	-2.47	19.55	1.0	0.05439	2.18	0.3903	2.0	0.05198	0.9	-0.07	307	103	327	6	331	11	106	99	327	6
JUA25-143.FI	0.45228	72058	593	1.5	-4849	-2.75	19.36	0.8	0.05415	1.52	0.3854	1.2	0.05198	0.8	-0.07	312	74	327	5	330	7	105	99	327	5
JUA25-42.FIN	0.53741	34916	270	2.1	-1843	-3.45	19.51	0.9	0.05379	1.76	0.3867	1.5	0.05206	0.9	0.02	282	82	327	5	330	8	116	99	327	5
JUA25-111.FI	1.66031	10711	83	0.8	-2734	-82.5	20.36	2.1	0.06286	4.05	0.5549	8.1	0.05237	2.1	0.93	524	183	328	13	363	28	63	90	328	13
JUA25-142.FI	0.43632	70760	583	0.9	-4177	-3.24	19.31	0.8	0.05269	1.69	0.3749	1.3	0.05233	0.8	-0.14	238	76	329	5	322	7	138	102	329	5
JUA25-68.FIN	0.57053	27739	217	2.4	-1482	-4.66	19.50	1.1	0.05481	2.18	0.3915	1.9	0.05242	1.1	0.53	272	107	329	7	332	11	121	99	329	7
JUA25-133.FI	3.02161	5990	49	1.5	-335.7	-3.56	19.73	1.5	0.05091	4.17	0.3598	4.0	0.05245	1.4	0.03	-44	208	329	9	307	22	-743	107	329	9
~~JUA25-83.FIN~~	~~2.44756~~	~~10839~~	~~84~~	~~2.3~~	~~-541.7~~	~~-4.4~~	~~19.51~~	~~1.2~~	~~0.07485~~	~~3.51~~	~~0.5448~~	~~3.5~~	~~0.05252~~	~~1.2~~	~~0.12~~	~~799~~	~~145~~	~~330~~	~~8~~	~~429~~	~~24~~	~~41~~	~~77~~	~~330~~	~~8~~

JUA25-44.FIN	0.46879	28393	218	1.3	-1960	-2.65	19.30	0.9	0.05211	1.97	0.3775	1.7	0.05260	0.9	0.15	193	94	330	5	324	10	171	102	330	5
JUA25-40.FIN	1.25629	16003	124	2.0	-1831	-3.01	19.41	1.1	0.05479	2.80	0.3929	2.6	0.05268	1.1	0.00	201	131	331	7	331	15	165	100	331	7
JUA25-55.FIN	0.5103	49963	379	1.7	-2552	-3.48	19.19	0.8	0.05620	1.74	0.4109	1.6	0.05270	0.8	0.14	396	78	331	5	347	9	84	95	331	5
JUA25-32.FIN	0.47742	15320	124	1.7	-901	-5	19.32	1.1	0.05453	3.01	0.3888	2.8	0.05267	1.0	0.42	244	128	332	7	327	16	136	101	332	7
JUA25-78.FIN	-1.1468	11886	91	1.9	-683.9	-2.7	19.16	1.1	0.05611	3.23	0.4000	2.7	0.05284	1.1	0.06	184	142	332	7	335	15	180	99	332	7
JUA25-3.FIN2	0.37528	42398	325	2.4	-3854	-6.22	19.09	0.9	0.05235	1.72	0.3847	1.5	0.05286	0.9	0.06	227	79	332	6	329	9	146	101	332	6
JUA25-9.FIN2	1.75428	10126	77	2.7	-637.1	-23.2	19.39	1.2	0.05327	3.16	0.3923	3.0	0.05295	1.3	0.84	152	162	332	8	328	17	218	101	332	8
JUA25-59.FIN	3.50681	18676	141	1.9	-1159	-4.19	19.25	1.0	0.06255	3.68	0.4490	3.5	0.05300	1.0	0.00	457	156	333	6	366	19	73	91	333	6
JUA25-84.FIN	1.86675	20300	156	0.2	-1076	-2.76	19.11	0.9	0.05166	2.31	0.3800	2.2	0.05299	0.9	0.05	123	107	333	6	322	12	270	103	333	6
JUA25-73.FIN	0.54129	20715	163	1.3	-1538	-2.72	18.99	0.9	0.05462	2.21	0.3974	2.0	0.05317	0.9	0.02	281	110	334	6	336	11	119	99	334	6
~~JUA25-34.FIN~~	~~3.72342~~	~~24401~~	~~189~~	~~1.9~~	~~-1088~~	~~-4.61~~	~~19.08~~	~~1.0~~	~~0.07137~~	~~3.23~~	~~0.5315~~	~~3.5~~	~~0.05321~~	~~1.0~~	~~0.32~~	~~728~~	~~130~~	~~334~~	~~7~~	~~421~~	~~23~~	~~46~~	~~79~~	~~334~~	~~7~~
JUA25-97.FIN	1.51377	21570	172	1.1	-1898	-3.94	18.94	1.0	0.05507	2.44	0.4002	2.1	0.05331	1.0	-0.10	284	110	335	7	338	12	118	99	335	7
JUA25-46.FIN	2.38406	11316	89	1.7	-749.1	-4.58	19.22	1.2	0.06033	3.09	0.4370	3.0	0.05336	1.2	0.11	440	138	335	8	362	18	76	93	335	8
~~JUA25-13.FIN~~	~~6.8896~~	~~16140~~	~~137~~	~~0.7~~	~~-967.7~~	~~-5.53~~	~~19.68~~	~~1.7~~	~~0.12729~~	~~7.16~~	~~1.1443~~	~~8.7~~	~~0.05353~~	~~1.9~~	~~0.79~~	~~1123~~	~~243~~	~~336~~	~~13~~	~~620~~	~~77~~	~~30~~	~~54~~	~~336~~	~~13~~
JUA25-75.FIN	1.4295	27400	217	2.0	-2059	-5.21	19.10	1.1	0.05631	2.06	0.4116	1.9	0.05350	1.1	0.01	381	92	336	7	348	11	88	96	336	7
JUA25-117.FI	1.65148	36194	283	2.2	-2042	-3.83	18.90	0.8	0.05814	2.06	0.4257	2.0	0.05362	0.9	0.28	416	93	337	6	356	12	81	94	337	6
JUA25-25.FIN	-2.8276	6285	48	2.9	-439.8	-7.99	20.03	1.8	0.05368	4.47	0.3731	4.0	0.05385	2.8	0.04	142	216	337	18	310	22	237	109	337	18
JUA25-129.FI	1.70169	18936	154	0.4	-973.8	-3.51	19.17	1.4	0.05779	3.39	0.4211	3.2	0.05370	1.3	0.03	248	132	337	8	346	16	136	97	337	8
JUA25-41.FIN	5.73751	5037	38	0.9	-299.9	-6.16	19.42	2.1	0.06311	5.47	0.4513	5.3	0.05394	2.1	0.18	578	209	338	13	351	32	58	96	338	13
JUA25-53.FIN	0.72711	25180	188	1.7	-1147	-3.27	18.81	1.1	0.05446	2.41	0.4051	2.4	0.05389	1.1	-0.02	211	121	338	7	341	14	160	99	338	7
JUA25-94.FIN	1.69207	19489	152	1.3	-2114	-3.04	18.78	1.1	0.05348	2.44	0.3970	2.2	0.05392	1.1	0.18	222	120	338	7	337	13	153	101	338	7
JUA25-58.FIN	1.50739	17130	126	1.9	-1230	-4.56	19.22	1.4	0.06155	3.99	0.4205	3.4	0.05399	1.5	0.06	422	157	339	10	347	19	80	98	339	10
JUA25-139.FI	2.76873	7676	62	1.5	-368.4	-3.5	19.22	1.6	0.06023	4.19	0.4459	4.6	0.05405	1.5	0.26	312	171	339	10	349	22	108	97	339	10
JUA25-11.FIN	1.92959	13649	105	1.1	-732.3	-3.5	18.85	1.2	0.05649	2.85	0.4179	2.7	0.05416	1.1	0.01	244	146	340	8	348	16	139	98	340	8
JUA25-135.FI	-0.4555	38065	305	0.9	-2123	-4.14	18.74	1.1	0.05343	1.86	0.3974	1.6	0.05433	1.0	0.04	265	88	341	7	338	9	128	101	341	7
JUA25-123.FI	2.62763	33040	252	1.4	-2267	-3.49	18.95	0.9	0.06586	3.05	0.5867	13.2	0.05444	1.8	0.99	600	101	341	11	401	24	57	85	341	11
JUA25-76.FIN	0.45472	46714	351	0.8	-3748	-2.8	18.48	0.8	0.05498	1.63	0.4132	1.5	0.05468	0.8	0.03	336	76	343	5	350	9	102	98	343	5
JUA25-28.FIN	0.25606	28227	222	2.4	-1689	-3.4	18.50	0.9	0.05461	1.99	0.4145	1.9	0.05482	0.9	0.05	308	97	344	6	349	11	112	99	344	6
JUA25-137.FI	0.05083	66974	530	1.3	-3414	-5.53	18.44	0.8	0.05264	1.48	0.3962	1.3	0.05492	0.8	0.18	267	69	345	5	337	8	129	102	345	5
JUA25-26.FIN	1.15196	17383	138	1.6	-939.1	-4.37	18.58	1.3	0.06659	3.44	0.5013	3.4	0.05501	1.3	0.03	585	161	345	9	408	24	59	85	345	9
JUA25-8.FIN2	-0.5522	10569	80	2.0	-578.7	-4.33	18.78	1.4	0.05724	3.45	0.4230	3.2	0.05502	1.4	0.04	260	161	346	9	351	19	133	99	346	9
JUA25-19.FIN	0.4315	32289	245	1.1	-1553	-3.89	18.21	0.9	0.05246	1.85	0.4022	1.8	0.05542	0.9	0.20	225	92	348	6	341	10	154	102	348	6
JUA25-17.FIN	-0.0588	101128	771	0.4	-6305	-4.19	18.16	0.8	0.05367	1.40	0.4141	1.2	0.05547	0.8	0.01	309	67	348	5	351	7	113	99	348	5
~~JUA25-144.FI~~	~~3.22757~~	~~13424~~	~~108~~	~~2.2~~	~~-905.4~~	~~-4.68~~	~~18.57~~	~~1.3~~	~~0.08320~~	~~4.59~~	~~0.6336~~	~~4.8~~	~~0.05569~~	~~1.3~~	~~0.15~~	~~774~~	~~197~~	~~349~~	~~9~~	~~479~~	~~36~~	~~45~~	~~73~~	~~349~~	~~9~~
~~JUA25-72.FIN~~	~~3.95458~~	~~20279~~	~~151~~	~~2.4~~	~~-1227~~	~~-3.93~~	~~18.28~~	~~1.2~~	~~0.09987~~	~~4.80~~	~~0.8033~~	~~5.6~~	~~0.05590~~	~~1.2~~	~~0.63~~	~~1136~~	~~187~~	~~350~~	~~8~~	~~551~~	~~44~~	~~31~~	~~64~~	~~350~~	~~8~~
JUA25-114.FI	0.51258	27703	169	1.4	-15149	-91.1	18.72	1.5	0.05423	2.34	0.4064	2.1	0.06470	13.4	-0.03	274	103	351	25	342	12	128	102	351	25
JUA25-33.FIN	1.07203	24601	186	1.7	-1119	-7.02	18.20	1.1	0.05519	2.31	0.4295	2.0	0.05614	1.1	0.08	338	102	352	8	359	12	104	98	352	8
JUA25-96.FIN	4.27591	29445	229	1.4	-3459	-6.44	17.97	1.3	0.06795	4.71	0.5244	5.0	0.05764	1.7	0.16	552	172	361	11	405	28	65	89	361	11
JUA25-45.FIN	3.60656	15827	109	1.9	-1630	-26.9	19.10	1.7	0.05556	2.90	0.4072	2.4	0.05856	4.8	0.03	323	130	363	30	342	14	112	106	363	30
~~JUA25-124.FI~~	~~6.11818~~	~~10777~~	~~87~~	~~2.0~~	~~-14118~~	~~-94.5~~	~~19.19~~	~~3.3~~	~~0.12212~~	~~8.31~~	~~1.2027~~	~~11.6~~	~~0.06118~~	~~4.7~~	~~0.00~~	~~1053~~	~~242~~	~~379~~	~~31~~	~~580~~	~~75~~	~~36~~	~~65~~	~~379~~	~~31~~
~~JUA25-93.FIN~~	~~9.50029~~	~~42803~~	~~280~~	~~3.9~~	~~-1785~~	~~-6.89~~	~~17.01~~	~~1.9~~	~~0.14042~~	~~6.75~~	~~1.7814~~	~~10.2~~	~~0.06305~~	~~2.6~~	~~0.90~~	~~1508~~	~~225~~	~~393~~	~~20~~	~~786~~	~~95~~	~~26~~	~~50~~	~~393~~	~~20~~
~~JUA25-108.FI~~	~~17.2232~~	~~17557~~	~~107~~	~~2.2~~	~~-969.3~~	~~-9.21~~	~~15.47~~	~~2.6~~	~~0.25305~~	~~5.48~~	~~3.6199~~	~~8.5~~	~~0.07798~~	~~3.6~~	~~0.94~~	~~2594~~	~~197~~	~~483~~	~~33~~	~~1188~~	~~115~~	~~19~~	~~41~~	~~483~~	~~33~~
~~JUA25-82.FIN~~	~~33.3548~~	~~2250~~	~~8~~	~~8.8~~	~~-88.7~~	~~-7.95~~	~~10.72~~	~~4.4~~	~~0.53800~~	~~5.05~~	~~7.8362~~	~~4.7~~	~~0.11269~~	~~4.0~~	~~0.18~~	~~3836~~	~~143~~	~~682~~	~~51~~	~~2138~~	~~80~~	~~18~~	~~32~~	~~682~~	~~51~~

JUA25-29.FIN	0.79647	28605	80	1.5	-2114	-3.07	6.66	1.0	0.07117	1.59	1.4905	1.4	0.15236	1.0	0.08	907	70	913	17	923	17	101	99	913	17
JUA25-134.FI	-0.0142	63295	176	0.7	-3444	-2.71	6.59	0.9	0.06987	1.44	1.4647	1.2	0.15282	0.9	-0.03	902	59	916	15	913	14	101	100	916	15
JUA25-6.FIN2	4.08412	5524	15	0.7	-360	-3.31	6.81	1.8	0.09090	3.51	1.8594	3.3	0.15369	1.7	0.18	1220	149	918	29	1028	47	75	89	918	29
~~JUA25-5.FIN2~~	~~0.67177~~	~~22321~~	~~54~~	~~0.8~~	~~-1479~~	~~-8.08~~	~~6.11~~	~~1.6~~	~~0.06694~~	~~1.89~~	~~1.5585~~	~~2.0~~	~~0.17045~~	~~1.7~~	~~0.11~~	~~750~~	~~84~~	~~1011~~	~~31~~	~~944~~	~~24~~	~~135~~	~~107~~	~~1011~~	~~31~~
JUA25-12.FIN	-3.8737	4949	12	0.8	-283.7	-4.46	6.07	2.0	0.07195	4.27	1.6840	4.1	0.17065	1.9	-0.02	726	188	1011	35	953	54	139	106	1011	35
JUA25-15.FIN	5.00098	8016	21	0.6	-1019	-3.83	6.46	1.8	0.07398	3.29	1.6207	3.1	0.16175	1.7	0.22	825	138	967	29	937	41	117	103	967	29
JUA25-61.FIN	0.40005	31691	85	0.6	-1463	-5.38	6.27	1.0	0.06950	1.96	1.5572	1.9	0.16283	1.1	0.11	862	86	971	19	948	23	113	102	971	19
JUA25-98.FIN	0.09512	107396	276	0.2	-8070	-2.2	6.20	1.0	0.07240	1.50	1.6237	1.2	0.16406	1.0	0.15	946	62	978	17	973	15	103	100	978	17
JUA25-79.FIN	0.04737	124789	320	0.3	-6404	-3.65	6.12	0.8	0.07314	1.17	1.6738	1.0	0.16436	0.8	0.15	987	49	980	14	994	13	99	99	980	14
JUA25-87.FIN	0.59364	16063	39	0.6	-1504	-18.7	6.04	1.3	0.07268	2.41	1.6753	2.2	0.16905	1.3	0.07	881	105	1005	24	992	27	114	101	1005	24
JUA25-21.FIN	-1.786	23436	62	1.0	-1325	-9.62	6.33	2.3	0.07449	2.72	1.6760	2.7	0.16677	1.6	0.65	878	110	996	28	966	33	113	103	996	28
JUA25-36.FIN	0.39409	78591	185	0.4	-12108	-2.66	5.93	0.9	0.07252	1.23	1.7147	1.1	0.17110	0.9	0.21	973	51	1017	17	1013	14	105	100	1017	17
JUA25-57.FIN	0.04661	52119	123	0.7	-3397	-3.01	5.93	0.9	0.07393	1.50	1.7414	1.3	0.17081	0.8	0.04	984	61	1016	16	1017	16	103	100	1016	16
JUA25-100.FI	1.0619	33260	79	0.9	-2087	-3.78	5.78	0.9	0.07297	1.70	1.7579	1.6	0.17491	0.9	0.15	943	73	1038	18	1020	20	110	102	1038	18
JUA25-103.FI	0.20384	105533	262	0.1	-8480	-2.27	5.95	1.0	0.07495	1.38	1.7345	1.3	0.17123	0.9	0.30	1023	53	1018	18	1020	15	100	100	1018	18
JUA25-24.FIN	1.06244	25447	62	3.1	-1701	-3.46	5.95	1.2	0.07502	1.92	1.7746	1.8	0.17094	1.1	0.17	994	79	1015	21	1023	23	102	99	1015	21
JUA25-48.FIN	0.08249	30261	71	0.6	-2138	-3.48	5.89	0.8	0.07485	1.74	1.7831	1.6	0.17201	0.9	0.08	1007	74	1022	17	1028	21	102	99	1022	17
JUA25-150.FI	0.6783	28163	72	1.1	-2033	-5.18	5.93	1.1	0.07702	2.05	1.7983	1.9	0.17173	1.1	0.08	1036	84	1020	21	1032	25	98	99	1020	21
JUA25-99.FIN	1.58481	14400	37	0.7	-1109	-9.13	5.88	1.3	0.07798	2.73	1.8362	2.4	0.17507	1.3	0.05	986	119	1037	25	1038	34	105	100	1037	25
JUA25-92.FIN	1.8571	17429	45	2.3	-1688	-6.93	5.64	1.2	0.07446	2.64	1.8738	2.7	0.18120	1.3	0.23	939	113	1071	26	1041	35	114	103	1071	26
JUA25-120.FI	0.55286	33907	79	0.8	-3357	-2.56	5.66	0.9	0.07602	2.11	1.8319	1.5	0.17748	0.9	-0.03	992	72	1052	17	1047	19	106	100	1052	17
JUA25-128.FI	-0.0277	170162	404	0.1	-9771	-3.03	5.72	0.8	0.07496	1.20	1.8161	0.9	0.17605	0.8	-0.01	1037	50	1044	15	1048	12	101	100	1044	15
JUA25-66.FIN	-0.0394	81888	192	0.7	-4897	-4.59	5.49	0.8	0.07381	1.46	1.8330	1.2	0.18304	0.8	0.01	996	61	1083	16	1056	17	109	102	1083	16
JUA25-49.FIN	0.32238	51193	111	1.5	-3817	-2.86	5.53	0.9	0.07519	1.73	1.8878	1.4	0.18306	0.9	0.01	1004	70	1084	18	1068	19	108	102	1084	18
JUA25-126.FI	0.55565	39719	95	1.5	-2419	-3.47	5.69	0.9	0.07723	1.64	1.8895	1.4	0.17867	0.9	0.13	1072	66	1058	17	1070	19	99	99	1058	17
JUA25-102.FI	0.3827	123180	289	0.4	-11147	-4.07	5.65	0.9	0.07740	1.61	1.9060	1.2	0.18154	1.7	0.32	1095	63	1060	20	1077	16	97	98	1060	20
JUA25-56.FIN	1.17352	56815	130	0.7	-3066	-10.7	5.65	1.4	0.07716	1.67	1.9406	1.7	0.18380	1.4	-0.03	1063	74	1085	28	1086	23	102	100	1085	28
JUA25-50.FIN	3.26995	12156	28	3.0	-853.4	-4.77	5.72	1.3	0.08201	2.89	1.9985	2.6	0.17997	1.3	0.12	1059	122	1064	25	1091	36	101	98	1064	25
JUA25-140.FI	-0.0611	28946	74	0.4	-1310	-5.27	5.42	1.8	0.07908	2.08	2.0679	2.1	0.19289	1.4	0.20	1088	80	1134	29	1121	28	104	101	1134	29
JUA25-20.FIN	-0.2115	23382	50	0.9	-1158	-4.25	5.33	1.0	0.07901	1.96	2.0681	1.9	0.18873	1.0	0.19	1095	75	1113	20	1128	24	102	99	1113	20
JUA25-60.FIN	0.01482	91751	194	0.6	-5425	-8.07	5.08	0.8	0.07600	1.59	2.0673	1.4	0.19824	0.8	0.07	1046	64	1165	17	1129	19	111	103	1165	17
JUA25-23.FIN	0.16478	100771	218	0.8	-7436	-8	5.26	1.0	0.07801	1.37	2.0825	1.3	0.19392	1.0	0.35	1101	56	1141	20	1135	17	104	100	1141	20
JUA25-64.FIN	0.17152	81785	172	0.9	-5903	-4.65	5.20	0.9	0.07853	1.37	2.0982	1.1	0.19423	0.9	0.08	1114	55	1143	19	1144	16	103	100	1143	19
JUA25-67.FIN	-0.3096	31154	63	0.7	-1875	-5.29	4.96	1.1	0.07990	2.01	2.2278	1.7	0.20558	1.0	-0.03	1105	82	1203	23	1178	24	109	102	1203	23
JUA25-38.FIN	1.07776	35715	90	1.6	-2E+05	-13.8	5.03	1.3	0.07839	2.07	2.1939	1.9	0.20556	1.2	0.25	1110	82	1202	27	1183	27	108	102	1202	27
JUA25-18.FIN	0.1506	163559	354	0.8	-8357	-3.79	5.29	0.9	0.08459	1.25	2.2113	1.1	0.19041	0.9	0.12	1282	48	1122	19	1185	15	88	95	1122	19
JUA25-54.FIN	0.03328	626645	1208	1.0	-30532	-3.22	4.96	0.8	0.08118	0.93	2.3018	0.8	0.20399	0.7	0.17	1209	37	1196	16	1210	11	99	99	1196	16
JUA25-115.FI	0.42337	71695	145	0.7	-3975	-2.96	5.04	0.8	0.08364	1.26	2.3250	1.1	0.20056	0.8	0.05	1258	52	1177	17	1214	16	94	97	1177	17
JUA25-148.FI	0.05395	197884	400	0.5	-10148	-3.6	4.70	0.8	0.08348	1.32	2.4597	1.0	0.21566	0.8	-0.04	1236	51	1258	17	1255	14	102	100	1258	17
JUA25-69.FIN	1.32235	36796	69	0.6	-2814	-12.3	4.46	1.3	0.08195	2.02	2.6198	2.0	0.23051	1.3	0.17	1175	85	1333	31	1284	29	114	104	1333	31
JUA25-22.FIN	0.4759	66206	98	1.5	-3686	-3.36	3.61	0.9	0.09825	1.44	3.7770	1.1	0.27966	0.9	0.10	1556	54	1590	25	1585	19	102	100	1556	54
JUA25-132.FI	0.05815	214143	312	0.9	-12957	-4.86	3.23	0.8	0.10367	1.13	4.4608	0.9	0.31270	0.9	0.24	1671	44	1751	26	1719	16	105	102	1671	44
JUA25-39.FIN	0.49158	90122	127	1.2	-24234	-7.64	3.21	0.9	0.10559	1.28	4.6303	1.2	0.31576	0.9	0.44	1694	47	1766	28	1749	20	104	101	1694	47
JUA25-81.FIN	0.15525	284183	373	2.8	-17095	-3.48	3.25	0.6	0.10572	1.02	4.5200	0.7	0.30854	0.6	-0.08	1706	38	1739	19	1732	13	102	100	1706	38
JUA25-62.FIN	-0.0843	96057	126	2.2	-5855	-2.35	3.21	0.8	0.10737	1.34	4.5889	1.2	0.31268	0.8	0.24	1713	49	1754	25	1739	20	102	101	1713	49
JUA25-91.FIN	0.06739	126969	166	0.8	-10305	-2.86	3.12	0.8	0.11049	0.96	4.9528	0.9	0.32137	0.8	0.52	1789	35	1796	27	1807	16	100	99	1789	35

U-Pb data from JUA 26.

01 November 2022, Instituto de Geociências, Universidade							Data for Tera-Wasserburg plot						Data for Wetherill plot								Dates							
Identifier	f206c	206Pb	Uppm	Th/U	206Pb/ 204Pb	1s%	238U/ 206Pb	1s%	207Pb/ 206Pb	1s%	208Pb/ 206Pb	1s%	207Pb/ 235U	1s%	206Pb/ 238U	1s%	Rho	208Pb/ 232Th	1s%	207Pb/ 206Pb	2s (abs)	206Pb/ 238U	2s (abs)	207Pb/ 235U	2s (abs)	Conc (%) 6/8 -7/6	Conc (%) 6/8 -7/5	Idade Preferida	2s abs
~~344-JUA26-~~	~~-2.31~~	~~2787~~	~~549~~	~~0.8~~	~~-156.84~~	~~-3.3~~	~~437.97~~	~~2.1~~	~~0.04697~~	~~6.97~~	~~0.1372~~	~~16.9~~	~~0.0153~~	~~6.7~~	~~0.00242~~	~~2.0~~	~~0.05~~	~~0.0007~~	~~8.79~~	~~138~~	~~282~~	~~16~~	~~1~~	~~15~~	~~2~~	~~11~~	~~102~~	~~16~~	~~1~~
~~294-JUA26-~~	~~26.95~~	~~869~~	~~69~~	~~1.9~~	~~-44.911~~	~~-6.6~~	~~242.30~~	~~6.8~~	~~0.06264~~	~~####~~	~~0.4283~~	~~32.9~~	~~0.0376~~	~~14.6~~	~~0.00586~~	~~3.9~~	~~0.04~~	~~0.0021~~	~~9.7~~	~~765~~	~~442~~	~~38~~	~~3~~	~~35~~	~~10~~	~~5~~	~~108~~	~~38~~	~~3~~
308-JUA26-(	3.09	8867	640	0.7	-385.61	-3.5	160.02	1.2	0.04628	3.59	0.1198	7.84	0.0406	3.5	0.00637	1.2	-0.02	0.002	4.48	-248	184	41	1	40	3	-17	102	41	1
221-JUA26-3	-2.74	9132	656	0.6	-459.08	-4.2	156.14	1.8	0.04853	5.93	0.0919	8.09	0.0426	5.7	0.00645	2.1	0.05	0.0018	7.44	-143	345	41	2	42	5	-29	98	41	2
248-JUA26-2	-19.3	1982	137	1.0	-77.97	-4.7	175.31	4.6	0.05544	####	0.2341	22.2	0.0481	11.1	0.00647	3.9	0.06	0.0025	12.6	511	467	42	3	47	10	8	89	42	3
405-JUA26-1	-1.02	22675	1345	1.6	-1327.2	-7.4	115.83	1.7	0.04874	4.38	0.2728	5.25	0.0589	4.0	0.00883	1.7	0.00	0.0026	4.41	69	214	57	2	58	5	83	98	57	2
307-JUA26-(	-1.3	7574	331	1.7	-353.16	-5.2	92.61	1.4	0.05053	4.03	0.2537	4.52	0.0778	4.2	0.01101	1.4	0.23	0.0034	3.55	4	217	71	2	75	6	1742	94	71	2
255-JUA26-3	-14.4	2651	100	1.2	-87.501	-5	94.70	3.9	0.05182	####	0.2317	14.8	0.0732	9.9	0.01129	3.5	-0.01	0.0045	10.3	314	510	72	5	70	14	23	103	72	5
266-JUA26-3	-10.1	4954	203	0.7	-172.37	-4.9	90.98	1.9	0.05164	7.44	0.119	8.98	0.0772	6.5	0.01145	1.9	0.03	0.0038	7.16	-83	275	73	3	74	9	-88	99	73	3
223-JUA26-(	13.04	2420	83	1.5	-112.77	-4.1	84.98	2.4	0.05805	8.00	0.2806	8.96	0.0943	7.3	0.01256	2.4	-0.02	0.0043	6.33	531	285	80	4	88	12	15	91	80	4
402-JUA26-1	1.945	5064	204	1.8	-297.72	-5.5	81.07	2.2	0.05004	5.66	0.3026	14.1	0.0846	5.1	0.01267	2.0	0.12	0.0039	4.67	-5	270	81	3	81	8	-1582	100	81	3
295-JUA26-3	4.249	3115	115	1.7	-140.25	-4.7	82.66	2.2	0.05257	7.22	0.3253	9.47	0.0869	6.8	0.01280	2.2	-0.10	0.0046	5.74	166	313	82	4	83	11	49	99	82	4
391-JUA26-1	1.788	9097	347	1.6	-568.38	-4.6	79.03	1.7	0.04880	4.18	0.2261	3.96	0.0866	4.0	0.01297	1.6	0.05	0.0038	3.64	-25	209	83	3	84	6	-334	99	83	3
252-JUA26-2	1.03	6477	226	1.1	-222.9	-6.7	79.41	1.4	0.05024	4.65	0.2146	17.7	0.0879	4.4	0.01302	1.4	-0.01	0.0042	5.18	-19	210	83	2	84	7	-444	99	83	2
276-JUA26-(	0.403	35034	779	1.7	-1541	-3.3	48.64	0.9	0.04925	2.08	0.2473	2.8	0.1418	2.0	0.02079	0.9	0.13	0.0065	1.87	62	100	133	2	134	5	215	99	133	2
235-JUA26-1	1.276	7704	89	1.4	-344.87	-3.5	26.17	1.6	0.05580	4.66	0.2132	4.53	0.2948	4.2	0.03897	1.6	-0.05	0.0122	4.07	88	240	246	8	257	19	281	96	246	8
379-JUA26-1	0.863	18897	229	3.4	-901.69	-3.7	25.67	1.0	0.05203	2.25	0.4529	1.69	0.2840	2.1	0.03926	1.0	0.10	0.0118	1.39	193	111	248	5	252	9	128	99	248	5
282-JUA26-(	0.301	#####	1235	1.9	-5572.3	-6.2	24.88	1.4	0.05257	2.45	0.2775	2.09	0.2927	2.1	0.04047	1.3	0.11	0.0122	1.4	243	113	256	6	260	9	105	98	256	6
220-JUA26-(	1.893	63889	713	1.6	-2262.8	-8.5	24.45	1.5	0.07335	2.78	0.2535	2.74	0.4132	2.2	0.04156	1.5	-0.05	0.013	1.8	922	123	262	8	351	13	28	75	262	8
389-JUA26-1	-0.43	14517	156	1.7	-873.41	-2.8	22.88	1.0	0.05298	2.88	0.2407	3.08	0.3233	2.9	0.04382	1.1	0.07	0.014	2.3	213	132	276	6	280	14	129	99	276	6
~~409-JUA26-~~	~~-0.31~~	~~14826~~	~~150~~	~~0.5~~	~~-1063.3~~	~~-6.6~~	~~22.59~~	~~1.9~~	~~0.07675~~	~~6.03~~	~~0.1364~~	~~8.14~~	~~0.4757~~	~~5.7~~	~~0.04477~~	~~2.0~~	~~-0.03~~	~~0.0302~~	~~7.75~~	~~942~~	~~280~~	~~282~~	~~11~~	~~390~~	~~37~~	~~30~~	~~72~~	~~282~~	~~11~~
293-JUA26-3	0.179	20341	207	0.8	-947.49	-3.3	22.78	1.2	0.05311	2.54	0.1217	2.81	0.3269	2.4	0.04484	1.1	0.11	0.0141	2.46	194	128	283	6	284	12	146	100	283	6
287-JUA26-3	0.379	77918	801	0.5	-4100.9	-5.3	21.79	0.9	0.05256	2.08	0.1194	39.1	0.3321	1.8	0.04619	0.9	0.05	0.0137	3.03	247	95	291	5	290	9	118	100	291	5
318-JUA26-7	1.635	14669	144	1.2	-992.54	-2.9	21.63	1.1	0.05346	3.02	0.1736	2.9	0.3413	2.5	0.04686	1.1	-0.15	0.0148	2.67	159	129	295	6	294	12	185	100	295	6
~~304-JUA26-(~~	~~-1.37~~	~~11902~~	~~119~~	~~1.5~~	~~-519.78~~	~~-4.4~~	~~21.10~~	~~1.5~~	~~0.05807~~	~~3.89~~	~~0.2399~~	~~3.91~~	~~0.4017~~	~~4.0~~	~~0.04797~~	~~1.5~~	~~0.15~~	~~0.0153~~	~~3.6~~	~~436~~	~~212~~	~~302~~	~~9~~	~~338~~	~~23~~	~~69~~	~~89~~	~~302~~	~~9~~
275-JUA26-(	0.092	48565	468	0.4	-1955.3	-5.2	20.94	0.8	0.05419	1.79	0.1278	7.16	0.3606	1.8	0.04822	0.8	0.22	0.0145	2.2	303	86	304	5	311	9	100	98	304	5
317-JUA26-7	0.28	#####	1617	0.5	-10248	-4.8	20.72	1.0	0.05359	1.50	0.079	2.4	0.3590	1.2	0.04857	1.0	0.08	0.0146	2.33	324	68	306	6	311	7	94	98	306	6
224-JUA26-7	0.14	33100	323	0.6	-1623.4	-8.7	20.87	1.5	0.05398	3.03	0.0807	4.65	0.3569	2.7	0.04869	1.6	0.07	0.0137	3.77	244	150	306	9	307	14	126	100	306	9
291-JUA26-3	-0.35	47559	445	0.8	-2434.9	-3	20.74	0.8	0.05340	1.81	0.1187	2.56	0.3599	1.6	0.04871	0.8	-0.06	0.0144	1.94	284	83	307	5	311	9	108	99	307	5
~~267-JUA26-7~~	~~0.428~~	~~12526~~	~~118~~	~~3.2~~	~~-387.91~~	~~-6.7~~	~~20.88~~	~~1.4~~	~~0.06935~~	~~4.22~~	~~0.3539~~	~~6.22~~	~~0.4603~~	~~3.6~~	~~0.04881~~	~~1.6~~	~~-0.11~~	~~0.0106~~	~~2.85~~	~~704~~	~~152~~	~~307~~	~~9~~	~~377~~	~~21~~	~~44~~	~~81~~	~~307~~	~~9~~
372-JUA26-1	1.414	3975	42	1.9	-271.78	-4.8	22.23	3.5	0.05165	9.13	0.3264	7.65	0.3383	8.5	0.04889	3.6	-0.21	0.0153	5.73	126	411	307	21	281	41	244	109	307	21
234-JUA26-1	0.805	10402	94	2.7	-472.89	-3	20.65	1.0	0.05482	3.02	0.3992	2.38	0.3663	2.7	0.04920	1.0	-0.03	0.0158	2.29	274	136	309	6	315	15	113	98	309	6
302-JUA26-(	-1.26	14094	129	1.2	-630.38	-2.2	20.59	1.1	0.05229	2.84	0.1816	3.54	0.3534	2.6	0.04962	1.1	0.03	0.0158	2.47	99	134	312	7	303	14	314	103	312	7
403-JUA26-1	-0.04	16583	171	0.9	-928.99	-7.6	20.20	1.3	0.05175	3.74	0.1249	4.31	0.3614	4.0	0.04975	1.3	-0.09	0.0141	4.02	166	172	313	8	308	21	189	101	313	8
380-JUA26-1	-0.38	16851	163	0.9	-825.33	-3.4	20.32	1.1	0.05402	2.70	0.305	55.2	0.3704	2.4	0.04985	1.0	-0.20	0.0164	2.97	168	125	313	6	316	13	186	99	313	6
303-JUA26-(	-0.64	8048	74	3.0	-345.14	-3.6	20.52	1.4	0.05427	3.81	0.4284	2.64	0.3694	3.6	0.05004	1.3	0.05	0.0157	2.21	100	191	315	8	310	19	315	101	315	8
315-JUA26-7	1.452	16277	154	0.2	-977.8	-3.6	20.23	1.1	0.05414	2.40	0.0363	6.19	0.3724	2.2	0.05024	1.1	0.10	0.0178	7.59	262	114	316	7	319	12	121	99	316	7
311-JUA26-7	0.142	7442	71	1.4	-380.04	-4.3	20.67	2.1	0.05932	8.97	0.2444	6.9	0.3997	8.1	0.05031	2.0	0.10	0.0168	5	177	230	316	12	311	28	179	102	316	12
357-JUA26-1	0.901	30006	287	0.8	-2389.7	-6	20.13	1.0	0.05424	2.31	0.1433	3.86	0.3756	2.2	0.05031	1.0	0.07	0.0147	2.07	260	106	316	6	322	12	122	98	316	6
251-JUA26-2	-0.59	27538	230	1.0	-968.12	-3.8	20.04	1.0	0.05540	2.87	0.1382	3.8	0.3894	2.7	0.05038	1.0	-0.03	0.0165	2.72	306	138	317	6	331	15	104	96	317	6
231-JUA26-1	0.102	27887	242	0.8	-1210.2	-2.8	19.97	0.9	0.05447	2.03	0.5299	77.1	0.3771	1.8	0.05076	1.0	0.03	0.0177	2.26	279	93	319	6	324	10	114	99	319	6
350-JUA26-9	-0.31	39258	353	0.9	-2276.5	-3.3	19.84	0.8	0.05282	1.67	0.1345	2.46	0.3723	1.5	0.05085	0.8	0.10	0.0162	1.99	259	82	320	5	322	9	124	99	320	5
415-JUA26-3	5.288	9604	93	3.6	-32290	-57	20.11	1.3	0.05312	3.37	0.507	2.8	0.3720	3.3	0.05097	1.2	0.00	0.0163	1.98	149	158	320	7	313	18	215	102	320	7
261-JUA26-3	0.942	49984	416	2.9	-1295.7	-7	19.79	1.1	0.06091	2.67	0.417	2.51	0.4332	2.8	0.05109	1.1	0.31	0.0171	1.39	607	115	321	7	362	16	53	89	321	7
377-JUA26-1	-0.1	12309	118	2.0	-611.83	-3.5	19.78	1.3	0.05143	3.15	0.2761	2.85	0.3662	3.1	0.05114	1.3	0.10	0.0151	2.49	168	155	321	8	316	18	191	102	321	8
385-JUA26-1	0.973	16419	163	1.3	-861.1	-4.4	19.93	1.6	0.05640	4.10	0.1953	4.43	0.3870	3.5	0.05115	1.5	-0.05	0.0155	4.14	402	169	321	10	328	20	80	98	321	10
359-JUA26-1	1.644	27426	243	2.0	-2177.9	-4.8	19.56	1.2	0.05461	3.28	0.2824	4.97	0.3870	3.2	0.05134	1.2	0.03	0.0161	2.47	237	133	323	8	329	17	136	98	323	8
238-JUA26-1	1.158	26412	231	2.1	-1151.8	-6.3	19.47	0.9	0.05462	2.51	0.2949	2.18	0.3910	2.3	0.05180	0.9	0.00	0.0164	1.93	292	115	325	6	332	14	111	98	325	6
363-JUA26-1	0.429	57042	511	0.2	-5540.4	-3.3	19.41	0.8	0.05274	1.76	0.0303	7.29	0.3758	1.5	0.05179	0.8	-0.09	0.0157	3.91	249	81	325	5	323	8	131	101	325	5
225-JUA26-8	3.562	15218	126	1.6	-630.05	-5	19.57	1.2	0.05610	3.06	1.7965	86.8	0.3986	2.9	0.05171	1.3	0.01	0.0168	2.83	364	140	326	8	336	17	89	97	326	8
392-JUA26-1	3.636	8705	85	1.9	-538.62	-5.1	19.83	2.2	0.05557	4.48	0.3017	4.67	0.3992	4.7	0.05192	2.1	0.12	0.0155	4.16	294	219	326	13	334	26	111	98	326	13
233-JUA26-1	-1.49	11396	103	1.8	-512.97	-5.7	19.62	2.0	0.05330	5.57	0.2714	4.45	0.3698	4.7	0.05194	2.0	-0.17	0.0154	3.86	183	255	326	13	313	26	178	104	326	13
349-JUA26-9	-0.03	20220	186	1.6	-1104.1	-3.6	19.52	1.0	0.05267	2.30	0.2127	2.4	0.3786	2.1	0.05196	1.0	-0.02	0.0155	2.01	166	112	326	6	323	12	196	101	326	6
227-JUA26-1	0.223	20512	172	1.5	-946.73	-3.5	19.31	1.0	0.05490	2.30	0.2281	3.04	0.3995	2.3	0.05235	1.0	0.10	0.017	2.43	274	109	329	7	337	13	120	97	329	7
249-JUA26-2	-0.6	23761	202	1.5	-849.59	-3.7	19.24	0.9	0.05242	2.26	0.2258	2.25	0.3772	2.2	0.05256	0.9	0.10	0.0168	1.85	173	109	330	6	322	12	191	103	330	6
297-JUA26-(	0.2	31274	276	0.0	-1414.1	-4.3	19.28	1.1	0.05338	2.29	0.004	18.5	0.3869	2.0	0.05284	1.2	-0.03	0.0254	20.7	267	105	330	7	329	11	124	100	330	7
332-JUA26-8	0.251	5001	46	1.2	-345.01	-4.1	19.65	2.9	0.05793	6.97	0.2091	6.83	0.4184	7.3	0.05269	3.0	0.16	0.0175	5.9	213	386	330	19	337	42	155	98	330	19
351-JUA26-9	0.321	42959	388	1.8	-2304.1	-4.3	19.10	1.2	0.05364	2.31	0.272	2.68	0.3993	2.2	0.05306	1.2	0.03	0.0162	1.99	323	107	333	8	339	13	103	98	333	8
263-JUA26-3	0.055	19635	167	2.3	-590.37	-4.6	18.81	1.0	0.05400	2.65	0.3406	2.46	0.4013	2.4	0.05373	1.0	0.16	0.0172	1.92	230	130	337	7	338	14	147	100	337	7
421-JUA26-1	5.112	20981	225	3.1	1324.69	9.62	19.43	3.5	0.05377	6.61	0.51	5.75	0.4008	5.9	0.05387	3.1	0.10	0.0165	3.35	205	294	338	21	336	35	165	101	338	21
329-JUA26-8	0.457	50740	435	0.2	-3554.1	-3.2	18.61	1.0	0.05279	1.59	0.0357	4.35	0.3996	1.6	0.05452	0.9	0.24	0.0198	3.38	261	77	342	6	339	9	131	101	342	6
280-JUA26-(	-0.26	29778	260	1.1	-1507.8	-5	18.34	1.0	0.05264	2.21	0.1604	2.51	0.4017	2.1	0.05527	1.0	0.05	0.0172	2.05	172	106	347	7	339	12	202	102	347	7
365-JUA26-1	0.702	37473	338	0.3	-3597.9	-6	17.50	1.4	0.05479	2.44	0.1034	8.72	0.4401	2.7	0.05812	1.5	0.07	0.0189	3.41	281	112	364	11	366	16	129	99	364	11
226-JUA26-9	0.627	#####	779	0.7	-4241.1	-5.5	15.91	1.0	0.05993	1.68	0.105	2.06	0.5250	1.6	0.06342	1.0	0.19	0.0188	1.68	550	76	396	8	427	11	72	93	396	8

247-JUA26-2	1.737	8346	53	0.9	-295.69	-6.8	14.75	2.2	0.05741	6.14	0.103	9.31	0.5305	5.4	0.06927	2.3	-0.08	0.0171	7.24	209	291	431	20	430	39	206	100	431	20
387-JUA26-1	0.61	18929	116	1.4	-1043.3	-4.3	13.25	1.1	0.05455	2.81	0.1767	3.22	0.5662	2.5	0.07654	1.2	0.06	0.0234	3.02	253	128	475	11	450	18	188	106	475	11
346-JUA26-9	1.203	11423	72	1.6	-584.97	-7.1	13.27	3.0	0.06321	6.05	0.2675	6.64	0.6632	4.8	0.07893	3.0	-0.05	0.0252	5.68	482	257	489	28	507	39	101	96	489	28
406-JUA26-1	0.103	35821	212	1.6	-2114.5	-2.8	12.28	1.0	0.05943	1.93	0.2156	1.77	0.6694	1.6	0.08270	0.9	0.00	0.0256	1.53	481	88	512	9	518	14	106	99	512	9
296-JUA26-5	2.023	19889	117	1.4	-828.44	-7.1	12.32	2.6	0.06064	3.93	0.2109	5.55	0.7010	3.6	0.08281	2.3	0.21	0.0233	4.52	593	170	518	25	541	33	87	96	518	25
~~322-JUA26-7~~	~~0.114~~	~~#####~~	~~733~~	~~0.1~~	~~-10190~~	~~-4.8~~	~~11.62~~	~~0.8~~	~~0.11235~~	~~1.50~~	~~0.0329~~	~~3.63~~	~~1.3348~~	~~1.4~~	~~0.08636~~	~~0.8~~	~~0.08~~	~~0.043~~	~~3.42~~	~~1824~~	~~55~~	~~534~~	~~8~~	~~859~~	~~16~~	~~29~~	~~62~~	~~534~~	~~8~~
325-JUA26-8	2.047	15577	83	1.4	-1139.5	-3.5	11.59	1.1	0.05996	2.62	0.1891	2.89	0.7189	2.5	0.08781	1.1	0.00	0.0268	2.48	433	116	542	11	540	20	125	100	542	11
333-JUA26-8	-0.05	45450	246	1.9	-3072.9	-3.2	11.30	1.3	0.05982	2.34	0.2607	2.02	0.7358	1.9	0.08971	1.3	-0.04	0.0258	1.86	524	102	553	14	557	16	106	99	553	14
240-JUA26-1	0.089	33790	145	2.5	-1530.1	-3.1	10.06	0.9	0.06110	1.94	0.3351	2.99	0.8447	1.7	0.10051	0.9	-0.01	0.0313	1.71	569	87	617	10	617	16	108	100	617	10
301-JUA26-6	0.695	49589	238	1.2	-2171.3	-6.8	9.95	1.4	0.05814	2.59	0.1731	3.75	0.8155	2.5	0.10142	1.4	0.13	0.0286	2.91	517	111	622	16	605	22	120	103	622	16
375-JUA26-1	-0.23	20454	96	1.2	-1115.9	-2.6	9.92	1.0	0.06108	2.08	0.1641	3.12	0.8443	1.8	0.10221	1.0	-0.03	0.0311	2.41	541	100	627	12	619	17	116	101	627	12
386-JUA26-1	0.253	60358	284	1.4	-3350.9	-3.3	9.84	0.6	0.06105	1.30	0.1842	1.39	0.8690	1.2	0.10246	0.6	0.03	0.0304	1.31	619	56	629	8	633	12	101	99	629	8
408-JUA26-1	1.732	18124	64	1.0	-1084	-5	7.05	2.2	0.08085	4.55	0.1737	5.15	1.6084	4.8	0.14403	2.2	0.27	0.0485	4.75	1044	200	866	36	956	60	83	91	866	36
309-JUA26-6	0.44	89619	291	0.3	-3965.1	-3.6	6.99	1.1	0.07665	1.47	0.0472	2.35	1.5243	1.3	0.14508	1.1	0.24	0.0452	2.09	1073	58	872	18	935	15	81	93	872	18
364-JUA26-1	1.86	21243	68	0.7	-2098.5	-4.4	6.66	1.1	0.06956	2.26	0.109	3.41	1.4690	2.2	0.15152	1.1	0.16	0.0486	2.75	815	100	912	17	911	25	112	100	912	17
343-JUA26-9	1.872	12347	36	2.5	-666.37	-5.3	6.67	1.7	0.06690	3.47	0.5952	42.4	1.4172	3.6	0.15392	1.6	0.28	0.0468	3.56	691	167	921	28	881	44	133	105	921	28
414-JUA26-1	1.475	12394	38	1.4	-4098.7	-3.8	6.53	1.1	0.07209	2.52	0.1848	3.14	1.5519	2.4	0.15603	1.3	-0.03	0.046	2.58	869	106	933	22	930	29	107	100	933	22
241-JUA26-2	0.161	52678	144	0.8	-2245.3	-5.7	6.23	0.9	0.07409	1.75	0.1182	2.38	1.6425	1.8	0.16134	0.8	0.24	0.0515	2.37	980	70	963	15	982	20	98	98	963	15
353-JUA26-1	0.203	#####	332	0.5	-6707.1	-4	6.14	1.1	0.07349	1.48	0.0733	2.08	1.6548	1.3	0.16485	1.1	0.29	0.0492	1.97	992	61	983	19	992	17	99	99	983	19
373-JUA26-1	0.274	21885	64	2.6	-1342.9	-3.1	6.05	1.3	0.07454	2.38	0.3324	2.24	1.6952	1.9	0.16669	1.3	0.04	0.047	2.13	975	100	992	24	1000	24	102	99	992	24
268-JUA26-3	-0.05	72668	199	0.8	-2421.1	-3.8	6.05	1.2	0.07557	1.72	0.1002	2.33	1.7300	1.6	0.16722	1.1	0.22	0.0439	2.3	1048	71	996	21	1015	21	95	98	996	21
400-JUA26-1	0.572	47079	143	0.6	-2657.8	-5.1	6.04	1.2	0.07639	2.64	0.0998	10.4	1.7282	2.1	0.16754	1.3	0.03	0.0502	4.05	1034	109	998	24	1023	30	96	98	998	24
217-JUA26-1	0.317	34054	89	0.8	-1655.9	-4.4	5.96	1.0	0.07216	1.81	0.1054	2.37	1.6935	1.5	0.16969	1.0	0.04	0.0534	2.34	952	73	1009	19	1001	20	106	101	1009	19
394-JUA26-1	0.121	32813	93	0.9	-2182.9	-2.2	5.96	0.9	0.07419	1.88	0.1144	2.63	1.7224	1.5	0.16996	0.9	-0.07	0.0507	2.28	950	79	1011	18	1007	20	106	100	1011	18
310-JUA26-6	0.328	31832	82	2.5	-1468.6	-4.9	5.95	1.5	0.07196	2.07	0.3208	2.29	1.6795	1.8	0.17015	1.6	0.30	0.0534	2	936	90	1012	30	996	24	108	102	1012	30
417-JUA26-1	0.326	65173	182	1.5	13194.7	3.15	5.92	1.0	0.07360	2.29	0.1769	2.21	1.7338	2.0	0.17004	1.0	0.01	0.049	2.04	985	88	1012	19	1016	24	103	100	1012	19
283-JUA26-5	-0.58	25541	70	0.9	-1430.5	-3.2	5.91	1.1	0.07408	2.27	0.1291	6.09	1.7443	2.1	0.17029	1.2	0.02	0.0466	3.25	1016	92	1013	23	1014	27	100	100	1013	23
416-JUA26-1	0.696	60432	193	0.9	32049.4	6.47	6.00	1.8	0.07071	2.43	0.1299	3.48	1.6617	2.0	0.17043	1.6	0.09	0.0483	2.65	902	100	1013	31	992	26	112	102	1013	31
259-JUA26-3	0.016	#####	961	0.1	-10148	-5.9	5.93	1.4	0.07546	2.02	0.0249	3.95	1.7692	1.5	0.17111	1.3	-0.04	0.0541	2.59	1036	83	1017	25	1031	19	98	99	1017	25
245-JUA26-2	0.862	29623	77	0.8	-1184.5	-3.7	5.94	1.0	0.07492	1.87	0.112	2.55	1.7605	1.6	0.17118	1.0	0.11	0.0533	2.45	984	75	1017	19	1021	20	103	100	1017	19
345-JUA26-9	0.065	46779	125	0.8	-2490.4	-4.1	5.95	1.0	0.07472	1.79	0.1146	3.49	1.7369	1.5	0.17083	0.9	0.03	0.0503	1.9	989	71	1018	16	1016	19	103	100	1018	16
316-JUA26-7	1.847	29340	82	0.9	-1808.7	-6	5.93	1.2	0.07380	2.03	0.1225	2.28	1.7221	1.8	0.17079	1.1	0.05	0.0515	2.29	965	84	1019	19	1012	25	106	101	1019	19
337-JUA26-8	3.203	6577	18	1.0	-433.35	-5.7	5.99	1.6	0.07288	3.42	0.1463	5.25	1.7429	3.2	0.17339	1.6	-0.01	0.055	4.23	835	153	1027	30	995	43	123	103	1027	30
422-JUA26-1	0.781	#####	424	0.4	6850.38	6.44	5.86	1.7	0.07818	2.26	0.0546	3.54	1.8491	1.5	0.17330	1.6	0.03	0.055	3.55	1111	92	1029	30	1060	20	93	97	1029	30
367-JUA26-1	1.304	32843	93	1.3	-2916.8	-3.7	5.79	1.6	0.07532	2.47	0.1765	3.09	1.8265	2.1	0.17657	1.5	0.07	0.0495	2.9	1010	105	1047	29	1046	28	104	100	1047	29
260-JUA26-3	-0.21	#####	374	0.4	-4560	-3.4	5.63	1.1	0.07448	1.78	0.0633	2.34	1.8434	1.2	0.17950	1.1	0.18	0.0508	1.91	1019	72	1064	21	1058	16	104	100	1064	21
407-JUA26-1	0.052	#####	768	1.4	-16100	-4	5.51	1.2	0.07577	1.77	0.1928	2.16	1.9157	1.3	0.18370	1.2	-0.09	0.051	1.35	1052	72	1086	24	1084	17	103	100	1086	24
269-JUA26-4	-0.06	24314	61	1.1	-792.37	-4	5.52	1.3	0.07704	2.25	0.1684	2.98	1.9398	2.2	0.18384	1.3	0.20	0.0553	2.8	1068	94	1086	26	1087	28	102	100	1086	26
381-JUA26-1	0.344	39942	100	0.9	-1914.4	-3.9	5.36	0.8	0.07593	1.52	0.114	2.57	1.9670	1.3	0.18801	0.8	0.03	0.0571	2.22	1031	64	1110	16	1097	17	108	101	1110	16
371-JUA26-1	1.041	5641	14	0.8	-403.37	-3.6	5.58	3.0	0.07727	5.06	0.125	7.82	1.9630	5.2	0.18957	2.1	0.26	0.0647	7.21	919	200	1116	42	1042	72	121	107	1116	42
399-JUA26-1	0.866	31463	81	0.6	-1945.4	-3.5	5.27	1.0	0.07693	1.98	0.0925	4.62	2.0301	1.8	0.19166	1.1	0.10	0.0571	2.88	1055	83	1132	21	1114	25	107	102	1132	21
305-JUA26-6	0.303	49061	117	1.1	-2177.2	-6.5	5.19	0.9	0.07849	1.45	0.1503	1.64	2.0865	1.3	0.19328	0.9	-0.03	0.0572	1.49	1112	60	1138	19	1140	17	102	100	1138	19
360-JUA26-1	-0.45	27085	65	0.5	-2607.8	-1.7	5.21	1.1	0.07815	1.63	0.1043	4.17	2.1111	1.6	0.19479	1.0	0.18	0.064	3.04	1091	64	1145	22	1141	22	105	100	1145	22
347-JUA26-9	-1.21	8931	23	1.1	-487.76	-4.4	5.18	2.4	0.08659	5.28	0.285	39.8	2.2919	4.1	0.19587	2.9	0.02	0.0613	6.08	1236	219	1149	60	1187	60	93	97	1149	60
401-JUA26-1	1.006	17662	44	0.8	-1036.5	-2.6	5.17	1.1	0.08089	1.90	0.1024	2.98	2.2021	1.7	0.19652	1.1	0.13	0.056	2.61	1156	77	1155	23	1170	25	100	99	1155	23
413-JUA26-1	1.341	29346	74	1.3	-4996.7	-3.7	5.12	1.1	0.07903	1.80	0.1816	4.01	2.1522	1.8	0.19749	1.1	0.04	0.0594	2.47	1112	72	1160	24	1159	24	104	100	1160	24
288-JUA26-5	1.342	25676	64	0.8	-1424.2	-5.2	5.26	2.4	0.07665	2.64	0.1089	4.09	2.0962	2.6	0.19788	1.4	0.41	0.0528	3.68	1040	105	1162	30	1140	34	112	102	1162	30
246-JUA26-2	0.651	34409	83	1.7	-1390.3	-6.1	5.16	2.2	0.08444	3.31	0.2666	4.21	2.3055	3.0	0.19742	2.0	0.13	0.0562	3.22	1224	133	1167	46	1206	41	95	97	1167	46
219-JUA26-3	0.613	34425	77	0.7	-1651.6	-4.7	5.05	1.1	0.08010	2.30	0.0929	3.76	2.1849	2.1	0.20045	1.1	0.13	0.0593	3.28	1139	94	1177	24	1165	30	103	101	1177	24
366-JUA26-1	0.401	69765	167	0.7	-6572.2	-3.3	5.03	0.7	0.07913	1.24	0.0878	1.87	2.1858	1.0	0.20048	0.7	0.08	0.0591	1.87	1146	49	1177	15	1171	15	103	100	1177	15

289-JUA26-5	0.283	58896	134	0.8	-3044.4	-2.7	5.04	0.7	0.08126	1.36	0.1116	1.78	2.2575	1.1	0.20066	0.7	0.06	0.0597	1.68	1198	55	1178	16	1195	16	98	99	1178	16
239-JUA26-1	0.156	80748	175	0.6	-3722.2	-6.1	5.03	1.0	0.08060	1.47	0.08	2.58	2.2222	1.3	0.20024	1.0	0.09	0.062	2.06	1175	58	1179	21	1182	19	100	100	1179	21
419-JUA26-1	1.038	39594	90	1.2	4035.45	3.08	4.99	1.4	0.07851	2.31	0.148	3.03	2.1954	2.4	0.20186	1.3	0.16	0.0651	3.05	1115	90	1184	28	1178	31	106	101	1184	28
420-JUA26-1	3.246	16431	40	0.8	1298.27	2.89	5.05	1.2	0.08223	2.41	0.1014	4.78	2.2596	2.0	0.20269	1.1	-0.05	0.0595	3.45	1109	95	1187	25	1181	28	107	101	1187	25
336-JUA26-6	0.344	90033	218	0.7	-5414.1	-11	4.83	1.3	0.08124	2.34	0.1191	6.82	2.3284	2.1	0.20978	1.4	0.17	0.0571	2.93	1177	93	1226	31	1213	30	104	101	1226	31
330-JUA26-8	0.718	25583	58	0.8	-1888.3	-4.6	4.84	1.0	0.08318	1.85	0.1021	3.03	2.3861	1.6	0.21002	0.9	0.05	0.0602	2.89	1209	75	1227	21	1231	23	102	100	1227	21
237-JUA26-1	1.833	63853	131	1.0	-2563.8	-5	4.80	0.8	0.09365	1.89	0.15	3.43	2.6826	1.6	0.20996	0.8	0.02	0.0709	2.63	1446	70	1228	18	1319	25	85	93	1228	18
324-JUA26-7	0.131	65148	138	0.5	-5012.1	-2.9	4.79	0.9	0.08219	1.36	0.0656	3.66	2.3908	1.3	0.21054	0.9	0.28	0.0656	2.66	1220	54	1231	19	1236	18	101	100	1231	19
323-JUA26-7	0.372	48719	109	2.7	-3664.7	-3.6	4.79	1.1	0.08231	1.84	0.3683	1.97	2.3886	1.4	0.21136	1.0	-0.06	0.061	1.44	1216	79	1235	23	1237	22	102	100	1235	23
321-JUA26-7	0.063	51510	114	0.9	-3957.3	-2.7	4.76	0.9	0.08209	1.58	0.1151	2.37	2.4125	1.4	0.21238	0.9	0.09	0.0606	2.01	1220	66	1240	21	1239	20	102	100	1240	21
388-JUA26-1	0.089	82907	185	2.3	-4963.6	-6.6	4.64	0.9	0.08474	1.48	0.2806	1.68	2.5034	1.1	0.21726	0.8	-0.09	0.0605	1.4	1277	58	1266	19	1271	17	99	100	1266	19
279-JUA26-4	-0.05	53545	113	1.0	-2698.9	-3.6	4.62	0.9	0.08374	1.41	0.1318	1.69	2.5361	1.3	0.21883	0.8	0.22	0.0678	1.79	1243	55	1274	19	1274	18	103	100	1274	19
339-JUA26-9	1.405	23740	53	0.9	-1381.5	-4.5	4.60	1.3	0.08692	2.46	0.1304	3.52	2.6122	2.1	0.22178	1.2	0.06	0.0615	2.99	1281	98	1289	29	1289	32	101	100	1289	29
338-JUA26-8	1.612	50683	97	4.1	-2696.6	-7	4.46	1.4	0.08575	2.19	0.4878	1.96	2.7028	1.9	0.22686	1.3	0.10	0.0684	1.78	1296	85	1317	32	1324	27	102	99	1317	32
274-JUA26-4	0.028	96843	199	0.8	-3842.3	-3.3	4.45	0.9	0.08653	1.15	0.4253	71.8	2.6944	1.1	0.22740	0.8	0.59	0.068	1.84	1317	45	1319	20	1327	15	100	99	1319	20
265-JUA26-3	-0.49	51064	100	0.7	-1650.7	-4.2	4.36	1.0	0.08826	1.44	0.0966	2.9	2.8330	1.2	0.23161	0.9	0.36	0.0691	2.08	1343	57	1348	24	1359	18	100	99	1348	24
254-JUA26-2	-0.09	#####	261	1.2	-4649.3	-2.9	4.08	0.7	0.08933	1.01	0.1542	1.31	3.0493	0.8	0.24659	0.7	0.10	0.0739	1.23	1389	40	1420	17	1416	12	102	100	1420	17
253-JUA26-2	-0.38	28687	49	1.0	-961.58	-4.4	3.78	0.9	0.09601	1.59	0.1352	2.4	3.5076	1.4	0.26782	0.9	0.10	0.0783	2.35	1499	60	1528	23	1523	22	102	100	1499	60
331-JUA26-6	9E-04	49267	87	0.9	-3517.6	-3.8	3.75	0.8	0.09441	1.35	0.1196	3.19	3.5385	1.2	0.27037	0.8	0.13	0.0832	2.02	1483	54	1541	22	1526	20	104	101	1483	54
374-JUA26-1	0.007	#####	280	0.5	-8835.9	-3	3.70	0.7	0.09717	0.90	0.0907	3.37	3.6488	0.9	0.27212	0.7	0.38	0.0828	1.36	1558	35	1550	21	1559	14	100	99	1558	35
290-JUA26-5	-0.02	#####	321	0.3	-10048	-2.4	3.67	0.7	0.09640	1.03	0.0398	1.93	3.6412	0.7	0.27418	0.7	0.00	0.0692	1.96	1535	38	1561	18	1556	12	102	100	1535	38
232-JUA26-1	0.15	67910	97	1.6	-2935.3	-4.5	3.16	0.8	0.10644	1.35	0.2106	1.7	4.6651	1.2	0.31850	0.8	0.11	0.0907	1.67	1714	52	1784	27	1754	19	104	102	1714	52
281-JUA26-4	0.08	#####	189	2.3	-6579.7	-4	3.14	0.9	0.10632	1.50	0.3055	2.19	4.6956	1.1	0.32100	0.9	-0.02	0.0872	1.21	1714	57	1793	30	1767	19	105	101	1714	57
~~393-JUA26-1~~	~~-0.08~~	~~44313~~	~~69~~	~~2.0~~	~~-3036.3~~	~~-4~~	~~3.17~~	~~1.1~~	~~0.10522~~	~~1.43~~	~~0.2536~~	~~1.88~~	~~4.6568~~	~~1.3~~	~~0.32226~~	~~0.9~~	~~0.30~~	~~0.0894~~	~~1.36~~	~~1682~~	~~54~~	~~1798~~	~~28~~	~~1750~~	~~23~~	~~107~~	~~103~~	~~1682~~	~~54~~
277-JUA26-4	-0.08	#####	187	0.6	-6632	-3	2.93	1.2	0.11522	1.64	0.127	6.97	5.4209	1.4	0.34388	1.3	0.31	0.1051	2.31	1860	58	1902	43	1886	24	102	101	1860	58
335-JUA26-6	0.24	#####	276	0.8	-11307	-5.9	3.00	1.7	0.12548	2.03	0.0574	4.63	5.8337	1.6	0.33877	1.6	0.26	0.0566	9.56	2009	71	1878	53	1952	29	93	96	2009	71

U-Pb data from JUA 30

University of Brasilia							Data for Tera-Wasserburg plot				Data for Wetherill plot					Dates									
Identifier	f206c	206Pb	Uppm	Th/U	206Pb/ 204Pb	1s%	238U/ 206Pb	1s%	207Pb/20 6Pb	1s%	207Pb/ 235U	1s%	206Pb/ 238U	1s%	Rho	207Pb/ 206Pb	2s (abs)	206Pb/ 238U	2s (abs)	207Pb/ 235U	2s (abs)	Conc (%) 6/8 -7/6	Conc (%) 6/8 -7/5	Idade Preferida	2s abs
JUA30-77.I	-0.72	11214	797	1.3	-509.3	-4.9	156.14	1.1	0.04813	3.46	0.0427	3.2	0.00656	1.1	0.27	-232	188	42	1	42	3	-18	100	42	1
~~JUA30-13.I~~	~~0.25~~	~~28287~~	~~1016~~	~~2.1~~	~~-874.1~~	~~-5.4~~	~~86.90~~	~~1.0~~	~~0.05865~~	~~2.30~~	~~0.0946~~	~~2.3~~	~~0.01164~~	~~0.9~~	~~0.06~~	~~438~~	~~113~~	~~75~~	~~1~~	~~92~~	~~4~~	~~17~~	~~81~~	~~75~~	~~1~~
~~JUA30-29.I~~	~~4.69~~	~~20485~~	~~750~~	~~2.6~~	~~-1232~~	~~-5.2~~	~~83.66~~	~~1.3~~	~~0.06654~~	~~3.40~~	~~0.1150~~	~~3.9~~	~~0.01222~~	~~1.3~~	~~0.47~~	~~637~~	~~144~~	~~78~~	~~2~~	~~109~~	~~8~~	~~12~~	~~72~~	~~78~~	~~2~~
JUA30-4.FI	-2.51	7432	251	1.1	-334.1	-6	76.97	1.6	0.05491	5.00	0.0982	4.6	0.01329	1.6	-0.08	271	208	85	3	94	8	31	91	85	3
JUA30-103	0.78	21264	698	2.5	-1046	-6.2	73.40	1.2	0.05148	2.66	0.0992	2.4	0.01407	1.5	0.13	156	120	90	3	96	4	58	94	90	3
~~JUA30-128~~	~~-111~~	~~1937~~	~~5~~	~~0.0~~	~~188.09~~	~~130~~	~~-21.33~~	~~-209.2~~	~~-0.07177~~	~~-240.38~~	~~-5.0801~~	~~-49.3~~	~~-0.84488~~	~~-48.6~~	~~0.00~~	~~4266~~	~~133~~	~~118~~	~~155~~	~~1625~~	~~153~~	~~3~~	~~7~~	~~118~~	~~155~~
JUA30-107	2.73	9938	159	3.4	-424.9	-7.1	38.39	2.8	0.05408	5.24	0.1997	4.6	0.02800	2.7	0.12	161	247	178	10	181	16	111	98	178	10
~~JUA30-68.I~~	~~-2.29~~	~~8926~~	~~133~~	~~2.1~~	~~-322.8~~	~~-6.2~~	~~33.06~~	~~1.6~~	~~0.06310~~	~~5.06~~	~~0.2675~~	~~6.3~~	~~0.03208~~	~~2.4~~	~~-0.11~~	~~360~~	~~205~~	~~203~~	~~9~~	~~237~~	~~21~~	~~57~~	~~86~~	~~203~~	~~9~~
JUA30-40.I	0.53	22549	245	1.7	-1516	-3.1	24.80	0.9	0.05348	2.30	0.3004	2.1	0.04080	0.9	-0.01	209	115	258	5	264	10	123	98	258	5
JUA30-76.I	1.48	17193	189	2.6	-1102	-27	24.79	1.2	0.05100	2.81	0.2843	2.4	0.04154	1.4	-0.07	90	127	262	7	251	11	292	104	262	7
~~JUA30-98.I~~	~~1.33~~	~~32959~~	~~375~~	~~1.5~~	~~-1508~~	~~-6~~	~~24.39~~	~~1.2~~	~~0.06340~~	~~2.50~~	~~0.3626~~	~~2.3~~	~~0.04178~~	~~1.2~~	~~0.04~~	~~601~~	~~112~~	~~264~~	~~6~~	~~312~~	~~12~~	~~44~~	~~84~~	~~264~~	~~6~~
JUA30-30.I	1.88	21379	234	2.4	-1384	-7.2	23.78	1.1	0.05734	2.86	0.3336	2.7	0.04278	1.1	0.25	363	127	270	6	288	13	74	94	270	6
JUA30-10.I	0.18	16648	158	1.0	-880.6	-4.8	23.41	1.3	0.05135	2.89	0.3041	2.6	0.04348	1.2	0.03	62	128	274	6	266	12	439	103	274	6
JUA30-1.FI	-0.13	37743	353	1.1	-2791	-39	22.61	0.8	0.05237	1.67	0.3239	1.5	0.04576	2.3	0.02	241	74	288	12	284	7	120	102	288	12
JUA30-51.I	-0.16	19088	191	1.0	-861.7	-6.3	21.84	1.3	0.05557	2.87	0.3539	2.5	0.04679	1.3	-0.06	251	129	295	7	303	13	118	97	295	7
JUA30-93.I	1.08	18902	175	3.0	-1685	-3	21.19	1.0	0.05463	2.29	0.3624	2.4	0.04811	1.0	0.23	261	110	303	6	310	12	116	98	303	6
JUA30-100	-0.13	21935	208	0.6	-983.8	-3.3	21.06	1.0	0.05514	2.31	0.3639	2.0	0.04831	1.0	0.12	256	115	304	6	312	11	119	97	304	6
JUA30-121	14.7	2408	23	1.8	-118.1	-3.9	22.16	2.4	0.05883	6.09	0.3839	5.8	0.04944	2.2	0.07	592	237	310	14	306	33	52	101	310	14
JUA30-75.I	0.75	23741	225	1.5	-1499	-3.8	20.49	0.9	0.05935	3.04	0.4050	3.3	0.04937	1.0	0.08	364	120	310	6	334	15	85	93	310	6
JUA30-118	0.47	22147	200	1.3	-3369	-77	21.95	2.4	0.06343	4.18	0.4173	3.3	0.05013	4.0	0.00	499	118	313	22	346	18	63	91	313	22
JUA30-125	4.88	3935	37	2.0	-172.4	-6.2	21.15	2.0	0.06142	5.37	0.3886	4.7	0.05017	2.1	0.03	324	237	315	13	316	25	97	100	315	13
JUA30-5.FI	0.83	15769	133	2.2	-633.1	-3.1	20.43	1.1	0.05512	2.55	0.3764	2.3	0.05017	1.1	0.12	231	127	315	7	320	13	136	99	315	7
JUA30-148	-0.66	7144	64	2.4	-467.6	-12	20.83	2.1	0.05997	9.28	0.3890	6.4	0.05039	2.5	-0.02	137	227	316	15	308	26	231	103	316	15
JUA30-144	-0.17	23974	207	0.3	-1904	-4.4	20.27	1.4	0.05331	2.70	0.3770	2.5	0.05068	1.3	-0.15	311	124	318	8	323	14	102	99	318	8
JUA30-25.I	1.1	12461	111	1.5	-613.9	-5.3	20.29	1.4	0.05802	3.99	0.3867	3.4	0.05076	1.3	-0.06	288	172	319	8	322	19	111	99	319	8
JUA30-99.I	0.06	20984	189	2.4	-964.7	-2.9	20.17	1.2	0.05392	2.75	0.3726	2.5	0.05089	1.1	0.03	180	125	320	7	317	13	177	101	320	7
JUA30-64.I	-0.09	32199	305	1.5	-1473	-10	20.15	1.6	0.05268	3.33	0.3690	2.6	0.05101	1.7	-0.02	177	152	321	10	318	15	181	101	321	10
JUA30-131	0.4	30757	286	2.3	-1334	-4.7	20.12	1.4	0.05670	2.29	0.3976	2.0	0.05121	1.4	0.14	358	112	322	9	338	12	90	95	322	9
JUA30-22.I	-0.17	33734	296	1.0	-1608	-9.2	19.67	0.9	0.05333	1.74	0.3763	1.6	0.05132	0.9	0.05	281	82	322	6	323	9	115	100	322	6
JUA30-18.I	0.19	123226	1040	0.8	-8321	-4.6	19.63	0.9	0.05475	1.54	0.3851	1.3	0.05139	0.9	0.04	354	71	323	6	330	7	91	98	323	6
JUA30-149	0.37	24817	214	1.3	-1533	-2.5	19.84	1.1	0.05534	2.12	0.3904	2.0	0.05151	1.1	0.14	295	100	324	7	331	11	110	98	324	7
JUA30-57.I	0.56	21407	183	1.3	-1012	-2.8	19.67	0.9	0.05329	2.25	0.3798	2.0	0.05158	0.9	-0.09	234	104	324	6	324	11	139	100	324	6
JUA30-32.I	0.23	29667	251	1.4	-1310	-3.8	19.58	1.1	0.05395	2.23	0.3903	2.9	0.05170	1.1	0.48	255	99	325	7	326	12	127	100	325	7
JUA30-28.I	-0.15	5508	47	0.9	-480.1	-2.9	19.99	1.7	0.05535	4.29	0.3747	3.8	0.05174	1.7	-0.04	-1	219	325	10	312	21	-23284	104	325	10
JUA30-84.I	0.63	19694	174	2.3	-1725	-3	19.64	1.0	0.05400	2.48	0.3834	2.3	0.05178	1.0	0.00	199	125	325	6	327	13	163	100	325	6
JUA30-81.I	0.26	88382	771	1.0	-7146	-2.4	19.48	0.8	0.05378	1.60	0.3846	1.3	0.05207	0.8	-0.07	277	73	327	5	329	7	118	99	327	5
JUA30-119	-2.41	9490	86	2.6	-345.9	-8.3	19.78	1.6	0.05775	3.83	0.4049	3.4	0.05239	1.6	0.99	281	160	329	10	335	20	117	98	329	10
JUA30-63.I	-1.12	12927	110	1.7	-569.4	-2.7	19.67	1.5	0.05416	2.83	0.3903	2.8	0.05265	1.4	0.20	166	142	330	9	328	15	199	101	330	9
JUA30-90.I	-0.05	70939	614	0.6	-3145	-3.8	19.15	0.8	0.05242	1.65	0.3813	1.4	0.05266	0.9	0.63	252	69	331	6	327	7	131	101	331	6
JUA30-41.I	0.56	13244	113	1.8	-834.1	-8.6	19.51	1.3	0.05699	3.40	0.4097	3.2	0.05273	1.4	-0.06	316	151	331	9	342	19	105	97	331	9
JUA30-87.I	1.97	18475	158	2.0	-1201	-7.6	19.30	1.1	0.05378	2.76	0.3897	2.5	0.05281	1.1	0.01	131	133	332	7	329	14	254	101	332	7
JUA30-82.I	1.02	26523	231	1.5	-2592	-3.6	19.26	1.0	0.05329	2.32	0.3874	2.1	0.05281	1.0	0.01	227	100	332	6	329	12	146	101	332	6
JUA30-95.I	2.59	14386	126	2.2	-1132	-4	19.46	1.3	0.05486	3.31	0.3897	3.0	0.05288	1.2	0.03	137	146	332	8	327	16	243	101	332	8
JUA30-74.I	2.09	2215	19	2.8	-162.7	-3.9	20.54	2.8	0.07607	6.56	0.4995	5.8	0.05415	2.5	0.00	854	236	339	17	374	38	40	91	339	17
~~JUA30-132~~	~~0.69~~	~~11938~~	~~101~~	~~1.4~~	~~-439.2~~	~~-4.3~~	~~18.63~~	~~1.4~~	~~0.06576~~	~~3.27~~	~~0.4946~~	~~3.4~~	~~0.05481~~	~~1.3~~	~~0.51~~	~~596~~	~~144~~	~~345~~	~~9~~	~~396~~	~~21~~	~~58~~	~~87~~	~~345~~	~~9~~
~~JUA30-53.I~~	~~0.95~~	~~21360~~	~~187~~	~~0.9~~	~~-903.3~~	~~-4.7~~	~~18.87~~	~~1.3~~	~~0.06619~~	~~3.44~~	~~0.5327~~	~~4.2~~	~~0.05564~~	~~1.9~~	~~0.13~~	~~623~~	~~146~~	~~348~~	~~13~~	~~418~~	~~27~~	~~56~~	~~83~~	~~348~~	~~13~~
~~JUA30-24.I~~	~~3.31~~	~~46122~~	~~396~~	~~0.9~~	~~-2078~~	~~-6.1~~	~~18.20~~	~~1.1~~	~~0.07841~~	~~2.71~~	~~0.6137~~	~~2.9~~	~~0.05608~~	~~1.1~~	~~0.18~~	~~974~~	~~125~~	~~351~~	~~8~~	~~475~~	~~23~~	~~36~~	~~74~~	~~351~~	~~8~~
~~JUA30-94.I~~	~~6.97~~	~~30515~~	~~250~~	~~2.4~~	~~-2106~~	~~-5.4~~	~~18.57~~	~~1.6~~	~~0.12082~~	~~5.93~~	~~1.0879~~	~~8.0~~	~~0.05665~~	~~1.8~~	~~0.90~~	~~1332~~	~~197~~	~~355~~	~~13~~	~~654~~	~~71~~	~~27~~	~~54~~	~~355~~	~~13~~
JUA30-58.I	0.34	41609	321	0.5	-2238	-3.7	16.89	1.1	0.05586	1.84	0.4638	1.8	0.06017	1.0	0.12	361	78	377	8	384	11	104	98	377	8
~~JUA30-50.I~~	~~2.68~~	~~41158~~	~~259~~	~~2.2~~	~~-25545~~	~~-76~~	~~19.59~~	~~2.1~~	~~0.05398~~	~~2.87~~	~~0.3936~~	~~2.6~~	~~0.06449~~	~~13.4~~	~~-0.04~~	~~227~~	~~114~~	~~378~~	~~68~~	~~330~~	~~13~~	~~167~~	~~115~~	~~378~~	~~68~~
JUA30-122	121	455	4	2.4	-24.94	-12	8.38	83.3	0.01766	450.26	1.0937	21.6	0.06238	8.0	0.24	1989	611	382	59	375	207	19	102	382	59

JUA30-17.I	1.3	13523	89	0.8	-695.9	-3.2	15.65	1.6	0.06395	2.82	0.5785	2.9	0.06630	1.6	0.03	549	118	415	12	450	19	76	92	415	12
~~JUA30-139~~	~~2.58~~	~~8495~~	~~40~~	~~1.5~~	~~-60.84~~	~~-42~~	~~100.51~~	~~8.5~~	~~0.50225~~	~~6.23~~	~~7.3025~~	~~10.6~~	~~0.07512~~	~~10.2~~	~~0.89~~	~~3096~~	~~367~~	~~436~~	~~85~~	~~1325~~	~~195~~	~~14~~	~~33~~	~~436~~	~~85~~
JUA30-135	-0.49	10187	65	2.5	-419.6	-5.1	14.64	2.0	0.06548	3.96	0.6363	3.5	0.07093	2.1	0.04	626	180	441	18	490	29	70	90	441	18
JUA30-55.I	0.1	68934	435	0.9	-3306	-5.2	14.09	0.9	0.05562	1.52	0.5557	1.3	0.07222	0.9	0.05	380	70	449	8	447	9	118	101	449	8
JUA30-62.I	-0.1	10848	64	0.7	-692.5	-31	13.01	4.7	0.06667	5.51	0.8666	10.0	0.08297	3.1	0.73	621	187	512	30	577	57	83	89	512	30
JUA30-59.I	0.51	84444	431	0.8	-5434	-4.8	11.46	0.8	0.05872	1.44	0.7237	1.3	0.08854	0.9	0.04	503	65	547	9	550	11	109	99	547	9
JUA30-15.I	-1.1	15852	76	2.7	-604.3	-2.7	11.21	1.2	0.05793	2.38	0.7224	2.2	0.09100	1.1	0.07	374	119	561	12	545	19	150	103	561	12
JUA30-101	1.89	33600	167	0.3	-1421	-5	10.85	1.2	0.06996	2.42	0.9074	2.3	0.09391	1.2	0.05	793	100	578	13	646	21	73	89	578	13
JUA30-38.I	0.96	20973	97	1.7	-1554	-5.9	10.29	1.1	0.06146	2.26	0.8246	2.1	0.09897	1.1	0.08	532	103	608	13	601	19	114	101	608	13
~~JUA30-72.I~~	~~2.59~~	~~191139~~	~~886~~	~~1.0~~	~~-5193~~	~~-12~~	~~10.34~~	~~1.6~~	~~0.12374~~	~~1.34~~	~~1.7360~~	~~1.7~~	~~0.10103~~	~~1.5~~	~~0.67~~	~~1986~~	~~49~~	~~619~~	~~18~~	~~1011~~	~~22~~	~~31~~	~~61~~	~~619~~	~~18~~
JUA30-35.I	0.36	52291	226	0.4	-3334	-2.8	9.85	1.0	0.06314	1.57	0.8944	1.4	0.10300	1.0	0.17	656	69	631	12	644	13	96	98	631	12
~~JUA30-124~~	~~5.06~~	~~70560~~	~~308~~	~~2.3~~	~~-1323~~	~~-10~~	~~9.76~~	~~1.2~~	~~0.10299~~	~~1.80~~	~~1.5019~~	~~1.9~~	~~0.10469~~	~~1.1~~	~~0.26~~	~~1637~~	~~73~~	~~641~~	~~14~~	~~920~~	~~23~~	~~39~~	~~70~~	~~641~~	~~14~~
JUA30-120	1.32	21148	97	1.6	-725	-4	9.55	1.0	0.06336	2.27	0.9292	2.1	0.10693	1.1	-0.01	606	107	654	13	659	20	108	99	654	13
JUA30-12.I	-0.2	97548	368	0.8	-3763	-5.6	9.69	2.8	0.07402	1.80	1.1432	2.6	0.11104	2.3	0.71	999	75	676	30	760	29	68	89	676	30
JUA30-91.I	0.26	15134	56	0.6	-894.5	-4.8	8.59	1.8	0.07223	2.95	1.1887	2.8	0.12153	1.6	0.27	853	122	738	22	772	33	86	96	738	22
JUA30-136	-0.91	32883	118	0.8	-1637	-4.5	8.32	2.0	0.07144	2.32	1.2500	2.7	0.12505	1.9	0.53	925	106	758	27	812	30	82	93	758	27
JUA30-126	-0.09	92677	376	0.4	-2911	-4.8	8.12	2.1	0.07699	1.31	1.3513	1.9	0.12905	1.9	0.72	1073	53	779	28	857	23	73	91	779	28
~~JUA30-130~~	~~0.78~~	~~126515~~	~~705~~	~~1.1~~	~~-3603~~	~~-5.2~~	~~13.40~~	~~9.0~~	~~0.10119~~	~~1.24~~	~~1.7824~~	~~3.6~~	~~0.13316~~	~~3.8~~	~~0.92~~	~~1610~~	~~44~~	~~792~~	~~58~~	~~980~~	~~53~~	~~49~~	~~81~~	~~792~~	~~58~~
JUA30-83.I	1.42	30524	102	0.5	-3123	-3.6	7.50	0.9	0.06640	1.66	1.2380	1.5	0.13591	1.0	-0.08	774	70	821	15	816	17	106	101	821	15
JUA30-109	0.01	38512	123	1.2	-2042	-2.1	7.25	0.9	0.07192	1.73	1.3929	1.6	0.13997	0.9	0.15	930	70	844	14	879	19	91	96	844	14
JUA30-45.I	0.63	42894	142	3.2	-3831	-4.7	7.38	1.4	0.07434	1.98	1.4169	1.9	0.14022	1.3	0.09	953	79	844	20	890	21	89	95	844	20
JUA30-14.I	1.14	77969	243	0.5	-12296	-77	7.07	2.1	0.07320	1.73	1.4688	2.4	0.14595	2.0	-0.06	970	72	876	34	905	30	90	97	876	34
JUA30-33.I	0.15	320274	951	3.2	-12760	-4.2	6.80	1.1	0.07751	1.20	1.6057	1.2	0.15057	1.1	0.40	1110	50	903	19	970	15	81	93	903	19
JUA30-89.I	-0.49	13478	39	1.8	-621.8	-3.5	6.78	1.4	0.07212	2.82	1.4928	2.6	0.15334	1.3	-0.19	791	122	918	23	902	32	116	102	918	23
JUA30-31.I	-0.02	74520	215	0.7	-3530	-3.6	6.52	0.8	0.07149	1.28	1.5266	1.2	0.15560	0.7	0.29	929	54	932	12	938	14	100	99	932	12
JUA30-134	0.52	20477	60	0.7	-750.5	-3.3	6.57	1.3	0.07325	2.38	1.5812	2.4	0.15682	1.2	0.20	900	100	937	21	946	28	104	99	937	21
JUA30-133	-0.03	49921	140	1.3	-1754	-3.6	6.54	1.4	0.07377	1.53	1.6058	1.6	0.15717	1.3	0.46	981	64	939	23	967	19	96	97	939	23
JUA30-106	0.2	6636	20	0.6	-310.7	-5.2	6.49	1.8	0.07427	4.36	1.5970	4.0	0.15841	1.9	0.09	848	191	949	35	952	49	112	100	949	35
~~JUA30-108~~	~~1.2~~	~~64758~~	~~178~~	~~1.1~~	~~-2700~~	~~-5.3~~	~~6.66~~	~~2.1~~	~~0.09868~~	~~1.47~~	~~2.1479~~	~~2.0~~	~~0.16007~~	~~2.0~~	~~0.44~~	~~1549~~	~~56~~	~~952~~	~~36~~	~~1153~~	~~27~~	~~61~~	~~83~~	~~952~~	~~36~~
JUA30-61.I	0.25	101843	285	0.3	-5526	-3.1	6.39	1.0	0.07215	1.21	1.5994	1.2	0.15962	1.0	0.33	968	55	955	18	969	16	99	99	955	18
JUA30-147	0.01	101817	275	0.5	-6078	-3.5	6.23	1.0	0.07517	1.47	1.6875	1.4	0.16243	1.0	0.23	1011	61	969	18	996	17	96	97	969	18
JUA30-142	0.4	38885	108	2.1	-3164	-3.4	6.21	0.9	0.07745	1.77	1.7306	1.4	0.16241	0.9	-0.04	1056	72	969	16	1013	19	92	96	969	16
JUA30-6.FI	-1.05	31809	87	0.6	-1390	-5.7	6.21	1.4	0.07353	2.84	1.6469	2.3	0.16327	1.3	0.42	933	120	974	24	977	30	104	100	974	24
JUA30-115	1.84	11274	33	0.7	-525.5	-4.5	6.30	1.7	0.07492	2.78	1.6608	2.6	0.16436	1.6	0.18	897	124	978	29	973	35	109	101	978	29
JUA30-105	0.23	49824	136	0.7	-2502	-3.5	6.17	1.0	0.07828	1.78	1.7569	1.5	0.16407	1.0	0.09	1067	72	978	18	1020	19	92	96	978	18
JUA30-27.I	0.33	80426	214	1.4	-6509	-3.2	6.17	1.0	0.07353	1.47	1.6644	1.3	0.16451	0.9	0.20	995	62	981	17	990	17	99	99	981	17
JUA30-88.I	0.13	40957	113	0.6	-2070	-4.3	6.14	1.0	0.07514	1.78	1.7042	1.5	0.16506	1.0	0.07	1005	75	983	18	1009	20	98	98	983	18
JUA30-9.FI	3.59	11880	30	0.9	-5114	-87	6.46	1.1	0.07412	2.79	1.6349	2.6	0.16732	3.4	0.02	904	116	985	52	957	32	109	103	985	52
JUA30-140	0.17	31413	86	0.4	-1522	-3.6	6.08	1.0	0.07371	2.08	1.6917	1.9	0.16627	1.1	0.13	976	86	990	20	1000	23	101	99	990	20
JUA30-7.FI	0.03	27688	70	1.4	-1286	-2.8	6.08	1.1	0.07307	1.74	1.6886	1.6	0.16735	1.0	0.25	951	74	996	18	996	21	105	100	996	18
JUA30-78.I	0.79	15392	42	0.6	-632.1	-5	6.02	1.2	0.07294	2.52	1.6985	2.4	0.16905	1.2	0.11	908	109	1005	22	996	31	111	101	1005	22
JUA30-11.I	-1.44	11111	28	1.2	-450.5	-3.7	6.13	1.4	0.07516	2.78	1.7459	2.6	0.17197	2.2	0.64	879	130	1005	28	997	33	114	101	1005	28
JUA30-112	0.19	234980	641	0.3	-18635	-4.1	5.96	0.8	0.07573	1.20	1.7548	0.9	0.16909	0.7	0.02	1049	48	1006	13	1029	12	96	98	1006	13
JUA30-116	0.51	152847	429	0.7	-5355	-5.2	6.00	0.9	0.07597	1.40	1.7625	1.1	0.16943	0.9	0.02	1049	57	1008	16	1028	15	96	98	1008	16
JUA30-52.I	-0.2	97609	265	0.6	-4241	-3.1	5.96	0.8	0.07301	1.36	1.7233	1.1	0.16985	0.8	0.12	986	60	1010	16	1012	15	102	100	1010	16
JUA30-65.I	-0.1	73074	202	0.4	-3544	-7.9	5.92	1.1	0.07365	1.66	1.7446	1.6	0.17126	0.9	0.03	953	63	1018	17	1015	20	107	100	1018	17
JUA30-97.I	1.15	132357	359	0.2	-6391	-4.1	5.89	1.2	0.07482	3.28	1.7408	1.3	0.17145	1.1	-0.15	971	54	1018	21	1017	16	105	100	1018	21
JUA30-20.I	3.84	10599	28	1.2	-820.8	-6	5.97	1.3	0.07215	2.62	1.6906	2.4	0.17248	1.4	0.01	834	121	1023	26	984	31	123	104	1023	26
JUA30-43.I	0.08	54043	142	0.7	-3323	-2.7	5.87	1.0	0.07490	1.69	1.7759	1.4	0.17251	1.0	0.09	1010	70	1025	19	1031	19	101	99	1025	19
JUA30-2.FI	3.79	8357	21	1.2	-331.8	-6.2	5.97	1.6	0.07556	3.23	1.7776	3.0	0.17516	1.9	0.09	915	137	1036	35	1010	41	113	103	1036	35
JUA30-39.I	0.89	14390	38	1.1	-935	-3.8	5.76	1.2	0.07316	2.43	1.7441	2.2	0.17524	1.2	0.09	875	105	1039	23	1010	29	119	103	1039	23
JUA30-104	-0.04	320239	890	0.3	-15819	-5.2	5.78	0.9	0.07362	1.22	1.7802	1.0	0.17526	0.9	0.24	993	51	1040	17	1035	13	105	100	1040	17
JUA30-47.I	0.11	105732	284	0.6	-8655	-4.5	5.82	1.1	0.07597	1.64	1.8185	1.4	0.17558	0.9	-0.36	1037	63	1042	17	1044	17	100	100	1042	17
JUA30-36.I	0.27	158962	405	0.2	-15152	-3.2	5.75	0.8	0.07497	1.37	1.8034	1.0	0.17605	0.8	-0.04	1016	55	1044	15	1044	13	103	100	1044	15
JUA30-8.FI	0.36	89939	222	0.9	-4626	-5.4	5.70	0.9	0.07631	1.42	1.8558	1.1	0.17717	0.9	0.02	1050	55	1052	17	1060	14	100	99	1052	17
JUA30-127	-0.07	209406	571	0.8	-6117	-3.9	5.71	1.0	0.07502	1.23	1.8198	0.9	0.17771	0.9	0.24	1032	49	1053	17	1051	13	102	100	1053	17
JUA30-113	0.04	107627	281	0.6	-6665	-3.8	5.61	0.9	0.07566	1.51	1.8478	1.1	0.17936	0.9	0.03	1037	59	1062	17	1057	15	102	101	1062	17
JUA30-123	0.53	133285	361	0.5	-6180	-7	5.51	1.0	0.07933	1.65	1.9721	1.4	0.18035	1.0	0.30	1141	66	1071	20	1104	19	94	97	1071	20

JUA30-150	0.73	166336	458	0.8	-9319	-7.8	5.57	0.9	0.07764	1.47	1.9236	1.2	0.18128	0.9	0.11	1092	57	1073	18	1090	16	98	98	1073	18
JUA30-60.I	0.15	59907	150	0.3	-4689	-2.8	5.64	1.4	0.07671	1.77	1.9222	2.0	0.18143	1.1	0.32	1042	68	1076	21	1073	19	103	100	1076	21
JUA30-21.I	0.36	115827	293	0.5	-4430	-5.8	5.50	0.8	0.07646	1.27	1.9232	1.1	0.18380	0.8	0.22	1067	53	1089	16	1089	15	102	100	1089	16
JUA30-141	0.27	136664	350	0.4	-9729	-8.9	5.46	1.2	0.07336	1.40	1.9093	1.6	0.18683	1.3	0.42	1001	58	1103	27	1078	20	110	102	1103	27
JUA30-37.I	0.21	290058	694	0.1	-23734	-3.3	5.40	0.8	0.07714	1.24	1.9856	1.0	0.18642	0.8	-0.03	1092	52	1104	17	1108	13	101	100	1104	17
JUA30-137	5.45	3926	10	0.9	-248.7	-19	6.00	3.1	0.09517	5.20	2.3584	5.1	0.19060	3.0	0.32	1113	236	1111	57	1111	76	100	100	1111	57
JUA30-54.I	0.16	116264	298	0.9	-5171	-5.6	5.34	1.0	0.07721	1.55	2.0176	1.3	0.18965	1.0	0.20	1073	63	1120	21	1113	18	104	101	1120	21
JUA30-49.I	0.21	123922	293	0.7	-8850	-3.3	5.29	1.2	0.08429	1.27	2.2713	1.4	0.19381	1.1	0.68	1277	49	1140	23	1195	20	89	95	1140	23
JUA30-42.I	0.38	21791	48	0.7	-1801	-33	5.46	2.5	0.08874	3.82	2.4417	5.7	0.20340	3.5	0.01	1186	108	1142	41	1152	38	96	99	1142	41
JUA30-73.I	0.43	633449	1615	0.7	-44863	-4.6	5.12	1.1	0.08146	1.20	2.1979	1.4	0.19601	1.1	0.58	1190	43	1152	23	1167	19	97	99	1152	23
JUA30-143	3.53	9667	24	0.9	-888	-4.4	5.58	5.0	0.08757	3.42	2.3087	3.0	0.19771	2.0	0.10	1157	131	1156	42	1168	43	100	99	1156	42
JUA30-85.I	0.24	160472	356	0.8	-11405	-4.6	5.05	0.9	0.08226	1.38	2.2662	1.4	0.20080	0.9	0.45	1210	52	1180	19	1193	18	98	99	1180	19
JUA30-138	0.45	105377	242	0.9	-4990	-8.7	5.10	1.6	0.10045	1.72	2.8489	1.9	0.20415	1.6	0.68	1596	65	1193	34	1351	27	75	88	1193	34
JUA30-67.I	0.1	32864	75	1.0	-1099	-3.6	5.02	1.5	0.07967	2.18	2.2120	1.6	0.20686	1.1	0.23	1082	69	1210	25	1175	22	112	103	1210	25
JUA30-46.I	0.41	54515	120	1.3	-5000	-2.5	4.85	0.9	0.08253	1.61	2.3603	1.3	0.20873	0.9	0.02	1197	62	1220	20	1222	19	102	100	1220	20
JUA30-79.I	0.79	67454	163	1.1	-2816	-5.7	4.88	1.2	0.07914	1.65	2.2899	1.7	0.21030	1.3	0.26	1115	65	1223	27	1195	23	110	102	1223	27
JUA30-111	0.1	187209	401	0.6	-23629	-2.8	4.81	0.8	0.08179	0.77	2.3793	0.9	0.21006	0.8	0.56	1224	30	1228	17	1234	12	100	100	1228	17
~~JUA30-80.I~~	~~3.24~~	~~31599~~	~~64~~	~~3.3~~	~~-1107~~	~~-6.8~~	~~5.35~~	~~5.7~~	~~0.13586~~	~~2.74~~	~~4.2428~~	~~4.4~~	~~0.22214~~	~~3.2~~	~~0.58~~	~~2117~~	~~90~~	~~1256~~	~~57~~	~~1593~~	~~64~~	~~59~~	~~79~~	~~1256~~	~~57~~
JUA30-71.I	0.41	90054	191	0.6	-7263	-2.8	4.66	0.9	0.08190	1.51	2.4435	1.2	0.21665	0.8	0.02	1188	59	1263	19	1252	17	106	101	1263	19
JUA30-129	0.19	40656	89	1.1	-1269	-3.9	4.64	1.0	0.08424	1.83	2.5148	1.8	0.21907	0.9	0.08	1228	67	1275	21	1264	24	104	101	1275	21
JUA30-66.I	0.03	232955	465	1.4	-8460	-3.1	4.45	0.9	0.08544	1.18	2.6808	1.0	0.22635	0.8	0.25	1310	46	1314	19	1321	15	100	99	1314	19
JUA30-96.I	0.9	45628	89	0.9	-2351	-6	4.50	1.4	0.09155	1.96	2.8738	1.8	0.22768	1.5	0.08	1387	82	1319	36	1363	27	95	97	1319	36
~~JUA30-110~~	~~1.68~~	~~98499~~	~~206~~	~~2.9~~	~~-3688~~	~~-8.7~~	~~4.53~~	~~2.5~~	~~0.12188~~	~~2.12~~	~~3.8068~~	~~2.1~~	~~0.23260~~	~~2.5~~	~~0.54~~	~~1931~~	~~78~~	~~1341~~	~~61~~	~~1580~~	~~34~~	~~69~~	~~85~~	~~1341~~	~~61~~
~~JUA30-70.I~~	~~-0.18~~	~~27645~~	~~55~~	~~2.4~~	~~-1269~~	~~-3~~	~~4.37~~	~~1.5~~	~~0.08597~~	~~2.20~~	~~2.7627~~	~~2.0~~	~~0.23423~~	~~1.3~~	~~0.02~~	~~1243~~	~~83~~	~~1358~~	~~31~~	~~1324~~	~~29~~	~~109~~	~~103~~	~~1358~~	~~31~~
JUA30-19.I	0.15	66886	128	0.9	-5677	-2.7	4.31	1.0	0.09072	1.56	2.8980	1.2	0.23538	1.0	0.05	1379	60	1360	24	1373	18	99	99	1360	24
JUA30-86.I	0.44	41113	79	1.1	-2823	-2.9	4.36	1.4	0.08619	1.82	2.7877	1.5	0.23710	1.0	0.25	1255	72	1369	26	1339	23	109	102	1369	26
~~JUA30-48.I~~	~~0.87~~	~~79135~~	~~177~~	~~1.1~~	~~-4990~~	~~-4.7~~	~~4.44~~	~~2.0~~	~~0.11140~~	~~1.19~~	~~3.6381~~	~~1.6~~	~~0.23822~~	~~1.8~~	~~0.76~~	~~1789~~	~~43~~	~~1374~~	~~45~~	~~1540~~	~~26~~	~~77~~	~~89~~	~~1374~~	~~45~~
JUA30-146	0.33	172055	325	0.4	-9229	-4.5	4.12	1.2	0.09241	1.40	3.1372	1.3	0.24831	1.0	0.12	1427	53	1427	26	1431	21	100	100	1427	26
JUA30-114	0	72259	131	0.9	-3846	-2.8	4.01	1.0	0.09399	1.55	3.2436	1.4	0.25208	1.0	0.25	1452	62	1449	26	1455	22	100	100	1449	26
JUA30-44.I	0.17	87483	151	0.8	-6251	-2.9	3.91	1.5	0.09263	1.79	3.3704	1.9	0.26135	1.4	0.35	1419	69	1492	39	1480	31	105	101	1492	39
JUA30-3.FI	0.05	317557	524	0.8	-13703	-4.4	3.85	0.6	0.09271	0.86	3.3510	0.7	0.26099	0.6	0.04	1463	33	1494	16	1493	11	102	100	1494	16
JUA30-102	0.27	70491	110	2.2	-3244	-4.2	3.40	1.0	0.11234	1.34	4.6160	1.2	0.29933	1.0	0.34	1796	48	1688	30	1744	20	94	97	1796	48
JUA30-117	0.09	72647	99	1.6	-2575	-3.3	2.94	0.9	0.11469	1.47	5.3605	1.1	0.34291	0.9	0.08	1836	53	1904	30	1875	20	104	102	1836	53
~~JUA30-92.I~~	~~0.11~~	~~182750~~	~~266~~	~~0.4~~	~~-13531~~	~~-3.6~~	~~3.23~~	~~0.8~~	~~0.12505~~	~~1.08~~	~~5.4411~~	~~0.9~~	~~0.31281~~	~~0.8~~	~~0.08~~	~~2011~~	~~38~~	~~1752~~	~~24~~	~~1885~~	~~15~~	~~87~~	~~93~~	~~2011~~	~~38~~
JUA30-23.I	0.72	85490	121	1.9	-3861	-4.7	3.10	1.2	0.12678	1.55	5.7634	1.6	0.32842	1.3	0.32	2033	59	1827	40	1929	27	90	95	2033	59
JUA30-34.I	0.08	41806	48	1.2	-2139	-4.6	2.60	1.7	0.12782	1.57	7.0016	1.2	0.38873	1.2	0.24	2034	56	2128	39	2099	22	105	101	2034	56
~~JUA30-145~~	~~15.1~~	~~9455~~	~~13~~	~~1.6~~	~~-686.1~~	~~-8.3~~	~~2.75~~	~~3.9~~	~~0.14956~~	~~8.18~~	~~4.1459~~	~~63.3~~	~~0.43425~~	~~8.6~~	~~0.77~~	~~2084~~	~~162~~	~~2254~~	~~227~~	~~2039~~	~~80~~	~~108~~	~~111~~	~~2084~~	~~162~~
~~JUA30-69.I~~	~~-545~~	~~11279~~	~~34~~	~~0.0~~	~~-544.7~~	~~-48~~	~~#####~~	~~-58.6~~	~~-0.23364~~	~~-110.63~~	~~######~~	~~-48.7~~	~~#######~~	~~-49.4~~	~~0.00~~	~~3623~~	~~425~~	~~7989~~	~~1433~~	~~3944~~	~~629~~	~~220~~	~~203~~	~~3623~~	~~425~~
~~JUA30-56.I~~	~~-334~~	~~87~~	~~0~~	~~0.1~~	~~-11.79~~	~~-67~~	~~8.80~~	~~15.0~~	~~-0.26113~~	~~-56.30~~	~~-7.5232~~	~~-65.9~~	~~-0.11939~~	~~-26.6~~	~~0.35~~	~~4107~~	~~214~~	~~-519~~	~~201~~	~~1623~~	~~79~~	~~-13~~	~~-32~~	-519	201
~~JUA30-16.I~~	~~-130~~	~~5821~~	~~17~~	~~0.0~~	~~-205.4~~	~~-41~~	~~19.44~~	~~266.2~~	~~-0.57929~~	~~-66.71~~	~~######~~	~~-36.0~~	~~-1.37204~~	~~-46.0~~	~~0.09~~	~~4283~~	~~294~~	~~-163~~	~~239~~	~~1594~~	~~152~~	~~-4~~	~~-10~~	-163	239
~~JUA30-26.I~~	~~70.5~~	~~235~~	~~0~~	~~0.1~~	~~-16.52~~	~~-16~~	~~5.94~~	~~18.8~~	~~-0.05067~~	~~-204.15~~	~~-7.9082~~	~~-44.6~~	~~-0.09709~~	~~-61.3~~	~~0.27~~	~~3766~~	~~222~~	~~-133~~	~~282~~	~~2073~~	~~174~~	~~-4~~	~~-6~~	-133	282

U-Pb data from JUA 31 (TAR31 – Stutz et al., 2022)

Instituto de Geociencias, Universidade de Brasilia							Data for Tera-Wasserburg plot				Data for Wetherill plot					Dates						Conc (%)	Conc (%)	Idade Preferida	2s abs
Identifier	f206c	206Pb	Uppm	Th/U	06Pb/204P	1s%	238U/206Pb	1s%	207Pb/206Pb	1s%	207Pb/235U	1s%	206Pb/238U	1s%	Rho	207Pb/206Pb	2s (abs)	206Pb/238U	2s (abs)	207Pb/235U	2s (abs)	6/8 -7/6	6/8 -7/5		
TAR31	8.936	2387	123	0.7	57.85559	141.761	377.42	1.1	0.04907	4.95	0.0180	5.7	0.00265	1.2	0.76	365	166	17	0	18	2	5	94	17	0
TAR32	66.124	1069	699	1.4	36.74331	42.1043	377.53	2.3	0.04593	10.56	0.0169	10.4	0.00272	2.2	0.06	1120	253	18	1	17	4	2	103	18	1
TAR33	4.8125	6526	368	0.9	403.4493	44.8467	364.71	1.0	0.05242	3.57	0.0198	3.9	0.00274	1.0	0.35	290	149	18	0	20	2	6	89	18	0
TAR34	3.6137	7037	247	0.8	185.7906	114.159	248.31	1.2	0.05062	4.33	0.0282	5.4	0.00403	1.2	0.81	249	174	26	1	28	3	10	92	26	1
TAR35	1.4184	9107	256	1.3	570.5956	95.0718	197.82	0.7	0.04672	1.70	0.0326	1.7	0.00506	0.7	0.21	104	51	33	0	33	1	31	100	33	0
TAR36	4.4402	3757	105	0.6	60.17954	216.436	184.00	1.2	0.04544	4.46	0.0340	4.7	0.00544	1.3	0.37	172	153	35	1	34	3	20	103	35	1
TAR37	0.226	13201	292	0.8	3944.946	57.0154	158.78	0.9	0.04533	1.11	0.0394	1.5	0.00630	0.9	0.68	75	50	40	1	39	1	54	103	40	1
TAR38	0.1037	8233	167	0.9	1252.372	172.545	146.67	0.6	0.04572	2.16	0.0430	2.2	0.00682	0.6	0.22	106	63	44	1	43	2	41	102	44	1
TAR39	0.4422	15365	331	1.0	532.8871	149.85	140.98	2.2	0.04670	2.09	0.0458	3.6	0.00712	2.2	0.86	119	54	46	2	45	3	39	101	46	2
TAR40	20.108	2176	510	1.1	75.62603	62.5097	132.06	1.9	0.05117	9.27	0.0496	8.2	0.00765	2.1	0.09	970	271	49	2	49	8	5	101	49	2
TAR41	~~17.865~~	~~9043~~	~~184~~	~~3.1~~	~~145.8633~~	~~31.5472~~	~~141.93~~	~~10.1~~	~~0.25883~~	~~24.40~~	~~0.3269~~	~~33.5~~	~~0.00768~~	~~12.0~~	~~1.00~~	~~2646~~	~~1137~~	~~49~~	~~12~~	~~265~~	~~159~~	~~2~~	~~19~~	~~49~~	~~12~~
TAR42	~~43.728~~	~~347~~	~~80~~	~~3.1~~	~~6.422897~~	~~44.2111~~	~~146.39~~	~~5.0~~	~~-0.04897~~	~~-29.75~~	~~-0.0560~~	~~-29.0~~	~~0.00773~~	~~4.9~~	~~0.10~~	~~1420~~	~~560~~	~~50~~	~~5~~	~~-56~~	~~30~~	~~3~~	~~-89~~	~~50~~	~~5~~
TAR43	0.046	29347	285	1.2	18352.42	102.673	70.83	0.8	0.04786	0.80	0.0932	0.6	0.01412	0.8	0.28	106	27	90	1	90	1	86	100	90	1
TAR44	~~4.9527~~	~~4611~~	~~373~~	~~0.5~~	~~117.0292~~	~~57.8536~~	~~50.08~~	~~4.4~~	~~0.06782~~	~~4.10~~	~~0.2028~~	~~5.9~~	~~0.02147~~	~~4.5~~	~~0.80~~	~~914~~	~~127~~	~~137~~	~~12~~	~~186~~	~~20~~	~~15~~	~~74~~	~~137~~	~~12~~
TAR45	~~2.9072~~	~~66058~~	~~316~~	~~1.5~~	~~450.594~~	~~458.746~~	~~31.99~~	~~2.4~~	~~0.07604~~	~~17.84~~	~~0.3399~~	~~20.9~~	~~0.03141~~	~~2.5~~	~~0.94~~	~~840~~	~~583~~	~~199~~	~~10~~	~~287~~	~~99~~	~~24~~	~~70~~	~~199~~	~~10~~
TAR46	0.1835	29296	106	2.6	126.8403	3311.89	24.78	0.8	0.05112	0.97	0.2843	1.2	0.04038	0.8	0.62	244	45	255	4	254	6	105	100	255	4
TAR47	0.3684	33637	110	1.9	10049.19	63.2931	22.36	0.6	0.05173	0.83	0.3188	1.0	0.04474	0.6	0.61	271	38	282	3	281	5	104	100	282	3
TAR48	0.0618	36969	116	1.3	2744.38	181.827	21.76	0.8	0.05276	0.95	0.3342	1.1	0.04598	0.8	0.53	317	43	290	5	293	6	92	99	290	5
TAR49	0.0245	76966	241	1.5	4183.042	87.2017	21.75	0.4	0.05194	0.83	0.3292	0.7	0.04598	0.4	0.09	281	37	290	3	289	4	103	100	290	3
TAR50	0.2246	110969	351	1.1	1725.435	484.401	20.86	0.6	0.05197	0.66	0.3433	0.8	0.04796	0.6	0.60	282	31	302	4	300	4	107	101	302	4
TAR51	0.3508	103061	307	1.0	10741.45	114.71	19.22	2.0	0.05673	1.44	0.4062	0.9	0.05216	1.9	0.71	478	63	328	12	346	5	69	95	328	12
TAR52	0.7062	22591	67	1.5	80.73093	777.284	19.14	0.5	0.05846	3.23	0.4203	3.5	0.05226	0.5	0.50	535	141	328	3	356	21	61	92	328	3
TAR53	0.1727	57705	150	1.4	6178.8	56.0482	18.83	0.8	0.05309	0.63	0.3890	0.8	0.05314	0.8	0.68	331	28	334	5	334	5	101	100	334	5
TAR54	0.4983	37895	110	1.1	3.192885	73219.1	18.78	0.6	0.05343	1.08	0.3913	1.2	0.05326	0.6	0.38	345	50	334	4	335	7	97	100	334	4
TAR55	0.3794	77237	201	1.4	11515.71	131.993	18.64	0.8	0.05281	0.28	0.3909	0.9	0.05367	0.8	0.97	320	13	337	5	335	5	105	101	337	5
TAR56	1.1105	18687	54	1.9	2378.731	122.053	18.58	0.6	0.05114	1.08	0.3785	1.0	0.05382	0.6	0.08	245	50	338	4	326	5	138	104	338	4
TAR57	0.6706	107406	310	1.7	43099.67	91.6315	18.41	0.8	0.05748	3.86	0.4300	4.4	0.05435	0.8	0.62	497	158	341	5	363	26	69	94	341	5
TAR58	9.8081	6240	206	3.0	126.0904	53.6758	18.32	1.3	0.05417	2.73	0.4088	2.4	0.05504	1.3	0.06	483	111	345	9	347	14	71	100	345	9
TAR59	0.6814	26429	49	1.6	2781.615	96.0042	12.81	0.8	0.06074	4.44	0.6545	5.2	0.07812	0.8	0.93	611	176	485	7	510	40	79	95	485	7
TAR60	0.2032	140479	251	0.2	5634.73	100.659	12.75	0.7	0.05636	0.50	0.6097	1.0	0.07846	0.7	0.87	465	22	487	7	483	7	105	101	487	7
TAR61	1.1717	81602	151	0.2	10099.87	83.7379	12.72	2.0	0.06950	11.54	0.7479	10.5	0.07883	1.8	0.43	810	402	489	17	560	85	60	87	489	17
TAR62	~~12.75~~	~~13941~~	~~305~~	~~0.3~~	~~412.5479~~	~~47.2846~~	~~13.17~~	~~4.5~~	~~0.14639~~	~~2.94~~	~~1.5895~~	~~2.1~~	~~0.08018~~	~~3.8~~	~~0.53~~	~~2302~~	~~116~~	~~496~~	~~37~~	~~963~~	~~26~~	~~22~~	~~52~~	~~496~~	~~37~~
TAR63	0.6425	28042	49	0.9	442.6249	1073.8	12.46	1.0	0.05694	0.56	0.6307	1.1	0.08034	1.0	0.87	488	25	498	10	496	9	102	100	498	10
TAR64	0.3497	79929	146	0.9	3459.159	42.5912	12.37	0.4	0.05702	0.66	0.6349	0.5	0.08086	0.4	0.05	491	29	501	4	499	4	102	100	501	4
TAR65	0.0168	46581	83	0.4	1985.398	164.666	12.32	1.1	0.05744	0.44	0.6431	1.0	0.08125	1.1	0.90	507	19	504	11	504	8	99	100	504	11
TAR66	3.6648	4332	92	1.6	36.32843	104.403	11.96	1.1	0.05639	3.50	0.6500	3.4	0.08371	1.2	0.17	671	127	518	12	510	30	77	102	518	12
TAR67	~~1.054~~	~~126458~~	~~219~~	~~1.2~~	~~15752.08~~	~~76.5015~~	~~11.42~~	~~0.7~~	~~0.06966~~	~~4.81~~	~~0.8411~~	~~5.5~~	~~0.08759~~	~~0.7~~	~~0.94~~	~~898~~	~~178~~	~~541~~	~~7~~	~~618~~	~~49~~	~~60~~	~~88~~	~~541~~	~~7~~
TAR68	0.1655	44037	71	2.1	3292.129	235.723	11.09	0.5	0.05815	0.68	0.7223	1.0	0.09015	0.5	0.82	534	30	556	5	552	9	104	101	556	5
TAR69	0.0571	190887	308	1.0	12794.68	63.9093	10.76	0.5	0.05870	0.33	0.7508	0.6	0.09293	0.5	0.83	555	15	573	5	569	5	103	101	573	5
TAR70	0.6461	14430	269	0.4	46.09995	148.522	10.65	1.3	0.05818	1.86	0.7573	2.0	0.09470	1.3	0.29	556	69	583	15	571	17	105	102	583	15
TAR71	0.2809	90647	136	0.4	7616.265	119.725	10.50	1.9	0.06934	1.34	0.9140	3.4	0.09545	2.0	0.99	906	54	588	22	658	32	65	89	588	22
TAR72	4.2767	16338	288	1.2	140.8579	59.2458	10.01	1.2	0.06136	1.77	0.8482	1.9	0.10069	1.2	0.17	658	78	618	14	622	18	94	99	618	14
TAR73	~~0.487~~	~~1257~~	~~24~~	~~3.5~~	~~145.2672~~	~~73.9904~~	~~10.21~~	~~2.7~~	~~0.05495~~	~~8.93~~	~~0.7233~~	~~8.6~~	~~0.10158~~	~~2.6~~	~~0.19~~	~~1218~~	~~258~~	~~623~~	~~31~~	~~534~~	~~84~~	~~51~~	~~117~~	~~623~~	~~31~~
TAR74	23.861	2412	44	1.1	44.44032	122.105	9.82	2.6	0.06151	5.62	0.8786	6.1	0.10446	2.6	0.07	859	165	639	32	619	58	74	103	639	32
TAR75	0.0257	289589	393	2.1	23618.8	129.431	9.43	0.7	0.06162	0.35	0.9002	0.6	0.10610	0.7	0.83	660	15	650	9	652	6	98	100	650	9
TAR76	2.2488	67347	85	1.9	3706.693	39.195	9.20	1.0	0.07882	11.82	1.1937	12.9	0.10882	1.0	0.85	1042	384	666	13	778	127	64	86	666	13
TAR77	6.3353	5749	91	0.2	24.12111	108.871	8.92	3.6	0.07838	4.21	1.3803	7.3	0.11992	3.7	0.68	1116	163	728	51	837	84	65	87	728	51
TAR78	1.8075	207086	240	1.7	2292.208	26.3212	7.85	3.4	0.08214	6.52	1.4308	2.9	0.12851	3.1	0.96	1210	234	779	46	901	34	64	86	779	46
TAR79	0.059	250920	275	0.7	8285.899	67.3296	7.20	0.7	0.06647	0.45	1.2700	1.0	0.13886	0.7	0.89	820	19	838	11	832	11	102	101	838	11
TAR80	~~0.0112~~	~~153401~~	~~148~~	~~0.5~~	~~5803.88~~	~~198.396~~	~~7.95~~	~~17.5~~	~~0.09365~~	~~0.97~~	~~1.8407~~	~~14.0~~	~~0.14150~~	~~13.3~~	~~1.00~~	~~1500~~	~~37~~	~~849~~	~~214~~	~~1037~~	~~199~~	~~57~~	~~82~~	~~849~~	~~214~~

TAR81	0.376	32718	31	2.8	3124.538	580.477	6.66	0.6	0.06950	0.71	1.4397	0.6	0.15025	0.6	0.28	912	29	902	10	906	7	99	100	902	10
TAR82	0.4325	119764	118	1.3	6753.807	24.2383	6.71	4.6	0.07297	1.82	1.5279	5.4	0.15135	4.3	0.97	1009	76	908	73	937	70	90	97	908	73
TAR83	0.0456	105567	104	1.1	5245.756	246.761	6.50	0.7	0.06882	0.43	1.4579	0.8	0.15397	0.7	0.84	892	18	923	12	913	9	103	101	923	12
TAR84	1.4813	267281	298	0.5	2944.477	35.5166	6.60	13.1	0.09348	6.68	2.0224	5.9	0.16335	11.1	0.95	1471	247	971	202	1119	82	66	87	971	202
TAR85	0.0561	148792	136	0.7	9772.809	144.609	5.91	1.8	0.07418	0.58	1.7323	2.1	0.16968	1.8	0.97	1045	23	1010	34	1020	28	97	99	1010	34
TAR86	0.0796	163362	131	1.1	24148.49	73.8357	5.67	0.7	0.07572	0.36	1.8419	0.7	0.17646	0.7	0.85	1087	14	1048	13	1060	9	96	99	1048	13
TAR87	0.5654	654504	566	0.6	3464.995	15.4606	5.86	6.7	0.10027	0.52	2.4394	6.3	0.17699	6.8	1.00	1628	19	1048	131	1246	90	64	84	1048	131
TAR88	0.0242	41365	35	0.7	10420.04	109.776	5.62	0.6	0.07376	0.71	1.8072	1.1	0.17805	0.6	0.77	1033	29	1056	12	1048	14	102	101	1056	12
TAR89	0.2988	12089	125	1.1	39506.05	131.117	5.63	1.0	0.07178	1.97	1.7714	2.2	0.17851	1.0	0.30	952	82	1058	20	1030	28	111	103	1058	20
TAR90	0.4701	155649	128	0.7	2454.032	95.1671	5.60	0.9	0.07646	1.37	1.8821	0.8	0.17875	0.9	0.11	1104	52	1060	18	1075	11	96	99	1060	18
TAR91	18.095	3166	34	2.9	91.05971	46.4951	5.67	2.2	0.07916	5.45	1.9320	5.7	0.18023	2.1	0.20	1096	171	1067	41	1062	68	97	100	1067	41
TAR92	0.2983	53599	43	0.6	6558.938	63.8549	5.57	3.5	0.07537	2.28	1.8973	5.7	0.18141	3.4	0.99	1072	91	1074	68	1074	76	100	100	1074	68
TAR93	2.0226	16026	152	1.1	102.0543	129.899	5.43	1.1	0.07557	1.71	1.9266	1.8	0.18499	1.0	0.32	1064	69	1094	21	1087	23	103	101	1094	21
TAR94	0.8186	510956	408	0.3	12655.17	55.26	5.58	7.1	0.09417	1.98	2.3917	5.1	0.18599	6.6	0.97	1507	76	1097	133	1235	75	73	89	1097	133
TAR95	1.7674	13059	132	0.8	7.565027	888.314	5.37	1.2	0.07421	2.65	1.9115	2.4	0.18746	1.2	0.01	1020	103	1107	24	1079	32	108	103	1107	24
TAR96	0.0084	307085	235	0.1	9557.306	369.965	5.33	0.6	0.07623	0.86	1.9702	0.9	0.18760	0.7	0.41	1100	34	1108	13	1105	13	101	100	1108	13
TAR97	0.5031	21483	17	1.1	7320.334	91.1461	5.29	1.0	0.07606	0.75	1.9837	1.1	0.18927	1.0	0.77	1095	30	1117	21	1110	15	102	101	1117	21
TAR98	0.092	543412	443	2.1	24046.55	15.6422	5.28	1.7	0.08174	0.50	2.1341	1.9	0.18977	1.7	0.97	1238	19	1120	35	1159	26	90	97	1120	35
TAR99	1.5091	377575	308	1.4	1102.321	4.44349	5.22	3.8	0.10303	0.61	2.7320	3.4	0.19287	3.7	0.99	1678	23	1136	77	1336	51	68	85	1136	77
TAR100	0.4901	199756	164	0.8	5210.797	62.4488	5.55	10.9	0.09065	1.94	2.3953	7.1	0.19452	8.5	1.00	1435	71	1141	181	1230	109	80	93	1141	181
TAR101	0.471	24947	219	2.3	233.0731	91.8764	5.14	1.0	0.07485	1.41	2.0165	1.3	0.19565	1.0	0.32	1051	56	1151	21	1119	18	110	103	1151	21
TAR102	0.5655	17668	155	1.5	320.3067	101.267	5.10	0.9	0.08731	4.56	2.5101	7.0	0.19973	1.7	0.91	1287	121	1158	20	1237	68	90	94	1158	20
TAR103	0.8002	15149	138	0.9	229.353	65.8848	5.10	1.3	0.07903	1.80	2.1519	2.0	0.19748	1.2	0.40	1153	68	1161	26	1161	27	101	100	1161	26
TAR104	0.0804	93302	70	1.1	5906.687	104.112	4.99	0.8	0.07852	0.40	2.1666	0.9	0.20059	0.9	0.90	1159	16	1178	19	1170	13	102	101	1178	19
TAR105	7.0723	2674	26	2.1	31.5256	66.799	5.04	2.1	0.07076	4.56	1.9303	4.5	0.20253	2.1	0.17	1030	153	1187	45	1069	63	115	111	1187	45
TAR106	0.0584	117555	82	1.0	7710.101	174.569	4.88	0.6	0.07883	0.32	2.2266	0.5	0.20497	0.6	0.86	1167	13	1202	14	1189	7	103	101	1202	14
TAR107	0.0247	187350	131	0.6	63111.12	75.6419	4.85	0.7	0.07809	0.29	2.2193	0.7	0.20623	0.7	0.92	1148	11	1209	15	1187	10	105	102	1209	15
TAR108	0.1696	239861	178	0.7	21510.77	543.151	4.84	0.5	0.08118	0.47	2.3063	0.7	0.20654	0.5	0.73	1225	18	1210	11	1214	10	99	100	1210	11
TAR109	0.098	94558	70	2.0	5696.849	50.3343	4.84	0.4	0.08051	0.44	2.2879	0.5	0.20659	0.4	0.52	1208	17	1211	9	1209	7	100	100	1211	9
TAR110	0.0139	466638	339	0.7	617355.8	114.218	4.82	0.5	0.08013	0.24	2.2861	0.5	0.20730	0.5	0.90	1199	9	1214	11	1208	6	101	101	1214	11
TAR111	0.1089	118258	80	0.7	12794.5	80.4377	4.81	0.4	0.07969	0.39	2.2860	0.5	0.20811	0.4	0.66	1188	15	1219	8	1208	7	103	101	1219	8
TAR112	0.0542	182870	129	0.6	8814.986	329.618	4.64	0.7	0.08144	0.27	2.4173	0.7	0.21575	0.7	0.92	1231	11	1259	16	1248	10	102	101	1259	16
TAR113	3.2683	13412	114	1.6	105.2202	119.322	4.71	2.2	0.09581	3.09	2.7858	2.8	0.21648	2.1	0.40	1501	108	1261	48	1343	40	84	94	1261	48
TAR114	4.6975	9862	78	1.3	118.7973	128.609	4.60	1.2	0.08004	2.14	2.4045	2.0	0.21890	1.2	0.13	1168	89	1275	28	1239	28	109	103	1275	28
TAR115	0.141	84716	59	0.6	3347.373	167.646	4.57	0.6	0.08047	0.46	2.4245	0.8	0.21895	0.6	0.81	1207	18	1276	13	1250	11	106	102	1276	13
TAR116	1.6832	8335	68	0.7	48.44547	139.149	4.59	1.1	0.07803	1.84	2.3802	2.1	0.21921	1.1	0.30	1139	80	1277	25	1231	29	112	104	1277	25
TAR117	4.1201	24013	203	1.4	442.013	71.4597	4.54	0.8	0.08106	1.86	2.4787	2.0	0.22102	0.8	0.17	1199	74	1287	18	1261	29	107	102	1287	18
TAR118	0.0477	417821	275	1.3	33632.67	45.4068	4.49	0.8	0.08251	0.38	2.5336	1.1	0.22292	0.9	0.96	1257	15	1297	20	1282	16	103	101	1297	20
TAR119	3.0322	11904	104	0.8	156.7858	57.1057	4.51	1.7	0.08394	2.15	2.6042	2.9	0.22336	1.9	0.53	1262	82	1298	43	1300	43	103	100	1298	43
TAR120	3.2429	10156	107	0.5	887.0353	60.2319	4.73	3.6	0.08358	2.67	2.6326	4.8	0.22501	3.4	0.73	1259	109	1302	80	1280	69	103	102	1302	80
TAR121	1.4639	13225	105	0.8	105.4454	105.412	4.44	0.9	0.08627	1.28	2.6970	1.3	0.22641	0.9	0.32	1333	50	1315	22	1325	20	99	99	1315	22
TAR122	3.6971	7566	59	1.9	267.8177	57.09	4.33	1.5	0.08534	2.22	2.7305	2.2	0.23358	1.6	0.31	1293	84	1352	38	1331	31	105	102	1352	38
TAR123	0.8386	10838	80	2.0	2065.848	73.0133	4.22	1.2	0.10062	2.30	3.3026	1.8	0.23881	1.1	0.19	1607	79	1380	28	1477	27	86	93	1380	28
TAR124	2.5249	12767	93	0.9	213.2759	83.522	4.10	1.1	0.08686	1.56	2.9312	2.0	0.24422	1.2	0.61	1341	61	1408	30	1384	30	105	102	1408	30
TAR125	0.0954	383083	216	0.7	4446.432	377.282	3.99	0.4	0.09263	0.51	3.1978	0.6	0.25034	0.4	0.54	1479	19	1440	9	1457	9	97	99	1440	9
TAR126	0.0642	213424	134	0.6	178504	80.2774	3.93	1.2	0.09251	0.54	3.2423	1.7	0.25497	1.2	0.98	1477	21	1464	33	1467	26	99	100	1464	33
TAR127	2.675	2600	20	2.9	261.561	39.4097	3.97	2.5	0.09009	3.90	3.2075	5.1	0.25611	2.2	0.63	1389	148	1467	58	1438	77	106	102	1467	58
TAR128	0.0998	79952	43	0.5	8793.745	101.337	3.87	0.6	0.09056	0.39	3.2291	0.6	0.25865	0.6	0.79	1436	15	1483	15	1464	10	103	101	1483	15
TAR129	0.0624	166635	98	1.1	19002.86	78.6517	3.75	0.8	0.09135	0.21	3.3516	1.0	0.26670	0.8	0.98	1453	8	1524	22	1493	15	105	102	1453	8
TAR130	0.043	16289	98	1.2	148.1517	175.988	3.48	1.1	0.09544	1.51	3.8000	1.4	0.28917	1.1	0.32	1523	55	1636	32	1589	23	107	103	1523	55
TAR131	0.5499	103869	666	0.5	906.0533	77.3863	3.52	0.9	0.09552	0.65	3.7324	1.1	0.28249	0.9	0.75	1535	25	1603	24	1577	17	104	102	1535	25
TAR132	0.055	277321	145	0.5	4168.54	327.991	3.54	0.3	0.09649	0.26	3.7543	0.4	0.28266	0.3	0.77	1556	10	1605	9	1583	7	103	101	1556	10
TAR133	0.6091	17774	108	2.2	267.4558	87.2352	3.41	1.1	0.09793	1.69	3.9720	1.6	0.29472	1.1	0.23	1568	65	1664	33	1624	26	106	102	1568	65
TAR134	0.0142	255548	137	1.0	79386.35	111.429	3.69	2.0	0.09805	0.61	3.6818	2.5	0.27211	2.0	0.99	1586	23	1551	55	1566	41	98	99	1586	23
TAR135	0.0767	85231	46	1.9	23928.29	157.699	3.40	1.3	0.09950	0.24	4.0319	1.4	0.29456	1.3	0.99	1614	9	1664	37	1640	22	103	101	1614	9
TAR136	0.2942	524840	284	0.4	6343.978	561.377	3.61	2.1	0.10125	0.85	3.8736	2.8	0.27780	2.1	0.99	1646	31	1580	59	1606	45	96	98	1646	31
TAR137	0.3588	407729	219	1.2	5319.945	16.3296	3.47	1.7	0.10513	0.70	4.1748	2.2	0.28851	1.6	0.99	1715	26	1634	46	1668	37	95	98	1715	26
TAR138	0.0032	125294	57	1.3	4136.356	235.111	3.06	0.5	0.10655	0.27	4.7930	0.5	0.32670	0.5	0.83	1740	10	1822	17	1784	8	105	102	1740	10
TAR139	0.0243	161826	72	1.9	4635.268	432.062	2.95	0.8	0.10846	0.24	5.0528	0.8	0.33863	0.8	0.96	1773	9	1880	27	1828	14	106	103	1773	9
TAR140	0.4392	23833	119	4.1	654.0709	88.7484	2.88	1.0	0.11249	1.26	5.4121	1.3	0.34935	1.0	0.38	1840	43	1930	33	1884	22	105	102	1840	43
TAR141	0.1227	171126	74	1.7	6506.366	103.59	2.80	0.6	0.11620	0.27	5.7018	0.6	0.35680	0.6	0.91	1898	10	1967	20	1932	11	104	102	1898	10
TAR142	2.8321	21747	105	1.5	671.8689	85.5014	2.81	0.8	0.12007	1.19	5.9340	1.2	0.35652	0.8	0.37	1948	44	1965	28	1963	22	101	100	1948	44
TAR143	1.5363	19280	96	2.3	483.393	66.4684	2.84	0.8	0.12174	1.73	5.9332	1.7	0.35390	0.8	0.21	1965	61	1952	28	1961	29	99	100	1965	61
TAR144	0.083	6598	32	1.8	44.21541	146.811	2.41	2.3	0.12008	1.92	7.0418	3.0	0.42675	2.3	0.59	1971	85	2283	88	2112	55	116	108	1971	85
TAR145	3.8596	17277	99	0.9	215.4437	57.9898	3.02	2.5	0.12256	1.47	5.8472	3.8	0.33426	2.3	0.50	1981	52	1854	73	1929	60	94	96	1981	52
TAR146	0.0773	226860	91	1.3	8862.838	268.821	2.56	0.8	0.12940	0.22	6.9460	0.7	0.39039	0.8	0.96	2089	8	2125	27	2104	13	102	101	2089	8
TAR147	0.03	596863	231	1.1	62048.41	67.8896	2.55	0.7	0.13551	0.32	7.3112	0.5	0.39214	0.7	0.91	2170	11	2133	26	2150	10	98	99	2170	11
TAR148	0.0318	265635	77	1.4	30718.35	236.715	1.88	0.8	0.18349	0.16	13.4188	0.7	0.53169	0.8	0.99	2684	5	2748	35	2709	13	102	101	2684	5
TAR149	1E-04	250954	69	0.6	5593.095	131.939	1.92	0.6	0.20048	0.57	14.4255	1.1	0.52198	0.6	0.95	2829	19	2707	26	2778	21	96	97	2829	19
TAR150	16.604	638	1	0.1	28.98997	60.4783	0.54	12.9	0.81094	3.74	365.0991	12.7	3.33606	11.8	0.95	4236	308	8696	1177	5732	253	205	152	4236	308

U-Pb data from HG1

	23 June 2022, Instituto de Geociências, Universidade de Brasí							Data for Tera-Wasserburg plot				Data for Wetherill plot							Dates								
Sample	Identifier	f206c	206Pb	Uppm	Th/U	206Pb/204Pb	1s%	238U/206Pb	1s%	207Pb/206Pb	1s%	207Pb/235U	1s%	206Pb/238U	1s%	Rho	207Pb/206Pb	2s (abs)	206Pb/238U	2s (abs)	207Pb/235U	2s (abs)	Conc (%) 6/8 -7/6	Conc (%) 6/8 -7/5	Idade Preferida	2s abs
HG1	~~AM030-70.F~~	~~13.70403~~	~~5445~~	~~173~~	~~1.6~~	~~-34.93~~	~~-25.1~~	~~308.93~~	~~4.0~~	~~0.06917~~	~~10.26~~	~~0.0306~~	~~8.5~~	~~0.00341~~	~~3.7~~	~~0.03~~	~~451~~	~~398~~	~~22~~	~~2~~	~~30~~	~~5~~	~~5~~	~~72~~	~~22~~	~~2~~
HG1	AM030-26.F	58.9936	3349	99	2.6	-21.8	-23.3	304.99	3.1	0.05179	12.67	0.0235	11.6	0.00351	2.8	0.09	284	442	23	1	23	5	8	97	23	1
HG1	AM030-66.F	3.728171	34554	1061	2.7	-230	-28	278.29	1.3	0.05059	3.35	0.0250	3.4	0.00363	1.3	-0.01	158	161	23	1	25	2	15	93	23	1
HG1	AM030-52.F	1.623823	15028	403	2.3	-67.13	-22.9	247.06	1.5	0.05051	5.68	0.0287	5.2	0.00414	1.6	0.00	-250	311	27	1	29	3	-11	93	27	1
HG1	~~AM030-45.F~~	~~16.63336~~	~~11703~~	~~315~~	~~1.6~~	~~-51.14~~	~~-36.3~~	~~236.29~~	~~2.6~~	~~0.07981~~	~~6.74~~	~~0.0458~~	~~6.9~~	~~0.00429~~	~~2.8~~	~~0.31~~	~~1058~~	~~240~~	~~28~~	~~2~~	~~45~~	~~6~~	~~3~~	~~61~~	~~28~~	~~2~~
HG1	~~AM030-54.F~~	~~-0.79036~~	~~23785~~	~~536~~	~~2.1~~	~~-124.1~~	~~-28.6~~	~~206.22~~	~~1.5~~	~~0.05616~~	~~8.39~~	~~0.0372~~	~~7.8~~	~~0.00496~~	~~1.5~~	~~-0.03~~	~~86~~	~~202~~	~~32~~	~~1~~	~~37~~	~~5~~	~~37~~	~~87~~	~~32~~	~~1~~
HG1	~~AM030-41.F~~	~~5.896833~~	~~7261~~	~~147~~	~~1.8~~	~~-63.66~~	~~-48.3~~	~~196.16~~	~~3.6~~	~~0.15483~~	~~8.00~~	~~0.1116~~	~~6.6~~	~~0.00542~~	~~5.4~~	~~-0.06~~	~~2322~~	~~225~~	~~35~~	~~4~~	~~107~~	~~13~~	~~2~~	~~33~~	~~35~~	~~4~~
HG1	AM030-114.	3.526631	12905	301	1.3	-420.1	-17.7	186.51	1.6	0.05450	6.19	0.0390	5.5	0.00547	1.7	0.16	-50	266	35	1	39	4	-71	91	35	1
HG1	AM030-95.F	0.866854	58154	559	1.2	-967.9	-44.5	77.74	2.4	0.05277	3.34	0.0887	2.4	0.01313	2.6	0.19	257	162	84	4	86	4	33	97	84	4
HG1	~~AM030-19.F~~	~~9.786849~~	~~465319~~	~~2514~~	~~0.2~~	~~177.46~~	~~7.11~~	~~51.25~~	~~2.0~~	~~0.14940~~	~~1.48~~	~~0.4105~~	~~1.3~~	~~0.01986~~	~~2.1~~	~~0.74~~	~~2329~~	~~49~~	~~127~~	~~5~~	~~349~~	~~8~~	~~5~~	~~36~~	~~127~~	~~5~~
HG1	~~AM030-12.F~~	~~2.63243~~	~~49806~~	~~254~~	~~1.6~~	~~-102.3~~	~~-56.6~~	~~46.75~~	~~1.2~~	~~0.06733~~	~~2.67~~	~~0.1933~~	~~2.3~~	~~0.02155~~	~~1.1~~	~~0.20~~	~~790~~	~~111~~	~~137~~	~~3~~	~~179~~	~~8~~	~~17~~	~~77~~	~~137~~	~~3~~
HG1	AM030-16.F	0.96896	24110	95	2.4	-162.1	-23.3	37.68	1.6	0.05065	4.91	0.1843	4.2	0.02685	1.5	-0.03	17	199	171	5	170	13	1001	100	171	5
HG1	AM030-5.FI	2.007658	43366	171	2.1	-186.6	-32.3	37.06	1.7	0.05122	2.97	0.1911	3.3	0.02742	1.9	0.53	184	128	174	7	177	11	95	99	174	7
HG1	~~AM030-109.~~	~~2.424519~~	~~146071~~	~~635~~	~~3.6~~	~~-3289~~	~~-23.4~~	~~35.20~~	~~0.9~~	~~0.06404~~	~~2.29~~	~~0.2506~~	~~2.4~~	~~0.02864~~	~~0.9~~	~~0.02~~	~~672~~	~~90~~	~~182~~	~~3~~	~~226~~	~~9~~	~~27~~	~~81~~	~~182~~	~~3~~
HG1	AM030-11.F	-1.82417	53737	165	1.9	-355.9	-21.1	27.84	2.3	0.05347	3.45	0.2581	2.8	0.03645	2.2	0.07	288	165	231	10	232	12	80	99	231	10
HG1	AM030-51.F	2.517782	95628	279	1.4	-30.69	-300	25.96	0.9	0.06025	2.42	0.3115	2.0	0.03874	1.0	-0.01	578	99	245	5	275	9	42	89	245	5
HG1	~~AM030-27.F~~	~~2.417234~~	~~######~~	~~2198~~	~~0.4~~	~~1062.5~~	~~15.3~~	~~18.78~~	~~1.2~~	~~0.08547~~	~~1.02~~	~~0.6264~~	~~1.5~~	~~0.05338~~	~~1.3~~	~~0.71~~	~~1319~~	~~40~~	~~335~~	~~8~~	~~493~~	~~12~~	~~25~~	~~68~~	~~335~~	~~8~~
HG1	AM030-98.F	-0.27622	150008	301	2.0	-5666	-15.7	16.80	0.6	0.05381	1.05	0.4457	1.0	0.05980	0.6	0.20	340	46	374	5	374	6	110	100	374	5
HG1	~~AM030-57.F~~	~~1.484952~~	~~106675~~	~~183~~	~~0.4~~	~~-326.8~~	~~-47.2~~	~~15.08~~	~~1.3~~	~~0.06736~~	~~1.96~~	~~0.6039~~	~~1.8~~	~~0.06706~~	~~1.3~~	~~0.21~~	~~809~~	~~88~~	~~418~~	~~10~~	~~478~~	~~14~~	~~52~~	~~87~~	~~418~~	~~10~~
HG1	~~AM030-39.F~~	~~3.566154~~	~~264011~~	~~432~~	~~0.9~~	~~-115~~	~~-196~~	~~14.95~~	~~0.8~~	~~0.08311~~	~~1.58~~	~~0.7734~~	~~1.3~~	~~0.06751~~	~~0.8~~	~~-0.08~~	~~1242~~	~~60~~	~~421~~	~~7~~	~~580~~	~~11~~	~~34~~	~~73~~	~~421~~	~~7~~
HG1	~~AM030-103.~~	~~2.475632~~	~~370008~~	~~710~~	~~0.6~~	~~-2009~~	~~-28~~	~~15.67~~	~~1.7~~	~~0.07907~~	~~1.23~~	~~0.7261~~	~~1.3~~	~~0.06821~~	~~1.8~~	~~0.53~~	~~1131~~	~~50~~	~~424~~	~~15~~	~~551~~	~~10~~	~~38~~	~~77~~	~~424~~	~~15~~
HG1	AM030-78.F	1.727855	507981	852	0.8	1005.3	38.8	14.43	2.8	0.06453	2.61	0.5883	1.9	0.07014	2.8	0.42	743	110	437	23	469	15	59	93	437	23
HG1	AM030-47.F	1.047017	391059	622	0.4	-717.9	-59.6	14.30	1.2	0.06565	1.21	0.6325	1.4	0.07067	1.1	0.43	778	51	440	10	497	11	57	89	440	10
HG1	AM030-83.F	0.332621	139226	224	1.5	-2518	-21.9	14.14	0.9	0.05746	1.64	0.5592	1.4	0.07132	0.9	-0.03	468	75	444	8	450	10	95	99	444	8
HG1	AM030-38.F	1.118459	106217	161	1.7	-873.5	-24.9	13.54	0.8	0.06527	1.92	0.6603	1.9	0.07422	0.8	0.10	746	83	461	7	513	15	62	90	461	7
HG1	AM030-107.	0.374791	182732	305	1.7	-51969	-28.7	13.34	1.1	0.05698	1.80	0.5866	1.9	0.07544	1.1	0.19	480	85	469	10	467	14	98	100	469	10
HG1	AM030-9.FI	-1.01775	56363	75	4.0	-273.4	-24	12.72	1.0	0.05752	1.97	0.6302	1.9	0.07922	1.0	0.26	464	86	491	9	494	15	106	99	491	9
HG1	AM030-75.F	0.583591	122782	175	0.9	-2896	-29.5	12.61	1.0	0.05922	2.20	0.6392	2.2	0.07966	1.0	0.17	542	100	494	10	500	17	91	99	494	10
HG1	AM030-55.F	-0.61927	55910	79	2.6	-374.9	-28.2	12.44	1.3	0.06274	2.96	0.6725	2.9	0.08108	1.3	-0.33	635	125	502	12	519	24	79	97	502	12
HG1	AM030-35.F	0.58065	189635	261	0.6	-931.5	-63.2	12.08	2.2	0.07016	4.47	0.7411	2.6	0.08344	2.1	-0.08	886	177	516	21	562	22	58	92	516	21
HG1	~~AM030-96.F~~	~~2.089678~~	~~188417~~	~~265~~	~~1.1~~	~~-4805~~	~~-17.6~~	~~11.91~~	~~0.7~~	~~0.07265~~	~~1.85~~	~~0.8487~~	~~1.8~~	~~0.08435~~	~~0.7~~	~~0.23~~	~~929~~	~~65~~	~~522~~	~~7~~	~~618~~	~~15~~	~~56~~	~~84~~	~~522~~	~~7~~
HG1	AM030-63.F	-0.09706	174006	226	1.9	-2266	-18.8	11.83	0.7	0.05855	1.17	0.6814	1.2	0.08488	0.8	0.39	540	54	525	8	526	10	97	100	525	8
HG1	AM030-37.F	4.182434	10124	12	0.1	-86.99	-16.4	11.77	1.8	0.06081	4.19	0.7177	3.9	0.09004	2.7	0.00	427	163	544	20	523	32	127	104	544	20
HG1	AM030-113.	0.087289	77396	99	1.1	-1030	-22.7	11.03	1.0	0.05905	2.35	0.7721	2.6	0.09175	1.0	0.08	507	94	566	11	575	21	112	98	566	11
HG1	AM030-105.	0.432809	378147	507	2.6	-19135	-31	10.89	1.0	0.06030	1.02	0.7667	1.1	0.09256	1.1	0.55	611	46	570	12	577	9	93	99	570	12
HG1	AM030-40.F	0.654821	254335	312	1.3	-2143	-30.4	10.82	1.1	0.06242	1.86	0.7743	1.6	0.09275	1.1	0.09	671	77	572	12	581	14	85	98	572	12
HG1	~~AM030-72.F~~	~~0.563711~~	~~483645~~	~~556~~	~~1.2~~	~~-6899~~	~~-26.9~~	~~10.85~~	~~1.3~~	~~0.06982~~	~~1.73~~	~~0.9080~~	~~1.3~~	~~0.09288~~	~~1.3~~	~~0.07~~	~~904~~	~~72~~	~~572~~	~~14~~	~~655~~	~~12~~	~~63~~	~~87~~	~~572~~	~~14~~
HG1	AM030-65.F	0.098183	345190	411	0.4	-2259	-24.5	10.80	1.0	0.06014	1.05	0.7628	1.4	0.09339	1.0	0.62	603	49	575	12	576	13	95	100	575	12
HG1	AM030-89.F	0.219379	474662	589	0.7	-3534	-15.5	10.76	0.7	0.05870	0.69	0.7589	0.7	0.09341	0.7	0.42	544	31	576	8	573	6	106	101	576	8
HG1	AM030-42.F	0.946817	169629	206	0.6	-1280	-23.7	10.72	1.1	0.06028	1.80	0.7625	1.6	0.09390	1.1	0.13	588	76	578	12	574	14	98	101	578	12
HG1	AM030-30.F	0.403919	158076	189	1.3	-1177	-21.2	10.65	0.9	0.05941	1.45	0.7771	1.4	0.09438	0.9	0.04	575	62	581	10	582	12	101	100	581	10
HG1	AM030-118.	0.140236	431120	532	1.3	-25395	-16.2	10.26	0.8	0.05928	0.78	0.8082	0.8	0.09811	0.8	0.46	567	35	603	10	600	8	106	100	603	10
HG1	AM030-13.F	0.041074	322819	344	0.9	-1598	-15.9	10.23	0.5	0.05962	0.66	0.8154	0.6	0.09808	0.5	0.24	585	29	603	6	605	6	103	100	603	6
HG1	AM030-29.F	1.679275	556539	631	145.9	1386.6	18.3	10.14	1.3	0.07110	1.35	0.9449	1.4	0.09935	1.3	0.51	949	55	610	15	674	14	64	91	610	15
HG1	AM030-53.F	-0.12691	181789	212	2.9	-1063	-20.3	10.11	0.7	0.06039	1.06	0.8271	1.1	0.09950	0.7	0.37	597	46	611	8	611	10	102	100	611	8
HG1	AM030-67.F	0.723397	127021	138	2.4	-648.3	-25.9	9.91	0.9	0.06177	1.47	0.8485	1.3	0.10156	0.9	0.07	641	63	623	11	622	13	97	100	623	11
HG1	AM030-117.	0.243259	129968	158	1.2	-8576	-18.3	9.78	0.7	0.06153	1.25	0.8660	1.2	0.10283	0.7	0.21	638	57	631	8	631	11	99	100	631	8
HG1	AM030-14.F	0.329766	246576	264	0.6	-1665	-21.3	9.77	1.4	0.06359	1.81	0.8779	1.7	0.10349	1.3	0.35	699	77	635	16	638	16	91	99	635	16
HG1	AM030-44.F	0.235228	716944	797	0.5	-2959	-31.7	9.67	1.5	0.06358	1.36	0.8925	2.0	0.10461	1.5	0.72	714	57	641	18	645	19	90	99	641	18
HG1	AM030-97.F	0.330477	543673	611	1.1	-23796	-14	9.59	0.8	0.06022	0.69	0.8810	0.8	0.10536	0.8	0.62	609	29	645	9	641	8	106	101	645	9
HG1	~~AM030-81.F~~	~~2.737706~~	~~284452~~	~~299~~	~~2.3~~	~~-1403~~	~~-38.5~~	~~9.22~~	~~0.9~~	~~0.09258~~	~~1.05~~	~~1.3885~~	~~0.9~~	~~0.10970~~	~~1.0~~	~~0.20~~	~~1463~~	~~40~~	~~671~~	~~12~~	~~884~~	~~10~~	~~46~~	~~76~~	~~671~~	~~12~~
HG1	AM030-120.	-0.14056	218729	247	0.8	-2E+05	-20.7	9.13	0.7	0.06201	0.97	0.9463	1.0	0.11014	0.7	0.30	658	41	673	9	674	10	102	100	673	9
HG1	~~AM030-15.F~~	~~0.489053~~	~~340090~~	~~342~~	~~0.6~~	~~-1391~~	~~-37.1~~	~~9.06~~	~~0.9~~	~~0.08420~~	~~1.24~~	~~1.2476~~	~~1.5~~	~~0.11019~~	~~1.0~~	~~0.59~~	~~1287~~	~~49~~	~~674~~	~~13~~	~~820~~	~~18~~	~~52~~	~~82~~	~~674~~	~~13~~
HG1	AM030-101.	0.344213	225824	249	0.8	-4070	-21.2	9.02	0.8	0.06291	1.27	0.9624	1.0	0.11133	0.8	0.05	682	56	680	11	683	10	100	100	680	11
HG1	~~AM030-69.F~~	~~0.696669~~	~~398939~~	~~390~~	~~1.5~~	~~-2459~~	~~-27.4~~	~~9.06~~	~~1.8~~	~~0.08160~~	~~1.25~~	~~1.2682~~	~~1.4~~	~~0.11226~~	~~1.6~~	~~0.61~~	~~1232~~	~~53~~	~~685~~	~~21~~	~~833~~	~~17~~	~~56~~	~~82~~	~~685~~	~~21~~

HG1	AM030-77.F	-0.2777	244769	238	0.6	-4615	-20.7	8.49	1.0	0.06505	1.51	1.0416	1.7	0.11839	0.9	0.36	769	66	721	13	722	18	94	100	721	13
HG1	AM030-24.F	0.827813	536639	497	2.1	-1392	-57.2	8.46	1.5	0.07644	1.06	1.2650	1.2	0.11930	1.4	0.68	1099	43	726	19	829	14	66	88	726	19
HG1	AM030-87.F	0.082627	85990	82	1.6	-887.5	-15.4	8.27	0.8	0.06488	1.23	1.0998	1.2	0.12214	0.8	0.23	747	52	742	11	750	13	99	99	742	11
HG1	AM030-74.F	0.125736	717934	651	0.1	-22533	-19.2	8.16	0.9	0.07268	0.93	1.2272	0.9	0.12305	0.8	0.44	997	37	748	12	812	10	75	92	748	12
HG1	AM030-116.	0.48643	400732	393	0.6	-18579	-30.9	7.88	0.9	0.06660	1.53	1.1470	1.2	0.12759	0.9	0.01	802	62	774	13	774	13	96	100	774	13
HG1	AM030-3.FI	0.085914	629067	525	0.5	-2916	-47.7	7.84	2.2	0.07075	2.89	1.1957	2.1	0.12899	2.2	0.08	922	123	782	32	797	24	85	98	782	32
HG1	AM030-48.F	0.714618	83140	69	6.1	-394.2	-16.9	7.56	0.8	0.07801	1.25	1.4444	1.2	0.13358	0.8	0.20	1119	53	808	13	903	15	72	89	808	13
HG1	AM030-102.	0.242438	85620	72	2.0	-1746	-12.5	7.03	0.7	0.07383	1.21	1.4801	1.3	0.14310	0.7	0.19	1003	48	862	11	916	15	86	94	862	11
HG1	AM030-104.	1.769806	55932	46	0.7	-2376	-14.7	6.78	1.4	0.07095	1.67	1.4565	1.9	0.15095	1.4	0.20	900	71	905	24	906	23	101	100	905	24
HG1	AM030-20.F	0.462708	461820	335	0.8	-2275	-28.8	6.55	1.1	0.08261	1.25	1.7078	1.1	0.15351	1.1	0.28	1244	50	920	19	1009	15	74	91	920	19
HG1	AM030-73.F	-0.18316	235053	170	0.8	-5482	-23.5	6.35	1.4	0.07345	1.90	1.5505	1.6	0.15874	1.4	0.16	1006	77	949	24	949	20	94	100	949	24
HG1	AM030-32.F	0.593529	457881	323	0.6	-1775	-40.2	6.29	1.1	0.07856	1.20	1.6924	1.4	0.15917	1.2	0.61	1147	48	952	21	1003	18	83	95	952	21
HG1	AM030-50.F	0.220698	823718	592	0.3	-1452	-68.4	6.32	1.2	0.07288	1.20	1.5518	1.4	0.15943	1.2	0.28	999	48	953	21	949	18	95	100	953	21
HG1	AM030-60.F	0.088433	355282	243	0.4	-2435	-18.3	6.16	0.8	0.07249	1.07	1.6180	1.0	0.16313	0.8	0.33	1006	38	974	14	976	13	97	100	974	14
HG1	AM030-86.F	0.162314	875686	633	0.1	-15690	-19.7	5.98	1.0	0.07331	0.82	1.6795	1.0	0.16821	1.0	0.78	1012	33	1002	19	999	12	99	100	1002	19
HG1	AM030-82.F	0.144277	481465	337	1.1	-7585	-19.4	5.95	0.8	0.07300	1.07	1.6807	1.0	0.16902	0.8	0.31	999	44	1006	15	1000	12	101	101	1006	15
HG1	AM030-22.F	0.052483	156822	104	0.9	-526.2	-27.8	5.92	1.0	0.07438	1.33	1.7141	1.5	0.16978	1.0	0.45	1038	57	1010	19	1010	19	97	100	1010	19
HG1	AM030-36.F	0.10048	628639	418	1.5	-4578	-24.5	5.89	0.7	0.07516	0.97	1.7248	0.9	0.17030	0.7	0.43	1063	38	1014	13	1017	12	95	100	1014	13
HG1	AM030-7.FI	0.080701	304229	188	1.5	-1064	-40.1	5.88	0.9	0.07369	1.31	1.7312	1.1	0.17075	0.8	0.10	1020	54	1016	16	1019	14	100	100	1016	16
HG1	AM030-112.	-0.05438	497932	337	0.2	-7165	-15.3	5.83	0.8	0.07386	0.88	1.8134	0.9	0.17243	0.7	0.34	1026	36	1025	14	1051	11	100	98	1025	14
HG1	AM030-43.F	0.295271	281929	184	1.1	-1788	-26.1	5.75	0.9	0.07776	1.15	1.8237	1.0	0.17414	0.9	0.31	1129	46	1035	18	1053	14	92	98	1035	18
HG1	AM030-18.F	0.209462	435582	271	2.9	-3806	-15.9	5.70	0.7	0.07468	0.94	1.7881	0.8	0.17555	0.7	0.15	1049	38	1042	13	1040	10	99	100	1042	13
HG1	AM030-93.F	0.63107	137529	91	2.1	-3861	-14.2	5.74	0.9	0.07302	1.25	1.8059	1.2	0.17587	1.0	0.19	993	51	1044	18	1045	15	105	100	1044	18
HG1	AM030-4.FI	0.214781	248260	150	1.1	-1053	-22.1	5.69	0.6	0.07478	1.02	1.8063	1.1	0.17605	0.6	0.22	1046	42	1045	11	1045	14	100	100	1045	11
HG1	AM030-108.	3.405876	88862	60	1.8	-2424	-25.2	5.61	1.0	0.09511	2.42	2.3769	2.6	0.17930	0.9	0.37	1446	90	1062	17	1216	35	73	87	1062	17
HG1	AM030-115.	0.079023	336414	225	1.4	-18335	-15.6	5.52	0.7	0.07480	0.89	1.8882	0.8	0.18212	0.7	0.38	1056	34	1078	13	1076	10	102	100	1078	13
HG1	AM030-61.F	0.49329	332109	207	2.5	-6044	-26	5.50	1.1	0.07868	1.30	1.9136	1.4	0.18288	1.1	0.38	1154	52	1082	22	1084	19	94	100	1082	22
HG1	AM030-71.F	0.030807	387680	242	1.9	-4294	-23.3	5.41	1.0	0.07925	1.48	1.9391	1.5	0.18492	1.0	0.34	1175	54	1093	21	1092	20	93	100	1093	21
HG1	AM030-46.F	-0.58478	205215	118	0.9	-809.1	-34.9	5.38	1.0	0.07906	1.29	2.0825	1.4	0.18683	1.0	0.08	1161	52	1104	20	1141	18	95	97	1104	20
HG1	AM030-85.F	0.825966	289568	175	1.2	-7852	-14.9	5.35	0.7	0.08991	0.83	2.3469	0.9	0.18751	0.7	0.48	1411	31	1109	13	1224	12	79	91	1109	13
HG1	AM030-10.F	0.09	118889	67	2.3	-500	-32.1	5.25	0.8	0.08171	1.32	2.1312	1.4	0.19158	0.8	0.42	1219	53	1129	17	1159	18	93	97	1129	17
HG1	AM030-106.	0.370391	442888	292	1.0	373193	29.7	5.22	1.1	0.08046	1.41	2.0696	1.3	0.19264	1.1	0.23	1194	57	1135	22	1137	17	95	100	1135	22
HG1	AM030-110.	-0.15617	417013	265	1.7	-7014	-15.3	5.24	0.8	0.07699	0.78	2.0702	0.9	0.19308	0.7	0.58	1109	32	1137	16	1135	13	103	100	1137	16
HG1	AM030-25.F	0.407166	178655	100	0.9	-720.1	-28.8	5.01	1.0	0.07975	1.11	2.1968	1.2	0.20123	1.0	0.54	1183	42	1181	21	1177	17	100	100	1181	21
HG1	AM030-49.F	-0.03185	531030	296	0.1	-1951	-23.2	4.97	0.9	0.07984	0.83	2.2217	1.0	0.20141	1.1	0.10	1218	58	1182	24	1186	14	97	100	1182	24
HG1	AM030-68.F	-0.04415	350704	192	0.5	-2308	-20.3	4.95	1.0	0.08507	1.38	2.3406	1.1	0.20296	1.1	0.28	1312	48	1190	23	1222	16	91	97	1190	23
HG1	AM030-76.F	0.149427	478553	261	1.9	-11817	-27.2	4.83	1.2	0.18002	1.15	5.0605	1.3	0.20812	1.2	0.61	2648	38	1218	27	1828	22	46	67	1218	27
HG1	AM030-17.F	0.299522	100183	49	1.0	-521.8	-25.2	4.79	1.1	0.08133	1.47	2.4185	1.6	0.21060	1.1	0.53	1220	57	1231	25	1248	24	101	99	1231	25
HG1	AM030-119.	1.17146	507349	302	1.8	-28161	-26.6	4.79	1.1	0.09130	0.99	2.6217	1.1	0.21069	1.1	0.53	1443	38	1232	24	1304	15	85	94	1232	24
HG1	AM030-2.FI	1.762745	57493	27	1.1	-187.9	-23	4.77	0.8	0.08042	1.41	2.3798	1.3	0.21212	0.8	0.15	1182	55	1239	19	1236	19	105	100	1239	19
HG1	AM030-88.F	0.048979	895771	496	0.8	-6222	-25.3	4.74	0.9	0.08307	0.81	2.4008	0.8	0.21225	0.9	0.59	1264	32	1240	21	1244	12	98	100	1240	21
HG1	AM030-80.F	0.124973	348397	177	0.6	-3661	-12.4	4.74	0.6	0.08202	0.80	2.4163	0.6	0.21262	0.6	0.09	1230	32	1242	13	1245	9	101	100	1242	13
HG1	AM030-31.F	0.855551	487060	256	1.2	-1160	-81.3	4.67	1.6	0.11450	2.02	3.2778	1.4	0.21699	1.6	-0.04	1850	73	1265	37	1473	22	68	86	1265	37

HG1	AM030-64.F	0.03049	418523	206	5.6	-5068	-18.6	4.48	0.8	0.08603	0.95	2.6201	1.0	0.22447	0.8	0.25	1329	37	1305	20	1304	14	98	100	1305	20
HG1	AM030-62.F	0.295935	289527	138	2.1	-3899	-18.9	4.33	0.6	0.08595	0.74	2.7516	0.9	0.23140	0.7	0.55	1327	28	1341	16	1340	13	101	100	1341	16
HG1	AM030-23.F	-0.05181	624718	299	0.5	-2406	-25.6	4.31	0.9	0.09086	1.13	2.8441	0.8	0.23348	0.8	0.17	1431	43	1352	20	1368	13	95	99	1352	20
HG1	AM030-84.F	0.560191	183395	84	0.9	-4547	-13.4	4.26	0.6	0.08760	0.87	2.9027	0.8	0.23668	0.6	0.16	1355	34	1369	15	1379	13	101	99	1369	15
HG1	AM030-99.F	0.145998	562610	282	1.1	-26540	-17.8	4.09	0.6	0.09014	0.66	3.0354	0.7	0.24520	0.6	0.44	1422	25	1413	15	1415	11	99	100	1413	15
HG1	AM030-58.F	0.193733	713995	323	1.8	-4962	-28.7	4.03	1.1	0.10943	1.34	3.6201	1.0	0.24985	1.1	0.25	1779	49	1437	29	1552	16	81	93	1437	29
HG1																										
HG1	AM030-92.F	0.42854	239281	102	1.3	-2733	-20.5	3.61	1.2	0.09590	0.98	3.7270	1.1	0.27869	1.1	0.60	1533	37	1583	30	1576	18	103	100	1533	37
HG1	AM030-34.F	0.474411	340295	130	1.2	-2293	-18.3	3.69	0.7	0.09811	0.71	3.7803	0.7	0.27186	0.6	0.44	1581	26	1549	18	1587	11	98	98	1581	26
HG1	AM030-56.F	0.226399	545926	226	1.2	-3854	-19	3.74	0.6	0.10076	0.57	3.7302	0.7	0.26796	0.6	0.53	1635	21	1530	16	1576	11	94	97	1635	21
HG1	AM030-8.FI	0.06118	565348	203	1.3	-2749	-27.6	3.39	0.7	0.10361	0.79	4.2032	0.8	0.29603	0.7	0.43	1684	29	1671	21	1673	14	99	100	1684	29
HG1	AM030-1.FI	0.052841	685330	236	1.3	-1884	-35.4	3.26	0.8	0.10930	1.01	4.5795	0.9	0.30838	0.8	0.32	1778	36	1732	25	1743	16	97	99	1778	36
HG1	AM030-111.	-0.16465	179344	72	2.1	-1899	-22.2	3.22	1.1	0.11124	1.22	4.7040	0.9	0.31245	1.1	0.31	1810	45	1752	33	1767	15	97	99	1810	45
HG1	AM030-33.F	0.132003	415241	148	1.7	-1918	-24.1	3.21	0.6	0.11328	0.79	4.8815	0.7	0.31275	0.6	0.50	1845	28	1754	17	1799	12	95	97	1845	28
HG1	AM030-79.F	0.167267	214569	76	3.1	-2464	-14.3	3.16	0.7	0.11406	0.93	4.9992	0.8	0.31693	0.7	0.20	1851	34	1774	21	1816	13	96	98	1851	34
HG1	AM030-94.F	0.398521	124324	41	2.9	-2261	-16.7	2.84	0.7	0.12157	0.78	6.0037	0.8	0.35752	0.8	0.25	1966	28	1957	23	1975	15	100	99	1966	28
HG1	AM030-59.F	-0.00175	563262	192	1.6	-2680	-43.9	3.00	1.6	0.12124	1.35	5.3971	1.2	0.33494	1.6	0.59	1969	49	1861	52	1883	22	95	99	1969	49
HG1	AM030-6.FI	-8.4E-05	654186	193	1.4	-2981	-24.2	2.78	0.7	0.12183	0.76	6.0019	0.8	0.35853	0.9	0.65	1982	29	1981	27	1977	13	100	100	1982	29
HG1	AM030-28.F	-0.04283	453992	132	1.2	-4079	-19.1	2.65	0.8	0.12827	0.70	6.6981	0.8	0.37883	0.8	0.58	2069	25	2069	28	2070	14	100	100	2069	25
HG1	AM030-91.F	0.201537	127475	38	1.3	-757.7	-26.2	2.55	0.9	0.13060	0.89	7.1772	1.1	0.39224	1.0	0.42	2098	31	2131	36	2133	19	102	100	2098	31
HG1	~~AM030-21.F~~	~~0.841754~~	~~314967~~	~~103~~	~~1.8~~	~~-192.3~~	~~-141~~	~~2.97~~	~~1.4~~	~~0.14627~~	~~1.09~~	~~6.7920~~	~~1.5~~	~~0.34260~~	~~1.3~~	~~0.73~~	~~2291~~	~~38~~	~~1896~~	~~44~~	~~2077~~	~~28~~	~~83~~	~~91~~	~~2291~~	~~38~~
HG1	AM030-90.F	-0.00084	######	708	1.9	-18596	-25	1.99	0.8	0.17993	0.74	12.3741	0.7	0.50434	0.8	0.55	2649	25	2631	35	2632	13	99	100	2649	25
HG1	~~AM030-100.~~	~~0.472254~~	~~461285~~	~~134~~	~~0.7~~	~~-22357~~	~~-26.3~~	~~2.34~~	~~0.8~~	~~0.18044~~	~~1.03~~	~~10.5179~~	~~1.1~~	~~0.42555~~	~~1.0~~	~~0.54~~	~~2652~~	~~34~~	~~2284~~	~~40~~	~~2479~~	~~21~~	~~86~~	~~92~~	~~2652~~	~~34~~

U-Pb data from HG2

	University of Brasilia								Data for Tera-Wasserburg plot				Data for Wetherill plot							Dates							
Sample	Identifier	Comments	f206c	206Pb	Uppm	Th/U	206Pb/ 204Pb	1s%	238U/206 Pb	1s%	207Pb/20 6Pb	1s%	207Pb/2 35U	1s%	206Pb/2 38U	1s%	Rho	207Pb/ 206Pb	2s (abs)	206Pb/ 238U	2s (abs)	207Pb/ 235U	2s (abs)	Conc (%) 6/8 -7/6	Conc (%) 6/8 -7/5	Idade Preferida	2s abs
HG2	~~AM031-26~~	LABXR31-32 (TAR21)	~~-2.96694~~	~~3606~~	~~325~~	~~1.5~~	~~-32.160256~~	~~-11~~	~~293.65~~	~~2.4~~	~~0.07281~~	~~10.05~~	~~0.0332~~	~~9.3~~	~~0.00353~~	~~2.4~~	~~-0.01~~	~~1036~~	~~348~~	~~23~~	~~1~~	~~33~~	~~6~~	~~2~~	~~70~~	~~23~~	~~1~~
HG2	AM031-76	LABXR31-32 (TAR21)	7.950734	4392	421	1.4	-61.5242025	-20	272.03	3.8	0.04583	13.06	0.0240	12.8	0.00385	4.1	0.17	-174	539	25	2	24	6	-14	104	25	2
HG2	AM031-75	LABXR31-32 (TAR21)	2.634364	14028	1271	1.4	-149.701306	-12	259.86	1.8	0.04843	4.83	0.0259	4.6	0.00386	1.9	0.12	-81	262	25	1	26	2	-31	96	25	1
HG2	~~AM031-116~~	LABXR31-32 (TAR21)	~~-5.87628~~	~~5838~~	~~544~~	~~0.4~~	~~-70.422887~~	~~-10~~	~~270.95~~	~~1.7~~	~~0.06739~~	~~4.63~~	~~0.0349~~	~~4.3~~	~~0.00394~~	~~2.4~~	~~0.03~~	~~623~~	~~214~~	~~25~~	~~1~~	~~35~~	~~3~~	~~4~~	~~73~~	~~25~~	~~1~~
HG2	~~Spot 14.FIN~~	~~LABXR002_2-TAR21~~	~~1890.552~~	~~117~~	~~36~~	~~2.4~~	~~-1.15002183~~	~~-89~~	~~396.38~~	~~22.3~~	~~0.07457~~	~~64.51~~	~~0.0178~~	~~56.4~~	~~0.00421~~	~~10.2~~	~~0.13~~	~~3011~~	~~466~~	~~27~~	~~6~~	~~16~~	~~20~~	~~1~~	~~165~~	~~27~~	~~6~~
HG2	AM031-12.I	LABXR30-31-32 (TAR	-8.32315	9302	259	0.7	-118.205928	-18	235.81	1.7	0.05036	5.27	0.0295	5.0	0.00436	2.0	-0.02	-122	287	28	1	29	3	-23	96	28	1
HG2	AM031-1.FI	LABXR30-31-32 (TAR	5.942829	11304	290	1.2	220.129911	14.3	221.37	1.0	0.05078	3.85	0.0335	5.1	0.00461	1.0	0.05	-115	176	30	1	33	3	-26	89	30	1
HG2	~~Spot 45.FIN~~	~~LABXR002_2-TAR21~~	~~253.2176~~	~~216~~	~~65~~	~~0.6~~	~~-17.8823757~~	~~-54~~	~~225.17~~	~~6.0~~	~~0.02387~~	~~36.24~~	~~0.0129~~	~~36.3~~	~~0.00469~~	~~6.7~~	~~0.08~~	~~1136~~	~~541~~	~~30~~	~~4~~	~~13~~	~~9~~	~~3~~	~~238~~	~~30~~	~~4~~
HG2	~~Spot 29.FIN~~	~~LABXR002_2-TAR21~~	~~16.72753~~	~~275~~	~~79~~	~~1.1~~	~~-1.66138327~~	~~-199~~	~~220.91~~	~~6.1~~	~~0.07208~~	~~14.16~~	~~0.0481~~	~~14.6~~	~~0.00478~~	~~6.0~~	~~-0.13~~	~~1675~~	~~362~~	~~31~~	~~4~~	~~47~~	~~14~~	~~2~~	~~65~~	~~31~~	~~4~~
HG2	~~AM031-82~~	LABXR31-32 (TAR21)	~~1.69058~~	~~4532~~	~~264~~	~~1.9~~	~~-47.0180227~~	~~-6.3~~	~~167.26~~	~~1.8~~	~~0.07249~~	~~4.05~~	~~0.0645~~	~~4.3~~	~~0.00636~~	~~1.7~~	~~0.21~~	~~635~~	~~184~~	~~41~~	~~1~~	~~63~~	~~5~~	~~6~~	~~65~~	~~41~~	~~1~~
HG2	AM031-52	LABXR31-32 (TAR21)	1.827214	8888	542	0.9	-78.2086623	-13	158.90	2.1	0.05549	7.90	0.0469	6.8	0.00644	2.2	-0.09	317	340	41	2	48	7	13	87	41	2
HG2	AM031-91	LABXR31-32 (TAR21)	-56.6696	2379	114	1.8	-31.960615	-29	175.08	3.9	0.05232	20.82	0.0477	17.9	0.00674	5.4	-0.03	1514	423	43	5	43	16	3	100	43	5
HG2	Spot 48.FIN	LABXR002_1-TAR21	-47.5591	251	47	0.7	-3.58320022	-95	150.73	6.2	0.05183	24.32	0.0466	21.8	0.00716	5.6	-0.25	1615	633	46	5	45	19	3	102	46	5
HG2	~~AM031-57~~	LABXR31-32 (TAR21)	~~-3.6048~~	~~6641~~	~~334~~	~~0.8~~	~~-77.0864531~~	~~-9.7~~	~~146.02~~	~~2.6~~	~~0.06243~~	~~6.79~~	~~0.0619~~	~~6.5~~	~~0.00731~~	~~2.5~~	~~0.09~~	~~743~~	~~228~~	~~47~~	~~2~~	~~60~~	~~8~~	~~6~~	~~78~~	~~47~~	~~2~~
HG2	~~AM031-92~~	LABXR31-32 (TAR21)	~~-13.7328~~	~~2733~~	~~106~~	~~1.1~~	~~-33.5424041~~	~~-28~~	~~154.80~~	~~15.9~~	~~0.18343~~	~~16.94~~	~~0.1134~~	~~5.5~~	~~0.00783~~	~~5.7~~	~~0.03~~	~~1605~~	~~223~~	~~50~~	~~6~~	~~104~~	~~11~~	~~3~~	~~48~~	~~50~~	~~6~~
HG2	AM031-103	LABXR31-32 (TAR21)	5.820034	11009	317	1.2	-115.276084	-8.2	83.11	1.2	0.05136	5.06	0.0894	5.1	0.01247	1.7	0.03	-98	237	80	3	86	8	-82	93	80	3
HG2	AM031-79	LABXR31-32 (TAR21)	-0.4333	10267	292	1.4	-104.059446	-8.7	80.74	1.4	0.04749	4.88	0.0808	4.4	0.01250	1.4	-0.04	-136	220	80	2	78	7	-59	102	80	2
HG2	Spot 17.FIN	LABXR002_1-TAR21	-9.14295	4795	449	1.6	404.490005	58	73.72	1.5	0.04699	4.75	0.0882	4.7	0.01357	1.4	0.12	497	180	87	2	86	8	17	102	87	2
HG2	AM031-48	LABXR31-32 (TAR21)	15.23063	9195	155	1.0	-71.9384871	-11	48.33	1.5	0.06553	5.37	0.1863	5.1	0.02106	1.5	0.13	586	216	134	4	170	16	23	79	134	4
HG2	AM031-36	LABXR31-32 (TAR21)	4.70396	11351	131	2.0	-70.632155	-19	36.08	1.8	0.04644	6.93	0.1755	6.6	0.02810	1.7	0.10	-279	356	179	6	164	21	-64	109	179	6
HG2	AM031-17.I	LABXR30-31-32 (TAR	-0.00131	45342	169	0.8	7850.08368	19.7	29.76	1.2	0.05423	2.05	0.2541	2.0	0.03383	1.1	0.19	319	99	214	5	229	8	67	94	214	5
HG2	Spot 25.FIN	LABXR002_2-TAR21	-3.53098	5228	172	1.3	-93.3019526	-70	27.82	2.6	0.05261	4.02	0.2605	5.1	0.03660	2.3	0.71	500	145	232	11	240	19	46	97	232	11
HG2	~~Spot 49.FIN~~	~~LABXR002_1-TAR21~~	~~-8.58581~~	~~3827~~	~~147~~	~~1.6~~	~~-132.424444~~	~~-54~~	~~27.58~~	~~1.8~~	~~0.06126~~	~~4.46~~	~~0.3082~~	~~4.0~~	~~0.03660~~	~~1.8~~	~~0.25~~	~~726~~	~~165~~	~~232~~	~~8~~	~~271~~	~~19~~	~~32~~	~~85~~	~~232~~	~~8~~
HG2	AM031-23.I	LABXR30-31-32 (TAR	-0.36472	41303	131	1.1	-1877.64263	-18	27.31	1.0	0.05010	2.62	0.2616	2.5	0.03686	1.1	0.03	114	123	233	5	235	11	204	99	233	5
HG2	AM031-105	LABXR31-32 (TAR21)	0.87651	54550	548	1.8	-489.54696	-10	27.22	0.9	0.05192	2.04	0.2686	1.9	0.03708	0.9	0.10	210	93	235	4	241	8	112	98	235	4
HG2	Spot 28.FIN	LABXR002_2-TAR21	7.793847	9747	323	2.0	-1803.08708	-30	26.50	1.3	0.04947	2.59	0.2637	2.9	0.03792	1.3	0.18	367	131	240	6	239	12	65	100	240	6
HG2	Spot 25.FIN	LABXR002_1-TAR21	-4.41475	8198	273	1.3	74.6633037	141	25.15	1.2	0.05025	3.16	0.2883	3.8	0.03971	1.3	0.08	377	121	251	6	256	17	67	98	251	6
HG2	Spot 15.FIN	LABXR002_1-TAR21	21.29129	2230	73	2.4	1806.35479	85.5	25.29	2.3	0.05379	5.58	0.2887	4.0	0.03977	2.2	-0.12	594	181	251	11	256	18	42	98	251	11
HG2	Spot 50.FIN	LABXR002_2-TAR21	8.118343	5824	189	1.7	-89.9599386	-85	24.84	1.2	0.05286	3.53	0.2951	3.6	0.03999	1.2	0.26	527	115	253	6	262	16	48	97	253	6
HG2	AM031-101	LABXR31-32 (TAR21)	1.014305	27061	250	2.0	-294.401536	-8	25.14	0.8	0.05581	2.19	0.3100	2.2	0.04033	0.8	0.20	327	99	255	4	272	10	78	94	255	4
HG2	AM031-109	LABXR31-32 (TAR21)	-1.19115	16977	157	2.0	-170.077504	-5.9	25.09	1.0	0.03772	3.55	0.2117	3.9	0.04061	0.9	0.08	-273	133	256	5	189	14	-94	136	256	5
HG2	AM031-43	LABXR31-32 (TAR21)	-0.26393	18554	157	2.4	-188.020866	-16	24.76	2.0	0.05235	5.01	0.2997	4.3	0.04152	2.1	0.07	135	253	262	11	263	20	195	100	262	11
HG2	Spot 29.FIN	LABXR002_1-TAR21	3.14675	7375	238	2.0	15.7278604	236	24.19	1.5	0.05078	2.25	0.2968	2.6	0.04162	1.5	0.28	367	128	263	8	263	12	72	100	263	8
HG2	~~Spot 42.FIN~~	~~LABXR002_2-TAR21~~	~~-9.7546~~	~~3130~~	~~100~~	~~1.7~~	~~-25.138583~~	~~-59~~	~~23.32~~	~~2.0~~	~~0.08926~~	~~7.38~~	~~0.5788~~	~~8.6~~	~~0.04344~~	~~2.1~~	~~0.37~~	~~1432~~	~~298~~	~~274~~	~~11~~	~~460~~	~~65~~	~~19~~	~~60~~	~~274~~	~~11~~
HG2	Spot 28.FIN	LABXR002_1-TAR21	3.335913	9699	298	1.0	140.439044	63.9	23.06	0.9	0.05459	2.61	0.3269	2.6	0.04346	0.9	0.02	437	101	274	5	289	12	63	95	274	5
HG2	AM031-107	LABXR31-32 (TAR21)	1.459755	31679	270	1.6	-284.168277	-7.7	22.70	1.2	0.05430	4.15	0.3550	5.4	0.04482	1.4	0.10	193	87	282	8	287	16	146	98	282	8
HG2	AM031-98	LABXR31-32 (TAR21)	1.644644	15879	126	1.5	-143.612913	-9.1	22.39	1.1	0.05082	2.80	0.3212	2.9	0.04546	1.1	0.20	159	144	286	6	278	15	181	103	286	6
HG2	Spot 66.FIN	LABXR002_1-TAR21	8.803264	5667	173	1.9	61.4360554	82	21.07	1.5	0.05453	3.04	0.3564	2.4	0.04745	1.5	-0.08	406	116	299	9	309	13	74	97	299	9
HG2	Spot 41.FIN	LABXR002_1-TAR21	21.05834	6675	198	1.7	-68.4352084	-90	20.91	1.4	0.05279	3.75	0.3366	3.5	0.04755	1.4	0.21	558	102	299	8	298	19	54	101	299	8
HG2	~~AM031-97~~	LABXR31-32 (TAR21)	~~5.625901~~	~~11745~~	~~84~~	~~1.2~~	~~-110.555392~~	~~-14~~	~~22.06~~	~~1.7~~	~~0.10237~~	~~5.70~~	~~0.6449~~	~~5.8~~	~~0.04816~~	~~2.2~~	~~0.05~~	~~1012~~	~~195~~	~~302~~	~~13~~	~~456~~	~~33~~	~~30~~	~~66~~	~~302~~	~~13~~
HG2	AM031-67	LABXR31-32 (TAR21)	1.187528	20716	144	2.0	-211.709388	-6.9	21.14	0.8	0.06119	2.89	0.4072	2.9	0.04863	1.0	0.12	482	92	306	6	338	14	63	91	306	6
HG2	AM031-44	LABXR31-32 (TAR21)	-0.07984	89724	684	1.1	-761.952594	-11	20.42	0.8	0.05554	1.56	0.3807	1.5	0.04915	0.8	0.09	403	73	309	5	327	8	77	95	309	5
HG2	Spot 9.FIN2	LABXR002_1-TAR21	9.565559	2859	74	1.1	-65.02849	-65	20.05	1.8	0.05957	5.27	0.4061	5.0	0.04993	1.7	-0.04	828	151	314	10	343	30	38	92	314	10
HG2	Spot 31.FIN	LABXR002_1-TAR21	1.423639	4942	134	1.1	9.0793232	542	19.78	1.5	0.05483	3.36	0.3731	3.2	0.05025	1.7	0.18	526	111	316	10	321	17	60	98	316	10
HG2	AM031-42	LABXR31-32 (TAR21)	-1.38874	62827	479	1.2	-637.279673	-11	20.03	1.1	0.05652	2.43	0.3941	2.2	0.05032	1.0	0.15	401	116	316	6	336	13	79	94	316	6
HG2	AM031-14.I	LABXR30-31-32 (TAR	0.244511	135395	329	1.8	-4062.85804	-13	19.84	0.6	0.05301	1.26	0.3693	1.0	0.05051	0.6	-0.09	301	55	318	4	319	6	105	100	318	4
HG2	AM031-112	LABXR31-32 (TAR21)	0.159925	21028	153	1.4	-236.12495	-13	20.26	0.9	0.05269	2.23	0.3621	2.1	0.05085	1.2	-0.03	224	101	319	7	311	11	143	103	319	7
HG2	Spot 63.FIN	LABXR002_1-TAR21	-0.92266	8900	251	1.3	178.111314	76.9	19.72	1.1	0.05112	3.03	0.3586	3.1	0.05087	1.1	0.26	348	111	320	7	310	17	92	103	320	7
HG2	AM031-46	LABXR31-32 (TAR21)	-0.78943	28553	232	2.2	-239.780456	-6.7	22.50	1.1	0.05144	1.97	0.3345	3.9	0.05167	3.5	0.46	188	90	322	21	285	13	171	113	322	21
HG2	AM031-29	LABXR31-32 (TAR21)	0.459133	30808	192	2.5	-258.218017	-7.6	19.67	0.8	0.05575	2.03	0.3965	1.9	0.05137	0.8	-0.03	349	90	323	5	337	11	92	96	323	5
HG2	Spot 48.FIN	LABXR002_2-TAR21	-0.97219	12231	320	1.5	228.135038	55.5	19.37	0.8	0.05140	1.88	0.3708	2.0	0.05173	0.8	0.18	291	85	325	5	320	11	112	102	325	5
HG2	Spot 66.FIN	LABXR002_2-TAR21	0.141292	7754	206	1.5	-219.703479	-55	19.21	1.4	0.05455	2.65	0.3984	2.4	0.05178	1.3	0.08	476	97	325	8	340	14	68	96	325	8
HG2	AM031-69	LABXR31-32 (TAR21)	0.510834	34358	234	1.8	-349.379153	-6.6	19.33	0.7	0.05321	1.81	0.3868	1.8	0.05238	0.8	-0.04	203	86	329	5	328	10	162	100	329	5
HG2	Spot 15.FIN	LABXR002_2-TAR21	-5.36054	6581	160	1.2	-95.6169036	-75	19.12	1.0	0.05394	2.90	0.3941	2.8	0.05246	1.0	-0.25	469	94	330	6	341	15	70	97	330	6
HG2	Spot 26.FIN	LABXR002_2-TAR21	5.165289	9171	232	2.1	-41291.936	-126	18.78	1.2	0.05632	2.33	0.4133	2.6	0.05294	1.2	0.06	483	94	333	8	350	16	69	95	333	8
HG2	AM031-90	LABXR31-32 (TAR21)	4.197832	23474	166	2.0	-183.073234	-8.2	19.27	1.6	0.05481	2.40	0.3917	4.7	0.05558	3.1	0.32	336	100	343	19	330	13	102	104	343	19

HG2	AM031-77	LABXR31-32 (TAR21)	1.346735	15678	96	3.2	-172.61001	-11	16.78	1.6	0.05577	3.90	0.5499	7.1	0.06959	3.8	0.13	269	132	423	28	378	28	157	112	423	28
HG2	AM031-87	LABXR31-32 (TAR21)	0.178227	41506	206	1.4	-352.270824	-10	14.66	0.9	0.05600	1.98	0.5370	2.0	0.06885	0.9	0.33	404	87	429	7	435	15	106	99	429	7
HG2	AM031-13.I	LABXR30-31-32 (TAR	0.477995	378527	669	1.2	-5835.56293	-21	14.28	1.7	0.05725	1.70	0.5522	1.7	0.07171	1.7	0.43	478	76	446	15	445	12	93	100	446	15
HG2	AM031-50	LABXR31-32 (TAR21)	1.643225	28218	149	2.2	-201.064853	-20	14.18	2.3	0.06147	3.19	0.6235	3.4	0.07217	2.2	0.30	602	164	449	19	488	27	75	92	449	19
HG2	Spot 42.FIN	LABXR002_1-TAR21	-0.32712	15169	286	0.1	-97.647004	-55	13.75	0.9	0.05505	2.24	0.5511	2.7	0.07287	0.9	0.42	447	93	453	8	448	18	102	101	453	8
HG2	AM031-68	LABXR31-32 (TAR21)	0.535569	40203	193	1.4	-370.165735	-9	13.59	1.0	0.05725	2.13	0.5885	1.9	0.07413	0.9	0.02	422	94	461	8	466	14	109	99	461	8
HG2	AM031-2.FI	LABXR30-31-32 (TAR	0.530612	197068	315	0.2	5955.3742	15.3	13.30	0.5	0.05651	1.01	0.5927	0.9	0.07550	0.5	0.02	447	47	469	5	472	7	105	99	469	5
HG2	AM031-100	LABXR31-32 (TAR21)	-0.01513	25545	119	1.0	-258.968133	-5.8	13.39	0.7	0.06082	2.10	0.6336	1.8	0.07554	0.7	-0.03	484	82	469	6	489	13	97	96	469	6
HG2	Spot 60.FIN	LABXR002_2-TAR21	6.331448	16645	298	0.2	396.964543	83	13.19	1.2	0.05674	1.77	0.5885	1.8	0.07618	1.2	0.40	467	77	473	11	469	13	101	101	473	11
HG2	AM031-30	LABXR31-32 (TAR21)	-0.48678	18563	81	1.5	-124.322826	-13	13.41	1.4	0.05574	3.42	0.5851	3.3	0.07624	1.4	0.01	340	151	473	12	461	24	139	103	473	12
HG2	Spot 12.FIN	LABXR002_1-TAR21	12.98074	3701	61	0.7	-9.83192553	-169	13.11	1.9	0.06075	4.73	0.6209	4.1	0.07654	2.0	0.15	742	173	475	18	487	32	64	98	475	18
HG2	AM031-16.I	LABXR30-31-32 (TAR	0.443922	170689	268	1.1	113021.338	21.8	12.65	1.2	0.05822	1.89	0.6254	1.7	0.07986	1.2	0.14	516	80	495	12	492	13	96	101	495	12
HG2	AM031-60	LABXR31-32 (TAR21)	-4.33754	84799	358	0.0	-844.650161	-6.4	12.91	1.5	0.05698	2.12	0.6306	1.7	0.08008	1.4	0.71	485	72	496	13	500	11	102	99	496	13
HG2	AM031-28	LABXR31-32 (TAR21)	0.170024	66837	281	1.8	-505.86364	-14	12.56	1.4	0.05951	2.35	0.6583	2.3	0.07996	1.4	0.35	565	101	496	14	513	20	88	97	496	14
HG2	AM031-34	LABXR31-32 (TAR21)	0.643085	27792	115	1.5	-234.902765	-8.3	12.57	0.8	0.06595	1.94	0.7268	1.7	0.08057	0.8	0.04	701	79	499	8	555	15	71	90	499	8
HG2	AM031-86	LABXR31-32 (TAR21)	-0.44182	63617	256	1.4	-551.262086	-7.6	11.55	0.7	0.05799	1.50	0.7046	1.4	0.08730	0.8	-0.08	480	71	539	8	541	11	112	100	539	8
HG2	Spot 61.FIN	LABXR002_2-TAR21	9.671797	9420	144	1.2	-3169520861	-42	11.16	1.4	0.05890	2.40	0.7355	3.5	0.08965	1.5	0.47	629	81	553	16	556	30	88	99	553	16
HG2	AM031-3.FI	LABXR30-31-32 (TAR	0.121786	370937	452	0.1	60894.7485	13.4	10.91	0.5	0.05789	0.71	0.7456	0.6	0.09203	0.5	0.10	519	31	567	5	566	6	109	100	567	5
HG2	AM031-113	LABXR31-32 (TAR21)	-0.49943	36556	149	0.9	-344.142008	-8.5	10.98	1.1	0.06253	2.14	0.7890	1.8	0.09243	1.2	0.05	620	92	569	13	590	16	92	97	569	13
HG2	AM031-94	LABXR31-32 (TAR21)	1.023614	93016	360	2.1	-585.781769	-15	10.59	0.8	0.06369	1.73	0.8493	1.7	0.09503	0.8	0.20	699	74	585	9	621	15	84	94	585	9
HG2	Spot 44.FIN	LABXR002_1-TAR21	1.436998	14463	206	0.4	-315.48785	-51	10.56	1.3	0.05901	2.05	0.7801	2.6	0.09516	1.3	0.50	548	91	586	15	589	21	107	100	586	15
HG2	AM031-85	LABXR31-32 (TAR21)	0.896337	36845	134	1.3	-247.535612	-9.8	10.55	0.6	0.05826	1.62	0.7735	1.5	0.09536	0.7	0.10	449	75	588	7	576	14	131	102	588	7
HG2	Spot 27.FIN	LABXR002_1-TAR21	1.544193	17188	223	0.0	102.982789	114	10.03	1.3	0.06085	1.47	0.8465	2.2	0.09962	1.3	0.59	624	63	612	15	621	20	98	99	612	15
HG2	Spot 10.FIN	LABXR002_2-TAR21	77.30955	1537	19	1.0	-91.4657628	-73	10.07	2.4	0.06287	5.81	0.8618	4.6	0.09976	2.1	-0.14	854	190	613	24	624	44	72	98	613	24
HG2	Spot 11.FIN	LABXR002_2-TAR21	-6.99346	4934	62	1.3	-17.8658302	-132	9.69	1.2	0.06214	3.13	0.8949	2.5	0.10244	1.2	-0.21	716	121	629	14	647	24	88	97	629	14
HG2	Spot 50.FIN	LABXR002_1-TAR21	9.269787	3013	41	0.8	-63.4276743	-80	9.64	2.0	0.06908	4.32	1.0274	3.9	0.10414	2.0	0.15	979	156	638	25	721	38	65	89	638	25
HG2	AM031-95	LABXR31-32 (TAR21)	0.413098	138722	526	1.9	-1078.88738	-12	9.77	1.7	0.06612	1.38	0.9692	1.8	0.10535	1.6	0.52	781	57	645	20	684	18	83	94	645	20
HG2	AM031-118	LABXR31-32 (TAR21)	1.993039	19790	69	2.0	-208.826436	-6.1	9.55	0.9	0.06435	1.99	0.9411	2.0	0.10746	1.1	0.34	604	93	657	14	659	19	109	100	657	14
HG2	AM031-93	LABXR31-32 (TAR21)	0.217597	71083	244	2.8	-600.164137	-11	9.29	1.0	0.06265	1.61	0.9456	1.4	0.10897	1.0	0.68	662	68	666	13	673	14	101	99	666	13
HG2	Spot 58.FIN	LABXR002_1-TAR21	0.345386	9005	116	0.9	197.835813	125	9.01	1.4	0.06630	2.86	1.0125	3.0	0.11160	1.4	0.31	783	118	682	18	707	31	87	96	682	18
HG2	AM031-9.FI	LABXR30-31-32 (TAR	-0.25517	141580	155	0.8	-10146.0485	-18	8.86	0.9	0.06854	1.85	1.0729	1.5	0.11370	0.9	0.06	846	74	694	12	738	15	82	94	694	12

HG2	AM031-45	LABXR31-32 (TAR21)	-0.01864	64244	204	0.6	-512.403411	-15	8.40	1.6	0.06833	2.65	1.1428	2.4	0.12037	1.5	0.16	824	113	732	20	773	25	89	95	732	20
HG2	AM031-80	LABXR31-32 (TAR21)	0.538487	38677	97	3.2	-311.955574	-7.1	7.59	0.6	0.06457	1.36	1.1968	1.4	0.13284	0.7	0.16	710	60	804	11	792	15	113	102	804	11
HG2	AM031-74	LABXR31-32 (TAR21)	0.23442	27163	67	1.1	-290.595509	-6.6	7.56	1.1	0.07228	2.12	1.3115	1.7	0.13492	0.9	0.12	912	85	815	14	840	19	89	97	815	14
HG2	Spot 31.FIN	LABXR002_2-TAR21	2.699798	19330	185	0.6	114.906233	112	7.38	0.8	0.06576	1.00	1.2541	1.1	0.13583	0.8	0.17	806	48	821	12	825	12	102	100	821	12
HG2	~~Spot 49.FIN~~	~~LABXR002_2-TAR21~~	~~-30.241~~	~~2082~~	~~21~~	~~0.5~~	~~79197960.1~~	~~98.4~~	~~7.38~~	~~4.6~~	~~0.09925~~	~~6.34~~	~~1.9271~~	~~7.6~~	~~0.13721~~	~~4.6~~	~~0.62~~	~~1568~~	~~226~~	~~826~~	~~72~~	~~1070~~	~~101~~	~~53~~	~~77~~	~~826~~	~~72~~
HG2	AM031-71	LABXR31-32 (TAR21)	16.12148	53872	134	0.5	-715.456755	-6.4	7.25	1.1	0.06548	1.34	1.2978	1.7	0.14159	1.1	0.15	718	50	852	17	829	18	119	103	852	17
HG2	AM031-41	LABXR31-32 (TAR21)	-0.30658	88119	218	0.1	-931.930163	-13	7.03	1.1	0.07431	1.99	1.4887	1.8	0.14316	1.1	-0.02	1038	86	862	18	923	22	83	93	862	18
HG2	AM031-89	LABXR31-32 (TAR21)	0.180373	30411	72	0.9	-289.383981	-6.3	6.95	0.7	0.06946	1.51	1.4101	1.4	0.14584	0.7	0.11	847	63	877	11	886	16	104	99	877	11
HG2	AM031-47	LABXR31-32 (TAR21)	-2.09962	30103	74	3.3	-289.68984	-13	7.11	2.8	0.06304	3.89	1.3265	4.6	0.14660	2.3	0.56	643	192	879	39	835	55	137	105	879	39
HG2	~~AM031-7.FI~~	~~LABXR30-31-32 (TAR~~	~~0.18021~~	~~######~~	~~1858~~	~~0.2~~	~~-46759.5506~~	~~-33~~	~~6.89~~	~~1.5~~	~~0.08476~~	~~1.41~~	~~1.7239~~	~~2.0~~	~~0.14672~~	~~1.6~~	~~0.69~~	~~1298~~	~~55~~	~~882~~	~~26~~	~~1014~~	~~25~~	~~68~~	~~87~~	~~882~~	~~26~~
HG2	AM031-88	LABXR31-32 (TAR21)	-0.16968	22647	51	0.7	-208.434486	-6.4	6.66	0.7	0.06550	1.78	1.3861	1.7	0.15212	0.8	0.13	700	84	912	12	869	20	130	105	912	12
HG2	AM031-63	LABXR31-32 (TAR21)	0.324733	69645	192	1.2	-617.666174	-9.6	6.85	2.5	0.07107	1.35	1.5307	2.2	0.15407	1.8	0.76	918	58	920	32	925	29	100	99	920	32
HG2	AM031-40	LABXR31-32 (TAR21)	0.891735	40917	94	1.2	-267.69095	-18	6.52	1.3	0.07707	2.30	1.6619	2.2	0.15448	1.4	0.20	1087	99	925	23	993	27	85	93	925	23
HG2	AM031-61	LABXR31-32 (TAR21)	1.276249	63170	147	0.9	-464.349695	-11	6.63	2.4	0.06854	1.61	1.5155	2.3	0.15793	1.8	0.71	845	70	943	33	923	30	112	102	943	33
HG2	Spot 62.FIN	LABXR002_2-TAR21	-5.9435	18340	164	0.5	91.8254238	160	6.38	1.3	0.07074	1.67	1.5678	1.7	0.15754	1.3	0.51	969	56	943	23	956	21	97	99	943	23
HG2	AM031-19.I	LABXR30-31-32 (TAR	-0.22238	48533	38	1.5	-22411.652	-20	6.38	1.7	0.07336	2.70	1.5758	2.5	0.15764	1.6	0.19	962	110	949	25	949	32	99	100	949	25
HG2	AM031-53	LABXR31-32 (TAR21)	0.842616	168215	373	0.5	-1193.77076	-8.8	6.44	1.0	0.07341	0.95	1.6305	1.3	0.16002	1.2	0.82	1001	37	950	19	967	13	95	98	950	19
HG2	Spot 47.FIN	LABXR002_1-TAR21	-2.96013	13578	116	0.3	-546.840839	-41	6.20	1.5	0.07618	1.71	1.6584	1.7	0.16140	1.7	0.69	1102	71	964	30	997	19	88	97	964	30
HG2	AM031-70	LABXR31-32 (TAR21)	2.598947	15337	32	1.0	-129.625522	-8.2	6.32	1.1	0.07224	2.23	1.6096	2.1	0.16176	1.1	0.13	883	99	965	19	957	27	109	101	965	19
HG2	Spot 14.FIN	LABXR002_1-TAR21	-2.70672	20988	174	0.8	-3310.96699	-95	6.05	1.1	0.07595	1.45	1.7045	2.3	0.16590	1.1	0.80	1085	58	989	21	1007	31	91	98	989	21
HG2	Spot 30.FIN	LABXR002_2-TAR21	5.48193	11246	87	0.8	1064.61253	46.7	6.04	1.0	0.07125	1.89	1.6165	1.9	0.16599	1.0	0.29	967	69	990	18	979	22	102	101	990	18
HG2	AM031-108	LABXR31-32 (TAR21)	-1.18315	36773	75	2.2	-353.585205	-8.7	6.10	1.5	0.08602	1.91	2.0268	1.9	0.16721	1.4	0.45	1302	82	995	26	1114	27	76	89	995	26
HG2	AM031-32	LABXR31-32 (TAR21)	1.280529	17750	35	3.6	-151.413555	-8.5	6.04	1.1	0.07539	2.14	1.7743	2.2	0.16799	1.1	0.22	1002	91	999	20	1018	29	100	98	999	20
HG2	~~Spot 59.FIN~~	~~LABXR002_2-TAR21~~	~~1.047264~~	~~19265~~	~~158~~	~~0.5~~	~~13.1590885~~	~~1315~~	~~6.08~~	~~4.1~~	~~0.09493~~	~~1.36~~	~~2.2224~~	~~3.6~~	~~0.17127~~	~~3.3~~	~~0.94~~	~~1519~~	~~51~~	~~1017~~	~~63~~	~~1190~~	~~47~~	~~67~~	~~85~~	~~1017~~	~~63~~
HG2	AM031-21.I	LABXR30-31-32 (TAR	0.360926	94157	60	0.6	2568.78842	21.8	5.81	0.8	0.07443	1.50	1.7742	1.4	0.17341	0.8	0.06	1011	61	1030	16	1031	17	102	100	1030	16
HG2	AM031-49	LABXR31-32 (TAR21)	0.332009	90798	198	1.8	-793.415464	-11	5.87	1.6	0.07120	1.60	1.7479	1.8	0.17479	1.4	0.35	947	59	1037	28	1014	21	109	102	1037	28
HG2	AM031-10.I	LABXR30-31-32 (TAR	0.115195	311671	211	0.3	-61795.3108	-19	5.63	0.6	0.07571	0.89	1.8789	0.8	0.17836	0.6	0.26	1073	36	1058	12	1073	11	99	99	1058	12
HG2	Spot 46.FIN	LABXR002_1-TAR21	3.499361	7763	60	0.6	-68.963572	-104	5.60	1.5	0.07932	2.91	1.9484	2.9	0.17969	1.5	0.23	1148	115	1065	29	1092	39	93	97	1065	29
HG2	Spot 65.FIN	LABXR002_1-TAR21	-4.41987	8481	66	0.9	-0.20077906	####	5.53	1.4	0.07660	2.53	1.9110	2.0	0.17975	1.3	0.13	1111	93	1065	26	1089	29	96	98	1065	26
HG2	Spot 57.FIN	LABXR002_1-TAR21	-0.01876	7145	56	0.6	-32.9292874	-96	5.56	1.6	0.08103	2.06	1.9944	2.1	0.18109	1.6	0.27	1223	87	1072	31	1111	28	88	97	1072	31
HG2	AM031-78	LABXR31-32 (TAR21)	-0.02215	221934	428	1.0	-2239.41611	-9.9	5.56	1.0	0.07560	1.14	1.9083	1.2	0.18123	0.9	0.51	1066	45	1073	19	1081	17	101	99	1073	19
HG2	AM031-39	LABXR31-32 (TAR21)	-0.24909	68622	135	1.0	-557.391466	-8.8	5.55	0.9	0.07739	1.49	1.9500	1.4	0.18212	0.9	0.26	1086	61	1078	18	1092	19	99	99	1078	18
HG2	Spot 44.FIN	LABXR002_2-TAR21	-6.01143	5904	43	0.9	-330.993327	-41	5.49	1.2	0.08568	3.41	1.2524	3.0	0.18301	1.2	-0.14	1290	126	1083	24	1159	41	84	93	1083	24
HG2	Spot 43.FIN	LABXR002_1-TAR21	0.903954	30681	227	0.4	-612.489638	-54	5.44	1.2	0.08071	1.17	2.0256	1.7	0.18457	1.2	0.76	1208	46	1092	24	1122	23	90	97	1092	24
HG2	AM031-65	LABXR31-32 (TAR21)	2.539823	90852	174	0.8	-693.158757	-12	5.44	0.8	0.08872	2.16	2.3398	2.7	0.18592	0.8	0.72	1286	73	1098	16	1188	32	85	92	1098	16
HG2	AM031-58	LABXR31-32 (TAR21)	1.333174	23195	43	2.3	-244.687038	-8.8	5.45	0.8	0.07344	1.52	1.9021	1.5	0.18630	0.8	0.13	981	63	1100	16	1067	20	112	103	1100	16
HG2	AM031-11.I	LABXR30-31-32 (TAR	0.410065	516610	343	2.3	-9519.60694	-27	5.35	1.0	0.07871	1.37	2.0121	1.2	0.18784	1.0	0.34	1147	51	1109	21	1117	16	97	99	1109	21
HG2	Spot 60.FIN	LABXR002_1-TAR21	-0.23038	32684	242	1.0	1075.03089	68	5.32	1.1	0.08107	1.56	2.0993	1.7	0.18875	1.2	0.56	1227	56	1114	24	1147	23	91	97	1114	24
HG2	AM031-4.FI	LABXR30-31-32 (TAR	0.146822	130226	85	1.0	-8574.78475	-17	5.30	0.7	0.07676	1.12	2.0165	1.1	0.18926	0.7	0.21	1084	46	1117	14	1117	14	103	100	1117	14
HG2	AM031-15.I	LABXR30-31-32 (TAR	0.608346	75691	49	0.5	-5258.70615	-18	5.31	1.1	0.08174	1.56	2.1291	1.4	0.18956	1.0	0.36	1230	58	1118	20	1154	19	91	97	1118	20
HG2	Spot 43.FIN	LABXR002_2-TAR21	-6.77068	3024	22	2.3	67.4475568	69.6	5.33	2.1	0.07019	3.51	1.7785	2.5	0.18851	2.0	0.05	911	152	1121	44	1034	32	123	108	1121	44
HG2	Spot 13.FIN	LABXR002_2-TAR21	2.921294	11188	65	0.6	-1102.53974	-77	5.29	1.5	0.07535	1.90	1.9343	2.5	0.19037	1.5	0.67	1077	82	1123	30	1089	33	104	103	1123	30
HG2	AM031-27	LABXR31-32 (TAR21)	-0.03031	340101	546	0.7	-3215.11336	-11	5.30	1.6	0.09374	1.83	2.4955	1.4	0.19205	1.5	0.27	1486	66	1131	32	1267	21	76	89	1131	32
HG2	AM031-106	LABXR31-32 (TAR21)	0.348092	32495	65	0.7	-348.582312	-10	5.33	1.3	0.07915	1.51	2.0981	1.6	0.19240	1.1	0.19	1106	58	1131	24	1130	22	102	100	1131	24
HG2	Spot 32.FIN	LABXR002_2-TAR21	5.671412	9283	63	1.2	-34.3702528	-228	5.20	1.2	0.08305	1.75	2.1942	1.6	0.19203	1.1	-0.01	1274	77	1132	23	1177	22	89	96	1132	23
HG2	AM031-20.I	LABXR30-31-32 (TAR	0.555637	132336	82	0.1	947798.276	36.3	5.26	1.3	0.07572	1.21	2.0212	1.6	0.19224	1.2	0.59	1078	52	1132	25	1122	23	105	101	1132	25
HG2	AM031-119	LABXR31-32 (TAR21)	1.539259	35553	68	1.1	-402.649335	-7.7	5.22	1.0	0.07848	1.36	2.1111	1.3	0.19454	0.8	0.30	1120	57	1147	17	1150	19	102	100	1147	17
HG2	AM031-110	LABXR31-32 (TAR21)	0.093044	62205	118	0.7	-522.146729	-8.6	5.14	0.8	0.07586	1.30	2.0591	1.1	0.19610	0.8	0.16	1049	52	1153	17	1130	16	110	102	1153	17
HG2	AM031-99	LABXR31-32 (TAR21)	2.59203	18729	33	2.7	-177.388964	-6.6	5.36	1.8	0.08584	1.97	2.3490	2.1	0.19754	1.4	0.26	1237	75	1157	30	1191	32	93	97	1157	30
HG2	AM031-81	LABXR31-32 (TAR21)	0.407689	44219	77	0.6	-459.251251	-7.5	5.04	1.3	0.07650	2.04	2.1145	1.7	0.20073	1.1	0.01	1050	79	1178	25	1144	23	112	103	1178	25
HG2	AM031-104	LABXR31-32 (TAR21)	0.111013	138013	254	0.2	-1520.52301	-5.8	5.03	0.6	0.08019	0.77	2.2373	0.7	0.20112	0.6	0.26	1182	30	1180	14	1190	10	100	99	1180	14
HG2	Spot 16.FIN	LABXR002_2-TAR21	0.032607	11912	78	1.3	90.5954786	122	4.96	0.9	0.07880	2.01	2.1936	1.8	0.20129	0.8	-0.14	1151	79	1182	18	1177	25	103	100	1182	18
HG2	AM031-5.FI	LABXR30-31-32 (TAR	0.908911	33601	18	1.3	-685.847942	-20	5.00	1.2	0.08153	2.01	2.2595	2.2	0.20251	1.1	0.34	1188	85	1187	23	1189	32	100	100	1187	23
HG2	Spot 18.FIN	LABXR002_2-TAR21	-5.64172	8285	55	0.7	-210.171846	-44	4.97	1.5	0.08193	2.68	2.2470	3.1	0.20257	1.5	0.36	1214	110	1188	33	1206	39	98	99	1188	33
HG2	Spot 10.FIN	LABXR002_1-TAR21	13.71897	4348	28	1.5	4.86294181	1033	4.85	2.1	0.08464	3.67	2.4291	3.5	0.20504	2.1	0.06	1330	146	1201	46	1242	49	90	97	1201	46
HG2	Spot 59.FIN	LABXR002_1-TAR21	0.913758	46650	326	0.5	-4.72997674	####	4.83	1.0	0.08490	1.29	2.4160	1.2	0.20524	1.0	0.52	1306	51	1203	22	1251	20	92	96	1203	22
HG2	AM031-64	LABXR31-32 (TAR21)	-0.01993	315507	540	0.3	-3186.15689	-7.4	4.89	1.0	0.08146	1.03	2.3641	1.4	0.20726	1.0	0.66	1216	40	1213	22	1223	21	100	99	1213	22
HG2	Spot 46.FIN	LABXR002_2-TAR21	-0.33412	18935	120	0.4	-116.020686	-125	4.78	1.1	0.08236	1.45	2.3373	1.6	0.20888	1.1	0.10	1245	58	1223	25	1226	22	98	100	1223	25
HG2	AM031-56	LABXR31-32 (TAR21)	0.053431	181345	306	0.3	-1953.91021	-6.3	4.78	0.6	0.08105	0.90	2.3799	0.8	0.21029	0.6	0.27	1209	36	1230	14	1235	12	102	100	1230	14
HG2	Spot 9.FIN2	LABXR002_2-TAR21	3.002068	27734	166	0.9	-62.9443327	-310	4.74	0.9	0.08101	1.92	2.3556	1.8	0.21069	0.9	0.23	1238	73	1232	19	1237	26	100	100	1232	19
HG2	Spot 57.FIN	LABXR002_2-TAR21	-8.35268	8644	57	1.0	-47.9828811	-119	4.77	1.5	0.08074	2.79	2.3444	2.4	0.21124	1.5	0.12	1230	108	1235	33	1221	34	100	101	1235	33
HG2	Spot 18.FIN	LABXR002_1-TAR21	0.450673	36123	225	0.1	994.334649	84	4.71	0.8	0.08031	1.35	2.3088	1.1	0.21187	0.9	0.32	1197	53	1239	20	1214	16	103	102	1239	20
HG2	AM031-115	LABXR31-32 (TAR21)	0.539956	184766	315	0.9	-1683.28911	-7.8	4.69	0.6	0.08669	0.79	2.5859	0.8	0.21461	0.6	0.34	1345	31	1253	13	1295	11	93	97	1253	13
HG2	AM031-59	LABXR31-32 (TAR21)	-0.30072	106146	177	0.5	-1382.99908	-10	4.68	0.8	0.08103	1.22	2.4179	1.1	0.21567	0.9	0.28	1204	48	1257	20	1245	17	104	101	1257	20
HG2	Spot 26.FIN	LABXR002_1-TAR21	7.219545	4828	29	0.5	80.4003899	80.8	4.65	1.3	0.08264	2.94	2.4332	2.9	0.21604	1.3	-0.19	1282	114	1260	31	1255	39	98	100	1260	31
HG2	Spot 12.FIN	LABXR002_2-TAR21	0.162475	12648	68	1.4	481.592624	46	4.76	4.2	0.10265	2.65	3.0938	5.0	0.21738	4.2	0.88	1648	97	1263	96	1424	75	77	89	1263	96
HG2	AM031-24.I	LABXR30-31-32 (TAR	-0.01522	568107	323	1.4	-9695.48497	-19	4.63	0.8	0.08585	0.95	2.5339	0.8	0.21721	0.8	0.25	1324	36	1267	18	1280	12	96	99	1267	18
HG2	Spot 16.FIN	LABXR002_1-TAR21	3.60543	11432	68	1.0	413.464018	118	4.60	1.5	0.08749	2.31	2.6254	2.7	0.21775	1.6	0.54	1387	92	1269	37	1302	41	92	97	1269	37
HG2	AM031-84	LABXR31-32 (TAR21)	0.060576	166176	272	1.2	-1450.392	-8.2	4.58	0.6	0.08351	0.95	2.5488	0.9	0.21961	0.6	0.19	1261	38	1279	14	1283	13	101	100	1279	14
HG2	Spot 27.FIN	LABXR002_2-TAR21	-1.48829	27494	160	0.6	556.538477	85	4.56	0.7	0.08460	1.45	2.5828	1.5	0.21966	0.7	0.18	1298	55	1280	16	1294	22	99	99	1280	16
HG2	Spot 34.FIN	LABXR002_2-TAR21	-3.99486	13788	82	1.0	-77.8759115	-100	4.52	1.0	0.08748	1.74	2.6704	1.9	0.22132	1.1	0.28	1359	67	1288	25	1317	29	95	98	1288	25
HG2	~~AM031-117~~	LABXR31-32 (TAR21)	~~3.101619~~	~~214204~~	~~350~~	~~1.0~~	~~-772.442959~~	~~-17~~	~~4.45~~	~~1.2~~	~~0.13443~~	~~3.06~~	~~4.1834~~	~~3.5~~	~~0.23044~~	~~1.3~~	~~0.45~~	~~1961~~	~~80~~	~~1334~~	~~30~~	~~1615~~	~~49~~	~~68~~	~~83~~	~~1334~~	~~30~~

HG2	AM031-120	LABXR31-32 (TAR21)	0.147544	59025	94	2.1	-638.257415	-8.7	4.34	1.1	0.09637	1.60	3.1049	1.5	0.23343	1.0	0.07	1527	55	1351	26	1425	24	88	95	1351	26
HG2	Spot 63.FIN	LABXR002_2-TAR21	5.197531	25227	151	0.4	970.169265	68.3	4.32	1.7	0.08973	2.04	2.8433	1.8	0.23341	1.7	0.65	1419	79	1351	41	1364	27	95	99	1351	41
HG2	Spot 58.FIN	LABXR002_2-TAR21	-4.97545	15902	93	0.8	227.454339	85.5	4.27	1.2	0.08368	1.57	2.6906	1.7	0.23519	1.2	0.46	1275	62	1361	29	1324	25	107	103	1361	29
HG2	AM031-102	LABXR31-32 (TAR21)	0.847533	53162	78	2.1	-584.087678	-6.2	4.33	1.2	0.09042	1.10	3.0223	1.5	0.23793	1.0	0.54	1395	44	1375	26	1396	23	99	98	1375	26
HG2	Spot 61.FIN	LABXR002_1-TAR21	-1.17227	19677	114	2.4	848.129779	57.2	4.19	1.5	0.09723	1.66	3.1791	1.8	0.24015	1.5	0.73	1575	58	1387	37	1449	28	88	96	1387	37
HG2	Spot 45.FIN	LABXR002_1-TAR21	-4.85657	6543	37	0.5	-84.5869575	-83	4.18	1.2	0.09768	2.74	3.2521	2.6	0.24034	1.2	0.19	1554	103	1388	30	1473	36	89	94	1388	30
HG2	AM031-62	LABXR31-32 (TAR21)	0.385237	375498	578	1.2	-2388.37977	-12	4.21	1.0	0.09154	0.88	3.0770	1.2	0.24122	0.9	-0.07	1438	32	1391	23	1420	18	97	98	1391	23
HG2	Spot 64.FIN	LABXR002_1-TAR21	0.006826	105192	648	0.1	2327.40923	59.2	4.18	1.8	0.09240	1.30	3.1351	1.9	0.23899	1.8	0.92	1481	55	1393	40	1438	31	94	97	1393	40
HG2	AM031-18.I	LABXR30-31-32 (TAR	0.003366	######	800	0.4	2027191.35	19.4	4.10	0.9	0.09265	1.28	3.0432	1.1	0.24542	1.0	0.03	1465	48	1414	26	1416	16	97	100	1414	26
HG2	AM031-37	LABXR31-32 (TAR21)	0.160253	84382	119	1.0	-658.192811	-9.2	4.10	1.1	0.07992	0.89	2.7778	1.2	0.24845	1.1	0.61	1191	34	1428	27	1342	19	120	106	1428	27
HG2	Spot 33.FIN	LABXR002_2-TAR21	2.115515	18470	95	1.0	-403.498164	-95	3.99	0.7	0.09259	1.86	3.2327	1.3	0.25079	0.7	0.03	1466	72	1442	18	1463	21	98	99	1442	18
HG2	AM031-31	LABXR31-32 (TAR21)	-0.00087	227134	299	0.9	-1926.29783	-8	3.99	0.7	0.09296	0.76	3.2521	0.8	0.25330	0.7	0.57	1473	28	1454	17	1468	13	99	99	1454	17
HG2	Spot 64.FIN	LABXR002_2-TAR21	5.138957	14570	79	1.4	-744.713453	-54	3.93	1.2	0.08885	1.89	3.1274	1.9	0.25539	1.2	0.33	1435	77	1466	31	1436	29	102	102	1466	31
HG2	Spot 13.FIN	LABXR002_1-TAR21	0.576262	83949	441	0.9	-4082.6623	-110	3.91	1.2	0.09459	0.65	3.3390	1.3	0.25556	1.3	0.85	1523	26	1466	33	1493	21	96	98	1466	33
HG2	AM031-8.FI	LABXR30-31-32 (TAR	0.320409	######	573	2.1	-27994.7965	-38	3.93	1.4	0.09692	1.42	3.4768	1.5	0.25621	1.4	0.52	1555	53	1469	36	1519	23	94	97	1469	36
HG2	Spot 62.FIN	LABXR002_1-TAR21	0.559583	99443	550	3.1	1077.87153	87.6	3.89	0.7	0.09653	0.88	3.3982	1.1	0.25638	0.7	0.58	1555	33	1471	18	1506	18	95	98	1471	18
HG2	AM031-96	LABXR31-32 (TAR21)	0.193105	122994	177	0.7	-1046.00486	-9.1	4.02	1.5	0.09849	0.97	3.5813	1.7	0.25843	1.3	0.82	1574	38	1476	36	1525	28	94	97	1476	36
HG2	Spot 32.FIN	LABXR002_1-TAR21	-0.17368	49461	255	1.0	-120.201122	-438	3.90	1.2	0.10076	1.32	3.5938	1.0	0.25761	1.2	0.34	1641	52	1477	31	1547	16	90	95	1477	31
HG2	Spot 41.FIN	LABXR002_2-TAR21	-1.29673	45837	227	1.3	-476.409729	-73	3.84	1.0	0.09507	0.96	3.4284	1.0	0.26020	1.0	0.45	1525	37	1490	27	1510	15	98	99	1490	27
HG2	AM031-111	LABXR31-32 (TAR21)	0.021215	265055	373	0.3	-2810.50939	-5.7	3.84	0.6	0.09454	0.60	3.4398	0.7	0.26203	0.6	0.63	1505	23	1502	17	1510	11	100	99	1505	23
HG2	Spot 30.FIN	LABXR002_1-TAR21	-0.39043	71930	367	0.2	696.088529	74.8	3.77	1.1	0.09322	0.80	3.3856	1.2	0.26624	1.2	0.84	1489	30	1521	32	1500	19	102	101	1489	30
HG2	AM031-54	LABXR31-32 (TAR21)	0.309028	130898	170	1.9	-923.104252	-11	3.52	0.8	0.10019	1.02	3.9587	1.2	0.28523	0.8	0.59	1604	37	1616	22	1621	18	101	100	1604	37
HG2	AM031-22.I	LABXR30-31-32 (TAR	0.090446	######	432	0.4	55039.9462	24	3.53	1.2	0.10067	1.07	3.9631	1.1	0.28653	1.1	0.48	1633	38	1622	32	1622	18	99	100	1633	38
HG2	Spot 47.FIN	LABXR002_2-TAR21	-4.06766	21040	98	0.7	-286.366403	-29	3.47	1.2	0.09636	1.81	3.8286	1.3	0.28675	1.1	0.08	1542	69	1625	33	1602	22	105	101	1542	69
HG2	~~AM031-66~~	LABXR31-32 (TAR21)	~~0.165929~~	~~119018~~	~~144~~	~~1.4~~	~~-1182.71958~~	~~-11~~	~~3.50~~	~~0.7~~	~~0.09526~~	~~0.87~~	~~3.8177~~	~~0.9~~	~~0.28711~~	~~0.7~~	~~0.43~~	~~1515~~	~~33~~	~~1626~~	~~19~~	~~1591~~	~~15~~	~~107~~	~~102~~	~~1515~~	~~33~~
HG2	Spot 33.FIN	LABXR002_1-TAR21	0.669849	62381	299	0.3	123.190932	278	3.45	1.1	0.10298	1.18	4.1297	1.5	0.29060	1.1	0.59	1673	43	1644	32	1658	24	98	99	1673	43
HG2	AM031-25.I	LABXR30-31-32 (TAR	0.366802	######	474	2.2	-11892.4124	-15	3.40	0.6	0.10264	0.86	4.1986	0.8	0.29557	0.6	0.20	1652	28	1668	18	1669	13	101	100	1652	28
HG2	AM031-83	LABXR31-32 (TAR21)	0.076891	203121	238	2.2	-2084.03454	-7.1	3.36	0.8	0.10646	0.79	4.4490	0.8	0.29984	0.8	0.48	1732	29	1688	23	1719	13	97	98	1732	29
HG2	~~AM031-6.FI~~	~~LABXR30-31-32 (TAR~~	~~-0.52152~~	~~721812~~	~~280~~	~~1.2~~	~~-13677.6859~~	~~-16~~	~~1.26~~	~~25.7~~	~~0.10689~~	~~0.75~~	~~11.7678~~	~~8.0~~	~~0.32939~~	~~6.3~~	~~0.00~~	~~1736~~	~~29~~	~~1735~~	~~168~~	~~2201~~	~~102~~	~~100~~	~~79~~	~~1736~~	~~29~~
HG2	Spot 17.FIN	LABXR002_2-TAR21	-1.32172	42782	168	2.0	-448.506888	-66	3.09	0.8	0.10970	0.88	4.9631	1.2	0.32483	0.9	0.65	1798	30	1813	27	1811	21	101	100	1798	30
HG2	AM031-114	LABXR31-32 (TAR21)	0.027401	129731	144	1.2	-1364.05909	-7.4	3.02	0.6	0.11409	0.68	5.2717	0.7	0.33287	0.5	0.38	1853	24	1850	17	1860	11	100	99	1853	24
HG2	AM031-55	LABXR31-32 (TAR21)	-0.6646	78522	81	1.2	-696.798665	-8.8	3.11	1.8	0.11961	0.99	5.6073	1.3	0.33508	1.2	0.76	1944	37	1857	40	1903	26	96	98	1944	37
HG2	Spot 11.FIN	LABXR002_1-TAR21	3.003997	10552	41	1.7	88.0074969	60.8	2.97	1.5	0.12444	1.18	5.8872	1.7	0.33423	1.5	0.70	2016	43	1870	53	1956	30	93	96	2016	43
HG2	Spot 34.FIN	LABXR002_1-TAR21	-0.8765	18554	74	0.9	-139.436473	-124	2.93	1.4	0.12133	1.65	5.7053	1.6	0.34108	1.5	0.37	1979	55	1891	49	1935	31	96	98	1979	55
HG2	AM031-72	LABXR31-32 (TAR21)	1.310832	49262	48	2.9	-612.785976	-6.4	2.91	0.7	0.12174	0.94	5.8857	0.9	0.34939	0.7	0.36	1964	33	1928	24	1952	15	98	99	1964	33
HG2	~~AM031-33~~	LABXR31-32 (TAR21)	~~0.057964~~	~~296922~~	~~258~~	~~1.4~~	~~-2541.47907~~	~~-11~~	~~2.51~~	~~1.2~~	~~0.11303~~	~~0.84~~	~~6.3608~~	~~1.0~~	~~0.40508~~	~~1.1~~	~~0.68~~	~~1839~~	~~31~~	~~2189~~	~~42~~	~~2022~~	~~18~~	~~119~~	~~108~~	~~1839~~	~~31~~
HG2	AM031-73	LABXR31-32 (TAR21)	0.08278	82876	69	1.2	-962.172673	-6.4	2.46	0.6	0.13553	0.74	7.6919	0.7	0.40928	0.6	0.23	2157	27	2209	22	2191	12	102	101	2157	27
HG2	Spot 65.FIN	LABXR002_2-TAR21	-0.84259	59971	170	0.9	-853.398098	-68	2.06	1.0	0.17024	1.04	11.5260	1.1	0.48710	1.0	0.54	2556	35	2557	41	2569	19	100	100	2556	35
HG2	~~AM031-38~~	LABXR31-32 (TAR21)	~~0.116796~~	~~214050~~	~~132~~	~~1.8~~	~~-1612.99067~~	~~-8.5~~	~~1.80~~	~~1.0~~	~~0.17406~~	~~0.73~~	~~13.7924~~	~~1.2~~	~~0.56823~~	~~1.0~~	~~0.79~~	~~2588~~	~~25~~	~~2892~~	~~47~~	~~2725~~	~~23~~	~~112~~	~~106~~	~~2588~~	~~25~~

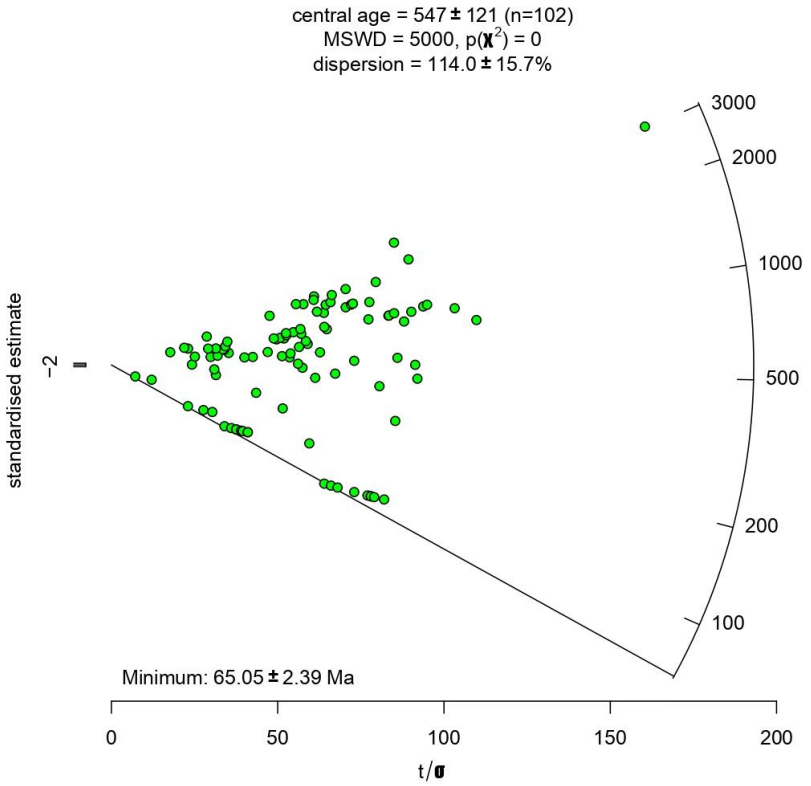
Anexo 3. Major and Trace Element Concentrations of Sedimentary Rocks Analyzed in this study . D.L. : Detection Limit

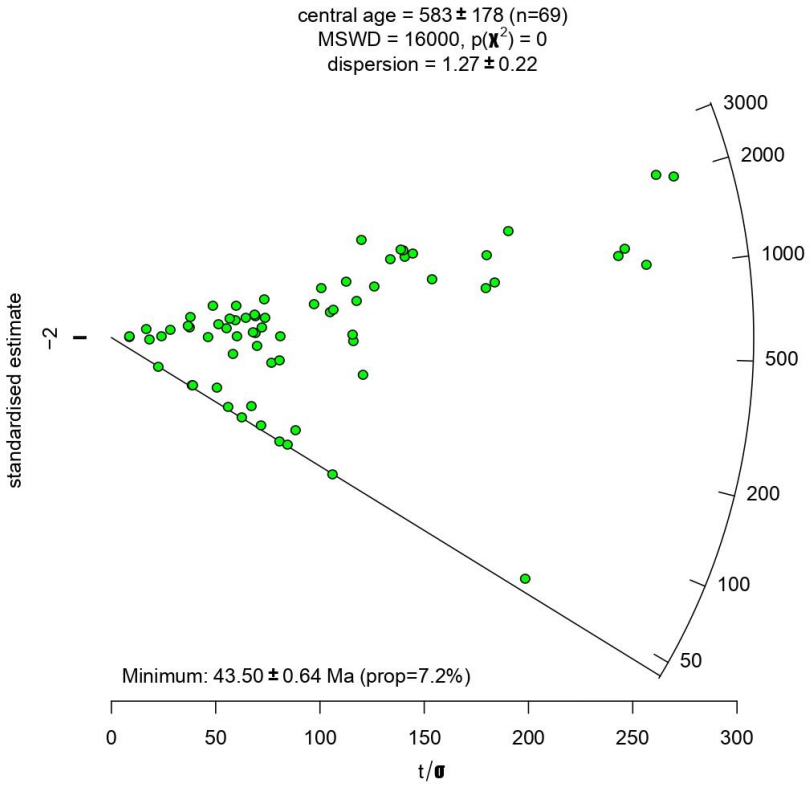
Sample		JUA 1	JUA 5	JUA 6	JUA 15	JUA 16	JUA 22	JUA 24	JUA 28	JUA 29	JUA 31	HG1	HG2
SiO_2	%	27.36	42.59	55.37	57.88	54.21	49.98	49.08	56.69	57.95	57.57	49.81	50.27
Si	ppm	127677.4465	198749.3583	258388.1656	270101.2646	252974.9405	233235.3353	229035.4193	264548.0424	270427.9248	268654.6269	232442.0178	234588.6416
Al_2O_3	%	8.43	12.57	10.38	10.51	11.89	15.56	12.12	15.86	14.77	9.19	12.41	15.50
Al	ppm	44614.9775	66525.5359	54935.1680	55623.1807	62926.7002	82349.8280	64143.9534	83937.5496	78168.8277	48637.2056	65678.7510	82032.2837
Fe_2O_3	%	3.59	3.52	3.69	4.67	4.61	7.20	4.65	6.17	6.79	2.72	4.92	4.80
Fe	ppm	25110.1630	24620.5498	25809.6104	32664.1953	32244.5268	50360.2154	32524.3058	43155.9068	47492.4809	19024.9703	34412.8139	33573.4770
MnO	%	0.13	0.039	0.053	0.065	0.063	0.045	0.068	0.033	0.038	0.082	0.120	0.055
Mn	ppm	1006.8154	302.0446	410.4709	503.4077	487.9182	348.5130	526.6419	255.5762	294.2999	635.0682	929.3680	425.9603
MgO	%	1.75	1.98	1.32	1.15	2.40	2.74	1.58	2.79	2.54	1.21	2.13	2.65
Mg	ppm	10554.2488	11941.3787	7960.9191	6935.6492	14474.3984	16524.9382	9528.9790	16826.4881	15318.7383	7297.5092	12846.0286	15982.1482
CaO	%	27.72	15.37	11.40	9.39	9.06	5.88	11.85	2.49	3.07	11.66	10.15	7.98
Ca	ppm	198141.5297	109864.1887	81486.7763	67119.3710	64760.5432	42030.0214	84703.3595	17798.4274	21944.2459	83345.2466	72551.8227	57040.7434
Na_2O	%	0.10	0.13	0.57	0.98	1.56	0.49	0.45	1.35	1.30	0.41	0.68	0.66
Na	ppm	741.8398	964.3917	4228.4866	7270.0297	11572.7003	3635.0148	3338.2789	10014.8368	9643.9169	3041.5430	5044.5104	4896.1424
K_2O	%	1.92	2.11	1.12	1.44	1.86	3.67	1.92	3.19	3.17	1.30	2.52	2.86
K	ppm	15938.9009	17516.1879	9297.6922	11954.1757	15440.8102	30466.5449	15938.9009	26481.8197	26315.7895	10791.9641	20919.8074	23742.3211
TiO_2	%	0.36	0.57	0.67	0.67	0.58	0.69	0.64	0.81	0.73	0.45	0.65	0.76
Ti	ppm	2158.1440	3417.0613	4016.5458	4016.5458	3477.0098	4136.4427	3836.7004	4855.8240	4376.2364	2697.6800	3896.6489	4556.0818
P_2O_5	%	0.12	0.19	0.16	0.21	0.16	0.19	0.20	0.21	0.25	0.16	0.20	0.21
P	ppm	523.9488	829.5856	698.5984	916.9104	698.5984	829.5856	873.2480	916.9104	1091.5601	698.5984	873.2480	916.9104
LOI	%	28.41	20.36	14.51	13.35	12.75	13.01	16.51	9.59	8.77	15.22	15.88	14.69
Total	%	99.89	99.43	99.24	100.32	99.14	99.45	99.04	99.19	99.37	99.96	99.46	100.44
Al/Si		0.35	0.33	0.21	0.21	0.25	0.35	0.28	0.32	0.29	0.18	0.28	0.35
CIA		22.09	41.65	44.23	47.09	48.79	60.78	46.01	69.29	66.20	40.74	48.18	57.41
Sc	ppm	8.17	12.62	9.62	10.07	9.97	15.17	12.21	15.69	13.97	8.49	11.87	15.5
Rb	ppm	79.80	85.20	47.30	55.80	65.0	148	84.6	122	118	66.2	101	115
Cs	ppm	3.82	5.04	2.70	2.94	4.13	10.6	8.47	8.57	8.31	5.94	7.95	9
Ba	ppm	473.00	531.00	316.00	250.00	399.0	482	235	348	332	421	346	271
Sr	ppm	401.00	261.00	443.00	180.00	312.0	198	170	644	175	185	296	242
Th	ppm	5.48	8.86	7.79	6.65	6.7	11.7	9.85	12	10.2	7.81	10.3	12
U	ppm	1.19	2.26	2.58	2.03	1.81	2.55	2.37	2.92	2.51	2.72	3.37	5.66
Y	ppm	11.5	17.7	23.2	20.3	19.0	26	25.1	29.4	28.1	23.4	24.2	27.8
Zr	ppm	72.50	112.00	200.00	255.00	170	142	183	252	198	184	177	152
Nb	ppm	5.64	9.27	11.20	11.70	8.34	12.2	10.9	13.3	11.6	7.76	12.1	13.7
Hf	ppm	2.04	3.08	5.20	6.44	4.49	3.92	4.81	6.63	5.28	4.85	4.84	4.2
Cr	ppm	24.20	43.80	37.30	34.60	37.8	57.9	41.7	60.2	53	31	48.5	60
V	ppm	76.30	121.00	81.90	66.30	73.0	108	117	116	106	91.3	81	110
Co	ppm	5.07	10.10	8.05	12.50	10.8	12.1	11	14.4	12	19.4	14.9	17.5
Cu	ppm	14.30	28.50	41.80	9.70	29.1	21.5	15.9	58.8	41.9	24.4	153	47.1
Ni	ppm	12.20	24.10	17.50	11.80	17.2	28.2	21.3	29.5	24.7	16.7	24.3	45.4
Zn	ppm	45.10	56.90	64.20	68.70	78.2	113	93	113	109	70.1	94.5	97.5
La	ppm	15.20	27.20	23.70	23.80	21.0	35.1	29.2	35.6	31.9	25.1	29.3	36.2
Ce	ppm	29.70	54.30	47.20	45.60	41.9	70.7	58.7	70.1	65.6	53.9	58.9	72.1
Pr	ppm	3.52	6.37	5.66	5.40	5.14	8.45	7.05	8.35	7.99	6.37	7.07	8.6
Nd	ppm	13.10	24.00	21.80	20.80	20.1	32.4	27.1	32	31.4	24.9	26.7	32.5
Sm	ppm	2.62	4.61	4.51	4.19	4.16	6.44	5.42	6.4	6.4	5.23	5.38	6.42
Eu	ppm	0.553	0.957	1.03	1.08	0.989	1.37	1.13	1.39	1.44	1.16	1.14	1.34
Gd	ppm	2.22	3.55	3.99	3.64	3.53	5.29	4.57	5.41	5.47	4.51	4.59	5.35
Tb	ppm	0.339	0.537	0.647	0.582	0.557	0.81	0.721	0.855	0.85	0.688	0.716	0.832
Dy	ppm	2.07	3.31	4.06	3.60	3.44	4.79	4.41	5.22	5.1	4.11	4.32	4.96
Ho	ppm	0.433	0.695	0.862	0.769	0.716	1.00	0.92	1.1	1.04	0.842	0.905	1.03
Er	ppm	1.18	1.92	2.35	2.12	1.95	2.69	2.55	3.06	2.78	2.24	2.45	2.79
Tm	ppm	0.183	0.297	0.368	0.327	0.299	0.407	0.39	0.472	0.424	0.339	0.369	0.417
Yb	ppm	1.18	1.92	2.41	2.19	1.95	2.62	2.56	3.08	2.74	2.16	2.46	2.71
Lu	ppm	0.185	0.294	0.366	0.343	0.301	0.401	0.387	0.474	0.417	0.332	0.375	0.411
Ta	ppm	0.51	0.84	0.95	1.02	0.75	1.12	0.99	1.21	1.06	0.73	1.1	1.26
Eu/Eu*		0.70	0.72	0.74	0.85	0.79	0.72	0.69	0.72	0.74	0.73	0.70	0.70
Cr/Th		4.42	4.94	4.79	5.20	5.64	4.95	4.23	5.02	5.20	3.97	4.71	5.00
Th/Sc		0.67	0.70	0.81	0.66	0.67	0.77	0.81	0.76	0.73	0.92	0.87	0.77
Rb/Sr		0.20	0.33	0.11	0.31	0.21	0.75	0.50	0.19	0.67	0.36	0.34	0.48

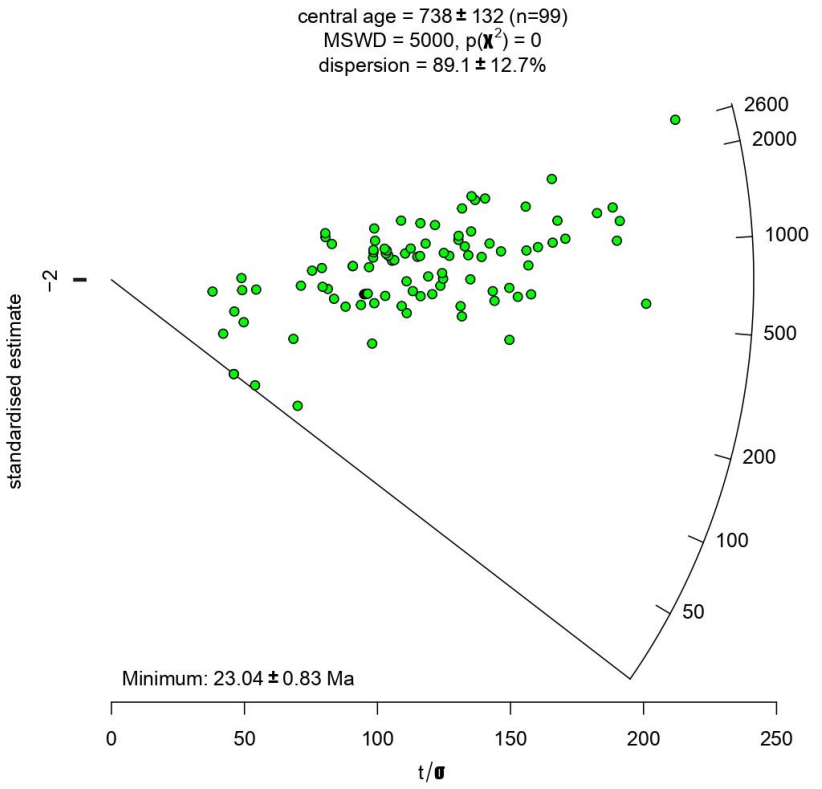
Sample	JUA 1	JUA 5	JUA 6	JUA 15	JUA 16	JUA 22	JUA 24	JUA 28	JUA 29	JUA 31	HG1	HG2
wt%												
SiO_2	27.36	42.59	55.37	57.88	54.21	49.98	49.08	56.69	57.95	57.57	49.81	50.27
Al_2O_3	8.43	12.57	10.38	10.51	11.89	15.56	12.12	15.86	14.77	9.19	12.41	15.50
Fe_2O_3	3.59	3.52	3.69	4.67	4.61	7.20	4.65	6.17	6.79	2.72	4.92	4.80
MnO	0.13	0.039	0.053	0.065	0.063	0.045	0.068	0.033	0.038	0.082	0.120	0.055
MgO	1.75	1.98	1.32	1.15	2.40	2.74	1.58	2.79	2.54	1.21	2.13	2.65
CaO	27.72	15.37	11.40	9.39	9.06	5.88	11.85	2.49	3.07	11.66	10.15	7.98
Na_2O	0.10	0.13	0.57	0.98	1.56	0.49	0.45	1.35	1.30	0.41	0.68	0.66
K_2O	1.92	2.11	1.12	1.44	1.86	3.67	1.92	3.19	3.17	1.30	2.52	2.86
TiO_2	0.36	0.57	0.67	0.67	0.58	0.69	0.64	0.81	0.73	0.45	0.65	0.76
P_2O_5	0.12	0.19	0.16	0.21	0.16	0.19	0.20	0.21	0.25	0.16	0.20	0.21
LOI	28.41	20.36	14.51	13.35	12.75	13.01	16.51	9.59	8.77	15.22	15.88	14.69
Total	99.89	99.43	99.24	100.32	99.14	99.45	99.04	99.19	99.37	99.96	99.46	100.44
Al/Si	0.35	0.33	0.21	0.21	0.25	0.35	0.28	0.32	0.29	0.18	0.28	0.35
CIA	80	84	82	76	49	61	46	69	66	41	48	57
ppm												
Sc	8.17	12.62	9.62	10.07	9.97	15.17	12.21	15.69	13.97	8.49	11.87	15.50
Rb	79.80	85.20	47.30	55.80	65.00	148.00	84.60	122.00	118.00	66.20	101.00	115.00
Cs	3.82	5.04	2.70	2.94	4.13	10.60	8.47	8.57	8.31	5.94	7.95	9.00
Ba	473.00	531.00	316.00	250.00	399.00	482.00	235.00	348.00	332.00	421.00	346.00	271.00
Sr	401.00	261.00	443.00	180.00	312.00	198.00	170.00	644.00	175.00	185.00	296.00	242.00
Th	5.48	8.86	7.79	6.65	6.70	11.70	9.85	12.00	10.20	7.81	10.30	12.00
U	1.19	2.26	2.58	2.03	1.81	2.55	2.37	2.92	2.51	2.72	3.37	5.66
Y	11.5	17.7	23.2	20.3	19.0	26.0	25.1	29.4	28.1	23.4	24.2	27.8
Zr	72.50	112.00	200.00	255.00	170.00	142.00	183.00	252.00	198.00	184.00	177.00	152.00
Nb	5.64	9.27	11.20	11.70	8.34	12.20	10.90	13.30	11.60	7.76	12.10	13.70
Hf	2.04	3.08	5.20	6.44	4.49	3.92	4.81	6.63	5.28	4.85	4.84	4.20
Cr	24.20	43.80	37.30	34.60	37.80	57.90	41.70	60.20	53.00	31.00	48.50	60.00
V	76.30	121.00	81.90	66.30	73.00	108.00	117.00	116.00	106.00	91.30	81.00	110.00
Co	5.07	10.10	8.05	12.50	10.80	12.10	11.00	14.40	12.00	19.40	14.90	17.50
Cu	14.30	28.50	41.80	9.70	29.10	21.50	15.90	58.80	41.90	24.40	153.00	47.10
Ni	12.20	24.10	17.50	11.80	17.20	28.20	21.30	29.50	24.70	16.70	24.30	45.40
Zn	45.10	56.90	64.20	68.70	78.20	113.00	93.00	113.00	109.00	70.10	94.50	97.50
La	15.20	27.20	23.70	23.80	21.00	35.10	29.20	35.60	31.90	25.10	29.30	36.20
Ce	29.70	54.30	47.20	45.60	41.90	70.70	58.70	70.10	65.60	53.90	58.90	72.10
Pr	3.52	6.37	5.66	5.40	5.14	8.45	7.05	8.35	7.99	6.37	7.07	8.60
Nd	13.10	24.00	21.80	20.80	20.10	32.40	27.10	32.00	31.40	24.90	26.70	32.50
Sm	2.62	4.61	4.51	4.19	4.16	6.44	5.42	6.40	6.40	5.23	5.38	6.42
Eu	0.553	0.957	1.03	1.08	0.99	1.37	1.13	1.39	1.44	1.16	1.14	1.34
Gd	2.22	3.55	3.99	3.64	3.53	5.29	4.57	5.41	5.47	4.51	4.59	5.35
Tb	0.339	0.537	0.647	0.582	0.557	0.810	0.721	0.855	0.850	0.688	0.716	0.832
Dy	2.07	3.31	4.06	3.60	3.44	4.79	4.41	5.22	5.10	4.11	4.32	4.96
Ho	0.433	0.695	0.862	0.769	0.716	1.000	0.920	1.100	1.040	0.842	0.905	1.030
Er	1.18	1.92	2.35	2.12	1.95	2.69	2.55	3.06	2.78	2.24	2.45	2.79
Tm	0.183	0.297	0.368	0.327	0.299	0.407	0.390	0.472	0.424	0.339	0.369	0.417
Yb	1.18	1.92	2.41	2.19	1.95	2.62	2.56	3.08	2.74	2.16	2.46	2.71
Lu	0.185	0.294	0.366	0.343	0.301	0.401	0.387	0.474	0.417	0.332	0.375	0.411
Ta	0.51	0.84	0.95	1.02	0.75	1.12	0.99	1.21	1.06	0.73	1.10	1.26
Sm/Nd	0.200	0.192	0.207	0.201	0.207	0.199	0.200	0.200	0.204	0.210	0.201	0.198
Eu/Eu*	0.70	0.72	0.74	0.85	0.79	0.72	0.69	0.72	0.74	0.73	0.70	0.70
ΩCe	0.98	0.99	0.98	0.97	0.97	0.99	0.99	0.98	0.99	1.03	0.99	0.98
Cr/Th	4.42	4.94	4.79	5.20	5.64	4.95	4.23	5.02	5.20	3.97	4.71	5.00
Th/Sc	0.67	0.70	0.81	0.66	0.67	0.77	0.81	0.76	0.73	0.92	0.87	0.77
Zr/Sc	8.87	8.87	20.79	25.32	17.05	9.36	14.99	16.06	14.17	21.67	14.91	9.81
LREE	1.04	1.88	1.67	1.62	1.52	2.49	2.08	2.48	2.34	1.86	2.07	2.53
HREE	1.22	1.97	2.45	2.23	2.00	2.69	2.60	3.15	2.80	2.23	2.49	2.76
MREE	1.14	1.81	2.15	1.93	1.86	2.68	2.39	2.84	2.82	2.29	2.37	2.75
MREE*	1.13	1.92	2.06	1.93	1.76	2.59	2.34	2.81	2.57	2.04	2.28	2.65

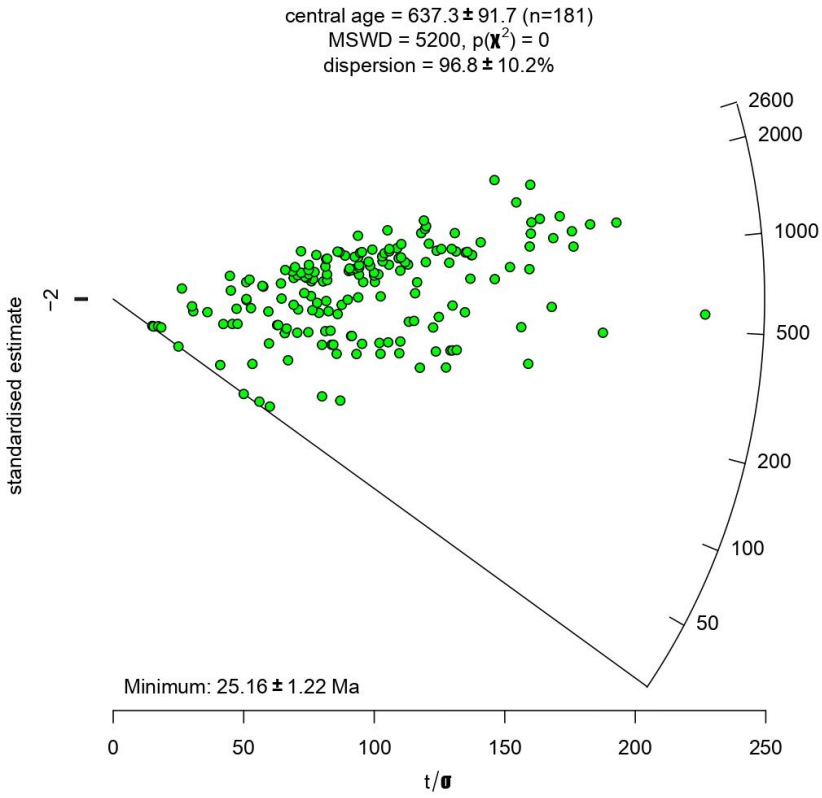
PAAS McLennan 1985 2001, Pour		JUA 1	JUA 5	JUA 6	JUA 15	JUA 16	JUA 22	JUA 24	JUA 28	JUA 29	JUA 31	HG1	HG2
wt%													
SiO_2	62.8	0.43566879	0.67818471	0.8816879	0.92165605	0.86321656	0.79585987	0.78152866	0.90270701	0.9227707	0.91671975	0.79315287	0.80047771
Al_2O_3	18.9	0.44603175	0.66507937	0.54920635	0.55608466	0.62910053	0.82328042	0.64126984	0.83915344	0.78148148	0.48624339	0.65661376	0.82010582
Fe_2O_3	6.5	0.55230769	0.54153846	0.56769231	0.71846154	0.70923077	1.10769231	0.71538462	0.94923077	1.04461538	0.41846154	0.75692308	0.73846154
MnO	0.1	1.3	0.39	0.53	0.65	0.63	0.45	0.68	0.33	0.38	0.82	1.2	0.55
MgO	2.2	0.79545455	0.9	0.6	0.52272727	1.09090909	1.24545455	0.71818182	1.26818182	1.15454545	0.55000000	0.96818182	1.20454545
CaO	1.3	21.3230769	11.8230769	8.76923077	7.22307692	6.96923077	4.52307692	9.11538462	1.91538462	2.36153846	8.96923077	7.80769231	6.13846154
Na_2O	1.2	0.08333333	0.10833333	0.475	0.81666667	1.3	0.40833333	0.375	1.125	1.08333333	0.34166667	0.56666667	0.55
K_2O	3.7	0.51891892	0.57027027	0.3027027	0.38918919	0.5027027	0.99189189	0.51891892	0.86216216	0.85675676	0.35135135	0.68108108	0.77297297
TiO_2	1.0	0.36	0.57	0.67	0.67	0.58	0.69	0.64	0.81	0.73	0.45	0.65	0.76
P_2O_5	0.2	0.6	0.95	0.8	1.05	0.8	0.95	1	1.05	1.25	0.8	1	1.05
Sc	15.9	0.51383648	0.79371069	0.60503145	0.63333333	0.62704403	0.95408805	0.76792453	0.98679245	0.87861635	0.53396226	0.74654088	0.97484277
Rb	160.0	0.49875	0.5325	0.295625	0.34875	0.40625	0.925	0.52875	0.7625	0.7375	0.41375	0.63125	0.71875
Cs	15.0	0.25466667	0.336	0.18	0.196	0.27533333	0.70666667	0.56466667	0.57133333	0.554	0.396	0.53	0.6
Ba	650.0	0.01256923	0.01941538	0.48615385	0.38461538	0.61384615	0.74153846	0.36153846	0.53538462	0.51076923	0.64769231	0.53230769	0.41692308
Sr	200.0	2.005	1.305	2.215	0.9	1.56	0.99	0.85	3.22	0.875	0.925	1.48	1.21
Th	14.6	0.37534247	0.60684932	0.53356164	0.45547945	0.45890411	0.80136986	0.67465753	0.82191781	0.69863014	0.53493151	0.70547945	0.82191781
U	3.1	0.38387097	0.72903226	0.83225806	0.65483871	0.58387097	0.82258065	0.76451613	0.94193548	0.80967742	0.87741935	1.08709677	1.82580645
Y	27.3	0.42124542	0.64835165	0.84981685	0.74358974	0.6959707	0.95238095	0.91941392	1.07692308	1.02930403	0.85714286	0.88644689	1.01831502
Zr	210.0	0.3452381	0.53333333	0.95238095	1.21428571	0.80952381	0.67619048	0.87142857	1.2	0.94285714	0.87619048	0.84285714	0.72380952
Nb	19.0	0.68947368	1.26315789	1.14736842	1.09473684	1.05789474	1.70526316	1.42631579	1.68421053	1.65263158	1.31052632	1.40526316	1.71052632
Hf	5.0	0.408	0.616	1.04	1.288	0.898	0.784	0.962	1.326	1.056	0.97	0.968	0.84
Cr	110.0	0.22	0.39818182	0.33909091	0.31454545	0.34363636	0.52636364	0.37909091	0.54727273	0.48181818	0.28181818	0.44090909	0.54545455
V	150.0	0.50866667	0.80666667	0.546	0.442	0.48666667	0.72	0.78	0.77333333	0.70666667	0.60866667	0.54	0.73333333
Co	23.0	0.22043478	0.43913043	0.35	0.54347826	0.46956522	0.52608696	0.47826087	0.62608696	0.52173913	0.84347826	0.64782609	0.76086957
Cu	50.0	0.286	0.57	0.836	0.194	0.582	0.43	0.318	1.176	0.838	0.488	3.06	0.942
Ni	55.0	0.22181818	0.43818182	0.31818182	0.21454545	0.31272727	0.51272727	0.38727273	0.53636364	0.44909091	0.30363636	0.44181818	0.82545455
Zn	85.0	0.53058824	0.66941176	0.75529412	0.80823529	0.92	1.32941176	1.09411765	1.32941176	1.28235294	0.82470588	1.11176471	1.14705882
La	44.56	0.34111311	0.61041293	0.53186715	0.53411131	0.47127469	0.78770197	0.65529623	0.7989228	0.71588869	0.56328546	0.65754039	0.81238779
Ce	88.25	0.33654391	0.61529745	0.53484419	0.51671388	0.47478754	0.80113314	0.66515581	0.79433428	0.74334278	0.61076487	0.6674221	0.81699717
Pr	10.15	0.34679803	0.62758621	0.55763547	0.5320197	0.50640394	0.83251232	0.69458128	0.8226601	0.78719212	0.62758621	0.69655172	0.84729064
Nd	37.32	0.35101822	0.64308682	0.58413719	0.55734191	0.53858521	0.8681672	0.7261522	0.85744909	0.84137192	0.66720257	0.71543408	0.87084673
Sm	6.88	0.38081395	0.67005814	0.65552326	0.60901163	0.60465116	0.93604651	0.7877907	0.93023256	0.93023256	0.76017442	0.78197674	0.93313953
Eu	1.22	0.45327869	0.78442623	0.8442623	0.8852459	0.81065574	1.12295082	0.92622951	1.13934426	1.18032787	0.95081967	0.93442623	1.09836066
Gd	6.04	0.36754967	0.58774834	0.66059603	0.60264901	0.58443709	0.87582781	0.75662252	0.89569536	0.90562914	0.74668874	0.75993377	0.88576159
Tb	0.89	0.38089888	0.60337079	0.72696629	0.65393258	0.6258427	0.91011236	0.81011236	0.96067416	0.95505618	0.77303371	0.80449438	0.93483146
Dy	5.33	0.38836773	0.62101313	0.76172608	0.67542214	0.64540338	0.89868668	0.82739212	0.9793621	0.95684803	0.77110694	0.81050657	0.93058161
Ho	1.05	0.41238095	0.66190476	0.82095238	0.73238095	0.68190476	0.95238095	0.87619048	1.04761905	0.99047619	0.80190476	0.86190476	0.98095238
Er	3.08	0.38311688	0.62337662	0.76298701	0.68831169	0.63311688	0.87337662	0.82792208	0.99350649	0.9025974	0.72727273	0.79545455	0.90584416
Tm	0.45	0.40666667	0.66	0.81777778	0.72666667	0.66444444	0.90444444	0.86666667	1.04888889	0.94222222	0.75333333	0.82	0.92666667
Yb	3.01	0.39202658	0.63787375	0.80066445	0.72757475	0.64784053	0.87043189	0.85049834	1.02325581	0.910299	0.71760797	0.81727575	0.90033223
Lu	0.44	0.42045455	0.66818182	0.83181818	0.77954545	0.68409091	0.91136364	0.87954545	1.07727273	0.94772727	0.75454545	0.85227273	0.93409091
Ta	0.00	0.00	0.00	0.00	0.00	0.00	0.00	0.00	0.00	0.00	0.00	0.00	0.00
		0	0	0	0	0	0	0	0	0	0	0	0
Eu/Eu*	0.58	0.34482759	0.33117816	0.35669092	0.34731432	0.35683651	0.34269902	0.34482759	0.34482759	0.35141665	0.36213821	0.34741056	0.34058355
ΩCe	1.00	0.70072151	0.72292751	0.74201034	0.84511051	0.78869616	0.71729408	0.69385409	0.72189433	0.74374882	0.72990498	0.70105941	0.69872751
Cr/Th	7.53	0.12994046	0.13200786	0.13038692	0.12872846	0.1289847	0.131331	0.13087721	0.13010655	0.13135355	0.13622101	0.13091439	0.13074697
Th/Sc	0.92	4.80006347	5.37344195	5.20455433	5.65544296	6.13238157	5.37904125	4.60163319	5.45289855	5.64791134	4.31442409	5.11819333	5.43478261
Zr/Sc	13.22	0.05073726	0.05310592	0.0612535	0.0499529	0.05083329	0.05834032	0.06102238	0.05785313	0.05522965	0.0695844	0.06563796	0.0585623
LREE													
HREE													
MREE													
MREE*													

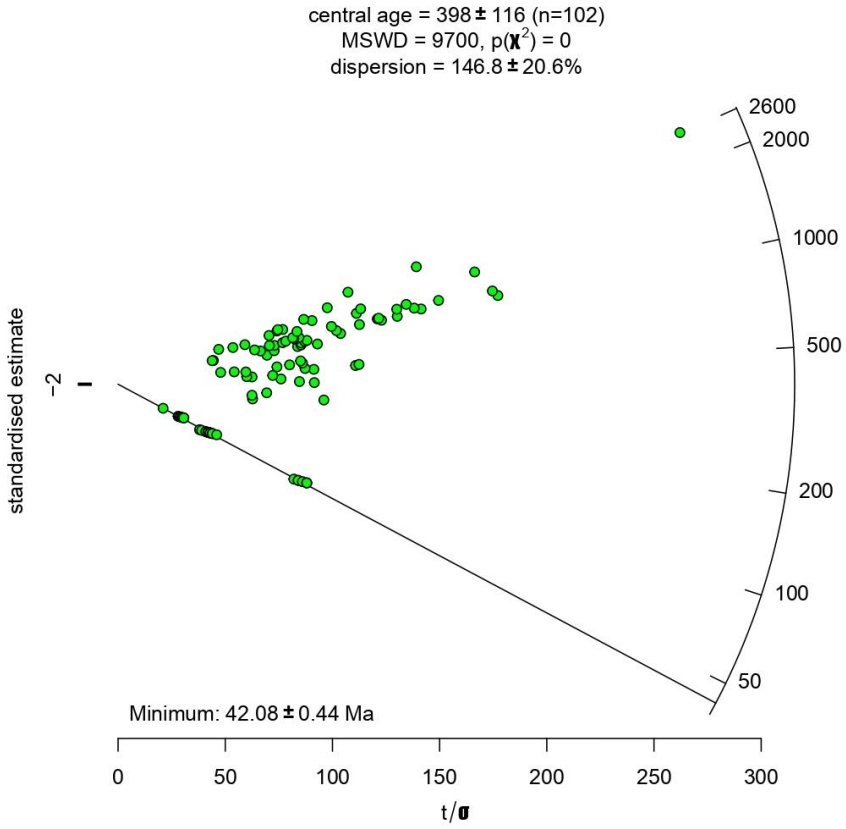
Anexo 4. Maximum Likehood Age (MLA)

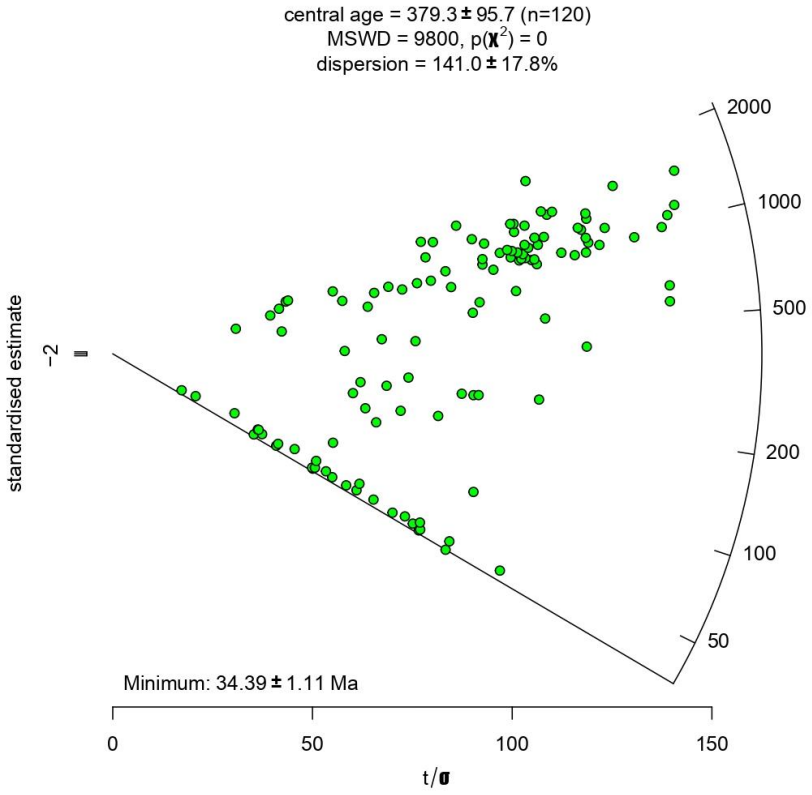


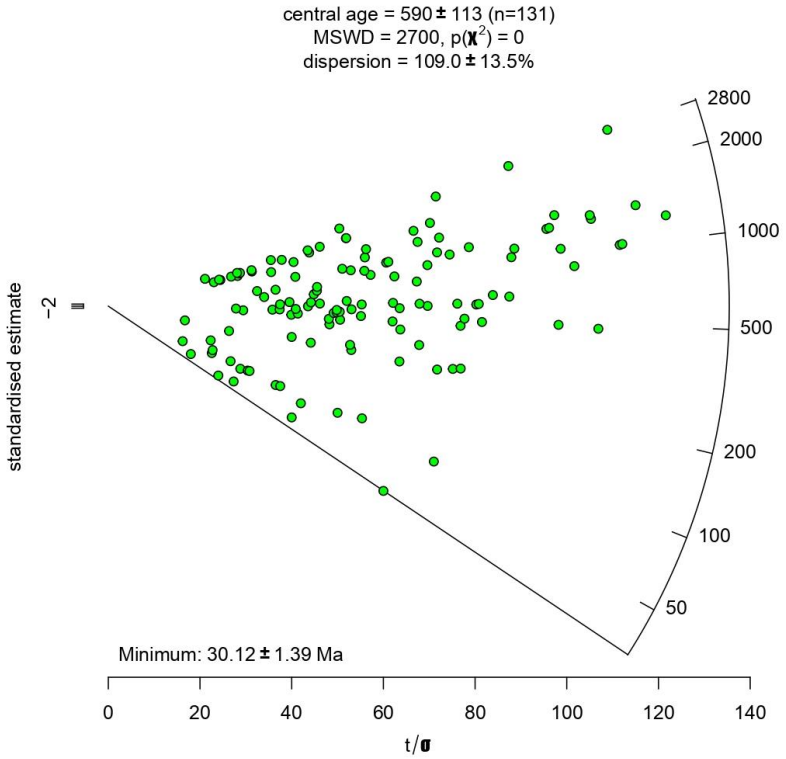


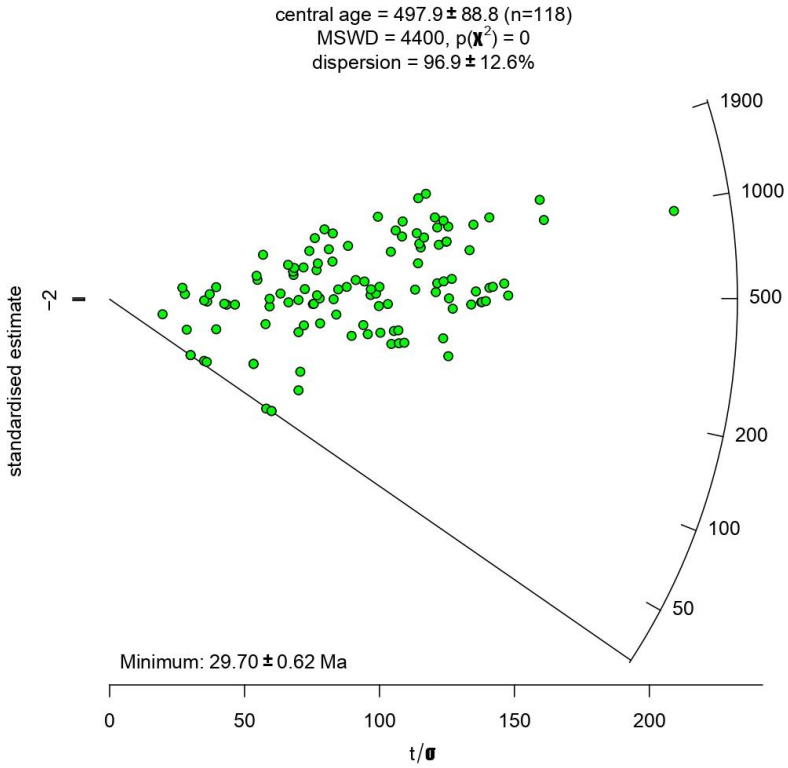

central age = 738 ± 132 (n=99)
MSWD = 5000, p(χ2) = 0
dispersion = 89.1 ± 12.7%
standardised estimate
−2
2600
2000
1000
500
200
100
50
Minimum: 23.04 ± 0.83 Ma
0
50
100
150
200
250
t/σ

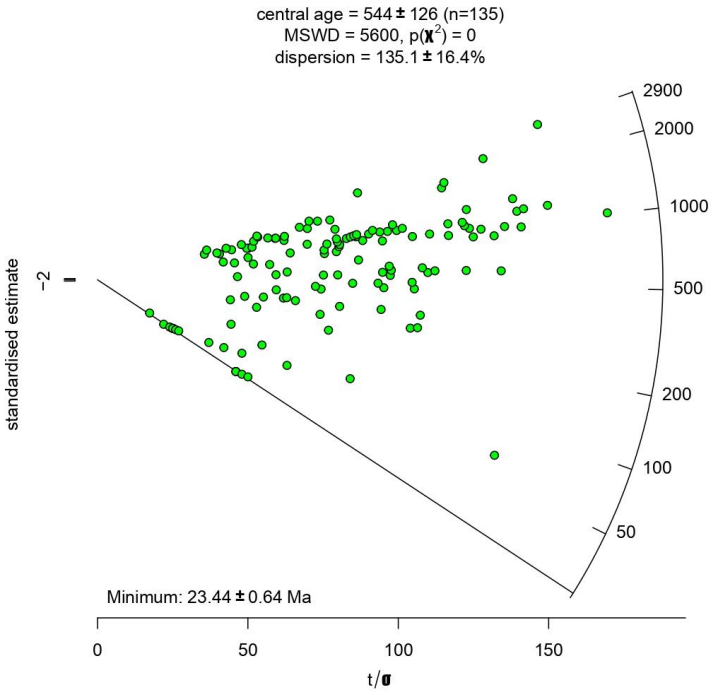

central age = 637.3 ± 91.7 (n=181)
MSWD = 5200, p(χ2) = 0
dispersion = 96.8 ± 10.2%
standardised estimate
−2
2600
2000
1000
500
200
100
50
Minimum: 25.16 ± 1.22 Ma
0
50
100
150
200
250
t/σ

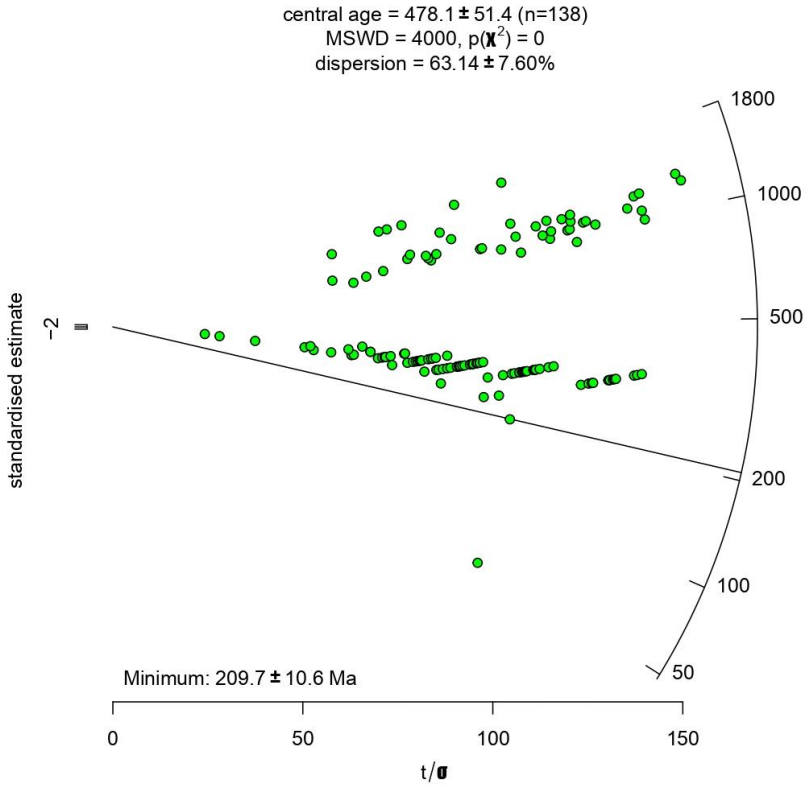

central age = 398 ± 116 (n=102)
MSWD = 9700, p(χ²) = 0
dispersion = 146.8 ± 20.6%
standardised estimate
−2
2600
2000
1000
500
200
100
50
Minimum: 42.08 ± 0.44 Ma
0
50
100
150
200
250
300
t/σ

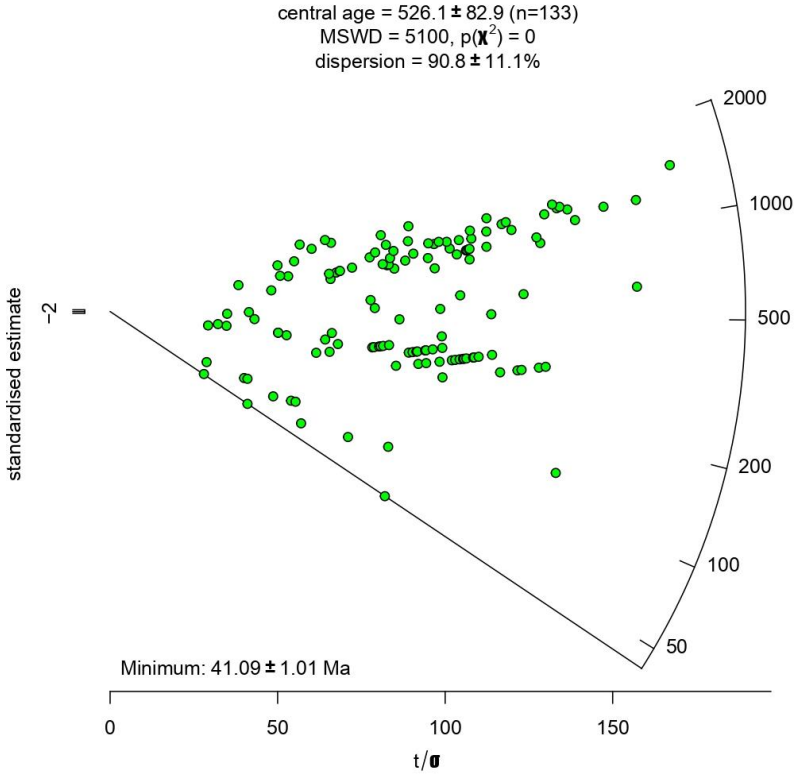

central age = 379.3 ± 95.7 (n=120)
MSWD = 9800, p(χ²) = 0
dispersion = 141.0 ± 17.8%
standardised estimate
−2
2000
1000
500
200
100
50
Minimum: 34.39 ± 1.11 Ma
0
50
100
150
t/σ

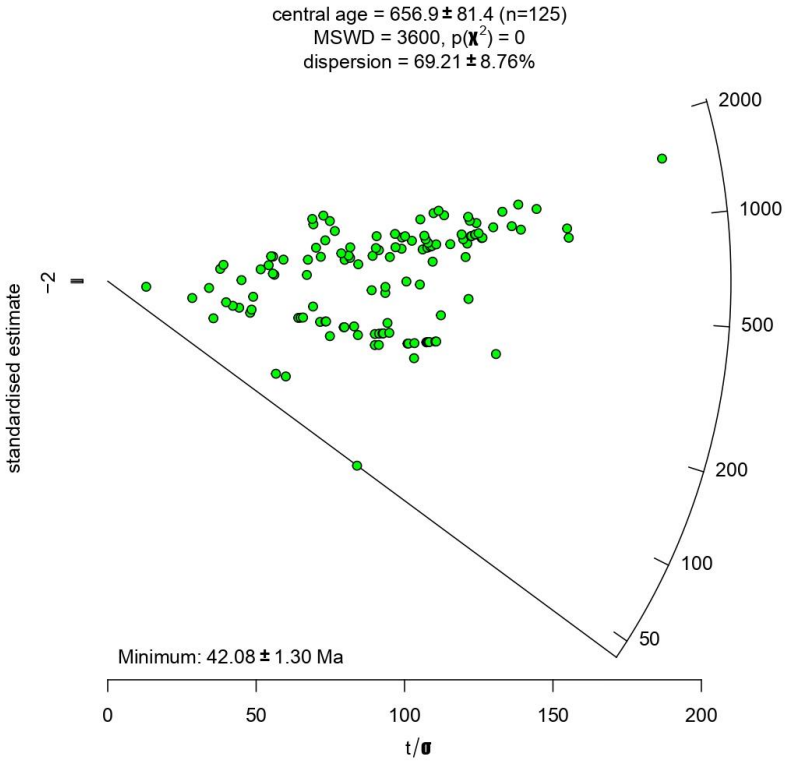

central age = 590 ± 113 (n=131)
MSWD = 2700, p(χ2) = 0
dispersion = 109.0 ± 13.5%
standardised estimate
−2
2800
2000
1000
500
200
100
50
Minimum: 30.12 ± 1.39 Ma
0
20
40
60
80
100
120
140
t/σ

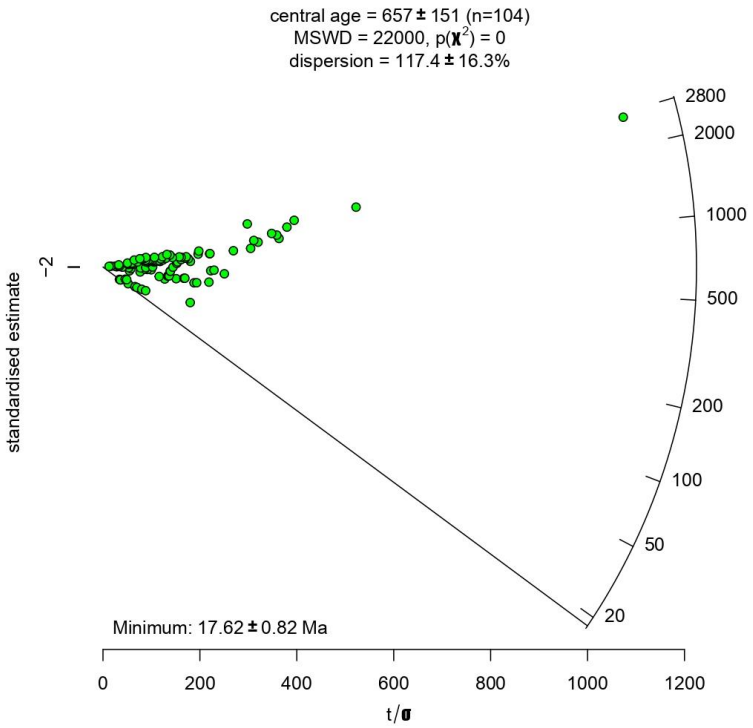

central age = 497.9 ± 88.8 (n=118)
MSWD = 4400, p(χ2) = 0
dispersion = 96.9 ± 12.6%
standardised estimate
−2
1900
1000
500
200
100
50
Minimum: 29.70 ± 0.62 Ma
0
50
100
150
200
t/σ


central age = 544 ± 126 (n=135)
MSWD = 5600, p(χ²) = 0
dispersion = 135.1 ± 16.4%
standardised estimate
2900
2000
1000
500
200
100
50
Minimum: 23.44 ± 0.64 Ma
0
50
100
150
t/σ

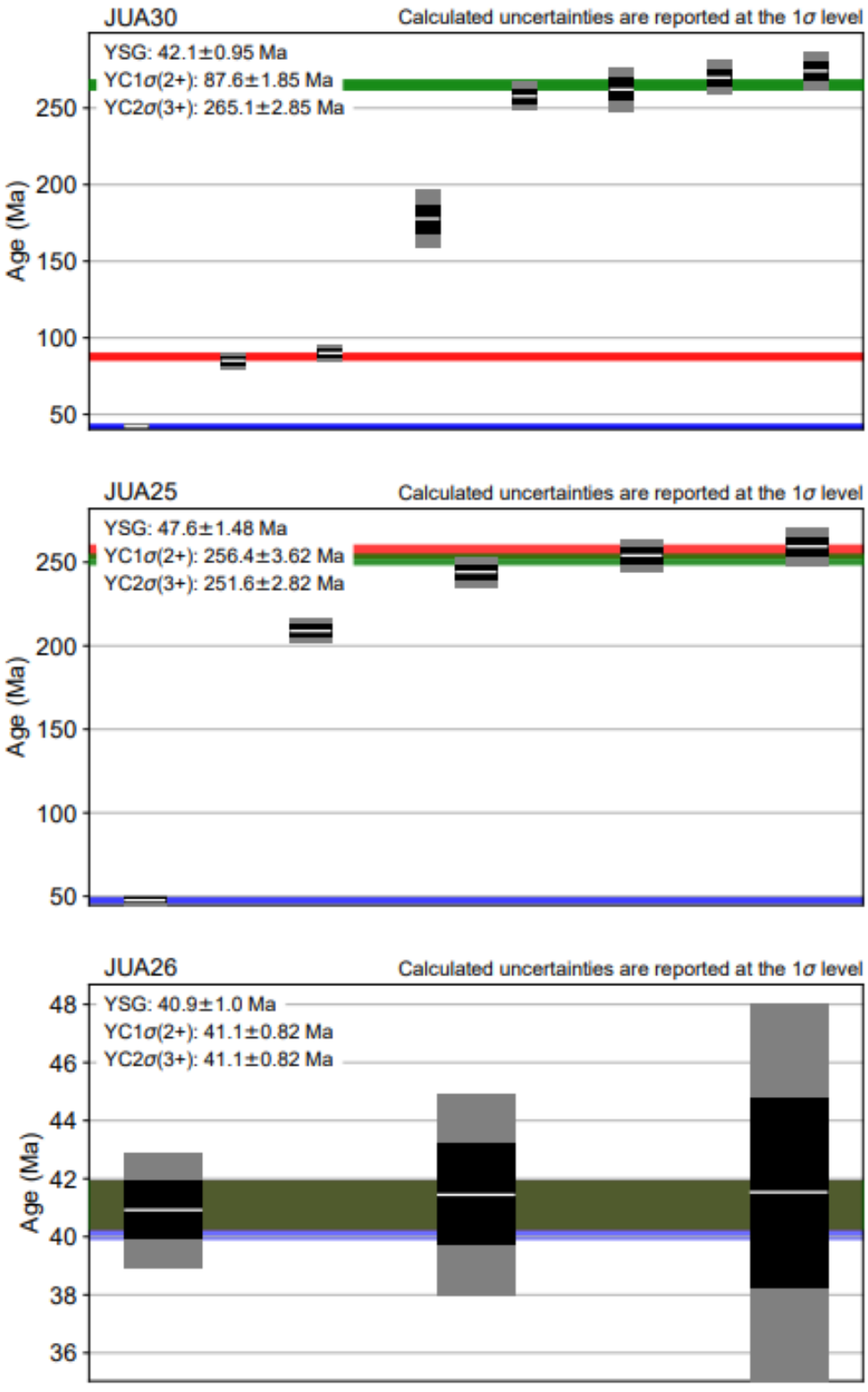

central age = 478.1 ± 51.4 (n=138)
MSWD = 4000, p(χ²) = 0
dispersion = 63.14 ± 7.60%
standardised estimate
1800
1000
500
200
100
50
Minimum: 209.7 ± 10.6 Ma
0
50
100
150
t/σ

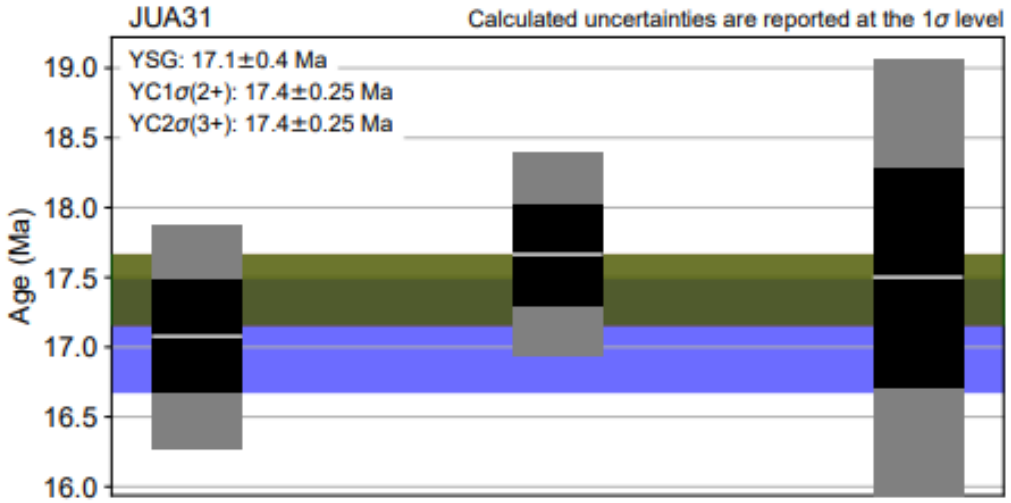

central age = 526.1 ± 82.9 (n=133)
MSWD = 5100, p(χ2) = 0
dispersion = 90.8 ± 11.1%
standardised estimate
−2
2000
1000
500
200
100
50
Minimum: 41.09 ± 1.01 Ma
0
50
100
150
t/σ

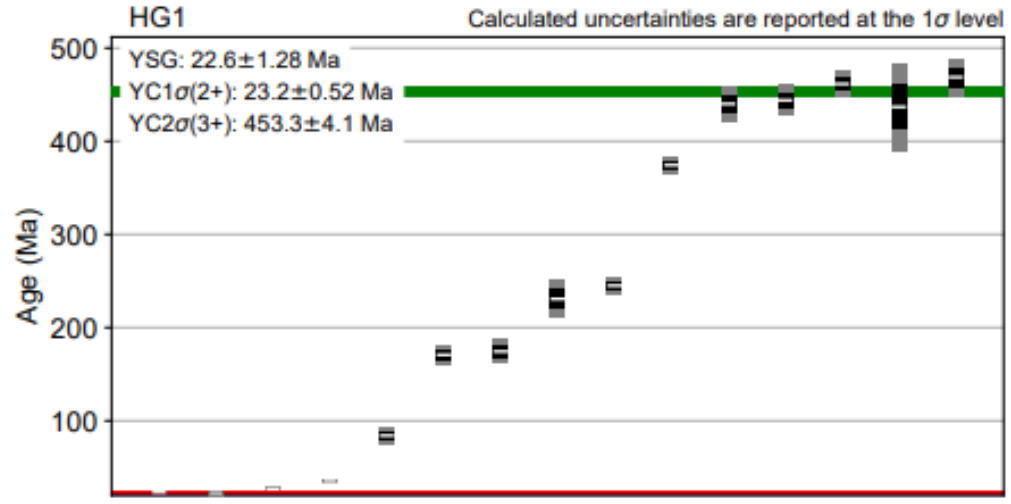

central age = 656.9 ± 81.4 (n=125)
MSWD = 3600, p(χ2) = 0
dispersion = 69.21 ± 8.76%
standardised estimate
−2
2000
1000
500
200
100
50
Minimum: 42.08 ± 1.30 Ma
0
50
100
150
200
t/σ

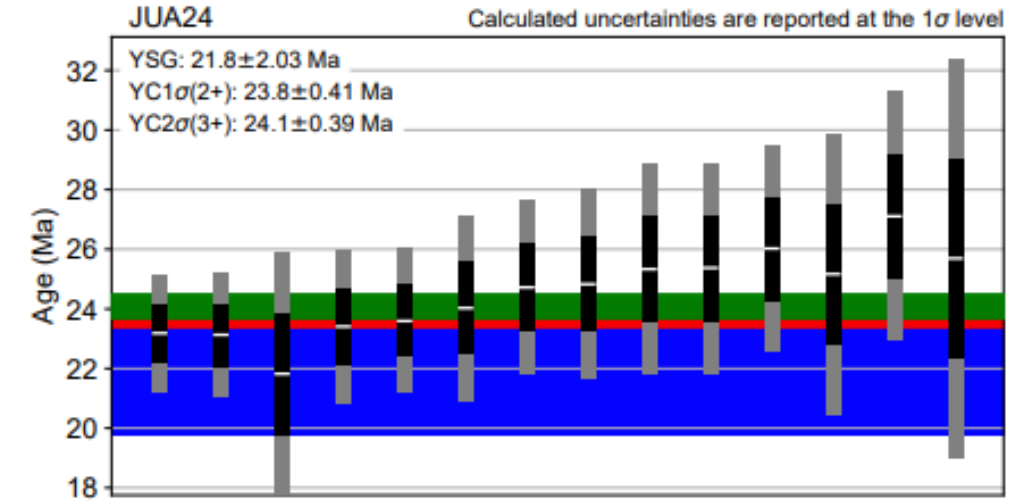

central age = 657 ± 151 (n=104)
MSWD = 22000, p(χ2) = 0
dispersion = 117.4 ± 16.3%
standardised estimate
−2
−1
2800
2000
1000
500
200
100
50
20
Minimum: 17.62 ± 0.82 Ma
0
200
400
600
800
1000
1200
t/σ

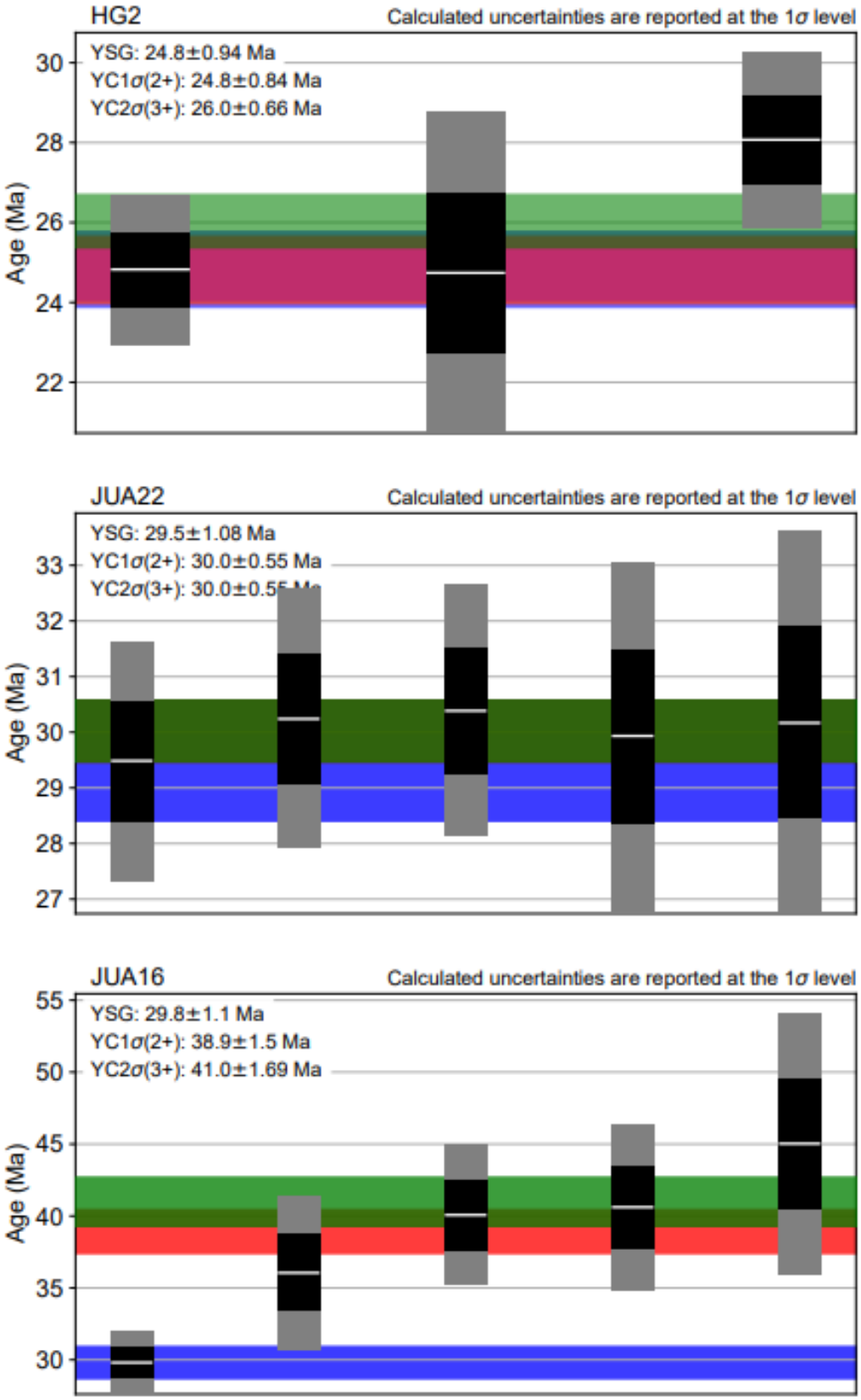
Anexo 5. Maximum Depositional Age (MDA)

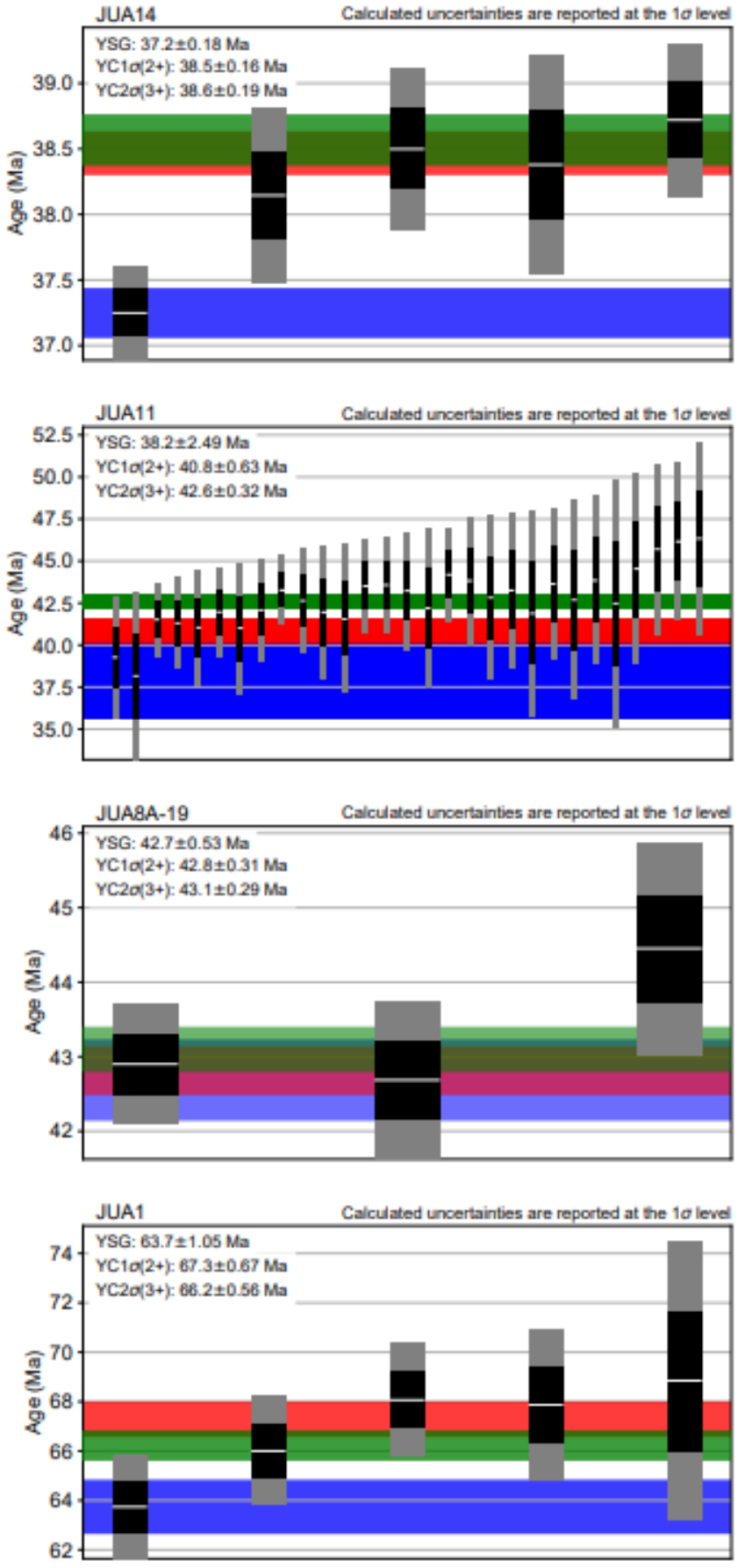



JUA31
Calculated uncertainties are reported at the 1σ level
YSG: 17.1±0.4 Ma
YC1σ(2+): 17.4±0.25 Ma
YC2σ(3+): 17.4±0.25 Ma
Age (Ma)
19.0
18.5
18.0
17.5
17.0
16.5
16.0

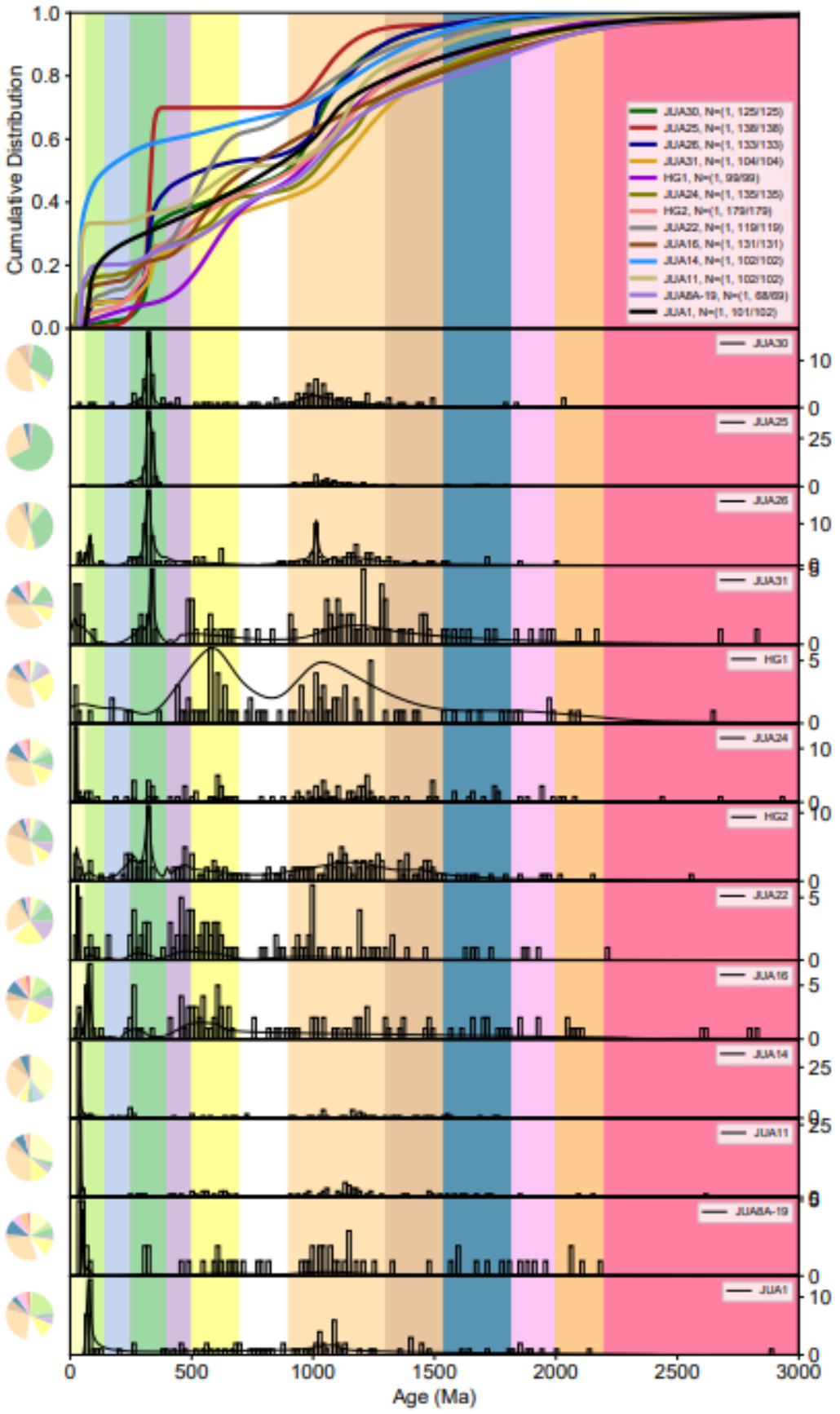

HG1
Calculated uncertainties are reported at the 1σ level
YSG: 22.6±1.28 Ma
YC1σ(2+): 23.2±0.52 Ma
YC2σ(3+): 453.3±4.1 Ma
Age (Ma)
500
400
300
200
100


JUA24
Calculated uncertainties are reported at the 1σ level
YSG: 21.8±2.03 Ma
YC1σ(2+): 23.8±0.41 Ma
YC2σ(3+): 24.1±0.39 Ma
Age (Ma)
32
30
28
26
24
22
20
18

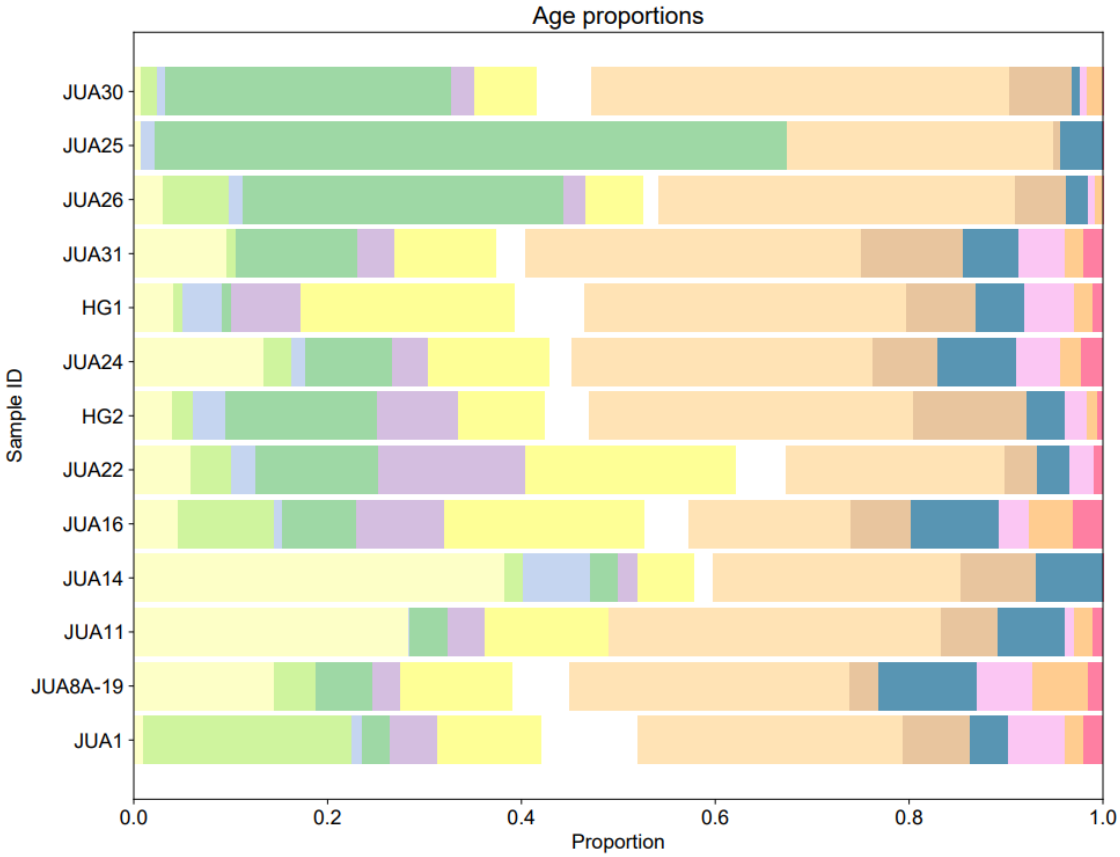

HG2
Calculated uncertainties are reported at the 1σ level
YSG: 24.8±0.94 Ma
YC1σ(2+): 24.8±0.84 Ma
YC2σ(3+): 26.0±0.66 Ma
Age (Ma)
30
28
26
24
22
JUA22
Calculated uncertainties are reported at the 1σ level
YSG: 29.5±1.08 Ma
YC1σ(2+): 30.0±0.55 Ma
YC2σ(3+): 30.0±0.55 Ma
Age (Ma)
33
32
31
30
29
28
27
JUA16
Calculated uncertainties are reported at the 1σ level
YSG: 29.8±1.1 Ma
YC1σ(2+): 38.9±1.5 Ma
YC2σ(3+): 41.0±1.69 Ma
Age (Ma)
55
50
45
40
35
30


JUA14
Calculated uncertainties are reported at the 1σ level
YSG: 37.2±0.18 Ma
YC1σ(2+): 38.5±0.16 Ma
YC2σ(3+): 38.6±0.19 Ma
Age (Ma)
39.0
38.5
38.0
37.5
37.0
JUA11
Calculated uncertainties are reported at the 1σ level
YSG: 38.2±2.49 Ma
YC1σ(2+): 40.8±0.63 Ma
YC2σ(3+): 42.6±0.32 Ma
Age (Ma)
52.5
50.0
47.5
45.0
42.5
40.0
37.5
35.0
JUA8A-19
Calculated uncertainties are reported at the 1σ level
YSG: 42.7±0.53 Ma
YC1σ(2+): 42.8±0.31 Ma
YC2σ(3+): 43.1±0.29 Ma
Age (Ma)
46
45
44
43
42
JUA1
Calculated uncertainties are reported at the 1σ level
YSG: 63.7±1.05 Ma
YC1σ(2+): 67.3±0.67 Ma
YC2σ(3+): 66.2±0.56 Ma
Age (Ma)
74
72
70
68
66
64
62

Anexo 6. Detrital zircon histogram



Anexo 7. Bar graphs samples

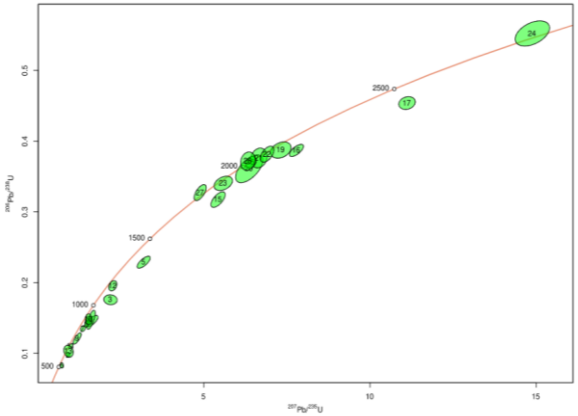


ANEXOS CAPITULO 5

Anexo 1. Samples location

Name	Code	Depth (m)	References	Location
Paleogene (P)	1APS 0024 AP	4770	This study	Amazon Fan Basin (2.556339, -49.354181)
	1APS 0024 AP	4665	This study	Amazon Fan Basin (2.556339, -49.354181)
Neogene (N)	1APS 0025 AP	1011	This study	Amazon Fan Basin (3.372100, -49.740289)
Quaternary (Q)	1APS 0025 AP	600	This study	Amazon Fan Basin (3.372100, -49.740289)
Northern Andes (NA)	AMZ-1		Mapes, R.W. (2009)	Aguarico River, Ecuador (0.04857°N, 77.3057°W)
	NA01		Pepper et al. (2016)	Delta - Caribbean coast (11.511030, -72.855890)
	NA02		Pepper et al. (2016)	Magdalena River system (9.786694, -74.815801)
	NA03		Pepper et al. (2016)	Magdalena River system (11.030854, -74.662604)
	NA04		Pepper et al. (2016)	Magdalena River system (10.950603, -74.758907)
	NA05		Pepper et al. (2016)	Magdalena River system (8.764512, -75.885191)
	NA06		Pepper et al. (2016)	Magdalena River system (6.824122, -73005229)
	NA07		Pepper et al. (2016)	Magdalena River system (2.614710, -75.356785)
	NA08		Pepper et al. (2016)	Magdalena River system (2.568122, -75.496008)
	NA09		Pepper et al. (2016)	Magdalena River system (2.464265, -75.562930)
	NA10		Pepper et al. (2016)	Andean highlands (0.474147, -78.062446)
	NA11		Pepper et al. (2016)	Tributary (Amazon River system) (-1.043799, -77.796650)
	NA12		Pepper et al. (2016)	Western Cordillera (0.324251, -79471773)
	NA13		Pepper et al. (2016)	Western Cordillera (-3.258791, -79.870847)
Central Andes (CA)	AMZ-17		Mapes, R.W. (2009)	Purus River (-4.0261, -61.5141)
	CA01		Pepper et al. (2016)	Central Andes (-22.157069, -62.793170)
	CA02		Pepper et al. (2016)	Central Andes (-23.249941, -64.140602)
	CA03		Pepper et al. (2016)	Central Andes (-25.014623, -58.129230)
	CA04		Pepper et al. (2016)	Central Andes (-26.660736, -58.636703)
	CA05		Pepper et al. (2016)	Central Andes (-5.89648, -76.10254)
	CA06		Pepper et al. (2016)	Central Andes (-8.33793, -74.59462)
	CA07		Pepper et al. (2016)	Central Andes (-9.65693, -7671890)
	CA08		Pepper et al. (2016)	Central Andes (-9.76080, -76.79600)
	CA09		Pepper et al. (2016)	Central Andes (-12.602997, -69.093975)
	CA10		Pepper et al. (2016)	Central Andes (-13.661263, -72.937880)
	CA11		Pepper et al. (2016)	Central Andes (-8.087023, -78.885215)
	CA12		Pepper et al. (2016)	Central Andes (-11.070220, -77.584415)
	CA13		Pepper et al. (2016)	Central Andes (-13.124683, -76.362626)
	CA14		Pepper et al. (2016)	Central Andes (-14.47544, -75.65164)
	CA15		Pepper et al. (2016)	Central Andes (-16.4245, -73.11711)
	CA16		Pepper et al. (2016)	Central Andes (-17.6000, -71.299167)
	CA17		Pepper et al. (2016)	Central Andes (-18.399425, -70.296888)
	CA18		Pepper et al. (2016)	Central Andes (-19.157089, -70.186656)
	CA19		Pepper et al. (2016)	Central Andes (-21.428065, -70.052807)
	CA20		Pepper et al. (2016)	Central Andes (-22.275285, -68.629725)
	CA21		Pepper et al. (2016)	Central Andes (-28.554654, -70.829347)
	CA22		Pepper et al. (2016)	Central Andes (-31.590655, -71.529943)
	CA23		Pepper et al. (2016)	Central Andes (-31.756327, -71.509948)
Craton (Negro River - NR)	AMZ-18		Mapes, R.W. (2009)	Negro River (-2.4352, -61.0622)
	AMZ-19		Mapes, R.W. (2009)	Negro River (-3.1807, -60.0054)
Bragantina Platform (BP)	GM-B5		Moizinho et al. (2022)	Barreiras Formation (-1.44324, -47.14211)
	GM-B6		Moizinho et al. (2022)	Barreiras Formation (-1.04827, -47.15256)
	GM-B7		Moizinho et al. (2022)	Barreiras Formation (-0.59094, -47.32145)
Amazon Fan (Holocene - H)	945-1		Mason et al. (2019)	Submarine Fan (6.9503, -47.9288)
	946-2		Mason et al. (2019)	Submarine Fan (6.9496, -47.9193)
	946-3		Mason et al. (2019)	Submarine Fan (6.9496, -47.9193)
	946-4		Mason et al. (2019)	Submarine Fan (6.9496, -47.9193)
	946-5		Mason et al. (2019)	Submarine Fan (6.9496, -47.9193)
	946-6		Mason et al. (2019)	Submarine Fan (6.9496, -47.9193)
	946-7		Mason et al. (2019)	Submarine Fan (6.9496, -47.9193)
	936-2		Mason et al. (2019)	Submarine Fan (5.6322, -47.7355)
	946-8		Mason et al. (2019)	Submarine Fan (6.9496, -47.9193)
	946-9		Mason et al. (2019)	Submarine Fan (6.9496, -47.9193)

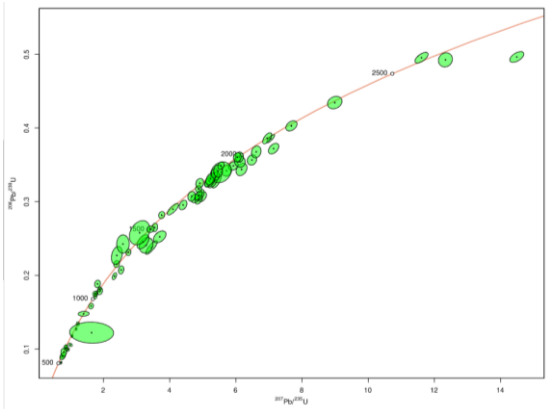
Anexo 2. U-Pb data from 1APS24_4770



University of Brasilia								Data for Tera-Wasserburg plot				Data for Wetherill plot					Dates								Conc (%)	Conc (%)	Best Age	2s (abs)
Identifier	Comments	f206c	206Pb	Uppm	Th/U	06Pb/204P	1s%	38U/206Pl	1s%	07Pb/206P	1s%	07Pb/235U	1s%	206Pb/238U	1s%	Rho	07Pb/206P	2s (abs)	2ssys (abs)	06Pb/238U	2s (abs)	2ssys (abs)	07Pb/235U	2s (abs)	2ssys (abs)	6/8 -7/6	6/8 -7/5		
Concordants																												
APS24_4770-100.FIN2	APS24_47	2.462402	29108	82	0.7	-321.227	-17.19735	6.90	2.2	0.08303	4.55	1.6356	4.5	0.14557	2.2	0.70	1166	171	171	875	36	37	969	53	53	75	90	875	36
APS24_4770-32.FIN2	APS24_47	2.181904	15855	36	2.5	-257.363	-5.806116	10.37	1.2	0.06789	2.57	0.9214	2.6	0.09759	1.2	0.21	754	117	117	600	14	14	654	26	26	79	92	600	14
APS24_4770-30.FIN2	APS24_47	1.414524	5857	12	3.6	-109.601	-5.210023	5.83	1.6	0.09181	3.97	2.1903	3.7	0.17572	1.6	-0.06	1290	159	159	1041	31	32	1134	52	52	81	92	1041	31
APS24_4770-73.FIN2	APS24_47	-0.57877	89252	273	2.1	-981.164	-15.06076	7.39	5.3	0.08154	2.80	1.6070	3.2	0.14741	3.7	0.69	1211	110	110	881	62	62	959	41	41	73	92	881	62
APS24_4770-4.FIN2	APS24_47	0.231696	64386	65	1.2	-1167.77	-6.828053	4.44	1.6	0.09776	1.61	3.1909	2.5	0.22878	1.5	0.72	1555	65	65	1325	37	38	1435	39	39	85	92	1325	37
APS24_4770-51.FIN2	APS24_47	0.892945	71558	379	0.2	-846.028	-11.26918	11.87	2.1	0.06160	3.91	0.7289	2.9	0.08249	1.7	-0.06	581	124	124	511	16	17	551	22	22	88	93	511	16
APS24_4770-46.FIN2	APS24_47	0.309686	79307	289	0.6	-1155.21	-8.086498	7.46	1.3	0.07288	2.11	1.3643	2.3	0.13494	1.3	0.41	975	92	92	815	19	20	872	28	28	84	94	815	19
APS24_4770-10.FIN2	APS24_47	0.951487	40660	66	1.8	-615.802	-9.16396	7.30	2.5	0.07665	2.10	1.4999	2.3	0.14459	2.2	0.54	1037	90	90	868	36	37	922	29	29	84	94	868	36
APS24_4770-19.FIN2	APS24_47	-1.39413	18310	110	1.1	-312.386	-7.41199	8.61	2.1	0.07229	4.07	1.1913	4.1	0.12093	2.7	0.77	791	162	162	734	35	36	774	42	42	93	95	734	35
APS24_4770-83.FIN2	APS24_47	0.566471	71025	150	0.7	-1005.48	-11.98223	7.07	2.2	0.07522	2.20	1.5353	2.6	0.14807	2.1	-0.04	1046	99	99	888	35	36	936	34	34	85	95	888	35
APS24_4770-16.FIN2	APS24_47	0.491077	67284	355	0.2	-1137.36	-9.778173	9.08	1.2	0.06492	1.81	1.0077	2.0	0.11062	1.2	0.35	748	73	73	676	15	16	703	20	20	90	96	676	15
APS24_4770-14.FIN2	APS24_47	0.977323	46922	60	2.7	-851.327	-7.441072	5.17	1.5	0.08315	2.24	2.2603	2.2	0.19553	1.5	0.31	1223	90	90	1150	32	33	1191	31	31	94	97	1150	32
APS24_4770-72.FIN2	APS24_47	-3.22831	29626	109	4.6	-426.103	-7.392635	10.40	1.3	0.06482	2.42	0.9292	6.2	0.10287	3.3	-0.17	691	99	99	627	36	36	626	20	20	91	100	627	36
APS24_4770-93.FIN2	APS24_47	19.08256	2484	7	0.0	-35.4152	-9.345134	8.75	20.0	0.07159	30.60	1.3528	16.5	0.14777	5.0	0.07	798	368	368	888	78	78	857	127	127	111	104	888	78
APS24_4770-20.FIN2	APS24_47	0.591422	221969	507	1.3	-2924.96	-12.13734	3.18	1.7	0.12220	1.52	5.4288	1.6	0.31734	1.4	0.64	1978	50	50	1774	43	45	1881	29	29	90	94	1978	50
APS24_4770-114.FIN2	APS24_47	1.516705	384129	287	0.3	-480.92	-51.98026	2.61	1.0	0.14412	0.81	7.7870	1.1	0.38687	0.9	0.68	2263	28	28	2104	34	37	2198	20	20	93	96	2263	28
APS24_4770-7.FIN2	APS24_47	0.393114	376793	192	1.2	-5443.34	-12.68849	2.19	0.8	0.17454	1.07	11.1145	0.9	0.45388	0.8	0.18	2593	36	36	2411	30	35	2530	16	16	93	95	2593	36
APS24_4770-21.FIN2	APS24_47	1.057857	117303	253	1.2	-1685.06	-11.29806	2.93	1.6	0.14027	10.93	6.7458	12.1	0.34451	1.5	-0.15	2009	56	56	1905	49	51	1956	35	35	95	97	2009	56
APS24_4770-75.FIN2	APS24_47	0.220824	109537	97	0.8	-1523.26	-11.06516	2.59	1.3	0.13585	1.75	7.3172	1.7	0.38739	1.2	0.30	2172	57	57	2109	45	47	2145	31	31	97	98	2172	57
APS24_4770-60.FIN2	APS24_47	-0.41718	68045	65	1.1	-909.513	-12.42201	2.80	2.1	0.12782	2.32	6.3645	2.6	0.36093	2.2	0.60	2032	89	89	1978	76	78	2017	47	47	97	98	2032	89
APS24_4770-89.FIN2	APS24_47	0.504162	87732	77	2.0	-1291.36	-8.471661	2.68	1.4	0.12987	1.94	6.6583	1.5	0.37618	1.5	0.17	2062	64	64	2052	53	55	2061	27	27	100	100	2062	64
APS24_4770-41.FIN2	APS24_47	0.263613	146241	74	1.6	-2105.68	-7.546707	2.65	1.2	0.13041	1.15	6.9042	1.2	0.38153	1.2	0.53	2087	40	40	2080	41	44	2096	22	22	100	99	2087	40
APS24_4770-1.FIN2	APS24_47	0.768984	68759	64	2.4	-1248.3	-9.667111	2.95	1.2	0.11725	1.95	5.5856	2.0	0.34030	1.2	0.37	1892	76	76	1886	40	42	1903	34	34	100	99	1892	76
APS24_4770-91.FIN2	APS24_47	0.362748	122300	84	2.3	-1821.62	-6.162819	1.84	1.4	0.19792	1.51	14.8839	1.4	0.55225	1.3	0.44	2785	46	46	2824	59	62	2803	23	23	101	101	2785	46
APS24_4770-15.FIN2	APS24_47	0.1792	126737	89	1.4	-2318	-5.518458	2.67	0.9	0.12339	1.18	6.4171	1.0	0.37000	0.9	0.30	1989	41	41	2027	33	36	2031	17	17	102	100	1989	41
APS24_4770-106.FIN2	APS24_47	0.226143	41500	34	3.4	-554.302	-6.444859	2.71	1.4	0.12356	1.61	6.3269	1.4	0.37173	1.4	0.15	1967	61	61	2038	47	49	2014	25	25	104	101	1967	61
APS24_4770-85.FIN2	APS24_47	0.342085	98598	102	2.2	-1528.02	-6.307014	3.12	1.5	0.10906	1.30	4.8911	1.5	0.32724	1.4	0.63	1755	47	47	1819	46	48	1789	26	26	104	102	1755	47

Discordants																													
APS24_4770_109.FIN2	APS24_47	12.53741	53017	768	6.4	-80.2195	-64.81925	52.54	4.6	0.24318	2.65	0.7992	9.2	0.02249	7.1	0.97	3095	84	84	143	20	20	581	76	76	5	25
APS24_4770_66.FIN2	APS24_47	18.92989	198560	1082	5.5	90.09754	8.401094	12.65	2.3	0.34478	2.01	4.0999	3.3	0.08437	2.3	0.76	3627	63	63	524	24	24	1604	49	49	14	33
APS24_4770_40.FIN2	APS24_47	8.060674	106877	265	12.4	-20.8329	-367.5393	13.36	2.4	0.20241	1.62	2.2106	2.0	0.08147	3.0	0.85	2809	53	53	503	29	29	1172	26	26	18	43
APS24_4770_102.FIN2	APS24_47	5.338368	78579	495	6.0	-269.14	-23.79096	17.28	1.1	0.15994	1.10	1.2986	1.3	0.05873	1.1	0.46	2437	37	37	368	8	8	845	14	14	15	43
APS24_4770_59.FIN2	APS24_47	7.408541	271774	758	0.4	156.9106	70.08902	8.96	1.6	0.24081	1.96	3.9028	3.0	0.11414	1.8	0.74	3089	59	59	696	23	24	1585	45	45	23	44
APS24_4770_44.FIN2	APS24_47	100.9951	307	1	-0.6	-5.8505	-14.36952	0.87	410.2	0.03700	166.95	3.8379	24.1	0.13673	11.7	0.39	2554	562	562	781	180	180	1664	323	323	31	47
APS24_4770_78.FIN2	APS24_47	6.212882	187357	543	2.0	85.06018	86.24864	9.74	1.8	0.19637	1.09	2.9250	1.7	0.10821	1.7	0.77	2781	37	37	661	21	22	1372	26	26	24	48
APS24_4770_55.FIN2	APS24_47	4.884004	68902	343	2.5	-319.999	-20.27016	17.29	2.8	0.16772	1.76	1.6660	3.8	0.07537	5.0	0.86	2495	59	59	461	43	43	953	42	42	18	48
APS24_4770_11.FIN2	APS24_47	6.364131	151561	383	5.3	23.01273	493.2025	11.40	2.2	0.16789	1.55	2.0649	1.9	0.09007	2.3	0.84	2517	54	54	555	24	25	1144	29	29	22	49
APS24_4770_36.FIN2	APS24_47	10.56274	105822	194	3.5	105.3643	62.78699	10.23	3.0	0.22393	2.38	3.2809	2.9	0.11776	3.4	0.68	2915	73	73	709	45	45	1440	40	40	24	49
APS24_4770_113.FIN2	APS24_47	5.507088	60744	243	0.8	-283.957	-22.54684	13.10	3.1	0.15182	1.39	1.7538	2.9	0.08261	3.0	0.75	2363	52	52	510	29	30	1016	38	38	22	50
APS24_4770_84.FIN2	APS24_47	4.839172	162314	647	2.0	-206.209	-48.04785	13.17	2.3	0.15843	1.33	1.8173	2.3	0.08275	2.4	0.77	2408	45	45	519	25	26	1030	29	29	22	50
APS24_4770_31.FIN2	APS24_47	11.90136	117408	184	1.7	109.5237	33.35187	6.38	1.8	0.21237	2.35	4.6724	2.0	0.15888	1.8	0.12	2885	79	79	954	33	34	1749	35	35	33	55
APS24_4770_42.FIN2	APS24_47	25.03385	1931	3	0.0	-27.8593	-12.43667	9.00	4.8	0.19254	8.96	3.0431	7.5	0.12449	4.2	0.08	2512	263	263	750	59	59	1283	143	143	30	58
APS24_4770_82.FIN2	APS24_47	17.18727	1954	5	0.0	-31.4052	-9.707231	9.68	6.8	0.20924	10.55	2.9517	8.9	0.12194	4.5	-0.07	2071	395	395	736	63	63	1232	130	130	36	60
APS24_4770_48.FIN2	APS24_47	3.983857	181167	406	11.8	-164.995	-96.12316	4.62	2.2	0.23268	1.43	7.1935	1.8	0.22608	2.4	0.78	3051	47	47	1308	57	58	2129	32	32	43	61
APS24_4770_105.FIN2	APS24_47	5.200337	127154	287	3.1	-66.0253	-194.6393	6.32	1.6	0.15969	2.22	3.5683	2.0	0.16029	1.5	0.22	2430	70	70	957	26	27	1538	30	30	39	62
APS24_4770_108.FIN2	APS24_47	7.590209	29786	55	6.8	-243.198	-14.21771	7.72	4.9	0.17952	3.03	4.0369	4.2	0.16940	4.9	0.80	2560	89	89	990	89	89	1574	75	75	39	63
APS24_4770_29.FIN2	APS24_47	2.379124	123796	306	2.8	-626.756	-22.76523	5.29	2.9	0.18706	1.67	5.2406	2.5	0.20419	2.6	0.73	2694	56	56	1191	57	58	1834	43	43	44	65
APS24_4770_90.FIN2	APS24_47	3.589522	174765	781	1.4	-80.6282	-154.4425	11.89	4.3	0.14178	1.21	2.4636	5.8	0.12491	5.6	0.97	2224	42	42	749	79	79	1152	76	76	34	65
APS24_4770_61.FIN2	APS24_47	4.65663	179515	571	3.1	-177.653	-77.36	6.98	3.2	0.15875	1.30	3.5613	2.8	0.16675	3.5	0.90	2418	45	45	983	63	64	1508	44	44	41	65
APS24_4770_63.FIN2	APS24_47	3.127668	3168	13	0.3	-39.9327	-9.242951	7.90	4.4	0.22333	7.04	5.8523	11.7	0.18570	8.0	0.82	2456	211	211	1035	137	137	1573	140	140	42	66
APS24_4770_53.FIN2	APS24_47	3.604605	103046	364	3.1	-785.715	-14.50036	14.40	4.8	0.15969	1.69	2.6059	5.3	0.13357	6.3	0.97	2398	59	59	777	92	92	1177	72	72	32	66
APS24_4770_18.FIN2	APS24_47	4.063426	129226	576	2.8	-543.937	-29.1792	5.47	4.9	0.20511	1.43	6.7708	5.1	0.24055	5.1	0.90	2854	45	45	1356	125	126	1997	94	94	48	68
APS24_4770_17.FIN2	APS24_47	3.542815	176241	637	2.3	-1339.61	-19.97811	7.00	3.3	0.14199	1.50	3.2185	3.6	0.16341	3.6	0.93	2240	50	50	967	64	65	1420	54	54	43	68
APS24_4770_8.FIN2	APS24_47	6.767877	131309	471	1.2	-733.68	-30.16694	20.27	11.8	0.16278	6.06	1.9593	7.5	0.11909	10.0	0.94	2291	186	186	703	136	136	1024	102	102	31	69
APS24_4770_23.FIN2	APS24_47	4.442813	1689	10	0.0	-30.716	-7.569354	9.04	4.4	0.14423	8.57	2.5381	9.1	0.13091	3.9	0.31	2021	350	350	785	58	58	1129	135	135	39	70
APS24_4770_101.FIN2	APS24_47	2.074157	154319	446	1.5	-1182.4	-14.98476	7.74	2.8	0.12129	1.61	2.2940	2.2	0.13974	2.6	0.81	1943	58	58	840	41	42	1197	30	30	43	70
APS24_4770_13.FIN2	APS24_47	2.999266	122991	180	5.4	-789.013	-24.38828	6.34	3.5	0.13105	1.65	3.0097	3.1	0.16834	4.0	0.89	2110	60	60	995	74	74	1397	49	49	47	71
APS24_4770_111.FIN2	APS24_47	0.518312	371520	629	1.2	-3411.28	-13.6634	5.75	4.0	0.14729	1.34	4.3870	5.5	0.19841	4.2	0.95	2305	47	47	1168	93	94	1625	84	84	51	72
APS24_4770_37.FIN2	APS24_47	2.534407	117797	145	3.1	-1457.24	-10.07839	8.63	6.3	0.16064	2.10	3.8852	4.4	0.19420	5.3	0.97	2415	67	67	1111	110	110	1520	73	73	46	73
APS24_4770_119.FIN2	APS24_47	1.991247	110501	214	5.0	-969.411	-12.44113	6.91	3.3	0.12060	1.63	2.6107	2.7	0.15912	3.1	0.36	1925	45	45	945	54	54	1281	39	39	49	74
APS24_4770_107.FIN2	APS24_47	2.1112	75181	162	3.9	-572.801	-19.37018	7.18	4.1	0.12145	1.58	2.7315	4.6	0.16410	4.7	0.92	1962	60	60	968	83	84	1301	66	66	49	74
APS24_4770_49.FIN2	APS24_47	2.937743	87220	325	7.5	405.74	-27.12732	7.23	6.0	0.14654	1.69	3.8516	5.2	0.19857	5.9	0.95	2287	60	60	1139	125	125	1522	84	84	50	75
APS24_4770_65.FIN2	APS24_47	4.300231	84110	203	5.0	-1056.65	-9.127123	5.90	3.0	0.12692	1.69	3.2140	2.5	0.18410	2.6	0.78	2048	53	53	1081	52	53	1437	39	39	53	75
APS24_4770_86.FIN2	APS24_47	5.027613	87445	233	2.5	-727.833	-13.49951	13.55	7.4	0.16147	3.26	2.9153	3.9	0.17264	5.2	0.92	2309	104	104	993	99	99	1299	64	64	43	76
APS24_4770_12.FIN2	APS24_47	0.741476	114121	115	4.9	-1650.81	-11.2272	4.52	2.1	0.12845	1.84	4.0152	1.8	0.22508	2.0	0.54	2060	67	67	1305	48	49	1629	30	30	63	80
APS24_4770_95.FIN2	APS24_47	2.682613	225457	371	1.1	-309.748	-50.01557	4.15	1.9	0.14290	1.07	5.0328	1.9	0.25546	1.8	0.82	2241	38	38	1458	47	48	1797	34	34	65	81
APS24_4770_50.FIN2	APS24_47	1.246853	37623	192	4.1	-433.258	-10.5876	12.00	1.9	0.07462	3.06	0.8920	3.2	0.08518	1.8	0.30	975	128	128	526	18	19	646	32	32	54	82
APS24_4770_118.FIN2	APS24_47	3.093342	67324	92	1.7	-451.304	-20.72702	4.74	4.3	0.12608	4.76	3.7477	1.9	0.22669	3.4	0.06	1987	165	165	1308	82	83	1573	30	30	66	83
APS24_4770_47.FIN2	APS24_47	2.017496	33946	68	3.2	-387.211	-9.623185	6.57	8.1	0.12536	1.87	4.2180	3.4	0.23918	3.2	0.85	2028	55	55	1358	84	85	1581	76	76	67	86
APS24_4770_24.FIN2	APS24_47	33.82472	1974	20	0.0	-35.5876	-13.28162	17.09	13.0	0.10699	27.23	0.3930	66.1	0.06425	8.6	-0.44	942	598	598	422	82	82	489	111	111	45	86
APS24_4770_99.FIN2	APS24_47	1.640583	81968	159	2.6	-760.92	-12.94497	4.65	3.4	0.11787	1.54	3.7840	2.3	0.23631	2.7	0.81	1907	58	58	1357	67	68	1569	37	37	71	86
APS24_4770_67.FIN2	APS24_47	1.423937	91633	192	2.8	-1032.82	-8.225156	5.45	5.2	0.11960	1.39	3.6323	2.7	0.22909	3.1	0.92	1929	51	51	1310	76	76	1508	49	49	68	87
APS24_4770_35.FIN2	APS24_47	0.889268	207830	361	0.9	-2100.01	-11.1876	9.12	1.0	0.07466	1.01	1.1486	1.1	0.11041	1.0	0.56	1040	40	40	675	13	14	774	12	12	65	87
APS24_4770_26.FIN2	APS24_47	3.152665	36298	168	0.8	-478.648	-7.513756	8.97	1.3	0.07664	2.54	1.1990	2.6	0.11350	1.3	0.40	993	105	105	692	18	18	790	28	28	70	88
APS24_4770_52.FIN2	APS24_47	1.412632	71301	211	1.8	-683.194	-14.19852	7.57	2.4	0.08171	1.79	1.5320	1.9	0.13632	2.2	0.79	1201	72	72	822	34	34	937	23	23	68	88
APS24_4770_110.FIN2	APS24_47	1.606556	31946	43	2.9	-448.738	-8.671928	4.57	1.8	0.10564	2.99	3.2086	2.1	0.22126	1.7	0.16	1652	104	104	1286	39	40	1449	32	32	78	89
APS24_4770_27.FIN2	APS24_47	2.16308	66891	129	2.3	-932.162	-8.262377	3.98	2.6	0.11548	1.48	4.1716	2.2	0.25086	2.1	0.71	1865	58	58	1481	57	58	1659	36	36	79	89
APS24_4770_112.FIN2	APS24_47	-0.23316	36460	68	0.6	-498.764	-6.870174	6.65	1.5	0.08350	2.03	1.7814	2.5	0.15337	1.4	0.56	1225	80	80	918	24	26	1028	31	31	75	89
APS24_4770_39.FIN2	APS24_47	45.17086	1064	1	-1.1	-20.1448	-19.94136	3.98	14.3	0.54838	36.45	30.7945	6.3	0.35657	6.7	0.03	3835	174	174	1851	210	211	3338	114	114	48	55
APS24_4770_64.FIN2	APS24_47	7.031506	99567	245	0.9	-553.579	-14.21717	4.29	3.4	0.16806	4.19	6.6323	6.9	0.28803	4.3	0.88	2222	136	136	1580	110	111	1853	85	85	71	85
APS24_4770_2.FIN2	APS24_47	0.754877	125518	174	1.2	-1764.25	-9.861571	4.51	5.9	0.15059	1.54	6.2417	4.4	0.30211	4.3	0.91	2335	51	51	1665	131	131	1916	86	86	71	87
APS24_4770_70.FIN2	APS24_47	1.396267	130783	164	1.3	-1156.49	-12.66984	3.29	1.1	0.15361	1.29	6.5292	1.3	0.30724	1.1	0.44	2366	43	43	1724	34	36	2042	23	23	73	84
APS24_4770_77.FIN2	APS24_47	1.729821	83743	97	3.9	-970.12	-13.99249	3.49	1.6	0.13445	2.28	5.3187	1.6	0.28903	1.7	0.09	2121	78	78	1634	49	50	1866	27	27	77	88
APS24_4770_43.FIN2	APS24_47	1.322047	124008	92	2.8	-1322.08	-11.23443	3.56	0.7	0.12426	1.08	4.8840	1.0	0.27989	0.7	0.23	2008	40	40	1590	20	24	1798	16	16	79	88
APS24_4770_62.FIN2	APS24_47	0.439953	96546	158	0.5	-1334.61	-8.10171	3.78	1.6	0.12115	1.04	4.6450	2.0	0.27679	1.8	0.84	1953	37	37	1566	49	50	1731	33	33	80	90
APS24_4770_5.FIN2	APS24_47	0.868	257044	190	1.7	-4175.73	-9.919598	3.22	2.6	0.13479	1.06	5.9282	1.8	0.31572	2.1	0.73	2156	38	38	1761	67	68	1958	34	34	82	90
APS24_4770_25.FIN2	APS24_47	0.643971	81595	182	2.8	-1173.94	-7.44419	3.74	2.6	0.11357	1.23	4.3142	2.0	0.27661	2.1	0.80	1834	47	47	1564	60	61	1685	36	36	85	93
APS24_4770_94.FIN2	APS24_47	0.496492	444883	568	0.4	-3638.53	-20.63004	3.56	2.2	0.09853	2.10	4.0254	3.4	0.29059	2.4	0.75	1546	79	79	1635	69	70	1606	52	52	106	102
APS24_4770_34.FIN2	APS24_47	0.027462	68129	37	2.0	-1154.07	-4.763023	2.81	0.9	0.11493	1.09	5.6965	1.0	0.35760	0.9	0.24	1859	41	41	1971	29	32	1929	17	17	106	102
APS24_4770_57.FIN2	APS24_47	-0.2312	61058	46	1.6	-964.182	-4.416213	2.57	0.9	0.12305	1.01	6.6229	1.0	0.38966	0.9	0.41	1981	37	37	2117	33	37	2057	17	17	107	103
APS24_4770_74.FIN2	APS24_47	1.155294	79478	72	0.8	-1042.03	-7.523224	2.63	1.2	0.12033	1.19	6.3862	1.4	0.38746	1.3	0.61	1940	45	45	2109	48	50	2027	23	23	109	104
APS24_4770_96.FIN2	APS24_47	0.402007	93484	98	1.0	-1359.24	-7.596678	2.63	1.5	0.11987	1.69	6.3622	1.8	0.38507	1.5	0.50	1924	61	61	2094	55	57	2016	31	31	109	104
APS24_4770_88.FIN2	APS24_47	1.178917	27915	21	2.6	-466.07	-5.973435	2.33	1.2	0.13378	1.67	7.8549	1.4	0.43710	1.1	0.25	2097	57	57	2330	44	47	2206	27	27	111	106

U-Pb data from 1APS24_4665

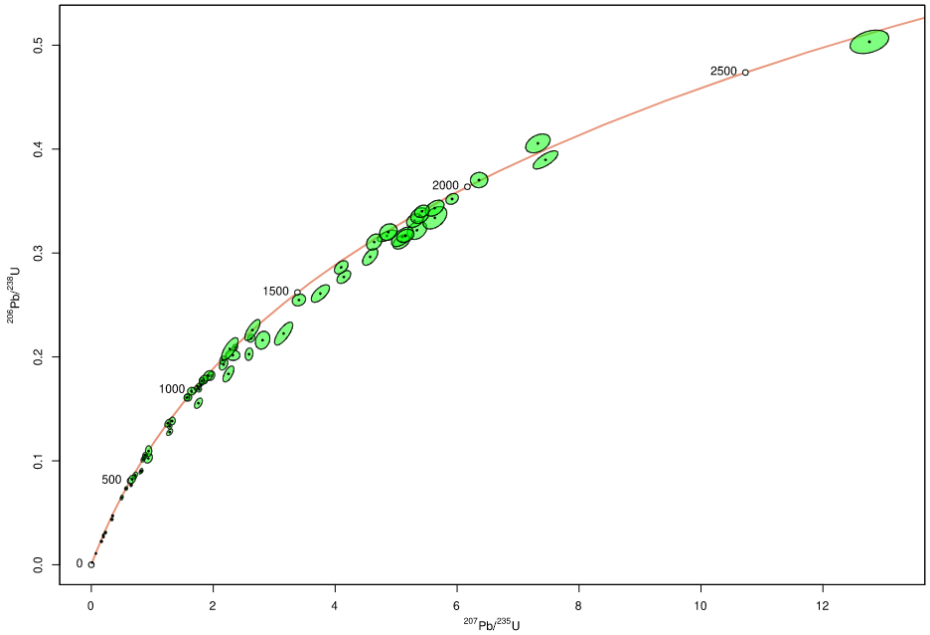


University of Brasilia								Data for Tera-Wasserburg plot				Data for Wetherill plot					Dates									Conc (%)	Conc (%)	Best Age	2s (abs)
Identifier	Comments	f206c	206Pb	Uppm	Th/U	206Pb/204	1s%	238U/206	1s%	207Pb/206	1s%	207Pb/235	1s%	206Pb/238	1s%	Rho	207Pb/206	2s (abs)	2ssys (abs)	206Pb/238	2s (abs)	2ssys (abs)	207Pb/235	2s (abs)	2ssys (abs)	6/8 -7/6	6/8 -7/5		
Concordants																													
APS24_4665-71.	APS24_4665	0.111626	628950	785	0.1	-6842.31	-7.02893	4.38	1.8	0.10266	1.12	3.4506	2.1	0.23781	1.6	0.83	1648	41	51	1369	40	40	1488	34	35	83	92	1369	40
APS24_4665-102	APS24_4665	0.261616	110044	407	1.2	-1444.75	-6.57519	12.22	1.0	0.06408	2.08	0.7159	1.8	0.08139	1.0	0.21	679	86	92	504	10	10	547	16	17	74	92	504	10
APS24_4665-104	APS24_4665	1.797165	47345	147	1.8	-564.829	-7.59841	10.07	1.2	0.06774	2.30	0.9234	2.0	0.09940	1.1	0.08	759	100	106	610	13	13	658	19	20	80	93	610	13
APS24_4665-79.	APS24_4665	0.026117	91062	109	1.7	-1143.36	-7.39406	4.00	1.4	0.10585	2.14	3.6994	2.1	0.25230	1.3	0.43	1691	76	81	1448	34	34	1558	35	36	86	93	1448	34
APS24_4665-46.	APS24_4665	-0.03685	22106	60	1.3	-289.757	-5.39566	9.55	1.0	0.06812	2.72	0.9961	2.7	0.10570	0.9	-0.34	703	104	109	647	11	11	682	24	24	92	95	647	11
APS24_4665-4.F	APS24_4665	0.13459	148812	192	1.0	-1817.98	-8.27344	4.85	1.1	0.08813	1.55	2.5325	1.3	0.20734	1.1	0.18	1354	59	66	1213	24	24	1277	19	20	90	95	1213	24
APS24_4665-63.	APS24_4665	1.703709	11426	14	3.2	-130.11	-7.61436	4.53	2.8	0.10396	2.88	3.2886	2.6	0.24074	1.8	0.18	1537	104	108	1387	47	47	1457	38	39	90	95	1387	47
APS24_4665-88.	APS24_4665	0.383569	378246	579	0.9	-3725.47	-9.37648	5.02	1.1	0.08348	1.07	2.3309	1.2	0.19881	1.0	0.49	1269	44	55	1167	22	22	1216	18	19	92	96	1167	22
APS24_4665-87.	APS24_4665	-0.09422	49869	96	1.3	-648.157	-6.63264	6.31	1.0	0.07411	1.96	1.6240	1.9	0.15826	1.0	0.13	966	77	83	946	17	17	969	22	23	98	98	946	17
APS24_4665-25.	APS24_4665	0.102175	78549	93	0.2	-1053.95	-10.2096	3.98	1.5	0.09299	1.98	3.1939	2.3	0.24559	1.6	0.50	1451	75	80	1412	41	41	1441	34	35	97	98	1412	41
APS24_4665-62.	APS24_4665	0.169154	119794	277	0.8	-1400.5	-6.59896	7.86	0.7	0.06656	1.12	1.1740	1.0	0.12718	0.7	0.11	801	49	60	771	10	10	786	11	12	96	98	771	10
APS24_4665-85.	APS24_4665	0.230021	65120	166	0.5	-821.503	-5.9767	8.48	0.8	0.06450	1.30	1.0524	1.1	0.11773	0.8	0.10	719	57	67	717	10	10	727	12	13	100	99	717	10
APS24_4665-97.	APS24_4665	2.506899	37478	65	2.5	-478.735	-6.09151	5.67	1.2	0.07790	2.06	1.8895	1.8	0.17855	1.1	0.18	1061	79	85	1058	21	21	1071	22	23	100	99	1058	21
APS24_4665-55.	APS24_4665	0.753502	56337	161	0.9	-708.667	-7.52473	9.83	1.0	0.06145	1.85	0.8738	1.6	0.10235	1.2	0.20	594	82	89	628	14	14	635	15	16	106	99	628	14
APS24_4665-38.	APS24_4665	0.158515	120137	202	1.0	-1561.8	-5.5639	5.86	0.9	0.07436	1.33	1.7530	1.1	0.17170	0.9	0.08	1002	55	64	1020	17	17	1023	15	16	102	100	1020	17
APS24_4665-64.	APS24_4665	-0.30132	52589	154	0.0	-694.382	-6.37404	10.19	1.9	0.06221	2.96	0.8622	2.9	0.10116	1.9	0.04	522	120	125	620	22	22	620	25	25	119	100	620	22
APS24_4665-107	APS24_4665	0.162096	136632	177	0.9	-1639.33	-6.80906	4.32	0.7	0.08570	1.20	2.7535	1.1	0.23117	0.8	0.12	1307	46	56	1339	19	19	1338	16	18	103	100	1339	19
APS24_4665-14.	APS24_4665	0.116771	125092	191	1.9	-1453.97	-6.86863	5.55	0.8	0.07542	1.33	1.8819	1.1	0.18102	0.8	0.22	1033	53	62	1072	16	16	1070	14	15	104	100	1072	16
APS24_4665-84.	APS24_4665	0.674544	45103	101	2.6	-590.891	-5.79479	7.45	0.9	0.06577	1.74	1.2245	1.6	0.13411	0.9	0.03	732	79	87	811	14	14	807	19	19	111	100	811	14
APS24_4665-120	APS24_4665	-0.19651	85849	152	0.7	-1311.46	-13.6794	5.72	0.8	0.07339	1.20	1.7814	1.1	0.17527	0.8	-0.01	985	50	61	1040	15	15	1034	14	16	106	101	1040	15
APS24_4665-48.	APS24_4665	-1.30104	23436	80	2.1	-330.287	-6.93283	11.30	1.3	0.06195	3.35	0.7685	3.3	0.08985	1.3	0.01	455	130	133	554	14	14	550	21	21	122	101	554	14
APS24_4665-43.	APS24_4665	2.974809	2060	5	0.0	-31.0352	-8.04353	9.79	6.3	0.12552	18.20	1.6396	16.6	0.12218	4.8	-0.04	1202	665	666	736	67	67	722	184	184	61	102	736	67
APS24_4665-103	APS24_4665	-0.34406	44217	64	2.5	-566.164	-6.5364	4.64	1.0	0.08049	1.52	2.3953	1.5	0.21532	0.9	0.10	1164	58	66	1255	22	22	1229	22	23	108	102	1255	22
APS24_4665-109	APS24_4665	0.996232	41022	71	1.1	-497.093	-6.48325	5.73	0.8	0.07205	1.71	1.7393	1.6	0.17494	0.8	0.06	917	70	77	1038	15	15	1016	19	20	113	102	1038	15
APS24_4665-92.	APS24_4665	1.488485	10044	33	2.7	-161.87	-18.1834	11.60	1.6	0.06368	4.43	0.7693	4.7	0.09037	2.3	0.47	371	179	182	556	23	23	540	29	29	150	103	556	23
APS24_4665-115	APS24_4665	0.107628	14268	45	1.2	-218.174	-19.6196	11.02	1.7	0.06205	4.49	0.7963	4.4	0.09557	2.3	-0.01	368	169	172	586	25	25	555	34	34	159	106	586	25
APS24_4665-69.	APS24_4665	0.216852	32230	64	1.7	-406.073	-6.23288	6.82	0.9	0.06538	3.11	1.3993	4.9	0.14778	0.9	0.09	630	86	89	888	14	14	840	21	21	141	106	888	14
APS24_4665-52.	APS24_4665	0.040982	111845	187	1.7	-1533.43	-4.32867	5.30	1.1	0.07067	2.20	1.8180	2.0	0.18838	1.1	0.13	912	91	97	1112	23	23	1047	26	27	122	106	1112	23
APS24_4665-119	APS24_4665	2.822898	8594	11	0.0	-118.539	-6.18301	4.06	2.6	0.08771	3.80	3.0906	4.1	0.25785	2.6	0.31	1196	168	172	1467	68	68	1377	69	69	123	107	1467	68
APS24_4665-68.	APS24_4665	-0.88776	16659	22	0.0	-210.657	-7.49602	4.59	2.4	0.07820	2.90	2.4019	2.8	0.22702	2.2	0.27	1010	125	129	1310	52	52	1226	43	44	130	107	1310	52
APS24_4665-67.	APS24_4665	-1.99795	15845	20	0.0	-230.873	-6.78077	4.21	2.1	0.07886	3.40	2.5877	3.0	0.24247	2.1	0.01	1023	148	152	1393	52	52	1267	45	46	136	110	1393	52

APS24_4665-116	APS24_4665	0.258217	243563	149	1.3	-2422.96	-8.26453	2.01	0.6	0.21004	0.66	14.4895	0.6	0.49638	0.6	0.55	2898	21	33	2596	25	25	2779	12	16	90	93	2898	21
APS24_4665-94.	APS24_4665	0.238155	241192	244	2.7	-2534.36	-8.47055	3.28	0.9	0.11796	1.18	4.9777	1.1	0.30687	0.9	0.35	1900	42	51	1723	28	28	1811	18	20	91	95	1900	42
APS24_4665-35.	APS24_4665	0.305613	358553	349	1.7	-3533.47	-9.16685	3.31	0.9	0.11653	1.13	4.8757	0.9	0.30261	0.8	0.44	1877	40	49	1702	25	25	1792	16	18	91	95	1877	40
APS24_4665-108	APS24_4665	0.052945	218053	197	1.6	-2732.57	-5.94188	2.92	1.0	0.13034	1.05	6.1719	1.1	0.34370	1.0	0.30	2077	38	47	1904	33	33	1992	20	22	92	96	2077	38
APS24_4665-58.	APS24_4665	0.42441	138204	130	2.2	-1464.67	-7.08958	3.28	1.1	0.11500	0.97	4.9105	1.1	0.30905	1.0	0.48	1863	34	44	1732	31	31	1796	18	20	93	96	1863	34
APS24_4665-99.	APS24_4665	0.779855	142996	119	2.3	-1228.29	-10.4292	2.70	0.9	0.13802	1.00	7.1411	0.9	0.37199	0.8	0.45	2188	36	46	2036	30	30	2124	16	18	93	96	2188	36
APS24_4665-7.F	APS24_4665	0.136409	162335	123	2.2	-1948.99	-6.04679	2.82	0.8	0.13163	1.12	6.4859	0.9	0.35660	0.8	0.14	2102	39	47	1963	27	27	2041	16	18	93	96	2102	39
APS24_4665-13.	APS24_4665	0.77373	85355	77	2.0	-803.525	-9.16817	3.28	0.8	0.11246	1.23	4.7652	1.1	0.30457	0.8	0.23	1818	48	57	1712	25	25	1776	20	22	94	96	1818	48
APS24_4665-113	APS24_4665	0.262939	360606	363	1.8	-3988.23	-7.52526	3.25	0.8	0.11208	0.76	4.8646	1.0	0.30815	0.8	0.61	1829	29	42	1730	23	23	1790	17	19	95	97	1829	29
APS24_4665-114	APS24_4665	0.241829	236904	232	1.3	-2815.5	-7.1164	3.02	1.2	0.11825	1.01	5.4139	1.1	0.32823	1.2	0.64	1916	37	47	1825	40	40	1886	19	21	95	97	1916	37
APS24_4665-21.	APS24_4665	0.112844	208346	190	1.6	-2242.52	-11.9992	3.05	1.3	0.11786	1.62	5.3094	1.3	0.32926	1.3	0.57	1913	62	69	1833	40	40	1866	23	25	96	98	1913	62
APS24_4665-106	APS24_4665	0.413945	110500	117	0.8	-1268.47	-7.72265	3.40	1.0	0.10771	1.30	4.4050	1.1	0.29545	0.9	0.35	1727	49	57	1666	28	28	1706	18	20	96	98	1727	49
APS24_4665-24.	APS24_4665	0.150927	331784	310	1.3	-3651.56	-8.43503	3.26	0.9	0.10970	1.24	4.6634	1.0	0.30729	0.9	0.11	1782	47	56	1725	27	27	1756	17	19	97	98	1782	47
APS24_4665-11.	APS24_4665	-0.00387	312866	261	2.4	-3875.72	-7.33179	2.93	0.9	0.12110	1.31	5.7182	1.1	0.34207	0.9	0.08	1951	47	55	1895	29	29	1930	18	20	97	98	1951	47
APS24_4665-8.F	APS24_4665	-0.21387	138101	103	1.1	-1846.98	-4.984	2.73	0.9	0.13053	1.23	6.6157	0.9	0.36756	0.9	0.16	2078	43	51	2018	30	30	2057	17	19	97	98	2078	43
APS24_4665-37.	APS24_4665	0.019482	242174	140	1.2	-3067.01	-5.93114	2.03	0.7	0.18136	1.03	12.3333	0.7	0.49250	0.8	0.10	2648	33	42	2577	32	32	2626	14	17	97	98	2648	33
APS24_4665-91.	APS24_4665	0.053791	101344	88	1.6	-1367.63	-5.53594	2.87	0.8	0.12245	1.05	5.9237	1.0	0.34868	0.7	0.27	1971	37	47	1926	25	25	1960	17	19	98	98	1971	37
APS24_4665-81.	APS24_4665	0.297346	154295	143	0.9	-1923.32	-9.38499	2.98	1.8	0.12113	2.56	5.5479	2.3	0.33988	1.7	0.21	1926	94	98	1882	55	55	1896	40	41	98	99	1926	94
APS24_4665-41.	APS24_4665	-0.02061	74158	65	1.6	-875.042	-6.66503	3.08	1.0	0.11445	1.15	5.2170	1.2	0.32683	0.9	0.51	1855	42	51	1820	29	29	1845	21	23	98	99	1855	42
APS24_4665-1.F	APS24_4665	0.358885	67678	52	2.8	-772.374	-6.64834	2.83	0.9	0.12520	1.39	6.1192	1.1	0.35455	0.9	-0.09	1991	49	57	1953	30	30	1985	19	21	98	98	1991	49
APS24_4665-72.	APS24_4665	-0.09656	196951	224	1.6	-2727.82	-5.94752	3.76	0.9	0.09575	1.22	3.5505	1.0	0.26499	0.9	0.14	1532	48	57	1514	24	24	1535	15	17	99	99	1532	48
APS24_4665-56.	APS24_4665	0.065742	321481	273	2.1	-3940.58	-6.02236	2.98	0.7	0.11620	1.14	5.3998	0.8	0.33501	0.7	0.02	1882	38	46	1861	22	22	1878	13	15	99	99	1882	38
APS24_4665-44.	APS24_4665	0.264416	145010	124	1.6	-1868.3	-5.69035	3.08	1.1	0.11445	0.95	5.1935	1.1	0.32833	1.0	0.60	1850	35	45	1830	31	31	1842	20	21	99	99	1850	35
APS24_4665-19.	APS24_4665	0.416461	122607	102	0.4	-1394.24	-7.51405	3.05	1.0	0.11472	1.23	5.2340	1.1	0.33093	1.0	0.40	1858	44	53	1840	31	31	1859	19	21	99	99	1858	44
APS24_4665-33.	APS24_4665	-0.07447	188578	167	1.1	-2423.46	-5.92102	3.16	0.6	0.11061	0.90	4.8716	0.8	0.31714	0.6	0.04	1789	34	46	1774	20	20	1793	14	16	99	99	1789	34
APS24_4665-49.	APS24_4665	0.7032	328151	247	1.2	-4247.44	-6.83158	2.59	0.6	0.13142	0.74	7.0526	0.7	0.38559	0.6	0.83	2107	26	39	2100	22	22	2114	12	14	100	99	2107	26
APS24_4665-82.	APS24_4665	0.180971	270845	187	1.4	-3127.03	-8.06155	2.28	0.8	0.14826	1.13	8.9882	1.0	0.43449	0.8	0.22	2325	37	46	2323	32	32	2332	18	20	100	100	2325	37
APS24_4665-83.	APS24_4665	0.156974	472583	509	0.1	-4406.98	-9.23189	3.51	1.0	0.10075	0.98	4.0979	1.7	0.28978	1.1	0.76	1631	36	46	1636	32	32	1638	27	28	100	100	1631	36
APS24_4665-90.	APS24_4665	0.145554	111084	82	1.8	-1263.31	-6.73828	2.46	0.9	0.13686	0.90	7.6793	0.9	0.40287	0.7	0.37	2170	32	42	2180	25	25	2188	16	18	100	100	2170	32
APS24_4665-3.F	APS24_4665	0.103427	199281	151	1.7	-2452.2	-5.62839	2.79	0.8	0.12245	1.07	6.1053	0.8	0.36041	0.8	0.07	1970	39	49	1981	26	26	1986	14	17	101	100	1970	39
APS24_4665-50.	APS24_4665	0.080211	166241	121	2.2	-2162.91	-6.36151	2.59	0.8	0.12927	0.80	6.9453	0.8	0.38608	0.8	0.63	2082	29	41	2103	27	27	2101	15	17	101	100	2082	29
APS24_4665-89.	APS24_4665	0.583781	64445	73	1.9	-745.26	-6.67686	3.82	0.8	0.09472	1.36	3.4182	1.3	0.26264	0.7	0.11	1482	51	59	1502	19	19	1502	19	20	101	100	1482	51
APS24_4665-27.	APS24_4665	-0.00223	133203	103	2.1	-1767.84	-5.35282	2.77	0.7	0.12103	1.00	6.0438	0.8	0.36026	0.7	0.12	1953	36	46	1981	24	24	1979	15	17	101	100	1953	36
APS24_4665-112	APS24_4665	0.027753	302232	273	1.7	-4035.38	-6.89379	2.95	0.8	0.11294	0.91	5.3522	0.7	0.33861	0.8	0.12	1843	36	48	1878	26	26	1874	12	15	102	100	1843	36
APS24_4665-54.	APS24_4665	-0.02699	186278	105	1.7	-2224.03	-6.79653	2.02	0.7	0.16768	0.71	11.6103	0.7	0.49538	0.6	0.64	2535	24	36	2592	25	25	2570	14	17	102	101	2535	24
APS24_4665-66.	APS24_4665	-0.19552	80578	68	3.3	-1181.33	-5.71075	2.90	1.0	0.11396	1.26	5.4628	1.0	0.34159	1.0	0.03	1853	41	48	1900	27	27	1888	17	19	103	101	1853	41
APS24_4665-105	APS24_4665	0.051452	169530	157	1.0	-2163.78	-5.33981	3.09	0.8	0.11001	1.20	4.9080	1.0	0.32511	0.8	0.16	1764	44	54	1815	26	26	1798	17	19	103	101	1764	44
APS24_4665-60.	APS24_4665	0.250429	74919	77	1.4	-920.076	-6.42949	3.56	0.7	0.09636	1.12	3.7583	1.0	0.28183	0.7	0.13	1535	41	51	1599	21	21	1580	15	17	104	101	1535	41
APS24_4665-80.	APS24_4665	-0.09218	261118	218	2.3	-3490.49	-6.25494	2.85	0.6	0.11357	0.80	5.5475	0.7	0.34887	0.6	0.28	1847	29	41	1928	20	20	1905	12	15	104	101	1847	29

Discordants																												
APS24_4665-96.	APS24_4665	6.946066	76033	1123	1.5	-30.6543	-210.291	49.16	1.2	0.16606	1.22	0.4703	1.4	0.02062	1.3	0.24	2487	42	50	132	3	3	390	10	10	5	34
APS24_4665-20.	APS24_4665	8.737439	101049	1761	8.8	72.70984	90.26937	74.98	4.1	0.15616	2.28	0.3342	3.2	0.01628	4.0	0.56	2345	71	75	104	8	8	289	16	16	4	36
APS24_4665-76.	APS24_4665	8.279443	123466	952	2.5	171.2851	27.06463	25.48	2.2	0.15853	1.20	0.9059	1.6	0.04145	1.7	0.71	2412	41	50	262	9	9	649	17	17	11	40
APS24_4665-6.F	APS24_4665	5.206016	171450	769	3.6	78.09765	134.3389	15.83	1.4	0.17478	1.55	1.5303	1.3	0.06389	1.4	0.36	2581	53	59	399	11	11	940	16	17	15	42
APS24_4665-2.F	APS24_4665	12.68446	274498	573	5.4	135.6847	5.769717	8.41	2.0	0.27298	1.53	4.7037	1.9	0.12605	1.8	0.69	3282	49	56	763	26	26	1751	33	35	23	44
APS24_4665-98.	APS24_4665	5.26115	224297	1176	7.8	168.3259	69.20777	18.37	3.4	0.16818	1.42	1.4053	3.1	0.06208	3.5	0.89	2514	47	54	387	26	26	880	36	37	15	44
APS24_4665-26.	APS24_4665	5.267477	137305	591	3.5	48.76939	196.0839	14.92	1.3	0.15139	1.19	1.4242	1.6	0.06912	1.7	0.05	2351	41	49	430	14	14	898	19	20	18	48
APS24_4665-10.	APS24_4665	5.113641	173664	476	7.9	-59.1158	-198.833	9.54	2.5	0.18265	1.63	2.7712	2.1	0.11310	2.9	0.82	2644	55	62	687	38	38	1339	30	30	26	51
APS24_4665-100	APS24_4665	3.345497	464687	1540	3.7	507.6834	31.01815	11.07	1.4	0.15465	1.18	1.9696	1.5	0.09192	1.4	0.41	2380	40	48	566	15	15	1099	20	21	24	52
APS24_4665-32.	APS24_4665	4.446532	228073	730	1.8	142.9757	82.33547	11.34	1.0	0.14675	1.31	1.8061	1.3	0.08848	1.0	0.44	2285	44	52	546	11	11	1043	17	18	24	52
APS24_4665-15.	APS24_4665	6.230533	360144	1290	2.5	295.5338	12.74736	12.27	1.4	0.13607	1.26	1.5608	1.5	0.08272	1.4	0.58	2163	46	54	512	14	14	950	19	20	24	54
APS24_4665-12.	APS24_4665	2.355742	652883	1708	0.9	705.6216	21.01027	9.43	1.4	0.15521	0.88	2.3371	1.5	0.10787	1.3	0.83	2390	30	41	659	16	16	1214	21	23	28	54
APS24_4665-118	APS24_4665	4.235388	118259	319	8.9	-327.68	-30.4522	9.10	2.6	0.16088	1.41	2.6286	2.6	0.12036	3.7	0.89	2442	52	60	725	49	49	1299	33	34	30	56
APS24_4665-23.	APS24_4665	1.473545	374746	1181	2.6	-422.054	-67.3468	11.64	2.1	0.11000	1.07	1.3775	2.1	0.09071	2.0	0.89	1776	39	49	558	22	22	874	26	27	31	64
APS24_4665-5.F	APS24_4665	1.82975	133830	248	5.4	-582.38	-20.7079	7.05	2.4	0.14182	1.12	2.9829	2.2	0.15317	2.3	0.87	2233	38	47	914	40	40	1381	33	34	41	66
APS24_4665-34.	APS24_4665	2.292438	295683	765	0.7	-333.64	-50.5868	9.65	1.7	0.11274	1.08	1.7188	1.9	0.10872	1.6	0.84	1816	39	49	664	20	20	999	26	27	37	66
APS24_4665-22.	APS24_4665	1.00432	303809	399	6.0	-499.855	-49.7448	4.55	2.1	0.20241	1.17	6.5407	2.2	0.23409	2.2	0.84	2825	38	46	1348	52	52	2023	38	39	48	67
APS24_4665-111	APS24_4665	4.44727	46329	152	1.5	-261.088	-14.4489	11.01	0.9	0.10373	4.12	1.3590	5.4	0.09047	0.9	0.08	1419	129	132	558	10	10	806	43	43	39	69
APS24_4665-74.	APS24_4665	1.263084	346546	629	1.7	-1004.66	-22.5572	6.27	1.7	0.13119	0.88	2.9994	1.5	0.16449	1.5	0.81	2100	30	41	982	27	27	1401	25	26	47	70
APS24_4665-30.	APS24_4665	0.472727	650299	811	1.0	-3187.78	-18.2785	4.82	2.9	0.17017	2.00	6.1327	4.9	0.24094	3.3	0.96	2496	68	73	1371	81	81	1861	82	82	55	74
APS24_4665-117	APS24_4665	3.431583	299168	624	0.4	-243.001	-65.2939	6.91	3.1	0.12636	1.73	3.2788	3.9	0.17495	3.0	0.95	1974	67	74	1026	57	57	1373	65	65	52	75
APS24_4665-93.	APS24_4665	2.334977	137155	646	3.7	-735.198	-15.8966	16.39	2.9	0.08453	1.80	0.7596	1.4	0.06876	2.3	0.65	1250	68	75	427	19	19	570	12	13	34	75
APS24_4665-86.	APS24_4665	4.294219	205010	277	6.1	-621.534	-30.119	5.29	4.3	0.17071	2.86	5.1785	2.6	0.24397	3.7	0.61	2463	83	86	1381	93	93	1812	49	50	56	76
APS24_4665-70.	APS24_4665	2.379275	133347	351	1.1	-895.299	-11.4802	9.14	2.4	0.09724	1.76	1.5716	2.1	0.11894	2.1	-0.01	1495	56	62	721	29	29	942	26	27	48	77
APS24_4665-95.	APS24_4665	0.756437	402342	559	1.5	-1363.1	-22.5751	4.54	1.0	0.13777	1.05	4.1973	0.9	0.22141	1.0	0.45	2175	37	46	1287	22	22	1668	15	17	59	77
APS24_4665-51.	APS24_4665	1.202993	286425	337	1.4	-1470.24	-20.8681	4.13	2.7	0.14195	1.24	5.0494	2.3	0.26023	2.6	0.88	2231	43	51	1480	70	70	1804	41	42	66	82
APS24_4665-61.	APS24_4665	0.546545	134186	172	3.6	-1251.83	-10.4271	4.25	2.8	0.14003	1.59	5.0025	2.9	0.25785	2.6	0.44	2181	45	50	1466	68	68	1782	46	47	67	82
APS24_4665-59.	APS24_4665	0.502719	272790	385	3.9	-2448.38	-8.894	4.76	1.9	0.12318	1.54	3.7800	2.1	0.22356	1.7	0.12	1964	36	41	1294	41	41	1568	33	34	66	83
APS24_4665-9.F	APS24_4665	0.603571	464386	530	2.9	-1518.44	-23.6994	4.07	1.0	0.13075	1.08	4.5042	1.2	0.24795	1.0	0.51	2087	38	47	1425	26	26	1723	19	21	68	83
APS24_4665-18.	APS24_4665	1.109938	153209	252	3.0	-1115.61	-11.0335	6.06	1.9	0.09647	1.17	2.2496	1.4	0.17102	1.7	0.67	1524	44	53	1014	31	31	1186	21	22	67	85
APS24_4665-65.	APS24_4665	0.651986	290566	335	1.1	-2178.2	-10.3057	3.90	0.8	0.12187	0.75	4.3446	0.9	0.25618	0.8	0.49	1971	27	40	1469	20	20	1698	14	17	75	86
APS24_4665-36.	APS24_4665	0.862723	14052	44	-0.1	-198.177	-7.95823	11.53	1.6	0.07260	3.21	0.9194	3.3	0.09040	1.9	0.08	839	139	143	556	20	20	637	31	31	66	87
APS24_4665-29.	APS24_4665	-6.02928	2308	5	0.0	-29.8071	-9.5746	9.29	7.0	0.11119	13.03	2.0227	10.1	0.15643	4.8	-0.02	1201	339	340	939	86	86	811	133	133	78	116
APS24_4665-47.	APS24_4665	0.751548	202973	205	1.4	-2158.09	-10.0791	3.76	4.0	0.13492	1.75	5.7289	2.5	0.30455	2.5	-0.49	2162	42	46	1682	72	72	1903	44	44	78	88
APS24_4665-16.	APS24_4665	0.62135	293861	285	1.5	-1764.95	-14.7698	3.44	1.2	0.13400	1.13	5.4494	1.1	0.29445	1.1	0.32	2128	39	48	1660	33	33	1885	19	21	78	88
APS24_4665-31.	APS24_4665	0.539923	557490	560	0.7	-2402.96	-18.36	3.66	0.9	0.12244	1.36	4.6667	1.2	0.27556	0.9	0.05	1950	41	48	1566	26	26	1752	19	20	80	89
APS24_4665-45.	APS24_4665	0.081977	487449	441	1.7	-5289.63	-7.35785	3.16	0.8	0.12979	0.83	5.7329	0.9	0.31695	0.8	0.49	2079	29	41	1773	24	24	1934	15	17	85	92
APS24_4665-40.	APS24_4665	0.39192	211953	218	2.0	-1873.56	-8.9228	3.52	1.3	0.11917	1.06	4.7719	1.2	0.29059	1.3	0.53	1918	39	48	1643	37	37	1772	20	22	86	93
APS24_4665-28.	APS24_4665	0.084528	261460	181	3.1	-3058.67	-6.41196	2.40	1.0	0.17661	0.84	10.3294	1.0	0.42052	0.9	0.67	2618	27	38	2262	34	34	2456	19	21	86	92
APS24_4665-53.	APS24_4665	0.571562	167989	161	2.1	-1433.74	-11.0697	3.48	2.3	0.12070	3.28	4.7227	2.6	0.28947	2.3	0.19	1906	120	124	1649	62	62	1769	48	49	87	93
APS24_4665-110	APS24_4665	0.550879	176612	182	2.1	-1779.17	-8.28519	3.41	1.0	0.11836	0.81	4.8356	0.9	0.29493	1.0	0.58	1921	30	42	1663	30	30	1789	15	17	87	93
APS24_4665-17.	APS24_4665	0.178617	251298	237	2.9	-2607.02	-9.04177	3.36	0.8	0.11596	1.11	4.7635	0.9	0.29746	0.7	0.13	1875	40	50	1677	22	22	1779	15	18	89	94
APS24_4665-101	APS24_4665	0.501369	2004359	1545	1.7	784.1899	121.3408	2.52	1.0	0.11975	0.90	6.6348	1.0	0.40018	1.0	0.60	1935	32	43	2165	37	37	2056	18	20	112	105

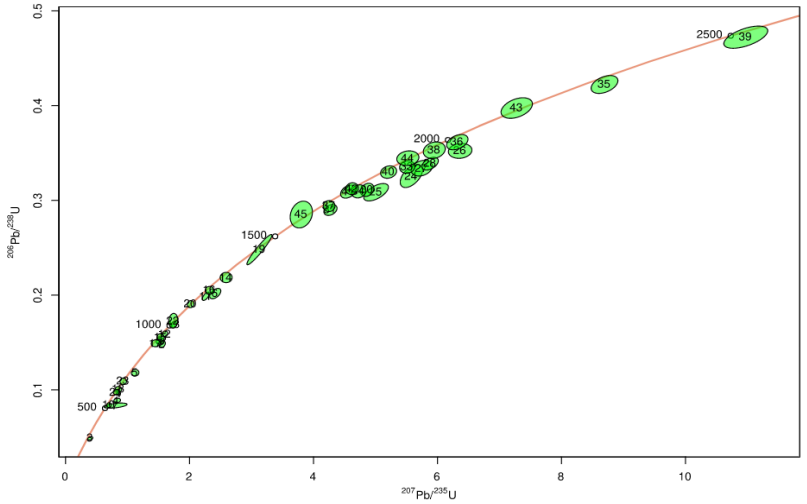
U-Pb data from 1APS25_1011



University of Brasilia								Data for Tera-Wasserburg plot				Data for Wetherill plot					Dates										Conc (%)	Conc (%)	Best Age	2s (abs)
Identifier	Comments	f206c	206Pb	Uppm	Th/U	206Pb/204	1s%	238U/206	1s%	207Pb/206	1s%	207Pb/235	1s%	206Pb/238	1s%	Rho	207Pb/206	2s (abs)	2ssys (abs)	206Pb/238	2s (abs)	2ssys (abs)	207Pb/235	2s (abs)	2ssys (abs)		6/8 -7/6	6/8 -7/5		
Concordants																														
APS25_1011-63.	APS25_10	0.670906	256248	405	0.5	-3297.38	-11.6474	4.61	2.3	0.10283	1.43	3.1544	1.9	0.22249	2.0	0.74	1650	53	53	1290	47	52	1434	31	33		78	90	1290	47
APS25_1011-29.	APS25_10	0.59989	171051	366	0.7	-3092.55	-5.82163	6.60	1.4	0.08164	1.21	1.7563	1.5	0.15543	1.3	0.48	1202	48	48	929	23	28	1020	20	22		77	91	929	23
APS25_1011-17.	APS25_10	1.249431	125643	440	1.2	-2017.58	-7.80855	11.14	0.8	0.06621	1.28	0.8248	1.3	0.08981	0.8	0.56	776	53	53	554	8	13	608	12	13		71	91	554	8
APS25_1011-24.	APS25_10	1.555714	146676	289	0.4	-1927.33	-11.7129	5.63	1.9	0.08960	1.39	2.2493	1.6	0.18364	1.7	0.61	1382	56	56	1082	34	39	1186	23	25		78	91	1082	34
APS25_1011-32.	APS25_10	1.487695	102937	163	2.7	-1829.25	-6.49661	5.05	1.3	0.09390	1.47	2.5869	1.0	0.20264	1.2	0.16	1460	57	57	1187	26	33	1293	14	18		81	92	1187	26
APS25_1011-13.	APS25_10	2.804489	27413	310	2.3	-534.801	-6.6539	37.85	1.0	0.05377	2.06	0.1994	1.8	0.02663	1.0	-0.02	255	102	102	169	3	5	184	6	6		66	92	169	3
APS25_1011-94.	APS25_10	1.127753	365542	1408	0.6	-2163.08	-19.8143	11.25	1.2	0.06525	1.16	0.8118	1.4	0.09006	1.3	0.62	763	51	51	555	14	17	601	13	14		73	92	555	14
APS25_1011-60.	APS25_10	1.224215	77624	203	1.5	-1288.33	-7.00796	7.90	1.0	0.07343	1.69	1.2848	1.6	0.12754	1.0	0.53	976	71	71	773	15	20	833	17	19		79	93	773	15
APS25_1011-61.	APS25_10	0.530315	29834	428	0.7	-573.652	-19.8756	46.61	2.3	0.05489	4.62	0.1665	4.3	0.02244	2.0	0.00	110	189	189	143	6	6	154	12	12		130	93	143	6
APS25_1011-11	APS25_10	0.737052	76424	345	2.0	-1260.13	-5.3341	13.09	0.8	0.06192	1.40	0.6539	1.2	0.07660	0.8	0.14	611	61	61	476	7	11	509	10	11		78	93	476	7
APS25_1011-10	APS25_10	0.113167	271790	427	0.5	-4669.13	-5.21914	4.88	1.9	0.09346	0.97	2.8096	1.7	0.21610	1.6	0.20	1475	36	36	1256	38	44	1341	27	29		85	94	1256	38
APS25_1011-10	APS25_10	-73.0667	613	96	2.1	-18.3255	-45.9691	920.93	19.0	0.12373	76.29	0.0149	18.8	0.00209	9.2	0.05	1620	508	508	13	2	2	14	5	5		1	94	13	2
APS25_1011-67.	APS25_10	1.708754	19848	148	1.9	-412.082	-4.6579	23.28	1.1	0.05642	3.00	0.3371	2.8	0.04366	1.2	0.03	273	128	128	275	6	8	290	14	14		101	95	275	6
APS25_1011-70.	APS25_10	8.355144	37703	153	1.8	-577.654	-10.3109	10.39	2.9	0.06865	2.84	0.9356	2.9	0.10236	1.8	0.28	763	114	114	627	22	25	660	27	27		82	95	627	22
APS25_1011-89.	APS25_10	0.14698	171128	214	1.5	-3217.17	-4.85967	3.90	1.4	0.10350	1.19	3.7566	1.6	0.26106	1.3	0.64	1653	45	45	1494	34	42	1571	26	29		90	95	1494	34
APS25_1011-7.F	APS25_10	-0.0864	27634	276	1.5	-768.257	-18.4816	33.46	1.0	0.05419	2.87	0.2324	3.2	0.03091	1.7	0.23	251	112	112	196	6	7	204	10	10		78	96	196	6
APS25_1011-10	APS25_10	0.46573	45557	188	2.0	-840.082	-5.03744	11.93	0.9	0.06109	1.80	0.7078	1.7	0.08426	0.9	0.11	590	79	79	522	9	13	543	15	16		89	96	522	9
APS25_1011-37.	APS25_10	0.258719	120642	286	0.8	-2559.9	-4.9649	7.53	0.8	0.06940	1.29	1.2862	1.1	0.13320	0.8	0.11	878	53	53	806	12	19	836	13	15		92	96	806	12
APS25_1011-10	APS25_10	0.689523	17357	540	1.3	-323.697	-5.0653	93.31	1.2	0.05056	3.31	0.0750	3.3	0.01084	1.2	-0.03	30	135	135	70	2	2	72	4	4		230	97	70	2
APS25_1011-50.	APS25_10	0.231502	180856	265	1.8	-3427.01	-5.13952	4.59	0.8	0.08732	1.12	2.6226	0.9	0.21788	0.7	0.24	1340	45	45	1270	17	27	1305	13	16		95	97	1270	17
APS25_1011-95.	APS25_10	0.163849	98936	180	1.0	-2016.75	-5.91884	5.22	1.3	0.08125	1.45	2.1685	1.3	0.19263	1.1	0.39	1192	58	58	1134	23	30	1165	18	20		95	97	1134	23
APS25_1011-10	APS25_10	0.069068	100420	202	0.9	-1853.63	-3.93531	5.92	0.6	0.07543	0.98	1.7694	0.9	0.16868	0.6	0.17	1053	40	40	1004	11	21	1031	12	15		95	97	1004	11
APS25_1011-47.	APS25_10	-0.58707	27797	105	1.7	-563.76	-5.37948	11.85	1.5	0.06113	2.12	0.7198	2.2	0.08621	1.4	0.34	577	105	105	532	14	17	546	18	19		92	97	532	14
APS25_1011-87.	APS25_10	0.273541	113388	209	2.9	-2183.75	-4.60461	5.53	1.0	0.07814	1.30	1.9660	1.2	0.18186	1.0	0.24	1112	52	52	1076	19	27	1103	16	18		97	98	1076	19
APS25_1011-65.	APS25_10	0.194342	149656	198	1.3	-2882.1	-4.89187	4.04	1.7	0.09735	1.31	3.4051	1.3	0.25474	0.9	0.17	1544	46	46	1464	25	36	1500	20	22		95	98	1464	25
APS25_1011-76.	APS25_10	0.451725	98195	681	2.2	-1844.35	-6.30526	21.44	0.9	0.05371	1.64	0.3502	1.6	0.04708	1.0	-0.07	274	65	65	296	6	8	303	8	9		108	98	296	6
APS25_1011-11	APS25_10	1.186598	34807	88	0.9	-638.31	-6.18861	7.32	1.3	0.06956	1.71	1.3252	1.6	0.13827	1.1	0.12	843	70	70	834	17	23	848	18	20		99	98	834	17
APS25_1011-11	APS25_10	-0.0954	41760	72	0.8	-820.739	-8.52456	4.99	0.9	0.08204	1.67	2.3218	2.0	0.20168	1.0	-0.03	1180	68	68	1183	21	30	1203	24	25		100	98	1183	21
APS25_1011-11	APS25_10	0.248704	211713	401	0.9	-3586.9	-5.61158	5.66	0.7	0.07609	1.06	1.8659	0.8	0.17730	0.7	0.03	1072	43	43	1051	14	23	1066	11	14		98	99	1051	14
APS25_1011-86.	APS25_10	-0.5104	39719	228	1.4	-775.232	-6.07635	15.91	1.5	0.05688	2.00	0.4991	2.0	0.06460	1.5	0.33	424	97	97	403	12	14	409	14	14		95	99	403	12
APS25_1011-83.	APS25_10	0.050478	124405	240	1.1	-2468.75	-5.52786	5.80	0.8	0.07411	1.24	1.7974	1.3	0.17294	0.8	0.89	1013	52	52	1027	15	24	1038	16	18		101	99	1027	15
APS25_1011-82.	APS25_10	-0.47668	20214	221	2.5	-415.739	-4.98988	35.35	1.4	0.05031	3.04	0.1980	2.9	0.02858	1.3	-0.04	14	174	174	182	5	6	183	10	10		1307	99	182	5
APS25_1011-1.F	APS25_10	0.013036	259522	383	0.9	-6079.53	-3.99833	4.79	0.7	0.08157	0.98	2.3562	0.8	0.20906	0.6	0.29	1209	39	39	1223	14	26	1228	11	15		101	100	1223	14
APS25_1011-10	APS25_10	0.411668	110708	194	0.7	-1905.05	-6.58501	5.63	1.7	0.07684	1.78	1.9156	1.7	0.18186	1.1	0.37	1070	73	73	1076	23	29	1079	23	25		101	100	1076	23
APS25_1011-10	APS25_10	0.079179	161466	277	1.7	-2897.17	-4.79683	5.09	0.8	0.07926	1.09	2.1552	0.9	0.19709	0.8	0.26	1152	42	42	1160	17	27	1164	13	17		101	100	1160	17
APS25_1011-6.F	APS25_10	0.151378	57573	173	2.0	-1305.86	-5.42805	9.93	1.1	0.06071	1.67	0.8472	1.5	0.10139	1.0	0.26	575	72	72	622	12	16	622	15	16		108	100	622	12
APS25_1011-11	APS25_10	-0.05221	58964	120	0.9	-1079.56	-4.29214	5.84	0.9	0.07357	1.44	1.7387	1.3	0.17168	0.8	0.78	972	58	58	1020	15	24	1019	16	18		105	100	1020	15
APS25_1011-93.	APS25_10	0.740559	48758	93	0.9	-987.33	-6.34518	5.69	1.0	0.07592	1.63	1.8398	1.5	0.17792	1.0	0.31	1031	70	70	1054	20	27	1052	19	21		102	100	1054	20
APS25_1011-11	APS25_10	1.398019	13228	58	1.3	-241.857	-7.67928	12.35	1.9	0.05985	3.87	0.6675	3.5	0.08215	2.0	0.28	372	176	176	508	20	22	507	28	29		137	100	508	20
APS25_1011-11	APS25_10	0.295451	141326	277	1.7	-2322.36	-5.62246	5.66	0.7	0.07382	1.08	1.8110	0.9	0.17686	0.7	0.05	1013	44	44	1049	13	23	1046	11	15		104	100	1049	13
APS25_1011-53.	APS25_10	0.056239	85749	254	0.4	-1811.68	-5.04974	9.41	1.0	0.06268	2.41	0.9402	2.2	0.10942	1.9	0.01	604	61	61	658	13	15	656	13	14		109	100	658	13
APS25_1011-20.	APS25_10	0.167392	32674	61	2.8	-781.001	-4.96952	6.20	0.8	0.07134	1.68	1.5876	1.5	0.16106	0.9	-0.02	934	71	71	962	16	23	958	19	21		103	100	962	16
APS25_1011-92.	APS25_10	0.573039	54201	173	0.3	-1001.5	-5.3455	9.76	1.0	0.06105	1.73	0.8716	1.5	0.10380	1.0	0.10	570	76	76	636	12	17	633	14	15		112	100	636	12
APS25_1011-2.F	APS25_10	-0.02879	59354	113	2.4	-1339.17	-4.78689	6.23	0.8	0.07063	1.41	1.5655	1.2	0.16082	0.8	0.06	916	58	58	961	14	22	956	15	17		105	100	961	14
APS25_1011-45.	APS25_10	6.2359	26705	113	1.6	-524.859	-4.90371	13.68	1.0	0.05622	2.05	0.5715	1.9	0.07344	1.0	0.11	343	99	99	457	9	12	454	14	15		133	101	457	9
APS25_1011-84.	APS25_10	-0.31117	70095	173	0.8	-1330.69	-4.98533	7.29	1.2	0.06573	1.45	1.2519	1.5	0.13624	1.1	0.45	780	61	61	822	17	22	817	17	19		105	101	822	17
APS25_1011-69.	APS25_10	0.562028	40700	64	1.6	-703.695	-7.80801	4.53	1.7	0.08470	1.67	2.6423	1.9	0.22586	1.8	0.73	1252	64	64	1313	39	45	1299	27	29		105	101	1313	39
APS25_1011-49.	APS25_10	0.678562	36195	111	1.5	-667.33	-6.08246	9.54	1.0	0.06044	1.84	0.8820	1.7	0.10551	1.0	0.10	546	84	84	646	12	17	638	16	17		118	101	646	12
APS25_1011-10	APS25_10	0.742685	43600	89	1.7	-846.037	-4.47254	6.01	1.0	0.07147	1.80	1.6435	1.6	0.16699	0.9	0.05	876	78	78	994	16	24	980	19	21		113	101	994	16
APS25_1011-75.	APS25_10	0.143358	507141	851	0.5	-9125.61	-8.36319	4.97	2.0	0.07898	1.65	2.2713	2.4	0.20772	2.1	0.72	1139	65	65	1213	46	51	1190	34	35		106	102	1213	46

APS25_1011-43	APS25_101	0.535531	240510	282	2.0	-3614.8	-8.49797	3.63	0.9	0.10809	1.04	4.1419	1.1	0.27693	0.9	0.48	1750	38	38	1574	26	37	1657	17	21	90	95	1750	38
APS25_1011-41	APS25_101	0.225655	371138	385	0.7	-5563.86	-9.81734	3.22	0.9	0.11755	1.02	5.0855	1.1	0.31073	0.9	0.44	1906	38	38	1742	28	40	1830	18	21	91	95	1906	38
APS25_1011-44	APS25_101	0.613786	137717	153	1.5	-2566.83	-6.57759	3.39	1.1	0.11164	1.28	4.5738	1.1	0.29630	1.1	0.57	1807	49	49	1670	31	42	1739	19	22	92	96	1807	49
APS25_1011-26	APS25_101	0.304038	1284403	1304	0.6	-7708.08	-19.9899	3.13	1.1	0.11927	1.06	5.3411	1.2	0.32189	1.1	0.28	1930	36	36	1795	34	45	1868	19	22	93	96	1930	36
APS25_1011-15	APS25_101	1.909762	76235	75	3.4	-1274.76	-7.14064	3.21	1.2	0.11784	1.25	5.1005	1.4	0.31562	1.2	0.58	1890	45	45	1763	36	46	1830	25	28	93	96	1890	45
APS25_1011-9.F	APS25_101	1.217602	81154	79	1.4	-1624.88	-5.26825	3.18	0.8	0.11662	1.18	5.1516	1.1	0.31659	0.8	0.27	1884	42	42	1771	24	38	1840	18	21	94	96	1884	42
APS25_1011-99	APS25_101	0.304543	93377	94	2.5	-1648	-6.30888	2.97	1.4	0.11988	1.00	5.6348	1.4	0.33389	1.3	0.42	1933	36	36	1864	40	49	1920	23	25	96	97	1933	36
APS25_1011-11	APS25_101	0.255999	50041	44	1.4	-889.304	-4.74262	2.58	1.0	0.13881	1.27	7.4502	1.1	0.38964	0.9	0.72	2178	44	44	2117	33	47	2157	20	23	97	98	2178	44
APS25_1011-46	APS25_101	-0.00337	131116	151	1.1	-2859.72	-4.17682	3.52	0.9	0.10312	1.11	4.0985	1.1	0.28623	0.9	0.42	1657	42	42	1620	26	37	1646	18	21	98	98	1657	42
APS25_1011-97	APS25_101	0.49866	74771	51	1.2	-1272.68	-5.48301	2.00	1.0	0.18367	1.15	12.7625	1.0	0.50324	0.9	0.35	2666	37	37	2621	40	57	2656	19	23	98	99	2666	37
APS25_1011-58	APS25_101	0.321891	115396	113	1.7	-2383.4	-5.05251	3.03	0.8	0.11578	1.17	5.3022	1.0	0.33128	0.8	0.27	1865	42	42	1842	25	39	1864	17	20	99	99	1865	42
APS25_1011-73	APS25_101	0.431439	132242	131	2.2	-2454.83	-5.36594	2.99	1.0	0.11702	1.21	5.3861	1.1	0.33601	0.9	0.21	1885	43	43	1865	28	42	1883	17	20	99	99	1885	43
APS25_1011-10	APS25_101	0.065591	227283	216	2.4	-4166.77	-4.36274	2.84	0.7	0.12081	0.85	5.9183	0.7	0.35207	0.6	0.26	1954	31	31	1943	21	38	1960	13	18	99	99	1954	31
APS25_1011-11	APS25_101	0.177734	115616	121	0.9	-2010.2	-5.98795	2.92	1.1	0.11831	1.23	5.6321	1.1	0.34315	0.9	0.42	1909	43	43	1899	30	43	1914	19	22	99	99	1909	43
APS25_1011-10	APS25_101	0.113791	100142	97	2.2	-2284.54	-4.603	3.16	0.8	0.11089	1.08	4.8486	1.3	0.31649	0.7	0.62	1787	39	39	1778	25	40	1791	16	18	99	99	1787	39
APS25_1011-3.F	APS25_101	0.940646	68819	72	2.2	-1315.8	-6.76083	3.24	0.9	0.10831	1.21	4.6397	1.1	0.31056	1.0	0.29	1750	47	47	1743	30	41	1758	19	22	100	99	1750	47
APS25_1011-22	APS25_101	0.115357	109228	115	1.7	-1998.63	-7.78603	3.16	1.0	0.11037	1.28	4.8716	1.2	0.32013	1.0	0.18	1768	46	46	1787	30	42	1787	20	23	101	100	1768	46
APS25_1011-5.F	APS25_101	0.064175	97669	88	1.6	-2361.25	-6.06151	2.95	0.7	0.11521	1.10	5.4241	0.9	0.34020	0.7	0.25	1865	41	41	1885	24	39	1882	16	20	101	100	1865	41
APS25_1011-21	APS25_101	0.668285	99196	83	2.4	-1839.87	-5.5515	2.70	0.8	0.12424	1.20	6.3602	0.9	0.37021	0.8	0.03	1994	45	45	2030	29	44	2022	16	20	102	100	1994	45
APS25_1011-68	APS25_101	0.038249	96713	80	3.7	-1926.83	-4.62516	2.48	0.9	0.13114	1.13	7.3252	1.1	0.40548	0.9	0.39	2086	39	39	2190	32	48	2143	19	23	105	102	2086	39
Discordants																												
~~APS25_1011-59~~	~~APS25_101~~	~~58.4941~~	~~1728~~	~~7~~	~~0.3~~	~~-26.0896~~	~~-13.3254~~	~~14.12~~	~~7.4~~	~~0.33058~~	~~6.88~~	~~3.8441~~	~~8.1~~	~~0.08643~~	~~5.0~~	~~0.47~~	~~3252~~	~~236~~	~~236~~	~~530~~	~~51~~	~~52~~	~~1475~~	~~130~~	~~131~~	~~16~~	~~36~~		
~~APS25_1011-31~~	~~APS25_101~~	~~5.350203~~	~~152111~~	~~1383~~	~~2.4~~	~~-358.214~~	~~-31.3026~~	~~28.71~~	~~1.3~~	~~0.13042~~	~~1.60~~	~~0.6373~~	~~1.4~~	~~0.03557~~	~~1.3~~	~~0.35~~	~~2055~~	~~56~~	~~56~~	~~225~~	~~6~~	~~7~~	~~498~~	~~11~~	~~12~~	~~11~~	~~45~~		
~~APS25_1011-12~~	~~APS25_101~~	~~5.096221~~	~~118864~~	~~1351~~	~~2.3~~	~~-247.102~~	~~-38.7729~~	~~35.13~~	~~2.1~~	~~0.11973~~	~~1.40~~	~~0.5004~~	~~2.2~~	~~0.03036~~	~~1.9~~	~~0.79~~	~~1927~~	~~47~~	~~47~~	~~193~~	~~7~~	~~8~~	~~409~~	~~15~~	~~15~~	~~10~~	~~47~~		
~~APS25_1011-62~~	~~APS25_101~~	~~11.68012~~	~~169023~~	~~3511~~	~~1.3~~	~~68.9327~~	~~148.5862~~	~~62.29~~	~~0.9~~	~~0.08817~~	~~1.81~~	~~0.1954~~	~~1.6~~	~~0.01603~~	~~1.0~~	~~0.06~~	~~1338~~	~~68~~	~~68~~	~~103~~	~~2~~	~~3~~	~~181~~	~~5~~	~~6~~	~~8~~	~~57~~		
~~APS25_1011-10~~	~~APS25_101~~	~~2.091285~~	~~8797~~	~~97~~	~~2.8~~	~~-144.213~~	~~-8.86791~~	~~33.67~~	~~8.4~~	~~0.10368~~	~~5.30~~	~~0.6197~~	~~7.0~~	~~0.04826~~	~~6.3~~	~~0.64~~	~~1516~~	~~203~~	~~203~~	~~301~~	~~37~~	~~38~~	~~475~~	~~56~~	~~56~~	~~20~~	~~63~~		
~~APS25_1011-23~~	~~APS25_101~~	~~2.950751~~	~~276484~~	~~935~~	~~1.5~~	~~-704.603~~	~~-34.0225~~	~~11.04~~	~~2.1~~	~~0.09611~~	~~1.42~~	~~1.3279~~	~~3.0~~	~~0.09697~~	~~2.6~~	~~0.78~~	~~1520~~	~~54~~	~~54~~	~~594~~	~~29~~	~~31~~	~~841~~	~~33~~	~~34~~	~~39~~	~~71~~		
~~APS25_1011-4.F~~	~~APS25_101~~	~~3.697898~~	~~411606~~	~~556~~	~~0.3~~	~~-4.51769~~	~~-4854.46~~	~~4.42~~	~~2.4~~	~~0.18244~~	~~1.25~~	~~6.1188~~	~~2.6~~	~~0.24243~~	~~2.4~~	~~0.84~~	~~2654~~	~~42~~	~~42~~	~~1390~~	~~59~~	~~64~~	~~1960~~	~~44~~	~~46~~	~~52~~	~~71~~		
~~APS25_1011-48~~	~~APS25_101~~	~~1.219662~~	~~483374~~	~~1075~~	~~1.6~~	~~-457.316~~	~~-92.7125~~	~~6.89~~	~~2.2~~	~~0.11836~~	~~1.36~~	~~2.4096~~	~~2.2~~	~~0.14778~~	~~2.2~~	~~0.80~~	~~1911~~	~~49~~	~~49~~	~~886~~	~~36~~	~~40~~	~~1233~~	~~32~~	~~34~~	~~46~~	~~72~~		
~~APS25_1011-30~~	~~APS25_101~~	~~1.752124~~	~~144576~~	~~326~~	~~2.5~~	~~-1534.84~~	~~-10.668~~	~~7.60~~	~~1.8~~	~~0.11412~~	~~1.25~~	~~2.1890~~	~~1.9~~	~~0.13770~~	~~1.7~~	~~0.70~~	~~1831~~	~~45~~	~~45~~	~~835~~	~~27~~	~~31~~	~~1161~~	~~26~~	~~27~~	~~46~~	~~72~~		
~~APS25_1011-11~~	~~APS25_101~~	~~1.429469~~	~~396160~~	~~1185~~	~~3.6~~	~~-2503.82~~	~~-17.6488~~	~~11.41~~	~~4.8~~	~~0.10267~~	~~1.00~~	~~1.5375~~	~~2.8~~	~~0.10994~~	~~3.0~~	~~0.94~~	~~1654~~	~~37~~	~~37~~	~~667~~	~~38~~	~~40~~	~~914~~	~~37~~	~~38~~	~~40~~	~~73~~		
~~APS25_1011-80~~	~~APS25_101~~	~~1.666858~~	~~485665~~	~~723~~	~~0.7~~	~~-1550.76~~	~~-24.9167~~	~~4.56~~	~~1.3~~	~~0.13802~~	~~1.09~~	~~4.2768~~	~~1.2~~	~~0.22350~~	~~1.4~~	~~0.64~~	~~2188~~	~~40~~	~~40~~	~~1296~~	~~32~~	~~39~~	~~1681~~	~~19~~	~~22~~	~~59~~	~~77~~		
~~APS25_1011-64~~	~~APS25_101~~	~~2.253733~~	~~131115~~	~~290~~	~~1.9~~	~~-1273.27~~	~~-12.0858~~	~~7.07~~	~~3.4~~	~~0.11529~~	~~1.11~~	~~2.5928~~	~~2.6~~	~~0.16421~~	~~2.7~~	~~0.53~~	~~1863~~	~~38~~	~~38~~	~~971~~	~~49~~	~~52~~	~~1258~~	~~42~~	~~44~~	~~52~~	~~77~~		
~~APS25_1011-19~~	~~APS25_101~~	~~1.765371~~	~~198060~~	~~337~~	~~1.3~~	~~-1867~~	~~-13.8569~~	~~6.24~~	~~2.5~~	~~0.11847~~	~~1.22~~	~~2.8933~~	~~2.5~~	~~0.17778~~	~~2.6~~	~~0.84~~	~~1911~~	~~43~~	~~43~~	~~1051~~	~~52~~	~~55~~	~~1351~~	~~37~~	~~39~~	~~55~~	~~78~~		
~~APS25_1011-25~~	~~APS25_101~~	~~2.531806~~	~~120139~~	~~185~~	~~2.5~~	~~-851.748~~	~~-14.2951~~	~~4.56~~	~~2.8~~	~~0.13826~~	~~1.50~~	~~4.5016~~	~~1.8~~	~~0.24183~~	~~2.1~~	~~0.78~~	~~2180~~	~~50~~	~~50~~	~~1391~~	~~52~~	~~57~~	~~1713~~	~~30~~	~~32~~	~~64~~	~~81~~		
~~APS25_1011-16~~	~~APS25_101~~	~~0.901368~~	~~704533~~	~~941~~	~~1.4~~	~~-3434.43~~	~~-18.0029~~	~~4.72~~	~~3.3~~	~~0.13133~~	~~0.91~~	~~4.4984~~	~~2.6~~	~~0.24785~~	~~2.6~~	~~0.94~~	~~2098~~	~~32~~	~~32~~	~~1410~~	~~68~~	~~72~~	~~1681~~	~~47~~	~~48~~	~~67~~	~~84~~		
~~APS25_1011-36~~	~~APS25_101~~	~~0.984084~~	~~390562~~	~~533~~	~~1.8~~	~~-2589.99~~	~~-16.0325~~	~~4.17~~	~~2.3~~	~~0.13198~~	~~0.99~~	~~4.7075~~	~~2.0~~	~~0.25670~~	~~2.0~~	~~0.59~~	~~2111~~	~~33~~	~~33~~	~~1462~~	~~53~~	~~58~~	~~1743~~	~~35~~	~~37~~	~~69~~	~~84~~		
~~APS25_1011-77~~	~~APS25_101~~	~~14.98438~~	~~3231~~	~~267~~	~~2.4~~	~~-58.3914~~	~~-5.99773~~	~~264.82~~	~~2.0~~	~~0.05831~~	~~8.39~~	~~0.0304~~	~~8.3~~	~~0.00396~~	~~1.9~~	~~0.00~~	~~308~~	~~254~~	~~254~~	~~25~~	~~1~~	~~1~~	~~30~~	~~5~~	~~5~~	~~8~~	~~85~~		
~~APS25_1011-90~~	~~APS25_101~~	~~2.242836~~	~~201899~~	~~388~~	~~0.5~~	~~-1269.49~~	~~-12.6314~~	~~5.03~~	~~4.8~~	~~0.13497~~	~~1.43~~	~~4.5430~~	~~2.4~~	~~0.25825~~	~~2.9~~	~~0.83~~	~~2120~~	~~49~~	~~49~~	~~1457~~	~~78~~	~~82~~	~~1691~~	~~45~~	~~47~~	~~69~~	~~86~~		
~~APS25_1011-74~~	~~APS25_101~~	~~3.99696~~	~~586956~~	~~709~~	~~1.6~~	~~442.4048~~	~~10.77923~~	~~3.45~~	~~1.7~~	~~0.20452~~	~~0.97~~	~~8.3226~~	~~1.7~~	~~0.29675~~	~~1.7~~	~~0.91~~	~~2844~~	~~31~~	~~31~~	~~1665~~	~~49~~	~~56~~	~~2249~~	~~29~~	~~31~~	~~59~~	~~74~~		
~~APS25_1011-11~~	~~APS25_101~~	~~3.052897~~	~~170260~~	~~210~~	~~2.2~~	~~-1397.24~~	~~-13.5485~~	~~3.85~~	~~1.9~~	~~0.15348~~	~~1.62~~	~~5.6237~~	~~1.1~~	~~0.27240~~	~~1.7~~	~~0.27~~	~~2349~~	~~55~~	~~55~~	~~1544~~	~~48~~	~~54~~	~~1914~~	~~19~~	~~23~~	~~66~~	~~81~~		
~~APS25_1011-72~~	~~APS25_101~~	~~1.494636~~	~~100668~~	~~93~~	~~1.4~~	~~-1719.51~~	~~-9.64501~~	~~4.76~~	~~5.8~~	~~0.16919~~	~~2.80~~	~~7.6733~~	~~4.7~~	~~0.29731~~	~~3.6~~	~~0.86~~	~~2448~~	~~113~~	~~113~~	~~1650~~	~~111~~	~~115~~	~~1977~~	~~117~~	~~118~~	~~67~~	~~83~~		
~~APS25_1011-35~~	~~APS25_101~~	~~3.221883~~	~~112316~~	~~136~~	~~2.1~~	~~-1153.47~~	~~-10.8386~~	~~3.89~~	~~1.8~~	~~0.13157~~	~~1.80~~	~~4.7453~~	~~2.3~~	~~0.26481~~	~~1.9~~	~~0.45~~	~~2077~~	~~60~~	~~60~~	~~1512~~	~~50~~	~~56~~	~~1749~~	~~35~~	~~37~~	~~73~~	~~86~~		
~~APS25_1011-28~~	~~APS25_101~~	~~1.441535~~	~~284002~~	~~260~~	~~1.1~~	~~-1850.83~~	~~-16.1524~~	~~2.99~~	~~2.4~~	~~0.18429~~	~~0.77~~	~~9.2582~~	~~2.0~~	~~0.36098~~	~~1.9~~	~~0.91~~	~~2680~~	~~25~~	~~25~~	~~1970~~	~~67~~	~~75~~	~~2334~~	~~39~~	~~41~~	~~74~~	~~84~~		
~~APS25_1011-81~~	~~APS25_101~~	~~0.716716~~	~~1077679~~	~~993~~	~~2.2~~	~~-1389.47~~	~~-50.6224~~	~~2.86~~	~~1.1~~	~~0.17316~~	~~0.87~~	~~8.5574~~	~~1.2~~	~~0.35588~~	~~1.2~~	~~0.72~~	~~2575~~	~~30~~	~~30~~	~~1956~~	~~39~~	~~51~~	~~2280~~	~~22~~	~~25~~	~~76~~	~~86~~		
~~APS25_1011-98~~	~~APS25_101~~	~~0.446121~~	~~39834~~	~~47~~	~~1.7~~	~~-748.806~~	~~-4.34857~~	~~3.45~~	~~1.3~~	~~0.12884~~	~~1.41~~	~~5.2530~~	~~1.7~~	~~0.29810~~	~~1.3~~	~~0.51~~	~~2043~~	~~50~~	~~50~~	~~1676~~	~~38~~	~~47~~	~~1847~~	~~29~~	~~31~~	~~82~~	~~91~~		
~~APS25_1011-79~~	~~APS25_101~~	~~0.48169~~	~~2098411~~	~~2353~~	~~1.2~~	~~-3480.86~~	~~-41.9774~~	~~3.82~~	~~2.1~~	~~0.11526~~	~~0.81~~	~~4.4682~~	~~2.0~~	~~0.27675~~	~~1.7~~	~~0.89~~	~~1872~~	~~29~~	~~29~~	~~1566~~	~~49~~	~~56~~	~~1698~~	~~34~~	~~37~~	~~84~~	~~92~~		
~~APS25_1011-12~~	~~APS25_101~~	~~0.902516~~	~~243298~~	~~236~~	~~1.5~~	~~-4806.85~~	~~-5.70203~~	~~3.29~~	~~1.4~~	~~0.12678~~	~~0.95~~	~~5.4337~~	~~1.1~~	~~0.31080~~	~~1.2~~	~~0.71~~	~~2036~~	~~34~~	~~34~~	~~1744~~	~~36~~	~~46~~	~~1881~~	~~19~~	~~23~~	~~86~~	~~93~~		
~~APS25_1011-38~~	~~APS25_101~~	~~0.219005~~	~~231535~~	~~275~~	~~1.2~~	~~-4052.77~~	~~-5.64837~~	~~3.54~~	~~1.6~~	~~0.11579~~	~~1.00~~	~~4.5639~~	~~1.4~~	~~0.28637~~	~~1.5~~	~~0.75~~	~~1878~~	~~34~~	~~34~~	~~1616~~	~~43~~	~~51~~	~~1734~~	~~23~~	~~26~~	~~86~~	~~93~~		
~~APS25_1011-14~~	~~APS25_101~~	~~0.005366~~	~~159066~~	~~148~~	~~1.7~~	~~-3626.55~~	~~-4.17829~~	~~3.05~~	~~0.8~~	~~0.10762~~	~~1.07~~	~~4.9275~~	~~1.0~~	~~0.32943~~	~~0.8~~	~~0.06~~	~~1737~~	~~39~~	~~39~~	~~1833~~	~~27~~	~~40~~	~~1801~~	~~17~~	~~20~~	~~106~~	~~102~~		
~~APS25_1011-96~~	~~APS25_101~~	~~1.832625~~	~~37884~~	~~46~~	~~0.0~~	~~-658.711~~	~~-6.48674~~	~~3.74~~	~~2.7~~	~~0.09687~~	~~2.12~~	~~3.7108~~	~~2.5~~	~~0.27863~~	~~1.9~~	~~0.73~~	~~1488~~	~~69~~	~~69~~	~~1574~~	~~46~~	~~51~~	~~1553~~	~~34~~	~~36~~	~~106~~	~~101~~		

U-Pb data from 1APS25_600



University of Brasilia								Data for Tera-Wasserburg plot				Data for Wetherill plot					Dates									Conc (%)	Conc (%)	Best Age	2s (abs)
Identifier	Comments	f206c	206Pb	Uppm	Th/U	206Pb/204	1s%	238U/206I	1s%	207Pb/206	1s%	207Pb/235U	1s%	206Pb/238U	1s%	Rho	207Pb/206	2s (abs)	2ssys (abs	206Pb/238	2s (abs)	2ssys (abs	207Pb/235	2s (abs)	2ssys (abs	6/8 -7/6	6/8 -7/5		
Concordants																													
APS25_600-36.	APS25_60	4.347298	21681	91	1.9	-350.608	-5.63683	11.38	1.2	0.06739	2.57	0.8329	2.6	0.08872	1.1	0.14	709	121	121	547	12	15	602	23	24	77	91	547	12
APS25_600-47.	APS25_60	0.144278	76911	194	1.8	-1177.38	-5.56676	6.81	1.0	0.07656	1.42	1.5593	1.3	0.14822	1.0	0.26	1069	55	55	890	16	22	951	16	18	83	94	890	16
APS25_600-85.	APS25_60	0.946857	18972	148	1.3	-272.343	-9.20818	20.69	1.3	0.05835	3.60	0.3993	4.1	0.04885	1.5	0.29	286	137	137	307	9	10	326	17	18	107	94	307	9
APS25_600-93.	APS25_60	0.279761	52174	210	2.7	-757.555	-5.18108	10.44	0.8	0.06434	1.51	0.8564	1.4	0.09599	0.8	0.09	707	68	68	591	9	14	625	13	14	84	94	591	9
APS25_600-20.	APS25_60	0.561153	23190	74	2.7	-408.427	-8.25164	8.56	1.0	0.06933	2.38	1.1222	2.2	0.11793	1.2	0.08	815	112	112	718	16	20	753	24	25	88	95	718	16
APS25_600-58.	APS25_60	0.187284	144991	284	0.9	-2191.59	-5.95687	5.04	1.3	0.08607	1.18	2.4145	1.5	0.20158	1.1	0.51	1309	47	47	1181	25	32	1235	22	24	90	96	1181	25
APS25_600-65.	APS25_60	2.277802	17459	78	2.1	-270.873	-5.76743	12.14	1.3	0.07050	11.06	0.8063	9.3	0.08335	1.3	0.50	465	124	124	515	13	16	536	30	30	111	96	515	13
APS25_600-86.	APS25_60	0.739881	237440	553	0.4	-2739.57	-11.1117	6.04	3.4	0.09775	1.84	3.1199	6.1	0.23257	6.4	0.91	1503	77	77	1271	132	133	1315	77	78	85	97	1271	132
APS25_600-92.	APS25_60	0.259736	47964	123	1.4	-725.337	-5.04781	6.64	0.9	0.07233	1.71	1.5259	1.7	0.15141	0.9	0.19	944	72	72	908	15	22	935	21	23	96	97	908	15
APS25_600-10:	APS25_60	0.541837	26418	123	1.2	-406.984	-5.27732	12.14	1.1	0.06089	2.42	0.7018	2.1	0.08387	1.2	0.01	476	111	111	519	12	15	532	17	18	109	97	519	12
APS25_600-56.	APS25_60	0.573217	136658	254	1.3	-1915.18	-6.03444	5.05	0.8	0.08232	1.21	2.2635	1.0	0.19879	0.9	0.65	1228	46	46	1168	18	27	1196	14	17	95	98	1168	18
APS25_600-39.	APS25_60	-0.19391	97347	222	0.6	-1708.4	-4.98049	6.28	0.8	0.07247	1.17	1.6028	1.1	0.15902	0.8	0.17	976	49	49	951	14	22	968	13	16	97	98	951	14
APS25_600-10:	APS25_60	-0.12364	218341	518	1.0	-3593.74	-3.68231	5.95	0.8	0.07495	1.12	1.7484	1.0	0.16870	0.8	0.16	1032	46	46	1004	14	23	1023	13	15	97	98	1004	14
APS25_600-3.F	APS25_60	0.167115	49931	78	2.8	-1098.69	-18.3649	4.57	1.0	0.08555	1.73	2.5908	1.5	0.21854	1.0	0.00	1271	53	53	1272	23	32	1291	20	22	100	99	1272	23
APS25_600-10:	APS25_60	0.571076	50159	126	1.3	-785.6	-6.96072	6.50	1.0	0.07252	1.64	1.5348	1.5	0.15506	1.1	-0.06	940	69	69	928	18	24	936	18	20	99	99	928	18
APS25_600-64.	APS25_60	0.036403	70904	130	0.8	-1114.8	-4.8111	4.88	0.8	0.08193	1.42	2.3227	1.2	0.20509	0.8	0.01	1193	56	56	1203	18	27	1212	17	19	101	99	1203	18
APS25_600-34.	APS25_60	-0.51393	24233	58	1.8	-425.972	-4.09255	6.76	1.0	0.06995	2.08	1.4549	2.0	0.14918	1.0	0.09	854	94	94	895	17	23	898	23	25	105	100	895	17
APS25_600-11(	APS25_60	2.040915	39638	172	3.0	-555.816	-8.28443	10.06	1.2	0.06213	2.56	0.8550	2.4	0.10064	1.2	-0.02	539	103	103	617	14	18	616	21	22	115	100	617	14
APS25_600-18.	APS25_60	-0.05792	325191	514	0.2	-5091.92	-6.68381	4.28	1.4	0.09213	0.99	3.1275	2.6	0.24800	2.6	0.95	1446	38	38	1413	59	62	1409	26	27	98	100	1413	59
APS25_600-35.	APS25_60	0.293537	101056	195	0.7	-1733.25	-5.02579	5.27	0.8	0.07679	1.33	2.0179	1.1	0.19046	0.8	0.10	1077	57	57	1123	17	26	1117	15	18	104	100	1123	17
APS25_600-75.	APS25_60	2.110863	20200	78	1.6	-308.783	-5.39011	10.34	1.2	0.06125	2.61	0.8170	2.4	0.09762	1.1	0.06	502	112	112	600	12	17	595	22	23	120	101	600	12
APS25_600-88.	APS25_60	0.278016	30878	69	1.0	808.1796	157.0821	5.90	1.4	0.07325	1.86	1.7374	1.7	0.17289	1.8	0.11	954	85	85	1024	32	36	1015	24	25	107	101	1024	32
APS25_600-68.	APS25_60	-0.90606	17952	63	1.2	-299.513	-4.87367	9.37	1.4	0.06245	2.43	0.9307	2.3	0.10898	1.3	0.03	571	111	111	666	16	20	658	22	23	117	101	666	16

APS25_600-29.	APS25_60	1.088048	55024	61	1.8	-898.701	-5.53194	3.20	1.8	0.12439	1.35	5.5785	1.3	0.32567	1.5	0.53	1992	48	48	1809	47	56	1905	24	27	91	95	1992	48
APS25_600-12(	APS25_60	0.428199	75260	101	2.1	-1050.34	-5.63845	3.33	1.6	0.11636	1.36	5.0092	1.6	0.30855	1.2	0.59	1881	48	48	1728	38	47	1806	27	29	92	96	1881	48
APS25_600-24.	APS25_60	0.015594	52802	55	1.3	-873.384	-5.37218	2.86	1.0	0.13170	1.41	6.3656	1.2	0.35223	0.9	0.11	2090	47	47	1941	32	45	2017	21	24	93	96	2090	47
APS25_600-55.	APS25_60	0.147038	123936	138	2.0	-1935.56	-5.52722	3.00	0.9	0.12375	1.30	5.7464	1.2	0.33396	1.0	0.27	1984	43	43	1854	31	43	1926	18	21	93	96	1984	43
APS25_600-30.	APS25_60	0.775518	115150	127	2.2	-1528.24	-7.17188	2.96	0.8	0.12507	1.09	5.8817	0.9	0.33877	0.8	0.45	2007	40	40	1878	25	40	1952	16	20	94	96	2007	40
APS25_600-25.	APS25_60	0.217577	655454	489	0.2	-11388.9	-5.53988	1.98	2.6	0.20936	1.06	15.4744	2.3	0.53932	2.5	0.54	2881	36	36	2734	109	116	2823	49	51	95	97	2881	36
APS25_600-81.	APS25_60	0.559943	147915	185	2.0	-2204.48	-5.53739	3.24	0.9	0.11274	1.11	4.8650	0.9	0.31109	0.9	0.24	1825	39	39	1743	27	39	1790	16	19	96	97	1825	39
APS25_600-40.	APS25_60	0.194624	152967	190	1.7	-2428.55	-4.90298	3.47	0.9	0.10610	1.12	4.2730	1.0	0.28986	0.8	0.32	1708	42	42	1639	24	36	1682	16	20	96	97	1708	42
APS25_600-67.	APS25_60	1.364895	468750	735	3.2	-112.013	-248.499	3.37	2.6	0.12648	0.92	6.3205	4.1	0.36354	4.2	0.91	2030	33	33	1956	136	139	1938	59	60	96	101	2030	33
APS25_600-26.	APS25_60	0.51249	81214	87	2.4	-1307.9	-5.31662	2.96	0.7	0.11816	0.99	5.5113	0.9	0.33521	0.8	0.09	1913	34	34	1864	25	39	1896	16	20	97	98	1913	34
APS25_600-79.	APS25_60	0.283321	107420	135	3.5	-1612.3	-5.77627	3.26	1.1	0.11053	1.12	4.7291	1.0	0.30949	0.9	0.15	1778	42	42	1735	28	40	1766	16	20	98	98	1778	42
APS25_600-105	APS25_60	1.435714	293063	285	1.5	-942.339	-23.3584	2.39	0.9	0.14949	1.05	8.6940	1.0	0.42232	0.9	0.42	2320	36	36	2266	35	50	2301	18	22	98	99	2320	36
APS25_600-14.	APS25_60	0.066615	61898	62	2.2	-1101.03	-5.46559	2.80	1.0	0.12661	1.13	6.3196	1.1	0.36146	0.9	0.39	2027	41	41	1985	32	45	2013	21	25	98	99	2027	41
APS25_600-61.	APS25_60	0.097709	157486	201	2.3	-2503.3	-4.84565	3.42	0.9	0.10528	1.17	4.2509	0.9	0.29399	0.8	0.02	1687	44	44	1659	25	37	1678	15	19	98	99	1687	44
APS25_600-108	APS25_60	0.169955	106677	123	2.3	-1459.18	-5.87912	2.86	1.1	0.12223	1.25	5.9482	1.2	0.35291	1.0	0.19	1961	44	44	1944	32	45	1963	19	22	99	99	1961	44
APS25_600-32.	APS25_60	0.474984	161931	124	1.7	-2499.55	-6.92116	2.14	1.2	0.16628	1.00	10.9730	1.3	0.47225	1.0	0.58	2500	33	33	2486	44	59	2505	25	29	99	99	2500	33
APS25_600-38.	APS25_60	0.381896	129578	143	2.1	-2131.51	-4.85265	3.04	0.8	0.11377	1.13	5.2113	1.0	0.32987	0.8	0.18	1835	42	42	1835	25	39	1849	17	20	100	99	1835	42
APS25_600-21.	APS25_60	0.131857	89328	102	2.8	-1472.49	-5.27165	3.24	0.9	0.10681	1.29	4.5614	1.1	0.30924	0.9	0.37	1715	46	46	1734	28	40	1736	18	21	101	100	1715	46
APS25_600-69.	APS25_60	0.230038	234871	298	2.4	-3276.5	-8.1557	3.20	0.8	0.10691	1.11	4.6206	0.9	0.31239	0.8	0.09	1723	40	40	1750	25	38	1747	15	19	102	100	1723	40
APS25_600-91.	APS25_60	0.061628	34739	35	1.4	-510.352	-5.59873	2.56	1.2	0.13352	1.56	7.2781	1.4	0.39744	1.1	0.40	2106	54	54	2156	40	53	2141	27	30	102	101	2106	54
APS25_600-95.	APS25_60	0.191922	42790	49	3.1	-684.681	-4.68764	2.92	0.9	0.11613	1.52	5.5216	1.3	0.34452	0.9	0.13	1859	55	55	1905	29	43	1899	23	26	102	100	1859	55
APS25_600-49.	APS25_60	-0.34377	18161	24	2.3	-323.574	-8.77003	3.62	1.5	0.09907	2.19	3.8030	1.9	0.28501	2.0	0.19	1530	77	77	1590	43	48	1581	30	32	104	101	1530	77
APS25_600-111	APS25_60	1.294553	92987	162	4.9	-1150.43	-10.3995	3.26	6.9	0.12868	2.21	7.7910	5.1	0.41633	4.8	0.58	2043	85	85	2139	155	159	2062	76	76	105	104	2043	85

Discordants

~~APS25_600-11~~	~~APS25_60~~	~~6.938703~~	~~1512~~	~~247~~	~~1.0~~	~~-24.183~~	~~-12.6685~~	~~321.54~~	~~6.4~~	~~0.18265~~	~~16.15~~	~~0.4346~~	~~389.5~~	~~1.99304~~	~~100.6~~	~~0.70~~	~~1145~~	~~382~~	~~382~~	~~-243~~	~~266~~	~~266~~	~~136~~	~~113~~	~~113~~	~~-21~~	~~-179~~
~~APS25_600-12.~~	~~APS25_60~~	~~2.765017~~	~~168227~~	~~4577~~	~~1.7~~	~~-737.547~~	~~-24.6802~~	~~79.84~~	~~2.8~~	~~0.12964~~	~~1.39~~	~~0.2516~~	~~2.9~~	~~0.01409~~	~~2.8~~	~~0.74~~	~~2092~~	~~51~~	~~51~~	~~90~~	~~5~~	~~5~~	~~228~~	~~12~~	~~12~~	~~4~~	~~40~~
~~APS25_600-66.~~	~~APS25_60~~	~~6.22946~~	~~121010~~	~~888~~	~~4.3~~	~~-131.194~~	~~-54.5112~~	~~19.72~~	~~2.0~~	~~0.17168~~	~~1.39~~	~~1.2891~~	~~2.4~~	~~0.05391~~	~~1.9~~	~~0.43~~	~~2545~~	~~44~~	~~44~~	~~338~~	~~13~~	~~14~~	~~824~~	~~26~~	~~27~~	~~13~~	~~41~~
~~APS25_600-10.~~	~~APS25_60~~	~~11.77969~~	~~150934~~	~~601~~	~~3.0~~	~~56.053~~	~~65.17653~~	~~9.71~~	~~3.6~~	~~0.20858~~	~~2.30~~	~~4.2326~~	~~6.4~~	~~0.15073~~	~~6.4~~	~~0.76~~	~~2834~~	~~74~~	~~74~~	~~865~~	~~97~~	~~98~~	~~1531~~	~~81~~	~~82~~	~~31~~	~~57~~
~~APS25_600-82.~~	~~APS25_60~~	~~2.049425~~	~~135001~~	~~1020~~	~~11.4~~	~~-204.683~~	~~-50.1675~~	~~20.27~~	~~4.6~~	~~0.13239~~	~~2.13~~	~~1.3500~~	~~5.6~~	~~0.07255~~	~~4.7~~	~~0.54~~	~~2116~~	~~69~~	~~69~~	~~445~~	~~40~~	~~41~~	~~787~~	~~54~~	~~54~~	~~21~~	~~57~~
~~APS25_600-80.~~	~~APS25_60~~	~~1.37736~~	~~183717~~	~~791~~	~~1.0~~	~~-966.413~~	~~-17.4332~~	~~10.50~~	~~1.4~~	~~0.12581~~	~~1.10~~	~~1.7594~~	~~2.6~~	~~0.09897~~	~~2.1~~	~~0.90~~	~~2018~~	~~40~~	~~40~~	~~600~~	~~21~~	~~23~~	~~1011~~	~~26~~	~~27~~	~~30~~	~~59~~
~~APS25_600-72.~~	~~APS25_60~~	~~2.723234~~	~~444189~~	~~884~~	~~1.4~~	~~-254.724~~	~~-74.3158~~	~~4.97~~	~~2.2~~	~~0.17573~~	~~0.99~~	~~5.2417~~	~~2.0~~	~~0.21550~~	~~2.0~~	~~0.87~~	~~2593~~	~~33~~	~~33~~	~~1250~~	~~46~~	~~51~~	~~1828~~	~~36~~	~~38~~	~~48~~	~~68~~
~~APS25_600-83.~~	~~APS25_60~~	~~1.399437~~	~~439759~~	~~1117~~	~~2.4~~	~~-364.435~~	~~-87.7938~~	~~6.90~~	~~3.3~~	~~0.13526~~	~~1.25~~	~~3.1669~~	~~2.9~~	~~0.16830~~	~~2.9~~	~~0.79~~	~~2146~~	~~43~~	~~43~~	~~992~~	~~53~~	~~55~~	~~1415~~	~~48~~	~~49~~	~~46~~	~~70~~
~~APS25_600-16.~~	~~APS25_60~~	~~4.000312~~	~~297886~~	~~784~~	~~1.3~~	~~188.9132~~	~~48.44285~~	~~6.52~~	~~2.3~~	~~0.13610~~	~~1.45~~	~~4.4043~~	~~11.7~~	~~0.20921~~	~~11.0~~	~~0.90~~	~~2158~~	~~49~~	~~49~~	~~991~~	~~103~~	~~103~~	~~1380~~	~~45~~	~~45~~	~~46~~	~~72~~
~~APS25_600-11~~	~~APS25_60~~	~~16.58994~~	~~111104~~	~~595~~	~~1.1~~	~~73.9744~~	~~59.1921~~	~~9.04~~	~~4.8~~	~~0.20025~~	~~3.33~~	~~7.4801~~	~~8.2~~	~~0.22509~~	~~7.0~~	~~0.46~~	~~2627~~	~~107~~	~~107~~	~~1268~~	~~159~~	~~161~~	~~1718~~	~~132~~	~~132~~	~~48~~	~~74~~
~~APS25_600-4.F~~	~~APS25_60~~	~~4.759329~~	~~643292~~	~~876~~	~~1.9~~	~~425.0114~~	~~13.24669~~	~~3.98~~	~~1.0~~	~~0.16770~~	~~0.94~~	~~5.8848~~	~~1.0~~	~~0.25283~~	~~0.9~~	~~0.55~~	~~2520~~	~~32~~	~~32~~	~~1451~~	~~24~~	~~35~~	~~1957~~	~~17~~	~~21~~	~~58~~	~~74~~
~~APS25_600-11~~	~~APS25_60~~	~~1.122081~~	~~291457~~	~~579~~	~~1.6~~	~~-1195.75~~	~~-20.0751~~	~~5.05~~	~~1.1~~	~~0.13292~~	~~0.99~~	~~3.6987~~	~~1.1~~	~~0.20081~~	~~1.1~~	~~0.56~~	~~2115~~	~~35~~	~~35~~	~~1178~~	~~23~~	~~31~~	~~1564~~	~~17~~	~~20~~	~~56~~	~~75~~
~~APS25_600-89.~~	~~APS25_60~~	~~2.691907~~	~~162105~~	~~269~~	~~13.2~~	~~-777.889~~	~~-17.8647~~	~~4.26~~	~~1.3~~	~~0.15333~~	~~1.21~~	~~5.1073~~	~~1.3~~	~~0.23901~~	~~1.3~~	~~0.21~~	~~2364~~	~~38~~	~~38~~	~~1378~~	~~31~~	~~39~~	~~1826~~	~~21~~	~~24~~	~~58~~	~~75~~
~~APS25_600-15.~~	~~APS25_60~~	~~2.079603~~	~~130420~~	~~201~~	~~0.8~~	~~-1161.16~~	~~-11.4319~~	~~4.40~~	~~1.3~~	~~0.14793~~	~~1.12~~	~~4.7718~~	~~1.5~~	~~0.23240~~	~~1.3~~	~~-0.10~~	~~2308~~	~~36~~	~~36~~	~~1343~~	~~31~~	~~39~~	~~1763~~	~~27~~	~~29~~	~~58~~	~~76~~
~~APS25_600-22.~~	~~APS25_60~~	~~0.906475~~	~~517010~~	~~719~~	~~2.8~~	~~-1851.06~~	~~-21.2906~~	~~3.93~~	~~1.2~~	~~0.16007~~	~~1.01~~	~~5.7627~~	~~1.4~~	~~0.25883~~	~~1.2~~	~~0.69~~	~~2436~~	~~34~~	~~34~~	~~1484~~	~~32~~	~~41~~	~~1929~~	~~22~~	~~25~~	~~61~~	~~77~~
~~APS25_600-17.~~	~~APS25_60~~	~~2.15073~~	~~176204~~	~~330~~	~~2.4~~	~~-1127.26~~	~~-14.5941~~	~~5.13~~	~~2.0~~	~~0.12560~~	~~1.14~~	~~3.4872~~	~~1.6~~	~~0.20458~~	~~1.9~~	~~0.77~~	~~2008~~	~~41~~	~~41~~	~~1193~~	~~41~~	~~46~~	~~1520~~	~~26~~	~~28~~	~~59~~	~~79~~
~~APS25_600-41.~~	~~APS25_60~~	~~0.715918~~	~~211039~~	~~334~~	~~1.4~~	~~-2450.8~~	~~-9.80357~~	~~4.34~~	~~1.9~~	~~0.13286~~	~~1.06~~	~~4.5046~~	~~1.8~~	~~0.24214~~	~~1.5~~	~~0.85~~	~~2111~~	~~38~~	~~38~~	~~1392~~	~~38~~	~~45~~	~~1705~~	~~34~~	~~36~~	~~66~~	~~82~~
~~APS25_600-73.~~	~~APS25_60~~	~~194.6205~~	~~85920~~	~~415~~	~~1.9~~	~~-988.447~~	~~-8.01127~~	~~12.92~~	~~1.7~~	~~0.07807~~	~~2.68~~	~~0.8047~~	~~1.7~~	~~0.07871~~	~~1.5~~	~~0.02~~	~~998~~	~~91~~	~~91~~	~~488~~	~~14~~	~~17~~	~~594~~	~~14~~	~~15~~	~~49~~	~~82~~
~~APS25_600-76.~~	~~APS25_60~~	~~2.236428~~	~~171859~~	~~535~~	~~2.8~~	~~-972.062~~	~~-18.3383~~	~~6.57~~	~~4.9~~	~~0.13029~~	~~1.37~~	~~3.9648~~	~~4.2~~	~~0.22453~~	~~4.3~~	~~0.90~~	~~2088~~	~~46~~	~~46~~	~~1268~~	~~97~~	~~99~~	~~1529~~	~~71~~	~~72~~	~~61~~	~~83~~
~~APS25_600-59.~~	~~APS25_60~~	~~2.760206~~	~~153005~~	~~324~~	~~1.1~~	~~-914.566~~	~~-15.856~~	~~5.77~~	~~1.0~~	~~0.09927~~	~~1.58~~	~~2.3841~~	~~1.2~~	~~0.17374~~	~~1.0~~	~~-0.01~~	~~1583~~	~~61~~	~~61~~	~~1031~~	~~20~~	~~27~~	~~1233~~	~~17~~	~~20~~	~~65~~	~~84~~
~~APS25_600-77.~~	~~APS25_60~~	~~1.899002~~	~~124053~~	~~242~~	~~1.0~~	~~-1411.6~~	~~-7.65933~~	~~5.38~~	~~1.6~~	~~0.09604~~	~~2.01~~	~~2.4854~~	~~1.0~~	~~0.19150~~	~~1.2~~	~~-0.04~~	~~1492~~	~~70~~	~~70~~	~~1127~~	~~26~~	~~33~~	~~1264~~	~~15~~	~~18~~	~~76~~	~~89~~
~~APS25_600-52.~~	~~APS25_60~~	~~14.63189~~	~~3195~~	~~13~~	~~0.0~~	~~-62.5452~~	~~-15.475~~	~~12.13~~	~~4.2~~	~~0.07444~~	~~7.50~~	~~1.1090~~	~~12.8~~	~~0.09904~~	~~3.7~~	~~0.90~~	~~618~~	~~300~~	~~300~~	~~602~~	~~41~~	~~42~~	~~532~~	~~60~~	~~60~~	~~97~~	~~113~~

APS25_600-62.	APS25_60	-277.552	38	1	-1.4	-1.87113	-37.3998	-8.04	-72.6	0.12497	113.49	-28.8718	-48.0	-0.60338	-33.7	0.00	3269	277	277	2397	909	910	3649	266	266	73	66				
APS25_600-5.F	APS25_60	4.725402	301945	351	2.3	-964.339	-28.8899	3.25	2.5	0.15597	1.56	7.4304	3.6	0.33113	2.1	0.67	2432	64	64	1843	67	73	2102	55	56	76	88				
APS25_600-57.	APS25_60	0.731873	213331	218	1.4	-2031.2	-13.2974	3.46	5.2	0.18888	1.16	9.9028	2.8	0.38857	3.0	0.49	2706	38	38	2069	111	116	2348	67	69	76	88				
APS25_600-13.	APS25_60	11.12514	105443	375	3.8	-196.298	-57.0741	5.60	5.3	0.23249	5.81	20.1536	10.7	0.46068	8.3	0.19	2700	121	121	2103	276	278	2260	178	179	78	93				
APS25_600-63.	APS25_60	3.938288	277165	347	1.8	-1083.45	-17.328	3.35	0.9	0.13956	2.09	5.7005	1.7	0.29968	0.9	-0.06	2150	68	68	1687	27	39	1913	27	29	78	88				
APS25_600-74.	APS25_60	0.952202	423652	580	0.8	-1301.91	-23.0525	3.30	1.9	0.14162	0.87	6.4109	2.2	0.32742	2.3	0.93	2234	31	31	1813	72	78	2005	36	37	81	90				
APS25_600-53.	APS25_60	1.301806	865918	1131	0.3	400.1463	44.83971	3.12	1.8	0.13997	0.95	6.4895	2.6	0.32753	2.4	0.95	2211	33	33	1795	62	67	2010	34	35	81	89				
APS25_600-71.	APS25_60	0.965367	411701	487	0.8	-1149.9	-26.9595	2.83	2.0	0.15692	1.46	7.8101	2.1	0.35441	2.0	0.86	2382	38	38	1940	61	68	2184	34	36	81	89				
APS25_600-70.	APS25_60	1.446372	155128	186	2.4	-1405.15	-9.70936	3.20	1.1	0.13571	1.15	5.8818	1.0	0.31348	1.1	0.46	2150	40	40	1757	36	47	1955	18	22	82	90				
APS25_600-84.	APS25_60	0.46326	69440	85	4.9	-933.477	-6.32342	3.30	2.6	0.13868	1.35	6.2427	1.6	0.32874	1.8	0.64	2183	46	46	1819	58	66	1992	30	33	83	91				
APS25_600-27.	APS25_60	0.887802	163859	188	11.1	-1793.84	-8.4614	3.11	0.9	0.13528	0.87	6.0763	0.9	0.32340	0.9	0.59	2150	31	31	1803	28	41	1980	17	20	84	91				
APS25_600-87.	APS25_60	-30.6374	27231	65	3.3	-386.512	-11.7247	5.19	17.5	0.13238	50.25	-14.0638	-66.9	1.73311	71.7	0.48	1803	174	174	1517	519	519	1750	183	183	84	87				
APS25_600-42.	APS25_60	0.9059	218934	287	1.9	-2248.38	-8.6605	3.60	0.7	0.11450	1.02	4.4165	0.8	0.27865	0.7	0.25	1848	37	37	1583	21	34	1711	13	18	86	93				
APS25_600-23.	APS25_60	0.662469	169815	230	0.7	-2152.12	-8.93695	3.65	1.3	0.11380	1.00	4.4421	1.5	0.27957	1.2	0.70	1838	36	36	1584	35	44	1704	26	28	86	93				
APS25_600-11(	APS25_60	4.001288	56042	70	2.0	-593.39	-10.9869	3.13	1.3	0.12401	1.76	5.6788	2.6	0.32412	1.6	0.92	2013	54	54	1800	49	57	1895	34	35	89	95				
APS25_600-43.	APS25_60	1.265647	1093540	1013	2.4	610.5407	65.13275	2.45	1.8	0.13135	0.81	7.8116	2.0	0.42925	2.0	0.93	2101	29	29	2279	76	84	2188	35	37	108	104				
APS25_600-96.	APS25_60	52.59758	66815	489	2.3	-400.583	-20.9704	11.38	7.0	0.17635	7.72	22.5997	31.3	1.15178	19.3	0.99	2313	101	101	2519	528	529	1795	202	202	109	140				
APS25_600-117	APS25_60	0.199237	1312261	1331	0.9	-6537.72	-18.0677	2.30	1.9	0.12900	0.87	7.9036	2.6	0.44916	2.8	0.96	2071	30	30	2335	90	94	2191	33	34	113	107				
APS25_600-98.	APS25_60	0.114385	1077730	1087	1.8	-7694.24	-13.0847	2.62	2.4	0.11317	0.75	6.7478	3.4	0.41243	2.7	0.76	1837	27	27	2191	92	98	2004	43	44	119	109				
APS25_600-94.	APS25_60	0.009795	1098480	946	2.8	-10712.5	-11.3403	1.84	2.6	0.16903	0.91	15.4210	4.9	0.67013	5.0	0.95	2531	31	31	3114	208	212	2733	69	69	123	114				
APS25_600-28.	APS25_60	-44.7088	53925	229	2.2	-190.292	-45.3979	5.45	11.4	0.06450	112.42	22.7961	32.4	0.58398	57.5	0.50	2132	211	211	2635	614	614	2392	285	285	124	110				
APS25_600-9.F	APS25_60	-14.2937	164499	425	3.2	192.0143	34.29442	4.13	6.2	0.18610	7.34	19.3955	11.2	0.93280	11.3	0.90	2417	128	128	3008	392	393	2352	165	165	124	128				
APS25_600-33.	APS25_60	-6.4209	41676	83	1.0	-235.674	-21.5382	3.50	7.2	0.13223	11.86	18.0178	17.4	0.73741	10.8	0.38	2197	113	113	2781	431	433	2224	173	173	127	125				
APS25_600-37.	APS25_60	25.55347	83253	129	-2.1	-871.278	-14.5529	6.94	35.3	0.15919	10.02	2.7564	579.8	-0.67866	-112.1	0.01	2215	117	117	2944	593	593	2281	200	200	133	129				
APS25_600-99.	APS25_60	3.461353	167735	251	6.5	1494.776	246.492	2.82	3.9	0.13253	2.53	16.7714	14.8	0.92860	15.1	0.51	2157	80	80	2901	378	379	2212	115	115	135	131				
APS25_600-10(	APS25_60	-0.48358	77950	93	1.6	-1107.46	-7.64691	3.55	18.3	0.12135	3.87	19.2226	36.3	0.87031	34.8	0.81	1889	93	93	2577	344	344	2012	97	97	136	128				
APS25_600-46.	APS25_60	26.35961	75286	157	1.4	-854.359	-15.7262	4.26	4.1	0.10491	9.22	-0.6820	-1081.2	0.47692	27.8	0.35	1459	129	129	2120	327	327	1510	133	133	145	140				
APS25_600-78.	APS25_60	0.067302	669973	646	0.9	-11667.8	-9.22534	2.27	3.1	0.11223	1.26	10.1813	8.7	0.59947	8.0	0.92	1825	47	47	2705	249	251	2188	85	85	148	124				
APS25_600-10(	APS25_60	0.216741	92168	133	4.7	-575.946	-20.94	2.73	5.4	0.16637	2.76	29.6074	28.6	1.41311	25.4	0.75	2516	106	106	3757	530	531	2626	154	154	149	143				
APS25_600-8.F	APS25_60	2.708684	351945	480	1.1	-173.55	-165.576	2.40	4.3	0.14021	1.48	15.6895	7.1	0.73128	6.2	0.45	2188	46	46	3288	317	320	2491	116	116	150	132				
APS25_600-10(	APS25_60	18.17176	53101	27	837.6	0.721749	2108.648	0.77	7.3	0.38356	1.75	87.5471	3.5	1.68106	3.6	0.41	3817	46	46	6066	267	275	4495	61	63	159	135				
APS25_600-45.	APS25_60	0.319836	471061	542	0.8	-2731.9	-21.735	1.94	5.1	0.18124	1.12	27.5705	7.1	1.16312	7.3	0.90	2653	41	41	4267	445	449	3022	137	138	161	141				
APS25_600-10.	APS25_60	6.838209	20690	81	1.6	-262.507	-11.225	6.50	6.4	0.10582	14.81	18.9622	129.3	2.60897	40.3	0.21	1612	175	175	2818	791	791	1717	250	250	175	164				
APS25_600-6.F	APS25_60	1.983926	200185	238	2.0	-1527.46	-12.3256	2.66	3.5	0.11408	2.11	17.3647	16.5	1.01406	11.9	0.52	1838	63	63	3291	472	474	2170	123	123	179	152				
APS25_600-7.F	APS25_60	7.978888	59506	72	3.4	-814.437	-11.4653	2.47	10.9	0.13980	7.92	-53.0183	-61.1	-2.67505	-48.6	0.56	2046	98	98	3666	595	595	2482	209	209	179	148				
APS25_600-97.	APS25_60	3.128431	333795	381	1.8	-2326.84	-16.5319	2.25	4.0	0.14948	1.58	35.9666	13.0	1.61921	12.5	0.94	2298	53	53	4187	609	610	2769	177	177	182	151				
APS25_600-1.F	APS25_60	40.75962	52575	144	-7.7	-123.517	-58.3346	2.71	13.6	0.18537	10.16	3.0422	621.6	0.35146	186.2	0.71	2522	154	154	5049	732	732	3044	249	249	200	166				
APS25_600-2.F	APS25_60	4.847401	145927	252	2.2	-1301.89	-15.8679	3.30	4.7	0.12074	4.50	32.4023	17.9	1.95753	15.2	0.82	1762	92	92	3850	652	653	2249	191	191	219	171				
APS25_600-10(	APS25_60	-3.57171	186458	195	0.8	-2673.32	-11.2056	1.73	4.8	0.14852	8.64	4.4412	1512.8	-0.10633	-1770.4	0.50	2078	98	98	4584	646	646	2778	178	178	221	165				
APS25_600-44.	APS25_60	13.30937	24686	49	1.6	-193.083	-9.32064	6.74	4.9	0.32769	7.30	355.2353	13.5	3.06861	13.3	0.99	2204	235	235	4894	988	990	2779	400	400	222	176				
APS25_600-60.	APS25_60	20.792	3018	22	-0.3	-60.2999	-132.279	3.29	992.2	0.86691	68.86	37.1751	207.4	4.01489	73.9	0.01	2405	562	562	5413	1297	1297	3710	421	421	225	146				
APS25_600-11(	APS25_60	34.50769	3974	33	-0.2	-62.5654	-24.0235	3.27	31.4	-0.08303	-179.61	-741.4698	-136.8	0.65473	479.7	-0.03	1542	312	312	3499	1366	1366	2856	544	544	227	123				
APS25_600-31.	APS25_60	107.6617	230279	273	0.7	-1446.62	-24.9053	2.10	13.1	0.15028	7.39	37.9686	33.0	1.72956	21.2	0.44	2206	154	154	5041	777	778	2964	219	219	229	170				
APS25_600-11(	APS25_60	5.054113	180349	195	3.7	-1381.4	-18.7533	1.42	6.3	0.20033	3.01	76.9749	10.6	2.52786	31.1	0.83	2761	95	95	6336	740	740	3592	186	187	230	176				
APS25_600-51.	APS25_60	-76.27	444	1	11645.0	-6.67358	-8.93136	3.36	46.7	1.28488	13.37	-1464.4161	-12.8	-11.61864	-13.2	0.40	3933	181	181	9047	1232	1235	5598	364	364	230	162				
APS25_600-54.	APS25_60	-100.953	296	0	-2.2	-10.7465	-30.0582	1.39	71.7	0.76017	27.25	-661.8030	-14.4	-7.61704	-19.0	0.25	3229	291	291	7520	1282	1284	4595	383	383	233	164				
APS25_600-90.	APS25_60	0.021281	1483335	1064	1.2	-5107.73	-33.9315	1.43	4.3	0.13606	1.16	31.3489	9.7	1.70586	9.5	0.96	2159	39	39	5144	569	571	3052	143	143	238	169				
APS25_600-19.	APS25_60	13.96394	214661	223	0.7	-3040.94	-11.7729	2.69	20.2	0.14046	3.59	53.6961	14.4	2.75007	13.5	0.88	2113	113	113	5711	775	777	2968	205	205	270	192				
APS25_600-11.	APS25_60	1.418923	1088688	2080	1.1	-2565.65	-55.0799	2.10	8.0	0.11736	1.98	24.7914	6.8	1.56112	6.8	0.75	1906	77	77	5223	514	519	2837	150	151	274	184				
APS25_600-11:	APS25_60	-111.24	46678	55	-5.6	-677.268	-23.7055	1.35	27.8	0.11555	56.55	-5365.8981	-25.9	-290.84360	-25.0	-0.04	2120	207	207	6017	1457	1459	3913	496	496	284	154				
APS25_600-48.	APS25_60	1.999743	171675	242	4.2	-693.934	-32.5092	1.97	6.3	0.12562	5.57	-18.3069	-152.6	0.70223	190.7	0.03	1878	135	135	5938	835	835	2800	207	207	316	212				
APS25_600-50.	APS25_60	47.1114	2372	1	0.6	-21.3738	-18.4951	1.62	48.1	0.93532	3.46	-11323.7412	-6.2	-97.52646	-7.5	0.80	4505	76	76	14498	2642	2663	6426	764	768	322	226				

Anexo 3. Detrital zircon histogram compilation. P1 = Paleogene; N1 = Neogene; NWA = Northern Western Andes; CA = Central Amazon; NR = Negro River (Amazon Craton)

